High Velocity Deformation of Solids

International Union of Theoretical
and Applied Mechanics

High Velocity Deformation of Solids

Symposium Tokyo/Japan
August 24-27, 1977

Editors
Kozo Kawata and **Jumpei Shioiri**

With 230 Figures

Springer-Verlag
Berlin Heidelberg New York 1978

Dr. Eng. KOZO KAWATA
Professor, Department of Materials,
Institute of Space and Aeronautical Science,
University of Tokyo

Dr. Eng. JUMPEI SHIOIRI
Professor, Department of Aeronautics,
Faculty of Engineering
University of Tokyo

ISBN-13: 978-3-642-67210-1 e-ISBN-13: 978-3-642-67208-8
DOI: 10.1007/978-3-642-67208-8

Library of Congress Cataloging in Publication Data

IUTAM Symposium on High Velocity Deformation of Solids, Tokyo, 1977.
High velocity deformation of solids.
At head of title: International Union of Theoretical
and Applied Mechanics. Bibliography: . Includes index.
1. Deformations (Mechanics) - Congresses. 2. Dynamic testing - Congresses.
3. Continuum mechanics - Congresses. 4. Fracture mechanics - Congresses.
I. Kawata, Kozo, 1923 -. II. Shioiri, Jumpei, 1924 -. III. International Union of Theoretical and
Applied Mechanics. IV. Title.
TA417.6.I17 1979 620.1'123 79-760

Softcover reprint of the hardcover 1st edition 1979

Offsetprinting: fotokop wilhelm weihert KG, Darmstadt · Bookbinding: Konrad Triltsch, Würzburg

2061/3020/543210

Preface

The IUTAM Symposium on High Velocity Deformation of Solids (August 24-27, 1977) was held at Science Council of Japan, under the sponsorship of IUTAM, Science Council of Japan, The Japan Society for Aeronautical and Space Sciences, Japan Society for the Promotion of Science, and The Commemorative Association for the Japan World Exposition (1970). The proposal of the symposium was accepted by the General Assembly of IUTAM in 1974, and the scientists mentioned below were appointed by the Bureau of IUTAM to serve as member of the Scientific Committee. The Symposium had as its theme High Velocity Deformation of Solids. The scope of the subjects were theory, experiment, and instrumentation, in macro- and micro-mechanics (from continuum to dislocation dynamics) concerning high velocity deformation of solids including metals, polymers and composite materials. These research fields were covered by 39 invited papers presented from 22 invited speakers and 16 invited discussers, in 9 scientific sessions chaired by the specialists invited shown in the programme. In Contents the full scientific programme is listed. Asterisk (*) shows the invited speech and non asterisk ( ) shows the invited discussion. Participants, numbered 91, came from 9 countries (Egypt, France, Japan, Poland, Saudi Arabia, Sweden, UK, USA, and USSR).

The topics discussed dealt mainly with: Micromechanical study of wave propagation behaviour, deformation and fracture of materials under dynamic loading, mainly of metals and composite materials (session 1, 2, 3 and 4), crack propagation problem (session 5), macro-mechanical analyses of high velocity deformation and fracture behaviours such as spalling, cratering, compression, analysis methods such as finite element method, etc. (session

6), various problems such as wave propagation in anisotropic media, combined dynamic stress effect, penetration, ricochet, supersonic and transonic impact, continuum theory of dislocation, etc. (session 7), high velocity deformation in structure, structural element and lamination forming (session 8 and 9). It is a great feature of the symposium that it were clarified that micro-mechanical treatments were necessary and powerful frequently for full understanding of various macroscopic behaviours of high velocity deformation and fracture.

With the advices and suggestions provided by the Local Organizing Committee, Organizing Executive Committee was responsible for the planning of the meeting, for the social activities, and for the editing of the Proceedings. The organizations of International Scientific Committee, Local Organizing Committee, and Organizing Executive Committee are listed below. Not in the last place owing to these committees, we may look back upon a very successful and enjoyable symposium.

We appreciate the contributions made by the following organizations in Japan: Science Council of Japan, The Japan Society for Aeronautical and Space Sciences, Japan Society for the Promotion of Science, and The Commemorative Association for the Japan World Exposition (1970).
I express my sincere thanks to the IUTAM Officers: Prof. H. Görtler, Prof. W. T. Koiter, Prof. D. C. Drucker, and Prof. F. I. Niordson, for their valuable guidance and cooperation, to the Representatives of The National Committee for Theoretical and Applied Mechanics of The Science Council of Japan: Prof. I. Tani, Prof. I. Imai, and Prof. M. Yoshiki, for their valuable guidance and arrangement, to the members of the Scientific Committee, the Local Organizing Committee,

and the Organizing Executive Committee, to all participants, for their hearty cooperation, and to the Springer Verlag for setting the scientific progress made by the symposium.

I do hope future IUTAM symposiums would be utilized actively and successfully as well as the one on High Velocity Deformation of Solids.

Tokyo, December 1977

S. Fukui
Chairman
Scientific Committee

Symposium Organizations

Scientific Committee

S. Fukui (Chairman), Professor Emeritus, Institute of Space and Aeronautical Science, University of Tokyo, Komaba, Meguro-ku, Tokyo 153, Japan; President, Institute of Physical and Chemical Research, Wako-shi, 351, Japan
K. B. Broberg, Professor, Lund Institute of Technology, S-22007 Lund, Sweden
D. C. Drucker, Dean, College of Engineering, University of Illinois, 106 Engineering Hall, Urbana, Illinois 61801, USA
K. Kawata (Secretary), Professor, Institute of Space and Aeronautical Science, University of Tokyo, Komaba, Meguro-ku, Tokyo 153, Japan
L. E. Malvern, Professor, Engineering Sciences Department, University of Florida, Gainesville, Florida 32611, USA
L. W. Morland, Professor, School of Mathematics & Physics, University of East Anglia, Norwich NR4 7TJ, UK
R. I. Nigmatulin, Professor, Institute of Mechanics, Moscow University, Moscow, V-234, USSR

Local Organizing Committee

S. Fukui (Chairman)
T. Hayashi, Professor, Osaka University, Toyonaka 560
S. Kawashima, Professor, Kyushu University, Fukuoka 812
K. Kawata (Vice Chairman)
T. Nakamura, Professor, Tokyo Institute of Technology, Tokyo 152
J. Shioiri, Professor, University of Tokyo, Tokyo 113 (Secretary)
K. Tanaka, Professor, Kyoto University, Kyoto 606
Y. Yamada, Professor, Institute of Industrial Science, University of Tokyo, Tokyo 106

Organizing Executive Committee

K. Kawata (Chairman), general, editor in chief
J. Shioiri (Vice Chairman), business, editor
K. Tanaka, programme
T. Hayashi, programme
A. Kobayashi, Associate Professor, Institute of Space and Aeronautical Science, University of Tokyo, Tokyo 153, accommodation, excursion

Editorial Committee

K. Kawata, Editor in chief
J. Shioiri, Editor

Symposium Sponsors

International Union for Theoretical and Applied Mechanics

Science Council of Japan

The Japan Society for Aeronautical and Space Sciences

Japan Society for the Promotion of Science

The Commemorative Association for the Japan World Exposition (1970)

Participants

Authors are identified by an asterisk *, coauthors by an asterisk with parentheses (*), and non present sole authors by parentheses.

Akasaka, T., Department of Precision Mechanics, Faculty of Science and Engineering, Chuo University, 1-13-27 Kasuga, Bunkyo-ku, Tokyo, 112 Japan

Aoki, S., Department of Physical Engineering, Tokyo Institute of Technology, 2-12-1 Ookayama, Meguro-ku, Tokyo, 152 Japan

Asada, K., Mitsubishi Heavy Industry, Co., Ltd., Arai-cho, Takasago-shi, Hyogo, 676 Japan

*Broberg, K.B., Division of Solid Mechanics, Lund Institute of Technology, S-22007, Lund, Sweden

Chadeyron, R., Commissariat a L'Énergie Atomique, Centre d'Etudes Scientifiques et Techniques d'Aquitaine, B.P.2, 33114 Le Barp, France

*Clifton, R.J., Division of Engineering, Brown University, Providence, Rhode Island, 02912 USA

*Davison, L., Explosives Physics Division, Sandia Laboratories, Albuquerque, New Mexico, 87115 USA

*Drucker, D.C., College of Engineering, University of Illinois, Urbana, Illinois, 61801 USA

*El Naschie, M.S., Civil Engineering Department, University of Riyadh, P.O. Box 800, Riyadh, Saudi Arabia

Fujii, T., Faculty of Engineering, Osaka City University, Sugimoto-cho, Sumiyoshi-ku, Osaka, 558 Japan

Fukuda, H., Institute of Space and Aeronautical Science, University of Tokyo, 4-6-1 Komaba, Meguro-ku, Tokyo, 153 Japan

Fukui, S., Institute of Physical and Chemical Research, Wako-shi, 351 Japan

*Fukuoka, H., Faculty of Engineering Science, Osaka University, Toyonaka, Osaka, 560 Japan

*Goldsmith, W., Mechanical Engineering Department, University of California, Berkeley, Calif., 94720 USA

(*)Hashimoto, S., Institute of Space and Aeronautical Science, University of Tokyo, 4-6-1 Komaba, Meguro-ku, Tokyo, 153 Japan

*Hayashi, Takuo, Department of Mechanical Engineering, Faculty of Engineering Science, Osaka University, Toyonaka, Osaka, 560 Japan

*Hayashi, Tsuyoshi, Department of Mathematics, Faculty of Science and Engineering, Chuo University, 1-13-27 Kasuga, Bunkyo-ku, Tokyo, 112 Japan

Hirao, M., Faculty of Engineering Science, Osaka University, Toyonaka, Osaka, 560 Japan

Ishikawa, H., Japan Automobile Research Institute, Yatabe-cho, Tsukuba-gun, Ibaragi, 300-21 Japan

*Jimma, T., Department of Mechanical Engineering, Tokyo Institute of Technology, 2-12-1, Ookayama, Meguro-ku, Tokyo, 152 Japan

*Johnson, W., Engineering Department, Cambridge University, Trumpington Street, Cambridge, CB2 1PZ, UK

((*)Kaibyshev, O., Ufa Aviation Institute, Karl Marx St. 12, 450025 Ufa-25, USSR)

*Kawashima, S., Department of Aeronautical Engineering, Faculty of Engineering, Kyushu University, Hakozaki, Higashi-ku, Fukuoka, 812 Japan

*Kawata, K., Institute of Space and Aeronautical Science, University of Tokyo, 4-6-1 Komaba, Meguro-ku, Tokyo, 153 Japan

Kawatate, K., Research Institute for Applied Mechanics, Kyushu University, Hakozaki, Higashi-ku, Fukuoka, 812 Japan

*Kinslow, R., Department of Engineering Science, Tennessee Technological University, Cookeville, Tennessee, 38501 USA

Kishi, T., Institute of Space and Aeronautical Science, University of Tokyo, 4-6-1 Komaba, Meguro-ku, Tokyo, 153 Japan

Kishida, K., Department of Precision Engineering, Faculty of Engineering, Osaka University, Suita, Osaka, 565 Japan

Kishimoto, K., Department of Physical Engineering, Faculty of Engineering, Tokyo Institute of Technology, 2-12-1 Ookayama, Meguro-ku, Tokyo, 152 Japan

*Kiyota, K., Yatsushiro College of Technology, Hirayama-shinmachi, Yatsushiro, 866 Japan

*Klepaczko, J., Institute of Fundamental Technical Research, Swietokrzyska 21, Warsaw, 00-049 Poland

*Kobayashi, Akira, Institute of Space and Aeronautical Science, University of Tokyo, 4-6-1 Komaba, Meguro-ku, Tokyo, 153 Japan

*Kobayashi, Shigeo, Department of Aeronautics, Faculty of Engineering, University of Tokyo, 7-3-1 Hongo, Bunkyo-ku, Tokyo, 113 Japan

Koga, T., National Aerospace Laboratory, 1880 Jindaiji, Chofu, Tokyo, 182 Japan

((*)Kohlin, N.N., Institute of Mechanics, Moscow University, Michurin Ave. 1, Moscow, V-234 USSR)

Kunishige, K., Sumitomo Metal Industry Co., Ltd., Amagasaki-shi, Hyogo, 660 Japan

Kuno, T., Department of Mechanical Engineering, Faculty of Engineering, Keio University, 3-14-1 Hiyoshi, Kohoku-ku, Yokohama, 223 Japan

Kuriyama, S., Institute of Physical and Chemical Research, Wako-shi, 351 Japan

(*)Kurokawa, K., Institute of Space and Aeronautical Science, University of Tokyo, 4-6-1 Komaba, Meguro-ku, Tokyo, 153 Japan

*Lee, E.H., Division of Applied Mechanics, Department of Mechanical Engineering, Stanford University, Stanford, Calif., 94305 USA

*Lindholm, U.S., Department of Materials Sciences, Southwest Research Institute, 8500 Culebra Road, San Antonio, Texas, 78284 USA

*Malvern, L.E., Engineering Sciences Department, University of Florida, Gainesville, Florida, 32611 USA

(*Mavljutov, R., Ufa Aviation Institute, Karl Marx St. 12, 450025 Ufa-25, USSR)

Mileiko, S.T., Institute of Solid State Physics of The Academy of Sciences of The USSR, Chernogolovka, Moscow District 142432, USSR

Miura, K., Institute of Space and Aeronautical Science, University of Tokyo, 4-6-1 Komaba, Meguro-ku, Tokyo, 153 Japan

*Mori, D., Institute of Space and Aeronautical Science, University of Tokyo, 4-6-1 Komaba, Meguro-ku, Tokyo, 153 Japan

Morimoto, Y., Department of Mechanical Engineering, Faculty of Engineering Science, Osaka University, Toyonaka, Osaka, 560 Japan

*Morland, L.W., School of Mathematics and Physics, University of East Anglia, Norwich, NR4 7TJ UK

*Mura, T., Department of Civil Engineering, Northwestern University, Evanston, Illinois, 60201 USA

Nagayama, K., High Energy Rate Laboratory, Faculty of Engineering, Kumamoto University, 2-39-1 Kurokami, Kumamoto, 860 Japan

Nakagawa, Kenji, Department of Precision Engineering, Faculty of Engineering, Osaka University, Suita, Osaka, 565 Japan

*Nakagawa, Noritoshi, Department of Mechanical Engineering, Faculty of Engineering, Kobe University, Rokkodai, Nada-ku, Kobe, 657 Japan

Nakagiri, S., Institute of Industrial Science, University of Tokyo, 7-22-1 Roppongi, Minato-ku, Tokyo, 106 Japan

Nakahara, I., Department of Mechanical Engineering, Faculty of Engineering, Tokyo Institute of Technology, 2-12-1 Ookayama, Meguro-ku, Tokyo, 152 Japan

*Nakamura, T., Graduate School of Science and Engineering at Nagatsuda, Tokyo Institute of Technology, 2-12-1 Ookayama, Meguro-ku, Tokyo, 152 Japan

(*Nigmatulin, R.I., Institute of Mechanics, Moscow University, Michurin Ave. 1, Moscow, V-234 USSR)

(*)Nojima, T., Department of Aeronautical Engineering, Faculty of Engineering, Kyoto University, Yoshida-honmachi, Sakyo-ku, Kyoto, 606 Japan

Okami, Y., Japan Automobile Research Institute, Yatabe-cho, Tsukuba-gun, Ibaragi, 300-21 Japan

Okano, S., Faculty of Engineering Science, Osaka University, Toyonaka, Osaka, 560 Japan

Okubo, H., National Defense Academy, Hashirimizu, Yokosuka, 239 Japan

Sakata, M., Department of Physical Engineering, Faculty of Engineering, Tokyo Institute of Technology, 2-12-1 Ookayama, Meguro-ku, Tokyo, 152 Japan

Sano, K., Research Laboratories, Kawasaki Steel Corp., 1 Kawasaki-cho, Chiba, 280 Japan

Sasaki, T., Department of Mechanical Engineering, Kobe University, Rokkodai, Nada-ku, Kobe, 657 Japan

Sawada, T., Faculty of Engineering, Tokyo University of Agriculture and Technology, Nakacho, Koganei, Tokyo, 184 Japan

*Sawaoka, A., Research Laboratory of Engineering Materials, Tokyo Institute Technology, Ookayama, Meguro-ku, Tokyo, 152 Japan

*Shioiri, J., Department of Aeronautics, Faculty of Engineering, University of Tokyo, 7-3-1 Hongo, Bunkyo-ku, Tokyo, 113 Japan

*Shioya, T., Department of Aeronautics, Faculty of Engineering, University of Tokyo, 7-3-1 Hongo, Bunkyo-ku, Tokyo, 113 Japan

*Shockey, D.A., Poulter Laboratory, Stanford Research Institute, Menlo Park, Calif., 94025 USA

*Stelly, M., Commissariat a L'Énergie Atomique, B.P.511-15, Paris (15e), France

Suhara, T., Research Institute for Applied Mechanics, Kyushu University, Hakozaki, Higashi-ku, Fukuoka, 812 Japan

Sunakawa, M., Institute of Space and Aeronautical Science, University of Tokyo, 4-6-1 Komaba, Meguro-ku, Tokyo, 153 Japan

Suzuki, H.G., Fundamental Research Laboratories, Nippon Steel Co., Ltd., 1618 Ida, Kawasaki, 211 Japan

Takahashi, Kiyoshi, Department of Applied Physics, Faculty of Engineering, University of Tokyo, 7-3-1 Hongo, Bunkyo-ku, Tokyo, 113 Japan

Takahashi, Kunihiro, Department of Mechanical Engineering, Faculty of Engineering, Keio University, 3-14-1 Hiyoshi, Kohoku-ku, Yokohama, 223 Japan

*Tanaka, K., Department of Aeronautical Engineering, Faculty of Engineering, Kyoto University, Yoshida-honmachi, Sakyo-ku, Kyoto, 606 Japan

Tanimura, S., College of Engineering, University of Osaka Prefecture, Mozu, Sakai, 591 Japan

*Ting, T.C.T., Department of Materials Engineering, University of Illinois at Chicago Circle, Chicago, Illinois, 60680 USA

(*)Toda, H., Department of Mechanical Engineering, Faculty of Engineering Science, Osaka University, Toyonaka, Osaka, 560 Japan

Toi, Y., Institute of Industrial Science, University of Tokyo, 7-22-1 Roppongi, Minato-ku, Tokyo, 106 Japan

Uchida, Takeshi, Heavy Apparatus Engineering Laboratory, Toshiba Corporation, 1 Toshiba-cho, Fuchu, Tokyo, 183 Japan

Uchida, Yukihiko, Faculty of Science and Engineering, Nippon University, 1-8-14 Kanda-Surugadai, Chiyoda-ku, Tokyo, 101 Japan

Urabe, N., Research Laboratories, Nippon Kokan Co., Ltd., 1-1 Minamitoda, Kawasaki-ku, Kawasaki, 210 Japan

Usami, S., Hitachi Research Laboratory, Hitachi Ltd., Hitachi-shi, 317 Japan

Wifi, A.S., Department of Mechanical Design and Production, Cairo University, Cairo, Egypt (Currently, Institute of Industrial Science, University of Tokyo)

*Wright, J.P., Weidlinger Associates, 110 East 59th Street, New York, N.Y., 10022 USA

Yamada, Toshiro, Department of Mechanical Engineering, Faculty of Engineering, Kyoto University, Yoshida-honmachi, Sakyo-ku, Kyoto, 606 Japan

(*Yamada, Yoshiaki, Institute of Industrial Science, University of Tokyo, 7-22-1 Roppongi, Minato-ku, Tokyo, 106 Japan)

Yamada, Yuji, Tamano Laboratory, Mitsui Engineering and Shipbuilding Co., Ltd., Tamano, Okayama, 706 Japan

Yamamoto, M., Institute of Industrial Science, University of Tokyo, 7-22-1 Roppongi, Minato-ku, Tokyo, 106 Japan

Yamamura, H., Faculty of Engineering Science, Osaka University, Toyonaka, Osaka, 560 Japan

*Yokobori, T., Department of Mechanical Engineering II, Tohoku University, Sendai, 980 Japan

Contents

Part 1 - 9 were presented at the corresponding sessions. Scientific Programme is as follows: Wednesday, August 24: Session 1 - 3; Thursday, August 25: Session 4 - 6; Friday, August 26: Session 7 - 9; Saturday, August 27: Excursion and personal discussion.

Analyses of High Velocity Tension of Bars of Finite Length of BCC and FCC Metals with Their Own Constitutive Equations

K. KAWATA, S. HASHIMOTO AND K. KUROKAWA

Institute of Space and Aeronautical Science,
University of Tokyo, 4-6-1, Komaba, Meguro-ku,
Tokyo 153, Japan

Summary

The concepts of high velocity ductility and high velocity brittleness are defined and it is stated that these phenomena are ruled by the crystal lattice system. The constitutive equations modelling high strength Al alloys are derived on the basis of thermal activated motion of dislocation. For a mild steel and high strength Al alloys, the behaviours of bars of finite length in high velocity tension are analysed basing upon their constitutive equations by finite element method. The difference and similarity between these two cases such as the existence and non-existence of sharp stress peak in wave front, are clarified.

1. Introduction

As suggested in the effect of crystal lattice systems on the relation of breaking elongation of thin bars of finite length vs. tensile velocity, it is considered necessary for the understanding of macromechanical behaviours in high velocity tension to introduce their own constitutive equations based upon their own crystal lattice systems. From this necessity the constitutive equations modelling high strength Al alloys are derived. The behaviours in high velocity tension of bars of finite length of a mild steel and Al alloys analysed by finite element method are known to show the interesting difference and similarity.

2. High Velocity Ductility and High Velocity Brittleness

The results of a series of high velocity tension test (Kawata et al. 1968)[1] indicate the existence of the lattice systems effect on the relation of breaking elongation ε_b vs. tensile velocity V_1 for pure metals and alloys especially in their annealed states as shown in Fig. 1. The tests cover the tensile velocity ranging from $10^{-5} ms^{-1}$ to 200 ms^{-1} (equivalent strain rate: $2 \times 10^{-4} s^{-1}$ to $4 \times 10^{3} s^{-1}$). The experimental values of β show remarkably clear tendencies as shown in Table 1.

Table 1. Crystal Lattice Systems Effect in High Velocity Breaking Elongation

Crystal lattice system	Material	Ratio of max. variation in ε_b to corresponding static breaking elongation ε_{bs}, β(%)
FCC	9/1 Cu-Zn	+20.0
	Cu	+11.3
	Al	+41.9
	Al 2S	+53.2
BCC	Fe	-40.1
	Mo	-56.6
HCP	Ti	+25.9
	Zn	-93.2

The terms of high velocity ductility or high velocity brittleness are defined as to express positive or negative values of β respectively. Table 1 shows that high velocity ductility appears for FCC materials, high velocity brittleness for BCC materials, and both high velocity ductility and brittleness for HCP materials. The fact that β is negative for Zn in contrast to positive β for Ti seems closely connected with the fact that axial ratio is 1.856 for Zn although it is 1.60 very close to FCC materials for Ti. Anyway, it is necessary to consider

micromechanical behaviour connected with crystal lattice system, to understand macromechanical behaviour of metallic materials.

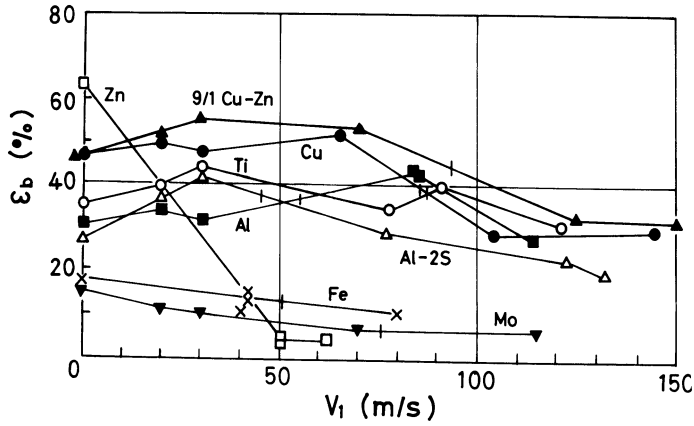

Fig. 1. Typical breaking elongation ε_b vs. tensile velocity V_1 relation in high velocity tension of annealed pure metals and alloys

3. On the Constitutive Equations Modelling FCC Metallic Materials Especially High-Strength Al Alloys and Their Characteristics

3.1 Derivation of the Constitutive Equations Modelling High-Strength Al Alloys [2] [9]

As shown in Fig. 2, general tendency of stress-strain diagrams in quasi static tension for high strength Al alloys [3] would be expressed approximately by elastic-linearly work hardening plastic type and be characterized with E: Young's modulus, E_p: tangent modulus in plastic region, and σ_y: yield stress. Known facts [4] ∿ [8] are summarized for the strain rate dependence of the flow stress in Al and some Al alloys in the strain rate range from 10^{-3} to $10^{3}s^{-1}$ as follows: (1) Strain rate dependence of flow stress of Al and some Al alloys in O-temper can be rationalized with simple theory for thermally activated motion of dislocations. (2) Principal effect of increased alloying is to increase athermal stress component. (3) Activation barriers

are probably forest dislocations. Constitutive equations modelling FCC metallic materials especially high strength Al alloys are derived basing upon the above mentioned.

3.2 Elastic-Perfectly Plastic Type

When Seeger's [5] flow rate with constant activation volume is adopted directly as plastic strain rate and zero athermal stress term is assumed, Eq. (1) is obtained, that gives elastic-perfectly plastic stress-strain relations as shown in Fig. 3, for the constants: $E = 7{,}190\ kg/mm^2$, $C_3 = 4.5 \times 10^{12} s^{-1}$, $U_0 = 30.3 \times 10^{-18}\ kg.mm$, $\sigma_0 = 19.42\ kg/mm^2$, k: Boltzmann's constant, $T = 300°\ K$. Eq. (1') gives practically the same behaviour when $C_1 = 2.32 \times 10^{11}\ (kg/mm^2)^{-1} s^{-1}$ is taken although the form of pre-exponential term is different.

$$\dot{\varepsilon} - \frac{\dot{\sigma}}{E} = C_3 \exp\left\{-\frac{U_0}{kT}\left(1 - \frac{\sigma}{\sigma_0}\right)\right\} \tag{1}$$

$$\dot{\varepsilon} - \frac{\dot{\sigma}}{E} = C_1 \sigma \exp\left\{-\frac{U_0}{kT}\left(1 - \frac{\sigma}{\sigma_0}\right)\right\} \tag{1'}$$

where σ is tensile stress, $\dot{\sigma}$ stress rate, and $\dot{\varepsilon}$ strain rate; E is Young's modulus, C_3 frequency constant, U_0 activation energy, k Boltzmann's constant, T temperature, σ_0 constant related to activation volume, and C_1 another constant related to frequency constant.

3.3 Elastic-Linearly Work Hardening Plastic Type

Eqs. (1), (1') are not enough to model high strength Al alloys. Such constitutive equations that give elastic-linearly work hardening plastic stress strain relations should be searched for. For this purpose constitutive Eqs. (2) ∿ (2") are considered, in which work hardening coefficient H and athermal stress term σ_g are introduced.

$$\dot{\varepsilon} - \frac{\dot{\sigma}}{E} = C_3 \exp\left\{-\frac{U_0}{kT}\left(1 - \frac{\sigma - \sigma_g}{\sigma_0\left(1 + H\left(\varepsilon - \frac{\sigma}{E}\right)\right)}\right)\right\} \tag{2}$$

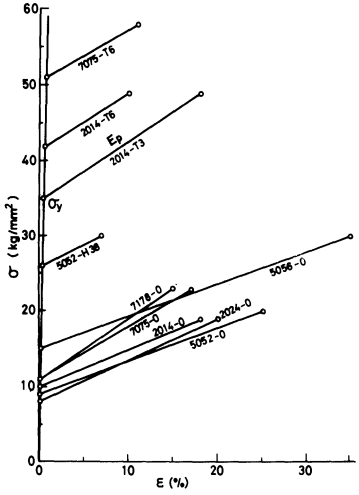

Fig. 2 Quasi-static stress-strain relation of high strength Al alloys, characterized by σ_y and E_p.

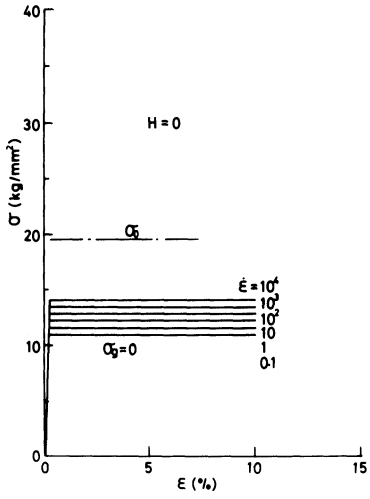

Fig. 3 Elastic-perfectly plastic stress-strain relation given by Eq. (1)

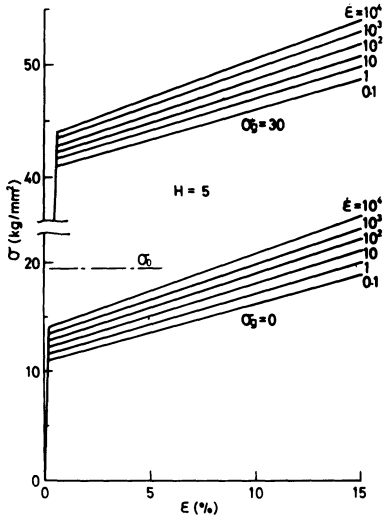

Fig. 4 Elastic-linearly work hardening stress-strain relation given by Eq. (2) for H = 5

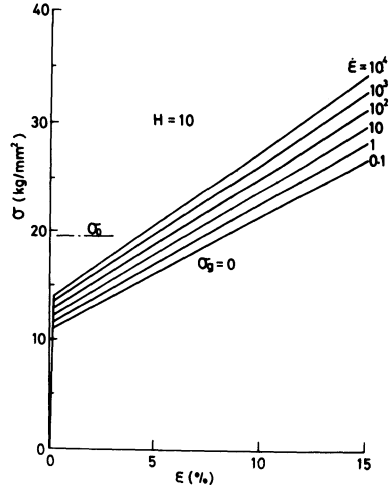

Fig. 5 Elastic-linearly work hardening stress-strain relation given by Eq. (2) for H = 10

$$\dot{\varepsilon} - \frac{\dot{\sigma}}{E} = C_1\sigma \quad \exp\left\{-\frac{U_0}{kT}\left(1 - \frac{\sigma - \sigma_g}{\sigma_0\left(1 + H\left(\varepsilon - \frac{\sigma}{E}\right)\right)}\right)\right\} \qquad (2')$$

$$\dot{\varepsilon} - \frac{\dot{\sigma}}{E} = C_3 \quad \exp\left\{-\frac{U_0}{kT}\left(1 - \frac{\sigma - \sigma_g}{\sigma_0\left(1 + H\left(\varepsilon - \frac{\sigma - \sigma_g}{E}\right)\right)}\right)\right\} \qquad (2'')$$

where σ, $\dot{\sigma}$, $\dot{\varepsilon}$, E, C_3, C_1, U_0, k, T, and σ_0 are the same with Eqs. (1), (1') respectively, and σ_g is athermal stress, and H work hardening coefficient.

Eq. (2) gives the stress-strain diagrams as shown in Figs. 4 and 5 for H = 5 and 10 respectively for example. Eq. (2') gives practically the same behaviour. About Eq. (2'') refer Fig. 13 and 5 (3).

The effect of introduction of athermal term σ_g to stress term in the numerator in Eqs. (2), (2') is to shift the curves in plastic region upward by σ_g, as shown in Fig. 4 for example. These constitutive equations are the searched elastic-linearly work hardening ones.

3.4 Relation between Micromechanical Constants and Macromechanical Constants

The process to determine the values of unknown micromechanical constants σ_g and H from given macromechanical constants σ_y and E_p is considered.

In all plastic range of linearly hardening material,

$$\sigma = \sigma_y + \frac{E_p}{1 - E_p/E} \cdot \varepsilon_p \qquad (3)$$

$$\dot{\sigma}/\dot{\varepsilon} = E_p \qquad (4)$$

where ε_p: plastic strain.

Using these conditions,

$$\left.\begin{aligned} (1 - E_p/E)\dot{\varepsilon} &= C_3 \exp\left[-\frac{U_0}{kT}\left(1 - \frac{\sigma_y - \sigma_g}{\sigma_0}\right)\right] \\ \frac{E_p}{(1 - E_p/E)} \cdot \frac{1}{\sigma_y - \sigma_g} &= H \end{aligned}\right\} \qquad (5)$$

Assuming $E_p/E \ll 1$,

$$\left.\begin{aligned} \sigma_g &= \sigma_y - \sigma_0 \left\{1 + \frac{kT}{U_0} \ln\frac{\dot{\varepsilon}}{C_3}\right\} \\ H &= E_p \Big/ \left\{\sigma_0 \left(1 + \frac{kT}{U_0} \ln\frac{\dot{\varepsilon}}{C_3}\right)\right\} \end{aligned}\right\} \qquad (6)$$

When the constants: $U_0/kT = 71.709$, $\sigma_0 = 19.42$ kg/mm^2, $C_3 = 4.5 \times 10^{12}$ s^{-1} are taken,

$$\left.\begin{aligned} \sigma_g &= \sigma_y - 11.530 - 0.6236 \log \dot{\varepsilon} \\ H &= E_p/(11.530 + 0.6236 \log \dot{\varepsilon}) \end{aligned}\right\} \qquad (7)$$

Calculated examples are shown in Table 2.

Table 2. Macromechanical and Micromechanical Constants of Ten High Strength Al Alloys

Material	σ_y * (kg/mm^2)	E_p * (kg/mm^2)	σ_g ** (kg/mm^2)	H**
2014 O	10	50.56	1	5.60
T6	42	61.95	33	6.86
2024 O	8	55.56	-1	6.15
T3	35	78.65	26	8.70
7075 O	11	73.62	2	8.15
T6	51	64.81	42	7.17
7178 O	11	78.43	2	8.68
5052 O	9	46.22	0	5.12
H38	26	58.82	17	6.51
5056 O	15	43.10	6	4.77

* Experimentally determined ($\dot{\varepsilon} = 10^{-4}$s^{-1}).

** Calculated from Eq. (7), using σ_y and E_p.

4. Behaviours in High Velocity Tension of Bars of Finite Length for BCC Metallic Material [2]

For the constitutive equation of mild steel of Johnston-Gilman type already shown in previous papers [10], [11]: Eq. (8), the behaviours in high velocity tension of bars of finite length are studied, by finite element method combined with Newmark 1/6 β method [12] ∿ [14], laying

emphasis on the ones after the reflections at the fixed ends.

$$\dot{\varepsilon} - \frac{\dot{\sigma}}{E} = \frac{4}{3} b \left[N_0 + \frac{3}{4} M(\varepsilon - \frac{\sigma}{E})\right] v^* \exp\left(-\frac{2\left[D + \frac{3}{4}H(\varepsilon - \frac{\sigma}{E})\right]}{\sigma}\right) \quad (8)$$

where $b = 2.5 \times 10^{-7}$ mm, $v^* = 3.2 \times 10^6$ mm/s, $N_0 = 3.75 \times 10^4 mm^{-2}$, $M = 10^9$ mm^{-2}, $D = 200$ kg/mm^2, $H = 10666$ kg/mm^2, $E = 2.15 \times 10^4$ kg/mm^2

Examples are shown in Figs. 6 ∿ 8. The remarkable characteristic of this BCC case is the existence of sharp stress peak at the stress wave front, after the reflection at the fixed ends of bars similarly with before the reflection, although its decay is observed of course.

5. Behaviours in High Velocity Tension of Bars of Finite Length for FCC Metallic Materials

For the constitutive equations modelling high strength Al alloys, the behaviours in high velocity tension of bars of finite length are analysed paying attention to both before and after the reflection of stress wave front at the fixed ends.

(1) σ, ε_p Distributions before the Reflection at the Fixed End

Two examples treating the cases for two pre-exponential forms and zero σ_g are shown in Figs. 9 and 10. Two significant characteristics of FCC materials are observed. The first is the non-existence of sharp stress peak at stress wave front, forming a striking contrast to mild steel. The second is the increasing formation of plateau in stress and plastic strain distributions with increasing work hardening coefficient H, showing a similar tendency with mild steel. There is practically no difference in behaviours between the two pre-exponential forms, that is, C_3 and $C_1\sigma$.

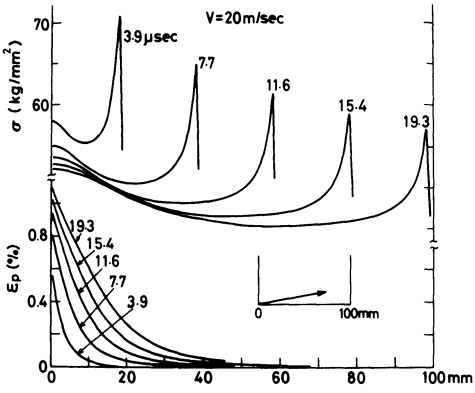

Fig. 6-1 High velocity tension of bar of finite length of a mild steel (V = 20 m/s)

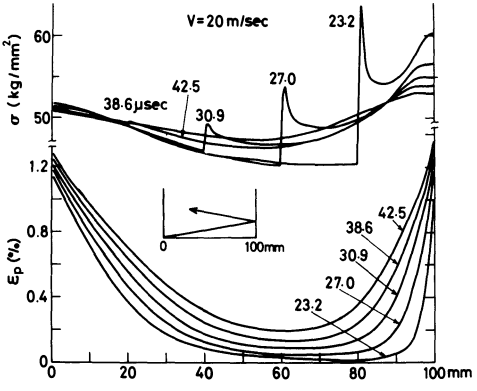

Fig. 6-2 High velocity tension of bar of finite length of a mild steel (V = 20 m/s)

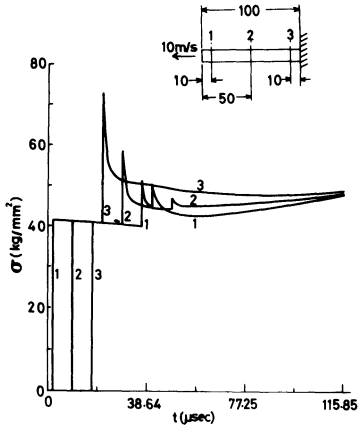

Fig. 7 Example of σ - t relation in high velocity tension of bar of finite length of a mild steel (V = 10 m/s)

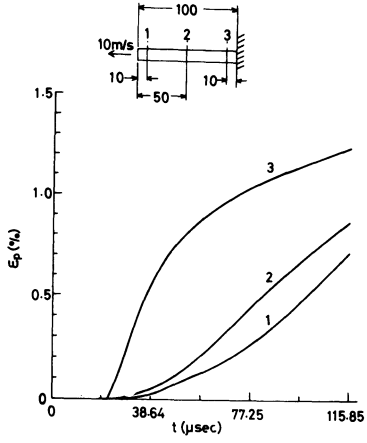

Fig. 8 Example of ε_p-t relation in high velocity tension of bar of finite length of a mild steel (V = 10 m/s)

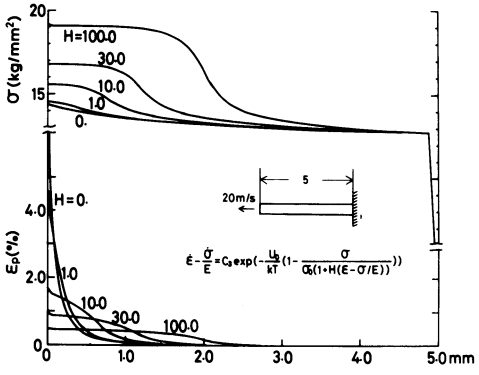

Fig. 9 High velocity tension of bar of finite length of material given by Eq. (2).

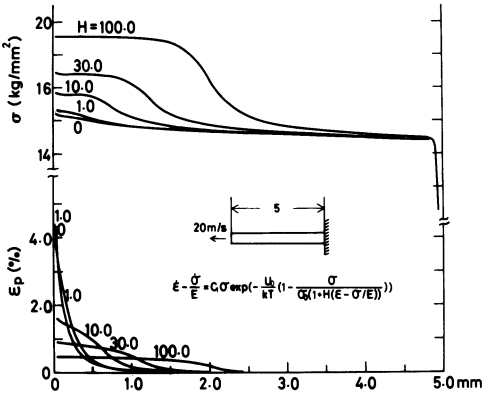

Fig.10 High velocity tension of bar of finite length of material given by Eq.(2')

(2) σ, ε_p Distributions after the Reflections at the Ends

As shown in Figs. 11 and 12, no essential difference occurs by the reflections. It is interesting that when time variations of stress and plastic strain are observed for three different points in the bar both stress and plastic strain tend to be equalize respectively.

(3) The effect of athermal stress term σ_g

As seen in the plot of $\sigma - \sigma_g$ (Fig. 13), its behaviours near wave front are nearly equal but in plastic strain growing region some differences are observed. This means that σ

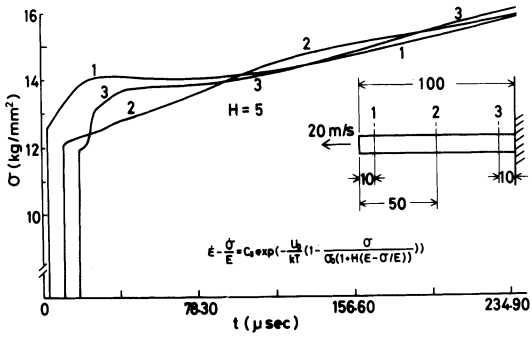

Fig. 11 Example of σ-t relation in high velocity tension of bar of finite length of material given by Eq. (2)

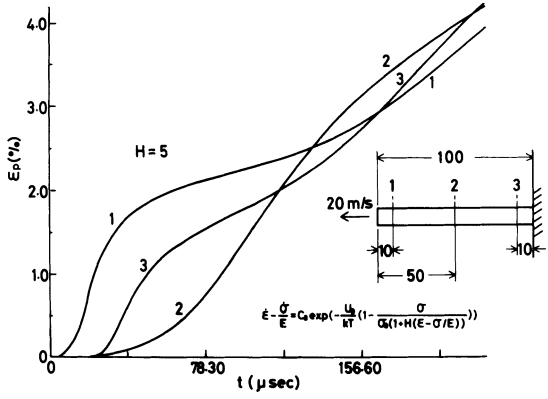

Fig. 12 Example of ε_p-t relation in high velocity tension of bar of finite length of material given by Eq. (2)

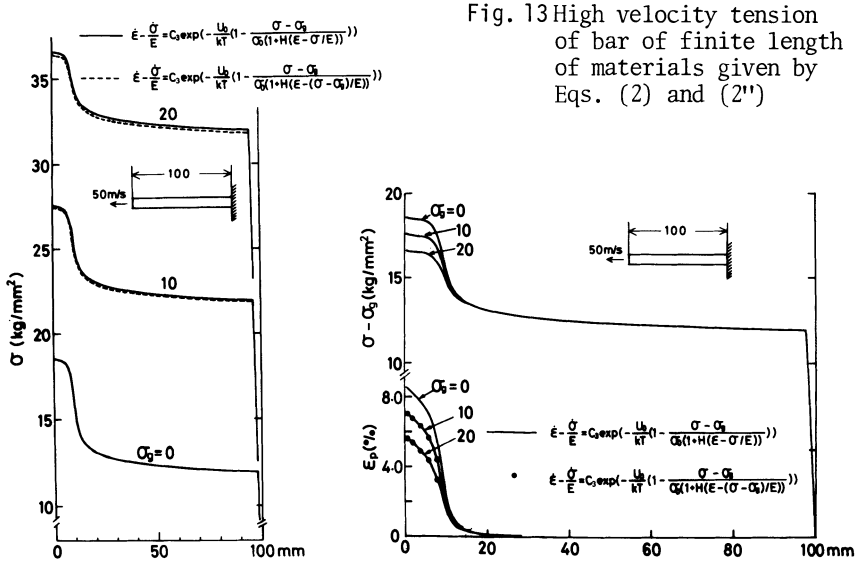

Fig. 13 High velocity tension of bar of finite length of materials given by Eqs. (2) and (2'')

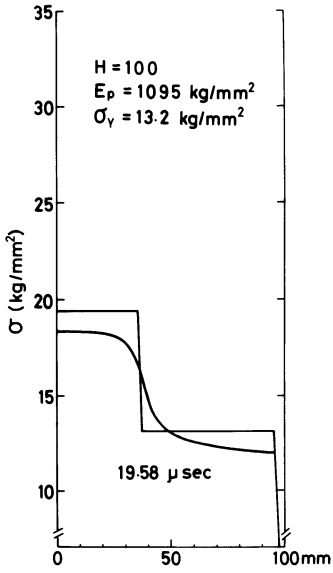

Fig. 14 (1)

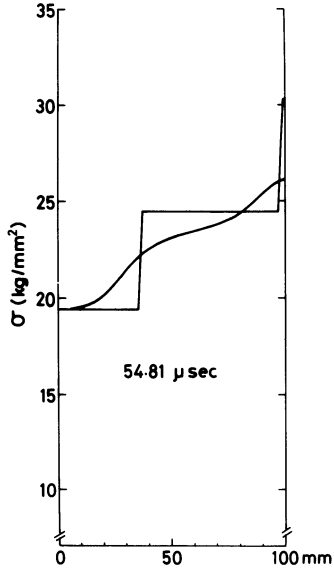

Fig. 14 (2)

Fig. 14 (1) ∿ (3)

Comparison of Eq. (2) and constant constitutive equation

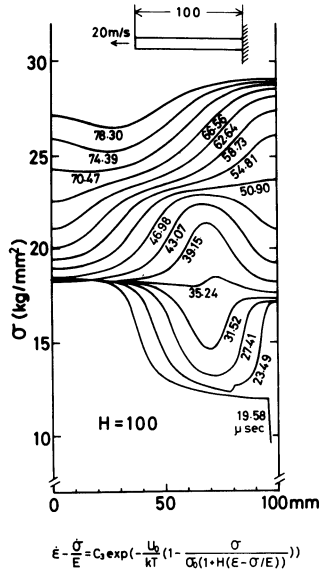

$$\dot{\varepsilon} - \frac{\dot{\sigma}}{E} = C_3 \exp\left(-\frac{U_0}{kT}\left(1 - \frac{\sigma}{\sigma_0(1 + H(\varepsilon - \sigma/E))}\right)\right)$$

Fig. 14 (3)

plot is shifted upward by σ_g near stress wave front and by a value a little smaller than σ_g for the region where plastic strain grows. The difference between the behaviours given by Eq. (2) and Eq. (2'') are little as seen in Fig. 13 and it is considered practically the same for these cases.

6. Some Discussions on the Applicability of Strain Rate Independent Theory

For the case of FCC type constitutive equation (2) with the constants: H = 100, bar length = 100 mm, tensile velocity = 20 m/s, comparison of Karman theory [15] is made as shown in Fig. 14. The constants for the strain rate independent theory are shown in the figure. For this case, the strain rate independent theory gives approximate values simulating general tendencies of the behaviours given by Eq. (2), although details of the stress profiles are not reproduced. So, the strain rate independent theory gives approximate values simulating general tendencies of correct behaviours, when a suitable stress-strain diagram of an selected $\dot{\varepsilon}$ is taken as constant constitutive equation.

7. Conclusion

(1) The concepts of high velocity ductility and high velocity brittleness are defind and their relations with crystal lattice systems are discussed. The importance of considering the crystal lattice system is emphasized for the study of high velocity deformation behaviour of metals.

(2) Constitutive equations modelling FCC materials especially high strength Al alloys are derived, based upon the experimental data in the strain rate range up to the order of $10^3 s^{-1}$.

(3) The mechanical behaviours in high velocity tension of bars of finite length are calculated for a mild steel and high strength Al alloys by finite element method, and the difference and similarity between BCC and FCC metallic materials are clarified.

(4) The existence and non-existence of sharp stress peak in the stress wave front in BCC and FCC materials respectively, seems to be connected with high velocity brittleness and high velocity ductility of these materials.

References

1. Kawata, K.; Fukui, S.; Seino, J.; Takada, N.: Some analytical and experimental investigations on high velocity elongation of sheet materials by tensile shock. IUTAM: Behaviour of Dense Media under High Dynamic Pressure. Paris: Dunod 1968, 313 - 323.

2. Kawata, K.; Hashimoto, S.; Kurokawa, K.: Analysis of high velocity tension of bars of finite length of materials obeying strain rate independent and dependent constitutive equations. Proc. 3rd Shock Technology Symposium (1976) 197 - 211.

3. Japan Society for Aeronautical and Space Sciences: Aerospace Engineering Handbook. Tokyo: Maruzen 1974, 483.

4. Holt, D. L.; Babcock, S.G.; Green, S.J.; Maiden, C.J.: The Strain-Rate Dependence of the Flow Stress in Some Aluminum Alloys. Trans. Am. Soc. Metals 60 (1967) 152 - 159.

5. Seeger, A.: The Generation of Lattice Defects by Moving Dislocations, and its Application to the Temperature Dependence of the Flow-Stress of F.C.C. Crystals. Phil. Mag. 46 (1955) 1194 - 1217.

6. Lindholm, U.S.; Yeakley, L.M.: Dynamic deformation of single and polycrystalline Aluminum. J. Mech. Phys. Solids 13 (1965) 41 - 53.

7. Shioiri, J.: Microscopic side of behaviours of metallic materials in high strain rate. Proc. 2nd Shock Technology Symposium (1975) 115 - 122.

8. Suzuki, H.: Strength of Metals. Tokyo: AGNE 1972, 50.

9. Kawata, K.: Recent development in macroscopic and microscopic theories of high velocity deformation mechanics. Preprint 25th Nat. Congr. Theor. Appl. Mech. (1975) 39 - 46.

10. Kuriyama, S.; Kawata, K.: Propagation of stress wave with plastic deformation in metal obeying the constitutive equation of the Johnston-Gilman type. J. Appl. Phys. 44 (1973) 3445 - 3454.

11. Kawata, K.; Kuriyama, S.: The development of macroscopic and microscopic theories of high velocity deformation. Harding, J.: Mechanical Properties at High Rates of Strain. London, Bristol: Inst. of Phys. 1974, 215 - 223.

12. Newmark, N.M.: A Method of Computation for Structural Dynamics. Proc. ASCE 85 No. EM3 (1959) 67 - 94.

13. Nakagiri, S.; Shimooka, H.: A Note on the Finite Element Approach to the Plastic Wave Propagation in Metal Obeying the Strain-Rate Dependent Constitutive Equation. CAS Research Paper 19 (1976) 39 - 44.

14. Kurokawa, K.; Kawata, K.: On the Dynamic Stress Concentration of Notched Plates as Induced by Tensile Stress Waves. Institute of Space and Aeronautical Science, University of Tokyo, Report No. 540 (1976) 47 - 89.

15. von Karman, T.; Duwez, P.: The propagation of plastic deformation in solids. J. Appl. Phys. 21 (1950) 987 - 994.

Dynamic Deformation of Materials and Structures Under Explosive Loadings

JOSEPH P. WRIGHT and MELVIN L. BARON

Weidlinger Associates
110 East 59th Street
New York, New York 10022

Introduction

Computerized analysis of materials and structures under explosive loadings has lead to the development of finite difference and finite element codes which are capable of treating nonlinear materials with a variety of dissipative mechanisms, such as thermal energy dependence, and hysteretic behavior in load-unload cycles in both shear and dilatation. Incremental plasticity theory is widely used for this purpose and a significant factor in this choice is the accompanying uniqueness - stability theory. The object of this paper is to review and illustrate this methodology for modeling nonlinear hysteretic materials and for analyzing the behavior under shock loadings of nonlinear media and structures embedded in such media.

Incremental Plasticity Theory

Classical incremental plasticity theory (e.g. see Ref. [1], p. 346 f.) provides a sound mathematical basis for the development of constitutive equations to represent diverse material behavior. Specifically, the plastic strain increment, $\dot{\varepsilon}^p_{ij}$, is related to the stress through a "flow rule" of the form

$$\dot{\varepsilon}^p_{ij} = \lambda \frac{\partial f}{\partial \sigma_{ij}} \tag{1}$$

where σ_{ij} is the stress tensor, f is a specified function of the stresses (and possibly other parameters), and λ is a non-negative function which must be determined as part of the solution of the problem. The equation

$$f(\sigma_{ij}) = 0, \tag{2}$$

called the yield condition, defines a surface in stress space and the yield surface is required to be everywhere convex in this space. Any portion of the yield surface may remain fixed (perfect plasticity), or move outward whenever the stress point is on that portion (work - hardening), or move inward so long as the stress point is not on that portion (e.g. kinematic hardening). In any case, work-softening is prohibited.

A plasticity model which satisfies the preceding guidelines is stable*) in the sense of Drucker, Ref. [2]. That is the constitutive equations together with the standard continuum mechanics equations (conservation of mass, momentum and energy) are properly posed so that solutions exist, are unique, and depend continuously on the initial and boundary data. These abstract mathematical properties are of considerable practical significance in the analysis of continuum problems. For example, if the solution does not depend continuously on the initial data, then small numerical errors (e.g. due to approximation or computer round-off) might propagate in such a manner as to make the entire solution worthless at a later point in time. Similarly, one would want to avoid problems with several solutions, or no solution, since the results may not correspond to a physical situation.

Cap Models

The cap model, Refs. [5] - [11], falls into the category of an incremental plasticity theory based upon the principles stated above. It is routinely used in finite element and finite difference calcu-

*) The use of the same function f in Eqs. (1) and (2) is referred to as an associated flow rule. Although non-associated flow rules are discussed in the literature, Refs. [3] and [4], their general use is not advised since stability proofs are difficult, often impossible, to obtain.

In this context, it is worth noting that constitutive equations based on endochronic theory have recently been shown to have non-unique solutions and are deemed unsuitable for use in general dynamic problems, Ref. [24].

lations to simulate the behavior of geological materials and buried structures subjected explosive loadings. Work has also been done to apply the cap model to earthquake problems. Various types of material behavior have been modeled with the cap model, including both the high and low pressure response of a number of geological materials such as sands, clays, and rocks. Anisotropy, strain rate effects in rocks, and temperature dependent effects have all been considered. The model developed in Ref. [11] is applicable from pressures of several bars to several megabars, and has been generalized to account for the observed increase in shear strength which occurs in the kilobar range.

For simplicity consider the (isotropic) cap model, Refs. [5] and [6], which employs a yield surface which is a function of only two invariants of the stress tensor. A typical yield surface is shown in Fig. 1 in which the coordinates are the pressure, p, and the square root of the second invariant of the deviatoric stress tensor $\sqrt{J_2'}$, i.e.

$$p = (\sigma_1 + \sigma_2 + \sigma_3)/3 \tag{3}$$

$$J_2' = [(\sigma_1 - \sigma_2)^2 + (\sigma_2 - \sigma_3)^2 + (\sigma_3 - \sigma_1)^2]/6 \tag{4}$$

where the σ_i are the principal stresses. Three different modes of behavior are possible for this model: elastic, failure and cap. Elastic behavior occurs when the stress point is within the yield surface which has two portions labeled failure envelope and cap. References [5] and [6] use a linearly elastic model inside the yield surface although various types of nonlinearly elastic or visco-elastic behavior can be modeled if warranted by test data.

During the failure mode of behavior, the stress point lies on the failure envelope which may be a movable (hardening) yield surface. In Refs. [5] and [6], the failure envelope is assumed to be fixed and is represented by a yield condition of the form

$$\sqrt{J_2'} - A + C \exp(-3Bp) = 0 \tag{5}$$

where A, B and C are material constants.

The cap mode of behavior occurs when the stress point lies on the movable cap and pushes it outward. The cap position and shape are related to the plastic strain history of the material through a hardening rule. In Refs. [5] and [6], the hardening rule is assumed to be of the form

$$\bar{\varepsilon}_v^p = W[1 - \exp(-3Dp)] \tag{6}$$

where W and D are material constants and for simplicity the shape of the cap is chosen as an ellipse. The cap does not move during purely elastic behavior. However, the behavior of the cap when the stress point lies on the failure envelope depends on whether the rock model or soil model is used. This distinction is made in order to model a phenomenon called dilatancy which is an inelastic volume change which appears in triaxial compression tests in rocks and some very dense sands, but is generally not present in most soils. When the stress point is on the failure envelope, the associated flow rule requires that the plastic strain increment be directed upward and to the left (see Fig. 1). Hence, the plastic strain increment during failure has a volumetric, or dilatant, component (as well as a shear component). For the rock model the cap position depends solely on the plastic strain generated when the stress point is on the cap; therefore the cap is stationary in this model when the stress point is on the failure envelope. This allows dilatancy to continue for as long as the stress point remains at failure. For the soil model, all plastic strain is included in $\bar{\varepsilon}_v^p$, so that the dilatancy associated with failure leads to a decrease in $\bar{\varepsilon}_v^p$, resulting in inward movement of the cap. This cap movement is halted if and when the cap reaches the stress point on the failure envelope. When this occurs the associated flow rule requires that the plastic strain increment lie between the outward drawn normals at the corner, Ref. [2]; the amount of dilatancy is then automatically controlled

so that the stress point does not lie outside the cap.

Tensile Behavior of Materials

Compressive states of stress appear to be adequately represented, both theoretically and practically, by the use of cap models. However, the state of the art in tensile modeling does not appear to have reached the same status.

Tensile failure of solids is typically associated with a phenomenon which is characterized as brittle. There may be ductile - like transitions but ultimately there appears a sudden relaxation from a measurable tensile stress to a zero stress. This relaxation frequently occurs in a time which appears instantaneous. As a result, tensile failure is often represented by some form of rate-independent stress-strain model. For example, the maximum principal tensile stress is monitored and set to zero whenever it reaches a specific value. Other, similar approaches involving the pressure and deviators have been used.

Little experimental information is available on the behavior of most solids after tensile failure, but what little there is indicates that these approaches are inadequate. A more important point is that these kinds of models violate the mathematical property of continuity and are thus potentially dangerous to use in calculations. In fact, simple one-dimensional numerical calculations have shown this danger to be quite real, Ref. [12]. In particular, extremely small changes in time step can be shown to lead to significant changes in calculated results.

An approach to tension modeling which appears both theoretically and practically acceptable is to use a rate-dependent theory. Tension models based on crack propagation concepts have been developed by several investigators. One such approach has been developed by the Stanfard Research Insitute, Refs. [13] and [14]. Work is currently under way, Refs. [15] and [16], to adapt such models for

use in wave propagation studies.

Soil-Island Calculations

Current methods for calculating the response of buried structures to explosive loadings sometimes employ a technique referred to as the soil-island approach, Fig. 2. In this method the ground response is first calculated as if the structure is absent (sometimes called a free-field calculation), and ground motions at the boundary of a region which contains the structure's location are saved. These boundary motions are then used in a second (usually more detailed) computation in which the structure is embedded in the ground. If the structure is at a considerable distance from the explosion and the boundary is placed at a reasonable distance from the structure, this can be an effective technique for reducing the interaction calculation to an acceptable size (Ref. [17]). This approach is particularly effective when a three-dimensional analysis is involved. For example, in vulnerability studies of protective structures subjected to high explosive or nuclear weapons, it is usual to model the ground as a series of layers (each of which is represented by a cap model) and to use a two-dimensional axisymmetric code (e.g. LAYER, Ref. [18]) to calculate the ground response in the vicinity of the structure. A local three-dimensional calculation is then performed with a three-dimensional code, such as TRANAL, Ref. [19].

Calculational Techniques

With the publication of several papers in the 1940's, John von Neumann laid the groundwork for both the current generation of digital computers and wave propagation calculations. Since then there has been continued evolution of computer capabilities so that it is now relatively easy to develop (or obtain) computer codes for dynamic calculations of various types. One and two dimensional calculations which were unthinkable a generation ago are now considered routine, and three dimensional calculations are becoming practical. Hence, the emphasis of this paper has been on how to model more complicated situations, rather than on how to integrate the equations of motion.

Nonetheless, a brief review of this part of the methodology is in order here.

In a review just two years ago, Ref. [20], nine specialized computer codes for doing three dimensional transient nonlinear calculations were briefly summarized. (Not included there were general purpose structural codes such as ANSYS, ASKA, NASTRAN, etc.) Codes for one and two dimensional wave propagation calculations have been adequately reviewed in Ref. [21]. Reference [22] has become a classic in this field and should not be overlooked.

Generally speaking, all of these codes integrate forward in time and permit different types of materials. The most commonly used time integration method for nonlinear wave propagation calculations is the explicit, central difference method with the artificial viscosity method of von Newmann and Richtmyer (see Ref. [23]). Other methods (e.g. implicit time integration) are sometimes used for structural problems but, for the high velocity motions and history dependent stress paths induced by explosive loadings, the traditional method appears to be the most economical. The TRANAL code, Ref. [20], is noted as an example of this methodology for calculating three dimensional problems. TRANAL is a finite element code which incorporates the cap model and which integrates the equations of motion using the central difference method. A calculation with 6,156 elements (21,480 degrees of freedom) and 660 time steps was performed in less than 32 minutes of computer time on the CDC (Control Data Corporation) 7600 with this code.

Concluding Remarks

Recent advances in computerized analysis of materials and structures under explosive loadings has been summarized. The use of incremental plasticity theory and the importance of stable material models has been emphasized. With the improvement of computer technology, three dimensional dynamic calculations involving complex material behavior are quickly becoming common place.

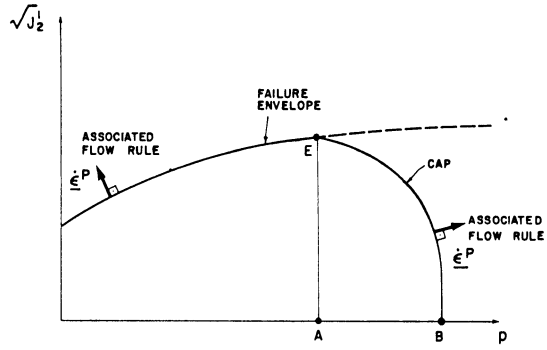

FIG. 1 TYPICAL YIELD SURFACE IN THE CAP MODEL FOR COMPRESSIVE STRESSES.

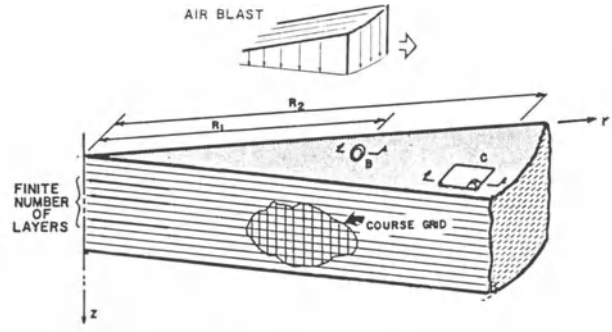

A FREE FIELD CALCULATION (2-D AXISYMMETRIC)
(FINITE DIFFERENCE)

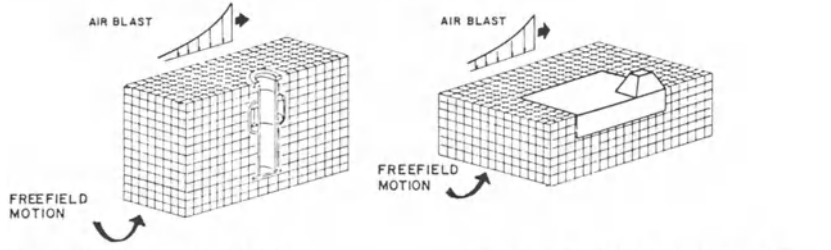

B. SOIL ISLAND (3-D) CONTAINING BURIED SILO STRUCTURE (FINITE ELEMENT)

C. SOIL ISLAND (3-D) CONTAINING PARTIALY BURIED RADAR STRUCTURE (FINITE ELEMENT)

FIG. 2 SOIL ISLAND CONCEPT

References

1. Malvern, L.E., Introduction to the Mechanics of a Continuous Medium, Prentice-Hall, Inc., Englewood Cliffs, New Jersey 1969.

2. Drucker, D.C., "On Uniqueness in the Theory of Plasticity", Quart. Appl. Math., Vol. 14, pp. 35-42, 1956.

3. Bleich, H.H., "On Uniqueness in Ideally Elastoplastic Problems in Case of Nonassociated Flow Rules", J. of Appl. Mech., Trans. ASME, Vol. 39, No. 4, pp. 983-987, December 1972.

4. Mroz, Z., "Nonassociated Flow Rules in Plasticity", Journal de Mecanique, VOl. II, No. 1, Paris, March 1963.

5. DiMaggio, F.L. and Sandler, I.S., "Material Model for Granular Soils", J. Engrg. Mech., Div., A.S.C.E., June 1971, pp. 935-950.

6. Sandler, I.S. and Rubin, D., "A Modular Subroutine for the Cap Model", Report No. DNA 3875F, Weidlinger Associates, New York, New York, January 1976.

7. Nelson, I., Baron, M.L., and Sandler, I.S., "Mathematical Models for Geological Materials for Wave Propagation Studies", Publ. in Shock Waves and the Mechanical Properties of Solids,, Syracuse University Press, Syracuse, New York, pp. 390-351, 1971.

8. Sandler, I.S., DiMaggio, F.L. and Baladi, G.Y., "Generalized Cap Model for Geological Materials", J. Geotech. Engrg. Div., A.S.C.E., Vol. 102, No. GT7, July 1976.

9. Sandler, I.S. and DiMaggio, F.L., "Anisotropy in Elastic-Plastic Models of Geological Materials", Weidlinger Associates, New York New York, (Presented at the Defense Nuclear Agency Meeting of Material Properties for Ground Motion Calculations), Park City, Utah, November 1973.

10. DiMaggio, F.L. and Sandler, I.S., "The Effect of Strain Rate on the Constitutive Equations forRocks", Report No. DNA 2801T, Weidlinger Associates, New York, New York, October 1971.

11. Rubin, D. and Sandler, I.S., "Development of a High Pressure Cap Model for Use in Computations of Ground Shock from Subsurface Explosions", Weidlinger Associates, New York, New York, December 1976.

12. Whitman, L. and Wright, J.P., "Tensile Behavior of Geological Materials in Ground Shock Calculations, III", forthcoming DNA report, Weidlinger Associates, New York, New York, 1977.

13. Shockey, D.A., Petersen, C.F., Curran, D.R., and Rosenberg, J.T., "Failure of Rock Under High Rate Tensile Loads", Publ. in New Horizons in Rock Mechanics, Fourteenth Symposium on Rock Mechanics, (page 709), 1973.

14. Seaman, L. and Shockey, D.A., "Models for Ductile and Brittle Fracture for Two Dimensional Wave Propagation Calculations", Army Materials and Mechanics Research Center Report, 1975.

15. Wright, J.P. and Whitman, L., "Tensile Behavior of Geological Material in Ground Shock Calculations, II", Report No. DNA (in process), Weidlinger Associates, New York, New York, March 1977.

16. Grady, D.E. and Hollebach, R.E., "Rate-Controlling Processes in Brittle Failure of Rock", Report No. SAND 76-0659, Sandia Laborities, Albuquerque, New Mexico, February 1977.

17. Nelson, I., "Analysis of Soil Structure Interaction on Site Defense (SD) Type Semi-Buried Structures, Part 1", HND-TR-75-20-ED-CS, Weidlinger Associates, New York, New York, 1975.

18. Baron, M.L., McCormick, J.M. and Nelson, I., "Investigation of Ground Shock Effects in Nonlinear Hysteretic Media", Publ. in Computational Approaches in Applied Mechanics, A.S.M.E. Computer Conference, pp. 165-190, 1969.

19. Baylor, J.L., Bieniek, M.P., Wright, J.P., "TRANAL: A 3-D Finite Element Code for Transient Nonlinear Analysis", DNA 3501F Weidlinger Associates, New York, New York, 1974.

20. Baylor, J.L. and Wright, J.P., "Three Dimensional Nonlinear Analysis", Publ. in Finite Element Analysis of Transient Nonlinear Structural Behavior, A.S.M.E. AMD-Vol. 14, Winter Annual Meeting, Houston, Texas, pp. 179-191, December 1975.

21. Structural Mechanics Computer Programs: Surveys, Assessments and Availability, edited by Pilkey et al, University Press of Virginia, Charlottesville, Virginia, 1974.

22. Methods of Computational Physics, edited by B. Adler et al, Vol. 3, Academic Press, New York, New York 1964.

23. Richtmyer, R.D. and Morton, K.W., "Difference Methods for Initial Value Problems", Interscience Publishers, New York, 1967.

24. Sandler, I.S., "On the Uniqueness and Stability of Endochronic Theories of Material Behavior", Report No. DNA 41337, Weidlinger Associates, New York, New York, October 1976.

Deformation Maps in the Region of High Dislocation Velocity

ULRIC S. LINDHOLM

Department of Materials Sciences
Southwest Research Institute
San Antonio, Texas

Summary

The form of the deformation map, as introduced by Ashby, is considered with emphasis on the region of high dislocation velocity (high stress). Of particular concern is the transition at high strain rates from a thermally activated to a linear viscous mode of deformation. New experimental data on aluminum and copper over a wide range in temperature and strain rates to 10^5 s^{-1} are presented. No evidence of the linear viscous mode was observed in these tests. Other data in the literature show a transition at strain rates on the order of 10^3 s^{-1}.

Introduction

Inelastic deformation of metals may occur by means of a number of distinct mechanisms. To describe the deformation process in terms of a constitutive equation, or set of equations, requires preknowledge of the operating mechanism(s) for the particular range of the relevant operative loading variables (stress, temperature, rate of deformation). Thus, both the form of the constitutive equation and the range of its applicability must be defined for each alloy of interest. Deformation maps, as introduced by Ashby [1], are a useful means of presenting this information graphically.

In this paper, we will examine the form of the deformation map in the region of high dislocation velocity, high strain-rate or high stress; these three being essentially equivalent. The maps are developed from a combination of analytical modeling of dislocation processes and of empirical data generation. We will proceed from some general considerations to specific quantitative data on aluminum and copper with particular emphasis on the transition

from thermal activation to linear viscous drag as the dominant rate controlling processes at high velocity.

Generalized Deformation Maps

Metals and other crystalline solids can deform plastically by means of a relatively large number of different mechanisms. The rate of plastic deformation is dependent, therefore, on the operative mechanism, or mechanisms if more than one is operative simultaneously, as well as the applied stress field and the temperature. When we are interested in a wide range of the pertinent variables, stress, temperature and strain rate, we can expect significant changes in the functional form of the constitutive relation at transition regions between operative mechanisms. Ashby [1] has introduced the deformation map, with axes of stress and temperature, for the purpose of delineating boundaries of those regions where specific mechanisms are dominant. The map may be accompanied by analytical or empirical constitutive relations to define the behavior within each region. The emphasis of Ashby's maps has been on the low stress or creep regions. Our purpose here is to concentrate on the regions of high stress which occur either at low temperature or at high strain rates.

The generalized form of the deformation map is given in Figures 1 and 2. Figure 1 is given in the Ashby form of stress vs. temperature with contours representing constant dislocation velocity or strain rate. Figure 2 presents an alternate form, more familiar to those working in high strain-rate effects, of stress vs. dislocation velocity (strain rate) with contour lines of constant temperature. In these figures, the stress is normalized by the shear modulus μ and the dislocation velocity by the elastic shear wave velocity, c_s. Conversion of dislocation velocity to strain rate is made by the usual kinematic relation, $\dot{\gamma} = \rho b v$. The dimensional scales on Figures 1 and 2 are based on nominal properties for aluminum with a dislocation density $\rho = 10^{10}$ cm^{-2}.

Major regions on these maps can be delineated based on four basic deformation mechanisms [2]. At the lowest stress levels, deformation occurs by diffusion controlled creep mechanisms. Significant

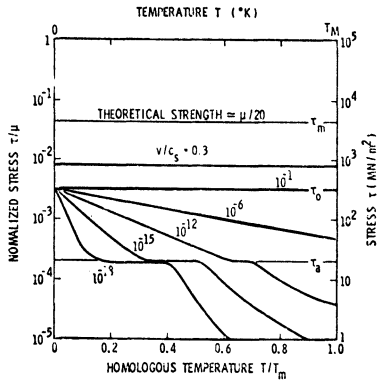

Figure 1. Generalized deformation map for high deformation rate region.

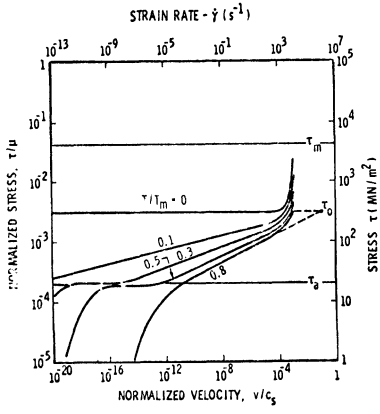

Figure 2. Generalized deformation map in terms of dislocation velocity (strain rate).

creep rates generally require temperatures above 0.5 T_m and for constant creep rate the stress drops rapidly with increasing temperature. Further subdivision of the creep range can be made based upon the type of diffusion controlled process involved [1, 2], but will not be discussed further here.

As the stress is increased by reducing the temperature or increasing the rate of deformation, for most metals there will occur a plateau or region where the flow stress is nearly independent of temperature variation over some range. At this athermal stress level, τ_a, the glide dislocations are held up at long range barriers which may be overcome only by further increases in the applied stress; i.e., the intrinsic barrier free energy is very large compared with kT so that random thermal fluctuation is not able to assist dislocation motion.

Upon further increase in applied stress, the principal resistance to dislocation motion is the interaction with short range barriers whose intrinsic free energy is comparable with kT. Therefore, these barriers may be overcome by random thermal fluction and thermal activation becomes the rate controlling mechanism. We again have a region where deformation rate may be strongly dependent on stress and temperature. In its simplest form, the

relationship between stress, τ, temperature, T, and strain rate, γ, in the thermal activation region is

$$\dot{\gamma} = \dot{\gamma}_o \exp - \frac{v^* (\tau_o - \tau)}{kT} \quad (1)$$

where $\dot{\gamma}_o$, τ_o and v* are constants. This simple model assumes that the activation barrier has a constant amplitude, τ_o, and constant width in the direction of dislocation motion proportional to the activation volume, v*. These assumptions correspond to the Seeger model for intersection of glide dislocations with stationary forest dislocations. There are other types of localized barriers such as Peierls stress, cross-slip, solute atom stress fields, etc. for which the variation in activation energy with stress amplitude may be nonlinear [3]; however, the Arhenius form of Equation (1) is retained. In the thermal activation region, stress increases with decreasing temperature and increasing dislocation velocity or strain rate. At T = 0 or $\dot{\gamma} = \dot{\gamma}_o$, the applied stress equals the barrier strength τ_o. The parameters τ_o, $\dot{\gamma}_o$ form bounds for the region of thermal activation.

If the applied stress exceeds τ_o, the dislocations may overcome all local barriers without assistance of the available thermal energy. At this point, viscous drag mechanisms (which are always present) become rate controlling. Several specific mechanisms have been proposed (see Ref. 2 for review), all of which result in a Newtonian viscosity and the drag force on the moving dislocation is given by

$$\tau b = Bv \quad (2)$$

where b is the Burger's victor and B is a drag coefficient. Alternately, Equation 2 can be expressed in terms of strain rate as

$$\tau = \alpha \dot{\gamma} \quad (3)$$

where $\alpha = B/\rho b^2$. The coefficients B or α are such that viscous drag becomes effectively rate controlling only at very high

dislocation velocity or strain rate. Experimental evidence to be discussed later indicates that viscous drag may become dominant at strain rates of the order of 10^3 to 10^4 s^{-1}. Such a transition is important because of the change from a comparatively weak (logarithmic) dependence on strain rate to a much stronger (linear) dependence. As shown in Figure 2, the slope of stress vs. strain rate turns up sharply in the viscous region, $\tau > \tau_o$. There may also be some weak dependence of the drag coefficient, B or α, on temperature.

The final limiting stress shown on Figures 1 and 2 is the theoretical strength, τ_m, which is taken to be approximately $\tau_m \simeq \mu/20$. The behavior in the neighborhood of the theoretical strength or the problem of relativistic effects as dislocation velocities approach the shear wave velocity will not be discussed in this paper.

The generalized deformation maps shown need further refinement and definition, but are presented to illustrate the general transitions occurring and to help guide the development of constitutive theory. The following experimental work is intended to verify certain regions of the map and specifically explore the transition region between thermal activation and viscous drag.

Experimental Procedure

Compression tests were performed on two metals, aluminum (1100-0), and copper (99.999% pure). Strain rate was varied over a wide range from 10^{-4} s^{-1} to 10^5 s^{-1} and temperature was varied from approximately 70K to 700K.

For strain rates below 100 s^{-1}, all compression tests were performed on a hydraulic testing machine. At rates from 100 s^{-1} to 3000 s^{-1}, a conventional split Hopkinson pressure bar of 1.25 cm diameter was used. These test techniques have previously been reviewed by Lindholm [4]. To achieve higher strain rates in order to define the potential transition into the viscous drag region, a split pressure bar system was modified as follows. The effective strain rate produced by the pressure bar technique is

proportional to the maximum elastic particle velocity in the bars and to the length of the compression specimen. Using maraging steel alloy bars with yield strengths in excess of 2,500 MN/m^2, the maximum particle velocity could be increased by nearly a factor of 10. Also, the specimen was reduced in size to 4 mm in diameter by 4 mm length, a dimension equal to approximately five times the maximum grain diameter in the polycrystalline test specimens. In reducing the specimen size (by approximately 1/3), it was also essential to correspondingly reduce the diameter of the pressure bars to assure that the area mismatch between bar and specimen is minimal and the interface remains planar during wave reflection. This reduced bar diameter also minimizes geometrical dispersion of the large amplitude pulses in the pressure bars. The actual pressure bar dimensions were 4.7 mm diameter by 300 mm length. Stress pulses were generated by axial impact from a bar of the same diameter. Other than the bar geometry and material properties, the test procedure was similar to the conventional Hopkinson pressure bar method [4]. Using this miniature pressure bar system and specimen, strain rates to 6×10^4 s^{-1} were achieved.

Results for Aluminum and Copper

Two alternate plots of typical data using the test procedures described are given in Figures 3 and 4 for 1100-0 aluminum. These are in the same form as the deformation maps although dimensional coordinates are used. Figure 3 shows compressive stress as a function of temperature for three widely different strain rates. The data points are taken from continuous stress-strain curves at a constant strain amplitude of $\varepsilon = 10\%$. The plotting of other constant strain amplitudes results in similar curves. Figure 4 shows the alternate plot of stress vs. strain rate at constant temperature.

It is apparent that two distinct modes of deformation are involved, both correlated by the simple thermal activation model given in Equation 1. The modes are defined based on the empirical data only and for reference purposes will be designated

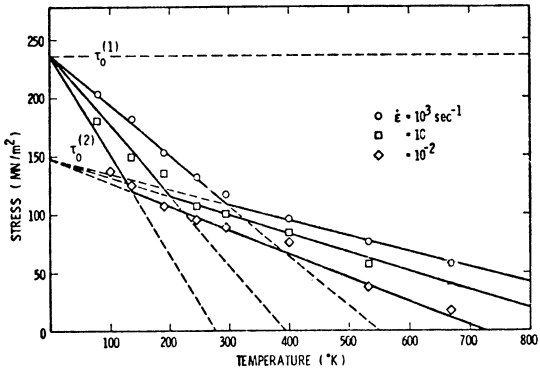

Figure 3. Flow stress for 1100-0 aluminum vs. temperature.

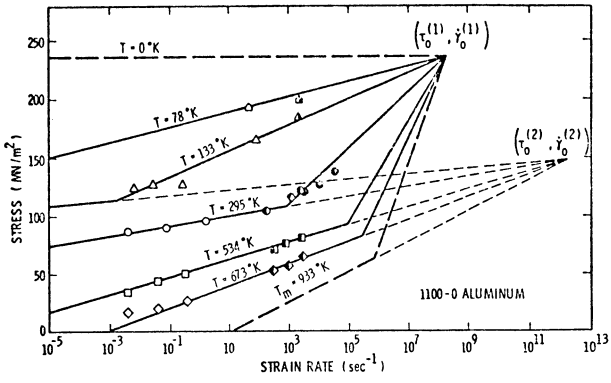

Figure 4. Flow stress for 1100-0 aluminum vs. strain rate.

by numerals 1 and 2, Mode 1 occurring at the higher stresses. The solid lines in Figures 3 and 4 are based on the following sets of constants from Equation 1.

		Mode 1	Mode 2
v^*	=	6.44×10^{-22} cm^3	3.76×10^{-21} cm^3
$\dot{\gamma}_o$	=	1.73×10^{8} s^{-1}	1.73×10^{12} s^{-1}
τ_o	=	234.4 MN/m^2	147.5 MN/m^2

The Mode 2 deformation occurs in a range usually attributed to the dislocation intersection model of Seeger [5]. The mechanism associated with Mode 1 is uncertain. A possible mechanism is the

nucleation of cross-slip as the temperature is decreased and the stress increased. This low temperature mode is also apparent in the low strain rate tensile data of Trozera, Sherby and Dorn [6] for pure aluminum. See particularly Figure 10 of Reference 6 which is contained in written discussion by Wiedersich.

If we now observe Figure 4, we see the same mode transition occurring with increasing strain rate. At ambient temperature (295K), the change in slope occurs at roughly 10^3 s^{-1}. Similar observations on strain rate effect in aluminum have led others [7] to conclude that this slope change was evidence of a transition to the viscous drag mechanism. However, in the present case, the low temperature, low strain rate data show that the transition is only to another thermally activated mode. The correlation of temperature effect and strain rate effect on flow stress over such a wide range is strong evidence of the thermal activation process.

Test results for copper obtained at 77K and 295K are shown in Figure 5 for two levels of compressive strain, 10% and 20%. These results show a lower strain rate and temperature sensitivity

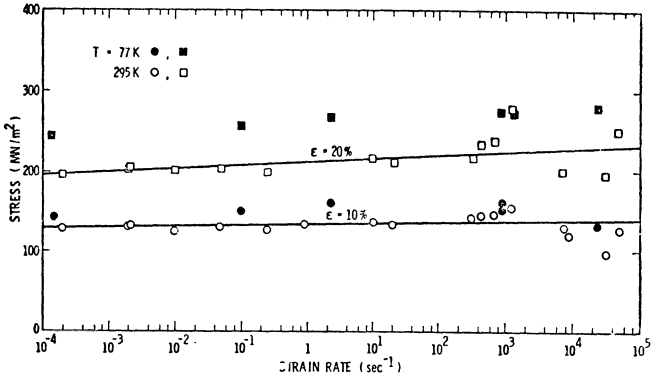

Figure 5. Flow stress for 99.999% copper.

than the aluminum and no change in mode over the wide range covered. The greater scatter in the data at the very highest rates can be attributed to the accuracy of the experimental technique in this region. Nevertheless, increases in stress of the

type that would accompany linear viscous damping are not present. Reducing the test temperature to 78K increased the stress level by less than 20% above the 295K data over the entire strain-rate range. Unfortunately, enough temperature data was not taken to compute all the activation parameters; however, the low sensitivity to temperature correlates with the low strain-rate sensitivity. Also, the present data does not indicate the presence of a second thermally activated mode in copper, either at low temperature or high strain rate.

It should be pointed out that other investigators [8, 9, 10], also using pressure bar techniques, have measured a sharp increase in flow stress at strain rates in the order of 10^3 s^{-1}. This increase has been attributed to viscous drag controlled deformation. Drag coefficients of the order 4-10 $kNsm^{-2}$ for copper at room temperature have been reported [10].

Conclusions

The construction of deformation maps is helpful in obtaining a consistent and complete picture of the deformation behavior for a given metal or alloy. They also assist in defining the range of applicability of the associated constitutive theory. For high velocity deformation, the deformation map and deformation mechanisms are not as well established as in the quasi-static or creep range. Thermal activation and viscous drag are relatively well established as the dominant mechanisms in this range. However, experimental mapping of the transition between these two mechanisms needs further work since there remains apparent inconsistencies among the reported results. This additional data is required in a region which is not available to simple experimental determination. The Hopkinson bar methods, which are widely used, must come under careful scrutiny when used for strain rates above about 10^4 s^{-1}. The limiting assumptions concerning uniaxial stress state, stress homogeneity and boundary constraint all become critical at these rates. However, improved alternate techniques are not yet available for large plastic deformation.

References

1 Ashby, M. F.: A first report on deformation mechanism maps. Acta Met., 20 (1972), 887-897.

2 Klahn, D.; Mukherjee, A. K.; Dorn, J. E.: Strain rate effects. Second Int. Conf. on Strength of Metals and Alloys, ASM (1970), 951-982.

3 Davidson, D. L.; Lindholm, U. S.: Effect of barrier shape in the rate theory of metal plasticity. Institute of Physics Conference Series No. 21 (London) (1975), 124-137.

4. Lindholm, U. S.: High strain-rate tests. Techniques in Metals Research. Vol. V, Part 1, Interscience, New York (1971).

5 Seeger, A.: The generation of lattice defects by moving dislocations and its application to the temperature dependence of the flow stress of F.C.C. crystals. Phil. Mag. 46 (1955), 1194-1217.

6 Torzera, T.A.; Sherby, O. D.; Dorn, J. E.: Effect of strain rate and temperature on the plastic deformation of high purity aluminum. Trans. ASM, 49 (1957), 173-188.

7 Hauser, F. E.; Simmons, J. A.; Dorn, J. E.: Strain rate effects in plastic wave propagation. Response of Metals to High Velocity Deformation, Interscience, New York (1961), 93.

8 Kumar, A.; Kumble, R. G.: Viscous drag on dislocations at high strain rates in copper. J. Appl. Phys., 40, (1969), 3475-3480.

9 Eddington, J. W.: The influence of strain rate on the mechanical properties and dislocation substructure in deformed copper single crystals. Phil. Mag., 17 (1969), 1189-1206.

10 Campbell, J. D.: Temperature and rate effects in metal plasticity. Archives of Mechanics, 27 (1975), 407-416.

Dislocation Configurations Due to Plate Impact

R. J. CLIFTON and P. KUMAR
Division of Engineering, Brown University
Providence, Rhode Island, U.S.A.

Summary

Plate impact recovery experiments are described in which single crystals of LiF are impacted by a thin flyer plate. Provisions are made to prevent reloading of the crystal by reflected waves or repeated impact. As a result, the crystal remains in position for subsequent removal to examine the dislocation configurations produced by a known stress pulse. Observation of dislocations by an etch pit technique shows large increases in dislocation density with closely spaced, long glide bands emanating from both front and rear surfaces. Comparatively short, widely spaced interior glide bands have lengths comparable to those predicted by applying the linear drag model of ultrasonic attenuation studies to the stress levels of the plate impact experiments.

Introduction

Plate impact experiments on single crystals provide a means for probing the dynamics of high speed dislocations as well as the nucleation and multiplication of dislocations. Early experiments of this type [1] focussed attention on the spatial attenuation of the stress amplitude at the leading wave front and the relation of this so-called "elastic precursor decay" to the dynamics of dislocations at the wave front. The general conclusion from these experiments is that the precursor decay is much greater than predicted from theory, provided that the decay is assumed to be due to movement of the initial dislocations at speeds less than elastic wave speeds. Various possible explanations of this discrepancy have been considered, including dislocation multiplication in the wave-front [2], front surface effects [3] and heterogeneous nucleation of dislocations [4]. Differentiation between these mechanisms, as well as such other possibilities as supersonic dislocations [5] and

dislocation breakdown into multiple dislocations at dislocation velocities approaching elastic wave speeds [6], should be facilitated by examination of dislocation configurations before and after impact.

Preliminary plate impact experiments intended to reveal post-impact dislocation configurations in LiF crystals have been reported by Flinn et al [7] for low velocity impacts (drop heights of less than 1 meter). These experiments show that marked increases in dislocation density can occur, even for the relatively low impact velocities imposed. However, detailed quantitative interpretation of these experiments is not possible because the wave profile was not monitored and reloading by reflected waves was not prevented. A more comprehensive series of plate impact recovery experiments on LiF crystals is being carried out by the authors [8,9]. Typical results and overall insights obtained from these experiments are reported in the following sections.

Experimental Setup and Procedure

A schematic of the plate impact recovery experiment is shown in Fig. 1. The objective of the experiment is to subject the single crystal specimen to a single, one-dimensional plane pulse with a duration of 0.25 μsec or less. Prevention of reloading by reflected waves is a primary requirement of the experiment because differences between dislocation configurations before and after impact are to be interpreted as due to the one-dimensional plane pulse. The specimen is impacted in a vacuum chamber by a thin aluminum flyer plate mounted in front of a projectile that is accelerated in a launching tube with a bore diameter of 6.35 cm. The velocity of the projectile is measured to an accuracy of better than 1% by recording the times at which 5 wire pins of known separation are contacted by the steel projectile plate at the front of the projectile. The flyer plate is separated from the steel projectile plate by a stiff foam spacer. The acoustic impedance of the foam is less than 0.5% of that of the aluminum flyer so that reflection of the initial compression wave at the aluminum-foam interface is essentially the same as reflection at a free surface. The duration of the initial pulse propagated into the specimen is equal to the round-trip transit

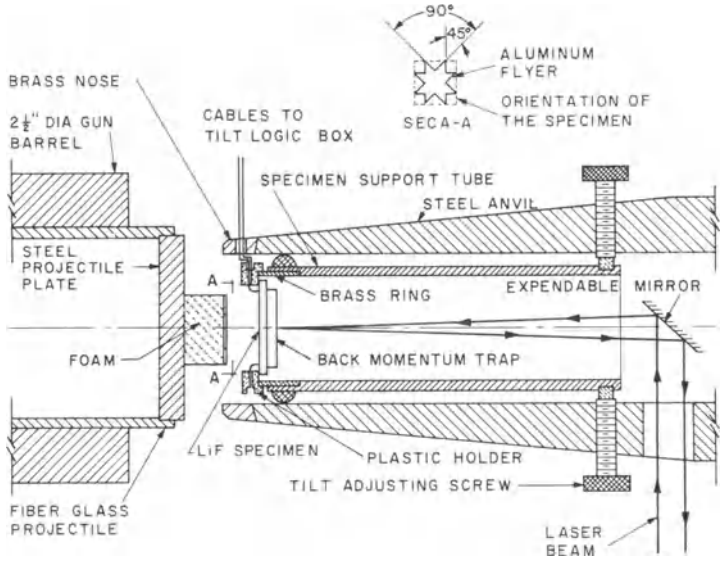

Fig. 1. Schematic of Single Crystal Recovery Experiment.

time for a longitudinal elastic wave in the flyer plate, provided that the acoustic impedance of the flyer is less than or equal to that of the specimen, and the yield strength of the flyer is high enough that yielding does not occur under the impact velocities employed. Both of the latter requirements are met for impact of high purity LiF crystals at projectile velocities less than 0.07 mm/μsec by using 6061-T6 aluminum flyer plates for which the acoustic impedance agrees with that of LiF to within 1%. The flyer plate has an eight-pointed star shape in order to prevent lateral release waves from influencing significantly the stress history in a central region of the crystal [10].

The single crystal specimen is a square plate of 99.9999% purity LiF, oriented for wave propagation along <100>. The specimen is backed by an impedance matching, unbonded, longitudinal momentum trap. As a result, the compression pulse generated by the flyer-specimen impact propagates into the momentum trap, reflects from the

free rear surface as a tensile pulse, and causes separation from the specimen when the reflected tensile pulse arrives at the unbonded interface. Under ideal conditions in which all plate faces are flat and parallel, all pieces are acoustically matched, and all pieces respond elastically, the specimen would be left at rest and unstressed. Subsequent, late impact of the specimen is prevented by stopping the projectile through impact of the projectile plate with the steel anvil. Thus, under ideal conditions the specimen remains in place and can be removed for examination of changes in dislocation configurations due to passage of the single pulse.

The ideal conditions listed here are, of course, not fully realized in actual experiments. However, actual experiments allow one to retain the principal feature of subjecting the specimen to a known pulse that leaves the crystal in place for subsequent examination of changes in dislocation configurations. Faces of the flyer, specimen, and momentum trap are made flat by lapping with a 3 micron alumina powder in a mineral oil. Periodic checking of the surfaces with a monochromatic light source and an optical flat allows production of surfaces with a flatness of approximately 1 light band per cm. The surface roughness is approximately 0.25 microns. Alignment of the impact faces by means of an optical technique [11] yields a parallelity at impact of better than 1×10^{-3} radians. This angular misalignment at impact is obtained from recorded times of contact of the flyer with conducting tabs of aluminum deposited on the impact face of the specimen [8]. The surface flatness and parallelity achieved are generally adequate for these deviations from ideal conditions to cause negligible adverse effects.

Deviations from ideal conditions that have the most effect on the experiments are those associated with inelastic deformation of the specimen and with stress wave transmission through the unbonded interface. The former is an inevitable consequence if the experiment is to be used to study the motion and generation of dislocations. However, the influence of dislocation motion on the pulse shape can be reduced by using crystals with low dislocation density and by using low amplitude, short duration pulses. To this end, initial dislocation densities are generally kept less than $5 \times 10^{4}/cm^{2}$

and the pulse amplitudes and durations are generally kept in a range where negligible decay is observed in non-recovery experiments on similar crystals. In addition, the pulse is monitored by means of a laser displacement interferometer [12] so that deviations between the actual pulse and the one predicted for ideal, elastic behavior are known.

The problem of achieving high fidelity stress wave transmission through the unbonded interface has proved to be difficult. One approach has been to lap the mating surfaces, ring them together, check the separation by observing Newton's rings due to interference of light reflected from the two surfaces, and bond the two pieces together with small drops of glue or foam at the corners. This approach has the drawback that an initial gap is left between the two faces. As a result, part of the compression pulse is reflected from the interface before the gap closes. This reflected wave then makes a round trip in the crystal and thereby subjects the crystal to a more complicated loading history than intended originally. However, once the gap closes and the reflected wave completes the round trip, essentially the entire pulse is transmitted to the momentum trap.

A second approach has been to put a thin layer of low viscosity (5 cp) silicone oil between the specimen and the momentum trap and assemble the pieces in a vacuum chamber at a pressure greater than the vapor pressure of the oil (~10 microns). (Again the assembled pieces are bonded at the edges by small drops of glue or foam to facilitate handling and maintain relative positions of the two pieces prior to impact.) This approach has the advantage that the leading part of the initial pulse is largely transmitted to the momentum trap so that the wave reflected back into the crystal has much smaller amplitude than for the case of a vacuum gap at the interface. However, it also has the disadvantage that the thickness and rheological properties of the oil are introduced as additional factors influencing the loading imposed on the specimen and the determination of that loading from the recorded motion of the free surface of the momentum trap. Examples of pulses obtained using both approaches are presented in the next section.

Plate Impact Results

The series of plate impact experiments on LiF crystals annealed at 600° C. consists largely of three types of experiments: (i) non-recovery, (ii) recovery--with a vacuum gap between specimen and momentum trap and (iii) recovery--with silicone oil between specimen and momentum trap. The non-recovery experiments differ from the recovery experiments in that no momentum trap is used and the motion of the specimen rear surface is monitored directly. Also, the flyer plates are generally circular and thicker (~3 mm) than for recovery experiments. Wave profiles for a series of experiments at different impact velocities are shown in Fig. 2. For linear elastic behavior of the flyer and the specimen the velocity of the free surface should jump to the projectile velocity and remain constant thereafter. Thus,

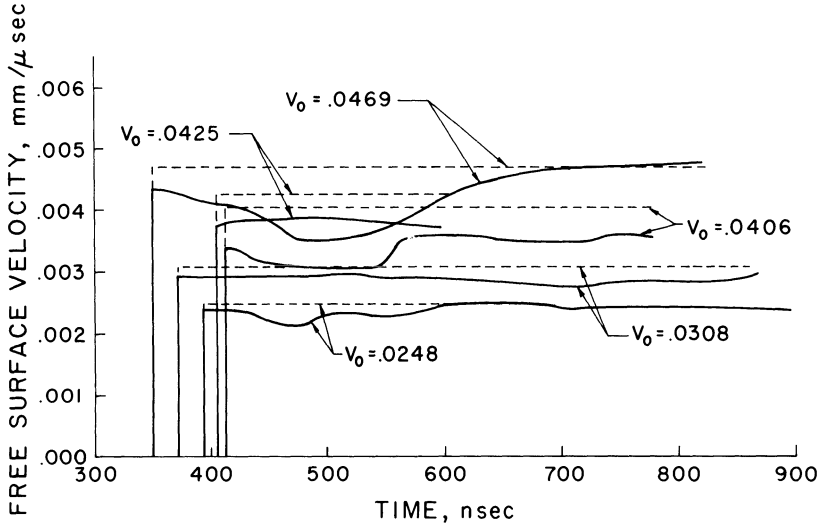

Fig. 2. Velocity-Time Profiles at Rear Surfaces of Specimens in Non-Recovery Experiments.

from Fig. 2 it appears that for impact velocities less than 0.03 mm/μsec and pulse durations less than 0.5 μsec the wave profiles show only minor deviations from those predicted for the linear elastic case. For impact velocities of 0.04 mm/μsec and larger there are clear signs of inelastic wave phenomena. On the basis of these experiments, the recovery experiments were designed for impact velocities less than 0.025 mm/μsec.

A typical velocity-time profile for a recovery shot without a substance between the specimen and momentum trap is shown in Fig. 3. The thickness of the flyer is such that the expected pulse duration is 250 nsec. However, because of an initial gap between the specimen and momentum trap, approximately 110 nsec of the pulse is reflected at the interface and only the remaining 140 nsec of the pulse appears in the main transmitted pulse. The remainder makes a round trip in the specimen and arrives at t = 1452. The tail following the main pulse and the second part of the reflected pulse increase nonlinearly with increasing projectile velocity and appear to be related to plastic deformation of the specimen. The longitudinal momentum transmitted to the momentum trap is equal to the area under the curve in Fig. 3 from t = 896 to t = 1765 times $(\rho c_l/2)$ where ρc_l is the acoustic impedance of aluminum. Measurement of this area indicates that the transmitted momentum is approximately 3.8% greater than the initial momentum of the flyer plate. This comparison provides a rough check of the measured velocity-time profiles and also indicates that the longitudinal momentum trap has effectively trapped nearly all of the longitudinal momentum.

A velocity-time profile for a recovery shot with silicone oil (5 centipoise viscosity) between the specimen and momentum trap is shown in Fig. 4 for the case of a projectile velocity comparable to that of Fig. 3. In Fig. 4 the duration of the initial pulse is approximately equal to the round trip transit time in the specimen. However, the amplitude of this pulse is approximately 15% less than expected from elastic wave theory. Another important difference between the velocity-time profile of Figs. 3 and 4 is the reduced amplitude and duration in Fig. 4 of the first part of the reflected

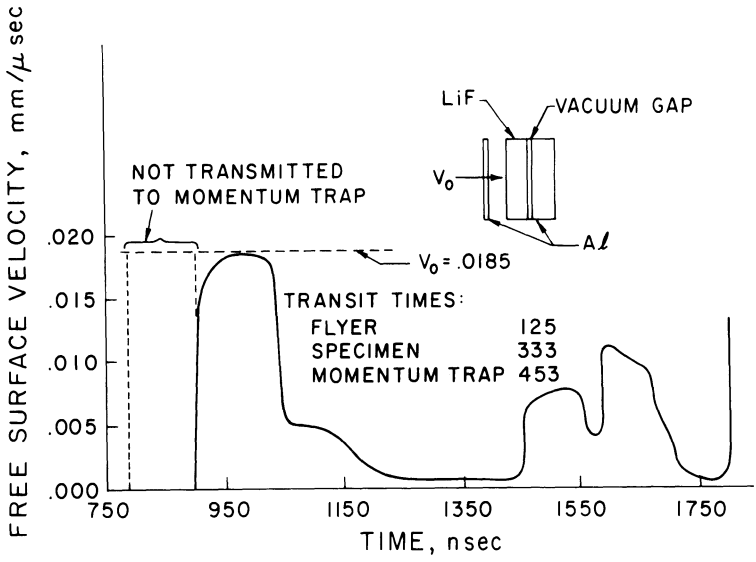

Fig. 3. Velocity-Time Profile at Rear Surface of Momentum Trap for Recovery Experiment with Vacuum Gap Between Specimen and Momentum Trap.

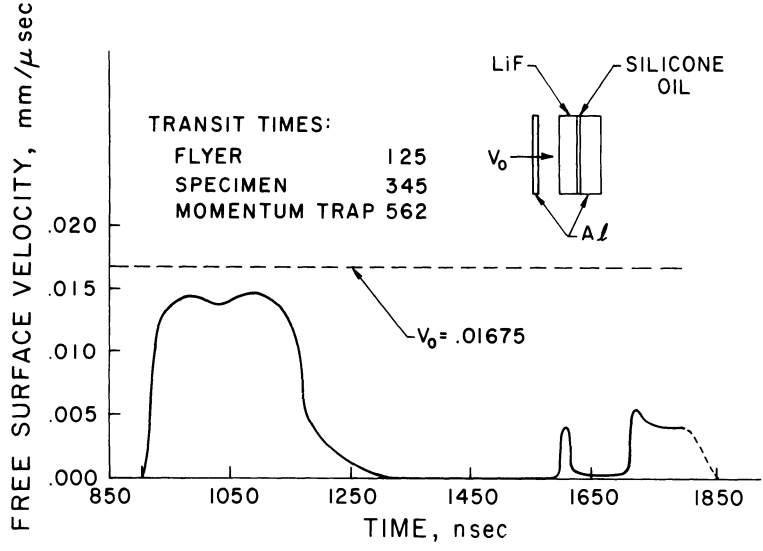

Fig. 4. Motion of Rear Surface of Momentum Trap Experiment with Silicone Oil Between Specimen and Momentum Trap.

pulse that arrives after a round trip in the specimen. This difference is of course due to more of the leading part of the initial pulse being transmitted through the oil layer to the momentum trap. Measurement of the area under the velocity-time profile in Fig. 4 from $t = 907$ to $t = 1850$ indicates that the momentum transmitted to the momentum trap is approximately 1.5% less than the initial momentum of the flyer plate. Thus, the LiF-Oil-Al configuration also allows nearly all of the momentum to be transferred to the momentum trap.

Dislocation Configurations Produced

In recovery experiments the specimen generally remains in position, supported by drops of glue or foam at the corners. Often, and especially at relatively high impact velocities, the specimen has a number (say 1-5) of cracks on (100) planes perpendicular to the impact face. In most cases when these cracks are present the specimen is separated into several pieces by cracks extending either all the way through the crystal or until they intersect another crack at right angles. The most common crack planes are the midplanes coinciding with lines joining opposing re-entrant corners of the star. Thus, when cracks develop they generally expose (100) planes in the central region of the crystal where dislocations are to be observed. If such planes are not exposed as a result of the impact experiment, then they are exposed afterwards by cleaving with a sharp chisel. In either case, dislocations produced during fracture remain near the fracture surface and are removed by using a 2% NH_4OH solution to dissolve a 5-10 μm thick surface layer.

Etch pits [13] marking the intersection of dislocations with an (001) face perpendicular to the impact face are shown schematically in Fig. 5. A schematic representation is used in order to enhance contrast for the photographic reproduction used for this book. However, the glide bands shown are the same as those in a particular experiment, except that individual etch pits in glide bands are not shown and the number of glide bands near the surfaces is reduced to keep the picture from appearing uniformly dark in these regions.

Interpretation of these glide bands is facilitated by noting that the primary slip systems in LiF consist of the six slip systems with {110} slip planes and <110> slip directions. In the central part of the crystal loaded by waves of one dimensional strain the two families of slip planes perpendicular to the impact face are unstressed whereas the other four slip systems are stressed equally. Evidence of glide band formation on all stressed slip systems is shown in Fig. 5, whereas there is no evidence of slip on the unstressed slip planes which intersect the surface shown along lines perpendicular to the impact face. Glide bands parallel, and at 45°, to the impact face correspond, respectively, to the intersection of screw and edge dislocation segments with the observed surface.

The dislocation configurations in Fig. 5 are characterized by long glide bands emanating from the boundaries and comparatively short glide bands in the interior. Furthermore, the lengths of interior edge and screw bands are approximately the same. In addition, there are a large number of individual dislocations that do not appear to be part of any glide band structure. Overall, the dislocation density in the middle third of the crystal is approximately $10^{6}/cm^{2}$ and increases to greater than $10^{7}/cm^{2}$ at the impact and rear surfaces. This is a marked increase in dislocation density from an initial density of $5 \times 10^{4}/cm^{2}$, except within 50 μm of the lapped surfaces where the density was greater than $5 \times 10^{7}/cm^{2}$.

The long glide bands can often be traced to regions of the impact and rear surfaces where scratches and/or foreign particles have contributed to glide band initiation. The lengths of these glide bands are frequently greater than the distance a dislocation could move if driven at sub-sonic velocities for the duration of the applied pulse. Furthermore, the lengths of bands emanating from front and rear surfaces are nearly the same even though forward moving dislocations emanating from the front surface remain under the driving force of the initial pulse significantly longer than backward moving dislocations emanating from the rear surface. For these reasons it is believed that the long glide bands are initiated to

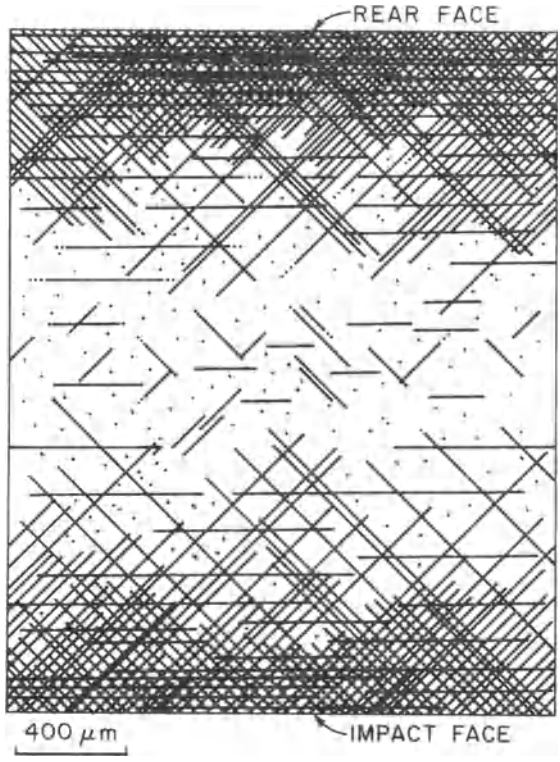

Fig. 5. Schematic of Etch Pits on (100) Face Perpendicular to Impact Face. (Recovery Experiment with Vacuum Gap; V_o = 0.0223 mm/μsec; Pulse Duration of 0.248 μsec)

accommodate geometric imcompatiblility of mating surfaces and that these glide bands continue to extend after the applied stress is removed due to the repulsive force between dislocations of like sign. Resistance to ejection of the dislocations at the boundary is provided by the opposing force resulting from the intersection of glide bands. The length of the long glide bands presumably increases with the number of dislocations necessary to accommodate the given incompatibility. It should also decrease with increasing yield stress, due to arrest of dislocations at higher stress levels. Partial confirmation of the latter hypothesis comes from experiments on hard irradiated crystals which have a much higher yield stress (more than tenfold) and resulted in much shorter glide bands (less than one tenth) emanating from the boundary even though the surface preparation was

the same as for annealed specimens and the recorded wave profiles were also similar to those for annealed specimens.

The interior glide bands contain, on the average, approximately 20 etch pits. If the outermost etch pits in the longer interior bands are viewed as marking the limits of the region swept out by the leading dislocation loop (circular loop in view of the equality of lengths of edge and screw bands), then the average velocity of the leading dislocation can be estimated by dividing the half-length of the glide band by the duration of the pulse. For this calculation it appears reasonable to take the pulse duration to be that of the initial pulse because of the relatively small amplitude and duration of the reflected pulses. Also, the reversal of sign of the resolved shear stress that occurs during reflection from the free front surface of the specimen tends to nullify the effect of reflected pulses on final loop diameter. For a glide band length of 0.23 mm and a pulse duration of 0.25 μsec the estimated average dislocation velocity is 0.46 mm/μsec or approximately 7% of the longitudinal elastic wave speed. Thus, the average dislocation velocities in these experiments appear to be small relative to those at which breakdown and relativistic effects are expected to play important roles.

An interesting insight into the rate controlling mechanism for dislocation motion in high purity LiF crystals at the stress levels of the experiments is obtained by substituting the experimentally determined dislocation velocity and resolved shear stress into the model for linear drag on a dislocation:

$$\tau b = Bv \qquad (1)$$

where τ is the resolved shear stress (approximately 0.6 Kbar for the initial pulse in the experiment corresponding to Fig. 5), b is the Burgers vector ($b = 2.84 \times 10^{-8}$ cm fo LiF), v is the dislocation velocity and B is the drag coefficient. The resulting value of the drag coefficient is $B = 3.7 \times 10^{-4}$ dyne-sec/cm^2, which is comparable to values obtained in ultrasonic attenuation experiments [14-16]. This suggests that the dominant mechanism controlling the motion of dislocations in the plate impact recovery experiments is

the intrinsic resistance of the clear lattice, as in the case of the small amplitude vibration of dislocations in ultrasonic attenuation studies. More detailed interpretation of the recovery experiments awaits the development of constitutive models that incorporate the main features of the dislocation configurations shown in Fig. 5. In particular, more realistic models of the behavior of groups of dislocations appear to be required. These models should relate the dislocation line length per unit volume to the density of loop centers and the diameters of loops. The dislocation density at any position should include contributions from expanding loops nucleated in other regions. Furthermore, the modelling of the interaction of dislocation loops through their long range stress fields appears important for an adequate description of glide band formation. The wave profiles and dislocation configurations obtained in plate impact recovery experiments comprise a rich data base for excluding unsatisfactory constitutive models.

Acknowledgements

Support by the National Science Foundation through Grant ENG 76-01426 is gratefully acknowledged, as well as support from the NSF Materials Research Laboratory at Brown University.

References

1 Johnson, J. N.; Jones, O. E.; Michaels, T. E.: Dislocation Dynamics and Single-Crystal Constitutive Relations: Shock-Wave Propagation and Precursor Decay. J. Appl. Phys. 41 (1970) 2330-2339.

2 Hermann, W.; Hicks, D. L.; Young, E. G.: Attenuation of Elastic-Plastic Stress Waves. Shock Waves and the Mechanical Properties of Solids (J. J. Burke and V. Weiss eds.). Syracuse: Syracuse University Press 1971.

3 Study, P.L.; Nidick, E.; Uribe, F.; Mukherjee, A. K.: Effects of Microstructure and Temperature on Dynamic Deformation of Single Crystal Zinc. Metallurgical Effects at High Strain Rates. New York: Plenum 1973.

4 Gupta, Y. M.; Duvall, G. E.; Fowles, G. R.: Dislocation Mechanism for Stress Relaxation in Shocked LiF. J. Appl. Phys. 46(1975) 532-546.

5 Weertman, J.: Dislocation Mechanics at High Strain Rates. Metallurgical Effects at High Strain Rates. New York: Plenum 1973.

6 Weiner, J. H.; Pear, M.: Breakdown in High-Speed Edge Dislocation Motion. Phil. Mag. 31 (1975) 679-688.

7 Flinn, J. E.; Duvall, G. E.; Tinder, R. F.: Dislocation Multiplication in Lithium Fluoride Single Crystals under Impact Loading. J. Appl. Phys. 46 (1975) 3752-3749.

8 Kumar, P.: An investigation of Dislocation Motion and Generation in LiF Single Crystals Subjected to Plate-Impact. Ph.D. Thesis, Brown University, May 1976.

9 Clifton, R. J.: Some Recent Developments in Plate Impact Experiments. Propagation of Shock Waves in Solids. New York, ASME 1976.

10 Kumar, P.; Clifton, R. J.: A Star-Shaped Flyer for Plate Impact Recovery Experiments. J. Appl. Phys. 48 (1977) to appear.

11 Kumar, P.; Clifton, R. J.: Optical Alignment of Impact Faces for Plate Impact Experiments. J. Appl. Phys. 48(1977) 1366-1367.

12 Barker, L. M.; Nollenbach, R. E.: Interferometer Technique for Measuring the Dynamic Mechanical Properties of Materials. Rev. Sci. Instr. 36 (1965) 1617 - 1620.

13 Gilman, J. J.; Johnston, W. G.: The Origin and Growth of Glide Bands in Lithium Fluoride Crystals. Dislocations and Mechanical Properties of Crystals. New York, Wiley 1957.

14 Fanti, F.; Holder, J.; Granato, A. V.: Viscous Drag on Dislocations in LiF and NaCℓ. J. Acoust. Soc. Amer. 45 (1969), 1356-1366.

15 Suzuki, T.; Ikushima, A.; Aoki, M.: Acoustic Attenuation Studies of the Frictional Force on a Fast Moving Dislocation. Acta Met. 12 (1964) 1231- 1240.

16 Mitchell, O. M. : Drag on Dislocations in LiF. J. Appl. Phys. 36 (1965) 2083 - 2084.

Experimental Studies on the Behaviour of Dislocations in Copper at High Rates of Strain

J. SHIOIRI, K. SATOH and K. NISHIMURA*

Department of Aeronautics, Faculty of Engineering, University of Tokyo.
Bunkyo-Ku, Tokyo, Japan.
* Now, Nippon Steel Corporation.

Summary

Two experimental works concerning the behaviour of dislocations at high rates of strain in polycrystalline OFHC copper are reported. The first work is time resolved measurements of the ultrasonic attenuation and velocity in specimens undergoing dynamic deformation. The highest strain rate imposed was about 80 /sec. From the ultrasonic data the density of the mobile dislocations was estimated as a function of the strain rate. The second work is measurements of the flow stress in a strain rate range from 1×10^3 to 2.5×10^4 /sec and at 293°, 573° and 773° K. A sharp increase in the strain rate sensitivity which means a transition in the rate controlling mechanism appeared at a strain rate of about 1×10^4 /sec. The behaviour of dislocations in this transition range is discussed.

Introduction

In fcc metals such as copper and aluminium, the intrinsic drag on dislocations is given in a linear form [1]:

$$v = \tau b / B \ , \qquad (1)$$

where v is the velocity of a dislocation, τ is the resolved shear stress, b is the Burgers vector, and B is the dislocation damping constant. Since the value of B is very small, in the strain rate range lower than about

10^3 /sec, the dominant rate controlling mechanism for dislocation motion is not the above drag but a thermally aided cutting of localized extrinsic obstacles. At least in case of pure metals, the dominant obstacles may be the forest dislocations. A simplified analysis given by Seeger [2] interprets the existing experimental results [3,4] fairly well. However, there is a possibility that the actual process is more complicated. The experimental results by Edington [5] indicate that the cell structure of dislocations should be considered. On the other hand, when the strain rate is higher than about 10^3 /sec, it has been reported very often that the strain-rate sensitivity of the flow stress increases rapidly. Many investigators have attributed it to an explicit appearance of the intrinsic drag [4], while a question has been raised by Lindholm [6] concerning the experimental technique in such a very high strain rate range.

In this paper, two experimental works are presented. The first one is time resolved measurements of the ultrasonic attenuation and velocity in polycrystalline OFHC copper specimens undergoing dynamic deformation. The second one is measurements of the flow stress in the strain-rate range where the transition in the rate controlling mechanism is expected to appear. The material of specimens was again polycrystalline OFHC copper, and measurements were made at widely different temperatures.

Ultrasonic Experiment

1. Experimental

In order to develop a more direct method of detecting the behaviour of dislocations than the flow stress measurement, two of the present authors [7] have tried time resolved measurements of the ultrasonic attenuation and velocity changes in specimens undergoing dynamic defor-

mation. However, the analysis of the experimental results given in the previous papers was not necessarily satisfactory. In this paper, a somewhat detailed discussion will be presented together with an outline of the method and results of the experiment.

The devised ultrasonic apparatus has a resolution time of about 10 μsec. Set-up around the specimen is shown in Fig.1. The ultrasonic frequency was 11 MHz. Measurements were made on polycrystalline OFHC copper vacuum annealed at 700° C for 3 hr. The highest strain rate imposed was 83 /sec. The results on the ultrasonic attenuation and velocity changes induced by deformation are shown in Fig.2, and summarized as follows:

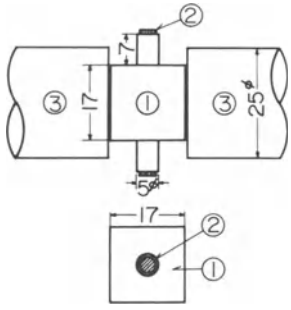

Fig.1. Set-up around specimen. (size in mm)

1. Specimen.
2. X-cut quartz transducers.
3. Hopkinson pressure bars.

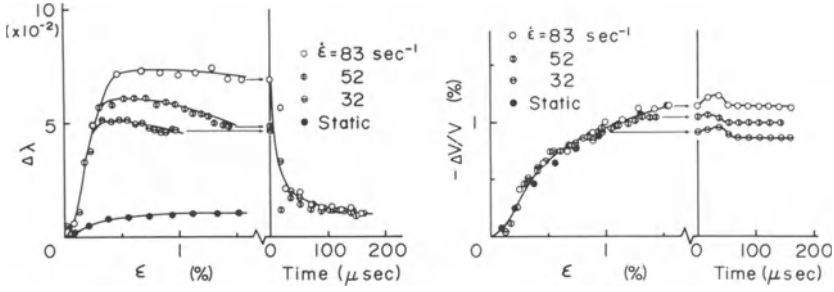

Fig.2. Ultrasonic attenuation and velocity changes, $\Delta\lambda$ and $\Delta V/V$ respectively, against strain ε and time after deformation.

(i) during deformation, the attenuation change $\Delta\lambda$ is strain-rate sensitive, whereas the velocity change $\Delta V/V$ is not;

(ii) after dynamic deformation, $\Delta\lambda$ rapidly falls near to the value under static deformation, whereas $\Delta V/V$ shows no remarkable change;

further, from (i) and (ii)

(iii) $\Delta\lambda$ and $\Delta V/V$ after deformation are insensitive to the previous strain rate;

(iv) $\Delta\lambda$ and $\Delta V/V$ can be divided into rate sensitive and rate insensitive parts, but the rate sensitive part of $\Delta V/V$ is negligibly small.

The above rate sensitivities of $\Delta\lambda$ and $\Delta V/V$ were confirmed by changing the strain rate $\dot{\varepsilon}$ stepwise [7].

2. Discussion

Edington [5] reported that the cell structure of dislocations was formed in dynamic deformation as well as in static deformation. The foregoing summary (iii) of the experimental results corresponds with the above Edington's result. In the following analysis, formation of the cell structure in dynamic deformation will be postulated. In the present experiment the strain is small, but Göttler [8] pointed out formation of the cell structure from a very early stage of deformation.

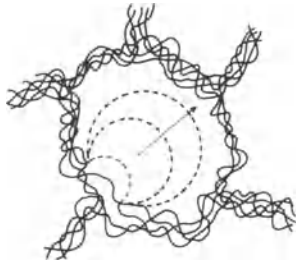

Fig.3. Cell structure.

---- Mobile dislocations
——— Cell wall dislocations

Under the cell structure, as shown in Fig.3, plastic deformation is caused by the glide motion of the mobile dislocation loops, which bow out from the cell wall and move across the interior of the cell until they are absorbed again into the cell wall. The strain rate in this deformation process is given by

$$\dot{\varepsilon} \propto \dot{n} a_c b \quad , \tag{2}$$

where $\dot{n}$ is the emission rate of mobile dislocation loops from the cell wall, a_c is the cross-sectional area of the cell. The emission of mobile dislocation loops may be thermally aided process.

The rate controlling mechanism in the glide motion of mobile dislocation loops may be the intrinsic drag given by (1). Therefore, the lifetime of mobile dislocation loops, the time required for crossing the cell interior, may depend upon the stress. However, in case of fcc metals, the strain rate dependence of the flow stress in the strain rate range lower than about 10^3 /sec is very small, and, accordingly, the lifetime of mobile dislocation loops will depend upon the strain rate very weakly. On the contrary, as is given by (2), the emission rate of mobile dislocation loops, $\dot{n}$, should be proportional to the strain rate. Thus, the instantaneous density of mobile dislocation loops may be nearly proportional to the strain rate. Now, by putting together the foregoing summary (iv) of the experimental results with the above consideration, it may be concluded that the rate sensitive parts of $\Delta\lambda$ and $\Delta V/V$ are the contribution of the mobile dislocation loops while the rate insensitive parts are that of the cell wall dislocations.

In Granato-Lücke's theory [9], a dislocation is simulated by an elastic string. In case of the cell wall dislocations, the loop length between adjacent tangle nodes is very small. Accordingly, the contribution of the cell

wall dislocations to $\Delta\lambda$ and $\Delta V/V$ can be given by the low frequency approximation of Granato-Lücke's theory;

$$\Delta\lambda = \Omega\Lambda L^4 B\omega t_1/\pi^3 C \qquad -\Delta V/V = \Omega\Lambda L^2 t_2/2\pi^2 \ , \qquad (3)$$

where Λ and L are the density and mean loop length of dislocations, respectively; ω is the circular frequency of the ultrasonic wave; t_1 and t_2 are constants determined by the distribution function of the loop length; Ω is a factor determined by the orientation of the slip system; B and C ($=\frac{1}{2}Gb^2$) are the damping constant and line tension of a dislocation, respectively, and G is the modulus of rigidity.

In case of the mobile dislocation loops the motion due to the ultrasonic stress is superimposed upon the main motion. For simplicity, the following assumptions are made:

(a) the lifetime of the mobile dislocation loops is sufficiently longer than the ultrasonic period;
(b) the intrinsic drag which is the rate controlling mechanism of the mobile dislocation loops is linear as is given by (1).

On the above assumptions, Granato-Lücke's theory may be applicable in its original form. Though the mobile dislocation loops are not necessarily long enough, their natural frequency at the critical position for bowing out (Fig.3) is zero, and after the critical position is passed the frequency turns imaginary. Thus, for the contribution of the mobile dislocation loops the high frequency approximation of Granato-Lücke's theory may hold;

$$\Delta\lambda = \pi\Omega\Lambda C/B\omega \ , \qquad \Delta V/V = 0 \ . \qquad (4)$$

Göttler [8] pointed out that the cell wall dislocations are distributed over all the slip systems nearly equally while the mobile loops belong mostly to the primary slip system. On these conditions, the orientation factor Ω is derived as follows:

for cell wall dislocations

$$\Omega = (E/15G)(1 - 2\nu)/(1 - \nu^2) \ , \qquad (5)$$

for mobile dislocation loops

$$\Omega = (3E/32G)(1 - 2\nu)/(1 - \nu^2) \ , \qquad (6)$$

where E is Young's modulus and ν is Poisson's ratio. The above derivation was made for polycrystalline materials by taking an average with respect to the orientation of the grains. The Schmid factor of the primary slip system with respect to the main compression axis was assumed to be 0.5, and the direction of the ultrasonic wave transmission shown in Fig.1 was taken into account.

Table 1. Density and mean loop length of cell wall dislocations and density of mobile dislocation loops. (strain $\varepsilon = 0.01$)

Cell wall dislocations	Mobile dislocation loops	
	strain rate /sec	Λ /cm^2
$\Lambda = 1.2 \times 10^9$ /cm^2	32	2.3×10^7
	52	2.9×10^7
$L = 2.0 \times 10^{-5}$ cm	83	4.0×10^7

The density and mean loop length of the cell wall dislocations can be evaluated by substituting (5) and the experimental data of the rate insensitive parts of $\Delta\lambda$ and $\Delta V/V$ into (3). Similarly, the density of the mobile dislocation loops is obtained from (4), (6) and the experimental data of the rate sensitive parts of $\Delta\lambda$ and $\Delta V/V$. The experimental fact that the rate sensitive part of $\Delta V/V$ is negligibly small [summary (iv) of experimental results] coincides with the second equation of (4). Some of the results are shown in Table 1. For the constants and moduli the following values were used: $B = 7 \times 10^{-4}$ dyn·sec/cm^2 [1], $t_1 = 120$ and $t_2 = 6$ [9], $\nu = 0.35$, $E = 1.23 \times 10^{12}$ dyn/cm^2, $G = 0.4 \times 10^{12}$ dyn/cm^2. The values of the density and mean loop length of the cell wall dislocations and the density of the mobile dislocation loops seem accept-

able. In Fig.4, the density and mean loop length of the cell wall dislocations in the static deformation and after the dynamic deformation are plotted against strain. The strain dependencies of the density and mean loop length are also reasonable.

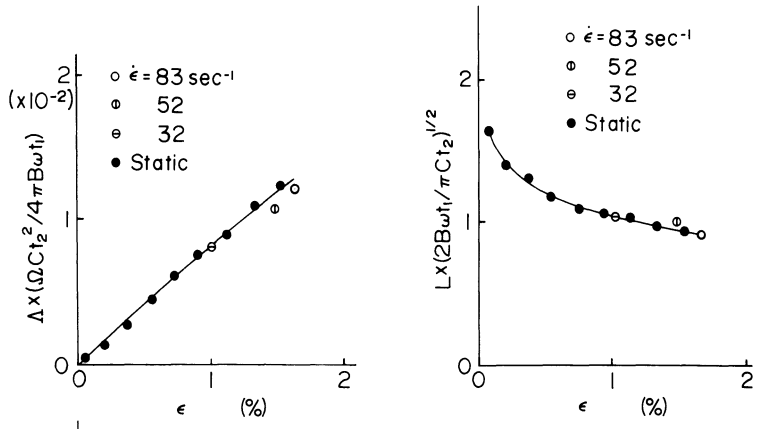

Fig.4. Density and mean loop length of cell wall dislocations against strain ε. Density Λ and loop length L are shown in non-dimensional forms.

The above analysis of the data was made postulating the formation of the dislocation cell structure. On the other hand, if this is not the case, the mobile dislocations should cut through an array of the forest dislocations with the aid of thermal activation. If the density of the dislocations is not so low, the lifetime of the mobile dislocation loops, the time required for one jump motion, may be negligibly short compared with the ultrasonic period. In this case, $\Delta\lambda$ and $\Delta V/V$ may be given by

$$\Delta\lambda = \frac{\pi\Omega G \left(\frac{d\dot{n}}{d\tau}\right)_{\tau=\tau_0} a_j b}{\omega} \qquad \Delta V/V = 0 \quad , \qquad (7)$$

where $\dot{n}$ is the rate at which a thermally aided jump of the mobile dislocation loops occurs per unit volume, a_j is the area swept by a mobile dislocation loop in one

jump, τ_0 is the resolved shear stress due to the main compression. It must be noted that $\Delta V/V$ is again zero. Equations (4) and (7) represent two extreme cases. In order to identify the actual process further experiments especially at different ultrasonic frequencies and temperatures seem necessary.

Flow Stress Measurement

1. Experimental

Flow stress measurements over a strain rate range from 1×10^3 to 2.5×10^4 /sec were performed on polycrystalline OFHC copper at 293°, 573° and 773° K with the split Hopkinson pressure bar method. Small specimens, 2 mm both in diameter and length , were used. The above size and diameter-length ratio were adopted to minimize the effects of the inertia and the end surface friction. A schematic diagram of the apparatus is shown in Fig.5. The pressure bars were made of maraging steel and their diameter was 10 mm. Specimens were vacuum annealed at 650° C for 3 hr after machining.

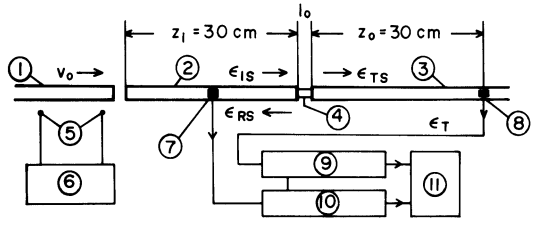

Fig.5. Schematic diagram of the split Hopkinson pressure bar apparatus.

1. Impact bar. 2. Incident bar. 3. Transmitter bar. 4. Specimen. 5. Position sensors. 6. Electronic counter. 7, 8. Strain gauges. 9, 10. Digital memories with a common quartz controlled time base. 11. Pen recorder.

In tests at very high strain rates, the effect of the geometrical dispersion of elastic waves in the pressure bars becomes significant. Miklowitz [10] showed that when a step velocity $S(t)V_0$ or a step pressure $S(t)P_0$ is imposed upon one end of a circular elastic bar, where $S(t)$ is the Heaviside function, the axial strain $\varepsilon_{zz}(t)$ at a long distance z from the end can be approximated by essentially the same form,

$$\varepsilon_{zz}(t) \approx \frac{V_0}{c_0} F[\frac{z}{a}, \frac{c_0 t}{a}] \quad \text{or} \quad \varepsilon_{zz}(t) \approx \frac{P_0}{E} F[\frac{z}{a}, \frac{c_0 t}{a}] \quad , \qquad (8)$$

where

$$F[\frac{z}{a}, \frac{c_0 t}{a}] = \frac{1}{3} + \int_0^D A_i(-\xi) d\xi \quad , \qquad D = (\frac{4}{3\nu^2 z/a})^{\frac{1}{3}} (\frac{c_0 t}{a} - \frac{z}{a}) \quad ,$$

$A_i(\ )$ is the Airy function, c_0 is the velocity of the longitudinal wave in a thin bar, $2a$ is the diameter of the bar, E and ν are respectively Young's modulus and Poisson's ratio. Further, Kennedy and Jones [11] pointed out that the effect of the non-uniformity in the pressure distribution on the end surface is not so significant when $z/a >$ 40 (the dynamic Saint-Venant's principle).

In the split Hopkinson pressure bar apparatus, if the inertia of the specimen is neglected

$$\varepsilon_{IS}(t) + \varepsilon_{RS}(t) = \varepsilon_{TS}(t) \qquad (9) \qquad \dot{\varepsilon}(t) = -(2c_0/l_0)\varepsilon_{RS}(t), \qquad (10)$$

where ε is the strain of the specimen, ε_{IS}, ε_{RS} and ε_{TS} are respectively the strain amplitudes of the incident, reflected and transmitted pulses at the specimen side ends of the pressure bars and l_0 is the length of the specimen. From (8)

$$\varepsilon_{IS}(t) = \frac{v_0}{2c_0} F[\frac{z_i}{a}, \frac{c_0 t}{a}] \quad , \qquad (11)$$

where v_0 is the impact bar velocity and z_i is the length of the incident bar. If the flow stress of the specimen is given by

$$\sigma = f(\varepsilon, \dot{\varepsilon}) \quad , \tag{12}$$

the output of the transmitter bar strain gauge, $\varepsilon_T(t)$, to be obtained experimentally is derived utilizing (8) in the form of the Duhamel integral

$$\varepsilon_T(t) = \int_0^t F\left[\frac{z_0}{a}, \frac{c_0(t - t_1)}{a}\right] \frac{d}{dt_1}\varepsilon_{TS}(t_1)\,dt_1$$
$$\varepsilon_{TS}(t) = \frac{A_0}{EA} f\,[\varepsilon(t), \dot{\varepsilon}(t)][1 + \varepsilon(t)] \quad , \tag{13}$$

where z_0 is the distance from the specimen end to the transmitter bar gauge and A_0 and A are respectively the cross-sectional areas of the specimen and the transmitter bar. For determining $f(\varepsilon, \dot{\varepsilon})$, evaluation of $\varepsilon_{TS}(t)$ from measured $\varepsilon_T(t)$, i.e. inversion of the first equation of (13), becomes necessary. In actual practice, by assuming $f(\varepsilon, \dot{\varepsilon})$ in the form of

$$\sigma = f(\varepsilon, \dot{\varepsilon}) = K(\dot{\varepsilon})\sqrt{\varepsilon} \quad , \tag{14}$$

$K(\dot{\varepsilon})$ was determined by fitting $\varepsilon_T(t)$ calculated utilizing from (9) to (14) to the experimental $\varepsilon_T(t)$. In the above procedure, $K(\dot{\varepsilon})$ was considered a function of the nominal strain rate, and the following time lags were taken into account. The first one is due to the inertia effect of the specimen, and was assumed equal to l_0/c_{0s}, where c_{0s} is the longitudinal wave velocity in the specimen. The second one is the effect of the local temperature rise of the pressure bars in the high temperature tests. The amount of this lag was evaluated comparing the results of the test impacts at the room and elevated temperatures. A further lag was observed, which is roughly inversely-proportional to the impact velocity v_0. Its amount was about 0.5 μsec for $v_0 = 52.17$ m/sec. Presumably, this lag is due to imperfect contact at the specimen and pressure bar interfaces.

The above method based upon (14) gives a first approxima-

tion to $f(\varepsilon, \dot{\varepsilon})$. A second approximation was obtained by evaluating directly $\varepsilon_{TS}(t)$ from the experimental $\varepsilon_T(t)$ utilizing the relationship between $\varepsilon_{TS}(t)$ and $\varepsilon_T(t)$ calculated with the first approximation to $f(\varepsilon, \dot{\varepsilon})$. However, the difference between the obtained results was not so significant, and this implies that (14) is a fairly good assumption at least for copper.

In Fig.6, the incident and the first reflected waves in the incident bar under free end condition are plotted in

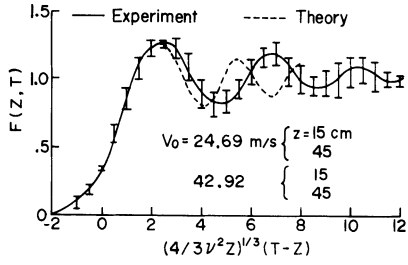

Fig.6. Experimental and theoretical $F[Z, T]$.

$$Z = \frac{z}{a}, \quad T = \frac{c_0 t}{a}.$$

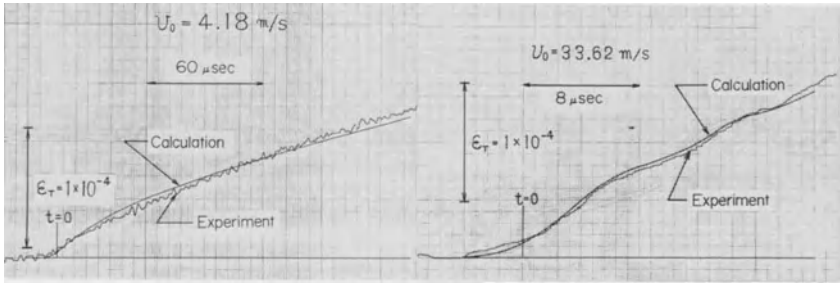

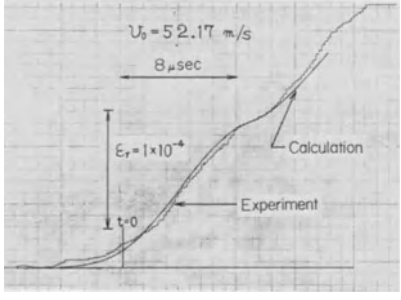

Fig.7. Examples of the output of the transmitter bar strain gauge, $\varepsilon_T(t)$. Calculated curves are also shown. (293° K)

the form of $F[\frac{z}{a}, \frac{c_0 t}{a}]$ for two different impact velocities. The broken curve is a theoretical one given by (8). In the data analysis, an experimentally determined function was used. From these measurements, c_0 in the pressure bar was also determined.

Examples of the experimental $\varepsilon_T(t)$ are shown in Fig.7. In Fig.8, the experimental values of the flow stress σ at $\varepsilon = 0.20$ obtained through the foregoing data analysis procedure are plotted against the strain rate $\dot{\varepsilon}$. The strain rate sensitivity of the flow stress changes abruptly at a strain rate of about 1×10^4 /sec.

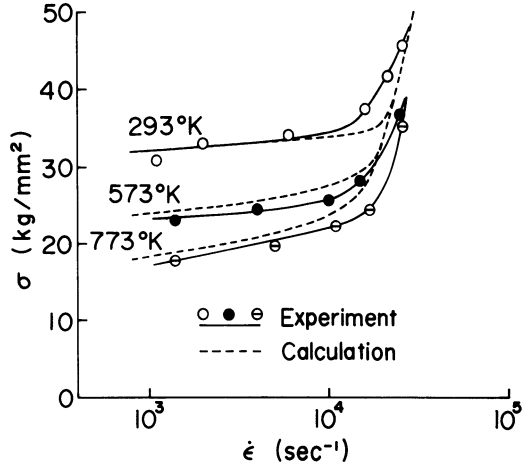

Fig.8. Flow stress σ against strain rate $\dot{\varepsilon}$. ($\varepsilon = 0.20$)

2. Discussion

In Fig.7, in order to examine the function of the apparatus together with the validity of the data analysis procedure, $\varepsilon_T(t)$ calculated utilizing from (9) to (14) is compared with the experimental one. In this figure $t = 0$ indicates the time when the non-dispersive wave front would arrive, where the foregoing time lags are taken into account. In this calculation, $K(\dot{\varepsilon})$ in (14) was

regarded as a function of the instantaneous strain rate instead of the nominal strain rate and determined from the experimental flow stress at $\varepsilon = 0.20$ shown in Fig.8. A slight systematic deviation presumably caused by the assumed strain dependence of the nominal flow stress, $\sqrt{\varepsilon}(1+\varepsilon)$, is observed. It was recognized from the calculation that the wavy shape of $\varepsilon_T(t)$ seen in cases of very high strain rate is due to the shape of the dispersion function $F[\ ]$. In spite of a large area mismatch between the specimen and the pressure bars in the present experiment, $\varepsilon_T(t)$ calculated with $F[\ ]$ for no area mismatch follows the wavy shape of the experimental $\varepsilon_T(t)$ fairly closely.

Kumar and Kumble [12] derived the average velocity of a dislocation moving across a forest of dislocations in the form of

$$v = \frac{a l^{-1}}{\nu^{-1}\exp[(U_0 - l b^2 \tau^*)/kT] + aBl^{-1}/\tau^{**}b} \quad , \tag{15}$$

where l is the distance between the forest dislocation, a is the area swept by a dislocation loop after cutting a forest dislocation, ν is the frequency factor, U_0 is the activation energy, k is Boltzmann's constant, T is the absolute temperature, and τ^* and τ^{**} are shear stresses. The first term in the denominator is the time necessary for a thermally aided cutting of a forest dislocation, and the second is the time required for one jump under the control of the intrinsic drag (1). When the strain rate is very high, there is a possibility that a thermally aided cutting at one intersection point successively causes an athermal cutting at the adjacent intersection points and thus a long free loop is formed as a result of one thermal event. Further, when such a long loop intersects a forest dislocation during its motion, there is also a possibility that the forest one is cut athermally and therefore such a long loop has a large free

path length. If the length of such a loop and that of free path are respectively given by nl and $\frac{1}{2}nl$, the shear strain rate becomes

$$\dot{\gamma} = \frac{\frac{1}{2}N(nl)^2 b}{(n\nu)^{-1}\exp[(U_0 - lb^2\tau_e)/kT] + nlB/2\tau_e b} \quad , \tag{16}$$

where $\tau_e = \tau - \tau_G$, τ is the flow stress, τ_G is the long range back stress and Nnl is the density of the mobile dislocations. The thermal activation term should be put equal to zero when $U_0 - lb^2\tau_e < 0$, but since the frequency factor ν is very large ($\approx 10^{13}$ /sec), (16) holds mathematically through the whole range of $\tau_e > 0$. Equation (16) can describe the transition in the rate controlling mechanism according as

$$(n\nu)^{-1}\exp[(U_0 - lb^2\tau_e)/kT] \gtrless nlB/2\tau_e b \quad . \tag{17}$$

Kumar and Kumble considered τ^* and τ^{**} in (15) assuming the thermal and phonon damping components of stress to be additive, while, in the present treatment, it was assumed that the same force $\tau_e b$ acts per unit length of a mobile dislocation whether it is captured by the forest dislocations or moving freely.

The calculated curves shown in Fig.8 are obtained from (16) by putting $U_0 (\approx \frac{1}{2}Gb^3) = 40$ kcal/mol, $l = 2.5 \times 10^{-6}$ cm, $n = 20$, $B = 7 \times 10^{-4}$ dyn·sec/cm^2 [1], $b = 2.5 \times 10^{-8}$ cm, $Nnl = 2.7 \times 10^7$ /cm^2, $\tau_G = 0$, $\dot{\gamma} = 2\dot{\varepsilon}$ and $\sigma = 2\tau$. A fairly good agreement with the experimental results is seen, but further work seems necessary to attribute conclusively the experimentally observed change in the strain rate sensitivity to the explicit appearance of the intrinsic drag.

In the above analysis, after Kumar and Kumble's treatment, a distributed array of the forest dislocations was assumed. The possibility of the formation of the dislocation cell structure and its effects, if it is formed, in the very high strain rate range are important subjects to be studied.

Conclusions

1. The ultrasonic wave method can provide time-resolved information on dislocation behaviour under dynamic deformation. Experimental results on copper in the strain rate range up to about 1×10^2 /sec seem to suggest a possibility of the formation of the cell structure. Assuming the cell structure formation, the following conclusion was drawn from the ultrasonic data: the density of the cell wall dislocations does not depend upon the strain rate, while that of mobile dislocation loops increases with an increase in the strain rate. In order to obtain more decisive information, measurements over a wide range of ultrasonic frequency seem necessary.

2. The results of the flow stress measurements on copper at 293°, 573° and 773° K show an abrupt change in the rate sensitivity at a strain rate of about 1×10^4 /sec. An analysis based upon the mobile dislocation motion controlled alternately by the thermally aided cutting of the forest dislocations and the intrinsic drag during jumping motions seems to account for the experimental strain rate sensitivity in the above transition region. However, it is difficult to say that a conclusion has been reached concerning the identification of the rate controlling mechanisms.

Figures 1 and 2 are reproduced from Ref.[7] by courtesy of Institute of Physics.

References

1 Vreeland, T., Jr.: Dislocation velocity in copper and zinc. A. R. Rosenfield; G. T. Hahn; A. L. Bement, Jr.; R. I. Jaffee (eds.): Dislocation Dynamics. McGraw Hill, New York, 1968, 529-549.

2 Seeger, A.: The mechanism of glide and work hardening in face-centered cubic and hexagonal close-packed

metals. J. C. Fisher; W. G. Johnston; R. Thomson; T. Vreeland, Jr. (eds.): Dislocations and Mechanical Properties of Crystals. Wiley, New York, 1957, 243-329.

3 Lindholm, U. S. ; Bessay, R. L. : A survey of rate dependent strength properties of metals. Technical Report AFML-TR-69-119. Air Force Materials Laboratory, Wright-Patterson Air Force Base, Ohio, 1969.

4 Campbell, J. D.: Dynamic plasticity, macroscopic and microscopic aspects. Mat. Sci. Eng. 12 (1973) 3-21.

5 Edington, J. W.: The influence of strain rate on the mechanical properties and dislocation structure in deformed copper single crystals. Phil. Mag. 19 (1969) 1189-1206.

6 Lindholm, U. S.: Review of dynamic testing techniques and material behaviour. Conference Series No. 21. Institute of Physics, London, 1974, 3-21.

7 Shioiri, J.; Satoh, K.: An ultrasonic wave study of the behaviour of dislocations under high strain rate deformations. Conference Series No. 21. Institute of Physics, London, 1974, 154-162.

8 Göttler, E.: Versetzungsstruktur und Verfestigung von [100]-Kupfereinkristallen (I. Versetzungsanordnung und Zellstructur zugverformter Kristalle). Phil. Mag. 28 (1973) 1057-1076.

9 Granato, A.; Lücke, K.: Theory of mechanical damping due to dislocations. J. Appl. Phys. 27 (1956) 583-593.

10 Miklowitz, J.: On the use of approximate theories of an elastic rod in problems of longitudinal impact. Proc. 3rd U. S. National Congress of Applied Mechanics. ASME, 1958, 215-224.

11 Kennedy, L. W.; Jones, O. E.: Longitudinal wave propagation in a circular bar loaded suddenly by a radially distributed end stress. J. Appl. Mech. (Trans. ASME, E) 91 (1969) 470-478.

12 Kumar, A.; Kumble, R. G.: Viscous drag on dislocations at high strain rates in copper. J. Appl. Phys. 40 (1969) 3475-3480.

Dislocation Concepts in the Mechanics of Rapid Deformation of Metals

R.I.NIGMATULIN and N.N.KHOLIN

Institute of Mechanics
Moscow University, USSR

Summary

Inelastic behaviour of metals and alloys has been investigated in a wide range of variation of strain rates. An equation has been proposed for the rate of formation of dislocations in which all possible mechanisms for the production and annigilation of dislocations have been taken into account. The possibility for a common description of static and dynamic experiments on the basis of certain mechanism of propagation and multiplication of dislocations has been examined. The problems of quasi-static compression in short rods at a constant strain rate, propagation of Luders front in rods, propagation of elastoplastic waves in rods and plates have been numerically solved. Using the models developed, two stages in the creep and superplastic deformation in metals and alloys of fine-grain structure have been studied.

Governing relationships

We shall consider the case of uniaxial-stressed and uniaxial-strained states. Let loading be applied along the axis denoted by I, and let the axes 2 and 3 be mutually perpendicular. We shall take $\sigma_2 = \sigma_3$, and $\varepsilon_2 = \varepsilon_3$, where σ_2 and σ_3 are the components of the stress tensor, ε_2 and ε_3 are the components of the total strain tensor. We shall assume that

$$\varepsilon_i = \varepsilon_i^e + \varepsilon_i^p \,, \quad i = 1,2,3 \tag{I.I}$$

where ε_i^e are the components of elastic strain tensor, ε_i^p are the components of plastic strain tensor. The elastic strain tensor is related to the stress tensor by the Hooke low:

$$\sigma_1 = (\lambda+2\mu)\varepsilon_1^e + 2\lambda\varepsilon_2^e, \quad \sigma_2 = \lambda\varepsilon_1^e + 2(\lambda+\mu)\varepsilon_2^e \qquad (I.2)$$

where λ and μ are the Lame coefficients. By virtue of plastic incompressibility of the material from the equations (I.I) and (I.2), we obtain the following governing relationship for uniaxial-stressed and uniaxial-strained states:

$$\sigma_2 = \sigma_3 = 0, \quad \sigma_1 = E(\varepsilon_1 - 4\varepsilon^p/3), \quad \tau = \sigma_1/2 \qquad (I.3)$$

$$\varepsilon_2 = \varepsilon_3 = 0, \quad \sigma_1 = (\lambda+2\mu)\varepsilon_1 - 8\mu\varepsilon^p/3, \quad \tau = \mu(\varepsilon_1 - 2\varepsilon^p) \qquad (I.4)$$

where $\varepsilon^p = (\varepsilon_1^p - \varepsilon_2^p)/2$. These relationships have an obvious physical meaning: stress increases with increasing total strain, and relaxes owing to plastic strain. The properties of a particular material should be given due consideration in selecting the physical model for Furthermore, we shall suppose that the plastic shearing rate $\dot{\varepsilon}^p$ depends on the dislocation flow density:

$$\dot{\varepsilon}^p = b n u(\tau, n) \qquad (I.5)$$

where b is the Burgers vector, n is the dislocation density, $u(\tau,n)$ is the mean dislocation rate. In the paper /I/ it has been shown that the static description of the behaviour of dislocation clusters can be replaced by the description of a certain averaged dislocation loop. The mean rate of an isolated dislocation depends on the maximum shearing stress τ /2/. In order to account for the closing action of dislocations we shall assume that

$$u(\tau, n) = u^0(\tau)\varphi(n) \qquad (I.6)$$

where $u^0(\tau)$ is the rate of an isolated dislocation without an account of the interactions, $\varphi(n)$ is a function accounting for the closing action of adjacent dis-

location, $\varphi(n) \approx 1$ for $n \ll n_*$, and $\varphi(n) \ll 1$ for $n \gg n_*$, where n_* is the strengtheninge constant. The value $1/\sqrt{n_*}$ characterizes the critical distance between dislocations at which they are closed. For sufficiently large τ, we may use the approximation suggested in /2/:

$$u = u_s \exp(-\tau_*/\tau)\,\varphi(n), \quad \varphi(n) = \exp(-n/n_*) \qquad (I.7)$$

where u_s is the shearing elastic velocity of sound, τ_* is a constant of the material. The relation (I.7) satisfactorily approximates the experimental data in the range of τ values where the dislocation slip rate is controlled by the viscous retardation mechanism /3/. For sufficiently small τ, the dislocation rate is controlled mainly by the thermofluctuation mechanism in which the time of slip from one obstacle to another depends largely on the time of retention before an obstacle, but not on the time of displacement from one active barrier to the other. In this range of τ values the dislocation rate is satisfactorily approximated by the exponential relationship:

$$u^{\circ}(\tau) = u_*\left(\frac{\tau}{\tau_H} - 1\right)^K \qquad (I.8)$$

where u_* and K are constant parameters, τ_H is the Peierls-Nabarro stress. In the superplastic flow, the dislocation rate is controlled by the thermoactive slip of granular dislocations as in the case of creepage of screw dislocations with steps. In this case the rate of an individual dislocation is of the form /4/:

$$u^{\circ} = u^* \operatorname{sh}(\tau/\tau^*) \qquad (I.9)$$

where u^* and τ^* are constant parameters.

With due regard for the possible mechanism of production and annihilation of dislocations, we write the kinetic equation for the total rate of dislocation formation as /5/:

$$\dot{n} = m b n u^{\circ} \varphi + \dot{\Phi}^{\circ} \psi - \alpha n^2 \qquad (I.10)$$

where the first term on the right-hand side of the equation (I.10) describes the production of dislocations as a result of multiple slip, $\dot{\Phi}^{\circ}(\tau)$ is the production of dislocations at Franck-Ryde type sources, and the function $\psi(n)$ accounts for the inhibiting action of adjacent dislocations at the source and is similar to the function $\varphi(n)$ ($\psi(n) \approx 1$ for $n \leqslant n_*$ and $\psi(n) \ll 1$ for $n \gg n_*$). The term $\alpha(\tau) n^2$ describes the annihilation of dislocations due to pairwise interaction of dislocations of opposite signs. For small grain sizes ($d \leqslant$ 10 microns) the coefficient admits negative values. For large grain sizes ($d \gtrsim$ 100 microns) the Franck-Ryde source is not so effectiv as the multiplication of dislocations as a result of multiple slip /6/. In this case the relation (I.10) can be rewritten as

$$\dot{n} = m b n u^{\circ} \varphi - \alpha n^2, \quad m(d) > 0 \qquad (I.11)$$

For sufficiently small n , the relation (I.11) can be expressed in the form:

$$\dot{n} = m b n u^{\circ} \varphi = m \dot{\varepsilon}^{p} \qquad (I.12)$$

After integrating (I.12), we obtain

$$n = n_o + m \varepsilon^{p} \qquad (I.13)$$

where n_o is the initial dislocation density. Forcoarse grain materials the relation (I.13) is corroborated by the experimental results. If during deformation the parameter n attains such a high value, that $n \gg n_*$ say as in the creepage of metals, then the relation (I.11) has to be applied. In the deformation of metals of fine-grain superplastic structure, strengthening of metal does not take place at all, i.e. $n \ll n_*$. In this case the pairwise interaction of dislocations can be discarded and the relation (I.10) rewritten as

$$\dot{n} = m\dot{\varepsilon}^{p} + \Phi^{o}\psi \quad , \quad m(d) < 0 \qquad \text{(I.I4)}$$

In the steady stage of superplastic flow and in the second steady creep stage the exeess of generated dislocations is compensated by their annihilation, so that $\dot{n} = 0$. Applying the equations (I.II) and (I.I4) for these stages, we obtain an expression for the function $\alpha(\tau)$ and $\Phi^{o}(\tau)$:

$$\alpha(\tau) = mb\,u^{o}(\tau)\,\varphi(n_c)/n_c \qquad \text{(I.I5)}$$

$$\Phi^{o}(\tau) = -mb\,n_s\,u^{o}(\tau)\,\varphi(n_s)/\psi(n_s) \qquad \text{(I.I6)}$$

where $n_c(\tau)$ and $n_s(\tau)$ are the limiting values of dislocation density in creepage and in superplasticity corresponding to maximum shearing stress τ attained at the moment when the balance $\dot{n} = 0$ is established. Substituting the relations (I.I5) and (I.I6) into the right-hand part of the equation (I.IO) we find

$$\dot{n} = m\dot{\varepsilon}^{p}\left[1 - \frac{n}{n_c}\cdot\frac{\varphi(n_c)}{\varphi(n)} - \frac{n_s}{n}\right], \; n_s \ll n_c \qquad \text{(I.I7)}$$

Under certain specific range of variation of the characteristic grain size d , a combined action of the dislocation mechanisms determining the deformation of coars-grain and fine-grain materials is possibles. In this case the relation (I.I7) has to be used.

Quasi-static and dynamic deformation in uniaxial-strained and uniaxial-stressed states

We shall now examine a case where the strain rate is not great, and the stresses are uniform along the rod. We shall assume such conditions of uniformity for the stress along the rod that are applicable to sufficiently short specimens. Let the law governing the strain be given in the form of constant strain rate,

i.e. $\dot{\varepsilon}_1 = \text{const}$. Using the relations (I.3),(I.5),(I.7) and (I.I2) we shall write a closed system of equations describing the quasi-static deformation in short rods at a constant strain rate:

$$\dot{\varepsilon}^p = b n u \,, \quad \dot{\tau} = E(\dot{\varepsilon}_1 - 4\dot{\varepsilon}^p/3)/2, \quad \dot{n} = m\dot{\varepsilon}^p$$
$$u^0 = u_s \exp(-\tau_*/\tau) \,, \quad \varphi(n) = \exp(-n/n_*) \qquad (2.I)$$

with the initial conditions $t = 0 \;\; \varepsilon_1 = \varepsilon^p = 0 \,, \;\; n = n_0$.

The solutions of the system (2.I), derived with the help of a computer, were compared with the corresponding experimental data obtained by Marsh and Campbell /8/ for the quasi-static compression of short rods made of low-carbon steels of different granularities (346,495,773,2033 mm^{-2}). A method has been developed for determining the kinetic parameters from the solution of the inverse problem /7/ . Fig.I shows the dependense of the kinetic parameters on the granularity. The following values were taken for the constants of low-carbon steel: E = 2,IxI0^6 bar, λ = I,096xI0^6 bar, μ = 0,906xI0^6 bar, u_s = 3,2xI0^5 cm/sec, b = 2,5x I0^{-8} cm.

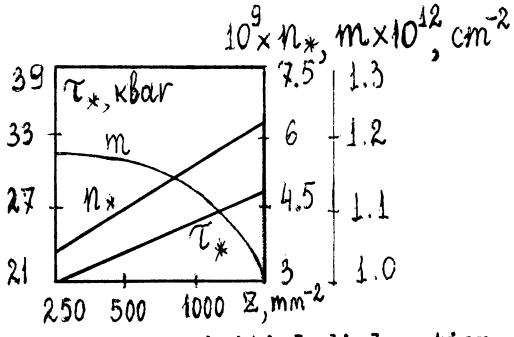

Fig.I

By varying the initial dislocation density the effect offinitial dislocation density on the upper creep limit was studied. For a granularity of 2033 mm^{-2}, the calculated data (solid line), and for the sake of comparison, also the data reported in /8/ are shown in Fig.2.

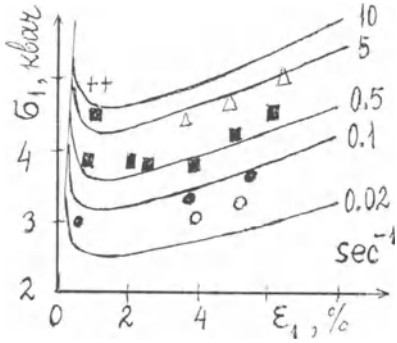

Fig.2

In the strain rate variation range from 0.I to I0 sec^{-I} there is satisfactory agreement between the calculated and the experimental results. For small $\dot{\varepsilon}_1$, close to the static value, the theory gives a lower σ_1, because for small $\dot{\varepsilon}_1$, and consequently, for small τ, the viscous mechanism of dislocation slip predominates over the thermofluctuation mechanism, and therefore the approximation applied gives a higher value to the dislocation rate.

The kinetic effects described above are also exhibited in the propagation of shock waves in metals. We shall express the system of equations of a one-dimensional plane motion of the medium in Lagrangian variables as follows:

$$\frac{\partial \varepsilon_1}{\partial t} = \frac{\partial v}{\partial \tau}, \quad \rho_0 \frac{\partial v}{\partial t} = \frac{\partial \sigma_1}{\partial \tau}, \quad \frac{\partial \varepsilon^p}{\partial t} = b n u \qquad (2.2)$$

In order that the system (2.2) may be closed, we have to use a governing relationship in the form of (I.3) if we are considering the head-on collison of rods, or in the form of (I.4) for the head-on collison of plates.

We shall now consider the two-dimensional collison of a plate of thickness l (impinging body) on a plane target of thickness L. The initial conditions are

$$t=0 \quad \rho=\rho_0 \,,\ \tau=0 \,,\ \sigma_1=0 \,,\ \varepsilon_1=\varepsilon^p=0$$
$$v(r,0)=v_0 \ \text{for}\ -l\le r<0 \,,\ v(r,0)=0 \qquad (2.3)$$

and the boundary condition are for $0<r\le L$ $\sigma_1(-l,t)=\sigma_1(L,t)=0$. In solving this problem the kinetic parameters were taken to be of the values given elsewhere for solving the quasi-static problem on the deformation of short rods at a constant strain rane. Fig.3 shows the calculated values (solid line) for the dependence of the mass velocity of the substance in front of an elastic forerunner v_d on the coordinate r in the target for two impinging velocities of I00 and I50 m/sec. The results obtained in experiments /9,I0/ for low-carbon steel and Armco iron are shown in the same figure for the sake of comparison.

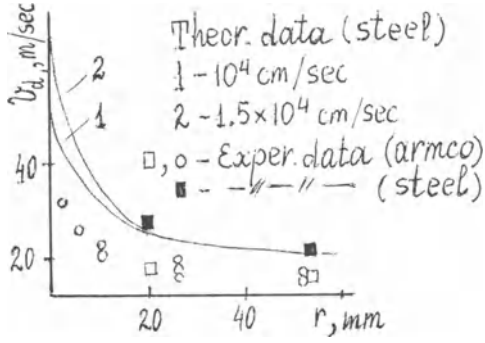

Fig.3

Fig.4 shows the $\sigma_1-\varepsilon_1$ dependence for a fixed cross-section of the target. It is obvious that stress relaxation takes place almost elastically though there is a small amount of plastic deformation in the dynamic yield point range.

Satisfactory agreement between the experimental and theoretical results demonstrates that the results derived in the calculations of quasi-static deformation in rods (uniform plastic deformation) can be used for

predicting the dynamic behaviour of materials.

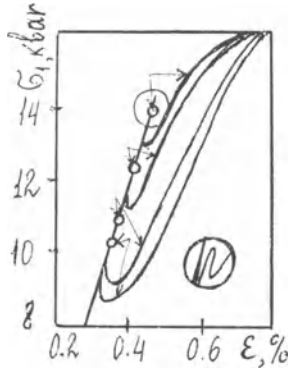

Fig.4

Propagation of Luders front (quasi-static plasticity wave

During elongation of long rods the uniformity of plastic deformation along the rod length is disrupted as is indicated by the generation of Luders fronts near the target. The cross-section, where the Luders wave has not still reached, undergoes elastic deformation, but those section, where the wave has already reached, exist in a plastic state. A boundary value problem has to be formulated for investigating such a process. The situation is analogous to the case of flame propagation. The problem of flame propagation is solved with the help of the equations of state and the reaction kinetic with due regard for the transfer of heat to the layers before the flame front. We shall now formulate this problem in a coordinate system moving with the front. The system of equations describing the propagation of Luders front along the rod is of the form:

$$\rho d\varepsilon_1/dx = dv/dx,\ \rho v dn/dx = bmnu - dq_v/dx$$
$$\sigma_1 = 2\tau = const.,\ \varepsilon = \varepsilon_{10} + 4\varepsilon^p/3,\ \varepsilon^p = (n-n_0)/m \qquad (3.I)$$

Unlike in the case of (I.5), here we have a flow of dislocations along the rod due to cross slip /6/. Among various possible lows for q_v , we shall consider the

law $q = -\chi(\sigma_1, n)\,\partial n/\partial x$, where $\chi(cm^2/sec)$ is the cross slip factor. It can be shown that such a law for q admits a unique solution for the rate and structure of the quasi-static plasticity wave. The boundary conditions for (3.I) are

$$\begin{aligned} x = -\infty &, \quad \varepsilon_1 = \varepsilon_{10} = \sigma_1/E, \quad \dot{\varepsilon}^p = 0, \quad n = n_0, \quad v = v_0 \\ x = +\infty &, \quad \varepsilon_1 = \varepsilon_{1e}(\sigma_1), \quad \dot{\varepsilon}^p = 3(\dot{\varepsilon}_{1e} - \dot{\varepsilon}_{10})/4, \quad n = n_e, \quad v = v_e \end{aligned} \qquad (3.2)$$

where v_0 determines the plasticity wave velocity, and $\varepsilon_{1e}(\sigma_1)$ is the static diagram ($\dot{\varepsilon}_1 \to 0$) for the elongation of the specimen. The value of v_0 , as in the theory of flame propagation, is determined from the condition for the passage of the integral curve through two points corresponding to the initial and final states. In order that a solution may exist, it is necessary that these states be stationary ($\dot{\varepsilon}^p = 0$). In order that these states may be stationary, it is necessary to correct the relationship (I.5) near these states assuming that $u = 0$. Similar truncation of the kinetics is also used in combustion problems.

Creepage and superplasticity

Creepage and superplasticity of metals and alloys exhibit certain common features which make it possible to investigate them theoretically. The first two stages in creepage (logarithmic and stationary stages) are characterized by a change in the internal structural dislocations, and the third stage by external destruction of the material. Therefore, only the first two stages in creepage can be described by means of the locally uniform model developed in the previous pages. To describe the third stage we have to introduce an additional parameter characterizing the destruction of the material. The logarithmic state of creepage is charac-

terized by multiplication and closing of dislocation which ultimately lead to a decrease in the creep rate. Using the relations (I.5) and (I.7), Gilman /2/ investigated the thirst stage in LiF single crystals. The second stationary stage in creepage is characterized by intensive annihilation of dislocations of opposite signs in adjacent slip planes when closing of dislocations gives rise to energy conditions for the diffusion of dislocations over short distances. Similarly a balance is established between the annihilated and generated dislocations during superplastic deformation at the stationary stage, so that

$$\dot{n} = 0 \tag{4.I}$$

Unlike in the case of creepage, noticeable increase in the dislocation density is not observed during superplastic deformation, and therefore in the equation (I.6) we can take that

$$\varphi(n_s) \approx \psi(n_s) \approx 1 \tag{4.2}$$

from the relation (I.5) when τ =const., the following expression is obtained for the strain rate at the stationary superplastic state:

$$\dot{\varepsilon}_1 = b n_s(\tau)\, u^* \operatorname{sh}(\tau/\tau^*) \tag{4.3}$$

The $\dot{\varepsilon}_1(\tau)$ dependence is determined from experiments. A comparison of (4.2) with the experimental data /II/ makes it possible to express $n_s(\tau)$ in the following form:

$$n_s(\tau) = n_s^* (\tau/\tau^*)^l \tag{4.4}$$

where n_s^* and l are constant parameters. Substituting (4.2) and (4.4) into (4.3) we obtain:

$$\dot{\varepsilon}(\tau) = \frac{3}{4} b n_s^* \left(\frac{\tau}{\tau^*}\right)^l u^* \operatorname{sh}\left(\frac{\tau}{\tau^*}\right) \tag{4.5}$$

The parameters ℓ, τ^* and $n_e^* u^*$ can be determined from the experimental dependence $\varepsilon_1(\tau)$ at three characteristic points. The values of the kinetic parameters n_s^* and u^*, or the values of the coefficient m can be determined only from comparison of the numerical solution of the problems for the nonstationary stage where $\dot{n} > 0$. Consider the elongation of rods made of superplastic alloy Zn-22%Al at a constant rate of movement of end faces v_0, so that

$$\dot{\varepsilon}_1 = v_0/(\ell_0 + v_0 t)$$

where ℓ_0 is the initial rod length. A comparison of the expression (4.5) and corresponding experimental dependence obtained for this alloy having a grain size of I.8 microns at T=523°K /II/ gives τ^* =0.308 kbar, ℓ =I.5, $b n_e^* u^*$ =4.05xI0^{-3} sec, and the Burgers vector was taken to be equal to 2.5xI0^{-8} cm. We shall write the closed system of equations for supperplastic deformation of rods as

$$\dot{n} = m b u (n - n_s), \quad \dot{\tau} = E(\dot{\varepsilon}_1 - 4\dot{\varepsilon}^p/3), \quad m < 0$$
$$\dot{\varepsilon}^p = b n u, \quad \dot{\varepsilon}_1 = v_0/(\ell_0 + v_0 t) \qquad (4.6)$$

This system is closed by the equation (I.9) and the initial conditions t=0, $n = n_0$, $\varepsilon_1 = \varepsilon^p = 0$, $\tau = 0$. From a comparison of the numerical solution of the problem of the nonstationary stage of superplasticity with the experimental data, we obtain the following values for the kinetic parameters:

$$n_s^* = 1.4 \times 10^9 \text{ cm}^{-2}, \quad u^* = 1{,}16 \times 10^{-2} \text{ cm/sec}, \quad m = -10^8 \text{ cm}^{-2}$$

The upper limit for the creep at the initial stage of plastic deformation depends on the preliminary heat treatment given to the material. In the model deve-

loped here this situation is accounted for by the fact that the calculations for the initial stage of superplastic deformation leads to a redistribution of $n_s^* \cdot u^*$, determined for the stationary stage, between the parameters n_s^* and u^*. Fig.5 shows the experimental and calculated data (dotted line). Different curves correspond to different strain rates at the initial deformation stage: I- $2 \times 10^{-4} sec^{-1}$; 2- $2 \times 10^{-2} sec^{-1}$; 3- $2 \times 10^{-1} sec^{-1}$. The kinetic parameters were determined from the condition that the calculated curve may fit with the experimental curve for $\dot{\varepsilon}_1 = 2 \times 10^{-2} sec^{-1}$. The other two plots were used as a check for the calculations.

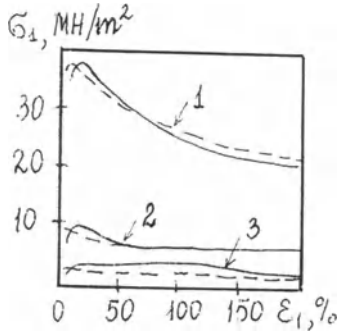

Fig.5

Unlike the superplasticity, annihilation of dislocations during the creep takes place at a very high dislocation density $n \gg n_*$. We shall write the closed system of equations for creep of rods as

$$\dot{n} = m\dot{\varepsilon}^p \left[1 - \frac{n}{n_c} \cdot \frac{\varphi(n_c)}{\varphi(n)}\right], \quad \tau = const$$
$$\dot{\varepsilon}^p = b n u(\tau, n), \quad n_c = const \qquad (4.7)$$

The initial conditions t=0, $n=n_0$ and $\varepsilon_1=\varepsilon^p=0$ complete the system (4.7). The kinetic parameters u_* and K were determined from the solution of the inverse problem for the first creepage stage without an account of the term αn^2 in (I.II); moreover, the values of m and n_* were taken from the solution of the problem of quasi-static deformation of short rods made of low-carbon steel. A comparison of the numerical solution of the system (4.7) with the experimental data for the nonstationary creepage stage makes it possible to determine the kinetic parameter n_c.

The values found for the kinetic parameters are as follows:

$$u_* = 32\ cm/sec\ ,\ K = 3.2\ ,\ n_c = 3.3\times10^{12}\ cm^{-2}$$

The values of τ_H was taken to be equal to $10^{-3}\ \mu$. Fig.6 shows the experimental /I2/ and calculated data (dotted line).

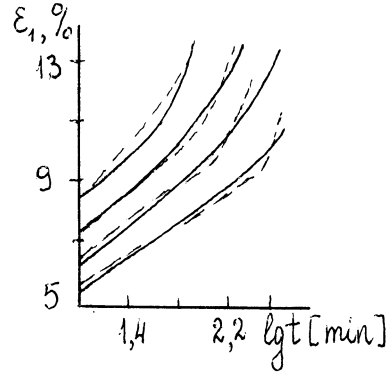

Fig.6

Literature

I Gillis, P.; Gilman, J.: Dynamical dislocation theory of crystal plasticity. Appl. Phys. 36 (I965) 3370 - 3374.

2 Gilman, J.: Microdynamics of plastic flow at constant stress. Appl. Phys. 36 (I965) 3370 - 3375.

3 Johnston, W.: Yield points and delay times in single crystals. Appl. Phys. 33 (I962) 2345-2349.

4 Kaibyshev O.: Plasticity and superplasticity of metals. Moscow, Izd. Metallurgizdat, I975.

5 Nigmatulin, R.; Kholin, N.: Dislocation kinetic of superplasticity and creep in metals. Doklady AN SSSR 23I (I976) 89-93.

6 Hull, D.: Introduction in the theory of dislocation. Moscow, Atomizdat, I968.

7 Nigmatulin, R.; Kholin, N.: On the model of elastoplastic medium with dislocation kinetics of plastic deformation. Mech. solids (I974) 34-42.

8 Marsh, K.; Campbell, J.: The effect of strain-rate on the post-yield flow of mild steel. Mech. Phys. Solids II (I963) 254-260.

9 Taylor, J.; Rice, M.: Elastic-plastic properties of iron. Appl. Phys. 34 (I962) 3234-3246.

I0 Jones, O.; Neilson, F.; Benedick, W.: Dynamic yield behavior of explosively loaded metals determined by a quartz transducer technique. Appl. Phys. 33 (I962) 435-443.

II Holt, D.:Recent developments in superplasticity. 25 (I968) 242-246.

I2 Nishihara; Tanaka : Tension and creep tests on mild steel. Proc. 5, Japan Nat. Congr. Appl. Mech., I955.

Some Results on the Dynamic Deformation of Copper

M. STELLY, R. DORMEVAL

Commissariat à l'Energie Atomique, Service Métallurgie
B.P.N°511-15 - 75015 PARIS, France

Summary.

The influence of strain rate and strain rate history on the mechanical behaviour of copper single crystals has been studied by means of compression tests. The shear strain rate range $10^{-4}s^{-1}$ - $8\ 10^{3}s^{-1}$ has been investigated. Dynamic tests were performed with an Hopkinson bar.
The strain rate behaviour can be divided into 2 regions. Above $10^{3}s^{-1}$ a linear relationship between shear stress and shear strain rates is observed. This can be explained by a viscous damping of dislocations. Static curves are sometimes over the dynamic ones depending of the strain rate.
Tests performed with change of strain rate have shown that strain rate history memory is never lost.
Results are compared with those obtained by tensile tests.

I - Introduction.

It is now well established that strain rate has an effect on metals and alloys mechanical behaviours. A great deal of experiments have been performed to measure strain rate effect and try to give satisfactory explanations to this phenomenon. Three zones have been clearly determined /1/ : at low strain rates a zone of very weak influence of strain rate, at medium strain rates (up to $10^{3}s^{-1}$) a region more sensitive to this parameter and finally at higher strain rates (above 10^{3} or $10^{4}\ s^{-1}$) a field where the influence of strain rate is very pronounced. This behaviour has been particularly studied for f.c.c. metals. Though copper was one of the most studied material there is still some lack in our knowledge. Many authors have performed tests to clear up the copper behaviour at high strain rates. Among others, Hopkinson bar tests have been used in compression /2-5/ or torsion /6-9/ and have shown unambiguously the influence of strain rate and also of mechanical history on the behaviour of that metal.

We have thought that studies on single crystals would be of interest to get more informations on copper behavior. So we have performed compression tests on single crystals of different orientations. We have particularly studied single crystals of <112> axe on which interrupted tests have been realized. This work follows and completes one on the tensile behaviour of copper single crystals /10/.

II - Specimens.

Specimens are obtained from 99.99 % copper by a method derived from Bridgman method. We put a short (10 mm) single crystal of choosen orientation at the bottom of the graphite mold and grow the specimen from this nucleus which can be used many times to get single crystals of the same orientation.
Single crystals, about 100 mm long, are cut by spark machining so as to obtain specimens 5 or 8 mm high for compression tests. For tension tests, samples have been shaped directly. Impact faces for compression samples are polished flat and parallel and a 24 h thermal annealing at 1000°C is performed to lower dislocation density. Finally specimens undergo a chemical and electropolishing. Dislocation density estimated by electron microscopy was about 10^6 per cm^2 /11/.

III - Experimental procedure.

At low strain-rates tensile tests were carried out with a standard Instron tensiometer, at medium strain-rates ($\dot{\gamma}$ = 10^{-2} to 10 s^{-1}) with an hydraulic Schenck Machine. High strain rates tests were performed in compression on a Hopkinson-bar and in tension on a specially built machine that we named Arbalete (Cross-Bow) /12/. Hopkinson bar principle is well known. Projectile, measure bars and impulse bar are in steel with a diameter of 12 mm and a length of 1 m. Strain gauges are sticked to measure bars near the specimen and strain-time curves are recorded on a magnetic record Biomation - Impact speed was limited to 20 m/s to avoid plastic deformation of measure bars. End faces near specimen were lubricated.

The dynamic tensile testing machine consists of two parallel guid-rails between which moves a projectile propelled by rubber bands. The speed range varies from 3 to 60 m s^{-1}. The specimen, positioned between the rails, is fixed at one end on a long fixed rod acting as a dynamometer and at the other end on a head which is hit by the projectile. Strain gauges attached to the dynamometer record load as a function of time. In a first approximation head speed is supposed constant which allows to derive stress-strain curves. Following Bell /13/ we have transformed these curves in shear stress-shear strain curves assuming a single system of slip during the whole test. For tension tests, we have used classical formulas and for compression tests those proposed by Taylor /14/.

IV - Compression tests.

Constant strain-rate tests.

Two types of specimens were used. The first one was an orthocylinder 8 mm in diameter and 8 mm high and the second one a parallelepiped with a section of 4 x 5 mm^2 and a height of 5 mm. The parallelepipedic specimens had their axe in the close vicinity of the <112> direction and faces were of (111) and (110) types. These orientations were chosen to give a symmetrical mode of deformation and to present two planes of great interest in the deformation study by microscopy.

Tests results are given on fig. 1. to 4.

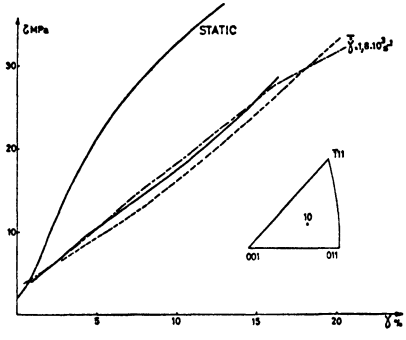

Figure 1

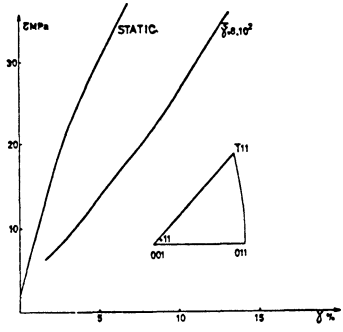

Figure 2

We can see that for samples 10 and 11 (which were cylindrical) the dynamic curves obtained with mean shear strain-rates of $1.8\ 10^{3} s^{-1}$ and $8\ 10^{2}\ s^{-1}$ respectively are always below the static ones. This behaviour has soon been reported by Nagata and Yoshida on aluminium and copper single crystals /15-16/ and by Larrecq on aluminium single crystals /17/. They have shown that, depending on the initial orientation of the specimens the dynamic curves can be below or above the static curves. Dynamic curves for orientation 10 are not similar to those found by Edington /3/ for an adjoining orientation.

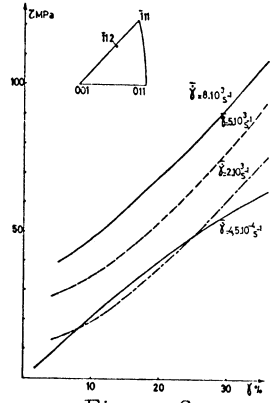

Figure 3

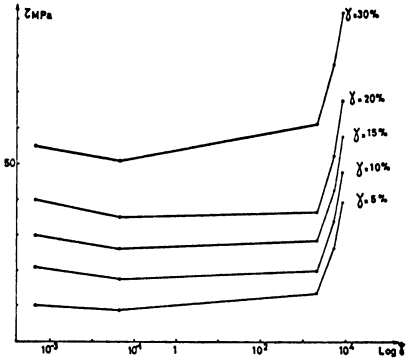

Figure 4

For the <112> orientation, as expected the static curve shows only two stages. The linear stage II extends up to a shear strain of about 10 to 12 % and then begins the parabolic stage III. The three dynamic mean curves have the same shape : they are all curved upwards. They are also nearly parallel and the higher the strain rate, the higher the shear stress. We can see that the curve obtained at $\dot{\gamma} = 2\ 10^{3} s^{-1}$ is over the static one ($\dot{\gamma} = 4.5\ 10^{-4} s^{-1}$) up to 8 %, under up to about 25 % and then is still over. We must note that these dynamic tests were performed at higher shear strain rates than with cylindrical specimens.

In the (τ , ln $\dot{\gamma}$) diagram we can separate two fields (fig.4). The first spreads up to about $10^{3} s^{-1}$. For a given shear strain the shear stress varies very little ; stress levels for $\dot{\gamma} = 4.5\ 10^{-2} s^{-1}$ are always somewhat under those for $\dot{\gamma} = 4.5\ 10^{-4}\ s^{-1}$ or for $\dot{\gamma} = 2\ 10^{3} s^{-1}$ producing a minimum on the curves. In the second field, strain rate has a great influence on shear stress ; there

exists a linear relation between shear stress and strain rate for each strain level (fig. 5).

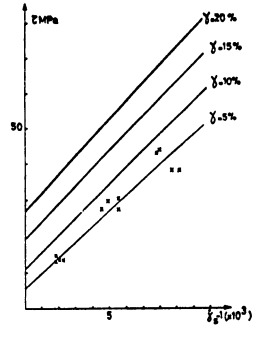

Figure 5

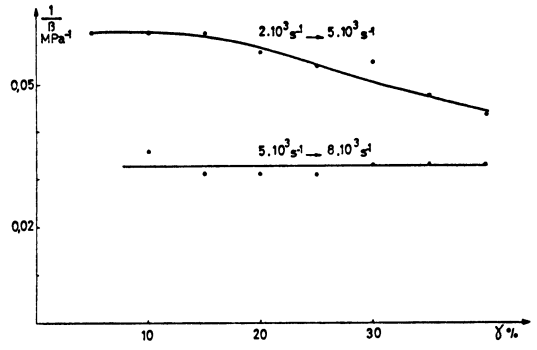

Figure 6

We can define a strain rate sensitivity parameter as follows /9/ :

$$\beta = \left(\frac{d\,\tau}{d\,\ln\,\dot{\gamma}}\right) \simeq \frac{\Delta\,\tau}{\ln\,\dot{\gamma}_2/\dot{\gamma}_1}$$

Below $\dot{\gamma} = 10^3\ s^{-1}$ this parameter has a very low value, possibly negative. Over $10^3 s^{-1}$ this parameter takes values of the order of 16 to 30 MPa (fig.6). Between $\dot{\gamma} = 2\ 10^3 s^{-1}$ and $5\ 10^3 s^{-1}$ the parameter increases with strain but between $5\ 10^3 s^{-1}$ and $8\ 10^3 s^{-1}$ it remains constant.

Incremental strain-rate tests.

For this type of tests we have only worked with the parallelepipedic specimens.

Two methods can be used (fig.7) :

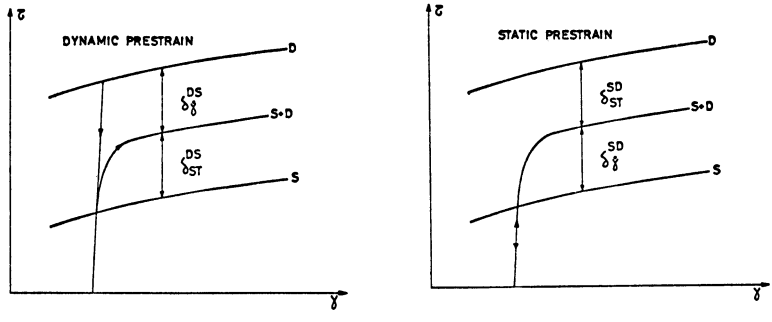

Figure 7

- deform statically the specimen up to a given strain and then make a dynamic test.
- deform dynamically the specimen then statically.

Due to the apparatus used we cannot change the strain rate suddenly. We are obliged to discharge the specimen after the first part of the test, to place it in the other apparatus and to reload at the new strain rate. Thus tests are not conducted in the same way as other workers did with an instantaneous jump of strain rate. It is possible that, due to our method, the specimen microstructure would be changed and that we do not study only the influence of a strain rate change but also of a structure change. But we think that the structure change effect would be very weak for this metal and would influence the beginning of the test after the strain rate change. By the way we cannot get the beginning of the curves because stress and strain are still inhomogeneous along the sample and because lateral inertia introduces oscillations which are important at the just test beginning /18/. It is then expected that the interruption of tests has no influence on results.

Two sets of tests have been performed ; in each the static shear strain rate was $4.5\ 10^{-4} s^{-1}$ but the dynamic strain rates were $2\ 10^{3} s^{-1}$ or $8\ 10^{3} s^{-1}$. For each curve, we have performed one or two tests.

Upward changes.

- from $\dot{\gamma} = 4.5\ 10^{-4} s^{-1}$ to $\dot{\gamma} = 2\ 10^{3} s^{-1}$ (fig.8 and 9). Results for prestrained specimens are entangled with the purely static or dynamic ones at low strain but they are located between the two after a shear stress of 30 %. They never come again under the static curve as do the dynamic curve between 8 and 25 %.
- from $\dot{\gamma} = 4.5\ 10^{-4} s^{-1}$ to $\dot{\gamma} = 8\ 10^{3} s^{-1}$ (fig.10). All the curves are located between the static and dynamic ones. They do not trend to reach the purely dynamic curve. Curves with 25 % and 50 % prestrain have not the same behaviour than others at high shear strains.

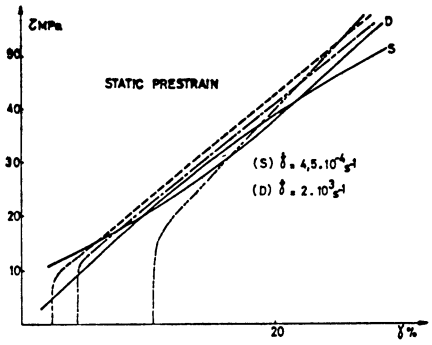

Figure 8

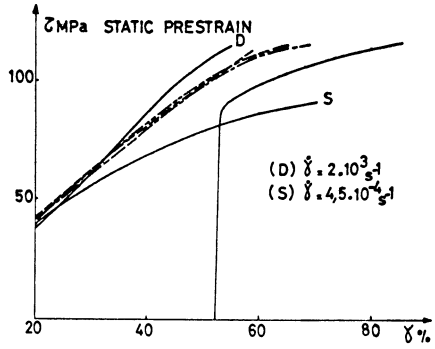

Figure 9

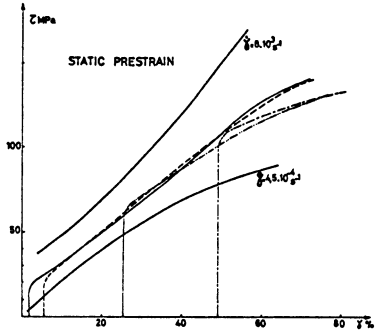

Figure 10

Downward changes (fig. 11 and 12).

Irrespective of the initial strain rate, the curves are situated upon the static curve and are very near from one another at least for low deformations.

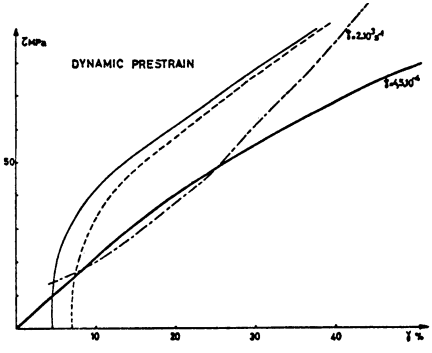

Figure 11

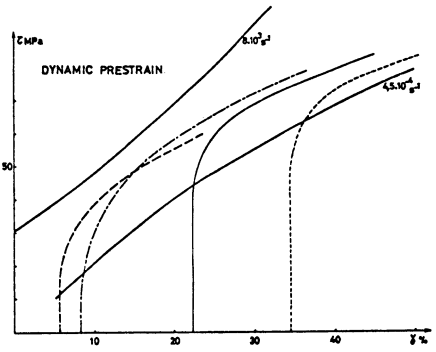

Figure 12

V - Discussion.

Constant strain-rate tests.

The diagram of fig.4 shows that two fields can be distinguished in the behaviour of copper single crystals between $\dot{\gamma} = 10^{-4} s^{-1}$ up to $\dot{\gamma} = 10^{4} s^{-1}$. This has previously been established on copper single crystals by Edington /3/ or Dusek et al /4/ in compression or Dormeval et al /10/ in tension. The transition between these two areas is situated about $\dot{\gamma} = 10^{3} s^{-1}$.

Similar results have been found for polycrystals or single crystals of f.c.c. metals /1/ and the two fields are related to two different deformation mechanisms. At strain-rates below $10^{3} s^{-1}$ the deformation is thermally activated. At higher strain rates, deformation is controlled by the viscous damping of dislocations /19/. In this case strain rate and stress are related by :

$$\tau = \tau_b + \alpha \dot{\gamma}$$

α can be expressed in function of mobile dislocation density and viscous damping parameter B by :

$$\alpha = \frac{B}{\rho b^2}$$

(b is the dislocations Burgers vector).

It is obvious that in each field a single phenomenon does not occur but that the two mechanisms compete /20/. This competition is specially noticeable in the transition zone around $10^{3} s^{-1}$.

Values of α have been calculated from fig.5. The mean value $4.5\ 10^{3}$ Pa.s., is quite in good agreement with values of other authors /3,4, 16, 10/. Values of B are in the range 1 to $8\ 10^{-5}$ Pa.s. /4 - 21 to 24/. From these values one can calculate the mobile dislocation density. We have found values ranging from $4\ 10^{6}$ per cm^2 to $3\ 10^{7}$ per cm^2. These low densities are however in accordance with those found in dynamic tension tests /10/ : from $2\ 10^{6}$ to 10^{7} per cm^2. They require high dislocation speeds ranging about 300 to 3000 m/s according to the relation $\dot{\gamma} = \rho b V$ and thus need high stresses. This is especially true in tension tests where an initial stress peak can be noticed on dynamic curves /10/.

We can also note that the value of α does not change noticeably up to a shear strain of 40 % which in turn means that the mobile dislocation density does not vary very much in this strain range. Concerning the curves for $\dot{\gamma}$ below $10^3 s^{-1}$ and specially the fact that curves for $\dot{\gamma} = 10^{-4} - 10^{-3} s^{-1}$ are over curves for $\dot{\gamma} = 10^2 - 10^3 s^{-1}$, it would be interesting to study, for different initial orientations, the behavior all over the range $10^{-4} - 10^3 s^{-1}$. It is possible, as suggested by fig.4, that a minimum exists on the curve (τ , ln $\dot{\gamma}$) for some value of $\dot{\gamma}$.

Incremental strain-rate tests.

As shown on fig.7, we can define four parameters to describe the behavior in the two sets of incremental strain-rate tests. They are relative to the influence of the previous history which is supposed to be divided in two terms : one representing the strain rate effect for the "same" structure ($\delta_{\dot{\gamma}}$) and the other the effect of the difference of history for the same strain rate (δ_{ST}).
The strain rate effect parameter $\delta_{\dot{\gamma}}$ has a similar behaviour for the two sets of tests (fig. 13 and 14) except for static tests realized after a dynamic prestrain at $\dot{\gamma} = 2\ 10^3\ s^{-1}$ for which this parameter is sometimes negative. A plateau is reached between 10 to 20 % of shear strain. The level of this plateau is not far from the value which can be determined by the intersection of the linear elastic part of the stress-strain curve and the tangent to the initial plastic portion of this curve. After the plateau $\delta_{\dot{\gamma}}$ rises, as it does for

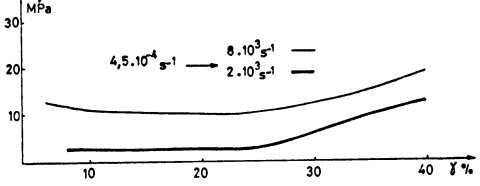

Figure 13

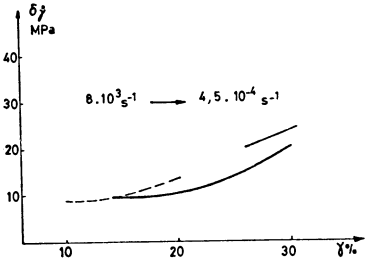

Figure 14

high values of prestrain. Plateau levels are identical for tests between $\dot{\gamma} = 8\ 10^{3} s^{-1}$ and $\dot{\gamma} = 4.5\ 10^{-4} s^{-1}$ irrespective of the initial value of $\dot{\gamma}$. These values are about 10 MPa. For tests at $\dot{\gamma} = 2\ 10^{3}\ s^{-1}$ after a static prestrain the plateau levels are low (2.5 MPa) which must be connected with results obtained at constant strain-rates.

This strain-rate effect parameter may be connected with the activation volume derived from the thermal activation strain rate analysis, only suitable in the low strain rate range. We have attempted this connection for the tests with prestrain at $\dot{\gamma} = 4.5\ 10^{-4} s^{-1}$ and deformation at $\dot{\gamma} = 2\ 10^{3} s^{-1}$ the lowest dynamic strain rate studied. We have used the relation $v = kT \left(\frac{\Delta \ln \dot{\gamma}}{\delta \sigma}\right)$ which is similar to that derived by Klepaczko /9/. For low shear strains v is constant ($\sim 29\ 10^{-27} m^{3}$) due to the plateau of $\delta \sigma / \delta \ln \dot{\gamma}$ after decreases when γ increases. For $\gamma = 40\ \%$ we obtain $v = 6\ 10^{-27} m^{3}$ value which is not far from that which can be extrapoleted from Klepaczko's work. The decrease of v with γ was also found by this author. We are fully aware of the limitations of our results : we have not performed incremental tests by rapid variations of $\dot{\gamma}$, we are not sure to be in the thermal activation field but the similitude of the results is noticeable. This may be fortuitous and once again it would be necessary to perform tests at lower strain-rate first to define the limit of strain rate for which thermal activation analysis may be used and second to study the influence of higher low strain rate that is to say to limit the jump height. Thus it would be possible to define unambiguously the domain of validity of thermal activation analysis and then the activation volume and to use this analysis to derive more informations on the deformation mechanism and dislocations density.

For tests between $\dot{\gamma} = 4.5\ 10^{-4} s^{-1}$ and $8\ 10^{3} s^{-1}$ the parameter $\delta \sigma / \delta \ln \dot{\gamma}$ may be considered partly as the contribution due to phonon damping of dislocations. We are not informed of a theory which can be used to explain the results.

The other parameter δ_{ST} may describe history influence on the structure that is to say, for example, the difference in mobile dislocation density between samples tested at low or high strain rates.

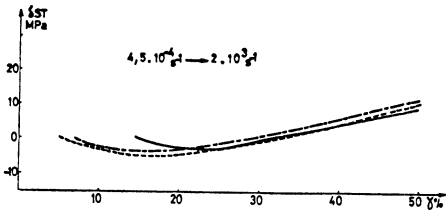

Figure 15

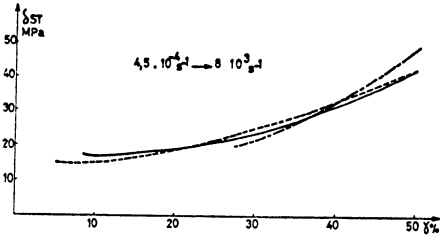

Figure 16

Its variations are plotted on fig. 15 to 18. The main point is that δ_{ST} never vanishes except for results obtained with incremental tests finished at $\dot{\gamma} = 2\ 10^3 s^{-1}$. So single crystals never forget the strain-rate history contrary to what happens for polycrystalline copper /6-7/. Studies by electron microscopy are carried on to explain this behaviour.

For dynamically prestrained specimens, values of δ_{ST} are close, to 15 to 20 MPa so that the ratio $\delta_{ST} / \delta_{\dot{\gamma}}$ is about 2 between $\gamma = 10$ and 25 %, value very close to that found by Glenn and Bradley for similar tests on polycrystalline copper /2/.

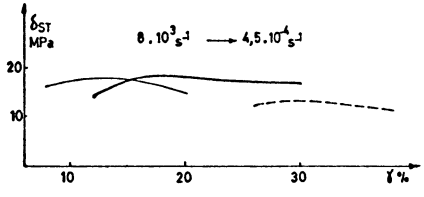

Figure 17

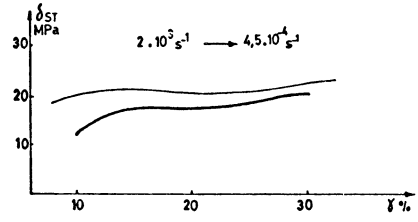

Figure 18

Comparison with tension tests.

We shall recall some results obtained in tension /10/ before comparing tension and compression tests.

For all orientations tested (fig. 19), stress-time curves have the

same general features (fig.20). It is possible to distinguish four zones more or less pronounced according to specimen orientation and test conditions : at the beginning of the test, a stress peak is reached between 40 and 100 μs. After relaxation, stress rises again strongly then more slowly. After a maximum value stress decreases up to rupture by a chisel point mechanism.

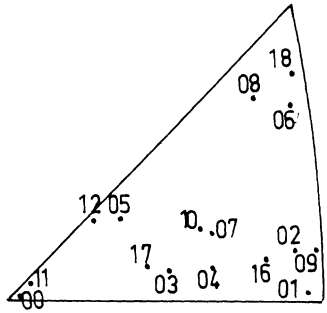

Figure 19

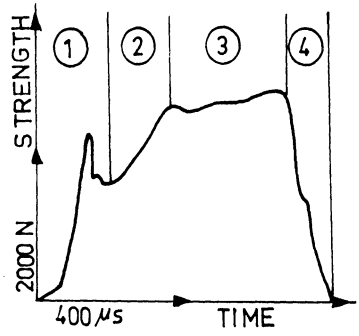

Figure 20

Stress-time curves have been transformed in shear stress-shear strain curves with a single glide hypothesis. In all cases dynamic shear stresses are greater than the static ones for the same shear stress. Stress variations with strain rate are reported on fig.21.

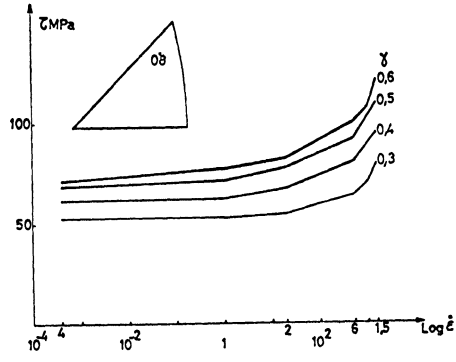

Figure 21

Below about $10^2 s^{-1}$, stress levels are nearly constant ; on the other hand we can note a rapid rise over $5\ 10^2 s^{-1}$, stress curves for a given strain are linear functions of strain rate. The coefficient α of the relation $\tau = \tau_B + \alpha \dot{\gamma}$ is about $7\ 10^3$ Pa.s., value near those found in compression and by other authors.

Interrupted tests have also been performed with only static pre-strains (it is not possible to stop a dynamic test). The initial peak is always very high (fig.22), over the stress for the same strain in the pure dynamic test. The flow shear stress is weaker for interrupted tests than for dynamic tests but stronger than for static tests. We have not realized enough tests to generalize but it seems that there does not either exist a fading memory effect in tension.

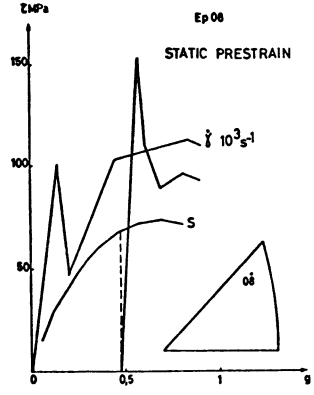

Figure 22

So we have obtained similar results in tension and compression, the only great difference is that in tension the dynamic shear stress shear strain curve is always over the static one contrary to that found in compression.

We think that this difference is due to the facts that for most of the orientations specimen axis rotation is not the same in tension and compression and that microscopical structure is certainly unlike. A study by electron microscopy would be necessary to elucidate this behavior.

Conclusions.

Compression tests performed on copper single crystals with strain rates ranging from 10^{-4} s^{-1} to 8 10^3 s^{-1} have shown that :

- the strain rate behaviour can be divided into 2 regions. Above $10^3 s^{-1}$ a linear relationship between shear stress and shear strain rate is observed of the type

$$\tau = \tau_B + \alpha \dot{\gamma}$$

with $\alpha = 4.5\ 10^3$ Pa.s. This behaviour must be related to viscous

damping mechanism on dislocations and a mobile dislocation density of about 10^7 per cm^2 may be calculated.

- low strain-rate curves are over curves obtained for a strain rate of $10^3 s^{-1}$ indicating that a minimum must exist in the stress-strain-rate diagram.

Tests performed with strain-rate changes either to lower strain rate or to greater strain rate have given the following results :

- incremental test curves never trend toward the purely dynamic or static curves. The fading memory effect which has been display for copper polycrystals is not observed for single crystals.
- the parameter $\delta_{\dot{\gamma}}^{\circ}$ describing the strain-rate effect for the "same" structure is equal to about 10 MPa for tests performed between $\dot{\gamma}^{\circ} = 8\ 10^3\ s^{-1}$ and $\dot{\gamma}^{\circ} = 4.5\ 10^{-4}\ s^{-1}$ irrespective of the initial strain rate value.
- for dynamically prestrained specimens values of the parameter δ_{ST} showing the effect of a difference of history for the same strain-rate are close to 15 to 20 MPa.
- the ratio $\delta_{ST} / \delta_{\dot{\gamma}}^{\circ}$ is about 2 between $\gamma = 10\,\%$ and $25\,\%$ for dynamically prestrained specimens.
- a slighty different behaviour is observed for samples statically prestrained in stage II or III of the single crystal stress - strain curve.
- observations by electron microscopy seem necessary to explain the variations of δ_{ST}.

Comparison with tensile tests shows a similar value of α at high strain rates. Incremental tensile tests indicate that there does not exist a fading memory effect.

Acknowledgements.

The authors wish to express their gratitude to M.C.Guillaume for stimulating discussions. Experimental works were performed with the assistance of Mme.L.Lardreau and M.A.Matagne. It is a pleasure to thank them.

References.

1. Campbell J.D. - Dynamic plasticity of metals . Udine 1970 - Springer Verlag.

2. Glenn T. ; Bradley W. - The origin of strain-rate sensitivity in OFHC copper. Met. Trans. 4 (1973) 2243-2348.

3. Edington J.W. - The influence of strain rate on the mechanical properties and dislocation substructure in deformed copper single crystals. Phil. Mag. 19 (1969) 1189-1206.

4. Dusek F. et al. - Response of Cu single crystals to high loading rates. Czech. J. Phys. B 26. (1976) 538-555 and 559-564.

5. Kumar A. ; Kumble R.G. - Viscous drag on dislocations at high strain rates in copper. J. Appl. Physics. 40-9 (1969) 3475-3480.

6. Klepaczko J. ; Duffy J. - Strain rate and temperature memory effects for some polycristalline f.c.c. metals in Mechanical Properties at high rates of strain. Institute of Physics conf. ser. N°21 (1974).

7. Eleiche A.M. ; Campbell J.D. - The influence of strain-rate history on the shear strength of copper and titanium at large strains. University of Oxford Report 1106/74 (1974).

8. Senseny P.E. ; Duffy J. ; Hawley R.H. - The effect of strain rate and strain rate history on the flow stress of four close packed metals. Brown University Report (1976).

9. Klepaczko J. - Thermally activated flow and strain rate history effects for some polycrystalline f.c.c. metals. Mat. Sci. Eng. 18 (1975) 121-135.

10. Dormeval R. ; Stelly M. ; Caput M. - Comportement en traction dynamique de monocristaux de cuivre - ICSMA 4 proceedings Nancy France (1976) Vol.3. 1141-1145.

11. Caput M. - Private communication.

12. Buchalet C. - Etude théorique et expérimentale des essais de traction à grande vitesse. Recherche d'un modèle général de comportement - Rapport CEA R-4162 (1970).

13. Bell J.F. ; Green R.E. - An experimental study of the double slip deformation hypothesis for face-centred cubic single crystals. Phil. Mag. 15 - 135 (1967) 469-476.

14. Taylor G.I. - The distortion of crystals of aluminium under compression . in the scientific papers of G.I. Taylor Vol.1. 205 - Ed. Batchelor Cambridge 1958.

15. Yoshida S. ; Nagata N. - Deformation of Aluminium single crystals at high strain rates. Trans. JIM 8 (1967) 26-32.

16. Nagata N. ; Yoshida S. - Deformation of copper single crystals and polycrystals at high strain rates. Trans. JIM 13 (1972) 332-338.

17. Larrecq M. - Comportement mécanique de monocristaux d'aluminium. CEA Internal Report 1976.

18. DeVault G.P. - The effect of lateral inertia in the propagation of plastic strain in a cylindrical rod. J. Mech. Phys. Solids 13 (1965) 5.

19. Kumar A. ; Hauser F.E. ; Dorn J.E. - Viscous drag on dislocations in aluminium at high strain rates. Acta Met . 16 (1968) 1189-1197.

20. Klahn D. ; Mukherjee A.K. ; Dorn J.E. - Strain rate effects . ICSMA 2 Proceedings Asilomar (1970) Vol.3. 951-982.

21. Alers G.A. ; Thompson D.O. - J. Appl. Phys. 32 (1961) 283 cited by /22/.

22. Stern R.M. : Granato A.V. - Overdamped resonance of dislocations in copper. Acta Met. 10 (1962) 358-381.

23. Jassby K.M. ; Vreeland T. - An experimental study of the mobility of edge dislocations in pure copper single crystals. Phil. Mag. 21 - 174 (1970) 1147-1168.

24. Suzuki T. ; Ikushima A. ; Aoki M. - Acoustic attenuation studies of the frictional force on a fast moving dislocation. Acta. Met. 12 (1964) 1231-1240.

Dynamic Strength of Ti-Alloys and Al-Alloys

KICHINOSUKE TANAKA, KINYA OGAWA
and TAKETOSHI NOJIMA

Department of Aeronautical Engineering,
Faculty of Engineering,
Kyoto University, Kyoto, JAPAN

Summary

Continuous compression tests and incremental strain rate change tests of four kinds of titanium alloys and four kinds of aluminium alloys are carried out within the strain rate range of 10^{-4} $\sim 10^{3}$/s and the temperature range of -195°$\sim$450°C. The experimental results reveal the effects of the strain rate and the temperature on the flow stress at 5% strain. The strain rate sensitivity obtained by the continuous tests or the incremental tests is also revealed. The thermal and the athermal components of stress are presumed and the relation between the activation volume and the thermal component of stress is discussed.

Introduction

It is very important to clarify the mechanical properties of materials at high strain rate. A succession of techniques for carring out high strain rate tests have been developed and the experimental results have been discussed from both macroscopic and microscopic aspects. Progress in this field has been described in recent reviews [1, 2], including the experimental results for titanium alloys and aluminium alloys.

This paper presents the experimental results for titanium alloys and aluminium alloys obtained by continuous compression tests and incremental strain rate change tests in a strain rate range of $10^{-4}\sim 10^{3}$/s (low and medium strain rate ranges) and a temperature range of -195°$\sim$450°C.

The split Hopkinson bar technique [3] has been applied in inves-

tigating the dynamic strength of various materials [4~6]. This technique has also been used in obtaining our experimental results [7].

The investigation of the mechanical properties of materials from a microscopic aspect [8, 9] is also significant. The clarification of the interrelation of microscopic and macroscopic phenomena has been a problem of long-standing [10]. History effect [11, 12] and force barrier shape [13] are treated recently.

Test materials and specimens

The eight kinds of materials listed in table 1 were tested. The chemical composition, heat treatment and Vickers hardness after the treatment are also shown in the table.

The diameter and the height of the cylindrical specimen are shown in table 1.

Table 1. Materials

Material	Chemical composition	Heat treatment	Vickers hardness	Specimen	Ref. no.
Ti		Annealed at 650°C for 2 hours	150	$7^{\phi}\times7$	
Ti-5Al	5.07%Al 2.29%Sn 0.32%Fe	Annealed at 800°C for 2 hours	330	$5^{\phi}\times7$	[14]
Ti-6Al	5.99%Al 4.14%V 0.22%Fe	Annealed at 700°C for 2 hours	435	$5^{\phi}\times7$	[15]
Ti-Mo	14.8%Mo 5.09%Zr 0.04%Fe	Annealed at 800°C for 2 hours	330	$5^{\phi}\times7$	
Al	99.997%Al	Annealed at 500°C for 1 hour	20	$8^{\phi}\times8$	[16] [17]
Al-Mg	1.08%Mg 0.01%Cu 0.06%Si 0.01%Fe	Annealed at 500°C for 1 hour	35	$8^{\phi}\times8$	[17] [18]
Al-Cu	4.01%Cu	Solution treated at 530°C for 1 hour Quenched in ice water Aged at 350°C for 36 hours	34	$5^{\phi}\times7$ $6^{\phi}\times7$	[16] [17]
A3B2 (2017)	(Duralumin)	Solution treated at 500°C for 1 hour Quenched in ice water Aged at 350°C for 2 hours	67	$6^{\phi}\times6$	[16] [17]

Test method

Continuous compression tests (constant temperature and constant strain rate) and incremental strain rate change tests (constant temperature, but the constant strain rate being abruptly

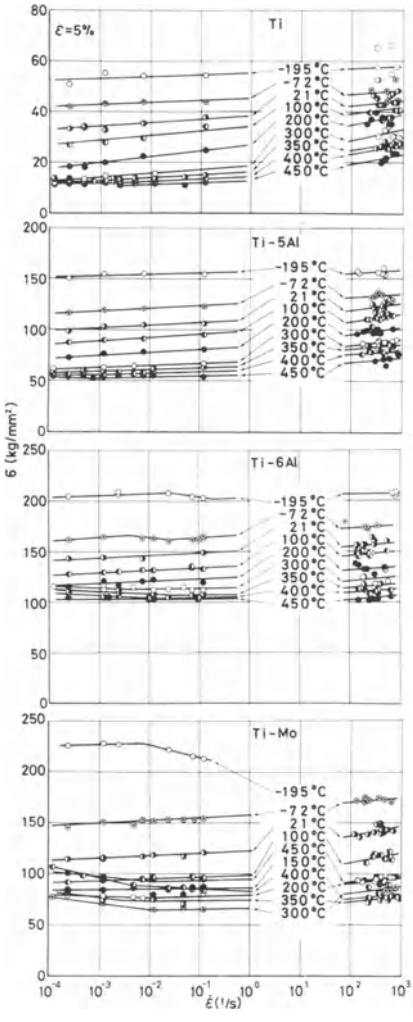

Figure 1. Effect of strain rate on the flow stress of four titanium alloys.

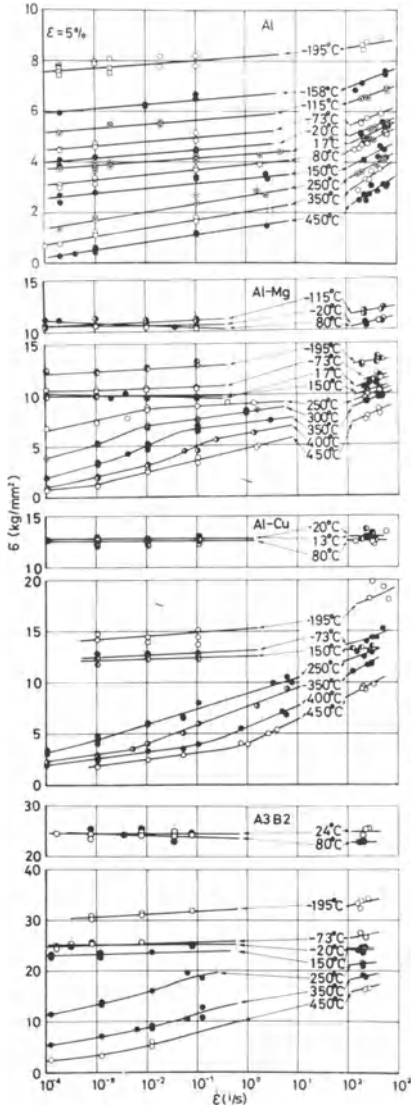

Figure 2. Effect of strain rate on the flow stress of four aluminium alloys.

changed to another strain rate) were carried out. The strain at which the strain rate was changed abruptly was 5%.
The strain rate was within the range of $10^{-4} \sim 10^{3}$/s. An Instron testing machine was used for the static (low strain rate) tests, and a split Hopkinson bar apparatus was used for the dynamic (medium strain rate) tests. The incremental tests in the dynamic region were carried out with a stepped striker bar [19]. A hydraulic testing machine was used to test aluminium alloys at a strain rate of about 1/s [20]. The temperature range in which the tests were performed was -195°∿450°C.

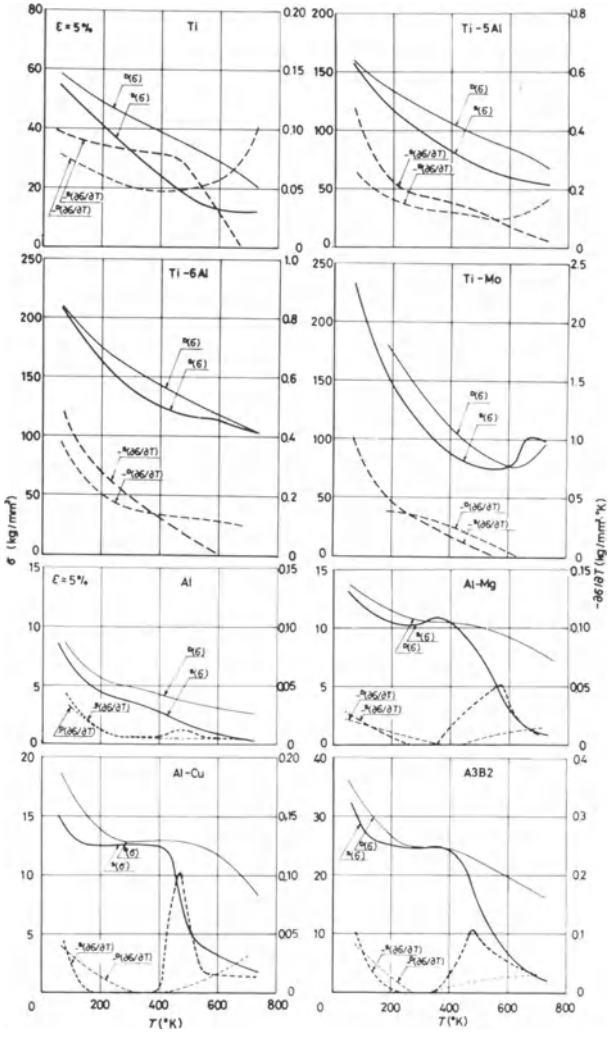

Figure 3. Effect of temperature on the flow stress and the temperature sensitivity.

Test results

The relation between the flow stress at 5% strain and the strain rate at various temperatures is illustrated in figure 1 for titanium al-

loys, and in figure 2 for aluminium alloys. The stress is the true stress and the strain is the true strain. Figure 3 illustrates the relation between the flow stress and the temperature. Superscripts S and D written on the left-hand side of the symbols denote the static value ($\dot{\varepsilon}\simeq 1\times 10^{-4}$/s) and the dynamic value ($\dot{\varepsilon}\simeq 2\times 10^{2}$/s).

The temperature sensitivity, $\partial\sigma/\partial T$, is also shown in figure 3. Figure 4 shows the strain rate sensitivity, $\partial\sigma/\partial\log\dot{\varepsilon}$. Superscripts C and I on the right-hand side indicate the value calculated from the slope of the curve in figure 1 and the value obtained experimentally by the incremental tests. In regard to the incremental tests, the strain rate was abruptly increased 10 times in the static tests and twice in the dynamic tests. In the case of aluminium, it has been proved that the amount of an abruptly increased strain rate has little effect on the static strain rate sensitivity [20].

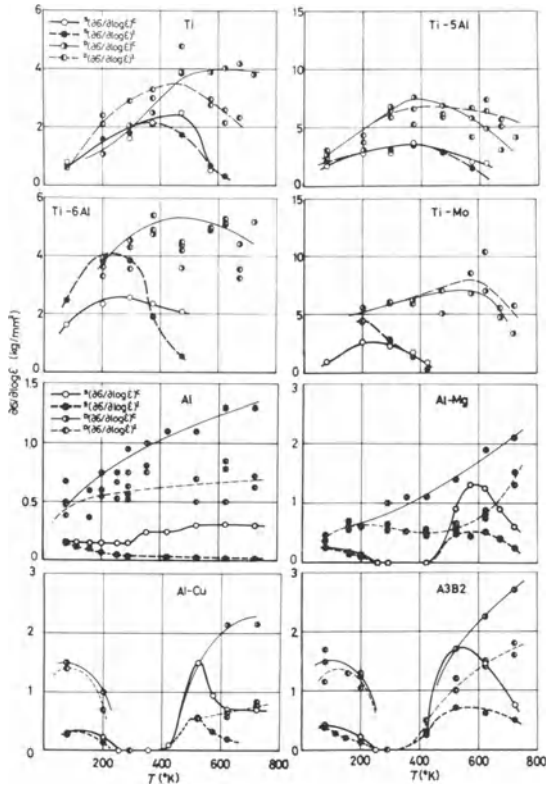

Figure 4. Effect of temperature on the strain rate sensitivity.

Consideration

The strain rate $\dot{\varepsilon}$ of thermally activated flow is expressed as

$$\dot{\varepsilon}=A\exp[-(H_0-\int v^*\,d\sigma^*)/kT]. \qquad (1)$$

A is a parameter proportional to the number and distribution of activation site and to the freqency of vibration of the dislocation segment, H_0, the total activation energy, and σ^*, the thermal component of stress, being expressed by

$$\sigma^*=\sigma-\sigma_G, \qquad (2)$$

where σ_G is the athermal component of stress. v^* is the activation volume, k Boltzmann's constant and T the temperature. In the case where the activation energy is given by $H_0-v\sigma^*$, the following relation exists [21]:

$$v^*=v+\sigma^*(\partial v/\partial\sigma^*)_T$$

Equation (1) is written as

$$kT(\ln\dot{\varepsilon}-\ln A)=-(H_0-\int v^*d\sigma^*). \qquad (1')$$

It is assumed that H_0 is constant, v^* is a function of σ^*, and A and σ^* are functions of $\dot{\varepsilon}$ and T. Differentiating equation (1') with respect to σ^*, the following is obtained.

$$v^*=kT[(\partial\ln\dot{\varepsilon}/\partial\sigma^*)_T-(\partial\ln A/\partial\sigma^*)_T] \quad (3)$$

It can be considered that A and σ_G do not change their values at an abrupt change of strain rate. Therefore, equation (3) becomes

$$v^*=kT(\partial\ln\dot{\varepsilon}/\partial\sigma^*)^{I}_{T}=kT(\partial\ln\dot{\varepsilon}/\partial\sigma)^{I}_{T}. \qquad (3')$$

The relation between v^* and T is illus-

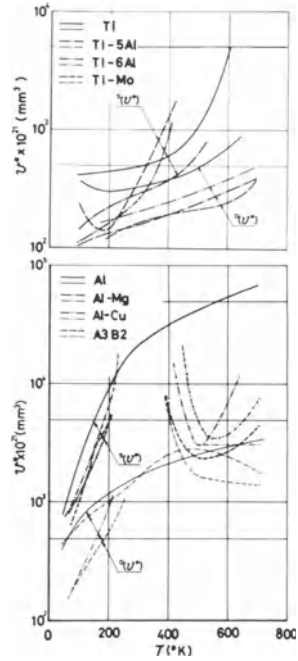

Figure 5. Effect of temperature on the activation volume.

Table 2. Numerical values

Material	$^{S}(T_c)$ °K	$^{D}(T_c)$ °K	$\ln A$	H_0 eV		H_0' eV
Ti	540	$^{D}(v^*)_{T=565}=^{S}(v^*)_{T=400}$	10 0.86	15 1.09	20 1.33	1.65
Ti-5Al	580	$^{D}(v^*)_{T=400}=^{S}(v^*)_{T=160}$	10 0.92	15 1.17	20 1.42	2.45
Al	290	$^{D}(v^*)_{T=290}=^{S}(v^*)_{T=75}$	10 0.46	12 0.51	14 0.56	0.66
A3B2	130	340, 300, 275	14 0.25	16 0.27	18 0.30	0.29

trated in figure 5. Differentiating equation (1′) with respect to T,

$$(\partial\sigma^*/\partial T)_{\dot{\varepsilon}}=k[\ln\dot{\varepsilon}-\ln A-T(\partial\ln A/\partial T)_{\dot{\varepsilon}}]/v^* \qquad (4)$$

is obtained. With the assumption that $(\partial\ln A/\partial T)_{\dot{\varepsilon}}$ can be neglected, it follows

$$(\partial\sigma^*/\partial T)_{\dot{\varepsilon}}=k(\ln\dot{\varepsilon}-\ln A)/v^*=(\ln\dot{\varepsilon}-\ln A)/[T(\partial\ln\dot{\varepsilon}/\partial\sigma)^{\mathrm{I}}_{T}]. \qquad (4')$$

Integration of this equation gives $\sigma^*(T)$. The boundary condition that $\sigma^*=0$ at temperature T_c is used. T_c is the temperature at which the σ-T curve changes its slope remarkably. The temperatures in static case ${}^{S}(T_c)$ for four materials and that in dynamic case ${}^{D}(T_c)$ for A3B2 are listed in table 2. Because ${}^{D}(T_c)$ is generally difficult to decide on the σ-T curve, the integration was carried out with the condition $\sigma^*={}^{S}(\sigma^*)_{T={}^{S}(T)}$ at $T={}^{D}(T)$, where ${}^{S}(v^*)_{T={}^{S}(T)}={}^{D}(v^*)_{T={}^{D}(T)}$ (table 2). This assumption means that v^* is a single valued function of σ^*. Corresponding to the given numerical values of $\ln A$, the σ^*-T relation is obtained and then the σ_G-T relation can be decided. These relations are illustrated in figure 6. It seems reasonable to suppose that σ^* and σ_G increase with the decrease of the temperature and that the values in dynamic tests are higher than those in static tests. From this point of view, the values of $\ln A$ of four materials in table 2 are less than 18, 11, 10 and 15, re-

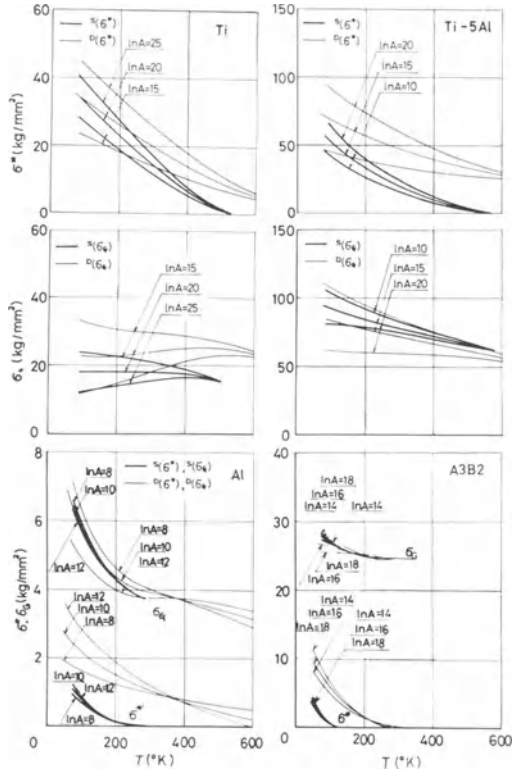

Figure 6. Effect of temperature on the thermal and the athermal components of stress

spectively.

Putting $\sigma^*=0$ in equation (1'), the total activation energy H_0 is given as

$$H_0=k\,{}^{S}(T_c)[\ln A-\ln{}^{S}(\dot{\varepsilon})]. \tag{5}$$

The values thus obtained are listed in table 2.

On the other hand, the activation energy H is given as

$$H=kT^2[-(\partial\ln\dot{\varepsilon}/\partial\sigma^*)^{C}_{T}(\partial\sigma^*/\partial T)^{C}_{\dot{\varepsilon}}+(\partial\ln A/\partial\sigma^*)_{T}(\partial\sigma^*/\partial T)^{C}_{\dot{\varepsilon}}-(\partial\ln A/\partial T)_{\dot{\varepsilon}}]$$
$$=kT^2[-(\partial\ln\dot{\varepsilon}/\partial\sigma^*)^{I}_{T}(\partial\sigma^*/\partial T)^{I}_{\dot{\varepsilon}}]. \tag{6}$$

Assuming $\ln A$=const. and putting $\sigma^*=0$ at $T=T_c$, the total activation energy H_0 is expressed as

$$H_0=kT_c^2[-(\partial\ln\dot{\varepsilon}/\partial\sigma^*)^{C}_{T}(\partial\sigma^*/\partial T)^{C}_{\dot{\varepsilon}}]_{T=T_c}.$$

The approximate values, H_0', defined as

$$H_0\simeq H_0'=kT_c^2[-(\partial\ln\dot{\varepsilon}/\partial\sigma)^{C}_{T}(\partial\sigma/\partial T)^{C}_{\dot{\varepsilon}}]_{T=T_c} \tag{6'}$$

are also written in table 2. Figure 7 shows the v^*-σ^* relation. It seems that the curves in the static range are almost continuous with those in the dynamic range for aluminium alloys, but it is not easy to say the same for titanium alloys.

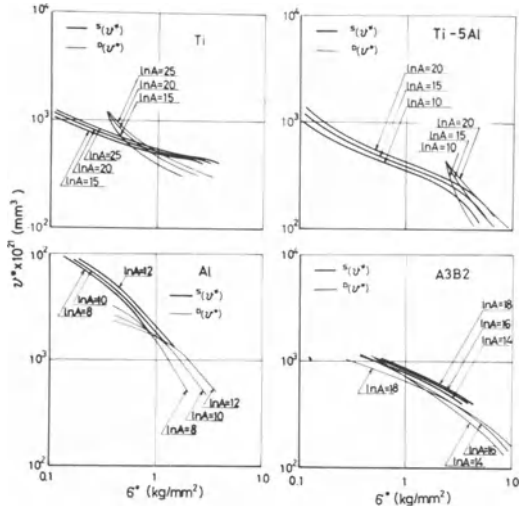

Figure 7. Activation volume against thermal component of stress.

Conclusions

1. Flow stress of Ti, Ti-5Al and Al increases steadily with the increase of the strain rate and the decrease of the temperature. Ti-6Al, Al-Mg, Al-Cu and A3B2 have the temperature range where the stress is independent of the temperature or decreases with the increase of the strain rate. Ti-Mo shows rather complicated behaviour.

2. The strain rate sensitivity calculated on the basis of con-

tinuous test results does not coincide generally with that obtained by incremental strain rate change tests, except in the case of Ti-5Al. The value of the former tends to be smaller in the cases of titanium alloys and larger in the cases of aluminium alloys comparing with the latter value.

3. Assuming that static deformation and dynamic deformation are controlled by the same single thermally activated process and $\ln A$ is constant, thermal and athermal components of stress are presumed. In the case of titanium alloys, the thermal and athermal components of stress are the same order, but, in the case of aluminium alloys, the former is far smaller than the latter.

4. The relation between the thermal component of stress and the activation volume in static range corresponds with that in dynamic range for aluminium alloys, but the correspondence is not so good for titanium alloys.

References

1 Campbell, J.D.: Dynamic plasticity: Macroscopic and microscopic aspects. Mat. Sci. Engg. 12 (1973) 3-21

2 Lindholm, U.S.: Mechanical properties at high rates of strain. The Institute of Physics, Conference Series Number 21, London (1974) 3-21

3 Kolsky, H.: An investigation of the mechanical properties of materials at very high rates of loading. Proc. Phys. Soc. B. 62 (1949) 676-700

4 Hauser, F.E.; Simmons, J.A.; Dorn, J.E.: Responce of metals to high velocity deformation. ed Shewmon, P.G.; Zackay, V.F., New York: Interscience Pub. (1961) 93-114

5 Chiddister, J.L.; Malvern, L.E.: Compression-impact testing of aluminium at elevated temperatures. Exp. Mech. 3 (1963) 81-90

6 Lindholm, U.S.: Some experiments with the split Hopkinson pressure bar. J. Mech. Phys. Solids 12 (1964) 317-335

7 Tanaka, K.; Kinoshita, M.: Compressive strength of mild steel at high strain rate and at high temperature. Bull. Jap. Soc. Mech. Engrs. 10 (1967) 429-437

8 Conrad, H.: Thermally activated deformation of metals. J. Metals July (1964) 582-588

9 Dorn, J.E.: Dislocation dynamics. ed Rosenfield, A.R.; Hahn, G.T.; Bement, A.L.; Jaffee, R.I., New York: McGraw-Hill (1968) 27-55

10 Dorn, J.E.; Goldberg, A.; Tietz, T.E.: The effect of thermal-mechanical history on the strain hardening of metals. Trans. AIME 180 (1949) 205-224

11 Duffy, J.: Mechanical properties at high rates of strain. The Institute of Physics, Conference Series Number 21, London (1974) 72-80

12 Klepaczko, J.; Duffy, J.: Mechanical properties at high rates of strain. The Institute of Physics, Conference Series Number 21, London (1974) 91-101

13 Davidson, D.L.; Lindholm, U.S.: Mechanical properties at high rates of strain. The Institute of Physics, Conference Series Number 21, London (1974) 124-137

14 Tanaka, K.; Ogawa, K.: The static and dynamic compressive strength of Ti and Ti alloys. Proc. Second Inter. Confer. Mat., Boston (1976) 1598-1602

15 Tanaka, K.; Ogawa, K.: Deformation of pure titanium and titanium alloys. Proc. 20th Jap. Cong. Mat. Res. (1977) 76-81

16 Tanaka, K.; Nojima, T.: Strain rate change tests of aluminium alloys under high strain rate. Proc. 19th Jap. Cong. Mat. Res. (1976) 48-52

17 Nojima, T.: Strain rate effect on the strength of aluminium and aluminium alloys. Proc. Second Inter. Confer. Mat., Boston (1976) 1785-1789

18 Tanaka, K.; Nojima, T.: Effects of temperature and strain rate on the strength of aluminium-1.1wt% magnesium alloy. Proc. 20th Jap. Cong. Mat. Res. (1977) 89-93

19 Tanaka, K.; Nojima, T.: Strain rate effect on the strength of aluminium. Proc. Inter. Confer. Mat., Kyoto Vol. 1 (1972) 176-183

20 Tanaka, K.; Nojima, T.: Strain rate change test on aluminium. Proc. 18th Jap. Cong. Mat. Res. (1975) 69-71

21 Luton, M.J.; Jonas, J.J.: A model for high temperature deformation based on dislocation dynamics, rate theory and a periodic internal stress. Acta Met. 18 (1970) 512-517

Steady State Deformation and Dynamic Restoration Processes During High Strain Rate and High Temperature Deformation in Metals and Alloys

T. NAKAMURA

Graduate School of Science and Engineering at Nagatsuta, Tokyo Institute of Technology, Meguro-ku, Tokyo, Japan 152

Summary

At strain rates from 10^{-3} to 10^{2} and temperature above 0.5 T_m, the flow behaviours of various metallic materials are classified into alminum type and copper type. The former has dynamic recovery as a Restoration process and the latter dynamic recrystallization. Copper type materials show smallest in the magnitude of temperature dependence and strain rate sensitivity exponent "m" value. Steady State flow Stress can be expressed as functions of product of strain rate and the reciprocal of the Arrhenius term of temperature dependence, and the values of stress exponent "n" value in it well correlates to the restoration processes of materials. It has been clarified from the observation of deformed microstructure that dynamic recrystallization as restoration process is occured soon after passing of the peak in flow curves. Finally, there has been good correlation between the deformation condition parameter and dynamically recrystallized grain diameters or dynamically recovered ones.

Introduction

Hot working an important process in which materials are applied the largest reduction and given a high strain rate deformation, among the various working operations undergone in the process from ingots to products. Results of the investigation to be presented hereafter, are on the analysis of the hot working process of various metallic materials mainly by mean of hot torsional deformation. The recent reports of other type of deformation in our country are also reviewed.

one of the purpose of the present investigation is to supply the basic data useful for hot working of metals by inquiring critically, the interrelation of flow stress, strain rate and temperature during a steady state deformation at the view point of mechanical approach. Special notice is taken on the fact that the characteristic of high temperature deformation of metals during hot working is the occurence of steady state deformation in which work hardening due to deformation equilibrates with dynamic restoration process as a thermal softening effects. Secondly, to consider the behaviours of deformation and restoration of metals at elevated temperature inclusively, the dynamic restoration process which contributes to the occurence of steady state deformation is investigated metallographically.

Steady State Deformation Behaviours

When metals are deformed at high temperature above $0.5T_m$, where T_m is melting temperature in degree Kelvin, with

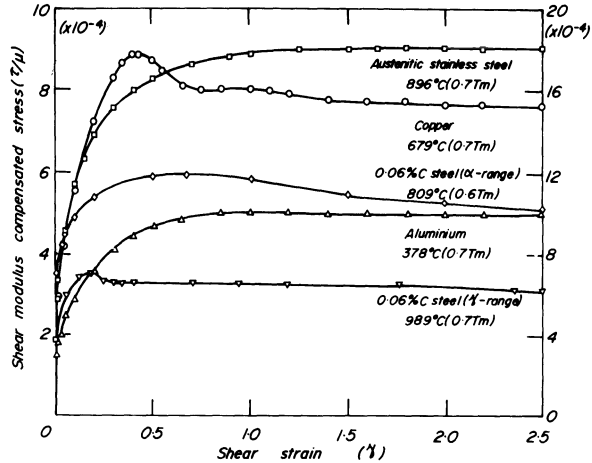

Fig. 1 Characteristic steady state deformation curves of Al, Cu, austenitic stainless steel and low carbon steel both in α and γ ranges, at 0.7 T_m or 0.6 T_m and shear strain rate of 0.12 sec^{-1}. Flow stress is expressed as the ratio of shear stress to shear modulus at the temperature of deformation. Shear modulus compensated flow stress of austenitic stainless steel is to be read in the right scale.

constant strain rates, the flow stress is constant in the larger strains, although it increases with strains during initial hardening region. Phenomenon of the steady state deformation occurrs also in the secondary creep, and has been studied extensively.

The characteristic shapes of the stress-strain curves for steady state deformation are shown in Fig.1 for typical metals at temperature of about 0.7 T_m [1,2]. These steady state deformation curves were roughly classified into aluminum type and copper type, in term of the approaching features to steady state. It would be considered that the reason of the changes of shapes of flow curves is due to the difference in the controlling mechanism of dynamic restoration process associated with deformation.

In aluminum in which dislocation climb is rapid, the initially work hardened structure is modified into a partially polygonized structure by the time the maximum stress is reached and further deformation leads to a sharpening of the sub-boundaries, followed by a migration of grains boundary when boundary angle is large enough. Since restoration is rapid, only a small maximum in the stress-strain curve, if any, is observed. While, in copper, dislocation climb is slower and sufficient strain energy is available to initiate the recrystallization as a restaration process. Therefore, copper softens during work hardening so as to exhibit a maximum in the stress-strain curve and fall into the steady state level. Thus, the materials belonging the copper type have a peaked stress-strain curve and those of alminum type show the stress-strain curve having no peak.

Temperature and strain Rate Dependence of Flow Stress

The magnitude of Temperature dependence of shere modulus compensated flow stress, flow stress divided by the shere modulus at the deformation temperature, was smaller below

Table 1. Temperature and strain rate dependences of flow stress up to large strain[3].

Material	$\tau_{10\%}$ T_h/T_m	τ_{max} T_h/T_m	Oder of magnitude of temperature dependence	Order of magnitude of τ/μ_T	Strain rate dependence "m" value
Al	0.4	0.4	2	3	$0.23(0.8T_m)$
Cu	0.55	0.4	4 smallest	2	$0.16(0.8T_m)$
SUS 304°	0.6	0.5	3	1 largest	$0.20(0.8T_m)$
αFe	0.4	0.4	1	4	$0.15(0.6T_m)$
γFe			1 largest	4 smallest	$0.16(0.8T_m)$

°JIS (18-8 stainless steel)

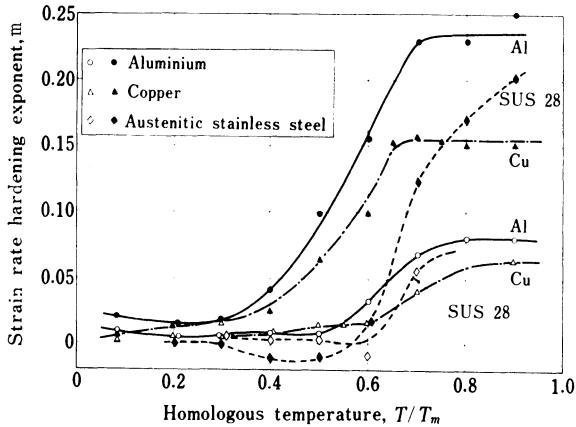

Fig. 2 Variation of strain rate sensitivity "m" value with homologous temperature in Al, Cu, and austenitic stainless steel. Black circles are obtained from strain rate dependence of 200 % strain or maximum flow stress, open circles from differential tests at strain of 100 % and before softening in the case of Cu.

0.5 or 0.6 T_m and became larger above ones. Thus, a transition which was shown as a knee in the relation between flow stress and temperature occurred at some temperature, T_h. The larger the strain, the lower became the transition temperature T_h which was about 0.6 $T_m$for strain of 0.2 % and 0.5 T_m the strain of 200 %.

Temperature and strain rate dependence of flow stress could be summarised as in Table 1 where the transition temperature T_h for flow stress at 10 % strain maximum flow stress,strain rate hardening exponent "m" and oder of magnitude of shear modulus compensated flow stress $\tau/\mu T$ are

given for four materilas[3]. The dependence of strain rate hardening exponent for steady state deformation on temperature are shown in Fig. 2[3]. The exponent "m" increased as temperature increased until the characteristic temperature was reached, above which "m" remained nearly constant except in stainless steel in which the exponent continued increase. The magnitude m was largest for alminum, i.e. dynamic recovery type material, and smallest for copper and low carbon steel, i. e. dynamic recrystallization one.

Interdependence of Flow Stress, Temperature and Strain Rate during steady State Deformation

The mechanical equation of state representing the interdependence of flow stress, temperature and strain rate in hot working are as follows:

Power law	$\dot{\varepsilon}=A_2\sigma^n\exp(-Q/RT)$	at low σ	(1)
Exponential law	$\dot{\varepsilon}=A_3\exp(\beta\sigma)\exp(-Q/RT)$	at high σ	(2)
Hyperbolic sine law	$\dot{\varepsilon}=A_1[\sinh(\alpha\sigma)]^{n'}\exp(-Q/RT)$	at all σ	(3)
	$\dot{\varepsilon}=f(\sigma)\exp(-Q/RT)$		(4)
	$f(\sigma)=Z=\dot{\varepsilon}\exp(Q/RT)$		(5),

where $\dot{\varepsilon}$ is strain rate, σ flow stress, T temperature, σ activation energy, Z Zener-Hollomon parameter, R gas constant, and A_1, A2, A_3, n, n' and $\beta=\alpha n$ are constants. Commonly used equations are (1), (2) and (3), however, none of these mathematical relationship have a strict theoretical foundation. The most convienient one which was proposed and widely used by sellers and Tegart is the power hyperbolic sine stress relationship, (3)[4-7]. This relationship is a development of the one proposed for creep by Garofalo[8], into the hot working condition region. The activation energy, Q, is approximately to that for creep or self diffusion. Further, at low stress ($\alpha\sigma<0.8$) the equation (3) reduces the power law relationship of equation (1). which is used well in creep. At high stress ($\alpha\sigma>1.2$), equation (3) is convertable to the exponential

Table 2 Constnts in equation (3) for heat resisting materials.

Alloy	ln A	n	α	Q	nα	Q/nα
	sec^{-1}		$(kg/mm^2)^{-1}$	kcal/mol	$(kg/mm^2)^{-1}$	$\frac{kcal\ kg}{mm^2\ mol}$
17 Cr	57.35	6.9	0.117	142.0	0.60	175
2.25Cr 1Mo	30.98	3.24	0.188	93.0	0.61	152
SUS 304	36.39	5.53	0.088	103.1	0.49	211
SUS 321	43.35	5.85	0.104	126.8	0.61	209
SUS 347	37.11	3.73	0.135	111.7	0.50	222
SUS 316	38.43	5.45	0.094	113.1	0.51	220
SUS 316M	37.85	4.92	0.106	115.7	0.52	221
SUS 317L	35.90	5.24	0.079	104.2	0.42	249
SUS 310	42.01	4.55	0.129	128.9	0.59	220
HK 40				130.2	0.52	249
Incoloy 802				97.4	0.38	260
Incoloy 800	26.37	2.95	0.108	78.9	0.32	247
Inconel 600	30.87	4.03	0.061	85.9	0.24	358
Hastelloy X				119.0	0.34	350
R 4286				139.0	0.34	408
Inconel 617				167.8	0.34	494
SSS 410				170.9	0.33	513
SSS 113M				118.2	0.20	513

relationship of equation (2), where the constants α and n are related by $\beta=\alpha n$ so that β and n can be determined from experimental data for high and low stress, respectively.

Tamura, Kamemura and Ichinose recently presented the sellers' constants for various heat resisting steels and alloys, which are tabulated in Table 2[9,10]. They reported that those values can be used successfully in predicting the deformation resistances in hot extrusion of such alloys.

The steady state flow stress can also be expressed as the product of the strain rate and the reciprocal of the Arrhenius term of temperature dependence, namely $\dot{\varepsilon}\exp(Q/RT)$, and this product is called the temperature compensated strain rate parameter, Z or the deformation condition parameter. This value is maintained constant during hot working test and value of Z increases either with increasing strain rate or decreasing temperature. For

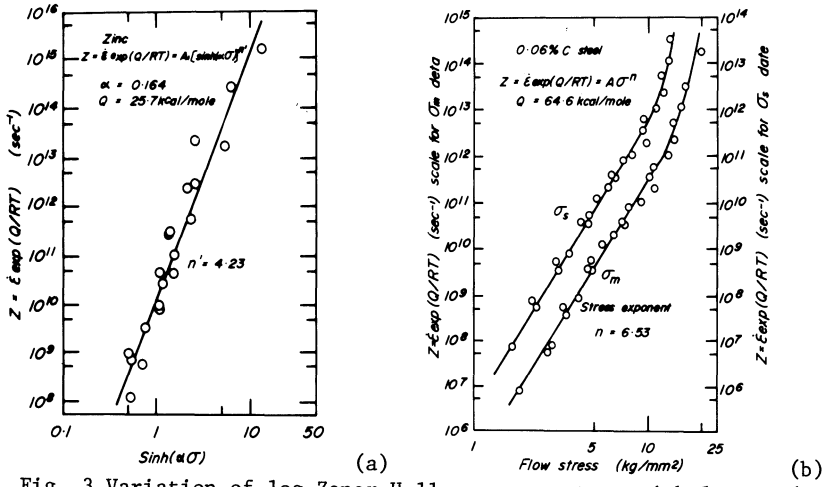

Fig. 3 Variation of log Zener-Hollomon parameters with log sin($\alpha\sigma$) in hot torsion of zinc (a), and relation between Z and peak flow stress (σ_m) and steady state flow stress (σ_s) for 0.06 % C steel (b).

the high values, the higher flow stress originates from the fewer thermally activated events per unit strain which arise from either temperature or the short duration accorded by a high strain rate.

The correlation of Z and flow stress allowed the representation of the data for different temperatures as a single straight line, as shown in Fig. 3(a). In the figure the plot of Z calculated by using the activation energy for self diffusion, Q=25.7kcal/mol, against sinh$\alpha\sigma$ in hot torsion of Zinc is shown. This type of plot provides a reliable method of interpolating data to obtain values of flow stress at any temperature or strain rate within the ranges studied. Fig. 3 (b) is the similar plot for 0.06 %C steel. From the such plots, the stress exponent "n" values were correlated with restoration process as: polygonization for n lower than 5, polygonization and recrystallization for n between 5 and 6, and recrystallization for n larger than 6.

Microstructure during High Temperature Deformation

The microstructure during high temperature deformation

are most important factors which determine flow stress and were widely investigated by Sakui and Sato[11], and recently by Sakui and Sakai[12] with using specimens deformed by an elegant tensile machine.

The reason why the large strain can be imposed to materials in hot working condition, is due to the approximately absent work hardening. In other words, the work hardening cannot be observed apparently, because of the dynamic equilibrium between the work hardening and the thermal softening process during deformation. The behaviours of metals in hot working remain unsolved, the reason of this, as mentioned above, is due to the complexity of the hot working mechanisms because of the superimposed effect of mechanical process due to deformation and microstructural evolution by the operation of dynamic restoration processes. Therefore, the microscopical features of the structure obtained by high temperature deformation, have the interest of variety. And then, the observation of the structure during hot working is one of the useful methods in consideration of plastic behaviours of metallic materials.

According to the results of the observations of quenched-in structure during hot working in various metals and alloys, the deformed microstructures are able to be classified into two groups. The first group contains Al, Al alloys, commercial purity α iron, ferritic iron alloys and austenitic stainless steels, and the second one Cu, Cu alloys, Ni, Ni alloys, γ range steels and high purity αiron. In the materials belonging to the first group, the sub-grains are deformed at the instance of quenching after deformation in spite of the degree of given strain whether large or small, and so-called polygonization phenomenon is observed. The characteristics of the second group materials are the development of substructures interior of strained grains during small strain in hot de-

formation, and the genaration of the eqiaxed recrystallized grains at large strains in steady state region. In the case of generation of the recryatallized grains, the peaked stress-strain curves can be obtained.

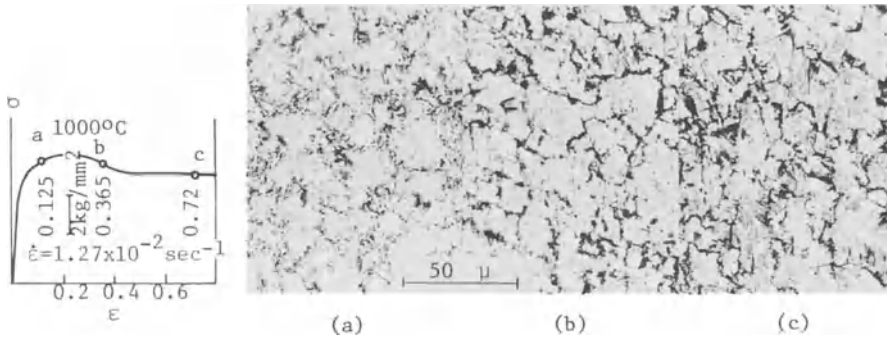

Fig. 4 Typical stress-strain curve and quenched-in microstructure of the each point on the curve, for 0.10 % C, 0.02 % Nb steel at 1000°C.

Fig. 4 illustrates quenched-in microstructures at the strain given at each point on the stress-strain curve for low carbon steel containing small amount of Nb deformed at 1000 C.[13] In the initial hardening range, austenitic grains became fine under the operation of dynamic recovery, and soon after passing the peak microstructure begins to change to recrystallized grains and dynamic recrystallization structure is well attained in the steady state of deformation. The same behaviour also are reported by Ohuchi [14] for such materials in the study relating controlled rolling. In these investigations, dynamically recrystallized grain structure cannot be observed at all, when peaked stress-strain curves are not obtained under the condition of high strain rate for the same material and same deformation temperature of Fig. 4. Therefore, it is concluded that the peaked flow curves are certainly appeared with occurrence of dynamic recrystallization. Fig. 5 illustrates the quenched-in microstructures of the each point on the plots representing the relations between the steady state flow stress andparameter Z. This plots have a knee point at the vicinity of $Z=10^{12}sec^{-1}$,

and at values of Z below the knee the equiaxed recrystallized grain structure was observed. It could be understood that the recrystallized grain size decreases with increasing the flow stress and the Z value up to the range of $Z<10^{12}sec^{-1}$. At the condition of $Z>10^{12}sec^{-1}$ althouth the recrystallized grains nucreate at grain boundaries. The large enough strain to cover the whole

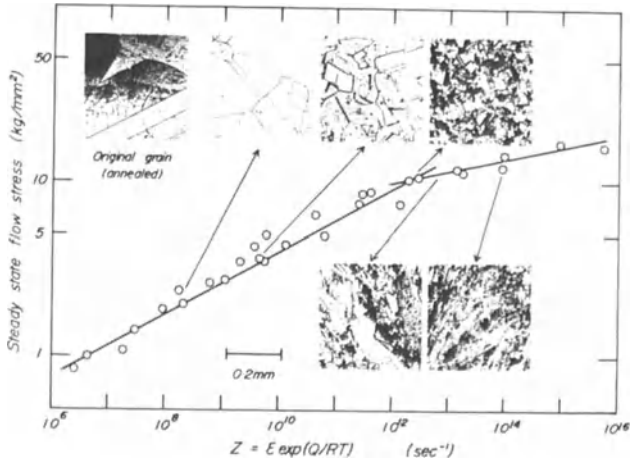

Fig. 5 Representation of proceedings of the dynamic recrystallisation on the plot of steady state flow stress with parameter Z.

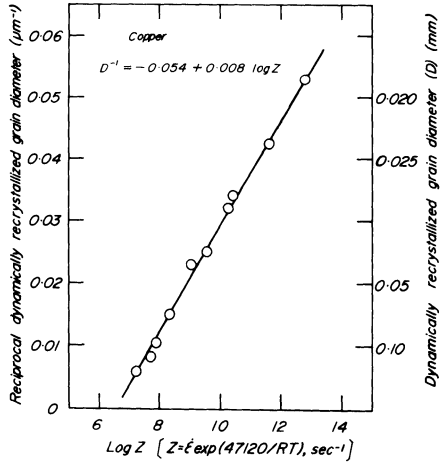

Fig. 6 Relation between the reciprocal dynamic recrystallized grain diameter and logarithm of temperature compensated strain rate.

structure, cannot be attained. Fig.6 illustrates the quantative relation between the deformation condition parameter Z and recrystallized grain size as shown in the previous figure, for the condition $Z<10^{12}sec^{-1}$. The good correlation which is shown in the figure, justified that the mechanism of deformation is thermally activated and resultant dynamically recrystallized grain size depends on the numbers of thermally activated events which are inversely proportional to parameter Z and also determine the hot working stress though relation shown in Fig.5. This fact considered as the same as the existence of the constant relation between the sub-grain size, parameter Z and flow stress in the dynamically recovery type materials.

References

1) Ohtakara, Y.; Nakamura, T.; Sakui, S.: Steady state deformation and restoration process in metals and alloys. Trans. Iron Steel Inst. Japan. 12 (1972) 207-216.
2) Nakamura, T.; Ueki, M.: Dynamic recrystallization in copper and mild steel during high temperature torsional deformation. J. Soc. Mat. Sci. Jap. 23 (1974) 182-188.
3) Ohtakara, Y.; Nakamura, T.; Sakui, S.: Temperature and strain dependences of flow stress in metals and alloys in torsional deformation. Trans. Iron Steel Inst. Jap. 12 (1972) 36-44.
4) Sellers, C. M.; Tegart, W. J. McG.: La relation entre la resistance et la structure dans deformation a chaud. Mem. Sci. Rev. 63 (1966) 731-746.
5) Jonas, J. J.: A comparison of creep and hot working strain rate relationship. Trans. A. S. M. 62 (1969) 300-303.
6) Jonas, J. J.; Sellers, C. M.; Tegart, W. J. McG.: Strength and structure under hot working conditions. Met. Rev. 14 (1969) 1-24.
7) Uvira, J. L.; Jonas, J. J.: Hot compression of Armco iron and silicon steel. Trans. Met. Soc. AIME 242 (1968) 1619-1626.
8) Garofalo, F.: An empirical relation defining the stress dependence of minimum creep rate in metals. Trans. Met. Soc. AIME 227 (1963) 351-356.
9) Tamura, M.; Kamemura, Y.; Ichinose, H.:Torsion tests of several high alloy steel and flow resistance in hot extrusion. Rep. 123rd Comm. Heat Resist. Metals and Alloys, Japan Soc. Prom. Sci. 18 (1977) 61-71.
10) Tamura, M.; Kamemura, Y.; Ichinose, H.: Effect of alloying element on the deformation resistance of austenitic stainless steels and Nickel base alloys at high temperature. ibid. 18 (1977) 189-

199.
11) Sakui, S.; Sato, K.: Fundamental studies of hot working of metals 1st Rep.-6th Rep. J. Jap. Inst. Met. 19 (1955) 659-663, 663-666, 704-707, 707-711; 20 (1956) 35-39, 281-285.
12) Sakui, S.; Sakai, T.: Deformation Behaviours of a 0.06 % Carbon Steel in the Austenite Range. Tetsu-to-Hagane. 63 (1977) 285-293, Effects of Strain, Strain Rate, and Temperature on the Hot worked Structure of a 0.06 % Carbon Steel ibid 62 (1976) 856-865.
13) Ueki, M.; Horie, S.; Nakamura, T.: Dynamic Restoration during Hot Deformation of Low Carbon Steels. Tetsu-to-Hagane 63 (1977) S241.
14) Ohuchi, C.: Hot Deformation Behaviours of Low Carbon Niobium and 1.8 % Alminum Steels, Comm. High Temp. Deformation Joint Comm. Iron Steel Basic Res. I.S.I.J. August(1977).

Impact Failure Mechanisms in Fiber-Reinforced Composite Plates

L.E.MALVERN, R.L.SIERAKOWSKI, and C.A.ROSS
University of Florida, Gainesville, Fla. 32611, USA
and N.CRISTESCU, University of Bucharest, ROMANIA
and University of Florida

Summary

Experimental studies of centrally impacted (0-90° lay-up) fiberglass-epoxy plates have revealed a sequential delamination mechanism, which appears to be a significant factor in the energy absorption at impact speeds below the speed required for perforation of the plate by a small rigid impactor. A linear relationship is found between impactor kinetic energy and total delamination area in this impact speed range (above a threshold speed) when the delamination does not extend to the edge of the plate.

Introduction

Because of their high strength-to-weight ratio as compared with conventional metal components, fiber-reinforced composite materials have become important for use in some parts of aircraft and space vehicles. Research on impact failure mechanisms has been motivated by the fact that their relatively poor impact resistance has limited applications of these composites where impact is a design consideration, for example in the compressor blades of jet engines. During take-off and flight, ingestion of stones, ice balls, birds and other objects may lead to impact loading of the blades [1]. Small hard impactors produce an effect similar to the effect on a stationary plate by a projectile fired from an air gun as in the experiments reported here. Ballistic perforation studies on fiberglass-epoxy plates were published by Gupta and Davids [2] in 1966. Askins and Schwartz [3] reported that a two-stage failure mode of heavy delamination followed by tensile loading of individual laminas increased energy absorption in composite backup panels for armor. They believed that the

tensile loading stage was the major energy absorber but that the delamination served to spread the deformation, involving more of the panel in the energy absorption. Additional references as well as experimental details of the investigation may be found in [3-10].

The impact perforation resistance of continuous fiber-reinforced plates is affected by many factors, including composite constituents, geometrical arrangement of the fibers, and fiber spacing. In examining the results of a study [4] of the effect of varying several of these factors it was noted in some 0^{o}-90^{o} layup fiberglass-epoxy plates, each with a total of 15 layers of fibers, that the number of fiber layers in each unidirectional lamina had a surprising effect on the results. It had been supposed that the alternating crossply arrangement would have greater perforation resistance than an arrangement with 5 laminas each containing 3 layers of fibers oriented in the same direction [referred to as a 3-3-3-3-3 arrangement] or a plate with three 5-layer laminas [5-5-5]. It turned out that both the 3-3-3-3-3 and the 5-5-5 plates showed somewhat better perforation resistance to normal impacts with 0.0143-kg blunt-ended steel cylinder impactors 9.7 mm in diameter by 25.4 mm long. Examination of some perforated and some partly penetrated plates led to the description of a sequential delamination mechanism [5], which appears to account for the good performance of the plates with multilayer laminas.

Sequential Delamination Mechanism

Delamination areas are clearly seen in the semitransparent epoxy matrix plates when a bright light is placed behind the plate as in the photograph of Fig. 1, which shows two delamination areas in a 3-lamina 5-5-5 plate. Fig.2 is a schematic diagram with three delamination areas, marked A_1, A_2, A_3. In impacts by a

blunt-ended cylinder of diameter D on plates with multi-layer laminas, at moderate speeds such that the shear cut-out of a circular plug does not extend all the way through the first lamina, the sequential delamination is begun when a strip of width D of the first lamina (parallel to the fibers) is pushed forward by the penetrator. This "generator strip" loads transversely the second lamina and initiates a separation between the first two laminas.

The generator strip from the first lamina is bounded by two through-the-thickness shear cracks, marked AA and BB in Fig. 2. This generator strip lengthens and the delamination area A_1 enlarges until the available energy is insufficient to continue the propagation of the delamination. A new generator strip may be formed in the second lamina (perpendicular to the first one in the 0^o-90^o layup plates), which initiates the area A_2 between the second and third laminas, and the process is then repeated with each subsequent delamination covering a larger area than the one before it.

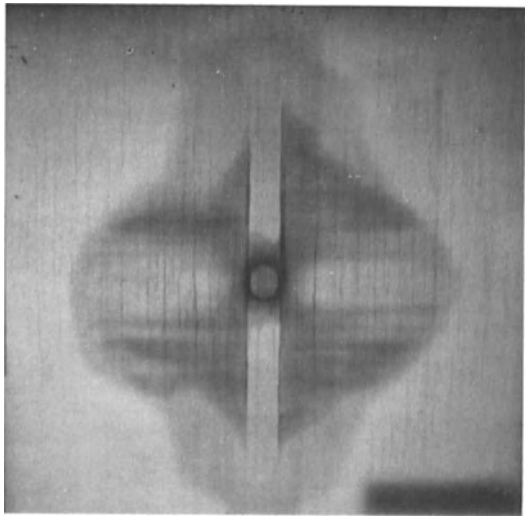

Fig.1. Generator Strip and two delamination areas in Type 5-5-5 plate.

In very high-speed impacts plugging may extend all the way through the plate with almost no delamination, al-

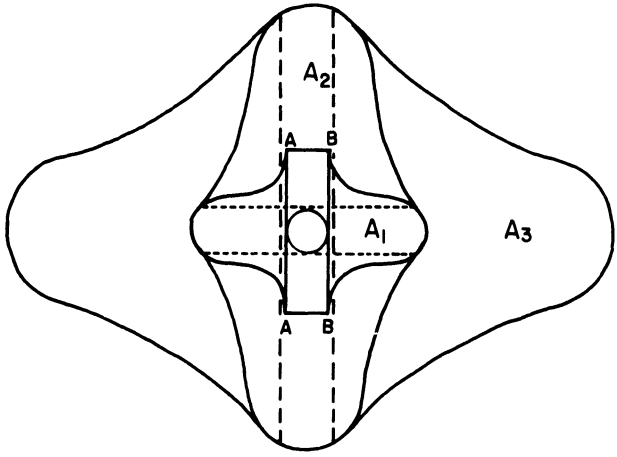

Fig.2.Schematic of three sequential delaminations. First generator strip is bounded by AA and BB.

though the hole enlarges so that the last laminas perforated show more tensile breaking and less clean shear cut-off. It can now be understood why in the first series of tests [4] at moderate speeds the delamination mechanism was more fully developed in plates with multilayer laminas than in the crossply arrangement with only one layer of fibers to the laminas. At these speeds the penetrator cuts through a single layer before there is time for a generator strip to form and initiate the sequential delamination. It was concluded [5] that the better perforation resistance of the plates with multilayer laminas could be attributed to the greater delamination, which involves a larger volume of the plate in the process. Fig.3, from a subsequent extensive series of tests [8], shows first generator strip length versus impact speed for three symmetrical layering arrangements, all with the same impactor and the same total of 15 layers of fibers in the 6.7-mm thick plates. All three show initially a monotonic increase of generator strip length with impact speed [at approximately the same slope], but for speeds above about 80 m/s the strips in the crossply plates are shorter because of the rapid perforation of the single layer. At the highest speeds the strip length of the 5-5-5 plate also

showed a drop, which may be associated with the fact that the delamination areas had reached the boundaries of the 150-mm square clamped plate. The point marked with a triangle is for the 300-mm square type 3-3-3-3-3 plate. Since it falls near the line of the 150-mm square type 3-3-3-3-3 plate, boundary interaction appears not to have affected the results.

Delaminated Area Versus Impactor Kinetic Energy

Some energy is absorbed by the delamination process itself and some by tensile breaking of the fibers and by matrix breakup. Details of the energy transformation from kinetic energy of the impactor to elastic strain energy of bending and stretching and kinetic energy in the dynamically deforming plate and final absorption by such dissipative processes as delamination and tensile breaking are not known.

Fig.4 shows a plot of the total delamination area versus impactor kinetic energy at speeds below the speed required for complete perforation in the 3-3-3-3-3 and 5-5-5 plate types [8]. The results for both agree well with the same straight line. At the higher speeds the experimental points for the 5-5-5 plates fall below the line because the delaminated areas have extended to the clamped boundaries.

The point for the 300-mm square type 3-3-3-3-3 plate falls near the line fitted to the 150-mm square plates, again indicating negligible boundary influence in the type 3-3-3-3-3 plates at these speeds where the delamination did not extend to the boundaries. The equation of the fitted line in Fig. 4 is

$$K = 3.5 + 0.315A \qquad (1)$$

for area A in cm^2 and kinetic energy K in joules. The implication of this result is that for one fixed type of impactor and plate, above a threshold impact speed, the total delamination area is a linear function of im-

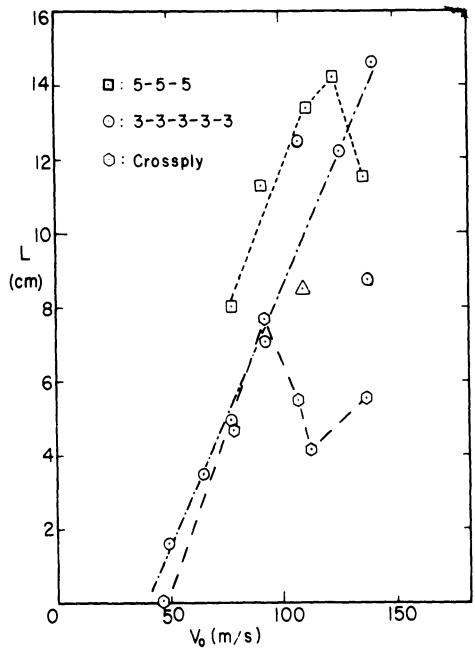

Fig.3.Generator Strip length L versus impact speed V_o for three symmetrical layering arrangements. Point marked with triangle is for the 300 mm square 3-3-3-3-3 plate.

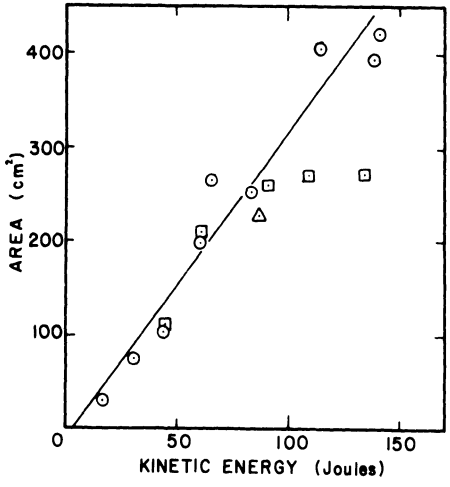

Fig.4. Total delamination area versus impactor kinetic energy for 3-3-3-3-3 plates (circle and triangle points and fitted line). Points and fitted line). Points marked with squares are for 5-5-5 plates.

pactor kinetic energy. The apparent fracture surface energy is constant at 1580 J/m^2 [or 0.158 J/cm^2, half the coefficient 0.315 in Eq.(1) since two surfaces are formed]. This is an order of magnitude higher than the fracture surface energies measured in static tests on pure epoxy double cantilever beam specimens [11]. It may be noted that several investigators have reported higher values of fracture surface energy in dynamic crack propagation than in static tests [12,13,14], as much as an order of magnitude higher in PMMA (Plexiglas) [13].

The details of the delamination crack propagation are not known, but the dynamic loading before delamination appears to involve mainly a flexural wave. The stress field around the delamination crack, which is caused by a combination of interlaminar flexural shear stress and the crack-opening loading from the generator strip, may be quite different from the stress field in the double cantilever beam specimens. Moreover the delamination proceeds along the interface between a fiber layer and the matrix, which may give different fracture surface energies from those of pure epoxy. Some reported static double cantilever beam tests on cleavage at the interface between E-glass fabric/epoxy laminates have shown fracture surface energies at least double those reported for unfilled epoxy specimens [15].

Continuing Studies

Current and planned studies include observation and analysis of the elastic flexural wave before delamination, and experiments designed to document the time history of the sequential delamination. Some calculations of the elastic response to a simulated impact loading applied as a pyramidal shaped pressure distribution over a square area at the center of the plate, were made with the DEPROP computer code [16]. The pres-

sure was assumed instantaneously applied and then decreased to zero linearly with time to give a loading time and total impulse comparable to the impact experiments. The code uses classical laminated plate theory neglecting shear strain. The transverse shear and interlaminar shear stresses were, however, estimated by integrating the equations of motion, neglecting inplane shear stresses and inplane inertia forces, so that

$$\partial\tau_{xz}/\partial z = -\partial\sigma_{xx}/\partial x \text{ and } \partial\tau_{yz}/\partial z = -\partial\sigma_{yy}/\partial y \qquad (2)$$

Values of normal stresses σ_{xx} and σ_{yy} were taken from the classical plate theory solution. Then the shear stresses τ_{xz} and τ_{yz} were determined by integrating in the z-direction (thickness) and using the stress free boundary conditions. The maximum interlaminar shear stress in a symmetric 3-lamina plate was estimated by this analysis to be 23.25 MPa [3370 psi] in a simulated impact at 107 m/s and 33.6 MPa [4780 psi] at 153 m/s impact speed. This compares with a static interlaminar single shear strength of 4100 psi quoted in the 3M specification sheet for crossplied Scotchply 1002 epoxy-glass composites. The calculation takes no account of delamination, and the simulated loading by a pyramidal pressure distribution does not reproduce the stress concentration at the edge of the blunt impactor. Thus details of the elastic stress distribution near the impact point are not given by the calculations.

Planned observations of the flexural wave include Moiré and strain gage techniques. A few strain gage records have been obtained, which verify that the primary deformation mode appears to be a flexural wave, in agreement with results recently reported by Daniel and Liber [17] for impacts on boron/epoxy and graphite/epoxy laminates. Muldary [18], however, has reported some impacts on glass-epoxy plates where membrane-type deformation was dominant.

Planned observations of the delamination history include fabrication of plates with conducting paths in them to be broken by the propagating delamination. This technique has been used successfully in our laboratory on some wedge loaded fracture specimens. It can also be used on plate specimens. Most of the plates fabricated in our laboratory have been fabricated by filament winding and matrix impregnation. Fabrication from prepreg tape should make it easier to build in the conducting paths. A few tests have been made of 0^{o}-90^{o} fiberglass/epoxy plates fabricated from prepreg tapes using an autoclave, e.g. Fig.1. These showed the same type of delamination patterns as the filament wound plates but at somewhat higher impact speeds. The threshold speed for delamination was about 2.5 times that of the filament wound plates. This may be attributed to the slightly higher volume fraction of fibers in the prepreg specimens.

A few plates were tested with an impactor having twice the length and mass of the impactors previously used. The threshold speed for delamination appeared to be of the same order of magnitude although slightly higher. The fracture surface energy also appears to be somewhat higher with the heavier impactor. Additional tests varying the mass and size of the impactor will be made, as well as static and dynamic three-point bend tests to measure delamination energies in flexural shear.

Conclusions

The superior perforation resistance of the multilayer lamina plates as compared to the crossply single-layer arrangement in the 0^{o}-90^{o} glass/epoxy plates is attributed to the sequential delamination mechanism, which spreads the deformation to a larger volume of the plate. Initiation of this mechanism requires the first lamina to resist perforation long enough for the generator strip to form, and, in the composite systems

studied, this requires multilayer laminas. It may be that the same effect could be achieved with a single layer of stronger fibers, but this has not been demonstrated.

The linearity of the relationship between the total delamination area and impactor kinetic energy above a threshold impact speed seems to imply that delamination is the principal energy absorbing mechanism at subperforation speeds in this composite system. This requires the dynamic delamination fracture surface energy to be an order of magnitude larger than the fracture surface energies measured in static double cantilever beam tests of pure epoxy specimens. This difference does not seem too unlikely in view of the reported differences between static and dynamic fracture surface energies in other materials [12,13,14], but the energy relationships need further investigation in other loading situations.

Acknowledgements

Most of the investigations reported here were performed under a grant from the U.S. Army Research Office, Durham, N.C. The earlier studies [4,5] were supported by the U.S. Air Force Armament Laboratory, Eglin Air Force Base, Florida.

References

1 Sun, C.T.; Sierakowski, R.L.: Recent advances in developing FOD resistant composite materials. Shock and Vibration Digest 4(2)(1975) 1-8.

2 Gupta, B.P.; Davids, N.: Penetration Experiments with Fiberglass-reinforced Plastics. Experimental Mechanics 6 (1976) 445-450.

3 Askins, D.R.; Schwartz, H.S.: Mechanical Behavior of Reinforced Plastic Backing Materials for Ceramic Armor. AFML-TR-71-283, Wright-Patterson Air Force Base, Ohio 1972.

4 Ross, C.A.; Sierakowski, R.L.: Studies on the Impact Resistance of Composite Plates. Composites 4 (1973) 157-161.

5 Cristescu, N.; Malvern, L.E.; Sierakowski, R.L.: Failure Mechanisms in Composite Plates Impacted by Blunt-Ended Penetrators. in Foreign Object Impact Damage to Composites, ASTM STP 568. Philadelphia: American Society for Testing Materials (1975) 159-172.

6 Ross, C.A.; Cristescu, N.; Sierakowski, R.L.: Experimental Studies of Failure Mechanisms in Composite Plates. Fibre Science and Technology 9 (1976) 177-188.

7 Ross, C.A. Sierakowski, R.L.: Delamination Studies of Impacted Composite Plates. Shock and Vibration Bulletin 46 Part 3. (1976) 173-182.

8 Sierakowski, R.L.; Malvern, L.E.; Ross, C.A.: Dynamic Failure Modes in Impacted Composite Plates. in Failure Modes in Composites III, ed. Chiao, T.T., New York: The Metallurgical Society of AIME (1976) 73-88.

9 Sierakowski, R.L.; Malvern, L.E.; Ross, C.A.; Strickland, W.S.: Failure of Composite Plates Subjected to Dynamic Loads. Proc. Army Symposium on Solid Mechanics, Watertown, Mass.: AMMRC 1976.

10 Sierakowski, R.L.; Ross, C.A.; Malvern, L.E.; Cristescu, N.: Studies on the Penetration Mechanics of Composite Plates. Final Report DAAG29-76-G-0085 to U.S. Army Research Office, University of Florida, Gainesville, Florida 1976.

11 Bascom, W.D.; Jones, R.L.; Timmons, C.O.: Mixed Mode Fracture of Structural Adhesives, Adhesion Science and Technology Vol. 9-B, ed. L.H. Lee, New York: Plenum Press, 1975, p.501.

12 Freund, L.B.: Dynamic Crack Propagation. in The Mechanics of Fracture, ed. Erdogan, F., ASME, New York (1976) 105-134.

13 Paxson, T.L.; Lucas, R.A.: An experimental investigation of the velocity characteristics of a fixed boundary fracture model. in Dynamic Crack Propagation, ed. Sih, G.C., Leyden: Noordhoff (1973) 415-426.

14 Broutman, L.J.; Kobayashi, T.: Dynamic crack propagation studies in polymers. in Dynamic Crack Propagation, ed. Sih, G.C., Leyden: Noordhoff (1973) 215-225.

15 Yeung, P.;Broutman, L.J.: The Effect of Glass-Resin Interface Strength on the Impact Strength of Fiber Reinforced Plastics. Presented at 1977 Reinforced Plastics Conference, Society of the Plastic Industries, February 1977.

16 Mente, L.J.; Lee, W.N.: DEPROP - A Digital Computer Program for Predicting Dynamic Elastic-Plastic Response of Panels to Blast Loadings. AFATL-TR-76-71 Air Force Armament Laboratory, Eglin Air Force Base, Florida 1976.

17 Daniel, I.M.; Liber,T.: Wave Propagation in Fiber Composite Laminates. Final Report NASA CR-135086, IITRI D6073-III, IIT Research Institute, Chicago, Illinois, 1976.

18 Muldary, P.F.: Dynamics of Elastic Plates. Masters Thesis, University of Minnesota 1975.

Computer Simulation of Dislocation Groups Dynamics Under Applied Constant Stress and Its Application to Yield Problems of Mild Steel

A.T. YOKOBORI,JR., T. KAWASAKI and T. YOKOBORI

Department of Mechanical Engineering II,
Tohoku University, Sendai, Japan

Summary

The number of dislocations emitted from the source under constant applied stress has been obtained in terms of simple and analytical formula by computer simulation on dislocation groups dynamics.

Based on this simulation and the previous one, yield model in bcc metals is proposed and the results are applied to the problem of the delay to the yield initiation under rapidly applied constant stress and of initial yield under constant rate of stress application in mild steel. The theoretical results are in good agreement with the experimental data on the temperature and the applied stress dependences of yield delay time and on the temperature and the stress rate dependences of upper yield stress in the mild steel using the same parameters, respectively.

Introduction

In previous papers [1][2][3] computer simulation was carried out for the problems of the same sign dislocation groups and of the positive and negative dislocation groups emission from a source and their movements under constant stress rate using the stress-velocity relation $v = M \tau_{eff}^{m}$. Thus the number of dislocations emitted until any time has been given by simple analytical formula [1][2][3].

On the other hand, Rosenfield and Hahn [4] studied dislocation groups dynamics under constant stress using

stress-velocity relation $v = K \exp(B\tau_{eff})$, but the analytical estimation of the dynamic behavior of dislocation groups and the number of dislocations emitted remain difficult. Furthermore, experimental equation of isolated dislocation velocity may be more reasonably represented by power relation such as $v = M\tau_{eff}^{m}$. Therefore, in this paper, the computer simulation for the problems of the same sign dislocation groups emission from a source and their movements under constant stress was carried out by using stress-velocity equation $v = M\tau_{eff}^{m}$.

Dynamic behaviour of the positive and negative dislocation groups moving is shown to be represented in good approximation by that of the same sign dislocation groups dynamics [3]. Thus, based on these results and the previous results, also the application has been made to the problem of delayed yield and the upper yield stress in mild steel

Simulation model and basic equations

The power relation between stress τ and velocity v was assumed for each individual dislocation in a linear array of parallel co-planar dislocations similar as in the previous paper [1 - 3].

$$v_i = M\tau_{eff,i}^{m} \qquad (1)$$

where $\tau_{eff,i}$: the effective stress on individual dislocation in terms of applied shear stress.

m : material constant

M : $v_0 (1/\tau_0^*)^m$

τ_0^* : a material constant representing the stress required to give a dislocation velocity $v_0 = 1$ cm/s

i : the index number of the dislocation in order of emission from the source. $\tau_{eff,i}$ is given as

follows:

$$\tau_{eff,i} = \tau_a + A \sum_{\substack{j=1 \\ i \neq j}}^{N} \frac{1}{x_i - x_j} \qquad (2)$$

where A is $Gb/2\pi(1-\nu)$ for edge dislocation, $Gb/2\pi$ for screw dislocation. G: shear modulus, ν: Poisson's ratio, b: the Burgers vector, τ_a: applied shear stress. An initial condition is that at t = 0, n = 1 and $x_1 = 0$, that is, at t = 0 one dislocation is at the source. On the other hand, the effective stress exerted on a source, $\tau_{eff,s}$ is written as:

$$\tau_{eff,s} = \tau_a - A \sum_{j=1}^{N} \frac{1}{x_j} \qquad (3)$$

Simulation model and method of computation is similar as in the previous paper [1 - 3]. In this paper calculation is carried out both for f c c metal and bcc metal. Therefore, experimental data [5 - 8] are used as material constant of this computation. Equations was programed and computed by NEAC2200-MODEL 700 computer, Computer Center, Tohoku University. In carrying out calculation, it is convenient to rewrite Eqns. (1)-(3) non-dimensional form; thus let us take

τ_0 : the specified applied stress, $1 Kg/mm^2$

ℓ : the specified length, say, 10^{-2}mm for bcc metal, 10^{-1}mm for fcc metal

t_0: the time which is required for an isolated dislocation to run the distance, ℓ under specified applied stress τ_0.

then

$$t_0 = \frac{\ell}{\tau_0^m M} \qquad (4)$$

Let us use variables in the terms of the non-dimensional form

$$\theta = t/t_0 \tag{5}$$

$$S_i = x_i/\ell \tag{6}$$

Using eqns (4),(5) and (6), then eqn. (1) redues to

$$\frac{dS_i}{d\theta} = \left[\frac{\tau_a}{\tau_0} + A \frac{1}{\tau_0 \ell} \sum_{\substack{j=1 \\ i \neq j}}^{N} \frac{1}{S_i - S_j} \right]^m \tag{7}$$

The flow chart for this analysis is shown in Fig.1.

Results of calculation

3.1 Dynamic behavior of individual dislocation in dislocation groups.

Under constant applied stress, for pure iron, the ratio of the position of the lead dislocation in the array to that of an isolated dislocation is shown in Fig. 2. From Fig.2 it can be seen that the ratio of the position is determined only by the factor $(H)_c \equiv (\tau/\tau_0)^4 \, t/t_0$ as far as τ and t is concerned, and represented by a function of $(H)_c$. It is also valid not only for the ratio of the position of the individual dislocation in the array to that of an isolated dislocation but also for the ratio of the velocity of and the effective stress on the individual dislocation to those of an isolated dislocation.Result in Fig.2 is similar to those for constant rate of stress application [1 - 3], except that the maximum value being slightly larger than the latter case. The results of calculations of other materials show that the dynamic behavior, such as the ratio of the position of, the effective stress on, and the velocity of the individual dislocation to those of an isolated dislocation is determined only by the dynamic factor $(H)_c \equiv (\tau/\tau_0)^{m+1} t/t_0$ or $\eta_c \equiv \tau^{m+1} t$ as far as τ, t and material constant is concerned. For instance, the

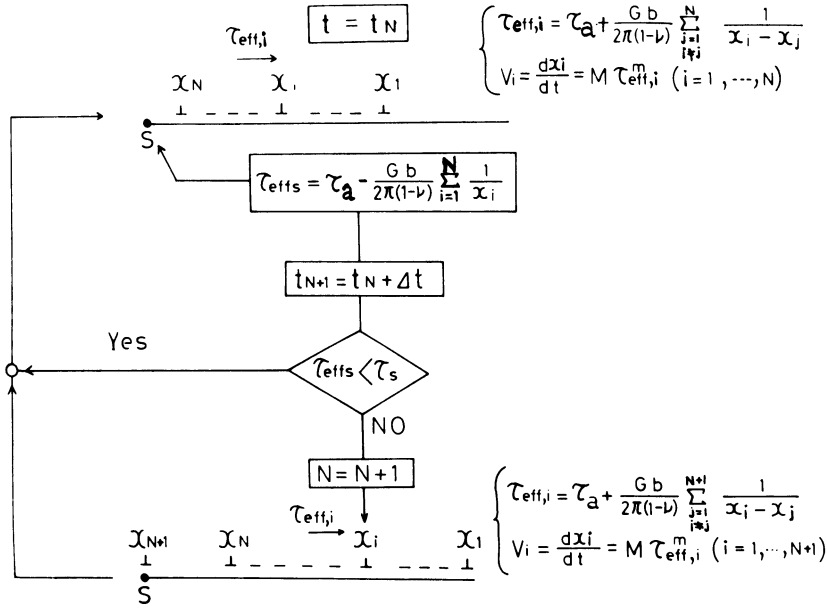

Fig.1. Flow chart by the simulation.

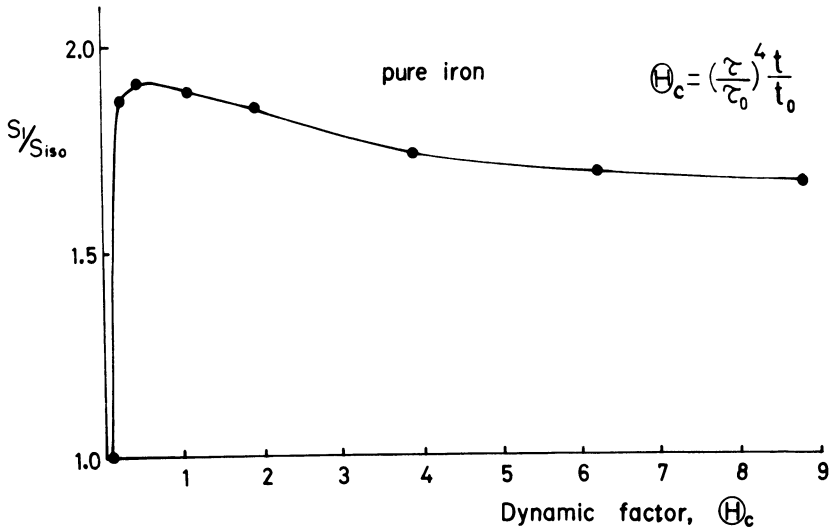

Fig.2. The ratio of the position of the lead dislocation to that of an isolated dislocation as a function of Θc. Solid circles are values calculated by computer.

		$\frac{S_1}{S_{iso}}$		$\frac{V_1}{V_{iso}}$		$\frac{\tau_{eff,1}}{\tau_{iso}}$	
τ/τ_0		5.0	10.0	5.0	10.0	5.0	10.0
Θ_c	N						
12.50	15	1.80	1.80	1.66	1.66	1.14	1.14
19.80	20	1.74	1.74	1.62	1.62	1.13	1.13
27.90	25	1.71	1.71	1.59	1.59	1.12	1.12

		$\frac{S_5}{S_{iso}}$		$\frac{V_5}{V_{iso}}$		$\frac{\tau_{eff.5}}{\tau_{iso}}$	
τ/τ_0		5.0	10.0	5.0	10.0	5.0	10.0
Θ_c	N						
12.50	15	1.01	1.01	1.32	1.32	1.07	1.07
19.80	20	1.14	1.14	1.37	1.37	1.08	1.08
27.90	25	1.21	1.21	1.39	1.39	1.09	1.09

		$\frac{S_{10}}{S_{iso}}$		$\frac{V_{10}}{V_{iso}}$		$\frac{\tau_{eff.10}}{\tau_{iso}}$	
τ/τ_0		5.0	10.0	5.0	10.0	5.0	10.0
Θ_c	N						
12.50	15	0.357	0.357	0.934	0.934	0.983	0.983
19.80	20	0.624	0.624	1.12	1.12	1.03	1.03
27.90	25	0.787	0.787	1.20	1.20	1.05	1.05

Table 1. The dynamic behavior of the lead, fifth and tenth dislocation in the array (for w238-2), (N is the number of dislocations emitted.)

Table 2. The maximum values of $\tau_{eff,1}/\tau_{iso}$, V_1/V_{iso}, and χ_1/χ_{iso} for various metals.

	m	τ_0^* kg/mm²	$\left(\frac{\tau_{eff,1}}{\tau_{iso}}\right)_{max}$	$\left(\frac{V_1}{V_{iso}}\right)_{max}$	$\left(\frac{\chi_1}{\chi_{iso}}\right)_{max}$
Al edge	1	8.5×10^{-5}	1.376	1.376	1.397
Fe edge	3	6.10	1.198	1.718	1.900
W238-2 edge	4	5.59	1.163	1.831	2.110
W edge	4.8	31.4	1.145	1.916	2.271
M_0	6.4	5.5	1.119	2.056	2.586

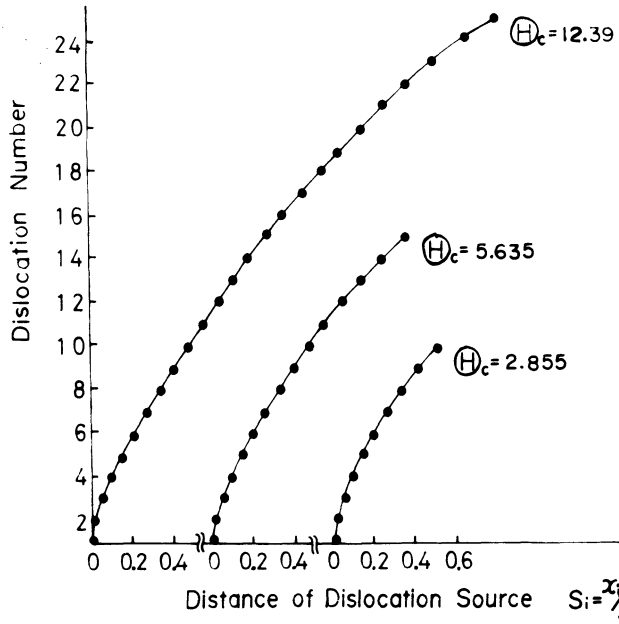

Fig.3. The position of each individual dislocation in the array at any time under constant stress.

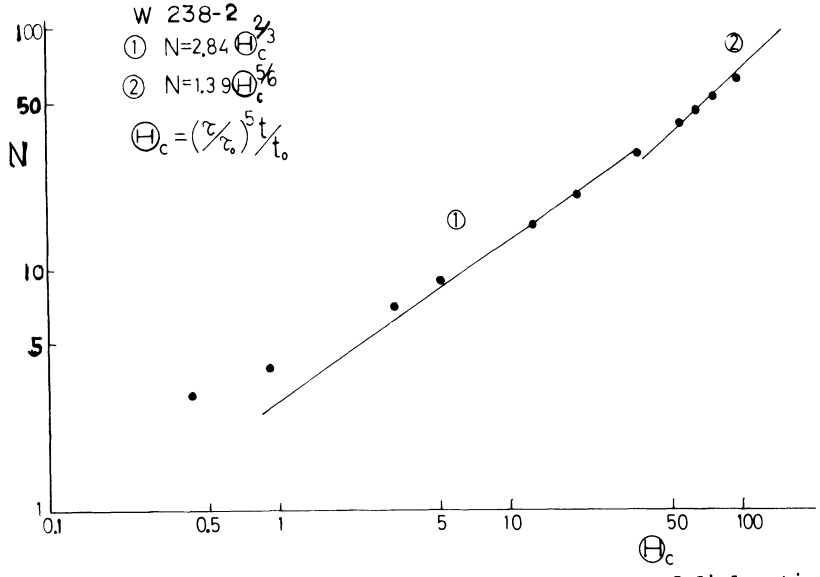

Fig.4. The relation between the number of dislocations emitted from a source and the dynamic factor for tungsten (w238-2). Solid circles are values calculated by computer.

dynamic behavior of the lead dislocation, the fifth dislocation, and the tenth dislocation in the array for tungsten (m = 4.0, $\tau_0^* = 55.9$ kg/mm^2) are shown as a function of (H)c in Table 1. In Table 2 it is shown

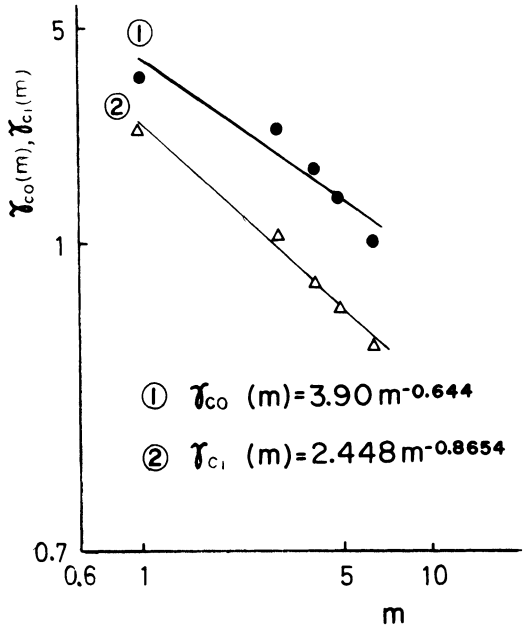

Fig.5. The value of $\gamma_{c0}(m)$ and $\gamma_{c1}(m)$.

Table 3. The dynamic factor η_c and the approximated formula for the number of dislocations emitted for various metals.

	m	η_c	for smaller N	for larger N
Al edge	1	$\tau^2 t$	$1850\,\eta_c^{\frac{1}{3}}$ (N<6)	$6.456\times10^5\,\eta_c^{\frac{2}{3}}$ (N>6)
Fe edge	3	$\tau^4 t$	$16.08\,\eta_c^{\frac{3}{5}}$ (N≤20)	$13.75\,\eta_c^{0.8}$ (N>20)
W 238-2 edge	4.0	$\tau^5 t$	$0.006216\,\eta_c^{\frac{4}{6}}$ (5<N≤30)	$0.0006581\,\eta_c^{\frac{5}{6}}$ (N≥30)
W	4.8	$\tau^{5.8} t$	$0.002591\,\eta_c^{\frac{4.8}{6.8}}$ (5<N≤30)	$0.0003143\,\eta_c^{\frac{5.8}{6.8}}$ (N≥30)
M_0	6.4	$\tau^{7.4} t$	$0.09984\,\eta_c^{\frac{6.4}{8.4}}$ (10<N≤30)	$0.03172\,\eta_c^{\frac{7.4}{8.4}}$ (N≥30)

that the maximum value of $\tau_{eff,1}/\tau_{iso}$ becomes larger as m decreases, whereas the maximum values of (v_1 / v_{iso}) and (x_1 / x_{iso}) become larger as m increases. The effect of the value τ_0^* on $(\tau_{eff,1}/\tau_{iso})$, (v_1/v_{iso}) and (s_1/s_{iso}) is small. These results are similar to the results for constant rate of stress application [1 - 3] except the value being slightly larger than the latter one. The configuration of the inverse pile-up of moving dislocations is shown in Fig.3, which is similar to the case under constant rate of stress application, but not so much conspicuous as for the latter case.

3.2 The number of dislocations emitted

The calculated value N, the number of dislocations emitted until any time t for tungsten is shown in Fig.4. Furthere, it was shown in general N is also determined by the dynamic factor $(H)_c$ or η_c and represented by the following simple formula in good approximation:

(i) for small N:

$$N = \gamma_{c0}(m)\left(\frac{M}{Gb}\right)^{\frac{m}{m+2}}\eta_c^{\frac{m}{m+2}}$$

$$= \gamma_{c0}(m)\left(\frac{b}{v_0 t}\right)^{\frac{m}{m+2}}\left(\frac{\tau_0^*}{G}\right)^{-\frac{m^2}{m+2}}\left(\frac{\tau_a}{G}\right)^{\frac{m(m+1)}{m+2}}. \qquad (9)$$

(ii) for large N:

$$N = \gamma_{c1}(m)\left(\frac{M}{Gb}\right)^{\frac{m+1}{m+2}}\eta_c^{\frac{m+1}{m+2}}$$

$$= \gamma_{c1}(m)\left(\frac{b}{v_0 t}\right)^{\frac{m+1}{m+2}}\left(\frac{\tau_0^*}{G}\right)^{-\frac{m(m+1)}{m+2}}\left(\frac{\tau_a}{G}\right)^{\frac{(m+1)^2}{m+2}}. \qquad (10)$$

where $\gamma_{c0}(m)$ and $\gamma_{c1}(m)$ is represented by the following formula respectively.(Fig.5)

$$\gamma_{c0} = 3.90m^{-0.644}$$

$$\gamma_{c1} = 2.45m^{-0.8654} \qquad (11)$$

For instance, for tungsten the line ① in Fig.4 is the theoretical one by Eqn.(9), and line ② is obtained by Eqn.(10). The good approximation formula for the computer calculated relations between N and η_c for various metals is shown in Table 3. Eqn.(9) and Eqn.(10) are similar form to equations of the number of dislocations emitted under constant stress rate, except the coefficients $\gamma_{co}(m)$ and $\gamma_{c1}(m)$ being different from $\gamma_0(m)$ and $\gamma(m)$ respectively.

The ratio of the number of dislocations emitted under constant stress rate up to time t to that under constant stress is shown in Table 4. It shows that the ratio is about 24～87% for smaller N, 20～57% for larger N, and it increases with increase of m.

Table 4. The value of $N_{\tau=\dot{\tau}t} / N_{\tau=const}$

m	1	2.6	3	4	4.8	6.4
for smaller N	0.867	0.446	0.403	0.33	0.291	0.238
for larger N	0.570	0.326	0.3	0.25	0.228	0.193

In the model described above, Eqn.(1) is used as the empirical formula. That is, the model does not require that the velocity of an isolated dislocation should be given by a thermally activated process. Next, let us consider the case in which the velocity v of an isolated dislocation is given by a thermally activated process. By the similar calculation as in the previous paper [2], the number N of dislocations emitted up to time t for larger N is represented by the following equation:

$$N = 2.45m^{-0.8654}\left(\frac{A_1 t \tau_a}{bG}\right)^{\frac{m+1}{m+2}} \exp\left\{\frac{-\frac{m+1}{m+2} H_k \ln\left(\frac{\tau_{oo}}{\tau_a}\right)}{4kT}\right\}. \quad (12)$$

where the velocity of an isolated dislocation $V=A_1 \exp(-H/kT)$, $H=H_k(1+\frac{1}{4}\ln\frac{16\tau_p^0}{\pi\tau^*})$, H_k = kind energy, $\tau_{oo}= e^4(16/\pi)\tau_p^0$, τ_p^0 is Peierls stress at 0°K. $m = H_k/4kT$, $\tau_o^* = \tau_{oo}(A_1/v_0)^{-1/m}$. τ^* is the effective stress. For usual materials such as pure iron (m=3 at room temperature) in the range between -100 and 0°C the value of (m+1)/(m+2) becomes from 0.85 to 0.80, and for pure aluminum (m=1 at room temperature) in the range between 0 and 300°C, (m+1)/(m+2) is from 0.67 to 0.60, which are practically not dependent on temperature. On the other hand, the change of the value of the logarithm of $\gamma_{c1}(m)$ with temperature change is neglected as compared with the value of the logarithm of $(b/tA_1)^{\frac{-m+1}{m+2}}(\tau_a/G)^{\frac{m+1}{m+2}}$ in Eqn.(12) in the range $573°K \geq T \geq 273°K$ for pure iron. Thus Eqn.(12) shows an equation of Arrehenius type. It is to be noted that the number N of dislocations emitted from the source up to time t from the instant of application of constant stress is expressed in terms of an apparent single rate process, and the apparent activation energy is (m+1)/(m+2) times the activation energy for the motion of an isolated dislocation, although the dislocation groups movement is not a single rate process, but consists of composite rate processes. For smaller number of N, using Eqn.(9) we obtain

$$N = 3.90 \times m^{-0.644}\frac{A_1 t \tau_a}{bG}^{\frac{m}{m+2}} \exp\left\{\frac{-\frac{m}{m+2} H_k \ln\left(\frac{\tau_{oo}}{\tau_a}\right)}{4kT}\right\}. \quad (13)$$

It can be seen that the argument made on Eqn.(12) also holds on Eqn.(13).

Application to the yield delay under rapidly applied constant stress and the yield stress of mild steel under constant stress rate.

Dislocation dynamics theory for yielding of steel by Johnston-Gilman and Hahn [9] is based on the equation of motion of an isolated dislocation, and does not consider moving of dislocation groups especialy with emission. In this paper, by using the results obtained in the present paper and the previous ones [1-3] on dislocation groups dynamics with emission, the stress and temperature dependences of the yield delay and the stress rate and temperature dependences of yield points were studied.

4.1 The yield delay

Let us denote N_0 as the number of dislocations emitted from a source up to time t under constant stress, and ρ as grown in dislocation density per unit volume. It may be assumed that when the total dislocation number ρN_0 emitted from sources per unit volume up to the time t increases and amounts to the certain specified value of N_0^*, yielding will occur. Then the yield criterion is represented by

$$N_0^* = \rho N_0 \tag{14}$$

Now, N_0 can be obtained by the simulation mentioned above and by the previous results [1 - 3]. Further, if the dislocation motion is subject to thermally activated process, then we can use the following relations.

$$\tau_0^* = \tau_{00}\left(A_1/v_0\right)^{-1/m}, \quad m = Hk/4kT,$$
$$m = 10 \sim 30 \text{ (for steel)}, \quad \frac{m+2}{m+1} = 1.03 \sim 1.09 \fallingdotseq 1.06 \tag{15}$$

Thus the delay time under rapidly applied constant stress is obtained as follows:

(i) for smaller N_0:

$$t = \left(\frac{N_0^*/\rho}{3.9}\right)^{1.1} \left(\frac{Hk}{4kT}\right)^{0.7084} \frac{bG}{A_1 \tau_{00}} \left(\frac{\sigma_y}{2\tau_{00}}\right)^{-\left(\frac{Hk}{4kT}+1\right)} \tag{16a}$$

For the value of m=10 ~ 30, m+1 ≃ m is valid, and then

$$t = \left(\frac{N_0^*/\rho}{3.9}\right)^{1.1} \left(\frac{Hk}{4kT}\right)^{0.7084} \frac{bG}{A_1 \tau_{00}} \left(\frac{\sigma_y}{2\tau_{00}}\right)^{-\frac{Hk}{4kT}} \tag{16b}$$

(ii) for larger N_0

$$t = \left(\frac{N_0^*/\rho}{2.45}\right)^{1.06} \left(\frac{Hk}{4kT}\right)^{0.917} \left(\frac{bG}{\tau_{00} A_1}\right) \left(\frac{\sigma_y}{2\tau_{00}}\right)^{-\left(\frac{Hk}{4kT}+1\right)} \tag{17a}$$

For the value of m=10 ~ 30, since m+1 ≃ m is valid,

$$t = \left(\frac{N_0^*/\rho}{2.45}\right)^{1.06} \left(\frac{Hk}{4kT}\right)^{0.917} \frac{bG}{\tau_{00} A_1} \left(\frac{\sigma_y}{2\tau_{00}}\right)^{-\frac{Hk}{4kT}} \tag{17b}$$

It is interesting that Eqns.(16)to (17) are apparently quite the same type as Eqn.(18) obtained [11] based on the Cottrell-Bilby locking mechanism.

$$t = t_0 \left(\frac{\sigma_y}{\sigma_0}\right)^{-\frac{1}{nkT}} \tag{18}$$

For mild steel, m=10 being assumed under room temperature, the comparison of the theory with the experimental data [10] are shown in Fig.7. It shows the agreement is good.

4.2 The yielding under constant stress rate

Let us denote N_0 as the number of dislocations emitted up to time t under constant stress rate [1-3]. If the dislocation motion is subject to thermally activated process, then substituting the value of N_0 in to Eqn. (14), the following relation is obtained;

(i) for smaller N_0:

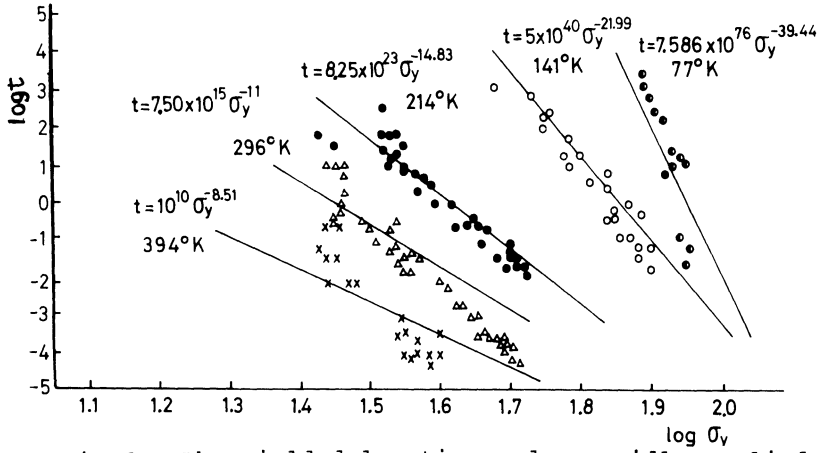

Fig.6. The yield delay time under rapidly applied constant stress. Points are experimental values. [10], solid lines are by Eqn.(16a)

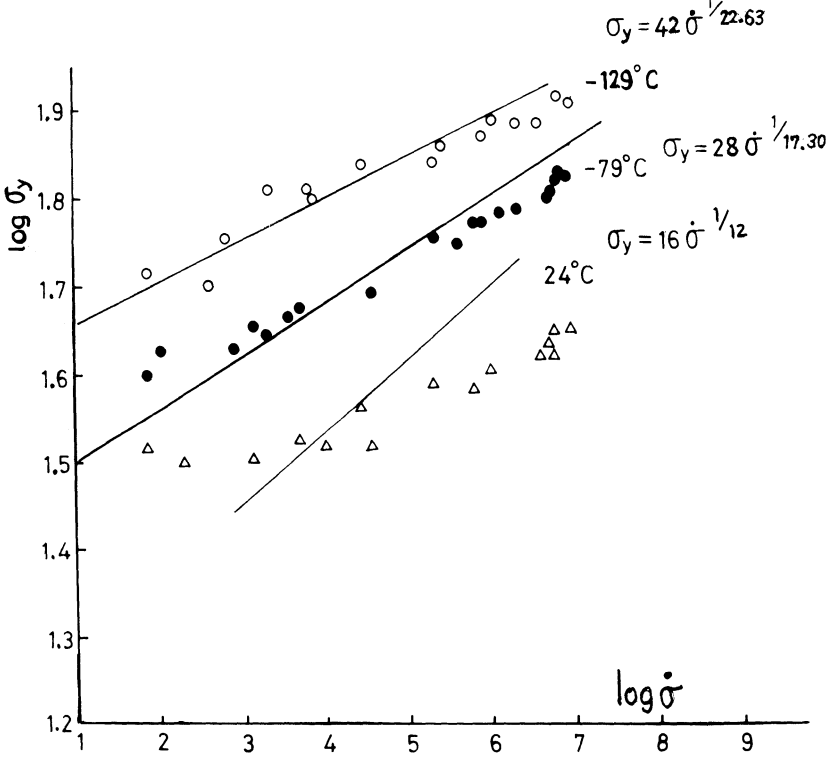

Fig.7. The upper yield point under constant stress rate. Points are experimental values.[10] Solid lines are by Eqn.(19a).

$$\sigma_y = 2\tau_{00}\left\{\frac{N_0^*/\rho}{3.38}\left(\frac{Hk}{4kT}\right)^{1.34}\right\}^{\frac{4kT}{Hk}}\left(\frac{Gb\dot{\sigma}}{2A_1\tau_{00}^2}\right)^{\frac{1}{(\frac{Hk}{4kT}+2)}} \quad (19a)$$

For the value of m = 10 ~ 30, since m+2 ≃ m+1 is valid

$$\sigma_y = 2\tau_{00}\left\{\frac{N_0^*/\rho}{3.38}\left(\frac{Hk}{4kT}\right)^{1.34}\right\}^{\frac{4kT}{Hk}}\left(\frac{Gb\dot{\sigma}}{2A_1\tau_{00}^2}\right)^{\frac{1}{(\frac{Hk}{4kT}+1)}} \quad (19b)$$

(ii) for larger N_0:

$$\sigma_y = 2\tau_{00}\left\{\frac{N_0^*/\rho}{1.396}\left(\frac{Hk}{4kT}\right)^{1.45}\right\}^{\frac{1}{(\frac{Hk}{4kT}+1)}}\left(\frac{Gb\dot{\sigma}}{2A_1\tau_{00}^2}\right)^{\frac{1}{(\frac{Hk}{4kT}+2)}} \quad (20a)$$

For the value of m = 10 ~ 30, since m+2 ≃ m+1 is valid

$$\sigma_y = 2\tau_{00}\left\{\frac{N_0^*/\rho}{1.396}\left(\frac{Hk}{4kT}\right)^{1.45}\left(\frac{Gb\dot{\sigma}}{2A_1\tau_{00}^2}\right)\right\}^{\frac{1}{(\frac{Hk}{4kT}+1)}} \quad (20b)$$

It is interesting that Eqns.(19) to (20) are apparently quite the same type as Eqn.(21) obtained [11] based on the Cottrell-Bilby locking mechanism.

$$\sigma_y = \sigma_0\left(\frac{t_0}{nkT}\frac{\dot{\sigma}}{\sigma_0}\right)^{\frac{1}{(\frac{1}{nkT}+1)}} \quad (21)$$

The comparison with the experimental data [10] is shown in Fig.8. The agreement is in fairly good.

4.3 Discussion

In f c c metal τ_0^* and m is small. When τ_0^* and m becomes small, the delay time and the stress rate effect becomes small as can be seen respectively by Eqns.(17a) and (20a) using Eqn.(9) or (10). Further N_0^* may be much smaller in f c c metal. These might explain that delayed and sharp yield can be obserbed in b c c metals only.

Conclusion

By computer simulation of dislocation groups dynamics under constant stress application, the following conclusions are obtained.

1) All dynamic behaviors of dislocation groups and the number N of dislocations emitted up to time t are determined only by the dynamic factor Ⓗc $(\equiv (\tau/\tau_0)^{m+1} t/t_0)$ as far as stress and time are concerned.
2) The number N of dislocations emitted up to time t is obtained by the simple and good approximation formulas.

Based on the present results and the previous ones, the application has been made to the yield problems of mild steel under rapidly applied constant stress and under constant stress rate, combined with new model of yield by dislocation groups dynamics. The following conclusions are obtained.

3) The theory proposed for yielding is in good agreement with the experimental data in literature.
4) The formulas of delay time and the upper yield stress are apparently quite the same type as obtained as based on the Cottrell-Bilby locking mechanism.

Literature

1. Yokobori,T., Yokobori,A.T.Jr. and Kamei,A., Phil. Mag., 30 (1974), 367
2. Tokobori,A.T.Jr., Yokobori,T. and Kamei,A., J.Appl. Phys., Vol.46 (1975), 3720
3. Yokobori,A.T.Jr., Yokobori,T. and Kamei,A. Trans. Japan Soc. Mech. Engrs. Vol.42 (1976) 1652
4. Rosenfield,A.R. and Hahn,G.T., Dislocation Dynamics, edited by Rosen field,A.R. Hahn,G.T., Bemet,A.L. and Jaffee,R.J., 1968 (McGraw-Hill) 255

5. Chaudhuri, A.R.,Patel.,J.R. and Rubin,L.F., J. Appl. Phys, 33 (1962), 2736

6. Turner,A.P.L. and Vreeland,T.Jr., Acta Metallurg., 18 (1970), 1225

7. Schadler, H.W., Acta Metallurg., 12, (1964), 861

8. Prekel,H.L., Lawler,A. and Conrad,H., Acta Metallurg., 16, (1968), 337

9. Hahn,G.T., Acta Metallurg., 10 (1962), 727

10. HedsicKson,J.A. and Wood.D.S., Trans.Amer.Soc. Met. 50 (1958) 498

11. Yokobori,T., J. Appl. Phys. 25 (1954) 593; Yokobori, T., Kolloid Zeitschrift. 166 (1959) 20

12. Cottrell, A.H. and Bilby, B.A., Proc. Phys. Soc. Lond. A62 (1949) 49

Computer Modeling of Microscopic Failure Processes Under Dynamic Loads

D. A. SHOCKEY, D. R. CURRAN AND L. SEAMAN
SRI International, Menlo Park, California

Abstract

High rate failure of structural materials takes place by rate processes occurring on the microlevel and involving nucleation, growth, and coalescence of voids, cracks, or shear bands. We have constructed computational models describing these processes and have used these models to predict macroscopic failure behavior in many materials under compressive, tensile, and shear loading conditions. This paper reviews the microphenomenology of dynamic failure, describes the approach used to obtain equations for the rate processes, and indicates the success of the resulting computer models in predicting dynamic failure behavior.

Introduction

Depending on material and loading conditions, high rate failure of solid materials occurs by the nucleation, growth, and coalescence of cracks, voids, or shear bands. [1] Under short-lived t e n s i l e pulses, materials such as Armco iron, beryllium, polycarbonate, and quartzite rock develop numerous planar, roughly circular microcracks, whereas materials such as commercial purity aluminum and copper, and structural aluminum, steel, and titanium alloys develop numerous roughly spherical voids. Under high rate c o m p r e s s i v e loads, these materials may deform and fail by developing a profusion of surfaces of intense shear strain. We have constructed computational models describing the development of these microfeatures and have used them to calculate the macrobehavior of failing specimens. This paper describes the approach used to obtain these models and presents examples of their application.

Brittle Tensile Failure

When subjected to high rate loads from impact, in-contact explosive, or intense radiation, Armco iron undergoes relatively brittle failure from nucleation, growth, and coalescence of planar cracks. [2] The fracture morphology is apparent from the cleavage facets on fracture surfaces, and from polished cross sections that show the traces of cracks at stages in their development before coalescence, Figure 1. The phenomenology of brittle

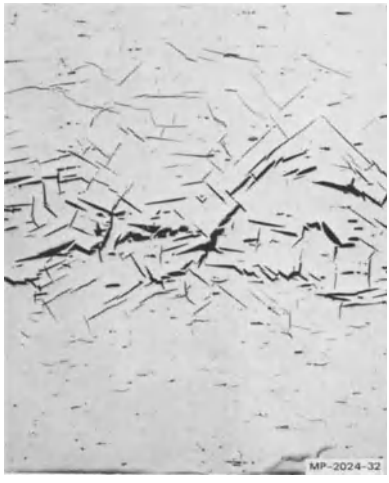

Figure 1. Polished Cross Section in Shock Loaded Armco Iron Revealing Internal Cleavage Cracks

tensile failure is even more clearly indicated in transparent materials such as the polycarbonate specimen shown in Figure 2. [3] Here, the internal penny-shaped cracks produced under planar impact are easily studied. The cracks are largely circular and have distinctive centers or starting points, suggesting that crack nucleation occurs at preferred sites in the material (some of which have been identified as inclusions and pores), and that crack growth occurs radially outward from the initiation site in a symmetric manner. The various fracture surface markings provide information about the growth history.

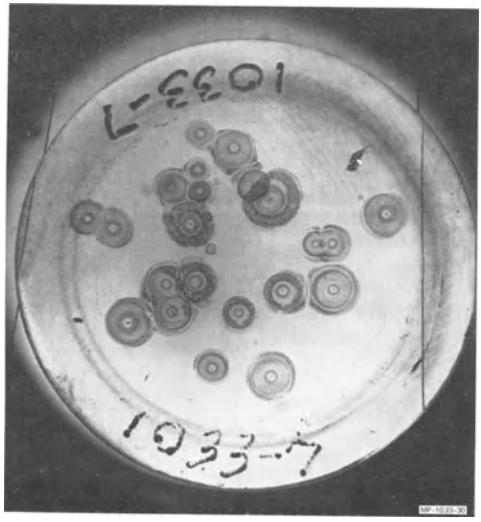

Figure 2. Internal Cracks in Polycarbonate Produced By A Short-Lived Tensile Pulse

The distribution in crack sizes suggests that nucleation occurs continually during the stress pulse life, the larger cracks being nucleated earlier than the smaller ones. Finally, the random location of the cracks reflects the nonuniform distribution in the material of inclusions and flaws. These observations suggest that to be physically realistic, any computational model of brittle tensile failure must include equations describing the nucleation, growth, and coalescence of penny-shaped cracks.

To obtain equations for microcrack nucleation and growth, we subjected specimens to simple, well-defined pulse loads to produce populations of cracks in various stages of development. The crack populations were quantitatively assessed and correlated with computed stress histories to obtain relationships for nucleation and growth rates. The procedure is now illustrated for Armco iron.

Armco iron flyer plates mounted on the leading edges of projectiles were accelerated in a light gas gun, Figure 3, to produce short tensile pulses in specimen plates of Armco iron under uniaxial strain conditions (Figure 3).

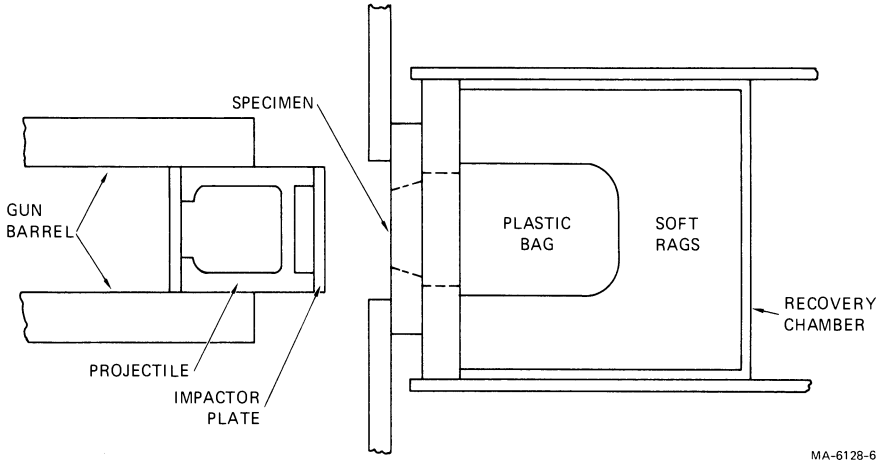

Figure 3. Schematic Diagram of Gas Gun Impact Facility Used To Produce Dynamic Fracture Damage in Materials Under Uniaxial Strain Conditions

The amplitudes and durations of the tensile pulses were controlled by the impact velocities and plate thicknesses, respectively; the pulse shapes were either measured or computed.

To reveal the internal fracture damage, we sectioned the specimens through the thickness, polished the surfaces, and examined them with a microscope (see Figure 1). The crack size distributions were determined by counting and measuring as a function of location the crack traces on the sectioned surface and converting these surface data to volume data with a statistical transformation code [4]. Figure 4 shows the crack size distributions for an Armco iron specimen. The curves are approximated by the equation

$$N_g(R) = N_o \exp\left(-R/R_1\right) \qquad (1)$$

where N_g is the cumulative number of cracks per cubic centimeter with radii greater than R, N_o is the total number per cubic centimeter, and R_1 is the characteristic size of the distribution.

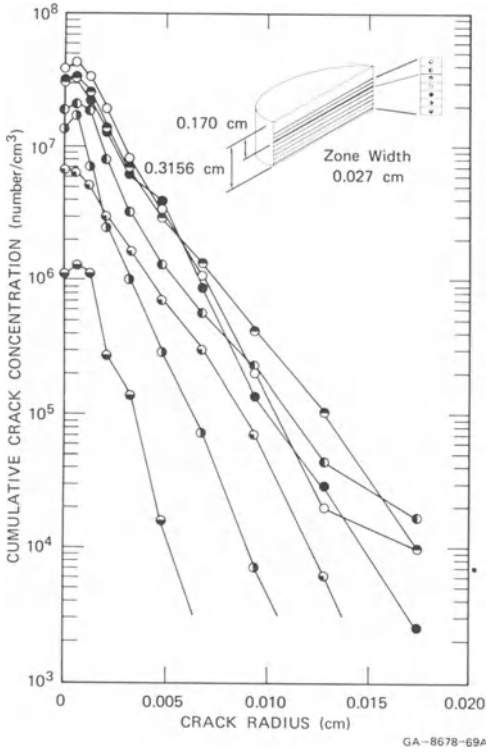

Figure 4. Crack Size Distribution at Several Distances Beneath the Impact Surface in a Specimen Plate of Armco Iron

The stress histories at various depths in the specimens were computed using PUFF, a one-dimensional, finite-difference wave propagation code. [5] The constitutive relation included yielding and work hardening and (after the equations for microcrack development were established) the stress relaxation arising from fracture damage. Microcrack nucleation and growth laws were deduced from iterative correlations of the measured microcrack size distributions and the computed stress histories. The measured microcrack distributions were best expressed by the following equations:

$$\dot{N} = \dot{N}_o \exp \frac{\sigma - \sigma_{no}}{\sigma_1} \qquad (2) \qquad \dot{R} = \frac{\sigma - \sigma_{go}}{4\eta} R \qquad (3)$$

where $\dot{N}$ and $\dot{R}$ are time rate of crack nucleation and growth, respectively, σ is the instantaneous tensile stress, and R is the radius of a penny-shaped crack. The remaining symbols are dynamic fracture parameters that are determined empirically by fitting the data. Figure 5 shows the agreement that was obtained between computed and measured distributions of damage in an impacted plate specimen of Armco iron. The dynamic fracture parameters for beryllium [6], polycarbonate [3], and quartzite [7] produced similar agreement between observed and computed damage.

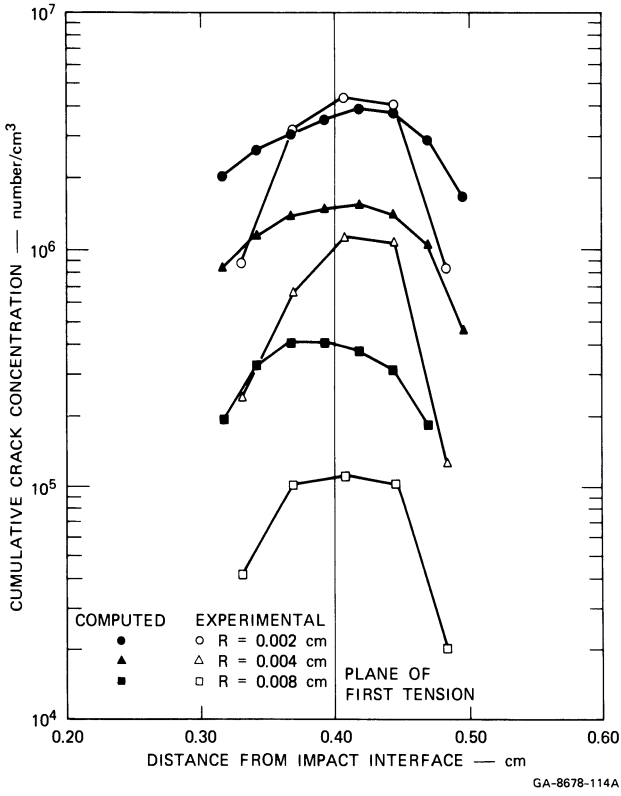

Figure 5. Comparison of Measured and Computed Crack Densities in a Shock Loaded Plate of Armco Iron

The nucleation and growth model has been extended to include the fragmentation that occurs in some materials such as ceramics and rock [8]. Growing cracks are allowed to

coalesce when the sum of the volumes of their magnified stress fields fills the volume of a computational cell. The fragment size distribution is computed from the crack size distribution at coalescence.

The fracture and fragmentation parameters obtained in simple one-dimensional strain experiments apply to other less simple loading situations. For example, experiments were performed in which a column of high explosive was detonated on the surface of a block of quartzite, and the fracture damage was assessed quantitatively [9]. A two-dimensional (axisymmetric) simulation using the fracture/fragmentation model developed from the one-dimensional plate impact procedure gave good agreement between computed and measured crater dimensions, subsurface fracture damage, and ejecta size distribution, Figure 6, although the spatial and velocity distributions of the ejecta were not closely predicted. Similar results were obtained from experiments and computer simulations for the case of right cylindrical rods impacting the rock surface. Finally, the extent of fracture damage produced by the explosion of 20 tons of liquid nitromethane buried in basalt was reasonably well predicted in a computational simulation [9].

Ductile Tensile Failure

In contrast to the planar cracks acquired by Armco iron under dynamic loads (Figure 1), polished cross sections of impacted plates of 1145 aluminum exhibit roughly spherical voids (Figure 7). This mode is also exhibited in structural alloys of iron [10,11], aluminum [2], and titanium [12] and is responsible for their good fracture toughness properties.

The equations for modeling ductile tensile failure of 1145 aluminum and OFHC copper were obtained by the plate impact technique described earlier for Armco iron.

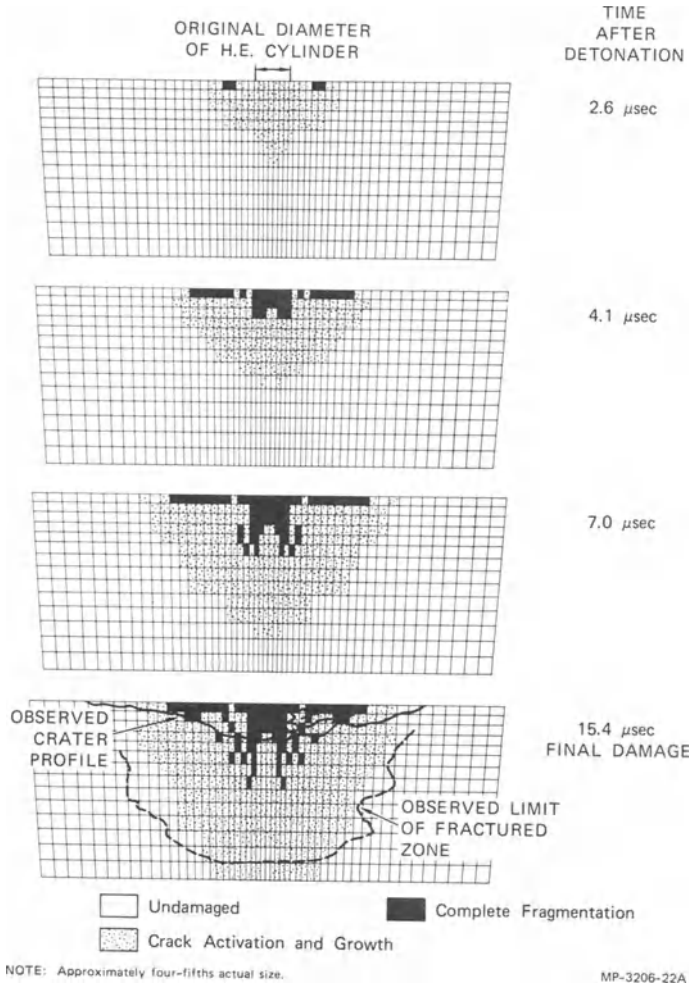

Figure 6. Successive Stages of Crater Formation and Sub-Crater Fracture Development in Quartzite Rock Computed for a Surface Explosion

The nucleation and growth expressions (1), (2) and (3) were found to also describe ductile void development. Agreement between observed and computed damage in 1145 aluminum is shown in Figure 8.

Shear Failure

Under high rate compressive loading conditions, where tensile failure is suppressed, solid materials often fail in

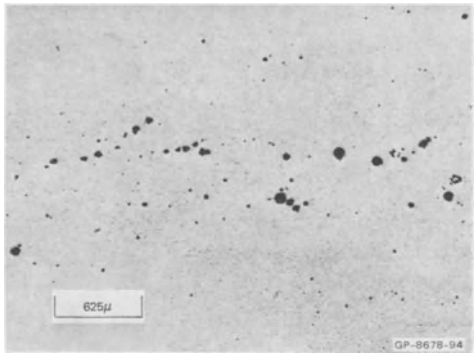

Figure 7. Polished Cross Section in Shock Loaded 1145 Aluminum Showing the Population of Internal Spherical Voids

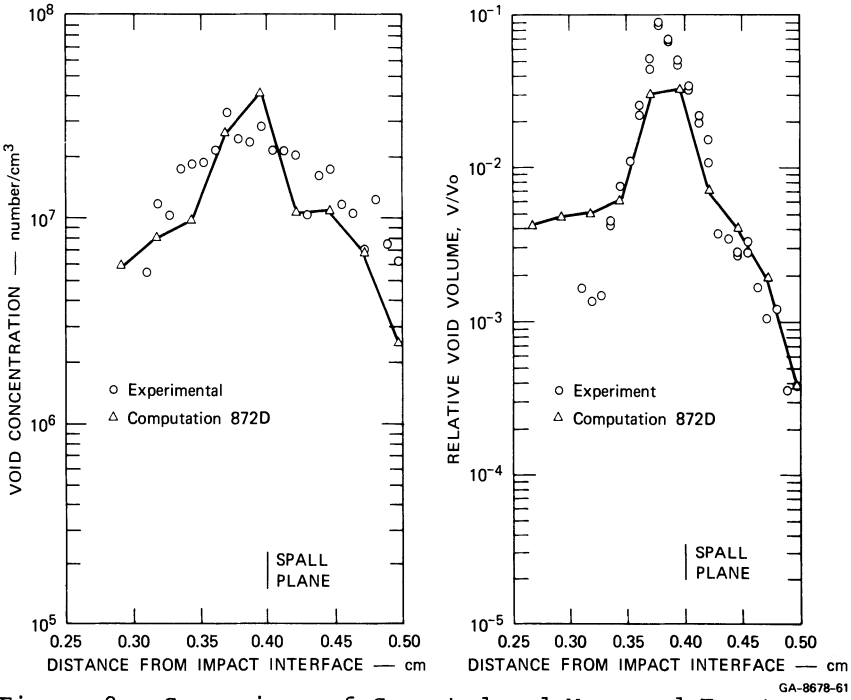

Figure 8. Comparison of Computed and Measured Fracture Damage in Shock Loaded 1145 Aluminum

shear by developing surfaces of intense plastic strain. This behavior, known as shear banding, is commonly observed in ballistic penetration of plates, exploding cylinders, impact forging, and in high-speed machining, and occurs according to the following mechanism [13]. Plastic flow first occurs at a number of discrete sites

where inhomogeneities raise the local stress above the yield stress, and local thermal softening overwhelms the work hardening, resulting in the propagation of a thin surface of high deformation into the material.

Local temperatures may rise so high that phase transformations result in some materials. In steels the austenite transitions temperature is often exceeded, and a thin band of white-etching martensite is formed when the cold material immediately adjacent to the shear band rapidly quenches the austenite. Thus shear bands in steel often appear as a network of white bands, Figure 9.

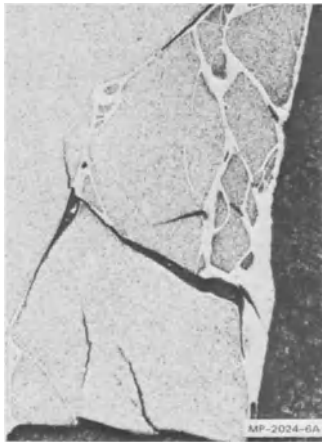

Figure 9. Network of White-Etching Shear Bands and Associated Cracks Near a Ballistic Performation in ESR 4340 Steel

Shear banding not only governs the deformation response of materials but may also strongly influence the fracture behavior. Shear bands are preferred sites for subsequent cracking, Figure 10, possibly because of residual tensile stresses or the embrittled state of quenched material.

To construct a computational model for the nucleation and growth of shear bands, we used an exploding cylinder technique [14,15], that allowed experimental and quantitative studies of shear bands in early stages of development. Cylinders of the specimen material were filled with chemical explosive of chosen density and power and enclosed by a thick-walled iron cylinder to stop the

expansion when the explosive was detonated. A series of experiments were designed to produce various levels of shear band activity. The numbers and sizes of shear bands on polished sections were correlated with stress and strain histories to help establish the laws describing shear band nucleation and growth. The nucleation rate was found proportional to the square of the rate of plastic strain energy increase and directly proportional to the plastic strain rate. The shear band growth rate was found proportional to the plastic strain rate and the size of the band. Coalescence and fragmentation of the specimen were assumed to occur in a computational cell when the total volume of shear bands equaled the cell volume.

We used this computational model to calculate the fragment size distribution from unconstrained exploding cylinders with varying diameters and wall thickness. A two-dimensional wave propagation code, TROTT, was used to simulate the running detonation and the subsequent expansion of the cylinder. The measured and computed fragment size distributions for two different steels (Figure 10) show good agreement.

Discussion

The dynamic failure models have been applied to a wide variety of materials and loading conditions and appear to be quite general. The values of the dynamic failure parameters in the models depend on microstructure [16] and temperature [17] and therefore behave as material properties. The models are based on detailed quantitative measurements of individual microfractures and shear bands observed in shock-loaded material, but these failure data appear in the model as statistical distribution functions and are treated as internal state variables in the continuum constitutive relations for the material. Thus the failure rate equations act as a link between microscopic and continuum behavior.

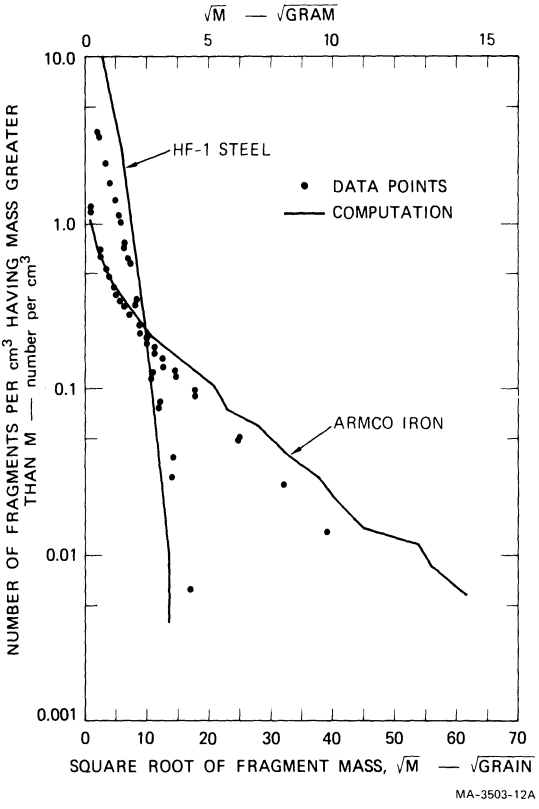

Figure 10. Comparison of Measured and Computed Fragment Size Distributions from Exploding Cylinder Experiments on Two Steels

References

1 D. R. Curran, L. Seaman, and D. A. Shockey, "Dynamic Fracture in Solids," Physics Today, January 1977.

2 T. W. Barbee, Jr., L. Seaman, R. Crewdson, and D. R. Curran, "Dynamic Fracture Criteria for Ductile and Brittle Materials," J. Materials, Vol. 7, pp. 393-401 (1972).

3 D. R. Curran, D. A. Shockey, and L. Seaman, "Dynamic Fracture Criteria for a Polycarbonate," J. Appl. Phys., Vol. 44, pp. 4025-4038 (1973).

4 L. Seaman, D. R. Curran, and R. C. Crewdson, "Transformation of Observed Crack Traces on a Section to True Crack Density for Fracture Calculations," submitted to J. Appl. Phys. 1977.

5 L. Seaman, "SRI PUFF 3 Computer Code for Stress Wave Propagation," Tech. Report AFWL-TR-70-99, Kirtland AFB, New Mexico, November 1970.

6 D. A. Shockey, L. Seaman, and D. R. Curran, "Dynamic Fracture of Beryllium Under Plate Impact and Correlation with Electron Beam and Underground Test Results," Final Report, Contract No. AFWL-TR-73-12, Air Force Weapons Laboratory, Kirtland AFB, New Mexico (January 1973).

7 D. A. Shockey, C. F. Petersen, D. R. Curran, and J. T. Rosenberg, "Failure of Rocks Under High Rate Tensile Loads," in New Horizons in Rock Mechanics, Proceedings 4th Symposium on Rock Mechanics, H. R. Hardy, Jr., and R. Stefanko, Eds., p. 709 (American Society of Civil Engineers, New York, 1973).

8 D. A. Shockey et al., "Fragmentation of Rock Under Dynamic Loads," Int. J. Rock Mech. Sci. and Geomech. Abstr., Vol. 11, pp. 303-317 (1974).

9 D. A. Shockey et al., "Development of a Capability for Predicting Cratering and Fragmentation Behavior in Rocks," Final Report, Contract DNA001-74-C-0195, Defense Nuclear Agency, Washington, D.C. (May 1975).

10 L. Seaman and D. A. Shockey, "Models for Ductile and Brittle Fracture for Two-Dimensional Wave Propagation Calculations," Final Report, Contract No. DAAG46-72-C-0182, Army Materials and Mechanics Research Center, Watertown, Massachusetts (February 1975).

11 D. A. Shockey et al., Final Report, Phase I, Contract No. DAAD05-73-C-0025, U.S. Army Ballistic Research Laboratories, Aberdeen Proving Ground, Maryland (December 1973).

12 D. A. Shockey, R. L. Jones, and K. C. Dao, "Effect of Grain Size on Dynamic Fracture Behavior of Titanium," Work in Progress on Contract DAAG29-75-C-0020, Army Research Office, Durham, North Carolina.

13 C. Zener and J. H. Hollomon, "Effect of Strain Rate Upon Plastic Flow of Steel," J. Appl. Phys., Vol. 15, No. 1, pp. 22-32 (January 1944).

14 L. Seaman, D. A. Shockey, D. R. Curran, and R. E. Tokheim, "Development of a Shear Band Model for Fragmentation in Exploding Cylinders," Final Report, Contract No. N00178-74-C-0450, Naval Surface Weapons Center, Dahlgren, Virginia (August 1975).

15 D. C. Erlich, L. Seaman, D. A. Shockey, and D. R. Curran, "Development and Application of a Computational Shear Band Model," Final Report, Contract No. DAAD05-76-C-0762, U.S. Army Ballistic Research Laboratory, Aberdeen Proving Ground, Maryland (June 1977).

16 D. A. Shockey, L. Seaman, and D. R. Curran, "The Influence of Microstructural Features on Dynamic Fracture," Metallurgical Effects at High Strain Rates, R. W. Rohde et al., eds. (Plenum Press, 1973).

17 D. A. Shockey, D. R. Curran, L. Seaman, and K. C. Dao, "Feasibility of Producing Fracture Damage with Repetitive Laser Pulses," Final Report, Contract No. DAAH01-75-C-1072, Redstone Arsenal, Alabama (August 1976).

Calculation of Spall Damage Accumulation in Ductile Metals

LEE DAVISON and M. E. KIPP

Sandia Laboratories
Albuquerque, New Mexico 87115, U.S.A.

Summary

In this article we review a theory of viscoplastic flow with spall damage accumulation, and describe its incorporation into a computer code for solving problems of propagation of plane waves of uniaxial strain. Solutions for plate-impact problems covering the range of sample thickness and impact velocity normally encountered in experimental investigations are discussed and shown to be in qualitative accord with observation. Calculated results are successfully interpreted in terms of existing spall criteria, indicating again the qualitative agreement of the new results with prior experience. These comparisons provide an indication of the range of validity of the simpler criteria.

1. Introduction

Spall damage is a type of fracture produced when large tensile stresses develop in material bodies through the interaction of stress waves. When present at low levels in ductile materials, this damage takes the form of a diffuse distribution of small rounded voids and may be characterized by the number density (typically $10^{4}/mm^{3}$) and average volume (typically $10^{-6}/mm^{3}$) of the voids. As the damage accumulates, it affects the gross mechanical properties of the material and thus interacts with the stress wave.

The deformation of a spalling ductile body comprises viscoplastic flow, the nucleation and growth of voids, and thermoelastic straining. Numerous investigations, both theoretical and experimental, of each of these phenomena have been conducted. On the basis of the knowledge thus gained, it seems most appropriate to describe the underlying response of the material using viscoplastic flow equations based on dislocation mechanics. Equations that have been proposed

for the nucleation and growth of spall voids are similarly motivated, or follow from experimental observations. Elastic behavior can be calculated in the usual manner, but with corrections introduced to account for the reduction in stiffness resulting from the presence of the voids. An internal-state-variable theory is an appropriate vehicle for combining these results, and a description of spallation has recently been developed on this basis [1]. The equations of this theory are complicated enough to necessitate resort to numerical solution for problems of practical interest, so a computer program implementing such calculations has been developed.

In Sec. 2 we give a brief review of the theory and describe the computer program in which it is implemented. We discuss a group of solutions covering the range of conditions most commonly encountered in experimental investigations of spall phenomena in Sec. 3. In Sec. 4 we compare the present results with previous work.

2. Theory and Computational Method

Our theory of elastic-viscoplastic deformation with spall-damage accumulation has been described in detail in Ref. 1. In that article the general theory was specialized to the case of uniaxial strain. This one-dimensional version of the theory forms the basis for the analysis presented here. In this section we briefly review the theory and its incorporation into a computer code. More detail on the latter topic is presented in a report by Kipp and Stevens [2].

One-dimensional motions of uniaxial strain can be described by the equation

$$\underset{\sim}{x} = (X_1, X_2, \hat{x}_3(X_3, t)) \tag{2.1}$$

giving the present cartesian position $\underset{\sim}{x}$ of each material point $\underset{\sim}{X}$ of the body. As is customary, we identify each material point $\underset{\sim}{X}$ with its position in a fixed homogeneous reference configuration in which it has the mass density ρ_R. The deformation gradient tensor associated with this motion is diagonal and, with $F = \partial \hat{x}_3 / \partial X_3$, can be written

$$\underset{\sim}{F} = \mathrm{diag}(1,1,F) \quad . \tag{2.2}$$

The momentum-balance equation has its usual one-dimensional form

$$\frac{\partial t_{33}}{\partial X_3} = \rho_R \frac{\partial^2 \hat{x}_3}{\partial t^2} \quad , \tag{2.3}$$

where t_{33} is the normal component of the Cauchy stress tensor on planes perpendicular to the direction of wave propagation. The principle of conservation of mass is represented by the equation $\rho = \rho_R/F$, where ρ is the mass density of the deformed material.

Our description of material behavior is based on the assumption that the deformation gradient tensor is composed of a part $\underset{\sim}{P}$ associated with the viscoplastic flow, a part $\underset{\sim}{M}$ representing the dilatation resulting from the nucleation and growth of spall voids, and a part $\underset{\sim}{E}$ arising as a result of thermoelastic deformation:

$$\underset{\sim}{F} = \underset{\sim}{E}\,\underset{\sim}{M}\,\underset{\sim}{P} \quad . \tag{2.4}$$

The part $\underset{\sim}{M}$ of this deformation gradient is a pure dilatation, and so has the form

$$\underset{\sim}{M} = (1-\mathfrak{N})^{-1/3}\,\mathrm{diag}(1,1,1), \tag{2.5}$$

where $\mathfrak{N}$, the spall damage, is the volume fraction of voids at a point in the material. The rates of nucleation and growth of voids have been studied by Barbee, et al. [3] in a pioneering series of experiments leading to the equation

$$\dot{\mathfrak{N}} = \{f\, v_o + [3A'\mathfrak{N}/(1-\mathfrak{N})]\}(1-\mathfrak{N})^2 \tag{2.6}$$

for the damage accumulation rate at a material point. In this equation f and A′ are functions of the spherical part of the stress and v_o, a material constant, is the nucleate-void volume. Since Eq. (2.6) has the form of an evolutionary equation for an internal state variable, we have incorporated $\mathfrak{N}$ into the theory on this basis.

Because of the symmetry of the uniaxial strain problem the part $\underset{\sim}{P}$ of the deformation gradient is of the form $\underset{\sim}{P} = \mathrm{diag}(P_{11},P_{11},P_{33})$ and, since the plastic flow is assumed to be isochoric,

$$\det \underset{\sim}{P} = P_{33}P_{11}^2 = 1 \quad . \tag{2.7}$$

Our calculation of $\underset{\sim}{P}$ is based on a dislocation-mechanical model according to which the rate of change of the longitudinal component is given by

$$\dot{P}_{33} = \frac{1}{2} BD_{(T)} f_{(m)} V P_{33} \quad . \tag{2.8}$$

The quantity B in this equation is the length of Burgers' vector, a material constant, while $D_{(T)}$ is the density of dislocations, $f_{(m)}$ is the fraction of these dislocations that is mobile, and V is the average velocity of the mobile dislocations. The quantities $D_{(T)}$ and $f_{(m)}$ are regarded as internal state variables, so their values are determined from evolutionary equations. The dislocation velocity V is a function of the excess of the maximum resolved shear stress $\tau = \frac{1}{2}(t_{33}-t_{11})(1-\vartheta)^{-2/3}$ over a threshold value. This threshold value, $\tau_{(A)}$, called the back stress, controls the onset of yielding. In order to incorporate strain hardening into the theory, we allow $\tau_{(A)}$ to evolve as an additional internal state variable. On the basis of this brief description we see that, to determine the part $\underset{\sim}{P}$ of the deformation gradient, we must solve a coupled set of first-order ordinary differential equations for the values of P_{33}, $D_{(T)}$, $f_{(m)}$, and $\tau_{(A)}$ at each point in the body.

In order to calculate the changes in temperature, θ, that occur in the body as a result of compression or dissipation we must solve an additional first-order ordinary differential equation representing the balance of energy at each material point.

Integration of the evolutionary and energy equations, and determination of P_{11} from Eq. (2.7), yields values for $\underset{\sim}{P}$ and $\underset{\sim}{M}$ so that $\underset{\sim}{E}$ can be determined from the equation

$$\underset{\sim}{E} = \underset{\sim}{F}\,\underset{\sim}{P}^{-1}\underset{\sim}{M}^{-1} \quad . \tag{2.9}$$

In problems analyzed in this article the thermoelastic deformations are quite small, so we use the linear stress relation

$$t_{ij} = [(K - \frac{2}{3}\mu)e_{kk} - 3\alpha K(\theta-\theta_R)]\delta_{ij} + 2\mu e_{ij} \quad , \tag{2.10}$$

where $\underset{\sim}{e} = \frac{1}{2}(\underset{\sim}{E}+\underset{\sim}{E}^{T})-\underset{\sim}{1}$ is the infinitesimal strain tensor, K is the bulk modulus, μ is the shear modulus, and α is the coefficient of thermal expansion. The elastic moduli are allowed to decrease linearly with damage, according to established formulae, so stress relief can occur as the spall begins to develop.

The theory outlined above has been incorporated into a computer code called WONDY [3] that solves second-order finite-difference analogs

of the balance and constitutive equations. This code accommodates several layers of material (each with its own constitutive equations) and permits imposition of a variety of boundary and initial conditions. Shock waves are treated by the method of artificial viscosity. Starting with the body in its specified initial state, the solution is advanced by increments of time (typically 10^{-8} s in the calculations reported here) that are related to the spacing of the material mesh by a numerical stability constraint. To advance the solution by one time step, the code progresses through the mesh substituting the stress calculated during the previous step into the difference analog of Eq. (2.3) and solving for the new positions of the mesh points. Compatibility requirements then yield the deformation gradient and particle velocity. Completion of this step of the solution requires determination of an updated value of the stress. This calculation entails integration of the evolutionary and energy equations to obtain $\mathcal{S}$, P_{33}, θ, and three dislocation parameters. The solutions of these equations frequently change so rapidly that they cannot be integrated using the relatively long time increments normally used for the momentum balance calculation, so they are solved on a subcycle basis using a standard integration subroutine.

Completion of the subcycle integration in each zone, and determination of P_{11} from Eq. (2.7), yields values for $\underset{\sim}{P}$ and $\underset{\sim}{M}$ so that $\underset{\sim}{E}$ can be evaluated using Eq. (2.9). Substitution of $\underset{\sim}{E}$ and θ into Eq. (2.10) yields an updated value of the stress in each zone and thus completes the computational step.

As many of these steps are taken as may be necessary to advance the solution over the desired time interval. A typical calculation of the sort discussed in the next section involves a 2 mm-thick impactor striking a 4 mm-thick target. In this case the 6 mm thickness of material was dissected into 120 zones and the computation was run for 450 time steps. This advanced the solution 3 μs (about 9 wave transits through the flyer). Obtaining this solution with a CDC 7600 computer required the use of about $100{,}000_8$ words of storage and occupied the central processor for about 65 seconds.

3. Computational Results

Experimental investigations of spallation usually involve impacting a thin slab of the material of interest against a thicker slab of the same material (a thickness ratio of 2 is common). A simplified (X,t)-diagram of the waves produced in this case is shown in Fig. 1.

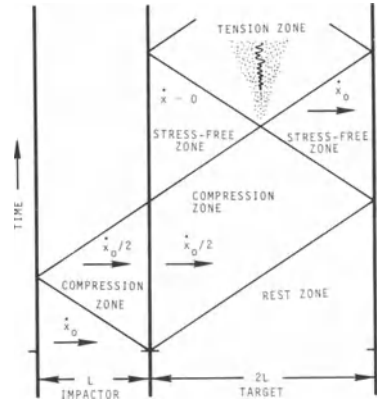

Fig. 1. When the thin impactor collides with the thicker target plate compression waves produced at the interface propagate into each plate. These waves reflect from the free surfaces as stress release waves. Interaction of the stress-release waves in the center of the target produces a regior of tension in which spall damage (indicated by dots) may develop.

Examination of this figure shows how the wave interactions that occur during this impact experiment can produce a region of tension in the interior of the thicker slab. It is in this region that damage may develop. The plane of maximum damage is called the spall plane. The detailed numerical solution of a problem essentially like that discussed above has been presented in Ref. 1.

In this article we consider a number of aspects of spallation that involve comparison of one solution to another as some of the parameters of the problem are varied. In order to permit this comparison, we have analyzed a series of cases involving impact of slabs of thickness 1, 2, 5 and 10 mm on targets that were, in each case, twice as thick as the impactor. The target and impactor were of aluminum, as characterized by the material constants used in our previous work. For each thickness, calculations were made for impact velocities covering the range necessary to produce damage up to peak void fractions of about 0.3.

The curves of Fig. 2 show the maximum damage level produced in the target as a function of the flyer velocity (or impact stress) for each of the four thickness combinations. The cross-hatched regions

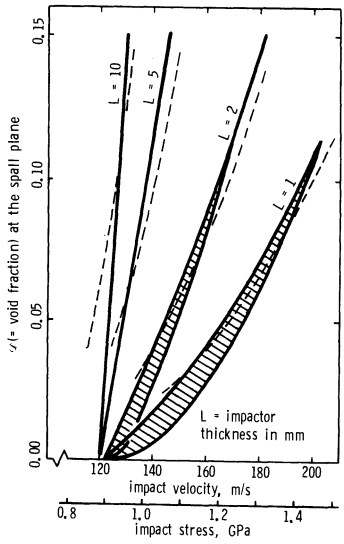

Fig. 2. The damage accumulated at the spall plane in a given impact increases with increasing thickness of the impactor plate (i.e. with increasing duration of load application) and with increasing impact velocity or stress. The shaded regions indicate cases where recompaction occurs from a peak level at the upper boundary to a final level at the lower boundary. The dashed lines are fit to the data using the criterion of Tuler and Butcher, as discussed in Sec. 4.

are those for which some recompression of the voids is produced by wave interactions subsequent to the one initiating the spall. The top border of the region gives the maximum value of $\mathcal{D}$ predicted to occur during the course of an experiment, and the bottom edge gives the final value after recompression. Recompression also occurs along the lower parts of the straight lines, but the regions involved are too narrow to show on the graph. Further examination of the calculations shows that high levels of damage accumulate in stages. Usually a void fraction distribution having a peak at about 0.15 would develop during the first tensile phase. Damage accumulation would cease during the subsequent recompression, but resume during the next tensile phase of the stress history. Some typical histories of damage accumulation are shown in Fig. 3.

Since the earliest investigations of spallation, it has been known that the stress required to produce a given level of damage increased as the duration of load application decreased. Much of the subsequent research on the subject has been directed toward obtaining a quantitative description of this effect. In experimental investigations it is customary to plot the velocity that an impactor must have to produce a given level of damage as a function of the

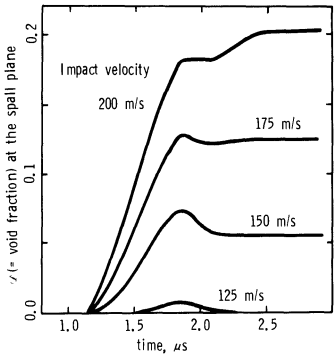

Fig. 3. Histories of damage accumulation at the spall plane for 2-mm thick impactors colliding with 4-mm thick targets at various relative velocities. The rate of damage accumulation increases with increasing impact velocity. When the damage is below about 0.15 the subsequent recompression wave is strong enough to produce some recompaction. Above this level no recompaction occurs and additional damage is produced during the second tensile phase.

thickness of the impactor. Such a plot is essentially one of the impact stress required to produce a spall as a function of the duration of the compression pulse. When our calculated values are plotted in this manner we arrive at the result shown on Fig. 4. We see that the material withstands impulses of short duration much better than those of longer duration, but that the effects become less pronounced when pulses of very long duration are being compared. On the other hand, it is also clear that the damage produced by a thick impactor depends in a very sensitive way on its velocity. All of these results are in qualitative accord with experimental observations.

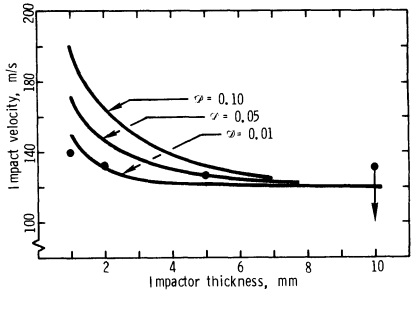

Fig. 4. Conditions of impactor thickness and velocity calculated to produce three given levels of damage. The resistance of the material to damage increases as the duration of load application is decreased. Failure occurs at a well defined stress level if the duration of load application is long. The dots represent thresholds calculated by Taylor's criterion, as discussed in Sec. 4.

A somewhat different view of the effect of stress pulse duration is presented in Fig. 5, which shows the increasing level of damage produced by impactors of fixed velocity but increasing thickness.

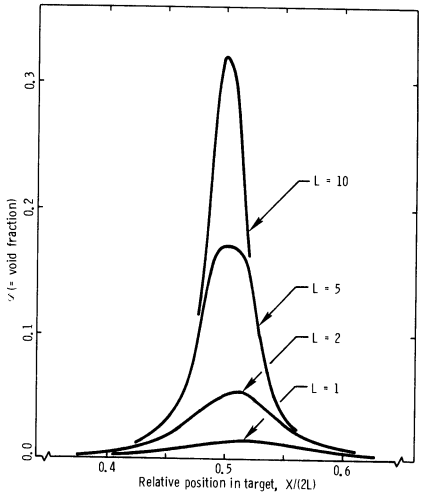

Fig. 5. Damage distributions produced by 150 m/s (stress of 1.1 GPa) collision of impactors of various thicknesses L with targets of twice this thickness. The short-duration impacts produce broad, low-level damage distributions while those of longer duration produce high levels of damage and sharply defined spall planes.

4. Spall Criteria

In this section we interpret earlier work on the problem of spallation in terms of the present theory. Two specific items are considered: (1) criteria for predicting spallation on the basis of wave-propagation calculations not incorporating damage accumulation and (2) methods for interpreting spall experiments by examination of free-surface velocity histories.

Spall Criteria for Use in Calculation. A spall criterion is simply a formal method for deciding whether or not some critical amount of material damage will occur under given conditions. Spall criteria are evaluated in terms of field variables calculated on the assumption that no damage is present.

The first spall criterion to have been considered is one of critical tensile stress--failure will occur on a plane at the instant the tensile stress first exceeds a critical value called the spall stress. Our calculations show that significant stress relief occurs as damage begins to accumulate and that the value calculated on the assumption that no damage develops will not accurately reflect the real situation. Nevertheless, we see from Fig. 4 that when compressive pulses of sufficiently long duration are introduced into the sample, damage

is produced at a critical level of impact velocity (equivalently, stress) and develops to high levels at impact velocities only slightly above the threshold value. Under this condition the critical stress criterion seems quite satisfactory. The curves of Fig. 4 also show, however, that the material is capable of resisting much higher velocity impacts if the duration of the stress pulse produced is short enough (less than about 1 μs in the present case). In this short-pulse regime large variations in impact stress produce only small variations in damage, so the critical-stress criterion is of limited utility.

A variety of spall criteria have been proposed to account for the increasing apparent strength of material when it is subjected to stress pulses of decreasing duration. Among these is the criterion of Tuler and Butcher [4]. According to a continuous-damage generalization of this criterion, a rectangular compression pulse of amplitude $|t_{33}| > t_s > 0$ and duration Δt will produce a peak damage level $\mathcal{D}$ given by

$$\mathcal{D} = \left(\frac{|t_{33}| - t_s}{t_s}\right)^{\lambda} \frac{\Delta t}{\tau} = \left(\frac{|t_{33}| - t_s}{t_s}\right)^{\lambda} \frac{2L}{U\tau} \qquad (4.1)$$

where t, τ, and λ (usually $\lambda = 2$ is chosen) are material constants. In deriving the second of these equations we have used the approximate relation $\Delta t = 2L/U$, where L is the thickness of the impactor plate and U is the wavespeed. When the parameter values $U\tau = 6$ mm, $t_s = 0.69$ GPa, and $\lambda = 2$ are chosen we obtain, for each of the four flyer thicknesses we have been considering, the dashed curves on Fig. 2. Except at very low damage levels, the fit to the more elaborate calculations presented in this paper is accurate enough to be quite useful. This agreement can easily be improved if attention is restricted to a specific damage level $\mathcal{D}_s$ as was originally intended by Tuler and Butcher. It also seems possible to improve the fit by changing the form of the stress-dependent factor in the criterion. We must remember, however, that no spall criterion can be expected to reproduce the results of a fully coupled theory over a broad range of conditions because it does not model all of the interactions actually taking place.

Spall Criteria for Use in Interpreting Experiments. Experimental investigations have often been conducted to determine the amplitude of a stress pulse that is just sufficient to initiate a spall. This has usually required conducting tests at various impact velocities until the critical degree of damage has been produced in a target plate. Taylor [5] has suggested an alternate procedure based on measurement of the velocity history of the stress-free back surface of a target plate impacted at a velocity comfortably above the expected threshold. A typical measurement produces a record like the calculated history shown in Fig. 6. The acceleration of the free surface beginning at the time t_B is attributable to the arrival of a tension-release wave

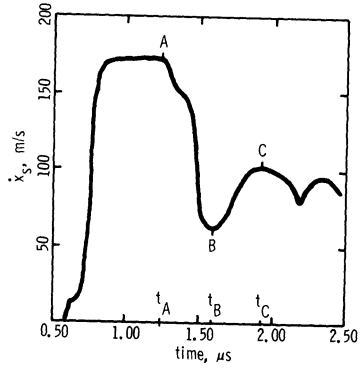

Fig. 6. A typical free-surface velocity history recorded experimentally corresponds closely to this history calculated for the case of a 2-mm-thick impactor colliding with a 4-mm-thick target at 175 m/s.

that is initiated at the spall plane when fracture occurs. According to Taylor's analysis, the stress at which a spall develops is given approximately by

$$t_{33} = \rho_R U \Delta \dot{x}_s / 2 \qquad (4.2)$$

where $\Delta \dot{x}_s = \dot{x}_s(t_A) - \dot{x}_s(t_B)$ is the pull-back velocity taken from the experimental record and U is the wavespeed. The advantage of Taylor's method lies in the fact that a spall threshold can be determined from a single test. It has the disadvantage that it fails to provide any direct indication of the degree of damage associated with the derived value of threshold stress. To determine this degree of damage, we have analyzed the free-surface velocity histories obtained in each of our calculations using Eq. (4.2). For the 1-mm, 2-mm, and 5-mm thick impactors the spall thresholds determined were, respectively, 1.03, 0.98, and 0.93 GPa. The variation over the range

of projectile velocities considered was less than ± 2% in each case. All of these stresses exceed the nucleation threshold of 0.80 GPa used in the calculations, but are entirely consistent with the usual interpretation of a spall stress. The impact velocity associated with each of these cases is shown by a dot on Fig. 4. The associated damage levels are seen to vary somewhat, but all fall in the range usually characterized as incipient spall. The method of interpretation breaks down when applied to the calculations for the thickest (10 mm) flyer. In this case the indicated spall strength decreased markedly with increasing impact velocity from a maximum of 0.97 GPa to a minimum of 0.69 GPa. The larger value is somewhat in excess of what one would expect on the basis of other evidence, and the lower value is clearly in error, as it lies below the nucleation threshold used in our calculation. The reason for the difficulty in interpreting the thick impactor calculations by Taylor's analysis has not been established.

As a final item, we consider the recent suggestion of Cochran and Banner [7] to the effect that the relative amplitude

$$R = \dot{x}_s(t_C)/\dot{x}_s(t_A) \qquad (4.4)$$

of the first and second peaks in the free surface velocity history (see Fig. 6) is a measure of the level of damage sustained in an experiment. We evaluated this ratio for each of our calculations, and obtained the curves of R versus flyer velocity shown on Fig. 7. The curves are of similar appearance to those Cochran and Banner obtained experimentally for uranium. Comparison of the R values with the damage level for each of our calculations confirms the

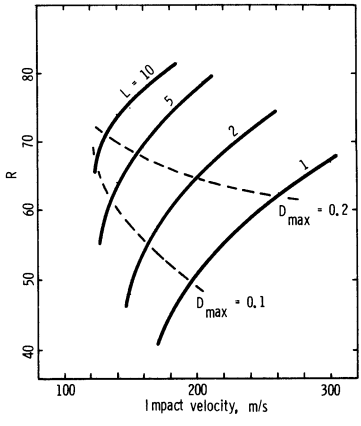

Fig. 7. When Cochran and Banner's damage estimate R is evaluated from calculated free-surface velocity histories results indicated by the solid curves are obtained. The dashed curves connect points on the solid curves at which the peak of the damage distribution is 0.1 and 0.2, respectively.

association of increasing values of R with increasing levels of damage (at the peak of its distribution) for a fixed thickness of impactor. However, comparison of results for different impactors indicates that a given value of R corresponds to smaller and smaller amounts of damage as the impactor thickness is increased. The dashed curves of Fig. 7 indicate conditions producing the fixed damage levels $\mathfrak{D}$ = 0.1 and 0.2. A better correlation of R to damage might be obtained if some other definition of damage than the value of the void fraction at the peak of its distiibution were adopted. One caution we note is that the value of R cannot accurately estimate damage in cases where it develops in stages to a final value, or where the final value is influenced by recompression. Ihis is because the damage distribution is still evolving after t_B, the last time at which information contributing to the value of R is obtained.

Acknowledgement

We are indebted to Dr. A. L. Stevens for numerous helpful discussions. This work was supported by U. S. ERDA, under contract AT(29-1)789.

References

1. Davison, L.; Stevens, A. L.; Kipp, M.E.: Theory of Spall damage accumulation in ductile metals. J. Mech. Phys. Solids 25 (1976) 11-28.

2. Kipp, M. E.; Stevens, A. L.: Numerical integration of a spall-damage viscoplastic constitutive model in a one-dimensional wave propagation code. Sandia Laboratories Report SAND 76-0061 (1976).

3. Barbee, T. W., Jr.; Seaman, L.; Crewdson, R; Curran, D.: Dynamic fracture criteria for ductile and brittle metals. J. of Materials 7 (1972) 393-401.

4. Lawrence, R. J.; Mason, D. S.: WONDY IV--A computer program for one-dimensional wave propagation with rezoning. Sandia Laboratories Report SC-RR-710284, Aug. 1971.

5. Tuler, F. R.; Butcher, B. M.: A criterion for the time dependence of dynamic fracture. Int. J. of Fracture Mechanics 4 (1968) 431-437.

6. Taylor, J. W.: Stress wave profiles in several metals in Dislocation Dynamics ed. A. R. Rosenfield, et al., McGraw-Hill Book Co. New York (1968) 573-589.

7. Cochran, S.; Banner, D: Spall studies in uranium. J. Appl. Phys. 48 (1977) 2729-2737.

Observation of Atomic Behavior in Crystal During Shock-Compression by Flash X-Ray Diffraction

K. KONDO, A. SAWAOKA and S. SAITO

Research Laboratory of Engineering Materials,
Tokyo Institute of Technology,
Ookayama, Meguro, Tokyo 152, JAPAN

Summary

Flash X-ray diffraction patterns of LiF single crystal during shock-compression have been successfully obtained up to 50 GPa. Some anomalous phenomena different from isotropic compression have been observed; the single crystal transforms to the imperfect one like a mosaic crystal, and the unit cell volume obtained from (200) interplanar spacing by FXD appears systematically smaller than the Hugoniot.

Introduction

The flash X-ray diffraction (FXD) technique is an usefull method to elucidate the microscopic structure of solids during shock-compression and release process because the FXD pattern brings some informations concerning the atomic arrangement. In traditional shock-wave studies, there has been a lack of understanding of disruptive forces within a shock-front and the effect of shock-wave passage on crystalline order. Moreover, volume and pressure under shock-compression are estimated by Rankin-Hugoniot relations based on the significant assumption that materials behave as the completely relaxed fuluid above the yield point.

The present authors intended that crystallography during shock-compression could be performed in the usual ex-

perimental room by using the following FXD system. We have constructed the FX generator[1] similar to Q. Johnson et al.'s and developed an X-ray detector by using an image intensifier (I.I.)[2]. This equipment has sufficient intensity and sensitivity to obtaine good diffraction patterns of polycrystalline LiF, NaCl, Si and SiO_2 etc. for molybdenum and copper Kα radiation under atmospheric pressure. The system has been combined with a small type of double stage light-gas gun for application to shock-wave studies[3].

Experimental Procedure

Schematic diagram of the experimental arrangement is shown in Fig. 1. The FX generator is combined with the gas gun at an angle of 80° to the projectile flight direction. The detector-assembly is placed on a precise mounting holder in the instrumentation chamber. The distances from the center of the back-surface of a specimen to the fluorescent screen of the detector and

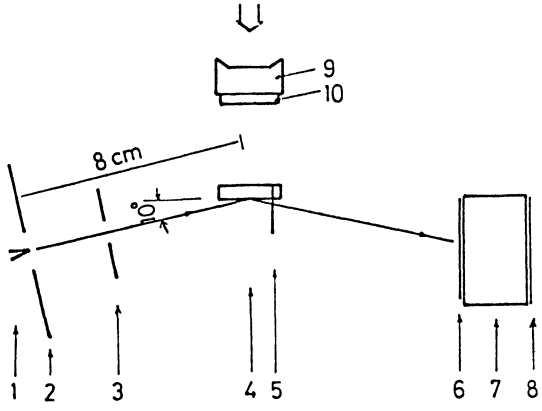

Fig. 1 Schematic diagram of the experimental arrangement.
1. Anode 2. Cathod 3. Collimator 4. Specimen
5. Trigger pin 6. Fluorescent screen 7. Image intensifier 8. Emulsion film 9. Projectile 10. Metal impactor

to the cathod plate are 80 mm, respectively. The detector can cover diffracted X-rays in the 2 θ range 10° to 30°. The diffracted X-rays from the specimen are approximately focused on the fluorescent screen at 20° 2 θ. Since reproducibility of the angle on the film is good, changes of the Bragg angle can be determind with a distance between recorded lines and a standard point marked on the film without a known line of normal condition to be compared to them. The error due to the above treatment is less than ±0.1° in 2 θ. The <100>-oriented crystal of LiF was shaped into a pellet of 15 mm in diameter. The surface was perpendicular to the shock direction. The crystal was cut and polished to the thickness calculated from G. E. Hauver and A. Melani's Hugonior[4] of LiF single crystal in order to synchronize the X-ray irradiation with the arrival of the shock-front at the back-surface of the specimen.

Results and Discussion

Figure 2 shows microphotometer tracings of typical diffraction records on LiF single crystal taken before

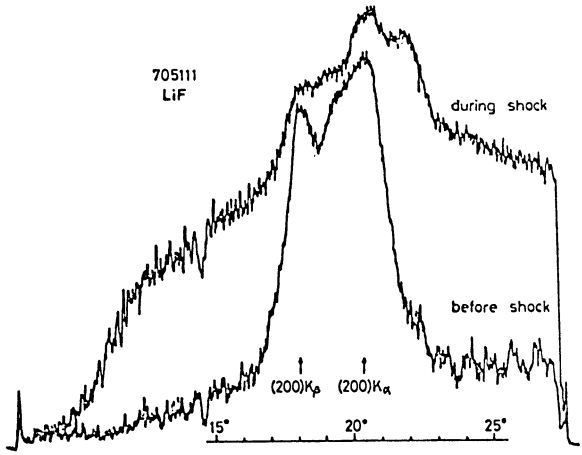

Fig. 2 Density pattern of FXD records by a microphotometer.

and during shock-conditions. These were taken using unfiltered molybdenum radiation. The projectile with a copper plate impacted the crystal at 1.831±0.013 mm/μsec parallel to (200) plane. The shock-pressure estimated is 24.0±0.3 GP_a using G. E. Hauver and A. Melani's Hugoniot of LiF[4]. The (200) Kα and Kβ lines can be seen in the normal condition and the additional line corresponding to the shock-compressed state can be seen at the higher angle position. The X-rays were irradiated at a few 10 *n*sec earlier than the shock arrival at the back surface of the specimen. Peak densities of the normal state during and before shock are equal to about 2.5. Although the density of the additional peak of the shock-compressed state is slightly lower and broader than that of the normal state, the difference is very small. Judging from the peak height and shape, the interplanar spacing of the crystal lattice is uniformly contracted, and then it is reconfirmed as pointed out by Q. Johnson et al.[5] that the shock compression is hydrostatic, and that crystal orientation can be preserved.

However, a remarkable increase of the back-ground diffraction exists around the peak compared to the pattern before shock and indicates that the direction of <100> crystal axis is distributed at several degree around the peak. It might be better to call it the broad peak indicating the distribution of the arrangements of crystallites rather than the back-ground. Since both the sharp and the broad peaks are much higher than those of the polycrystal diffraction records which are shown elsewhere, the disorder extent of each crystallite is not so random as polycrystal. It is, therefore, interpreted that the single crystal of LiF transforms to the imperfect one like a mosaic crystal which has a large disorder in the range of several degrees.

The peak of (200) Kα shock indicates 21.92±0.11° in 2 θ, thus the ratio of d to d_o results in 0.929±0.004, where d and d_o are the interplanar spacing corresponding to the shock and the normal states, respectively. Supposing hydrostatic compression and preservation of cubic symmetry, the change of the unit cell volume should be expressed by the cube of (d/d_o). Then, the volume change is estimated to be 0.801± 0.011. The data including the other pressure ranges indicate the significant results; the unit cell volume obtained from the (200) interplanar spacing which is measured by these FXD experiments appears systematically smaller than the Hugoniot volume. This indicates certainly the microscopic structure of the lattice during shock-compression or uniaxial-compression effect because we can observe only the perpendicular plane to the shock direction by FXD.

Literature

1) K. Kondo, A. Sawaoka and S. Saito: Proc. 4th Int. Conf. on High Pressure, Kyoto, 1974(the Physico-Chemical Soc. of Japan, Kyoto (1975) 845-850.

2) K. Kondo, A. Sawaoka and S. Saito: Japan. J. Appl. Phys., 14 (1975) 1585-1588.

3) K. Kondo, A. Sawaoka and S. Saito: to be published.

4) G. E. Hauver and A. Melani: Bull Am. Phys. Soc., 15 (1970) 1617.

5) Q. Johnson, A. C. Mitchell and L. Evans: Appl. Phys. Lett., 21 (1972) 29-30.

The Influence of High-Rate Deformation on Structure and Properties of Materials in the Presence of Stress Concentrators

R. Mavljutov and O. Kaibyshev

Ufa Aviation Institute, Karl Marx St., 12,
450025 Ufa-25/USSR

Summary

The propagation of shock waves in solid bodies is observed. The equipment and methods of measuring dynamic properties in wide temperature /up to 1200°C/ and strain rate /$\dot{\varepsilon} = 10^4$ sec^{-1}/ intervals are worked out.
Changes of the deformation mechanism with increasing $\dot{\varepsilon}$ are investigated on the model materials of copper and magnesium alloy.
It is established that with increasing strain rate up to dynamic loads /$\dot{\varepsilon} = 10^4$ sec^{-1} and more/ the transition to a multiple slip occurs. In plastic flow takes place as a result of slip in a great number of slip planes of the {111} <1$\bar{1}$0> system, in the magnesium alloy alongside with basal slip a non-basal one in the (10$\bar{1}$0), (10$\bar{1}$1) systems occurs.
In the magnesium alloy twinning is also activated. Under the conditions of dynamic loading twinning occurs in many systems simultaneously.
Taking into account the deformation characteristics of the materials: A dislocation type, stacking-fault energy, it is possible to describe changes in the deformation mechanism with increasing strain rates.
The change of a dislocation structure has been studied at increasing strain rates. Dislocation density increases 2-3 times as much at increasing strain rate by 6-7 orders of magnitude. The given result points at the fact that a high-rate deformation accomplishes at the expense of the increase in strain rates rather than in their number. The obtained results allow to give a structural explanation of the dynamic properties of the material and to explain an effect of stronger hardening of materials after impulsive loading.
The change of dynamic properties of the materials and their influence on the effect of stress concentration in real constructions are analyzed. The role of stress concentrators depending on a strain rate changes non-monotonously. At the calculation of details working at dynamic loading it is necessary to take into account both changes of properties and structure of materials and of the role of stress concentrators with strain rates.

On the Behaviour of the Process Region at a Fast Running Crack Tip

K.B. BROBERG
Division of Solid Mechanics,
Lund Institute of Technology, Lund,Sweden

Abstract

The energy dissipation at fast crack growth is studied. Whereas in the low velocity range the size of the process region (i.e. the region where micro-separations occur) is given by intrinsic dimensions of the material it is governed by the strength of the surrounding stress-strain field in the high velocity range. Therefore the energy dissipation per unit of crack growth is fairly independent of the crack tip velocity in the low velocity range but increases at least in proportion to the crack tip velocity in the high velocity range. At very high velocities the increase is strongly accelerated. The cause is to be sought in the changes of the near-tip stress field and in the associated changes of the micro-separation morphology.

Introduction

Recent experiments [1],[2],[3],[4] (see also [5]) have shown that the energy dissipation per unit of crack growth is extremely sensitive to the crack tip velocity in the high velocity range, see Fig. 1.

Basic Considerations of the High Velocity Range

The concept of *damage region* will be introduced, i.e. the region around the crack-tip where irreversible mechanisms work - plastic flow, micro-crack formation and growth, etc. Very small scale yielding and steady crack growth in the high velocity range is regarded.

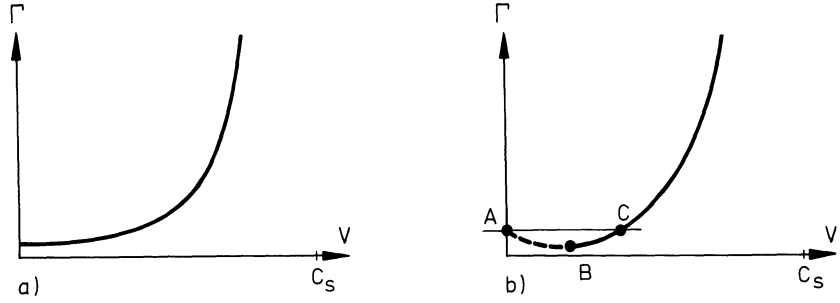

Fig. 1. Principle character of the relation between energy dissipation per unit of crack growth, Γ, and crack tip velocity, V, at small scale yielding. c_s is the propagation velocity of Rayleigh waves. In b) the Γ-V-curve possesses a minimum at the point B. For stability reasons therefore the part AB cannot be definitely given, and the part BC can be definitely given only for decelerating cracks.

Two different crack-tip velocities (in one and the same material), V_1 and V_2 (cases 1 and 2), will now be compared. It is known from dynamic analysis [6] that the near-tip stress-strain field changes with the crack-tip velocity even if the stress intensity factor is constant. However, for simplicity, such changes are disregarded in this section. Thus the near-tip stress-strain field is supposed to be uniquely described by an amplitude factor, only. Then the following statement can be made: If the damage region is known for case 1 it is also known for case 2, and if the stress intensity factor at case 1 is K_1 then it is $K_2=(V_2/V_1)^{\frac{1}{2}}K_1$ at case 2. This follows immediately from a study of Fig. 2. Obviously a material particle of case 2 at the distance $y_2=(V_2/V_1)b$ from the x-axis experiences exactly the same time history as a material particle of case 1 at the distance $y_1=b$ from the x-axis if $K_2=(V_2/V_1)^{\frac{1}{2}}K_1$. Consequently the same damage is produced at $y=y_2$ in case 2 as at $y=y_1$ in case 1. The energy dissipation per unit of crack growth is thus proportional to the velocity V of the crack-tip. This statement, which will be referred to as the *similarity argument*, will later

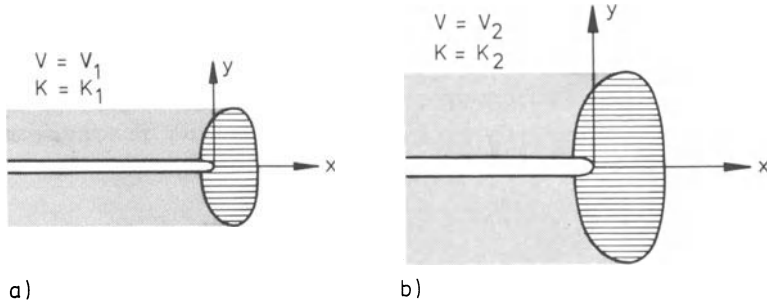

a) b)

Fig. 2. Damage region in case 1 (Fig. 2a) and case 2 (Fig. 2b). V is the crack tip velocity and K is the stress intensity factor. Coordinate directions x and y are shown. The sectioned regions are the damage regions, i.e. the regions where damage occurs. The dotted regions are the wakes of the damage region where no changes in the damage occur.

on be modified when the assumption made of stress-strain field similarity is removed.

Considerations of the Low Velocity Range

Near the crack tip there is a *process region* where micro-separations occur. The physical nature of these is not essential for the discussion in the following. However, it is helpful to make the specific assumption of hole growth starting from inclusions (dimple formation). The energy dissipation per unit of crack growth cannot be less than the energy needed to create a hole and to make it grow until coalescence with the main crack divided by the spacing between the holes. This will be called the *minimum energy requirement*, which implies that the results of the preceding section cannot be extrapolated to very low crack tip velocities, since they point towards zero energy dissipation at very slow crack growth.

The number of holes opened at very slow crack growth cannot considerably exceed the minimum number required for coalescence. The reason is simply that slow hole growth occurs under decreasing forces. This implies unloading

at neighbouring micro-separation kernels (here the inclusions), thus an impediment to hole formation at these sites. A comparison can be made with the fact, that only one necking occurs in a tensile bar at low loading velocities.

A simple but reasonably adequate model for slow crack growth consists of an unbroken sucession of cubic cells,

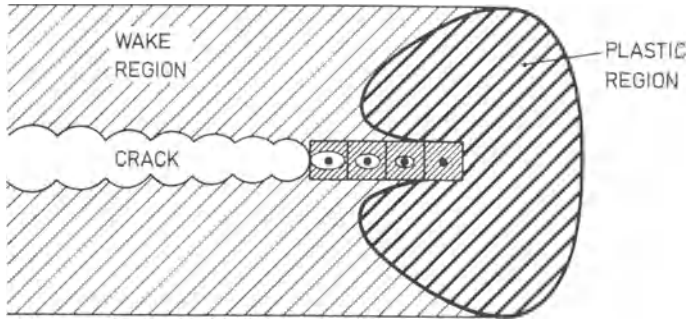

Fig. 3. Model for the process region at slow crack growth. In the originally cubic cells holes are opened at inclusions. At the innermost cell (the cell adjacent to the crack tip) coalescence between the hole and the main crack is about to take place.

each containing a micro-separation kernel, see Fig. 3. The (originally) cubic cells are extended in the y-direction under the action of increasing forces before hole formation, but afterwards (i.e. during hole growth) the extension occurs under decreasing forces [7].

The size of the plastic region as well as the energy dissipation in this region is completely determined by the *minimum energy requirement*, which in the model is interpreted as the energy needed to extend a cell until coalescence can take place. At very slow crack growth, therefore the total energy dissipation per unit of crack growth

is fairly independent of the crack tip velocity. However, already at surprisingly small crack tip velocities, changes of the plastic region are likely to take place due to rate effects [8]. Suppose, tentatively, that the remote stress required to propagate the crack at, say, the velocity 10 m/s is about the same as the one required for very slow crack growth. Then a lower energy dissipation than at very slow crack growth is expected in the plastic region due to its smallness (generally less than a few millimeters), which implies very short loading times. Thus surplus energy is available and also needed since cell extension to coalescence is likely to demand more energy at the higher velocity. Then, if the available energy is just what is needed the tentative assumption of unchanged remote stress is justified. The total energy dissipation is unchanged but the part due to micro-separation has increased and the part due to ordinary plastic flow has decreased. This result should be modified as the assumption of unchanged remote stress is removed. First one recalls that the cell size is fixed (by intrinsic dimensions of the material). Therefore the maximum amount of energy that can be consumed in a cell cannot be expected to be much larger than the energy consumption at very slow crack growth. This indicates that the total energy dissipation per unit of crack growth ought to decrease or to increase only moderately with increasing velocity as long as (essentially) no other micro-separations occur than those directly involved in coalescence with the main crack.

Transition Between the Low and the High Velocity Range

At crack tip velocities that are not very small compared to the propagation velocities of waves in the plastic region, more holes can be opened than those directly involved in coalescence with the main crack. The reason is simply that the unloading of the region surrounding a

growing hole propagates in a wave manner and, therefore, acts with a delay on neighbouring kernels of hole formation. (Compare high velocity elongation of bars where necking can take place at more than one site). The model in Fig. 3. should therefore be exchanged by the one shown in Fig. 4. The more the velocity increases the larger

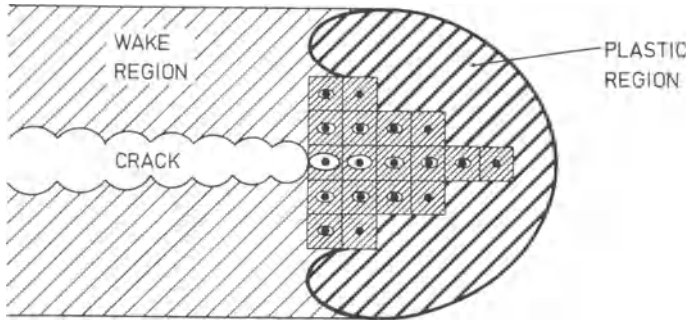

Fig. 4. Model for the process region at fast crack growth.

will the number of (activated) cells per unit of crack growth be.

At a sufficiently fast crack growth the dominating role of the cells in the plane of the crack disappears and the total number of cells becomes large enough for applying continuum mechanics on the region of micro-separations. The size of this region will no longer be tied to intrinsic dimensions of the material but instead to the strength of the surrounding stress-strain field. Then the high velocity range, previously schematically considered, is reached.

The same arguments as used for the low velocity range indicate that the relative part of the total energy dissipation that is due to plastic flow outside the cells should decrease with increasing velocity also in the

transition region. However, one additional mechanism must now be considered. An increased resistance to energy flow through the plastic region to the cells is expected because of the low propagation velocities of equivoluminal waves in a plastic region. The significance of this effect has been analysed in two previous investigations [8], [9]. The results indicate that the energy flow to the region of micro-separations is, in fact, impeded by the presence of low sound velocities, but only to a fairly low extent. Therefore it seems most probable that the fraction of the total energy dissipation that is due to ordinary plastic flow does not increase with the velocity in the transition range. In the high velocity range, the simple model previously considered, indicates that this fraction is independent of the velocity. This range will now be subject to a more detailed study.

Detailed Considerations of the High Velocity Range

The assumption previously made that the near-tip stress-strain field in the high velocity range is described uniquely by an amplitude factor, will now be removed.

In Fig. 5. curves of constant principal stress (the largest one) near a crack tip are shown for different tip velocities. If the linear scale is proportional to 1/V (thus different for the different curves) then it can be expected that micro-separation is initiated at approximately the same point in the figure for all V (say at the point marked x), because then the cells in the plane of the crack will experience approximately the same time history. But then the damage region (not shown in the figure) ought to increase faster in the y-direction than in proportion to V. This effect will be referred to as the effect of the *widening of the stress field*.

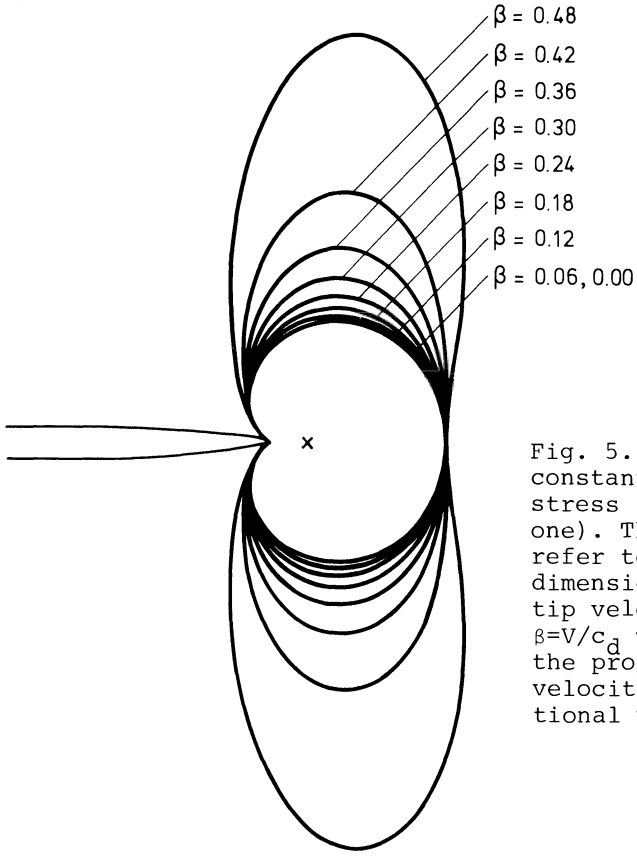

Fig. 5. Curves of constant principal stress (the largest one). The figures refer to the non-dimensional crack-tip velocity $\beta=V/c_d$ where c_d is the propagation velocity of irrotational waves.

It was tacitly assumed that the largest principle stress could serve as a guide to the changes of the damage region with the velocity. However, also the stress composition changes. In the static elastic case

$$\sigma_x = \sigma_y \tag{1}$$

just in front of the crack tip. Considerations of plastic flow [10] modify this relation to

$$\sigma_x \approx 0.6\sigma_y \tag{2}$$

In the dynamic elastic case [6]

$$\frac{\sigma_x}{\sigma_y} = \frac{2\beta^2(1-k^2)(2k^2-\beta^2)}{4k^3(1-\beta^2)^{\frac{1}{2}}(k^2-\beta^2)^{\frac{1}{2}}-(2k^2-\beta^2)^2} - 1 \tag{3}$$

where $\beta=V/c_d$ and $k^2=c_r/c_d$, c_r and c_d being the

propagation velocities of equivoluminal and irrotational waves. Assuming the crack-tip velocity to be about 70 percent of the Rayleigh wave velocity gives for Poisson's ratio 0.35 approximately

$$\sigma_x \approx 1.8\sigma_y \qquad (4)$$

Consideration of (1) and, especially, of the more accurate relation (2), shows that the stress state at slow crack growth is such as to favour growth of the material separations towards coalescence with the main crack (cf. [7]), see Fig. 6. On the other hand, at fast crack growth,

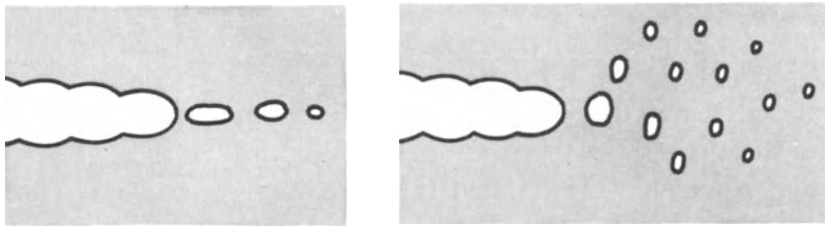

a) b)

Fig. 6. a) Shape of holes shown to be such as to favour coalescence with the main crack at low crack-tip velocities. b) Shape of holes at very fast crack growth.

as indicated by (4), material separations should tend to grow essentially transversely to the crack path, see Fig. 6b. The ultimate 'goal', the final coalescence of holes with the main crack, therefore ought to require comparatively more energy at high than at low velocities. Thus the tendency towards an increase of the energy dissipation per unit of crack growth faster than in proportion to the crack tip velocity (as indicated already by a study of the angular extension of the highly stressed region) is further accentuated. This effect will be referred to as the *changed micro-separation morphology*.

Besides its effect on the energy dissipation the change of the morphology of micro-separation implies increasing probability of coalescence involving off-side holes

as the crack tip velocity increases. This could explain why very rough fracture surfaces appear in the high velocity range.

In the discussion of the transition range the resistance to energy flow through the plastic region to the region of micro-separations caused by the low propagation velocities of equivoluminal plastic waves was mentioned. The same kind of effect - and perhaps much stronger - should prevail for the energy flow through the peripheral parts of micro-separations where irrotational waves can be much slower than in a homogeneous plastic region. Thus all propagation velocities can be much smaller than the elastic ones. Therefore the transfer of energy to the very neighbourhood of the crack-tip could be very much impeded. Still, as should be noted, such an effect would not influence the result arrived at when the simplified model (shown in Fig. 2.) was discussed, but could do so when coupled to the two superposed effects, the *widening of the stress field* and the *changed micro-separation morphology*. However, this opinion is rather speculative. The effect will be referred to as the *barrier effect*.

Conclusions

The investigation in the preceding sections enables a schematic construction of the relation between the energy dissipation per unit of crack growth and the crack tip velocity. Fig. 7. shows the composition in principle of the energy dissipation. The relative significance of the different sources naturally varies from one material to another. For example, rate effects on the plastic flow ought to be much more pronounced in materials exhibiting delayed yielding than in other ones and the change of micro-separation morphology may have another significance for micro-cracks (opened through cleavage) than for holes (opened at inclusions).

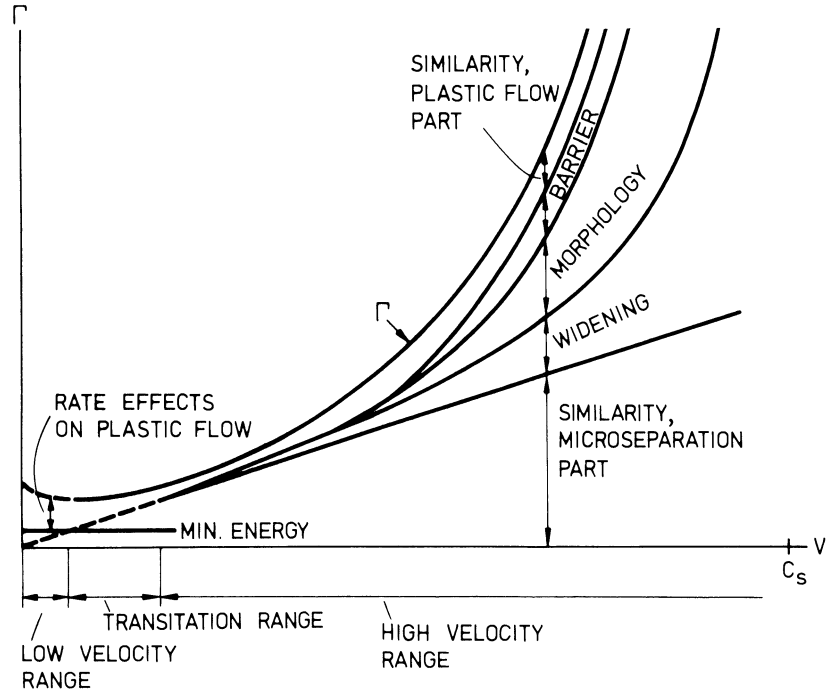

Fig. 7. Schematical construction of the energy dissipation per unit of crack growth, Γ, as a function of the crack tip velocity V. The different curves show how Γ is composed. 'Min. energy', 'Similarity', 'Widening', 'Morphology' and 'Barrier' stand for the concepts introduced in the text: 'Minimum energy requirement', 'Similarity argument', 'Widening of the stress field', 'Changed micro-separation morphology' and 'Barrier effect', respectively.

At some velocity branching seems to be inevitable, according to experiments. Its nucleation is probably favoured by the changes of the micro-separation morphology. Moreover sustained branching is unlikely to occur at low velocities because then any small initial length difference between the branches will lead to rapid arrest of the shorter one [11].

The anticipated strong influence of the character of the near-tip stress field ought to imply a rather high sensitivity of the total energy dissipation to the scale of yielding. Recent experiments also show such a sensitivity [2].

Acknowledgement

The present work has been carried out in close cooperation with a project supported by the Swedish Board for Technical Development.

References

1 Paxson, T.L. and Lucas, R.A., An experimental investigation of the velocity characteristics of a fixed boundary fracture model, Procedings of an International Conference on Dynamic Crack Propagation, ed. G.C. Sih, Nordhoff International Publishing, Leyden, The Netherlands (1973), 415-426.

2 Nilsson, F., Crack propagation experiments on strip specimens, Engng. Fracture Mech. 6(1974), 397-403.

3 Hahn, G.T., Gehlen, P.C., Hoagland, R.G., Kanninen, M.F., Popelar, C. and Rosenfield, A.R., Critical experiments, measurements and analysis to establish a crack arrest methodology for nuclear pressure vessel steels, Second Quarterly Progress Report on Task 62, Battelle, Columbus Laboratories, 505 King Avenue, Columbus, Ohio 43201, USA (1975).

4 Hahn, G.T., Gehlen, P.C., Hoagland, R.G., Kanninen, M.F., Popelar, C., Rosenfield, A.R. and deCamps, V.S., Critical experiments, measurements and analysis to establish a crack arrest methodology for nuclear pressure vessel steels, First Annual Progress Report on Task Agreement No. 62, Battelle, Columbus Laboratories, 505 King Avenue, Columbus, Ohio 43201, USA (1975).

5 Bergkvist, H., The motion of a brittle crack, J. Mech. Phys. Solids, 21 (1973), 229-239.

6 Broberg, K.B., The propagation of a brittle crack, Arkiv för Fysik, 18 (1960), 159-192.

7 Andersson, H., Analysis of a model for void growth and coalescence ahead of a moving crack tip, J. Mech. Phys. Solids, 25 (1977).

8 Broberg, K.B., On effects of plastic flow at fast crack growth, Fast Fracture and Crack Arrest, ASTM STP 627, eds. G.T. Hahn and F. Kanninen, American Society for Testing and Materials (1977).

9 Broberg, K.B., On dynamic crack propagation in elastic-plastic media, Proceeding of an International Conference on Dynamic Crack Propagation, ed. G.C. Sih, Nordhoff International Publishing, Leyden, The Netherlands (1973), 461-499.

10 Rice, J.R. and Rosengren, G.F., Plane strain deformation near a crack tip in a power-law hardening material, J. Mech. Phys. Solids, 16 (1968), 1-12.

11 Pärletun, L.G., Determination of the growth of branched cracks by numerical methods, Report from the Division of Solid Mechanics, Lund Institute of Technology, Box 725, S-220 07 Lund, Sweden.

Crack Propagation in Plastics Due to Impact

W. GOLDSMITH

Dept. of Mechanical Engineering
Univ. of Calif., Berkeley, CA, USA

F. KATSAMANIS

Chair of Mechanics, National
Techn. Univ., Athens, Greece

Summary

Crack propagation and the stress intensity at the tip of a crack resulting from impact loading were determined experimentally in narrow bars of polymethyl methacrylate and polycarbonate. Stress wave passage was monitored by strain gages mounted on the specimens. A 24-frame Cranz-Schardin camera recorded crack position and the stress intensity factor at its tip, the latter by means of a shadowgraphic technique known as the method of caustics, developed by Manogg [1] and Theocaris [2]. Static and dynamic stress intensity factors are obtained as functions of the assumed uniform stress at the crack section; the latter is based on the time-shifted strain measurement, the instantaneous intact specimen width and a dynamic Young's modulus obtained from measured propagation velocity and specimen density.

Introduction

During the last two decades, an enormous body of literature has been accumulated on the subject of crack propagation in brittle materials. The complexities of the dynamics of crack motion due to acceleration or, alternatively, kinetic energy are so great that a reasonably accurate analysis accounting for the separate effects of rapid crack opening, material motion, waves generated as the result of crack propagation, and non-uniform stress distribution, while slowly emerging [3-7], cannot be currently anticipated. Consequently, a wide variety of experimental techniques have been employed in an attempt to obtain an adequate understanding of dynamic fracture problems [8]. Stress intensity factors have been determined either by interferometric measurement of crack opening displacements [9] or by a shadowgraphic technique known as the method of caustics, which transforms a stress singularity into a corresponding optical singularity represented by a locus of concentration of light rays. This procedure was first used by Manogg [1] for transmitted light and subsequently expanded and more fully exploited by Theocaris and co-workers [2], [10-12] for

both transmitted and reflected light. Two recent contributions [13-14] utilizing a double cantilever beam specimen and a Charpy-type sample have evaluated the stress intensity factor obtained by the method of caustics under dynamic conditions.

This investigation involved an experimental study of the propagation of opening mode (Type I) edge cracks in flat specimens of two types of polymers due to the action of tensile components generated upon successive reflections from the free ends of initial compressive pulses generated by the impact of pneumatically propelled steel spheres. Although a large number of samples were tested, the sequel is limited to the presentation of static and dynamic results for a single geometry of each of the two materials. A more complete account of the results of the inquiry will be presented elsewhere.

Experimental Arrangement and Procedure

Notched flat rectangular specimens of polymethyl methacrylate (Plexiglas) and polycarbonate of bisphenol (Lexan) were tested in static tension in a standard commercial machine and were also subjected to longitudinal impact by 10 mm diameter steel spheres. Samples of about 3 mm thickness, 40 mm depth and lengths of 304-305 mm were edge-cut by a saw to produce rectangular notches of 5, 7 or 8 mm initial depths and thicknesses of 0.31-0.35 mm. One Plexiglas sample was also supplied with two 1.5 mm diameter holes on the centerline 10 mm on either side of the cut. Dynamic test specimens were mounted in two Styrofoam holders with the longer axis of symmetry horizontal and the shorter vertical. An aluminum disk about 4 mm thick was attached at the impact point to minimize chipping. Post-mortem photographs were taken of all reassembled specimens.

A single BLH-type FAE-12-12-12S9L foil strain gage with a resistance of 120Ω and a specified gage factor of 2.03 was cemented longitudinally to each of the dynamic test samples at distances of 14.5 and 74 mm ahead of the crack for the Plexiglas and Lexan bars, respectively. The gages were placed in a potentiometric circuit with one similar dummy gage and activated by a nominal 12 V car battery whose

output was ascertained for each shot. Signals were recorded and photographed on Tektronix storage oscilloscopes with a frequency response well into the MHz range.

The crack region was photographed with the aid of a 24-spark Cranz-Schardin camera capable of providing any desired uniform interframe time using an external oscillator. An internal control also permitted selection of constant interframe magnitudes in each of 5 groups of consecutive pictures that could be varied relative to each other by a binary factor. The light path from each spark was reflected by a concave mirror of about 5 m focal length, passing through the specimen ahead of the reference plane and thence through 24 individual apertures to a single film plate. The unit was triggered by a suitably delayed signal initiated by the sweep of the strain gage oscilloscope which, in turn, was activated by the voltage generated by shear in a barium titanate crystal pressed against the specimen near the impact point. A He-Ne laser served as the light source for the shadowgraphs in the static tests with a lens producing diverging rays.

An initial series of impact tests was conducted on a 466.5 x 11.0 x 10.95 mm PMMA and a 466.1 x 10.7 x 9.31 mm Lexan bar without notches to determine propagation velocity and pulse attenuation. Here, the swing of a 10 kp hammer of a Charpy impact tester (with a weight of 290 g) producing a velocity of about 3 m/s was utilized as well as ball impact. The latter were initially blown through a tube at velocities of 10-16 m/s, while a compressed gas gun capable of achieving speeds of 50-150 m/s was employed in later tests. Initial and rebound velocities were ascertained from oscilloscopically recorded signals generated by the interruption of two laser beams focussed on two light-sensitive elements 50 mm apart.

A schematic of the experimental arrangement is presented in Fig. 1.

Results and Discussion

The pulse propagation and attenuation tests served to establish the

value of the dynamic Young's modulus for the two substances; PMMA is generally regarded as strain-rate sensitive, whereas Lexan is considered to be nearly rate-independent [15-16]. The rod wave speed for Plexiglas was found to be $c_o = 2.11 \begin{smallmatrix} +4 \\ -1 \end{smallmatrix}$ % km/s within the ranges $\in$ = 0.2-2.0 x 10^{-3} and $\dot{\in}$ = 10-50 s^{-1}, produced by ball velocities of about 13 m/s or hammer drops through a fall height of 0.5 m. At sphere impact velocities of 120 m/s, where $\in$ = 19 x 10^{-3} and $\dot{\in}$ = 712 s^{-1} and fracture of the sample occurred, the propagation velocity increased to c_o = 2.3 km/s. On the other hand, the speed for Lexan for these conditions involving ranges of $\in$ = 0.2-40 x 10^{-3} and $\dot{\in}$ = 10-1000 s^{-1} was found to be c_o = 1.505 ± 1.3 % km/s, nearly constant. These speeds yield values of the dynamic moduli of 5240 MPa and 2800 MPa for PMMA and polycarbonate, respectively, based on measured densities of 1.18 and 1.23 for the two substances (c.f. [5], [16-17]). The static modulus for PMMA was selected as 3240 MPa [13][16], while that for polycarbonate was chosen as the dynamic value.

The attenuation of the stress amplitude σ of the wave was found as a function of travel distance x (in cm) in the domain of interest as:

$$\begin{aligned} &\text{(a)} \quad \sigma \text{ , MPa} = 10.14 \exp(-0.0028x), \; 20 \geqslant \sigma \geqslant 3 \text{ for PMMA} \\ &\text{(b)} \quad \sigma \text{ , MPa} = 8.83 \exp(-0.00156x), \; 15 \geqslant \sigma \geqslant 4 \text{ for Lexan} \end{aligned} \tag{1}$$

This result was used to adjust the wave amplitude from that at the gage position to both that at the impact point and that at the crack.

The stress intensity factor K_I is determined here from the transverse dimension of the brightly illuminated envelope, or caustic, that surrounds the dark zone created by the shadow method and that delineates the constrained circular plastic region around the crack extremity [1-2]. The light deviation produced in the high strain zone transforms the circular region in the specimen plane into a generalized epicycloid in the reference plane consisting of an outer, nearly circular envelope and an inner apple-shaped trace. For a tensile load, the outer pattern predominates; for compression, only the internal epicycloid is manifested when a stress nonuniformity exists. For tensile loads and non-parallel illumination, K_I is given by [10]

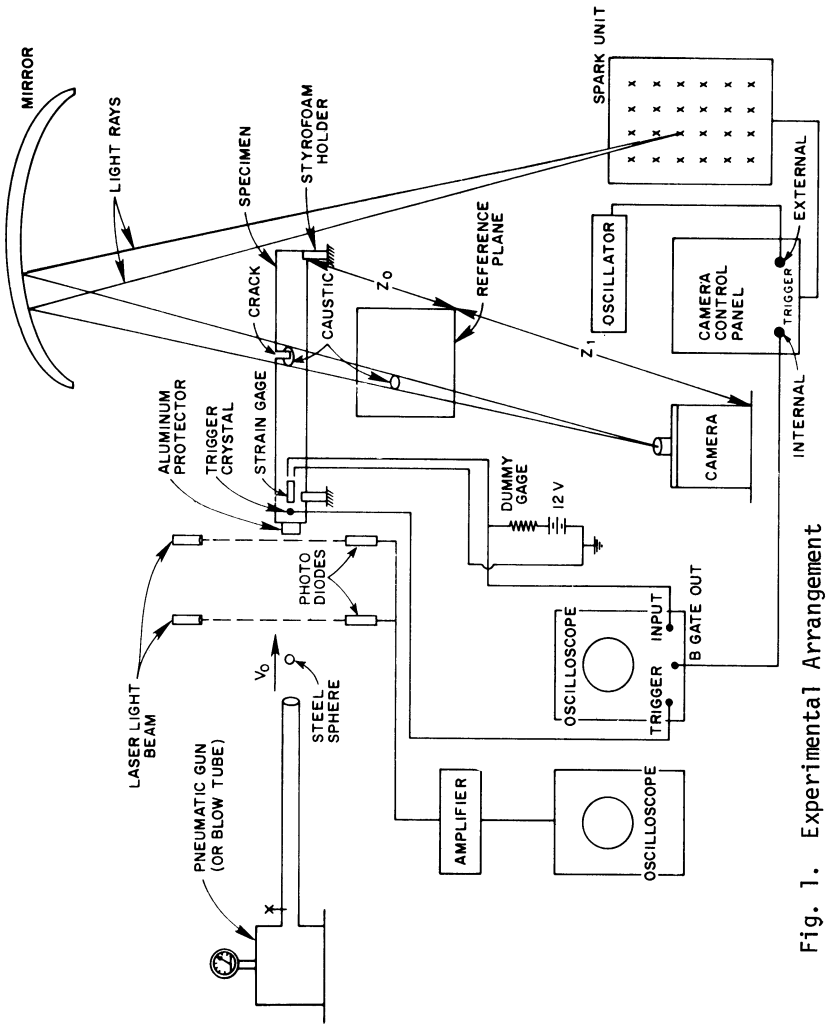

Fig. 1. Experimental Arrangement

$$K_I = 1.671\ (z_o t C_t)^{-1} (M)^{-1.5} (D_M^T/\delta)^{2.5} \qquad (2)$$

Here z_o is the distance between specimen and reference plane, t is the sample thickness, C_t is the photoelastic constant for transmitted light, M the magnification, D_M^T the actual transverse diameter of the caustic, and δ is the ratio of the transverse diameter of the outer envelope to the radius of the generating circle of the epicycloid, which has a value of 3.16 for an optically isotropic material. If z_1 is the distance from the focus to the specimen plane for diverging light and the distance from the reference plane to the focus for converging light, the magnification $M = (z_1 + z_o)/z_1$ or its inverse for the two cases, respectively. The value of D_M^T is the product of M and the transverse caustic diameter scaled from the photo.

The value of C_t for the two materials are not established with any degree of certainty, particularly for dynamic loading, due both to strain-rate and batch-to-batch material variations. The static value of C_t for PMMA was here chosen as 1.05×10^{-10} m^2/N as an average of the range of $0.99\text{-}1.08 \times 10^{-10}$ used previously [2][10-13], while a dynamic value of 0.53×10^{-10} m^2/N was determined experimentally for the conditions of the present tests. The latter corresponds to the data of [16] extrapolated to rise times in the domain of 10-100 μs. The corresponding values for Lexan were chosen from [16] as 1.44×10^{-10} (for a loading time of 1 s) and 1.66×10^{-10} m^2/N, differing from [15]; however, there the justification for the use of the technique of caustics in the case of viscoelastic materials is presented.

Static tension tests were conducted on two 305 x 39.9 x 3 mm Plexiglas specimens with central rectangular edge cracks of 5.1 x 0.34 mm and 7.1 x 0.315 mm, respectively. The fracture stresses for the two samples based on the crack cross section were found to be 11.53 and 10.0 MPa (or strains of 3.9×10^{-3} and 3.09×10^{-3}) for the shorter and longer cracks, respectively. The stress intensity factor varied linearly with applied stress σ at the crack according to

$$\text{(a)}\quad K_I,\ MN/m^{1.5} = 0.1\ \sigma\ \text{(in MPa)} \qquad 0 \leqslant \sigma \leqslant 11.53 \qquad (3)$$

$$(b)\quad K_I,\ MN/m^{1.5} = 0.096\ \sigma\ (\text{in MPa}) \qquad 0 \leqslant \sigma \leqslant 10.0 \tag{4}$$

for these two cases. These are slightly higher than the relation

$$K_I,\ MN/m^{1.5} = 0.082\ \sigma\ (\text{in MPa}) \tag{5}$$

obtained from [2]. The scatter of the present data relative to (3,4) is well within experimental error; the discrepancy with respect to the results of [2] may be due to either material dissimilarities or differences in crack tip geometry that appears to strongly affect the magnitude of the stress intensity factor [14].

The critical values K_{Ic} = 1.133 and 1.01 $MN/m^{1.5}$ found here for specimens with crack length to width ratios c/b = 0.128 and 0.178, respectively, are within the ranges of 0.89-1.32 and 0.88-1.92 cited by [18] and [19] and close to that of 1.18-1.67 given by [20]. This parameter is apparently a function of c/b, crack velocity and loading rate for identical materials; no relation has been suggested for a variation of K_{Ic} with kinematic parameters. The theoretical value for this quantity [20] translates into magnitudes of 1.42 and 1.37 $MN/m^{1.5}$ for the two cases, respectively. The lower measured magnitudes may be due to violations of the ideal case assumed in the analysis and to the relatively small sample width employed. No static tests were conducted on Lexan; [21] cites a range for the static value of K_{Ic} of 3-3.6 $MN/m^{1.5}$.

Fig. 2 reproduces the strain gage data, and Fig. 3 presents a typical shadowgraph frame for a notched Plexiglas and Lexan bar struck longitudinally by a 10 mm diameter steel sphere at velocities of 16.83 and 90.4 m/s, resulting in rebound speeds of 3.96 and 14 m/s, respectively. The strain gage for the PMMA bar was located 14.5 mm ahead of the crack near the bottom edge; that for the Lexan sample was mounted centrally 74 mm ahead of the crack. In both tests, the crack moved, to failure in the first instance, while arrest ensued in the Lexan. The particular wave velocities for these two cases were determined as 2.29 and 1.55 km/s, respectively, from the strain data. The pulses were translated backwards to the impact point for an eval-

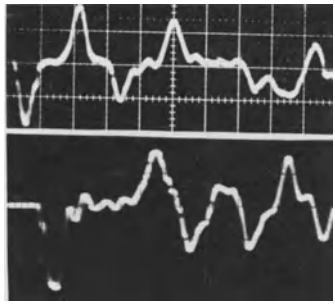

Fig. 2. Strain Gage Data from the Impact of 10 mm Diameter Steel Spheres

(a) 304 x 40 x 3.09 mm Plexiglas Bar with Central 7.3 x 0.315 mm Edge Crack at 16.83 m/s. Strain Scale: $\epsilon = 1.57 \times 10^{-3}$/div. Time Scale: 100 μs/div.

(b) 304 x 40 x 3.0 mm Lexan Bar with Central 8.0 x 0.35 mm Edge Crack Struck at 90.4 m/s. Strain Scale: $\epsilon = 7.97 \times 10^{-3}$/div. Time Scale: 100 μs/div.

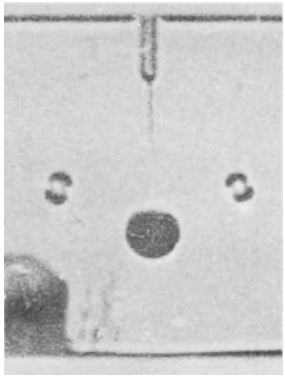

Polymethyl Methacrylate

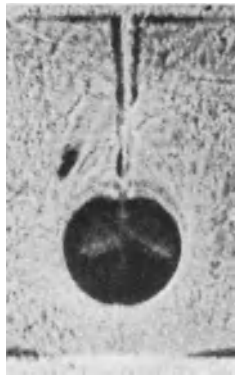

Polycarbonate

Fig. 3.

Typical Caustics Corresponding to the Data of Fig. 2.

uation of the impulse-momentum balance, and also projected forward to the crack position to determine the relation between stress and K_I. The first process required only an amplitude adjustment in accordance with (1), while the second additionally required a time shift due to wave transit and spark unit initiation delay as well as a correction accounting for the changing width of the specimen at the notch (during crack propagation) relative to that of the gage. The travel time was determined using average values for the wave speed (obtained from many tests) of c_o = 2.2 and 1.505 km/s for PMMA and Lexan, respectively, for purposes of uniformity; this involved a shifting error of no more than 2 μs. The variation in width was treated on the basis that the same stress was produced by a given

strain magnitude of the pulse at all longitudinal cross sections.

The fracture locus was a straight line for both samples; for PMMA, the bar exhibited two plateaus of crack arrest before the onset of catastrophic failure involving the passage of three consecutive tensile pulse components. The crack was permanently arrested in the Lexan specimen before complete penetration to the distal edge ensued; the absence of catastrophic failure is attributable to the lower amplitudes of subsequent tensile pulses resulting from higher material damping properties. A small bifurcation and a distinct plastic zone were discernable at the arrested crack tip. The propagation features for the two samples are presented in Fig. 4.

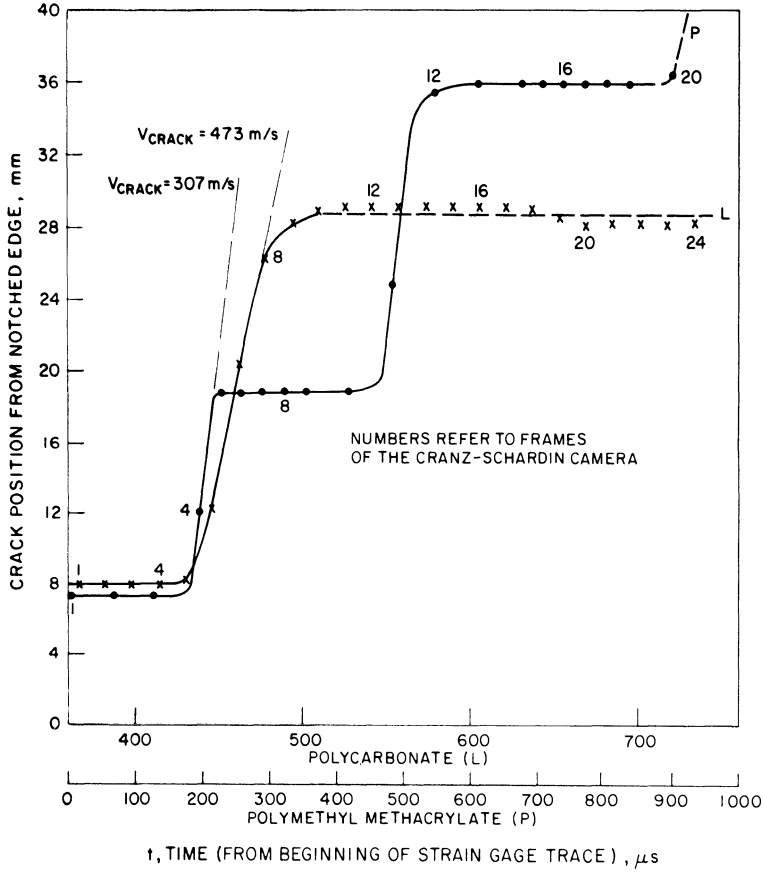

Fig. 4. Crack Propagation in the Specimens Tested

The present tests were not designed for a precise determination of the crack velocities as the photographic intervals were primarily selected to permit evaluation of K_I. A more accurate crack speed can be obtained either by more closely spaced frames during propagation or else by other techniques [18]. However, from these and other tests on PMMA, the crack velocity ranged from 625-700 m/s, with the preponderance of the data near the higher of these values when catastrophic failure occurred as the result of a single tensile pulse passage. This is in good correspondence with the peak crack velocities found by other investigators [5][17-18]. For stepwise propagation, on the other hand, the observed velocity was substantially lower, ranging from 250-340 m/s; this is in accord with the values found in Charpy tests [18] where the strain rates were much smaller than in the present sphere impact experiments. Literature references attribute the variability of the crack speed in PMMA to its dependence on loading rate and load amplitude as related to the amount of elastic energy stored [13] as well as to different conditions of slow crack growth, initiation and maintenance of unstable propagation. The crack speed for Lexan varied from 435-495 m/s, regardless of whether or not crack arrest occurred or catastrophic failure resulted from passage of one or more tensile pulses.

A reasonable impulse-momentum check was found when the static Young's modulus for the two materials was used in converting strain to force. For PMMA, the impulse was 0.0787 N-s and the momentum change was 0.0844 N-s when the strain was increased by 4% to account for the shift to the impact position. The corresponding values for Lexan were found to be 0.416 N-s and 0.426 N-s, respectively.

The dynamic stress intensity factor for the two materials is plotted in Fig. 5 as a function of crack position stress, determined as described above by multiplying crack strain and dynamic Young's modulus magnitudes cited earlier. Discrepancies due to finite interframe times occasionally required a single frame shift to match the maximum diameter of the caustic with peak strain. The trend shown exhibits a concave downward curve; however, in other tests the data appear to be distributed fairly evenly about a straight line. Only tensile com-

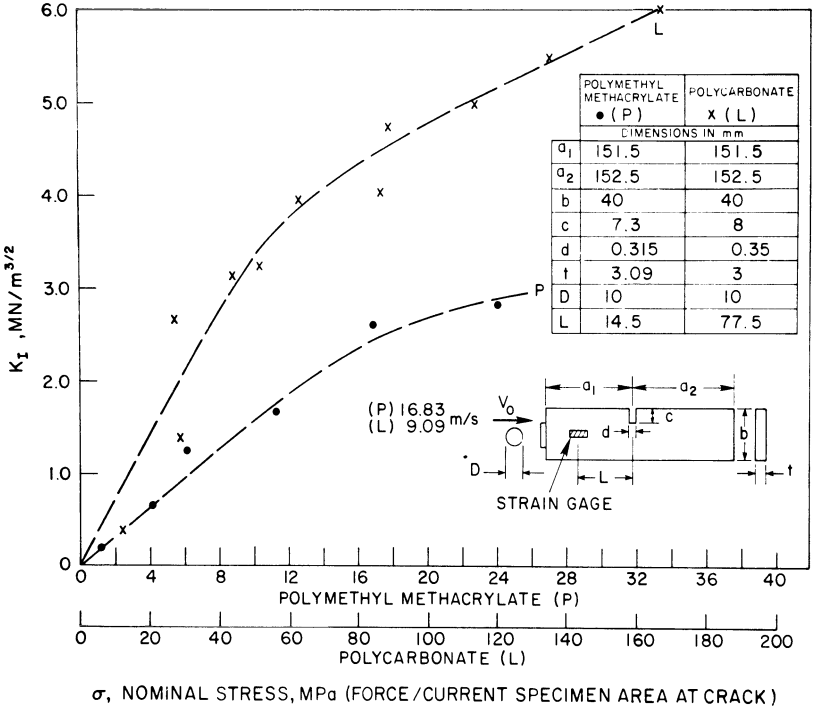

Fig. 5. Dynamic K_I vs. Stress at Crack Cross Section

ponents are examined here; the presence of stress irregularities under compressive stress is due to the finite width of the crack, at least in its initial configuration. The fracture strains for the two runs were of the order of 3.22 and 31.9 m∈, respectively; the associated values of stress are 16.9 and 89.3 MPa that correspond to maximum dynamic stress intensity factors of 2.83 and 6.03 MN/m$^{1.5}$ as determined from (2). These represent increases in K_I due to dynamic loading by factors of about 2.5 and 2, and may be compared to critical values K_{Ic} = 1.36 MN/m$^{1.5}$ and K_{Ic} = 0.82 MN/m$^{1.5}$ for unstable propagation and transition to crack arrest, respectively [17].

The shadowgraphic patterns for the hole do not indicate a completely uniaxial stress distribution where the major axis of the nearly elliptical dark zone (representing the outer envelope of a generalized epicycloid) would be in or perpendicular to the direction of loading for tension or compression, respectively. The axes are inclined to

the horizontal centerline indicating biaxial and probably non-uniform stress conditions. However, the stress calculated from the optical analysis of the light deviation [1][11] using the maximum diameter of the caustic obtained in tension of 14.1 MPa is not far from the value of 15.9 MPa based on a transposed strain 3.02×10^{-3} and the dynamic Young's modulus, although this close agreement was not observed in most of the tests. There, either the conditions for the use of the expression converting D_M^T to stress were not achieved or the value of C_t does not apply. The maximum diameter of the caustic appeared to be nearly proportional to the tensile strain at the crack as derived by translation from the gage measurement.

Acknowledgment

The generous assistance of Professor P. Theocaris, Director, and of the staff of the Laboratory for Testing Materials, The National Technical University of Athens, Greece, is gratefully acknowledged. The work was performed while the senior author was a Fulbright fellow under the auspices of the U.S. Educational Foundation in Greece.

References

1 Manogg, P.: Die Lichtablenkung durch eine elastisch beanspruchte Platte und die Schattenfiguren von Kreis- und Risskerbe. Glastech. Berichte 39 (1966) 323-329.

2 Theocaris, P.S.: Local yielding around a crack tip in Plexiglas. Trans. ASME, Ser. E, J. Appl. Mech. 37 (1970) 409-415.

3 Freund, L.B.: Crack propagation in an elastic solid subjected to general loading. I. II. III. J. Mech. Phys. Sol. 20 (1972) 129-140; 141-152; 21 (1973) 47-61.

4 Broberg, K.B.: On dynamic crack propagation in elastic-plastic media. In: Dynamic Crack Propagation, ed. by G.C. Sih. Leyden, Noordhoff, 1973, 461-499.

5 Bergkvist, H.: The motion of a brittle crack. J. Mech. Phys. Sol. 21 (1973) 229-239.

6 Lehnigk, S.H.: A macroscopic dynamic theory of stability and instability of cracks under impulsive loading. In: Dynamic Crack Propagation, ed. by G.C. Sih. Leyden, Noordhoff, 1973, 333-347.

7 Kfouri, A.P.; Rice, J.R.: Elastic/plastic separation energy rate for crack advance in finite growth steps. In: Fracture 1977, 1, Proc. 4th Int. Conf. on Fracture, ed. by D.M. Taplin. Univ. of Waterloo, Canada, 1977, 43-59.

8 Kobayashi, A.S., ed.: Experimental Techniques in Fracture Mechanics. SESA Monograph No. 1. Ames, Iowa State Univ. Press, 1973.

9 Sommer, E.: Experimental methods for the determination of stress intensity factors under various loading conditions. In: Prospects of Fracture Mechanics, ed. by G.C. Sih, H.C. van Elst and D. Broek. Leyden, Noordhoff, 1975, 593-607.

10 Theocaris, P.S.: Interaction of cracks with other cracks or boundaries. Int. J. Fract. Mech. 8 (1972) 37-47.

11 Theocaris, P.S.: Optical stress rosette based on caustics. Appl. Optics 12 (1973) 380-387.

12 Theocaris, P.S.: The reflected-shadow method for the study of the constrained zones in cracked birefringent media. J. Strain Analysis 7 (1972) 75-83.

13 Kalthoff, J.F.: Beinert, J.: Winkler, S.: Measurements of dynamic stress intensity factors for fast running and arresting cracks in DCB specimens. In: Proc. Symp. on Fast Fracture and Crack Arrest. Philadelphia, ASTM STP 627, 1977, 161-176.

14 Kalthoff, J.F.; Winkler, S.; Beinert, J.: The influence of dynamic effects in impact testing. Int. J. Fract., to appear.

15 Theocaris, P.S.: Method of caustics for the study of cracked plates made of viscoelastic materials. Int. J. Mech. Sci. 16 (1974) 855-865.

16 Raftopoulos, D.D.; Karapanos, D.: Theocaris, P.S.: Static and dynamic mechanical optical behaviour of high polymers. J. Phys. D.: Appl. Phys. 9 (1976) 869-877.

17 Carlsson, J.; Dahlberg, L.; Nilsson, F.: Experimental studies of the unstable phase of crack propagation in metals and polymers. In: Dynamic Crack Propagation, ed. by G.C. Sih. Leyden, Noordhoff, 1973, 165-181.

18 Radon, J.C.; Fitzpatrick, N.P.: Deformation of PMMA at high rates of strain. In: Dynamic Crack Propagation, ed. by G.C. Sih. Leyden, Noordhoff, 1973, 227-243.

19 Marshall, G.P.; Williams, J.G.: The correlation of fracture data for PMMA. J. Mat. Sci. 8 (1973) 138-140.

20 Kerkhof, F.: Anwendung der Bruchmechanik auf Hochpolymere. Kolloid-Z. u. Z. Polymere 251 (1973) 545-553.

21 Radon, J.C.: Influence of the dynamic stress intensity factor on cyclic crack propagation in polymers. J. Appl. Polymer Sci. 17 (1973) 3515-3528.

Loads and Crack Velocities During Dynamic Fracture

Akira Kobayashi and Nobuo Ohtani
Institute of Space and Aeronautical Science,
University of Tokyo, Komaba, Meguro-ku,
Tokyo, 153, JAPAN

Summary

Behaviors of loads and crack velocities observed during dynamic fracture in metals and viscoelastic solids, especially viscoelastic features such as the initial slow crack growth and the strain rate dependent crack propagation velocity profiles, are presented in connection with the applied strain rates and temperatures. The newly devised velocity gauge method to measure the very initial slow crack growth in viscoelastic solids is also briefly described.

Introduction

As a discusser's paper, the present authors would like to call attention to the viscoelastic features observed in the load and crack propagation velocity history during dynamic fracture. First, the initial slow crack growth behavior observed in both viscoelastic solids and metals, together with the newly devised modified gage method, is discussed. Then the strain rate dependent crack propagation velocity profiles in viscoelastic solids is presented.

Initial Slow Crack Growth Behavior

1) Viscoelastic Case

As is well-known, several techniques to measure the crack velocity are achieved [1], and the velocity gage

such as shown in Fig.1 is mostly used for viscoelastic case. However, this is not effective to measure the very initial transient portion of crack velocity profile

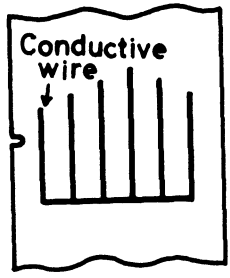

Fig.1 Conventional velocity gage

since the conductive wires are intermittently deposited. Then the modified velocity gage was devised by the present authors to scrutinize the initial part [2] as shown in Fig.2, in which the conductive silver coating materi-

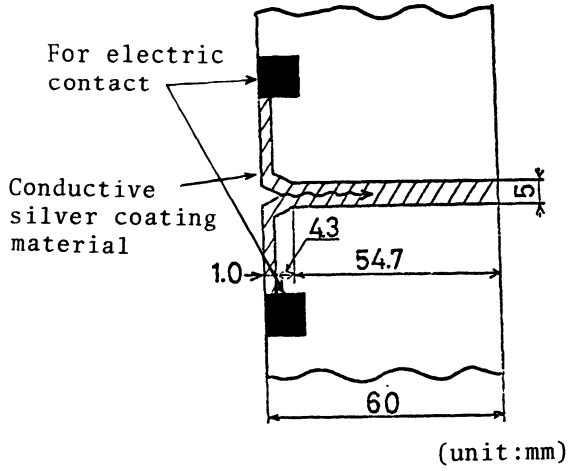

Fig.2 Modified velocity gage

als are deposited like a strip, so that the very initial portion of crack propagation can be measured continuously. The specimen size is shown in Fig.3, and the opening mode tension was applied. The load was measured by a load cell. Test results for PMMA(Polymethyl methacrylate)are shown in Fig.4. What we call the initial slow crack growth does not appear yet at 22°C, and it does at 53°C. So the temperature is a dominant fractor for a strain rate $\dot{\varepsilon} = 1.67 \times 10^{-4}$ /sec, where $\dot{\varepsilon}$=cross-head speed/specimen gage length. Further going to much slower strain rate of 1.67×10^{-6} /sec, the slow crack growth is observed even at the room temperature of 22°C. So the strain rate is influential this time.

2) Metallic Case

The conventional electric potential method was employed for velocity measurement. [3] Ti-6Al-4V alloys were tested. This alloy is rather supposed to be brittle at the room temperature, however, the initial slow crack growth is observed a little bit as shown in Fig.5. At the lower strain rate, the initial slow crack growth region is getting longer as shown in Fig.6. The crack velocity is also getting lower throughout as compared to Fig.5.

Strain Rate Dependent Crack Propagation Velocity Profile

In Fig.7, two dotted lines denote the boundary theoretical crack velocities calculated by the Berry's formula [4], and as the applied strain rates become lower, the obtained velocities are also getting lower. The conventional velocity gage method was employed.

In conclusion, the present authors would like to point out those viscoelastic features related to the applied

strain rates and/or temperatures observed during dynamic fracture.

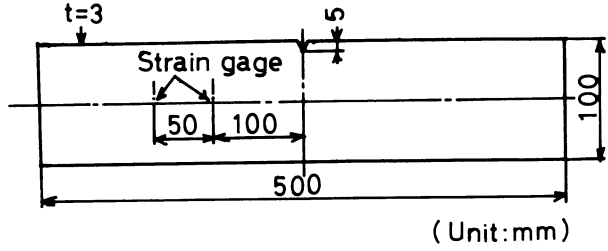

Fig.3 Specimen size

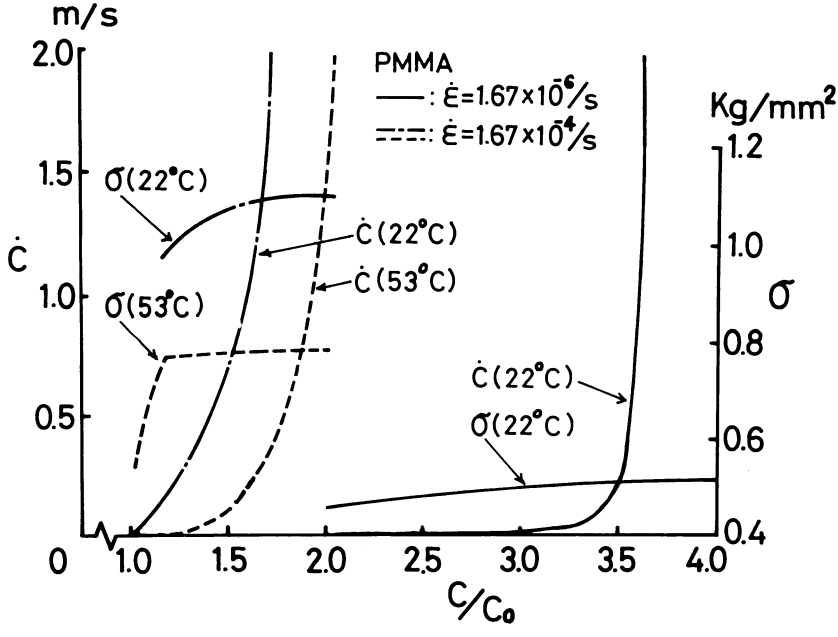

Fig.4 Crack velocity and load (PMMA)

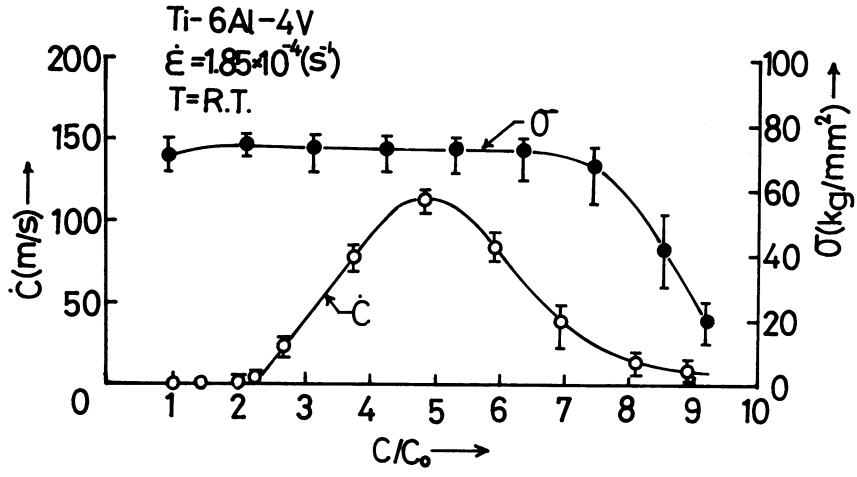

Fig.5 Crack velocity and load(Ti-6Al-4V)

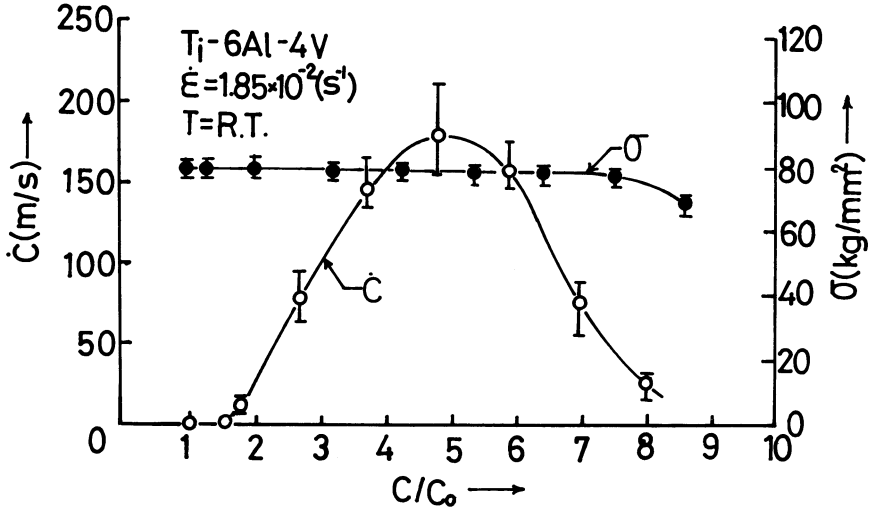

Fig.6 Crack velocity and load(Ti-6Al-4V)

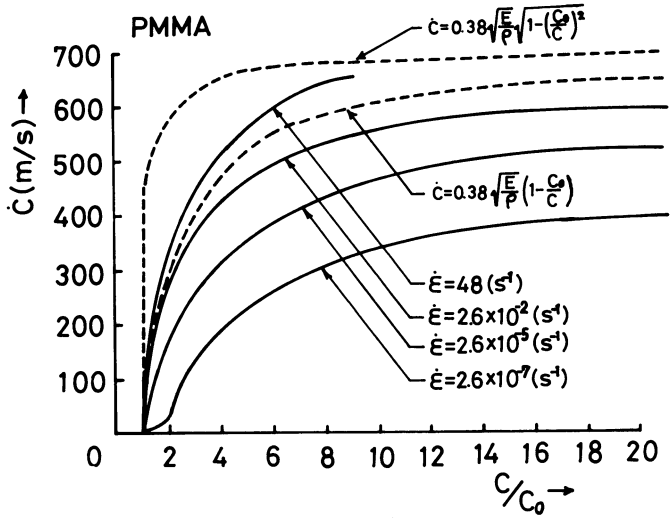

Fig.7 Crack velocity profiles (PMMA)

Acknowledgements

The authors are grateful to Professor Kozo Kawata for his encouragement. Mr. Masayuki Munemura and Mrs. Hiroshi Nakamura are appreciated for their assistance.

References

1. Liebowitz,H.(ed.), Fracture,Vol.II,N.Y.,Academic (1968) 545-547.

2. Kobayashi,A.;Ohtani,N.: Initial slow crack growth behavior followed by rapid brittle fracture in a viscoelastic solid. J.Appl.Polym.Sci. 21(1977) 1351-1358.

3. Kobayashi,A.;Ohtani,N.;Munemura,M: Dynamic crack propagation in aluminum alloys. Bull.Inst.Space. and Aero.Sci., University of Tokyo 13(1977) 517-528.

4 Berry,J.P.: Some kinetic considerations of the Griffith criterion for fracture-I. J.Mech.Phys. Solids 8(1960) 194-206.

Approximate Calculations of Spall and Cratering in High Speed Impact

DANIEL C. DRUCKER
University of Illinois at Urbana-Champaign

Abstract

Highly simplified pictures are presented of the state of stress and the response of ductile materials for spall of plates in uniaxial strain and for cratering of a half-space caused by the high speed impact of small particles or drops of water. Crater volumes are determined by an earlier analysis of Goodier modified to take the kinetic energy transfer ratio into account. Approximate solutions are proposed for speeds of impact from a fraction of the speed of sound in the target material to several times the speed of sound. For spall, the stress-separation relation is assumed to be given by a quasi-static plasticity solution. The ratio of the limit stress to the yield strength in shear is given by the ratio of interparticle distances to the diameters of those particles whose fracture or separation from the matrix material dominates the geometry of separation. A spall criterion is derived for high velocity impact which appears fairly insensitive to the fine details of separation on the microscale.

Introduction

Spall under uniaxial strain conditions and cratering due to impact of a particle or water drop on a half-space are among the most elementary of the complex problems of high velocity deformation of ductile solids. Yet realistic analytic solutions are not feasible, and even a truncated solution by computer is extremely time-consuming, and expensive with the simplest of assumed material behavior. Experimental studies also are difficult, time-consuming, and expensive.

It may well be that such problems are so complex that sufficient understanding to permit rational prediction and design can be achieved only through the most comprehensive set of computer solutions and experimental studies. Certainly, preliminary tests and as full a

computation as possible are desirable before going to the great expense of fabricating an elaborate new structure with a new material. However, the hope in all difficult problems is that a highly simplified approach containing the essence of the response will provide fundamental insight and incisive understanding of the controlling parameters. With a coherent set of principles as a guide, it is possible to move on to the far more complicated problems of practical importance, to guide the experimental work that will be needed, to be sure that computer solutions give meaningful results, and most important of all to choose appropriate materials and configurations for preliminary design purposes.

It is the purpose of this paper to present one such highly approximate approach for spall and another for cratering as illustrative examples. Space limitations do not permit more than an outline of the calculations but the reader should have no difficulty filling in the omitted steps and improving upon the crude approximations suggested.

The Simplified View of Spall

The problem of spall under conditions of uniaxial strain (plate impact or explosive tests) involves a wide variety of material and mechanics parameters. When cleavage is ruled out, the process of fracture is ductile on the microscale and involves complex details of hole growth and coalescence as described by McClintock. A simple, highly approximate, approach is suggested here based on geometry, plastic limit load, and elementary plane wave propagation pictures.

Fracture is considered to start from holes generated by the fracture of the larger inclusions (diameter d) or their separation from the matrix at the high tensile stress levels imposed. A very thin layer of thickness h, Figure 1, above and below a wavy surface joining holes or cracks lying in the vicinity of a single plane is supposed to deform plastically in tension. Spall follows the reduction of the net load-carrying area to zero.

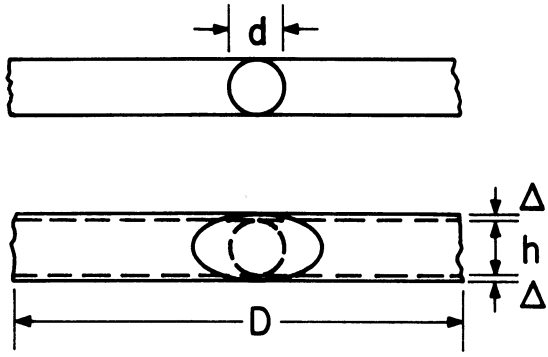

Figure 1. Layer Extending Plastically

The average triaxial stress state, σ_f, $\sigma_f - \sigma_o$, $\sigma_f - \sigma_o$ shown in Figure 2, at which this plastic deformation begins is given closely enough by an upper and lower bound plastic limit analysis of the geometric configuration of holes of spacing D.

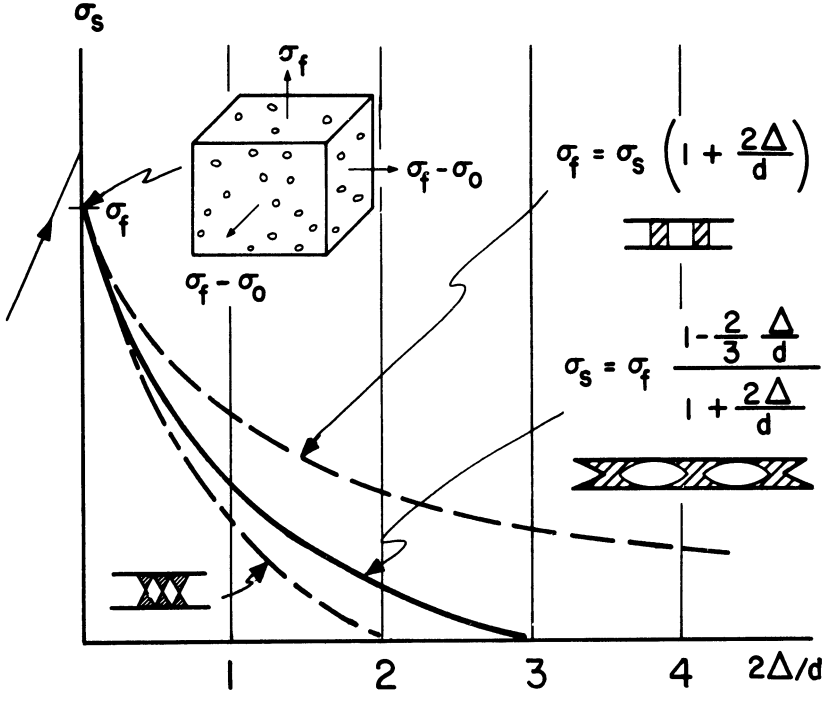

Figure 2. Average stress σ_s on surface of separation

Lateral spread of the holes is very rapid because volume remains constant during plastic deformation at limit load. All of the relatively large volume increase $(2\Delta)D^2$ represented by the small separation 2Δ of order d goes into increasing the volume of the hole. The rapid drop in the average stress σ_s from the initial limit value σ_f to zero, Figure 2, reflects the combination of the large reduction in load-carrying area and the decreasing lateral constraint as the holes coalesce. When Δ is a small multiple of d, $\Delta = \Delta^* = md/2$ with $m \cong 3$, separation is essentially complete and σ_s is close to zero. If the loading were static, the process would be highly unstable. Complete separation would follow immediately upon reaching the limit stress σ_f. Under dynamic loading, however, the stress level must be maintained for some time for incipient spall to be observable metallographically and for a longer time to actually result in a spall. This is quite apart from a rate effect which exists but is ignored at this level of approximation.

Wave transmission across the surface of incipient separation is affected by the continuously changing thickness and properties in the zone which is pulling apart. All of this complexity is condensed here to the stress-separation curve of Figure 2 and the assumption of a single plane of separation instead of a zone.

An upper bound on the limit stress σ_f can be obtained in terms of D/d from the layer picture of Figure 1 and a modification of the radial velocity field suitable for a circular cylinder of diameter D.

With h = d in Figure 1, $\sigma_f \leq \frac{4\sigma_o}{3}\left(\ell n \frac{D}{d} + \frac{D}{3d} + \frac{1}{4}\right)$.

A lower bound is given by the spherical hole solution $\sigma_f \geq 2\sigma_o \ell n D/d$

For a ratio of interparticle spacing to diameter of particle D/d=5, a reasonable estimate for the limit stress σ_f is $4\sigma_o$ where σ_o is a large offset yield strength (say σ at 0.01 strain). A value of $7\sigma_o$ seems appropriate for a rather clean material, D/d = 10, with few micron size inclusions.

Ignoring the very appreciable loss of lateral constraint, the stress on the surface of separation is given by:

$$\sigma_s = \sigma_f \frac{1 - \frac{1}{m}\frac{2\Delta}{d}}{1 + \frac{2\Delta}{d}} \qquad (1)$$

The guess, or recommendation, indicated in Figure 2 is to choose $m = 3$.

The drop in tensile stress from the incident tensile stress σ to the carrying capacity σ_s is equivalent to adding a compressive pulse $\sigma - \sigma_s$ at the surface of incipient separation. Each side of this interface then moves outward with respect to the mean velocity of the two surfaces at a relative velocity $\delta v = \frac{\sigma - \sigma_s}{\rho c}$, a direct carryover of the form $\sigma = \rho c v$ for an incident pulse.

The velocity of separation then is $2\delta v \equiv 2\frac{d\Delta}{dt} = 2\frac{(\sigma - \sigma_s)}{\rho c}$ with the stress σ_s a function of Δ in accord with Figure 2. This form for the relative velocity does not depend upon the shape of the incident tensile wave. It is determined solely by the instantaneous compression $\sigma - \sigma_s$ which must be added to the tensile stress σ to give σ_s on the surface of separation. As long as $\sigma > \sigma_s$ for the current value of Δ, σ may be any function of time.

The wave shape does affect the time available for separation because the subsequent reflections from the free surface can terminate the process before the time of passage of the wave; $T = L/c$ for the square wave of Figure 3. Therefore, the picture labelled as a limiting case in Figure 3 does require some modification for other pulse shapes. In general, the maximum tension and the associated plane of separation will not be located at L/2 from the free surface, nor will the time available for separation be L/c. However, the major separation activity occurs during the incidence of the higher stress levels and is not greatly affected by low stresses present in the rise and drop-off of the incident wave.

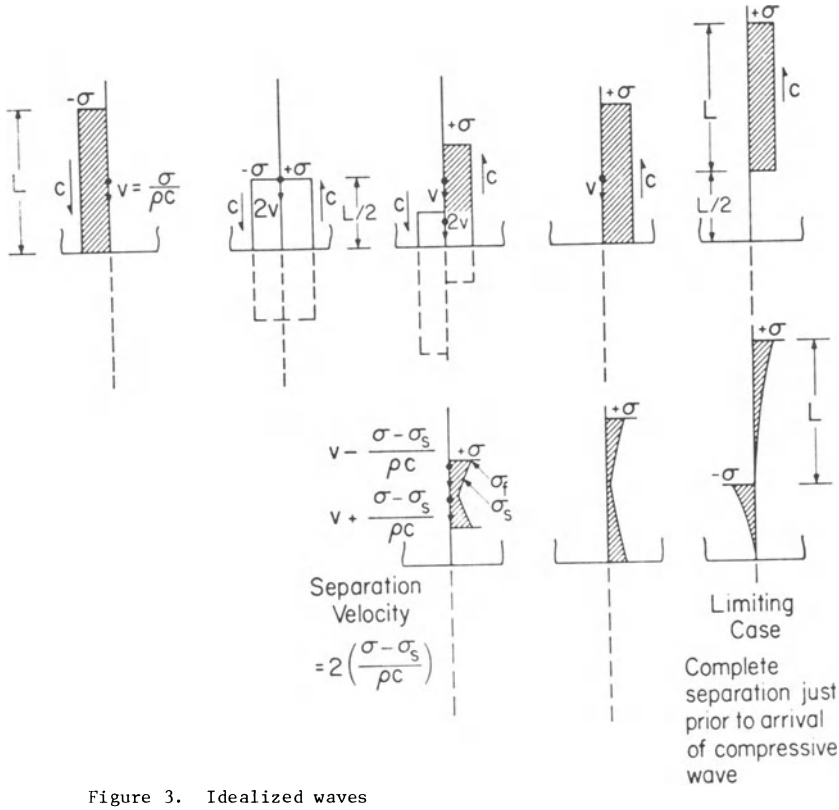

Figure 3. Idealized waves
Square entering pulse, single plane of separation for lower set of pictures, no separation or attenuation in upper set

A Spall Criterion

The criterion for spall which results from all of these idealizations and crude simplifications is just that the stress σ (a function of time) be high enough and applied for a long enough time to enable a critical separation $2\Delta^*$ of about 3d to be reached or exceeded.

Numerical solution and integration of $\frac{d\Delta}{dt} = \frac{\sigma - \sigma_s}{\rho c}$ as an equation in Δ (or σ_s) will determine whether or not Δ^* is exceeded. Formally, with T = L/c for a square pulse, separation occurs when

$$\rho c \Delta = \int_0^T (\sigma - \sigma_s) dt \geq \rho c m d/2 \cong \frac{3}{2} \rho c d \qquad (2)$$

The Simplified View of Cratering

The formation of a crater by the high velocity normal impact of a water drop or other particle on the flat surface of a semi-infinite target is, in one sense, on the opposite end of the spectrum from spall. Spall is governed by the behavior of the material in tension under the great lateral constraint of overall or average uniaxial strain, while cratering depends upon the response of the material to compression with far less lateral constraint in bulk and the presence of a free surface. However, both involve the enormous uncertainties of propagation of very high intensity stress waves through very disturbed regions of material. Both need a simple approximate means of solution to serve as a guide to the development of clear and appropriate basic premises or assessment of the usefulness and validity of any time or space truncated analytical or computer solutions presented for consideration.

There is a long history of attempts to provide this understanding for penetration and cratering under hypervelocity impact conditions with a wide variety of target and projectile materials. Interesting approximations have been suggested by many able and distinguished investigators. These range from the analysis by Birkoff, MacDougall, Pugh, and Taylor of the penetration P of a jet based on a simple hydrodynamic model $P = \ell_j \sqrt{\rho_j/\rho_t}$ where ℓ_j and ρ_j are the length and mass density of the jet and ρ_t the mass density of the target, to the plastic punching-out model of Goodier for particle impact with speed v_p which equates work to create the crater to the kinetic energy of the particle

$$\text{Crater volume} = \tfrac{1}{2}\rho_p v_p^2 \ (\text{particle volume})/\sigma_t \qquad (3)$$

σ_t, the punching-out stress given by Hill, is $\frac{2}{3}\sigma_y \left(1 + \ell n \frac{2E}{3\sigma_y}\right) + \frac{2\pi^2}{27} E_{tan}$ where σ_y is the initial yield strength of the target E its Young's modulus and E_{tan} its tangent modulus in the plastic range.

The essential concept proposed here is a simple modification of Goodier's approach; the volume of the crater is determined not by

the kinetic energy of the impacting particle but by the considerably smaller kinetic energy contained or trapped in that region of the target which then displaces to form the crater.

The lower the impact speed v_p for a given diameter d of water drop or any particle behaving as a "soft" impactor, the longer the time of impact and the larger the diameter of the target region in which there are outward radiating waves. Consequently, as is intuitively obvious and can be made reasonably quantitative, at the low end of the range of high velocity impact the kinetic energy available is a very small fraction of the energy of the incoming particle. Although momentum is conserved, energy transfer is inefficient because the particle has relatively small mass compared to the much larger mass of the region of the target that is in outward motion at the time the impact is essentially over. Furthermore, at the beginning of this range and below it, much of the kinetic energy that is deposited in the target lies outside the region of crater formation and simply continues to radiate out from the region of impact with acoustic speed c_t. On the contrary, at hypervelocity impact, v_p above c_t, the energy transfer is much more efficient for all particles and most of the kinetic energy deposited is available for crater formation. Vaporization of material and the complexity of flow at the rim of the expanding crater at the free surface will be ignored.

The well-understood situation for one-dimensional plane strain or plane stress impact serves as a reminder that over the high velocity range of interest, there is little need to distinguish between the impact of a liquid and a solid particle. The contact stress is of magnitude $\rho_p(v_p - u_i)^2$ or $\rho_p v_p c_p$ or $\rho_p c_t$ where subscript p refers to the particle, t to the target, u_i is the speed of the target material at the surface of impact and c is the speed of acoustic or shock waves. Impact stresses therefore are about $E\left(\frac{v_p}{c}\right)^2$ or $E\left(\frac{v_p}{c}\right)$ and become enormous compared to particle strength once v_p exceeds ¼ the speed of sound in the particle.

An Elementary Analysis of Cratering

Enormous impact stresses are far less troublesome conceptually for a ductile half-space target, Fig. 4, than for the impacting particle. Although comparable to the binding atomic forces and orders of magnitude above conventional yield stresses, the needed lateral constraint can be mobilized. The region immediately below the impactor goes into a state close to three-dimensional hydrostatic compression. It is not too unreasonable therefore for the purpose of estimating kinetic energy transfer to the target to replace the actual situation which is so much more complex with a uniform pressure pulse on a hemispherical surface of radius $r_i = d/2$ during a time interval somewhat less than the time of impact $t_i \cong d/(v_p - u_i)$

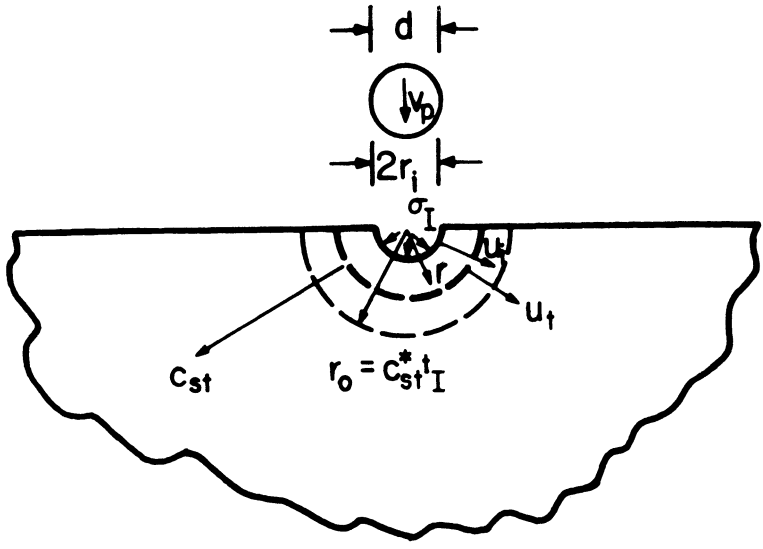

Figure 4. Impact of Spherical Particle (with modified half-space target)

The spherical waves shown radiating out to a hemispherical surface at a distance

$$c^*_{st} t_I \cong \frac{c^*_{st} d}{v_p - u_i} \cong r_o \tag{4}$$

are another crude approximation because the large vertical displacements of the free surface of the target disturb the radial symmetry appreciably and the average shock wave speed c^*_{st} is between the initial shock speed $c_{st} = c_t + k_t u_i$, with k_t about 1.5 or 2.0, and the acoustic speed c_t.

Nevertheless, fair estimates of the total kinetic energy in the target should be obtained with the spherical wave picture until the impact speed is so high (say $v_p/c_t > 3$) that the dominant motion is more a jet-like forward tunneling action of the particle.

If the modified target were to behave as an incompressible fluid, a steady radial outward velocity u_i at the hemisphere radius r_i would give rise to a radial velocity $u_t = u_i (r_i^2/r^2)$ at each larger radius r. Were the appreciable compressibility of the target material to be taken into account there would be still more rapid attenuation with r of the high values of u_t.

With these many oversimplifications, R_{KE} the kinetic energy transfer ratio from particle to target can be calculated to be $2r_i/r_o = d/r_o$ multiplied by the value u_i/v_p for one-dimensional impact or

$$R_{KE} = \frac{2r_i}{r_o} \frac{u_i}{v_p} = \frac{v_p - u_i}{c^*_{st}} \frac{u_i}{v_p} = \frac{v_p}{c_t} \frac{1 - u_i/v_p}{c^*_{st}/c_t} \frac{u_i}{v_p} \tag{5}$$

with $1 \leq c^*_{st}/c_t \leq 1 + k_t(u_i/v_p)(v_p/c_t)$

As for one-dimensional impact it is approximately true that the contact stress $\sigma_I = \rho_t c_{st} u_i = \rho_t (c_t + k_t u_i) u_i = \rho_p (v_p - u_i)^2$ so that

$$\frac{u_i}{v_p} \left[\frac{\rho_t}{\rho_p} \frac{c_t}{v_p} + 2 \right] = 1 - \left[\frac{\rho_t}{\rho_p} k_t - 1 \right] \left(\frac{u_i}{v_p} \right)^2 \tag{6}$$

This quadratic equation can be solved explicity for u_i/v_p but the approximate result

$$\frac{u_i}{v_p} = \frac{1}{\frac{\rho_t}{\rho_p}\frac{c_t}{v_p} + 1 + \sqrt{k_t \frac{\rho_p}{\rho_t}}} \tag{7}$$

is more informative.

At low speeds of impact $v_p << c_t$, $u_i/v_p = \rho_p v_p/\rho_t c_t$; R_{KE} is $\frac{\rho_p}{\rho_t}\left(\frac{v_p}{c_t}\right)^2$; and the total kinetic energy transferred, R_{KE} $(\frac{1}{2}\rho_p v_p^2)$, varies as v_p^4. In hypervelocity impact, R_{KE} is close to u_i/v_p which in turn, as v_p increases, approaches $1/(1 + \sqrt{k_t \rho_t/\rho_p})$ or about 1/3 for a water drop on aluminum or a glass sphere on steel. At $v_p = c_t$ R_{KE} is somewhat more than 1/10.

If all the kinetic energy in the target were converted to the punching-out of a spherical cavity, the crater volume would be given by Goodier's form (3) multiplied by the kinetic energy transfer ratio

$$\frac{\text{Crater volume}}{\text{Particle volume}} = (\tfrac{1}{2}\rho_p v_p^2) R_{KE}/\sigma_t \tag{8}$$

where σ_t is the applied pressure needed to create a cavity or crater.

The static pressure needed at the free surface of a half-space, Fig. 5, of perfectly plastic (non strain-hardening) material of yield strength σ_o is almost $3\sigma_o$. The pressure needed to continue the deformation is larger still.

The proposal here is to compromise crudely between the punching-out and the free surface value and to take $\sigma_t = 4\sigma_o$ where σ_o is the yield or flow strength at strains of order unity at the high rates of strain associated with the crater formation which occurs mainly after the major portion of the impulse is over.

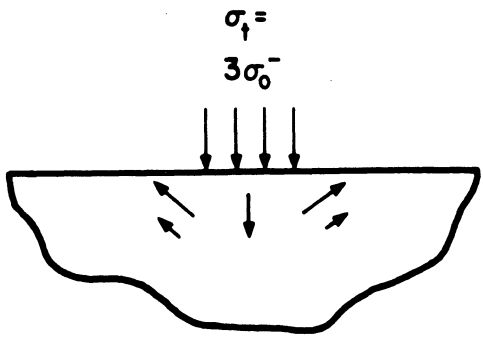

Limit Pressure on A Half Space

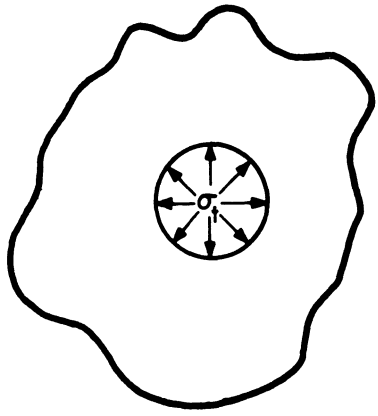

Punching-out Pressure For A Spherical Cavity

Figure 5. Limit Stress σ_t

The result (8) can be rewritten as

$$\frac{\text{crater volume}}{\text{particle volume}} = \left(\frac{E}{8\sigma_o}\right)\left(\frac{\rho_p v_p^2}{\rho_t c_t^2}\right)\left(\frac{u_i}{v_p}\right)\frac{v_p}{c_t}$$

$$\times \frac{1 - u_i/v_p}{1 + k_t\,(u_i/v_p)(v_p/c_t)} \qquad (9)$$

with a further approximation for R_{KE} (5) and use of $E = \rho_t c_t^2$. This form (9) when coupled with (7) does predict the v_p^4 variation reported for erosion at low to moderate speeds of impact, gives the v_p^2 variation at the highest speeds and provides a smooth tran-

sition over the entire range. In the neighborhood of $v_p/c_t = 1$, the transition from a v_p^4 to a v_p^2 variation will be close to v_p^3 which also is sometimes reported for erosion.

An interesting but far from accurate result given by (9) and (7) for the impact of a water drop on a structural aluminum target is that the volume of the crater is about equal to the volume of the drop at $v_p/c_t = 1$

Acknowledgement

This research was supported in part by the Advanced Research Projects Agency of the Department of Defense under Contract No. DAHC15-71-C-0253 with The University of Michigan. Helpful discussions with J. J. Gilman, B. Budiansky, E. H. Lee, F. A. McClintock, and J. R. Rice are gratefully acknowledged along with their disclaimers for the crude assumptions made here.

References

1 G. Birkhoff, D. P. MacDougall, E. M. Pugh, and G. I. Taylor, "Explosives with Lined Cavities," J. Appl. Phys. 19, 563 (June 1948).

2 D. R. Curran, L. Seaman, and D. A. Shockey, "Dynamic Failure in Solids," Physics Today, Jan. 1977, pp. 46-55.

3 J. N. Goodier, "On the Mechanics of Indentation and Cratering in Solid Targets of Strain-Hardening Metal by Impact of Hard and Soft Spheres," in vol. III-Theory, Proceedings of the Seventh Hypervelocity Impact Symposium (Nov. 1964), Feb. 1965, pp. 215-259.

4 R. J. Eichelberger and J. W. Gehring, "Effects of Meteoroid Impacts on Space Vehicles," J. Amer. Rocket Soc. 32, 1583 (Oct. 1962).

5 J. B. Feldman, Jr., "Volume-Energy Relation from Shaped Charge Jet Penetrations," Proc. 4th Symposium on Hypervelocity Impact, Vol. 2, 1960.

6 F. J. Heymann, "On the Shock Wave Velocity and Impact Pressure in High-Speed Liquid-Solid Impact," Trans. ASME 90, J. Basic Engineering, 400 (September 1968).

7 G. R. Johnson, "High Velocity Impact Calculation in Three Dimensions," Journal of Applied Mechanics, March 1977, Trans. ASME

vol. 99, Series E, pp. 95-100.

8 Roy Kinslow, Ed., "High Velocity Impact Phenomena," Academic Press, N.Y., 1970 includes:

J. K. Dienes and J. M. Walsh, "Theory of Impact: Some General Principles and the Method of Eulerian Codes," pp. 45-104.

R. G. McQueen, S. P. Marsh, J. W. Taylor, J. N. Fritz, and W. J. Carter, "The Equation of State of Solids from Shock Wave Studies," pp. 293-417.

J. W. Gehring, Jr., "Engineering Considerations in Hypervelocity Impact," pp. 463-514.

9 See also, "Applied Mechanics Surveys," Ed. H. N. Abramson, H. A. Liebowitz, J. M. Crowley, and S. Juhasz, Spartan Books, Washington, D. C. 1966. Articles by

W. Goldsmith, "Impact: The Collision of Solids," pp. 785-802.

H. G. Hopkins, "Dynamic Non-Elastic Deformation of Metals," pp. 847-867.

Fracture and Void Development in Hemi-Spherical Ended Perspex Rods Due to Stress Waves from Detonators

W. JOHNSON AND A.G. MAMALIS

Engineering Department
University of Cambridge
Cambridge, England

Summary

The paper mainly present results pertaining to fracture and void development in hemi-spherical ended rods of Perspex due to stress waves initiated by explosively loading one end of a rod with a detonator. The order in time, at which cracks or voids occur is examined using high speed photography; the crack and void locations are discussed in terms of stress optics. The different natures of the damaged zones created are illustrated and an explanation of resulting terminal fracture patterns is attempted. Previous related work on spheres is referred to.

Introduction

The phenomenon of the distal end spalling of long rods of fairly brittle material when subjected to an impulsive load at the other end is well known and has long been studied, see for instance the references and examples in Ref. (1). The results of subjecting spheres (typically of Perspex and plaster of Paris) to point explosive loads are less well known and have only relatively recently been published, see Refs. (2) to (6). Also, the examination of deformation and fracture in spheres, for comparative and other purposes, of ductile as well as brittle materials in quasi-static diametral compression is discussed in Refs. (7) and (8). Examinations of metal and acrylic thick spherical shells under impact load are described in Refs.

(9) and (10), and reference to work on fracture in explosively loaded bars containing transverse bores when end-shock loaded is given in Ref. (11).

The occurrence of spalls and fractures in rods due to shock loading is of obvious engineering importance in so far as bars and the like (e.g. thick plates which suffer scabbing[1]) are conventional constructional shapes for many engineering structures. The study of the break-up of spheres under impulsive attack is useful for appreciating shot behaviour in peening, ricochet, comminution and projectile fragmentation generally.

In the present work we have in a sense brought together the sphere and the long cylindrical rod and studied fracture at the distal-end due to near-end loading by a detonator, when the far end of the rod has a solid hemi-spherical (as opposed to a flat) termination. The interest of this kind of long bar for mechanical design is obvious.

Essentially the experimental set-up used is shown in Fig. 1; an exploded detonator generates a predominantly plane compressive pulse (designated the P-wave) of considerable intensity which approaches the end hemi-spherical free surface and is there reflected. It is considered that two reflected waves are generated; one is another P-wave and the other an S-wave. Both the latter reflected pulses are focussed or concentrated on the rod axis, each causing its own separate caustic curve or envelope and resulting in a well defined focus and fracture regions. In Fig. 2(a) we show a set of three calculated caustics and foci from Ref. (3) and in Fig. 3, the result of exploding a detonator (at A) on a Perspex sphere, which somewhat verifies them. (In Fig. 2(b), 0 is the centre of the sphere and x_1 x_2 are the distances from 0 of the foci on a polar diameter.)

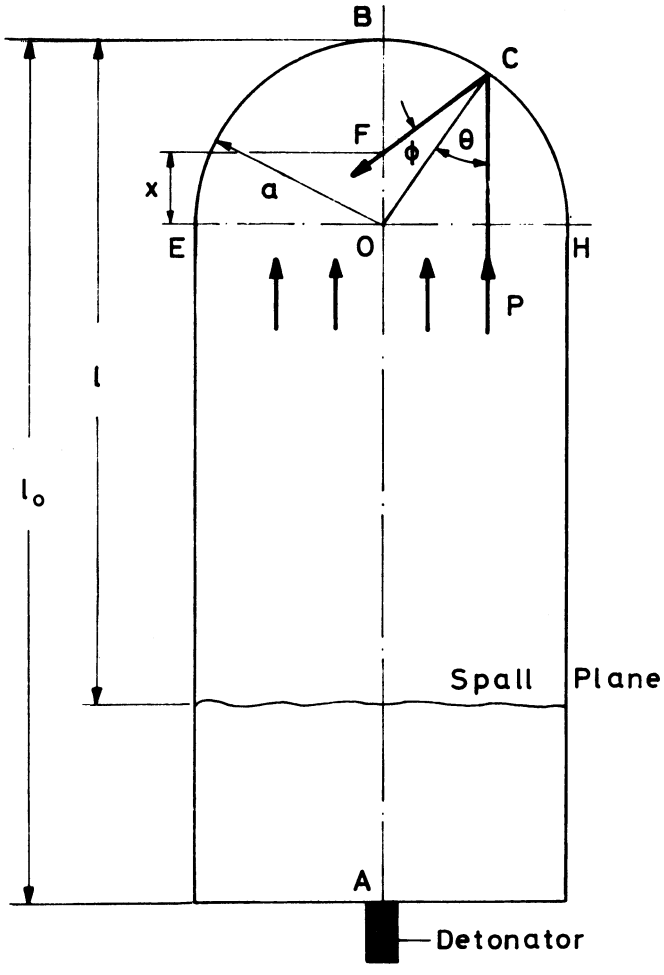

Fig. 1 A diametral cross-section of a solid Perspex hemispherical ended rod showing the detonator positioning and the reflection of a ray.

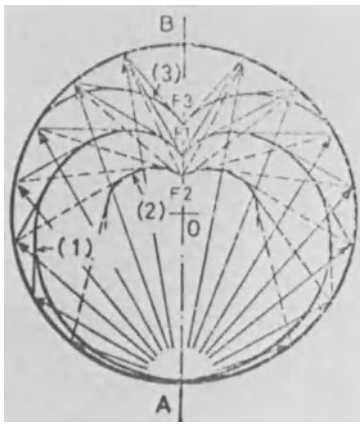

Caustics : (1) $C_P^{(P)} = C_S^{(S)}$

(2) $C_S^{(P)}$

(3) $C_P^{(S)}$

(a)

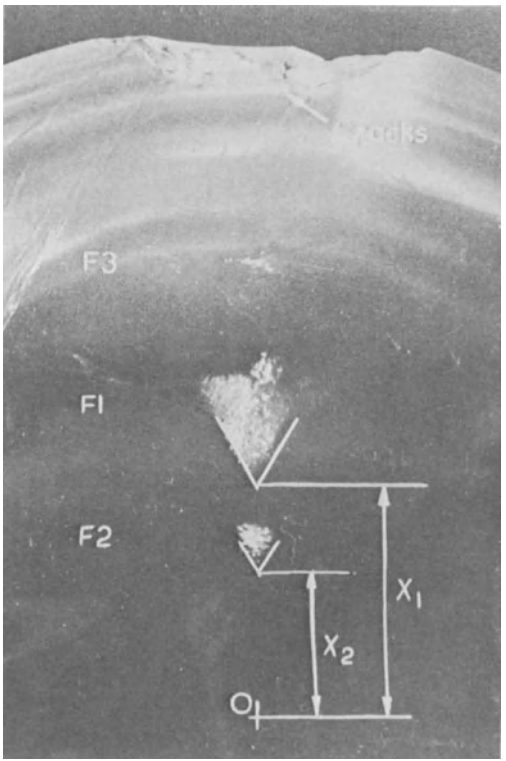

(b)

Fig. 2

A diametral cross-section of a solid Perspex sphere showing:

(a) The wave fronts (caustics) development.

(b) The shape and location of internal fractures.

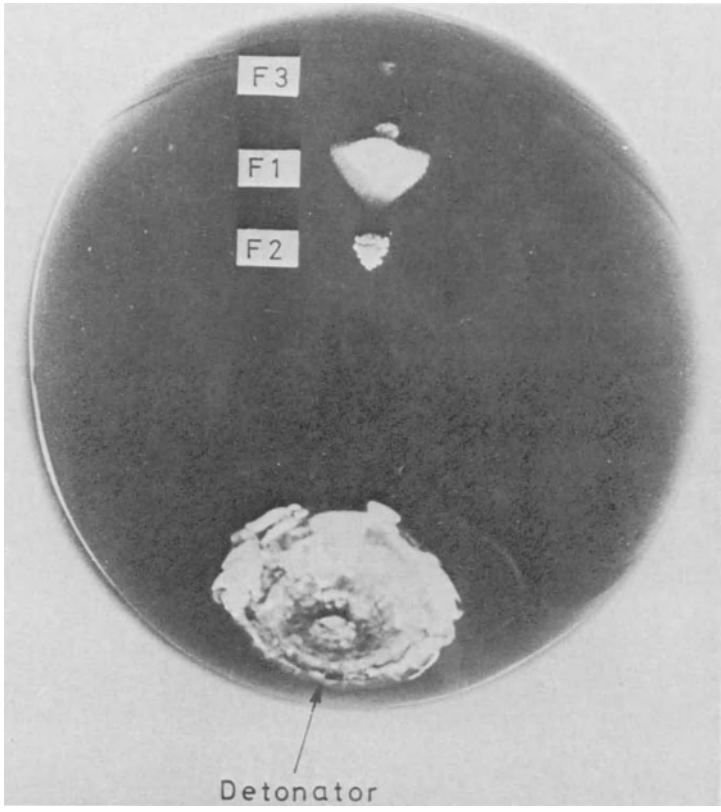

Fig. 3 An outside view showing the shape and locations of fractures in a solid Perspex sphere

Experimental Work

The circular section rods used as test specimens had wholly or plane-truncated hemi-spherical ends or plane ends. They were machined from Perspex acrylic stock the properties of which are described in Ref. (11). The dilatational speed for this material is C_d = 2010 m/sec and the transverse wave speed C_T = 965 m/sec. The rod diameters were 25.4 mm and their length, l_o, varied from 51 to 102 mm. A few Perspex specimens of diameter 19 mm were also investigated.

The impulsive loading was obtained by exploding I.C.I. No. 6 electrical detonators bonded to the flat end of each rod and placed on its axis of symmetry, see Fig. 1.

For purposes of comparison a few Perspex and plaster of Paris specimens (d = 25.4 mm and l_o = 37.5 mm) with hemispherical and truncated ends were statically compressed (without lubrication) through diametrically opposed rigid, smooth, parallel platens in an universal testing machine. The various fragments of the tested specimens were collected carefully and recombined; the terminal fracture results of these tests are shown in Fig. 4.

To photograph the evolution of the various internal fractures high-speed photography was employed; the set-up for photographic recording - at about 400,000 frames/sec - is similar to that described in Ref. (3).

To obtain information about the shape, actual size and location of the internal fractures, the rods, after detonation, were very carefully sliced along two planes parallel to a diametral one through the rod axis. These slices (about 4 mm thick) were polished carefully and then using a microscope the fractures were enlarged and photographed, see Figs. 5 and 6.

Fracture Location

In Fig. 1, a plane wave (supposedly due to a detonation at pole A) is considered to travel along the axis to the circular section rod and is shown incident on the distal hemi-spherical end; ray PC, is incident on the spherical surface at C with angle of incidence θ and angle of reflection ϕ. The reflected ray, CF, intersects the axis of the rod through AB at F and for various positions of C, CF defines an envelope. For an homogeneous elastic sphere, $\sin\theta/\sin\phi = 1$ if the rays PC and CF refer to incident and reflected dilatational waves, P-P (or incident and

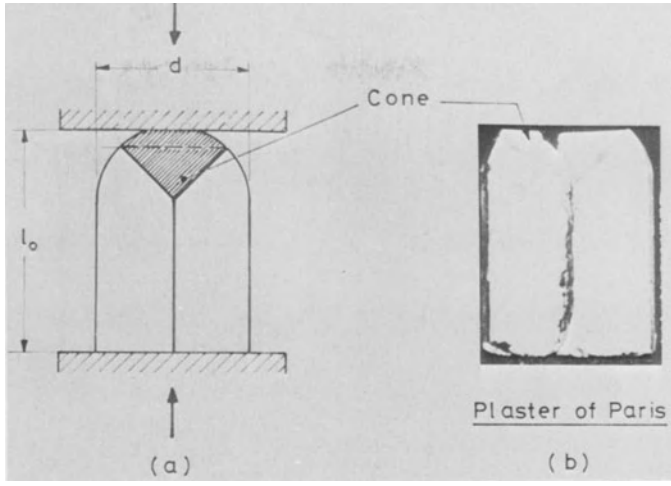

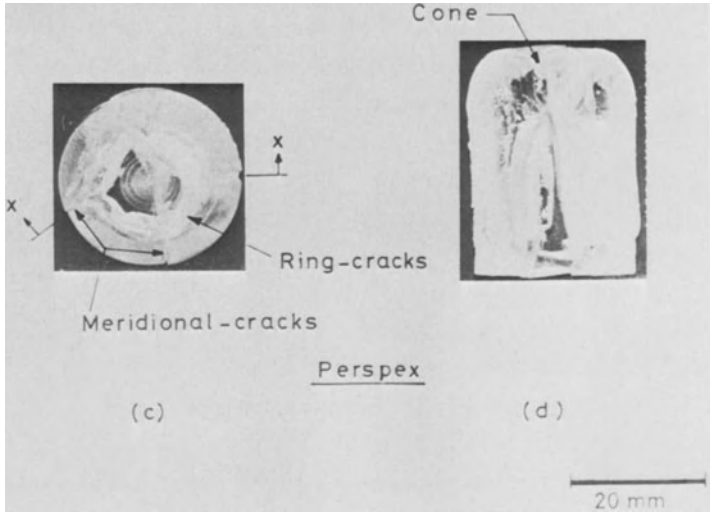

Fig. 4 Terminal fracture patterns in hemi-spherical truncated ended rods statically compressed.
(a) A schematic diagram showing the position of the applied load and the fracture pattern in section.
(b) Inside view for a plaster of Paris specimen.
(c) Outside top view and (d) inside (x-x) view for a Perspex specimen.

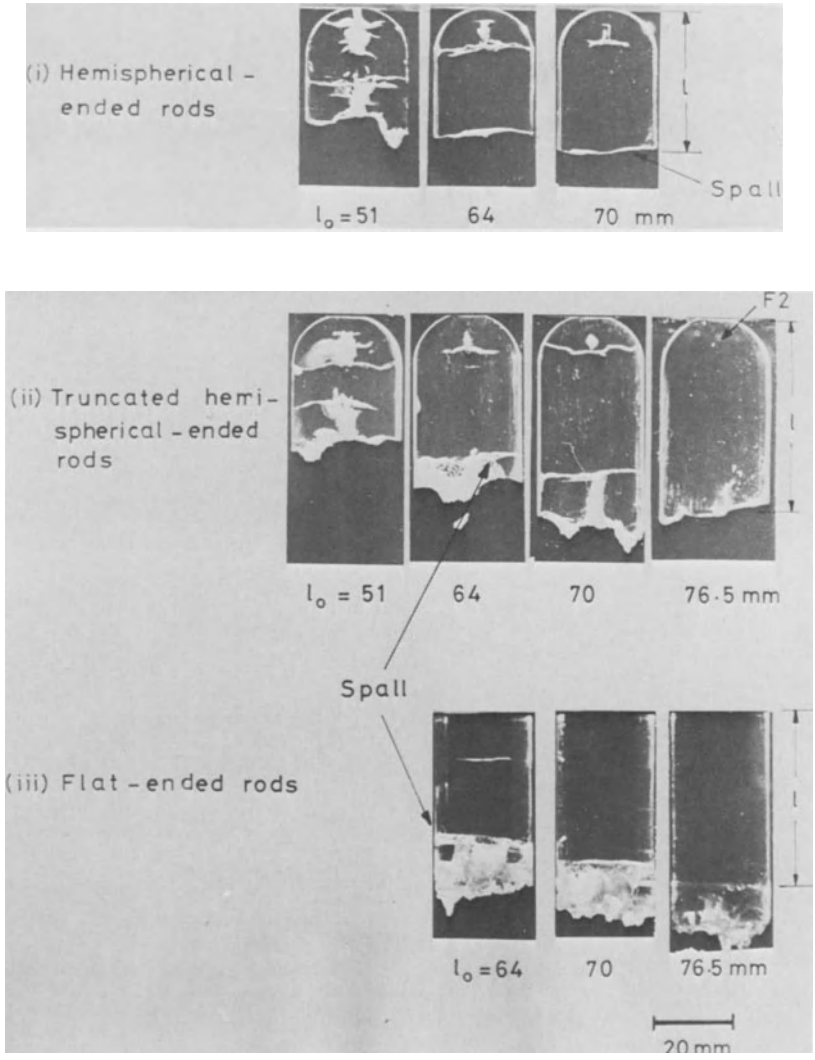

Fig. 5 Terminal fracture patterns in Perspex hemi-spherical, truncated and flat-ended rods of an initial diameter 25.4mm and various initial lengths; sliced specimens 4mm thick.

F 1 (x 80)

(a)

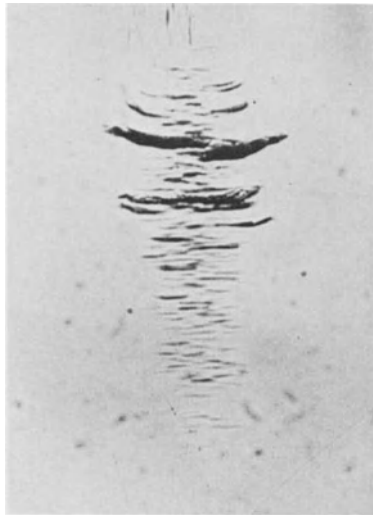

F 2 (x 80)

(b)

F 2 (x 80)

(c)

Fig. 6

Enlargement of fracture (diametral cross-section).
(a) and (b) Hemi-spherical ended rod (d=25.4 mm, ℓ_o=75mm).
(c) Hemi-spherical truncated ended rod (d=25.4mm, ℓ_o=74mm), after explosive loading.

reflected shear waves, S-S). If PC is an incident dilatational ray (P) and CF a reflected shear ray (S) and together denoted by P-S, (i.e. there is mode - conversion at C) then $\sin\theta/\sin\phi = C_d/C_T = n$, say. (For the combination S-P we would have $\sin\theta/\sin\phi = C_T/C_d = 1/n$; θ and ϕ are also supposed not to attain certain critical angles)[4].

The reflected rays thus give the caustic curves whose cusps or foci lie on centre-line AB, compare Fig. 2(a), and their position is easily found; each is associated with the limit when C approaches B. We have, see Fig. 1,

$$x\theta \simeq (a - x)\,\phi \quad \text{or} \quad x/a \simeq 1/(1 + \theta/\phi). \qquad (1)$$

When $\theta=\phi$, (P-P and S-S combinations), $x/a = 0.5$ and thus a first fracture F1 is expected at 0.5a below the anti-pole, B.

For $\theta/\phi = n$, a P-S combination,

$$x/a \simeq 1/(1 + n) = 0.32, \text{ for Perspex.} \qquad (2)$$

A fracture, F2, is thus expected at 0.68a below the anti-pole. If there was an S-P combination,

$$\theta/\phi = 1/n \text{ and } x/a = n/(n + 1) \simeq 0.67, \text{ for Perspex.} \qquad (3)$$

Results

1. Number of Fractures

Only two fractures i.e. F1 and F2 were found, unlike the case of the sphere. This is probably to be expected in view of the predominantly compressive nature of the fracture initiating pulse, P.

2. Fracture Detection

In the case shown as Fig. 7(e), an F2 fracture was detected, but no F1; but both fractures are found to occur

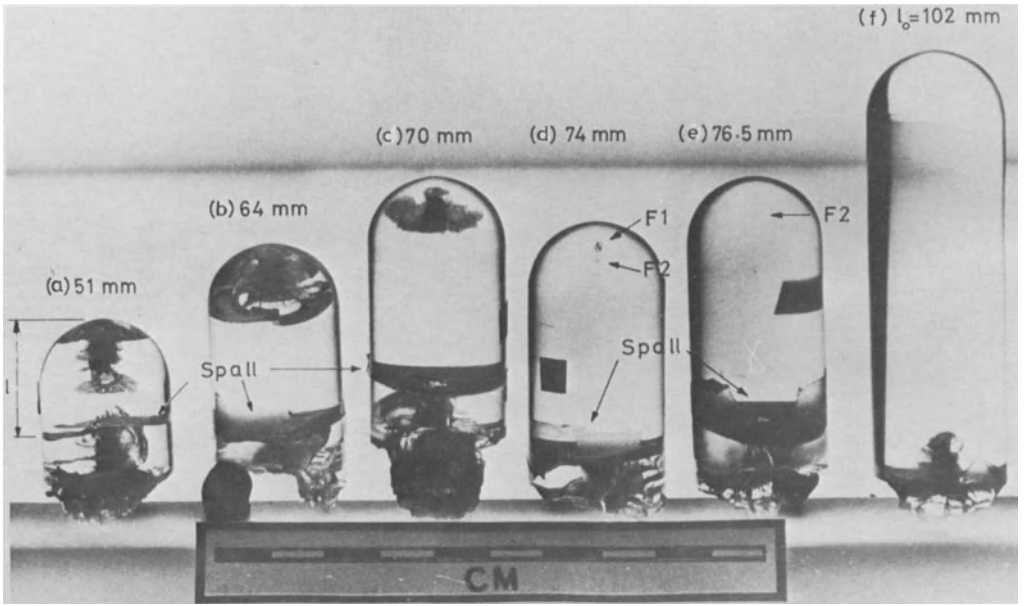

Fig. 7 Terminal fracture patterns in Perspex hemi-spherical ended rods of an initial diameter 25.4mm and various initial lengths, (outside view), after explosive loading.

for the next shorter rod, (d). We suppose the reason for this is that an S-type mode of particle movement more easily generates visible damage than does a P-type, for this material with this geometry*.

3. Fracture Location

In the Table 1 the calculated (or theoretical) locations for the cusps of fractures (and voids), i.e. as from (1) and (2) above, are compared with the values measured using a travelling microscope; the lowest point on the axis is assumed to be the focus or identifying point for F1 and F2. Refer to the enlarged views of the F1 and F2 regions in Fig. 6. The former overestimates the latter; this is as might be expected since the pulse is not plane, but slightly spherical. (For point shock-loading with a sphere, $x/a = 1/3$.)

4. Times to Fracture Initiation

The high-speed photographs of Figs. 8 and 9 show F1 appearing after about 35 μsec. (The times marked in the photographs were calculated from assuming the camera framing speed to be 400,000 frames/sec, filming being initiated by the detonation.) The time for a P-pulse to travel from the detonator to the opposite end the thence to F1 would be expected to be $(\ell_o + a/2)/C_d = (74 + 6.3)/2010 \times 10^3$ sec = 40 μsec. The discrepancy is probably due to lack of precision in the knowledge of the framing speed.

The fracture F2, appears about 12 μsec after it; this seems excessive if we consider it to be solely an effect due to the P-wave reflection as (in part) an S-wave.

---

* Kolsky, in Ref. (12) observes that, "As far as is known the reflected shear wave does not, in general, influence fracture phenomena in brittle solids".

Table 1

	ℓ_o (mm)	F2 (Perspex)			F1 (Perspex)			Spall	
		x/a		Vertical Length of Fracture (mm)	x/a		Vertical Length of Fracture (mm)	$(\ell_o - \ell)$ (mm)	
		Measured	Calculated		Measured	Calculated		Perspex	Plaster of Paris
Hemi-spherical ended rods	102							-	-
	76.5	0.29	0.32	1.23				32	36
	75	0.25		1.45	0.46	0.50	1.74	32	34
	74	0.22		1.63	0.45			33	36
	70							32	33
	64	0.21		1.84				32	36
	51							32	30
Truncated hemi-spherical ended rods	102							-	-
	76.5	0.30	0.32	1.32				32	36
	75							33	31
	74	0.28		1.49	0.50	0.50		33	33
	72	0.26		1.66	0.49			31	36
	70							32	35
	64	0.21						32	33
	51							32	34
Flat ended rods	102							-	
	76.5							34	
	75							33	
	74							33	
	72							32	
	70							33	
	64							32	
	51							33	

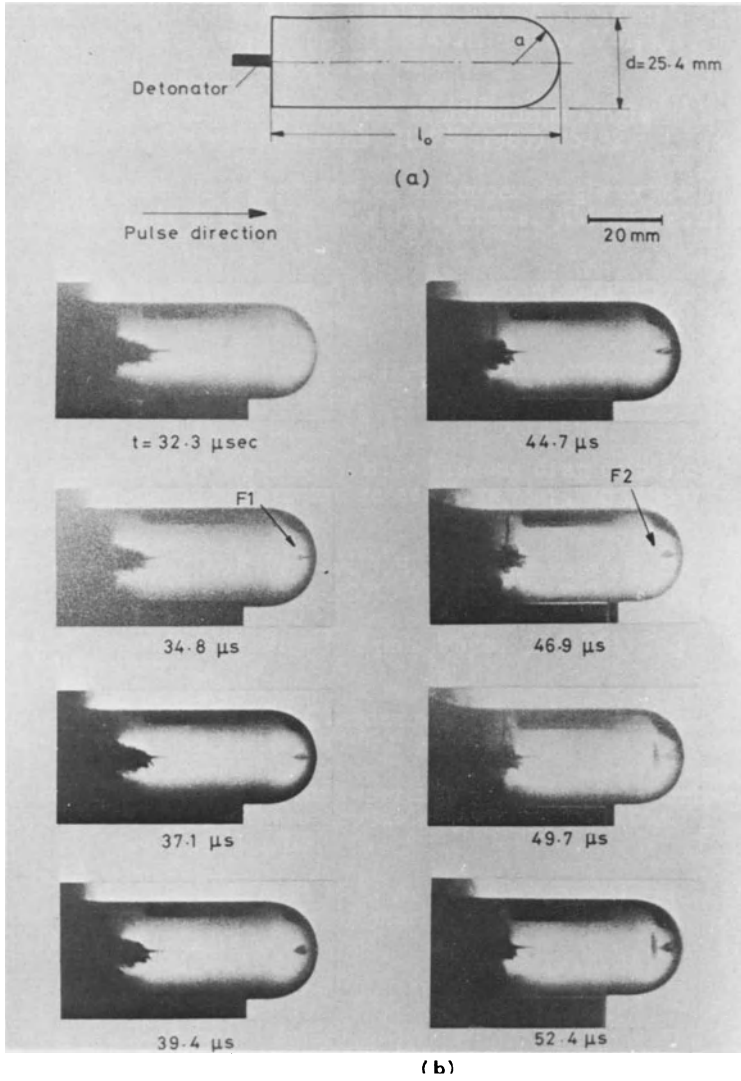

Fig. 8 Showing the development of internal fractures in a Perspex hemi-spherical ended rod of an initial diameter 25.4mm and an initial length 74mm, (speed 400,000 frames/sec).

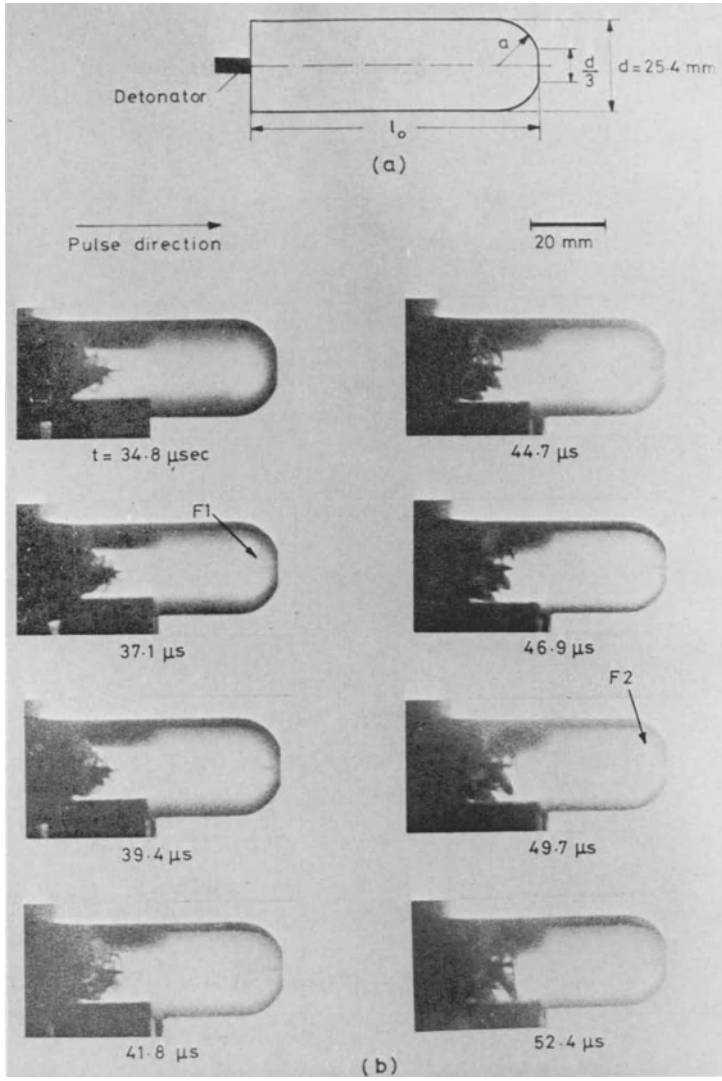

Fig. 9 Showing the development of internal fractures in a Perspex hemi-spherical truncated ended rod of an initial diameter 25.4mm and an initial length 74mm, (speed 400,000 frames/sec).

5. Results for Truncated Hemi-Spherical Ended Rods

The fracture and void formation in respect of location, times and physical appearance are substantially similar to those for the wholly hemi-spherical-ends; the foci positions are very slightly modified (as would be expected) and the F2 fracture planes appear to be more curved when we compare Figs. 8(b) and (c).

6. Fracture Plane Growth

The growth of F2, into a large crack transverse to the rod axis is very notable, compare Figs. 7(c), (d) and (e).

7. Fracture Form

In Fig. 6 enlarged views of the two fracture regions are shown. Their specific characters are similar to those found in an explosively loaded sphere with planes of fracture, or successions of small voids, variously orientated for F1 and relatively large parallel planes perpendicular to the axis for F2.

8. A Spall Plane at the Detonation End of the Rod

A conspicuous feature of the terminal fracture patterns, see Figs. 5 and 7, is the appearance of a transverse spall plane at a constant distance from the detonator where $(\ell_o - \ell)$ is about 2.5 to 3 time the radius of the rod.

9. Quasi-Static Compression of Round Ended Rods

The resulting terminal fracture patterns as shown in Fig. 4 have little or nothing in common with these explosively loaded rods. This was also found to apply in the case of solid Perspex spheres.

Conclusions

The fracture sites which occur at the distal round end of circular section rods whose length exceeds a few times their diameter, when end-loaded by a detonator, have similarities to those found for spheres. The stress wave initiated has a nearly plane front and this on reflection from the curved free surface causes two fractures - as opposed to three in the case of the sphere - at reasonably accurately calculable distances from the anti-pole. The time of emergence of the F1 fracture is reasonably predictable but the F2 fracture or void occurs later than expected. The physical damage caused at the F1 and F2 sites are similar to those found for the sphere.

Acknowledgement

The authors are indebted to the M.O.D. for supporting this work and Mr. H.J. James especially for his close interest and encouragement of it.

We are also grateful to Mr. D. Finch of the M.O.D. for his help in connection with the high-speed photography and to Mr. J.T. Holmes for the experimental assistance he has rendered and Miss L. Willis for typing our manuscript.

References

1. W. Johnson, Impact Strength of Materials, Ed. Arnold (1973).

2. E. Lovell, S.T.S. Al-Hassani and W. Johnson, Fracture in Solid Spheres and Circular Disks Due to a Point Explosive Impulse on the Surface, Int. J. Mech. Sci. 16, 193 (1974).

3. J.F. Silva-Gomes, S.T.S. Al-Hassani and W. Johnson, A Note on Times to Fracture in Solid Perspex Spheres Due to Point Explosive Loading, Int. J. Mech. Sci. 18, 543 (1976).

4. W. Johnson and A.G. Mamalis, Fracture Development in Solid Perspex Spheres with Short Cylindrical Projections (Bosses) Due to Point Explosive Loading, Int. J. Mech. Sci. 19, 309 (1977).

5. H. Rumpf and K. Schönert, Die Brucherscheinungen in Kugeln bei elastischen sowie plastischen Verformungen durch Druckbeanspruchung, Drittes Europäisches Symposion Zerkleinern, Cannes (1971), Dechema-Monographien, Band 69, 51 (1972).

6. H. Rumpf, Fracture Physics in Comminution, Dritte Internationale Tagung über den Bruch, München, PL IX-142 (1973).

7. W. Johnson, A.G. Mamalis and Y. Mihara, The Compression Loading of Solid Spheres of Plaster of Paris, Int. J. Mech. Sci. (in Press).

8. Y. Mihara and G.H. Daneshi, Part I: The Compression of Metal Spheres; A.G. Mamalis, Part II: The Static Compression of Perspex Spheres, 18th Int. M.T.D.R. Conf., London (Sept. 1977) (to be published).

9. J.D. Stachiw and O.H. Burnside, Acrylic Plastic Spherical Shell Windows under Point Impact Loading, Trans. A.S.M.E., J. Eng. Ind. B98, 563 (1976).

10. R. Kitching, R. Houlston and W. Johnson, A Theoretical and Experimental Study of Hemispherical Shells Subjected to Axial Loads between Flat Plates, Int. J. Mech. Sci. 17, 693 (1975).

11. W. Johnson and A.G. Mamalis, The Fracture in Some Explosively End-Loaded Bars of Plaster of Paris and Perspex Containing Transverse Holes or Changes in Section, Int. J. Mech. Sci. 19, 169 (1977)

12. H. Kolsky, Wave Propagation Effects and Fracture, Conf. on Mechanical Properties at High Rates of Strain, The Institute of Physics, Series No. 21, Oxford (1974), p. 201.

Spallation Resulting from High-Velocity Impacts

Ray Kinslow
Tennessee Technological University
Cookeville, Tennessee, U. S. A.

A high-velocity projectile impact generally creates a crater in the target, driving a strong shock wave into the material. If the target is sufficiently thin, a puncture will result. If the target is relatively thick, the shock wave will rapidly decay into a spherical elastic stress wave. When such a pressure wave encounters a free surface, it is reflected as a tensile wave.

The amplitude of the reflected waves may be of sufficient magnitude to produce fractures near and approximately parallel to the surface. The portion of the target material between the fracture and the rear surface is known as the "spall." The energy trapped in this spall may cause a rear surface bulge; or, if sufficiently great, the material may become detached from the target creating a shrapnel effect.

The fracture will be formed if the tensile stress reaches the critical dynamic strength (σ_c) of the target material. This fracture acts as a new free surface from which the tail of the pressure pulse is reflected. The tensile stress produced by this reflection may again reach the critical value, at which time a second fracture will be formed parallel to the first. The tail of the pulse is now reflected from this newly formed free surface and, if of sufficient magnitude, will produce additional fractures.

As an example, a sawtooth wave profile is assumed for both the simplicity of the calculations and because it may

roughly approximate an average pressure pulse. It has a length λ and a maximum amplitude of σ_o which is greater than the critical tensile strength σ_c of the material. From the geometry of the pulse, it may be seen that a fracture will be located at a distance $\Delta = (\sigma_c/\sigma_o)(\lambda/2)$ from the rear surface. In this case of the sawtooth pulse, other fractures also will be the distance Δ apart. If the pulse profile is not linear as assumed in this example, the distance between fractures will not be equal. By sectioning a damaged target and measuring the fracture location, one can determine the actual pulse profile.

The material velocity V_s can be determined by equating the impulse of the trapped part of the wave to the momentum of that portion of the material. The velocity of any spall resulting from this pressure pulse is $V_{sn} = [2\sigma_o - (2n - 1)\sigma_c]/\rho c$ where n denotes the spall number.

Another form often used to represent the pulse resulting from impact is the decaying exponential pulse $\sigma = \sigma_o \exp(-\alpha t)$ where α and t are the decay constant and time, respectively. The thickness of the first spall resulting from the reflection for a free surface is: $\Delta = -(c/2\alpha)\ln(1-\sigma_c/\sigma_o)$ and the spall velocity is $V_s = -2\sigma_c/\rho c \ln(1-\sigma_c/\sigma_o) = \sigma_c/\rho\alpha\Delta$.

Similar results can be determined for any pressure wave which will depend upon impact conditions and target material.

Micro-Dynamical Effects in High Speed Loading of Porous Metals

E. H. LEE and R. L. MALLETT
Stanford University

Summary

When porous metal is loaded in compression, after initial elastic deformation early plastic flow sets in due to stress concentration around the pores. Plastic pore collapse causes a stiffening of the stress-strain curve as the material approaches the compacted state. When the loading is rapid, the closing of the pores and associated reduction in their perimeters causes acceleration of material in the neighborhood of each cavity even for constant strain-rate loading, and the associated inertia forces result in an effective rate-effect. This is a system effect due to the micro-dynamics of the porous material, and will be superposed on any material rate-effect. Specific examples of pore collapse and the associated rate effect are presented for an aluminum alloy, based on finite-element evaluations of the process.

Introduction

Porous ductile metals constitute ideal media for the absorption of mechanical energy on impact. The free surfaces of the pores permit plastic flow to occur with local stresses of the order of the yield stress in simple compression. If the porosity is such that the pore volume comprises a significant part of the total volume, then the externally applied tractions required to generate plastic flow will also be of the order of the yield stress. External tractions which can generate plastic flow include the case of pure hydrostatic compression which produces plastic flow with volume compression of the porous medium because the pores collapse. This comprises a degree of freedom not available in homogeneous ductile metal. As the pores close up the porosity decreases and the external compressive traction needed to maintain

plastic flow increases. The averaged or macroscopic constitutive relation for the porous medium as a whole, modeled as a continuum, then exhibits the characteristics of a locking material, for which the yield stress increases with a concave upward stress-strain curve. If the external pressure is sufficient to close the pores completely, then no additional plastic flow can occur under increasing hydrostatic pressure and the bulk modulus will correspond to elastic response.

The decreasing surface area of the cavities as they collapse leads to a continuously increasing local collapse velocity because of the effectively incompressible nature of plastic deformation. For constant averaged or macroscopic rate of volumetric strain, new volume occupied by metal must replace pore volume the material being transported across the instantaneous pore surface of ever-decreasing area. Thus the local pore collapse accelerates, and if inertia forces are included, this acceleration demands larger compressive stresses to drive the system. If the whole process is carried out with a higher average applied strain-rate the inertia forces will be magnified and an apparent strain rate effect will be exhibited even if the response of the bulk metal is essentially rate independent, which is the case for many aluminum alloys for example.

The Analytical Model

The averaged, overall, stress-strain relation, expressing the response of a material element containing many pores, is termed the m a c r o s c o p i c stress-strain relation. This is deduced by analyzing the m i c r o s c o p i c motion in a single cell surrounding a pore cavity.

In a porous medium the pores are usually distributed randomly, and under load the stress fields around them will interact with neighboring fields to an extent depending on the porosity of the medium. Because of the randomness of the configuration it is virtually impossible to evaluate a precise load deformation relation, so that in order to include such interaction effects, we analyze a particular global distribution of pores - one

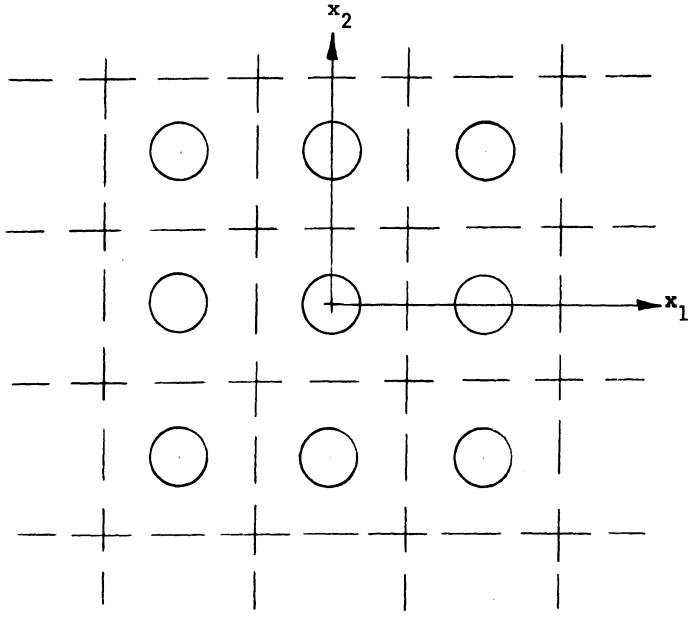

Figure 1. Global periodic distribution of circular cylindrical cavities.

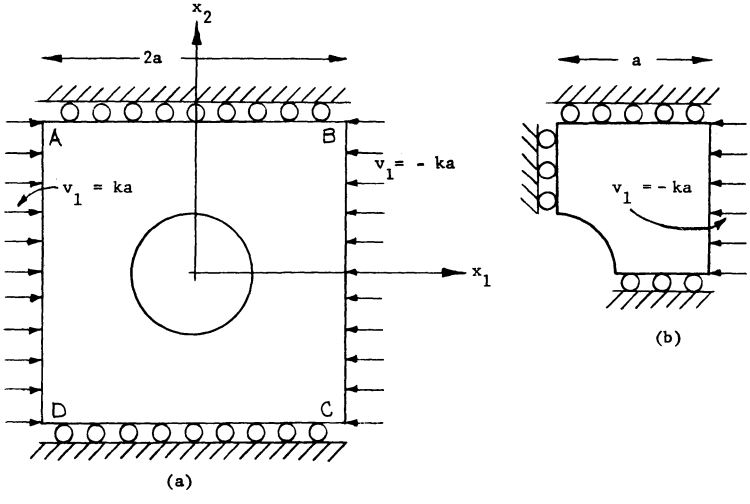

Figure 2. Equivalent single cell and quarter cell.

periodic on a square space mesh. Our first calculation is based on a two-dimensional array of circular cylindrical cavities as illustrated in Fig. 1.

We consider a problem of uniform one-dimensional compression set for an infinite porous medium as shown in Fig. 1, initially undeformed and moving with the initial velocity distribution

$$v_1 = - kx_1 \quad , \quad v_2 = v_3 = 0 \tag{2.1}$$

where v_i is the particle velocity. This prescribes the initial rate of strain

$$\dot{\varepsilon}_{11} = \partial v_1 / \partial x_1 = - k \tag{2.2}$$

to be a constant throughout the material. Because of the boundary conditions at the pore surfaces of freedom from traction, this uniform strain rate will change to a non-homogeneous distribution as time progresses, but each square cell surrounding a pore will deform like every other cell since its initial motion consists of uniform compression superimposed on the uniform velocity

$$v_1 = - k \bar{x}_1 \tag{2.3}$$

where $\bar{x}_1$ is the coordinate of the center of any particular cavity under study. Superimposing the constant velocity $k \bar{x}_1$ on the entire body brings to rest the centers of cavities initially at $x_1 = \bar{x}_1$ without affecting the equations of motion, so that these cavities will deform just as does the one centered at the origin in Fig. 1, and similarly for all other cavities. Moreover, anti-symmetry in the x_1 direction of the modified initial velocity field about the cavity centers, $x_1 = \bar{x}_1$, dictates that they remain at rest in the subsequent motion, which implies moving with constant velocity $- k\bar{x}_1$ for the prescribed initial velocity field (2.1). By a similar argument of superposing a constant velocity field $v_1 = k\bar{x}_1$,

where now $\bar{x}_1$ corresponds to cell boundaries parallel to the x_2 axis, it is clear that in the subsequent motion each of these boundaries moves with constant velocity $-k\bar{x}_1$ and that they remain straight and parallel to their initial directions. By symmetry for the infinite medium, the cell boundaries parallel to the x_1 axis remain at rest. Also by symmetry, there are no shear tractions on any of the cell boundaries. This lack of restraint permits motion along the boundaries of the material particles defining the boundaries. The initial zero velocity component v_3, symmetry about the x_1, x_2 plane and the considered unlimited extent of the body in the x_3 direction, determine the motion to be plane strain with no displacement in the x_3 direction.

The discussion above demonstrates that the deformation for any of the cells surrounding the cavities can be analyzed by solving for the motion of a single two-dimensional cell in plane strain with the boundary conditions shown in Fig. 2a:

$$\begin{aligned} &\text{BC and AD}, \quad x_1 = \pm a, |x_2| \leq a, \quad v_1 = \mp ka, \quad \sigma_{12} = 0 \\ &\text{AB and DC}, \quad x_2 = \pm a, \quad x_1 \leq a, \quad v_2 = 0, \quad \sigma_{12} = 0 \end{aligned} \tag{2.4}$$

where the upper sign is associated with the first boundary listed, and vice versa. On the cavity surface the traction is zero, hence the normal and shear components of the stress there are zero.

Symmetry and anti-symmetry of the geometry and boundary conditions for the single cell, Fig. 2a, determines that it is necessary only to solve the quarter cell problem shown in Fig. 2b in order to evaluate the stress and deformation distributions in the whole cell.

Since pore collapse must be investigated a theory valid for finite deformation is needed so that plastic flow and associated change in geometry of the cell and deformation of the cavity must be considered. To obtain complete stress information, elastic-plastic theory must be adopted [1], and the complexity of

the geometry requires a numerical evaluation using a finite-element procedure.

The elastic-plastic theory used in this study [2,3] assumes isotropic work-hardening based on the tensile Kirchhoff stress versus logarithmic plastic strain curve shown in Fig. 3.

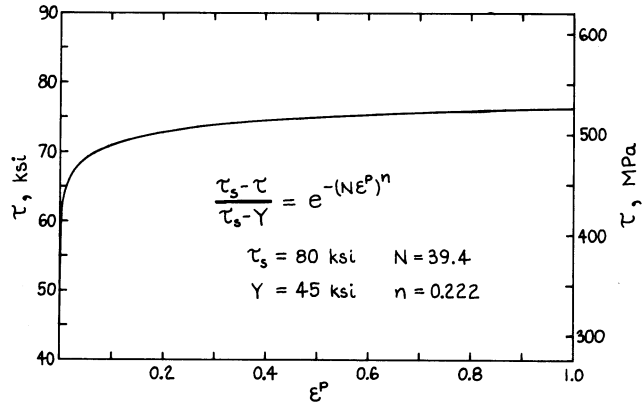

Figure 3 Stress-strain curve for aluminum alloy

This curve is intended to be typical of aluminum alloys at ambient temperatures and it represents the following analytic expression

$$\tau = \tau_s - (\tau_s - Y)\, e^{-(N\varepsilon^p)^n} \qquad (2.5)$$

suggested by Hockett and Sherby [4] for large strain of polycrystalline metals at low temperature. Y and τ_s designate the yield stress and steady-state saturation flow stress respectively and n and N designate dimensionless material constants which control the shape of the curve. Some large strain torsion experiments led to the adoption of the following values for these four parameters:

$$
\begin{aligned}
Y &= 45 \text{ ksi} \\
\tau_s &= 80 \text{ ksi} \\
n &= 0.222 \\
N &= 39.4
\end{aligned}
\tag{2.6}
$$

An incremental finite-element procedure based on the large deformation formulation of McMeeking and Rice [2] was adopted. The basic finite element employed was a four noded quadrilateral constructed from four constant strain triangles formed by the quadrilateral's diagonals. This element avoids the well known difficulties connected with the nearly incompressible deformations associated with plastic flow and has been discussed by Nagtegaal, Parks and Rice [5].

The history of stress and deformation for one-dimensional compression of the two dimensional porous media model was determined for three different values of porosity (defined as the ratio of pore volume to total volume) $p = \pi/32$, $2\pi/32$, $4\pi/32$, corresponding to the following initial pore radius to cell half width ratios: $r_o/a = 0.5/\sqrt{2}$, 0.5 , $0.5\sqrt{2}$. The finite-element network was obtained in each case by mapping an $n \times m$ rectangular array of quadrilateral elements onto the quarter cell (Fig. 2b) so that n and m denote the number of elements along the radial and circumferential edges of the quarter cell respectively. Specifically, 11×16 , 8×16 and 5×16 networks were used respectively for the three porosities. The radial dimension of the elements was chosen to increase with radial position so that the four edges of each element would initially be approximately equal. The solution obtained with the 8×16 network was compared with solutions using 4×8 and 6×12 networks in order to establish that a sufficiently refined finite-element mesh was being used. Fig. 4 shows the undeformed 8×16 finite-element network used for the $r_o/a = 0.5$ case ($p = 2\pi/32$).

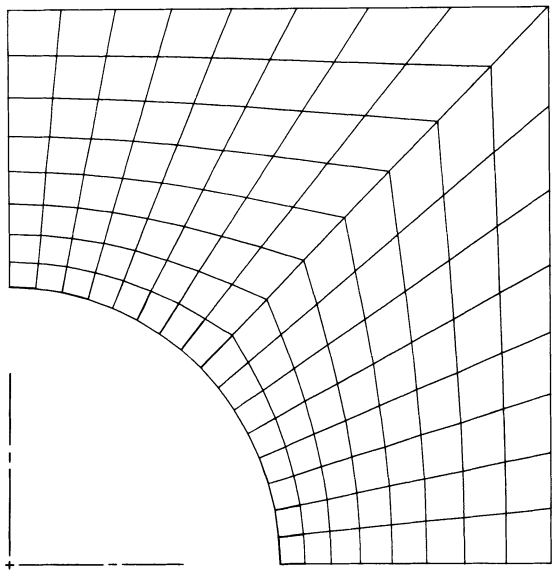

Figure 4. Undeformed finite-element network ($r_o/a = 0.5$)

Stress and Deformation Distributions

The finite element evaluation of the stress and deformation distributions was first carried out for quasi-static motion in which inertia forces were neglected. The porosities considered were not sufficiently close to unity to produce buckling of the cavity walls due to the compressive loading, as would, for example, have been the case with honeycomb material made of aluminum sheets.

Since the compressive deformation was initiated by the constant velocity motion of the right hand cell boundary in Figs. 2b and 4, as restrained by the fixed vertical line of symmetry $x_1 = 0$ (the left hand boundary in Figs. 2b and 4), plastic flow developed initially in the elements at the top of the cavity boundary. The region of plastic flow then gradually spread to include all the material above the cavity and eventually to include all material except for an elastic region occupying the lower right hand corner of the quarter cell in Fig. 2b.

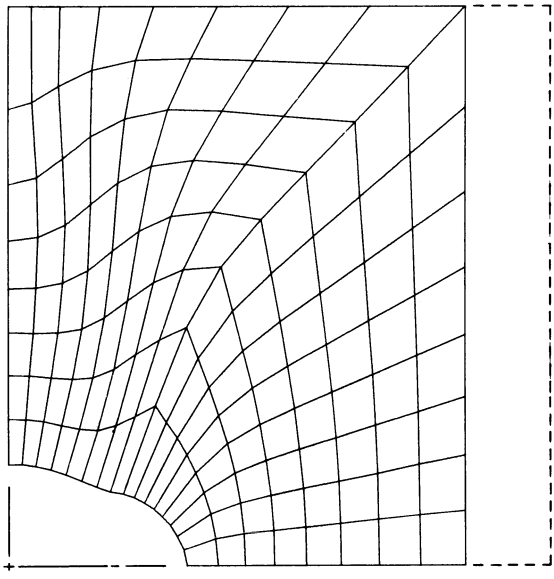

Figure 5. Deformed finite-element network ($r_o/a = 0.5$) .

Fig, 5 shows the deformed finite-element network for the $r_o/a = 0.5$ case after the cell width had been reduced by 16% and the cavity size had been reduced by about 76%. This amount of compression required 159 incremental steps of the computation. It is interesting to note that the cavity deforms into an approximately elliptical shape with its major axis parallel to the direction of compression. This feature can be understood by envisaging a cell defined by boundaries parallel to the x_1 axis in Fig. 1 passing through the centers of adjacent cavities. The cell then has the configuration of a notched specimen in compression so that plastic flow in the neck of the notch tending to increase its cross-section corresponds to narrowing the cavity perpendicularly to the direction of compression.

The solution for the stress distribution over the cell, Fig. 2a, determines the micro-stress component $\sigma_{11}(\pm a, x_2, t)$. Averaging this over the boundaries BC or AD (the distribution

being the same by symmetry) gives the macro-stress $\bar{\sigma}_{11}(t)$, associated with the average nominal compressive strain across the cell $2\,kat/2a = kt$: the compressive macro-strain $\bar{\varepsilon}_{11}$. The resulting macro-stress macro-strain relations for the three initial porosities considered are shown in Fig. 6. The stress has been non-dimensionalized with respect to the initial yield stress Y . The initial elastic response is evident, followed by macroscopic "hardening" of the porous material as the cavities close up.

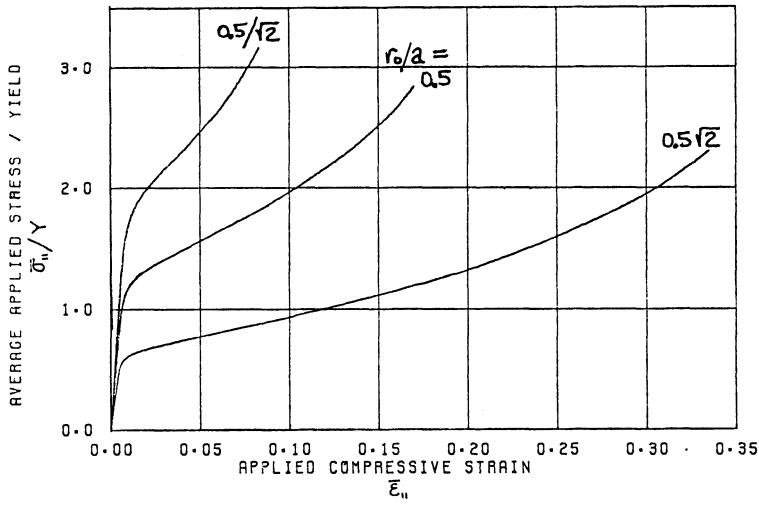

Figure 6. Computed macro-stress versus macro-strain curves for three values of pore radius to cell half-width ratio, r_o/a .

A detailed description of the quasi-static solution has been presented since such analyses can be shown to be valid for the investigation of many impact problems which arise in practice. For high strain rates, however, the influence of inertia forces can become significant, but wave propagation effects will still not appreciably influence the micro-motion in a single cell, as

shown in [6]. A method of computation was devised [6] which incorporated inertia effects but eliminated the consideration of wave propagation. This was necessary to ensure satisfactory accuracy without excessive computational costs.

In order to evaluate the effective strain rate influence arising from the inertia of accelerating material near the cavity boundaries, dynamic solutions were obtained for several values of the applied straining velocity, $v_1 = ka$, Fig. 2, or equivalently of the macroscopic compressive strain rate $k = v_1/a$. For quasi-static analysis in which inertia forces are neglected, the stress and strain solutions are independent of cell size and rate of compression if the progress of the motion is expressed by a representative strain magnitude, such as the macroscopic nominal strain kt. This follows from the fact that the plasticity law, (2.5), is rate independent. However incorporation of inertia terms introduces time scale effects. Dimensional analysis shows that although solutions for different cell sizes are geometrically similar, the applied strain rate must be scaled. We evaluated the solutions for a standard medium with cell dimension $a = 1"$, and for several values of the macroscopic nominal strain rate k. If the cell dimension in the medium is changed by a factor b, then the solution evaluated for the standard medium will correspond to a nominal strain rate k/b in the actual medium. Thus for a cell dimension $a = 10^{-3}$in, the solution evaluated for nominal macroscopic strain rate k will correspond to a strain rate $10^3 k$ in the porous medium.

Fig. 7 shows the macroscopic stress-strain relations for the standard medium computed for different values of the average strain rate, $v_1/a = k$, for initial porosity corresponding to $r_o/a = 0.555$. The compressive stress is averaged over the width of the cell so that the stress-strain relations correspond to one-dimensional strain of the bulk porous medium. These calculations were carried out [6] using the measured stress-strain curve introduced numerically into the program

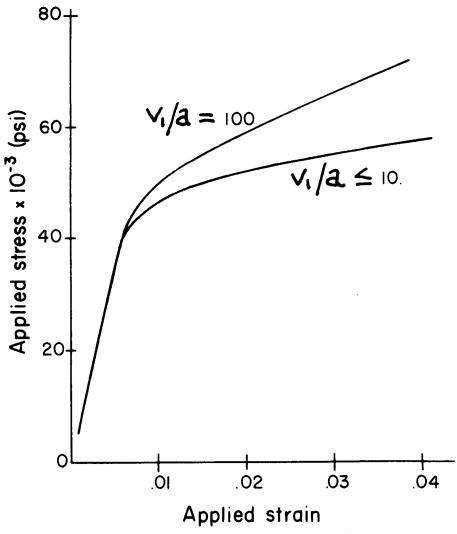

Figure 7. Computed macro-stress versus macro-strain curves for different applied strain rates, $k = v_1/a$ sec^{-1}.

and not through eq. (2.5). Since only small strains were generated this did not involve any discrepancy. Finite elements in the form of constant strain triangles were used rather than the four-noded quadrilaterals described in connection with the other calculations. However, it was ascertained that for this problem of compaction of a porous medium, the increase in the applied force is sufficiently rapid to cause an increase in elastic volumetric strain which eliminates the incompressibility constraint often encountered with elastic-plastic problems.

Fig. 7 indicates that there is a negligible effective strain rate influence for the standard medium unless the macroscopic rate of strain, k, exceeds 10 sec^{-1}. For higher strain rates, as described earlier, the inertia associated with the collapsing pores demanded an increased compressive force which

constitutes a system rate effect, even though the matrix material was assumed to obey a rate-independent plasticity law. Herrmann, [7], has shown using shock-wave propagation experiments that for the aluminum alloy 6061-T6 rate of strain influences are not observed below a strain rate of 10^4 sec^{-1}. Accepting these measurements and the porous medium calculations to be typical of an aluminum alloy, the microscopic configuration of the porous medium thus generates a system rate effect comparable with the material rate effect for pore separations of the order 10^{-3} in. Courser porous media will exhibit a greater system rate effect and for finer porous media material rate properties will dominate.

Discussion

The analyses of the response of a porous medium to compressive straining, based on the initial configuration of Fig. 1, incorporates the corresponding specific interaction effect between the pores. Earlier research on continuum models of porous media have incorporated simpler pore-interaction models such as the "composite spheres assemblage" of Hashin [8] which considers the body to be filled with spherical annuli having constant porosity and varying radii having no lower limit. Loading is limited to hydrostatic pressure and a hydro-dynamic continuum model is deduced. Carroll and Holt [9] developed an analogous model but utilized only one spherical annulus which generated a continuum model using the concept of a self-consistent body, such that under hydrostatic pressure deformation of the continuum was compatible with that of the embedded spherical annulus. Deformation local to the cavity was evaluated, leading to inertia effects similar to those discussed in the previous section. The advantage of analyzing a specific configuration, such as Fig. 1, is that interactions for other than hydrostatic pressure loading can be investigated. For example, one-dimensional strain parallel to the direction $x_1 = x_2$ would generate a different mode of interaction between pores.

Studies of the type presented in this paper would enable a continuum model to be formulated which would represent the

response of a porous medium. This could then be combined with the usual equations of motion to determine macroscopic stress and strain distributions. Inertia terms would appear and lead to wave propagation or vibration effects, but this would be associated with the macro-motion. The micro-motion on the scale of the individual cells would have been incorporated into the continuum model along with micro-inertia influences which are embodied in the strain-rate characteristics of the continuum model. Such influences would, for example, have an important bearing on the analysis of the propagation of shock waves through a porous body. The system rate influence would spread the shock wave profile and interact with the steepening of the profile associated with the concave upward characteristic of the macroscopic stress-strain curve already described. Thus the effect of inhomogeneities in the porous medium would exert an influence on wave propagation through the mechanism of a more complex homogeneous continuum model.

References

1 Lee, E. H.; Mallett, R. L.; McMeeking, R. M.: Stress and deformation analysis of metal forming processes. Numerical Modeling of Manufacturing Processes, Ed. R.F. Jones,Jr., H. Armen and J. T. Fong. ASME (1977) 19-33.

2 McMeeking, R.M.; Rice, J. R.: Finite-element formulations for problems of large elastic-plastic deformation. Int. J. Solids Structures 11 (1975) 601-616.

3 Lee, E. H.; Mallett, R. L.; Yang, W.H.: Stress and deformation analysis of the metal extrusion process. Comp. Meth. in Appl. Mech. Engg. 10 (1977) 339-353.

4 Hockett, J.E.; Sherby, O.D.: Large strain deformation of polycrystalline metals at low homologous temperatures. J. Mech. Phys. Solids 23 (1975) 87-98.

5 Nagtegaal, J.C.; Parks, D.M.; Rice, J.R.: On numerically accurate finite element solutions in the fully plastic range. Comp. Meth. in Appl. Mech. Engg. 4 (1974) 153-177.

6 Lee, E. H.; Mallett, R. L.; Ting, T.C.T.; Yang, W.H.: Dynamic analysis of structural deformation and metal forming. Comp. Meth. in Appl. Mech. Engg. 5 (1975) 69-82.

7 Herrmann, W.: Development of high strain rate constitutive equation for 6061-T6 aluminum. International Conference on the behavior of Materials, Kyoto, Japan, 1970.

8 Hashin, Z.; Theory of composite materials. Mechanics of Composites Materials- Ed. F. W. Wendt, H. Liebowitz, and N. Perrone. Pergamon (1970) 211-230.

9 Carroll, M. M.; Holt, A. C.: Static and dynamic pore-collapse relations for ductile porous materials. J. Appl. Phys. 43 (1972) 1626-1636.

Wave Propagation and Dynamic Response Analysis of Rate Dependent Materials

YOSHIAKI YAMADA, Professor

Institute of Industrial science
University of Tokyo
7-22-1, Roppongi, Minato-ku, Tokyo 106, Japan

Summary

A method is proposed for describing the constitutive equation which is convenient to the experimental determination of characteristic parameters representing the mechanical behavior as well as the execution of numerical analysis. It is based on the mechanical model of generalized Voigt type comprising elastic, plastic, and rate-dependent viscoelastic components being connected in series. The relation for the general three dimensional case is derived first and the implications of relevant terms are discussed in detail by considering the uniaxial stress field. Numerical example of the application of the proposed method concerns with the solution of one demensional viscoelstic wave propagation by the finite difference and finite element methods.

Mechanical Model Approach

The mechanical model on which the present formulation is based is essentially a series combination of the simple Maxwell, plastic, and simple Voigt (or Kelvin) elements as shown in Fig.1. For convenience of thermal stress analysis, the thermal component is also included. The total strain-rate $\{\dot{\varepsilon}\}$ is then given by

$$\{\dot{\varepsilon}\} = \{\dot{\varepsilon}_g^{\,e}\} + \{\dot{\varepsilon}^c\} + \{\dot{\varepsilon}^p\} + \{\dot{\varepsilon}^\theta\} + \Sigma\{\dot{\varepsilon}_i\} \qquad (1)$$

The elasic and creep strain-rates of the simple Maxwell model are given by

$$\{\dot{\varepsilon}_g^{\,e}\} = [C_g^{\,e}]\{\dot{\sigma}\} \qquad (2)$$

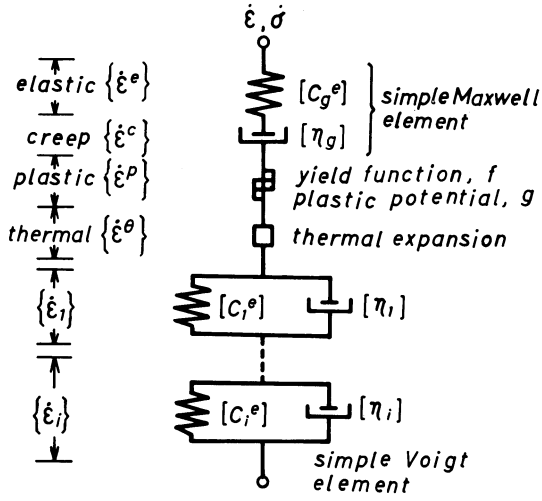

Fig.1 Generalized Voigt model

$$\{\dot{\varepsilon}^c\} = [\eta_g]^{-1}\{\sigma\} \tag{3}$$

and the strain-rate $\{\dot{\varepsilon}_i\}$ of a generic simple Voigt element is

$$\{\dot{\varepsilon}_i\} = [\eta_i]^{-1}\{\sigma\} - [\eta_i]^{-1}[D_i^e]\{\varepsilon_i\} \tag{4}$$

where $[C_g^e]$, $[D_i^e]$, $[\eta_g]$ and $[\eta_i]$ represent the flexibility, stiffness, and viscosity matrices respectively.

The plastic component is assumed to be derivable from the plastic potential $g(\sigma_{ij})$ as

$$\{\dot{\varepsilon}^p\} = \dot{\lambda}\{\partial g/\partial\sigma\} \tag{5}$$

Here the equivalent stress $\bar{\sigma}$ and equivalent plastic strain-rate $\dot{\bar{\varepsilon}}^p$ are introduced as follows

$$\text{plastic work-rate } \dot{W}^p = \lfloor\sigma\rfloor\{\dot{\varepsilon}^p\} = \bar{\sigma}\dot{\bar{\varepsilon}}^p \tag{6}$$

and

$$\bar{\sigma} = f(\sigma_{ij}) \tag{7}$$

Usually $\bar{\sigma}$ is defined such that it assumes the value which is equal to that of the yield function f evaluated from the current stress $\{\sigma\}$. Substituting $\{\dot{\varepsilon}^p\}$ form Eq.(5) into Eq.(6), we have

$$\dot{\lambda} = c\dot{\bar{\varepsilon}}^p, \quad c = \frac{\bar{\sigma}}{\lfloor\sigma\rfloor\{\partial g/\partial\sigma\}} \tag{8}$$

The strain-hardening hypothesis which we adopt in the present formulation states that

$$\bar{\sigma} = f(\sigma_{ij}) = f(\int\dot{\bar{\varepsilon}}^p dt,\ T) \tag{9}$$

Eq.(9) incorporates the effect of temperature T on the equivalent stress $\bar{\sigma}$. The differential form of Eq.(9) is

$$\dot{\bar{\sigma}} = \dot{f} = \lfloor\partial f/\partial\sigma\rfloor\{\dot{\sigma}\} = H'\dot{\bar{\varepsilon}}^p + (\partial\bar{\sigma}/\sigma T)\dot{T} \tag{10}$$

where H' represents the strain-hardening rate

$$H' = \partial\bar{\sigma}/\partial\bar{\varepsilon}^p \tag{11}$$

From Eqs.(8) and (10)

$$\dot{\lambda} = c\dot{\bar{\varepsilon}}^p = c\frac{\lfloor\partial f/\partial\sigma\rfloor\{\dot{\sigma}\} - (\partial\bar{\sigma}/\partial T)\dot{T}}{H'} \tag{12}$$

Substituting $\dot{\lambda}$ from Eq.(12) into Eq.(5)

$$\{\dot{\varepsilon}^p\} = c\frac{\lfloor\partial f/\partial\sigma\rfloor\{\dot{\sigma}\} - (\partial\bar{\sigma}/\partial T)\dot{T}}{H'}\{\partial g/\partial\sigma\} \tag{13}$$

It is worth pointing out that the effect of plastic equivalent strain-rate $\dot{\bar{\varepsilon}}^p$ on $\bar{\sigma}$ can be allowed for in the similar way as that of temperature T is included in Eqs. (10), (12), and (13).

Summing up the contributions from Eqs.(2), (3), (4) and (13) to Eq.(1)

$$\{\dot{\varepsilon}\} = ([C_g^e] + c\frac{\lfloor\partial f/\partial\sigma\rfloor\{\partial g/\partial\sigma\}}{H'})\{\dot{\sigma}\} + ([\eta_g]^{-1} + \Sigma[\eta_i]^{-1})\{\sigma\} - \Sigma[\eta_i]^{-1}[D_i^e]\{\varepsilon_i\} + \{\dot{\varepsilon}^\theta\} - c\frac{(\partial\bar{\sigma}/\partial T)\dot{T}}{H'}\{\partial g/\partial\sigma\} \tag{14}$$

By adopting the von Mises condition for the yield criterion f as well as for the plastic potential g, Eq.(14) assumes the following form in case of the isotropic

viscoelastic plastic material

$$\dot{\varepsilon}_{ij} = \frac{1}{2}C_{Gg}\dot{\sigma}_{ij} - \frac{1}{18}(3C_{Gg} - 2C_{Kg})\delta_{ij}\dot{\sigma}_{kk} + \frac{9\sigma'_{ij}\sigma'_{k\ell}}{4H'\bar{\sigma}^2}\dot{\sigma}_{k\ell}$$

$$+ \frac{1}{2}B_G\sigma_{ij} - \frac{1}{18}(3B_G - 2B_K)\delta_{ij}\sigma_{kk} - \Sigma\frac{1}{T_{Gi}}(\varepsilon_{ij})_i$$

$$+ \frac{1}{3}\Sigma\delta_{ij}(\frac{1}{T_{Gi}} - \frac{1}{T_{Ki}})(\varepsilon_{kk})_i \qquad (15)$$

where

$$B_G = \frac{1}{\eta_{Gg}} + \Sigma\frac{1}{\eta_{Gi}}\ , \quad B_k = \frac{1}{\eta_{Kg}} + \Sigma\frac{1}{\eta_{Ki}} \qquad (16)$$

C and η denote the elastic compliance and the coefficient of viscosity, with subscripts G and K which refer to the shear and bulk components respectively. T_{Gi} and T_{ki} represent the retardation time for a generic simple Voigt element $T_{Gi} = C_{Gi}\eta_{Gi}$ and $T_{Ki} = C_{Ki}\eta_{Ki}$. For simplicity, terms connected with thermal effects have been omitted in Eq.(15).

Eq.(15) can be written for the uniaxial stress field σ_x as the following by using the conventional notation and assuming that the coefficient of viscosity η_K for bulk deformation is infinite

$$\dot{\varepsilon}_x = (\frac{1}{E_g} + \frac{1}{H'})\dot{\sigma}_x + (\frac{1}{\eta_{Eg}} + \Sigma\frac{1}{\eta_{Ei}})\sigma_x - \frac{2}{3}\Sigma\frac{1}{T_{Gi}}(\varepsilon_x - \varepsilon_y)_i$$

$$\dot{\varepsilon}_y = (-\frac{\nu_g}{E_g} - \frac{1}{2H'})\dot{\sigma}_x - \frac{1}{2}(\frac{1}{\eta_{Eg}} + \Sigma\frac{1}{\eta_{Ei}})\sigma_x + \frac{1}{3}\Sigma\frac{1}{T_{Gi}}(\varepsilon_x - \varepsilon_y)_i \qquad (17)$$

where

$$\eta_{Eg} = 3\eta_{Gg}, \quad \eta_{Ei} = 3\eta_{Gi}, \quad T_{Gi} = \frac{\eta_{Gi}}{G_i} = \frac{\eta_{Ei}}{3G_i} \qquad (18)$$

E and ν are the Young's modulus and Poisson's ratio re-

spectively.

Eq.(17) features the inclusion of plasticity in terms of strain-hardening rate H' defined by Eq.(11). Further, it should be pointed out that characteristic parameters E_g, η_{Eg}, η_{Ei},.. can be variable, though they are regarded as constants in linear viscoelasticity. For example, the rate-dependent constitutive equation of Malvern type [1]

$$E\dot{\varepsilon} = \dot{\sigma} + k[\sigma - f(\varepsilon)] \tag{19}$$

is considered to be a special case of Eq.(17). In fact, Eq.(19) is obtainable from Eq.(17) by assuming nonlinear dashpot having a property

$$\frac{1}{\eta_{Eg}} = \frac{k[1 - f(\varepsilon)/\sigma]}{E} \tag{20}$$

More definitely, Eq.(14) or (15) is a generalization of the following constitutive equation of Perzyna [2,3]

$$\dot{e}_{ij} = \frac{1}{2G}\dot{s}_{ij} + \frac{1}{2\eta}\left\langle 1 - \frac{k}{\sqrt{J_2}}\right\rangle s_{ij}$$

$$\dot{\varepsilon}_{kk} = \frac{1 - 2\nu}{E}\dot{\sigma}_{kk} \tag{21}$$

The Johnston-Gillman's postulate [4] can also be included in Eq.(14) or (15) by introducing approproiate nonlinear coefficient of viscosity as well as retardation time.

Eq.(14) and its isotropic version of Eq.(15) are convenient to determine the characteristic material parameters from the test data obtainable at simple stress conditions. However, for the purpose of numerical analysis, particularly by the finite element method, inverted type of expression of Eq.(14) is preferable. Inversion can be effected [5] by an indirect procedure recapitulated in the following. In essence, it is to have an ex-

pression of $\dot{\lambda}$ in terms of $\{\dot{\varepsilon}\}$, which in Eq.(12) is given as a function of $\{\dot{\sigma}\}$.

We first have from Eqs.(1) through (5)

$$\{\dot{\varepsilon}\} = [C_g^e]\{\dot{\sigma}\} + \{\dot{\varepsilon}^\theta\} + \dot{\lambda}\{\partial g/\partial\sigma\} + ([\eta_g]^{-1} + \Sigma[\eta_i]^{-1})\{\sigma\} - \Sigma[\eta_i]^{-1}[D_i^e]\{\varepsilon_i\} \tag{22}$$

Premultiplying Eq.(22) by $[D_g^e] = [C_g^e]^{-1}$ and rearranging, we have

$$\{\dot{\sigma}\} = [D_g^e]\{\dot{\varepsilon} - \dot{\varepsilon}^\theta\} - \dot{\lambda}[D_g^e]\{\partial g/\partial\sigma\} - \{\dot{A}\} \tag{23}$$

where

$$\{\dot{A}\} = [D_g^e]([\eta_g]^{-1} + \Sigma[\eta_i]^{-1})\{\sigma\} - [D_g^e]\Sigma[\eta_i]^{-1}[D_i^e]\{\varepsilon_i\} \tag{24}$$

Substituting $\{\dot{\sigma}\}$ from Eq.(23) into Eq.(12) and solving for $\dot{\lambda}$

$$\dot{\lambda} = \frac{\lfloor\partial f/\partial\sigma\rfloor([D_g^e]\{\dot{\varepsilon} - \dot{\varepsilon}^\theta\} - \{\dot{A}\}) - (\partial\bar{\sigma}/\partial T)\dot{T}}{H_V'} \tag{25}$$

where

$$H_V' = H'/c + \lfloor\partial f/\partial\sigma\rfloor[D_g^e]\{\partial g/\partial\sigma\} \tag{26}$$

Introduction of $\dot{\lambda}$ from Eq.(25) to Eq.(23) leads to

$$\{\dot{\sigma}\} = [D_V^p]\{\dot{\varepsilon} - \dot{\varepsilon}^\theta\} - [D_V^c]\{\dot{A}\} - \{\dot{\sigma}^a\} \tag{27}$$

where

$$[D_V^c] = [I] - \frac{[D_g^e]\{\partial g/\partial\sigma\}\lfloor\partial f/\partial\sigma\rfloor}{H_V'}, \quad [D_V^p] = [D_V^c][D_g^e] \tag{28}$$

$$\{\dot{\sigma}^a\} = -\frac{[D_g^e]\{\partial g/\partial\sigma\}}{H_V'}(\partial\bar{\sigma}/\partial T)\dot{T} \tag{29}$$

Eq.(27) is an extension of the elastic-plactic con-

stitutive equation [6,7] to the material having rate-dependent component. It can be shown [5] that Eq.(27) covers the relation from the creep potential theory which is frequently employed in the elastic-plastic creep analysis of structural component.

One Dimensional Viscoelastic Wave Propagation

Although Eq.(14) and its inverted form given by Eq. (27) are quite general and applicable to the wide classes of continuum mechanics, we consider here the one dimensional case of viscoelastic wave propagation. Assuming isotropic material property along with the infinite coefficient of viscosity η_K for bulk deformation, relevant constitutive equation are from Eqs.(17) and (4)

$$\dot{\varepsilon} = \frac{\dot{\sigma}}{E_g} + \left(\frac{1}{\eta_{Eg}} + \Sigma\frac{1}{\eta_{Ei}}\right)\sigma - \Sigma\frac{\varepsilon_i}{T_{Ei}} = \frac{\dot{\sigma}}{E_g} + \frac{1}{\eta_{Eg}} + \Sigma\dot{\varepsilon}_i \quad (30)$$

where

$$\dot{\varepsilon}_i = \frac{\sigma}{\eta_{Ei}} - \frac{\varepsilon i}{T_{Ei}} \quad (31)$$

and notation T_{Ei} is used here for T_{Gi} defined by Eq.(18). For the simple Maxwell model, Eq.(30) reduces to

$$\dot{\varepsilon} = \frac{\dot{\sigma}}{E_g} + \frac{\sigma}{\eta_{Eg}}, \quad \text{or} \quad \dot{\sigma} = E_g\dot{\varepsilon} - \frac{\sigma}{T_{Eg}}, \quad T_{Eg} = \frac{\eta_{Eg}}{E_g} \quad (32)$$

In practical application, it is often advantageous to derive appropriate finite difference formulas from differential relations of Eqs.(30) and (32). A relation which assumes the linear variation of $\dot{\varepsilon}$ in time interval Δt of intergration has been described by Yamada [8] for the case of Eq.(30). An alternative is to assume the linear change of both $\dot{\varepsilon}$ and $\dot{\sigma}$. In this case, we have from Eq.(32), for example, the following finite difference formula

$$\Delta\sigma = \frac{E_g}{1 + \Delta t/(2T_{Eg})}\Delta\varepsilon - \frac{\Delta t/T_{Eg}}{1 + \Delta t/(2T_{Eg})}\sigma \qquad (33)$$

Yamada and Nagai [9] have employed successfully the finite difference relation of the type given by Eq.(33) in their analysis of one-dimensional viscoelasic stress wave propagation. In the computation, the integration scheme of Newmark with $\beta = 1/6$ is used. The choise of this value for β is equivalent to the assumtion of linear variation of particle acceleration during interval Δt and considered to be consistent with that made for $\dot{\varepsilon}$ and $\dot{\sigma}$ in deriving Eq.(33). Fig.2 depicts the finite element solution for one dimensional elastic wave in comparison to the analytical one. It can be seen that the finite element method gives completely accurate answer with the use of consistent mass matrix and the correct ratio of time step Δt to element length $\Delta\ell$, i.e. $\Delta t/\Delta\ell = 1/c$, where c represents the velocity of elastic wave propagation.

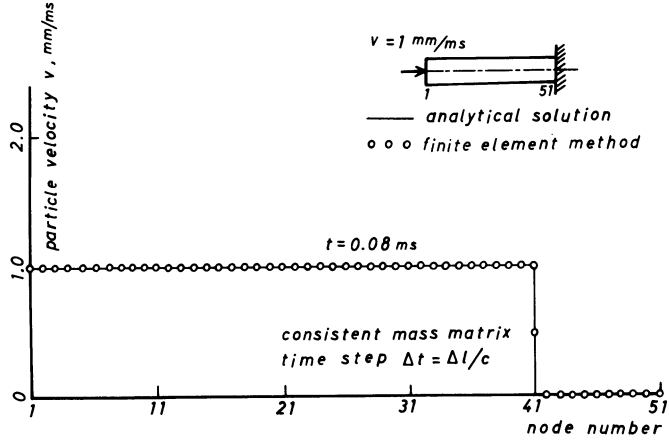

Fig.2 Elastic wave propagation with discontinuous wave front

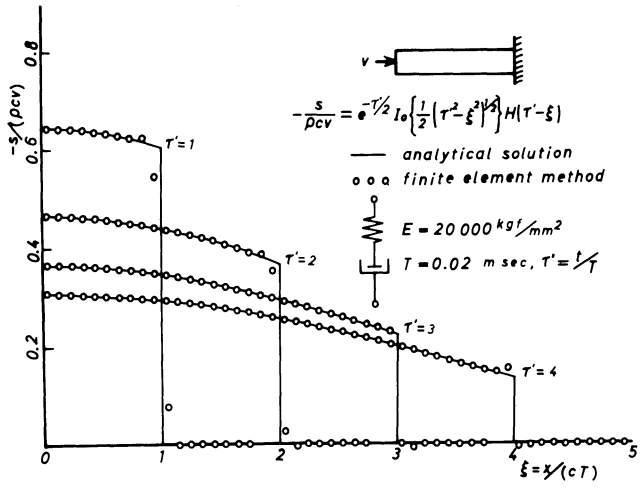

Fig.3 Viscoelastic wave propagation, simple Maxwell model

Fig.3 is an example showing the propagation of decaying wave in viscoelastic material. A simple Maxwell material is selected in this example. Again the agreement with the analytical solution [10] is satisfactory, not only in the stress wave form but also the magnitude of stress discontinuities s_R at wave front

$$-s_R/\rho cv = \exp(-\tau'/2), \quad \tau' = t/T \tag{34}$$

where ρ and v denote respectively the density and constant impact velocity, and τ' is a nondimensional measure defined by the ratio of natural time t to relaxation time $T = \eta_{Eg}/E_g$ of the simple Maxwell model.

In the finite difference solution, the constitutive relations such as Eq.(30) or (32) is directly combined with the equation of motion

$$\rho_0 \partial v/\partial t - \partial s/\partial x_0 = 0 \tag{35}$$

and an additional diffential relation

$$\partial v/\partial x_o - \partial e/\partial t = 0 \qquad (36)$$

where v denotes particle velocity. For convenience, we have used conventional stress s and strain e, material density ρ_o before deformation, and convected coordinate x_o in the above expressions.

Eqs.(35) and (36), together with the constitutive equation, lead to a system of differential relations along the characteristics of hyperbolic partial differential equation. For completeness of the finite difference computational scheme, we should further establish the Hugoniot type equation which refers to the momentum change at the discontinuous wave front. Yamada and Sawada [9] obtained the pertinent finite difference relations for the simple Maxwell material and applied them to the solution of wave propagation in the bar of finite as well as infinite length. Further, they extended the similar computational scheme on finite difference method to the generalized Voigt material which is composed of up to five elements (three elastic and two viscous elements) [10].

In this symposium, viscoelastic wave will be discussed by Nakagawa et al.[13]. Rate-dependent material having Malvern and/or Johnston-Gilman type of constitutive equation will be the topic of paper by Kawata et al. [14]. Besides these two symposium papers from Japan on rate dependent material, a work has been published by Yokoyama and Tsuzuki [15] on the wave propagation in a bar of pure copper characterized by Malvern's type of constitutive equation. Numerical experiments by the finite element method on Malvern and Johnston-Gilman materials have also been carried out by Nakagiri [16].

Concluding Remarks

Constitutive equations based on the mechanical model of the generalized Voigt type are summarized. The equations which are originally written for three dimensional case are considered to provide the necessary degree of sophistication for inelastic analyses and feature the easiness of experimental assessment of parameters characterizing the material properties. Parameters are not necessarily to be constant but can exhibit nonlinear behavior in the incremental expression of constitutive equations. It should be pointed out that the proposed equations incorporate plasticity effects, and therefore include the one used by Fukuoka [17] in the analysis of combined tension-torsion waves in elastic-plastic tubes. The author hopes the constitutive equations that have been proved to have many useful applications in quasistatic nonlinear analysis will be examined extensively in the field of dynamics.

References

1. Malvern, L.E., "The Propagation of Longitudinal Waves of Plastic Deformation in a Bar of Material Exhibiting a Strain-Rate Effect," J. Appl. Mech., vol. 18, 1951, pp. 203-208.

2. Perzyna, P., "The Constitutive Equations for Rate Sensitive Plastic Materials," Quart. Appl. Math., vol. 20, 1963, pp. 321-332.

3. Campbell, J.D., Dynamic Plasticity of Metals, International Center for Mechanical Sciences, Udine/Italy, Courses and Lectures No. 46, 1970.

4. Johnston, W.G., and Gilman, J.J., "Dislocation Velocities, Dislocation Densities, and Plastic Flow in LiF Crystals," J. Appl. Phys. vol. 30, 1959, pp. 129-144.

5. Yamada, Y., and Sakurai, T., "Basic Formulation and a computer Program for Inelastic Large Deformation Analysis," Pressure Vessel Technology, Part I, ASME,

1977, pp. 341-352.

6. Hill, R., "Some Basic Pricniples in the Mechanics of Solids without a Natural Time," J. Mech. Phys. Solids, vol. 7, 1959, pp. 209-225.

7. Yamada, Y., Yoshimura, N., and Sakurai, T., "Plastic Stress-Strain Matrix and its Application for the Solution of Elastic-Plastic Problems by the Finite Element Method," Int. J. Mech. Sci., vol. 10, 1968, pp. 343-354.

8. Yamada, Y., "Time Dependent Materials," Computer Programs in Shock and Vibration, The Shock and Vibration Information Center, Naval Research Lab., Washington, D.C., 1975, pp. 173-188.

9. Yamada, Y., and Nagai, Y., "Analysis of One-Dimensional Stress Wave by the Finite Element Method," Seisan-Kenkyu, Monthly J. of Institute of Industrial Science, Univ. of Tokyo, vol. 23, 1971, pp. 186-189.

10. Lee, E.H., and Kanter, I., "Wave Propagation in Finite Rods of Viscoelastic Material,", J. Appl. Phys. vol. 24, 1953, pp. 1115-1122.

11. Yamada, Y., and Sawada, T., "Analysis of Viscoelastic Wave Propagation with Particular Emphasis on Discontinuous Wave Front According to Finite Difference Method," J. of Japan Society for Technology of Plasticity, vol. 10, 1969, pp. 141-148 (in Japanese).

12. Yamada, Y., and Sawada, T., "Analysis of One Dimensional Viscoelastic Wave Propagation with Discontinuities," ibid., vol. 11, 1970, pp. 724-734 (in Japanese).

13. Nakagawa, N., Kawai, R., and Sasaki, T., "Identification of Dynamic Properties and Wave Propagation in Viscoelastic Bars," to be presented at this IUTAM symposium on High Velocity Deformation of Solids, August 24-27, 1977, Tokyo.

14. Kawata, K., Hashimoto, S., and Kurokawa, K., "Analysis of High Velocity Tension of Bars of Finite Length of bcc and fcc Metals with Their Own Constitutive Equations," as above.

15. Yokoyama, T., and Tsuzuki, M., "Analysis of Elastic/Viscoplastic Wave Propagation in a Bar by the Finite Element Method," J. of Japan Society for Technology of Plasticity, vol. 18, 1977, pp. 11-15, (in Japa-

nese).

16. Nakagiri, S., "Finite Element Analysis of the Elastic-Plastic Wave Propagation in Metal Obeying the Strain-Rate Dependent Constitutive Equation," Seisan-Kenkyu, Monthly J. of Institute of Industrial Science, Univ. of Tokyo, vol. 28, 1976, pp. 199-202 (in Japanese).

17. Fukuoka, H., "A Note on the Strength of the Combined Tension-Torsion Waves in Elastic-Plastic Tubes," Symposium on Foundations of Plasticity, Noordhoff, 1973, pp. 317-325.

Plane Wave Propagation in Anisotropic Jointed Media

L. W. MORLAND
School of Mathematics and Physics,
University of East Anglia,
Norwich, U.K.

Summary

The propagation of plane waves of combined longitudinal and transverse motion through a rock mass containing a major set of regularly spaced parallel joints is discussed. The continuum description adopted supposes that wavelengths are large compared with joint spacing, and joint slip is small compared with joint spacing. Elastic intact rock is assumed and joint motion is restricted to tangential slip governed by a Coulomb failure criterion and subsequent ideal slip, dilatancy is excluded to simplify the description and predictions. Plane strain in a plane containing the propagation direction and inclined joint normal normal is assumed. The mathematical constitutive description is equivalent to an anisotropic elastic-plastic theory with non-associated flow rule, even when the intact rock is isotropic, so the present wave results extend those of the classical isotropic model with associated flow rule. In the case of isotropic intact rock the three physical parameters governing the material response are the ratio of the bulk and shear elastic moduli of the rock, the joint friction coefficient, and the joint inclination. Detailed results are presented for this case.

Conditions for real characteristics (wave speeds) in both elastic and slip regions are obtained, and also conditions for the interleaving of the slip shear wave speed, elastic shear wave speed, slip longitudinal wave speed, and elastic longitudinal wave speed, which always occurs in the classical theory with associated flow rule. In the interleaving case it is shown that the ten types of wave interaction at a continuous interface between elastic and slip regions are correctly matched, but for non-interleaving some interactions are undertermined and some overdetermined. With the non-associated flow rule of this model, non-interleaving occurs for reasonable ranges of the three parameters, suggesting that non-associated flow rules are not acceptable.

As final illustration the five possible single-interface wave patterns initiated by a monotonic increasing normal pressure over a plane boundary are analysed, and it is found that only one type gives a non-trivial valid solution, restricted to particular ranges of the three parameters.

The detailed theory and illustrations are presented in Morland [1].

References

1. Morland, L. W.: Plane wave propagation in anisotropic jointed media. Q. J1 Mech. appl. Math., 30 (1977) 1-21.

Behavior of Materials under Dynamic Combined Stresses of Torsion and Tension

T.HAYASHI and N.TANIMOTO

Faculty of Engineering Science,
Osaka University.
Toyonaka Osaka, Japan

Abstracts

The paper is concerned with the experiment on the multi-axial stress-strain relations in time dependent materials. In order to examine the dynamic behavior of solid materials under combined stresses, a testing machine for applying the impulsive torque and tension simultaneously to the specimen has been desined. Experiments are performed with various ratios of torque to axial force by the equipment. During the loading process, the load ratios are kept constant, and we can obtain almost proportional loading. Equivalent strain rates are about 30 sec^{-1} to 50 sec^{-1} . The dynamic yield surfaces in the $\sigma - \tau$ plane are ellipse like Von Mises's yield surface in static loading, but the radii are larger than the static one and time dependent property is found clearly in biaxial loading too. The flow lure can be expressed by the Perzyna type formula.

Introduction

The behavior of the materials subjected to the dynamic plastic deformation depends on various factors e.g. strain rate, strain history, temperature, grain size and so on. Many investigations on the effect of those factors have been performed mainly under uniaxial stress state because of the simplicity of the theoretical analysis and the easiness of the experiment[1]. Recently, the theoretical researches[2,3,4,5] on the dynamic behavior of

materials under combined stresses have been worked out by some investigators, but it seems that few experimental studies on the constitutive relation under multiaxial dynamic stresses has been reported yet[6,7]. In the present paper, the yield surface and the flow rule of annealed aluminum under impulsive biaxial loading are obtained experimentally.

Testing Machine

Test equipment for applying the impulsive torque and tension simultaneously to the specimen is a torsion bar type device[8,9] as shown in Fig.1. AB is a striker bar of

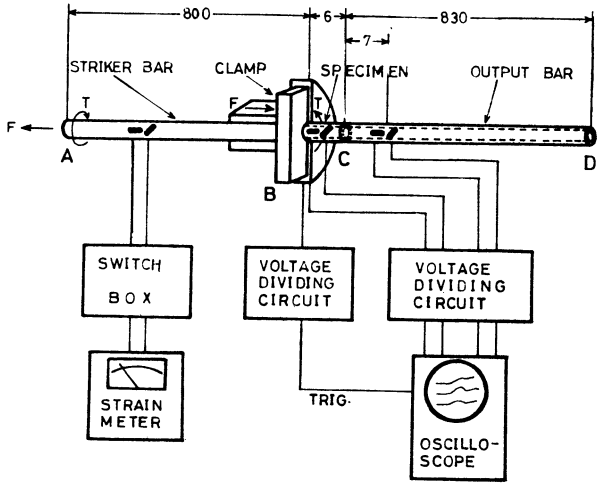

Fig.1 Schematic view of testing machine.

steel which is clamped at one end B and is twisted and pulled at the other end A to store the torque and axial force in the part AB. BC is a specimen of aluminum of thin walled cylinder. CD is an output bar which is used to measure the torque and the axial force applied to the specimen. Those three parts are pasted face to face

collinearly by the cement Bond E39Y6. The striker bar is made of carbon steel S45C which has a sufficiently higher yield stress than that of aluminum test specimen. Its dimension is 800 mm long with circular cross section of 10 mm diameter, and the clamped part of the bar about 10 mm long from the end B has been treated by the high frequency hardening in order to avoid the plastic deformation due to the clamping force. Copper tube is used as the output bar. Its dimensions are 830 mm in length, 10 mm in outside diameter and 1 mm of wall thickness. As the test specimen, commercially available pure aluminum (purity ; 99.7 %) is used. The shape and size of the specimens are shown in Fig.2. They have hut shaped ends

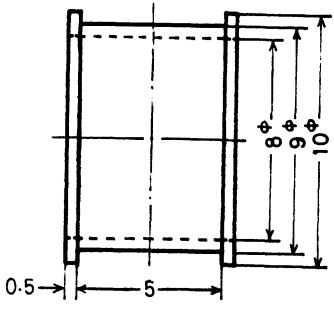

Fig.2 Specimen.

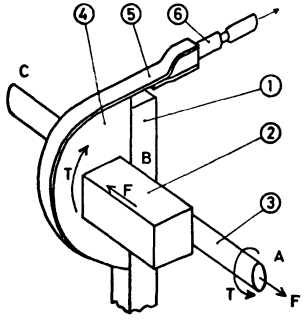

Fig.3 Clamp mechanism.

so that they can be bound well to the striker or the output bar. They were annealed before testing by keeping them at 400°C for 1.5 hours. Wire strain gauges are mounted on the specimen, one in the direction parallel to the axis and the other in the direction inclined to the axis by 45°, to measure the axial and shearing strains of the specimen, respectively. On the output bar, strain gauges are mounted in the same way as on the specimen, to measure the axial force and the torque applied to the specimen.

Having the strain energy stored in the part AB, if we release the clamp at B in an instant, the torque and the axial force will be applied to the specimen and the stress wave will be transmitted to the output bar. Applied forces were adjusted not to exceed the elastic limit of the output bar so that we could obtain the stresses in the bar by measuring its elastic strains. We assumed that the stress waves passing through the test specimen of aluminum had the same value as those of the output bar. Strains in the test specimen were obtained directly by the strain gauges (KFC-1-C1-11) on it.
Fig.3 shows the schematic view of the clamp mechanism. ① and ② are the rest stand to support the specimen. If we pull the metal band ⑤ in the direction of the arrow, the sector plate ④ holds the specimen firmly by the friction and the rotation of the specimen is restricted. The axial movement of the sector plate is also restrained by the stand block ② and so the axial force F of the specimen is supported by the stand ② through the sector plate ④. If the tension of the belt ⑤ is released in an instant by cutting the notch of the bar ⑥ with a chisel or by a brittle fracture of the notch, the torque and the axial force propagate simultaneously along the specimen BC and the bar CD.

Experimental Results and Discussions

The performance test of the equipment was done first in elastic range. The oscillogram obtained in the pure torsion impact test is shown in Fig.4. Beams (i) and (ii) show the outputs from strain gauges axially and symmetrically mounted on the output bar in the direction parallel to its axis. Beams (iii) and (iv) are the outputs from strain gauges mounted in the direction inclined to the axis by 45°. Comparing beam (i) or (ii) with beam (iii) or (iv), we find that the ratio of the former to

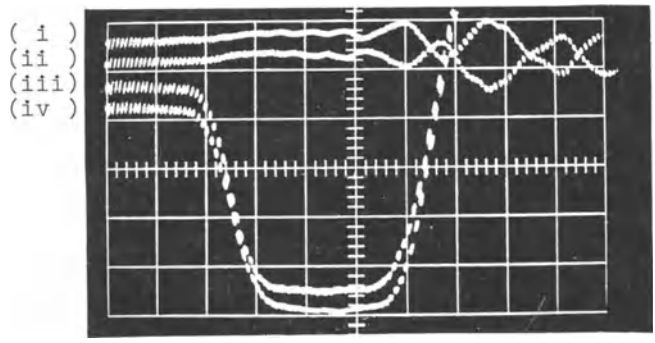

Fig.4 Oscillogram of pure torsion impact test.

the latter is about 10^{-2}. We find also that beams (iii) and (iv) are in good agreement with each other. They show that we can obtain almost pure plane waves by our device. The rise time of the impulsive load is about 100 μ sec.

Experiments were performed at the room temperature with several kinds of ratio of the torque to the tension. Figure 5 shows one of the osillograms obtained in our test. Beams (i) and (ii) in the figure show the outputs from strain gauges on the output bar, from which we can find the axial and shearing stress variations of the aluminum specimen with time. Beams (iii) and (iv) are the

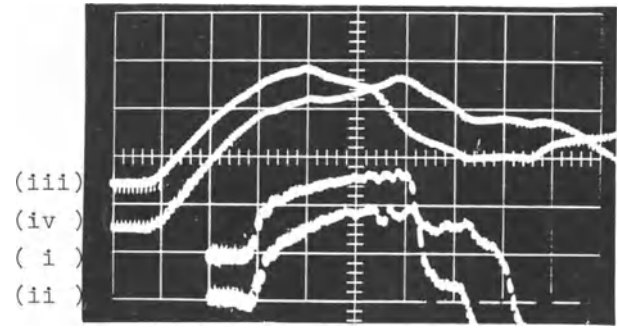

Fig.5 Oscillogram of impact test under biaxial loading.

outputs from strain gauges on the specimen, from which we can find its axial and shearing strain variations with time. The scales of the ordinate per dividion are 73×10^{-6} for beams (i) and (ii), and 2900×10^{-6} for beams (iii) and (iv). The time scale is 100 μsec per division, and after 320 μsec, all the beams are affected by the reflective wave from the end of the striker bar.

Stress paths in the specimen, obtained from beams (i) and (ii), are shown with thick solid lines in Fig.6. They

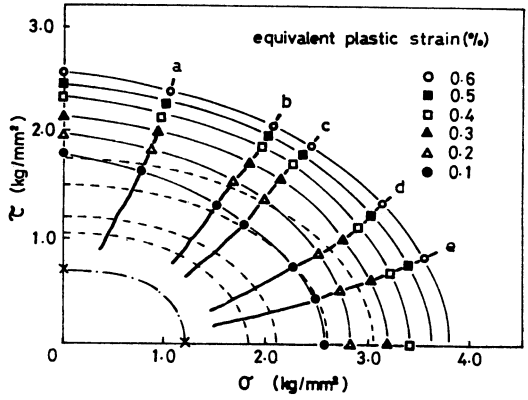

Fig.6 Yield surfaces in dynamic and static test.

show that the specimen is almost proportionally loaded during the loading process. The marks of X in the figure mean the yield points under static test, and the thin chain line is the initial yield surface of the material under static test. Thin solid lines in the figure show the yield surfaces under the dynamic loading, which are defined as contour lines passing through the equal equivalent strain points. The ratio between the major axis (tension stress axis) and the minor axis (shear stress axis) in the yield surface is about 1.51 except the equivalent plastic strain line of 0.1 per cent. Considering that the value of the ratio in Mises'yield surface is

$\sqrt{3}$, its deviation is about 13 percent. But it should be noted that equivalent plastic strain rates in our experiment are about 30 sec^{-1} to 50 sec^{-1}, and their values at each points in the figure differ from each other. The correction to the strain rate effect will be shown later. Thin broken lines in the figure are those obtained from the static tests of about 1.0×10^{-5} sec^{-1} plastic strain rate. Those lines correspond to the equivalent strains of 0.1, 0.2, 0.4 and 0.6 %. Comparing the dynamic yield surfaces with static ones, the former is larger than the latter. This means that aluminum is rate dependent in the combined torsion-tension dynamic loading as in the one-dimensional dynamic test.

If we assume the Mises' yield function as a plastic potential $F(\sigma_{ij})$, the flow rule will be expressed by

$$\dot{\varepsilon}^{P}_{ij} = \Phi \, \partial F / \partial \sigma_{ij} = \Phi \sigma'_{ij} \tag{1}$$

where $\dot{\varepsilon}^{P}_{ij}$ means the plastic strain rate and σ'_{ij} the deviatoric stress. According to the generalized Malvern's hypothesis, in which plastic strain rate is assumed to be a function of the over stress, Φ is expressed as follows.

$$\Phi = \Phi\left(\frac{1}{\bar{\sigma}_s} - \frac{1}{\bar{\sigma}}\right) \tag{2}$$

When the function Φ is linear, the flow rule is

$$\dot{\varepsilon}^{P}_{ij} = k\left(\frac{1}{\bar{\sigma}_s} - \frac{1}{\bar{\sigma}}\right)\sigma'_{ij} \tag{3}$$

where $\bar{\sigma}$ is the dynamic equivalent stress, $\bar{\sigma}_s$ is the static one and k is a material constant. In order to examine the validity of the rule under high velocity deformation, the material constant k was calculated from our experimental results. Table 1 shows the value of k taken every 25 μ sec from our experiment in Fig.6. Characters a$\sim$e in the table mean the stress paths shown in the figure and the stress ratios of τ/σ are 2.30, 1.05, 0.80, 0.44 and 0.25 respectively. The mean value of k is 174 sec^{-1} and the deviation from its mean value is less than 12 %. This suggests that the hypothesis holds approximately under dynamic combined stresses.

time (μs)	a	b	c	d	e
50	180	150	180	170	120
75	160	180	170	170	160
100	160	180	180	170	180
125	180	190	180	200	180
150	170	---	180	200	180
mean	170	175	178	182	164

Table 1 Values of k (sec^{-1})

In the case of proportional loading, the ratio $\sigma'_{ij}/\bar{\sigma}$ is constant, and so, we have the following relation from equation (3)

$$\sigma'_{ij} = \bar{\sigma}_s \left(\frac{\dot{\varepsilon}^P_{ij}}{k} + \frac{\sigma'_{ij}}{\bar{\sigma}} \right) = \bar{\sigma}_s \left(\frac{\dot{\varepsilon}^P_{ij}}{k} + C_{ij} \right) \tag{4}$$

or denoting the deviatoric stress corresponding to the strain rate $\dot{\varepsilon}^n_{ij}$ by σ^n_{ij}, we have

$$\sigma^n_{ij} = \sigma^m_{ij} + \frac{\bar{\sigma}_s}{k} \left(\dot{\varepsilon}^n_{ij} - \dot{\varepsilon}^m_{ij} \right) \tag{5}$$

By using eq. (5), the deviatoric stress σ^n_{ij} under the strain rate $\dot{\varepsilon}^n_{ij}$ can be estimated from the experimental datum σ^m_{ij} under the strain rate $\dot{\varepsilon}^m_{ij}$. Figure 7 shows the corrected yield

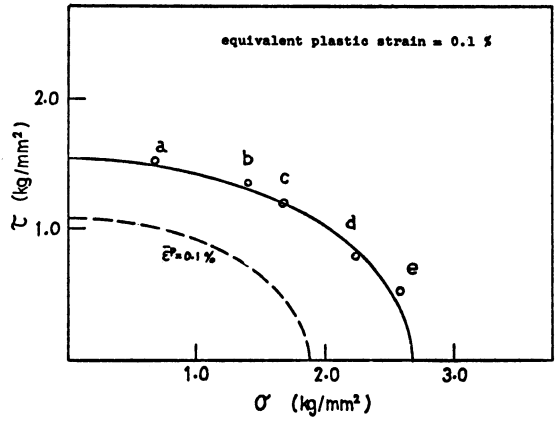

Fig.7 Corrected yield surface under dynamic loading

surface for 0.1 % equivalent strain. Broken line in the figure is Mises' yield surface in the static test and solid line is also an yield ellipse 1.43 times larger than the static one. The estimated stresses for the strain rate of 50 sec^{-1}, ploted in the figure, are almost on the solid line, and so, Mises' criterion holds even in the high velocity deformation.

Equation (1) means that the strain path should be normal to Mises' yield surface and the material obeys Prandtl-Reuss flow law. In our experiments, we have only two kinds of strain, axial strain ε_{11} and shearing strain ε_{12}, and so, the orthogonality condition becomes as follows.

$$k' = \left(\frac{\dot{\varepsilon}_{11}^{P}}{\sigma_{11}'}\right) \Big/ \left(\frac{\dot{\varepsilon}_{12}^{P}}{\sigma_{12}'}\right) = \qquad (6)$$

k' was also obtained from our experiments. Table 2 shows the values of k' taken every 25 μ sec. Total mean value of k' is 1.05. It suggests that the orthogonality condition holds approximately even in the dynamic loading, and the constitutive equation (3) of Perzyna type is valid under combined dynamic stresses.

time (μs)	a	b	c	d	e
50	1.3	0.8	1.4	0.8	1.4
75	1.1	1.1	1.4	0.8	0.8
100	1.1	1.0	1.2	0.8	0.9
125	1.2	0.9	1.2	0.9	1.3
150	1.3	0.9	1.2	0.8	1.1
mean	1.20	0.94	1.28	0.82	1.02

Table 2 Values of k'

Summary of Experimental Results

We have designed a testing machine which is used for applying the impulsive torque and tension simultaneously to the specimen and some experiments were performed for the

strain rate effect on the yield surface of aluminum under biaxial strains less than 0.6 %. In our experiments, different stress paths showed different strain rate histories during deformation, and so, stress values for any definite strain rate were estimated from our experimental data, which were used to obtain the yield surface corresponding to the definite strain rate. Experimental results showed that the dynamic yield surface thus obtained was in good agreement with Mises' criterion and the flow law for annealed aluminum could be expressed in Perzyna type formula by generalized Malvern's hyposesis.

References

1) Cristescu, N.: Dynamic plasticity, (1967), Noth-Holland.

2) Craggs, J.W.: J. Mech. Phys. Solids, Vol. 111 (1957).

3) Clifton, R.J.: Proc. 5th U. S. Nat. Congr. Appl. Mech., 465 (1966).

4) Fukuoka, H.: Proc. of the 16th Japan Nat. Congr. Appl. Mech., 109 (1966).

5) Rice, J.R.: Trans. ASME, Ser. E, 728 (1970).

6) Chatani, A. and Hosho, A.: Preprint of Japan Soc. Mech. Engrs. (in Japanese), 760-12, 216 (1976).

7) Lindholm, U.S. and Yeakley, L.M.: Exp. Mech. 7-1, 1 (1967).

8) Baker, W.E. and Yew, C.H.: Trans. ASME, Ser. E, 917 (1966).

9) Campbel, J.D. and Dowling, A.R.: J. Mech. Phys. Solids, Vol.18, 43 (1970).

10) Perzyna, P.: Quart. Appl. Math., 20, 321 (1963).

An Analysis of Elastic-Plastic Waves by the Continuum Theory of Dislocations

T. JIMMA and T. MASUDA
Department of Mechanical Engineering,
Tokyo Institute of Technology, Ookayama, Meguro-ku, Tokyo, Japan

Summary

Using the fact that stresses and plastic strains are discontinuous across a plane of continuously distributed moving dislocations, longitudinal and torsional waves in a linearly work- hardening material are studied.

1. Stress Field due to Moving Dislocations

Consider a uniform distribution of edge dislocations α_{zx} moving in the x direction as shown in Fig.1. The total Burgers vectors per unit length parallel to the y axis are b (dislocation density). Then, the dislocation stress may be constructed from the summation of a single dislocation, Weertman[1], as follows:

$$\tau_{xy} = \pm \frac{\mu b V^2}{2c_2^2} / \left(1 - \frac{V^2}{c_2^2}\right), \quad c_2 = \sqrt{\mu/\rho}, \qquad (1)$$

where upper signs are in $x<Vt$, lower signs in $x>Vt$. Consider another uniform distribution α_{zy} moving in the x direction as shown in Fig.2. The dislocation density is b, too. Then, following Chow and Mura[2], we have the dislocation stress as follows:

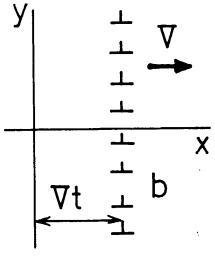

Moving Dislocations α_{zx}
Fig.1

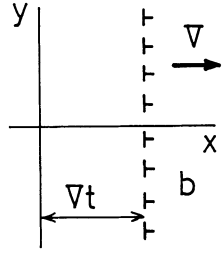

Moving Dislocations α_{zy}
Fig.2

$$\sigma_x = \pm \frac{\mu b V^2}{c_1^2} / (1 - \frac{V^2}{c_1^2}),$$

$$\sigma_y = \pm \mu b (\frac{1}{1-\nu} - \frac{V^2}{c_1^2}) / (1 - \frac{V^2}{c_1^2}), \qquad (2)$$

$$\sigma_z = \nu(\sigma_x + \sigma_y), \quad c_1 = \sqrt{(\lambda+2\mu)/\rho},$$

where upper signs are in $x<Vt$, lower signs in $x>Vt$.
Not only stresses but also plastic strains are discontinuous across the planes of uniformly distributed dislocations in Fig.1 and 2. If we assume null plastic strains in $x>Vt$, the plastic strains in $x<Vt$ are as follows:

$$\gamma^p_{xy} = b \quad \text{for Fig.1,}$$

$$\varepsilon^p_x = -\varepsilon^p_y = b, \ \varepsilon^p_z = 0 \quad \text{for Fig.2.} \qquad (3)$$

2. Torsional Step Loading in a Semi- Infinite Material

Consider the case when the surface of a semi-infinite material($x>0$) is suddenly given a shear stress $\tau_{xy} = \tau_1$ and a shear strain $\gamma_{xy} = \gamma_1$ at time $t = 0$.
The material is assumed to be a linearly work-hardening solid as shown in Fig.3, which satisfies the Tresca yield condition.

$$\tau_{xy} = \mu\gamma_e + F(\gamma_{xy} - \gamma_e) \qquad (4)$$

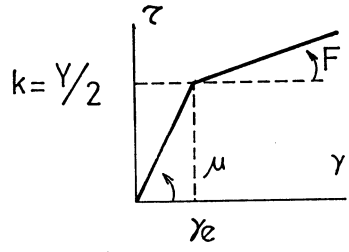

Fig.3

Then, the elastic wave front and the plastic wave front propagates by the speed c_2 and V respectively as shown in Fig. 4. If we assume the uniform distribution of moving dislocations α_{zx} on the plastic wave front, the dislocation stresses are given by (1). Superposing the stress of elastic wave front on the dislocation stress, and more adding a uniform stress on them in order to eliminate the stress in $x>c_2t$ where the elastic wave front does not reach, we have the stresses at time t as follows:

$$\tau_{xy} = \mu\gamma_e + \frac{\mu b V^2}{c_2^2} \Big/ \left(1 - \frac{V^2}{c_2^2}\right) = \tau_1 \quad \text{for } Vt>x>0,$$
$$\tau_{xy} = \mu\gamma_e = k \quad \text{for } c_2 t>x>Vt, \quad \tau_{xy} = 0 \quad \text{for } x>c_2 t. \tag{5}$$

The plastic strain $\gamma^p{}_1$ is equal to b, and we have:

$$\gamma^p{}_1 = b = \left(1 - \frac{F}{\mu}\right)(\gamma_1 - \gamma_e). \tag{6}$$

Moreover, from (4) we have:

$$\tau_1 = \mu\gamma_e + F(\gamma_1 - \gamma_e). \tag{7}$$

From (5), (6) and (7), the propagation speed of plastic wave front is obtained as

$$V = \sqrt{F/\rho}, \tag{8}$$

which coincides with the usual solution.

3. Longitudinal Step Loading in a Semi-Infinite Material

Consider the case when the surface of a semi-infinite material(x>0) is suddenly given a tensile stress $\sigma_x = \sigma_1$ at time t= 0. Since $\sigma_x > \sigma_y = \sigma_z$ and $\varepsilon_y = \varepsilon_z = 0$, the maximum shear stress and strain are expressed by

$$\tau = (\sigma_x - \sigma_y)/2, \quad \gamma = \varepsilon_x. \tag{9}$$

If the material is the linear work-hardening solid as shown in Fig.3,

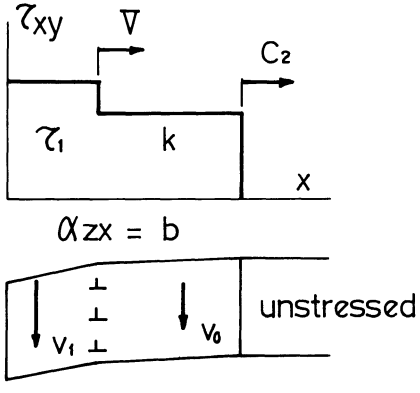

Torsional Step Loading
Fig.4

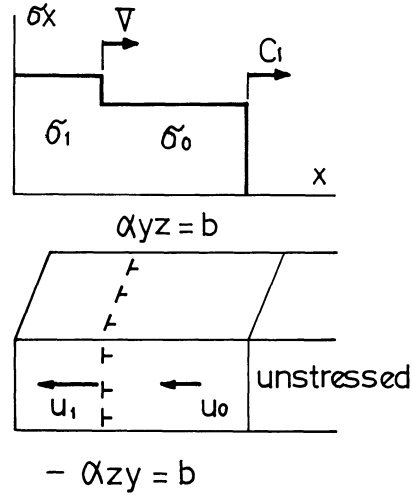

Longitudinal Step Loading
Fig.5

(4) is transformed into

$$\frac{\sigma_x - \sigma_y}{2} = \frac{Y}{2} + F(\varepsilon_x - \frac{Y}{2\mu}), \tag{10}$$

where $Y = 2k$ is a tensile yield stress.

The elastic wave front and the plastic wave front propagates by the speed c_1 and V respectively as shown in Fig.5.

(i) Elastic Wave Front($c_1 t > x > Vt$)

Using the relations of $\varepsilon_y = \varepsilon_z = 0$ and $\sigma_y = \sigma_z$, Hooke's law is reduced to

$$\sigma_x = (\lambda + 2\mu)\varepsilon_x, \quad \sigma_y = \sigma_z = \lambda\varepsilon_x. \tag{11}$$

Hence, the propagation speed of elastic wave front is

$$c_1 = \sqrt{(\lambda + 2\mu)/\rho}. \tag{12}$$

The elastic wave preceding the plastic wave front must satisfy the yield condition so that the stress and the strain in the elastic wave are:

$$\sigma_x = \frac{1-\nu}{1-2\nu} Y = \sigma_0, \quad \sigma_y = \sigma_z = \frac{\nu}{1-\nu}\sigma_0, \quad \varepsilon_x = \frac{Y}{2\mu}. \tag{13}$$

(ii) Plastic Wave($Vt > x > 0$)

If we assume two uniform distributions of moving dislocations - $\alpha_{zy} = \alpha_{yz} = b$ on the plastic wave front as shown in Fig.5, the dislocation stresses become

$$\begin{aligned} \sigma_x &= \pm \frac{2\mu b V^2}{c_1^2}/(1 - \frac{V^2}{c_1^2}), \\ \sigma_y &= \sigma_z = \pm \mu b(\frac{1+\nu}{1-\nu} - \frac{V^2}{c_1^2})/(1 - \frac{V^2}{c_1^2}), \end{aligned} \tag{14}$$

where upper signs are in $x < Vt$, and lower signs in $x > Vt$. Superposing (13) on (14), and more adding a uniform stress in order to eliminate the stress in the region of $x > c_1 t$, we have

$$\begin{aligned} \sigma_x &= \sigma_0 + \frac{4\mu b V^2}{c_1^2}/(1 - \frac{V^2}{c_1^2}), \\ \sigma_y &= \sigma_z = \frac{\nu}{1-\nu}\sigma_0 + 2\mu b(\frac{1+\nu}{1-\nu} - \frac{V^2}{c_1^2})/(1 - \frac{V^2}{c_1^2}). \end{aligned} \tag{15}$$

The strains in the plastic region are:

$$\varepsilon_x = \varepsilon^p{}_x + \varepsilon^e{}_x = 2b + [\sigma_x - 2\nu\sigma_y]/E,$$
$$\varepsilon_y = \varepsilon^p{}_y + \varepsilon^e{}_y = -b + [(1-\nu)\sigma_y - \nu\sigma_x]/E = 0. \tag{16}$$

Solving (10) and (16), we have:

$$\sigma_x = \left[\frac{E}{3(1-2\nu)} + \frac{4F}{3}\right]\varepsilon_x + \frac{2}{3}Y\left(1 - \frac{F}{\mu}\right),$$
$$\sigma_y = \left[\frac{E}{3(1-2\nu)} - \frac{2F}{3}\right]\varepsilon_x - \frac{2}{3}Y\left(1 - \frac{F}{\mu}\right), \tag{17}$$

$$\varepsilon^p{}_x = 2b = \frac{2}{3}\left(1 - \frac{F}{\mu}\right)\left(\varepsilon_x - \frac{Y}{2\mu}\right). \tag{18}$$

Substituting (15) and (18) into (10), we have the propagation speed of plastic wave:

$$V^2 = \left[\frac{4F}{3} + \frac{E}{3(1-2\mu)}\right]/\rho. \tag{19}$$

(19) coincides with the solution obtained by using the relation of $V = \sqrt{(\partial\sigma_x/\partial\varepsilon_x)/\rho}$ from (17).

4. Interaction of Longitudinal Waves

4.1 Interaction of Plastic Waves

Consider the interaction of plastic waves σ_1 and σ_2 as shown in Fig.6. Let the corresponding strain ε_x be ε_1 and ε_2. Then, the dislocation densities b_1 and b_2 are given from (18) as

$$b_{1,2} = \frac{1}{3}\left(1 - \frac{F}{\mu}\right)\left(\varepsilon_{1,2} - \frac{Y}{2\mu}\right). \tag{20}$$

The stresses at time t_1 in the region of II and III are obtained by substituting b_1 or b_2 in place of b in (15). At time t_2 after interaction, we can assume that two dislocations b_1 and b_2 pass each other as shown in Fig.6. Then, the stresses in region IV can be obtained by substituting $(b_1 + b_2)$ in place of b in (15).

$$\sigma_3 = \sigma_1 + \sigma_2 - \sigma_0 \tag{21}$$

The plastic strains in the region of II and III are:

$$\varepsilon^p_x = 2b_{1,2},\quad \varepsilon^p_y = \varepsilon^p_z = -b_{1,2}. \tag{22}$$

The plastic strains in region IV are:

$$\varepsilon^p_x = 2(b_1 + b_2),\quad \varepsilon^p_y = \varepsilon^p_z = -(b_1 + b_2). \tag{23}$$

(21) may be obtained from momentum considerations.

4.2 Interaction of Plastic Wave and Unloading Wave

We can solve the interaction in a similar way in which a part of dislocations stop moving at the intersection plane but the remains continue moving. In the case of weak plastic waves, it will be assumed that all the dislocations stop moving at the intersection plane.

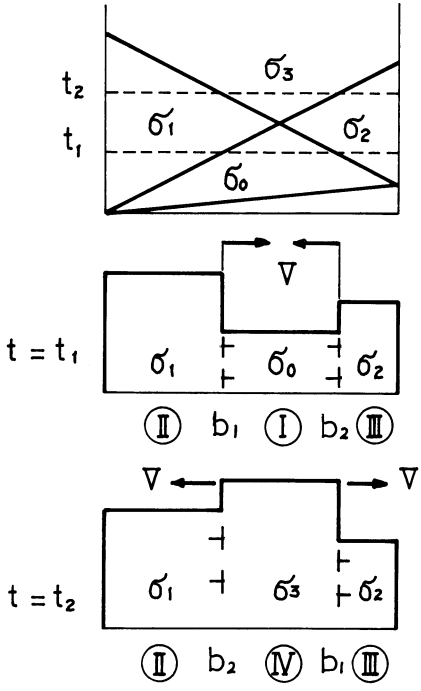

Interaction of Plastic Waves
Fig.6

We may extend this method to the analysis of the combined longitudinal and torsional step loading of a semi-infinite thin wall tube.

Acknowledgement

The authors express their sincere thanks to Prof. T. Mura for the guidance to the continuum theory of dislocations.

References

1 Weertman,J.: Response of Metals to High Velocity Deformation (New York: Interscience Publisher), 1961.

2 Chow,T.W.; Mura,T.: Plastic Bending of a Beam and the Theory of Dislocations.

Recent Results in Micromechanics

T. MURA

Materials Research Center and
Department of Civil Engineering
Northwestern University, Evanston, Illinois 60201

Summary

The elastic and plastic fields (displacement, stress, plastic strain) are investigated for a uniformly moving inclusion and a dislocation loop. From the results of analysis a new concept of essential distributions of dislocations is proposed. Finally, the energy release rate of a moving crack is given by the J integral and dislocation density tensors.

Introduction

Eshelby's inclusion problem [1] is extended to a dynamic case where an ellipsoidal inclusion is moving with a constant velocity. Since the stress field inside the inclusion becomes constant, the equivalent inclusion method [1] can be applied to the corresponding inhomogeneity problem. High velocity motion of interstitial atoms, vacancies, and neutrons during nuclear fission can be considered as an application. Another application is to estimate the stress concentration at the tip of a moving crack of paraboloidal shape, which is a special case of an ellipsoid.

A uniformly moving dislocation loop is considered with aim of application to high speed punching problems, where displacement discontinuity surface is created at the punch edge and propagates to the direction of punching. The surface condition for the semi-infinite block is approximately satisfied by considering two dislocations moving opposite directions.

A new concept of the essential dislocations is introduced which provides a convenient method to estimate

---

This research was partially supported by U.S. Army Grant No. DAAG 29-77-G-0092 to Northwestern University.

associated plastic strains from a given statically determinate stress field.

Finally, the energy release rate for a crack propagation is considered in connection with J integral and dislocation distribution. It is found that the energy release rate is the sum of J integrals and the total integration of Peach-Koehler force acting on dislocations.

Uniformly Moving Inclusions

When an infinitely extended homogeneous material develops a uniformly distributed eigenstrain (phase transformation strain, stress free strain, thermal expansion strain, plastic strain, etc.) in a domain Ω, an eigenstress (internal stress, self-equilibrium stress, residual stress, thermal stress, etc.) is induced in both inside Ω (inclusion) and outside Ω (matrix). The stress inside Ω becomes constant when Ω is ellipsoidal.

It will be shown that this stress uniformity inside Ω is also valid even when Ω is uniformly moving.

The displacement field $u_i(\underset{\sim}{x},t)$ in an infinitely extended homogeneous elastic medium caused by eigenstrain $\varepsilon^*_{ij}(\underset{\sim}{x},t)$ is expressed as (e.g. [2])

$$u_i(\underset{\sim}{x},t) = -(2\pi)^{-4} \frac{\partial}{\partial x_\ell} \int\int\int_{-\infty}^{\infty} C_{j\ell mn} \varepsilon^*_{nm}(\underset{\sim}{x}',t') N_{ij}(\underset{\sim}{\xi},\omega) D^{-1}(\underset{\sim}{\xi},\omega)$$

$$\exp\{i\underset{\sim}{\xi}\cdot(\underset{\sim}{x}-\underset{\sim}{x}') + i\omega(t-t')\} d\underset{\sim}{\xi} d\omega d\underset{\sim}{x}' dt' \qquad (1)$$

where $C_{j\ell mn}$ are the elastic moduli, $d\underset{\sim}{\xi} = d\xi_1 d\xi_2 d\xi_3$, $d\underset{\sim}{x}' = dx_1' dx_2' dx_3'$, D the determinant of the matrix with ij element $(C_{ipjq}\xi_p\xi_q - \rho\omega^2\delta_{ij})$, N_{ij} a cofactor of this matrix, ρ the density of the material, and δ_{ij} is the Kronecker delta.

When the distribution of ε^*_{nm} is moving with a constant velocity $\underset{\sim}{V}$, (1) can be written as

$$u_i(\bar{\underset{\sim}{x}}) = -i(2\pi)^{-3}\int\int_{-\infty}^{\infty}\xi_\ell C_{j\ell mn}\varepsilon^*_{nm}(\underset{\sim}{y})N_{ij}(\xi,-\xi\cdot\underset{\sim}{V})D^{-1}(\xi,-\xi\cdot\underset{\sim}{V})$$

$$\exp\{i\underset{\sim}{\xi}\cdot(\bar{\underset{\sim}{x}} - \underset{\sim}{y})\}d\underset{\sim}{\xi}d\underset{\sim}{y} \qquad (2)$$

and the associated stress components are

$$\sigma_{pq}(\bar{\underset{\sim}{x}}) = (2\pi)^{-3} C_{pqmn}\int\int_{-\infty}^{\infty}[\xi_n\xi_\ell C_{k\ell ij}\varepsilon^*_{ji}(\underset{\sim}{y})N_{km}(\xi,-\xi\cdot\underset{\sim}{V})D^{-1}(\xi,-\xi\cdot\underset{\sim}{V})$$

$$- \varepsilon^*_{nm}(\underset{\sim}{y})]\exp\{i\underset{\sim}{\xi}\cdot(\bar{\underset{\sim}{x}} - \underset{\sim}{y})\}d\underset{\sim}{\xi}d\underset{\sim}{y} \qquad (3)$$

where $\bar{\underset{\sim}{x}} = \underset{\sim}{x} - \underset{\sim}{V}t$. Furthermore, if ε^*_{nm} is uniformly defined in an ellipsoidal domain Ω, and only the point in Ω is considered, (2) becomes

$$u_i(\bar{\underset{\sim}{x}}) = (4\pi)^{-1} C_{j\ell mn}\varepsilon^*_{nm}\bar{x}_k\bar{G}_{ijk\ell} \qquad (4)$$

with

$$\bar{G}_{ijk\ell} = \int_{S^2} N_{ij}(\bar{\xi},-\bar{\xi}\cdot\underset{\sim}{V})D^{-1}(\bar{\xi},-\bar{\xi}\cdot\underset{\sim}{V})\bar{\xi}_k\bar{\xi}_\ell dS(\bar{\zeta}). \qquad (5)$$

In the above expression, S^2 is a unit sphere $\bar{\underset{\sim}{\xi}}\cdot\bar{\underset{\sim}{\xi}} = 1$ and $dS(\bar{\underset{\sim}{\zeta}})$ is the surface element of the unit sphere. The vectors $\bar{\xi}$ and $\bar{\zeta}$ are unit vectors related by

$$\bar{\zeta}_1 = \zeta_1/\zeta, \quad \bar{\zeta}_2 = \zeta_2/\zeta, \quad \bar{\zeta}_3 = \zeta_3/\zeta$$

$$\zeta_1 = a_1\bar{\xi}_1, \quad \zeta_2 = a_2\bar{\xi}_2, \quad \zeta_3 = a_3\bar{\xi}_3$$

$$\zeta = (\zeta_1^2 + \zeta_2^2 + \zeta_3^2)^{1/2} \qquad (6)$$

where a_1, a_2, a_3 are the principal axes of the ellipsoid. The integrals (5) can be easily evaluated numerically[3].

An interesting result obtained from (4) is that the stress components inside the inclusion are uniform (constant). Therefore, the equivalent inclusion method [1] can be easily applied to a uniformly moving inhomogeneity particle under a constant applied stress. The inhomogeneity particle has different elastic moduli than those of the matrix. The stress disturbance of the applied stress due to the inhomogeneity can be simulated by the eigenstress by choosing proper eigenstrains.

The stress just outside Ω can be evaluated from the stress field in Ω which is easily obtained from (4). The stress concentration at the tip of a moving paraboloidal crack, therefore, can be obtained as a special

case. The paraboloid is obtained from an ellipsoid by taking $a_1 \to \infty$, where the distance between a focus and the tip of the ellipsoid is kept constant.

Uniformly Moving Dislocations

When dislocations are continuously distributed in a space, the dislocation density at an arbitrary point is expressed by Kröner's formula [4]:

$$\alpha_{hi} = -\varepsilon_{h\ell k}\beta^*_{ki,\ell} \tag{7}$$

where $\varepsilon_{h\ell k}$ is the permutation tensor and β^*_{ki} is the plastic distortion. The plastic strain (eigenstrain) is

$$\varepsilon^*_{ki} = (1/2)(\beta^*_{ki} + \beta^*_{ik}). \tag{8}$$

α_{hi} is the density of the dislocations whose direction vector and Burgers vector are in the directions of the x_h and x_i axes, respectively.

When the dislocation distribution is moving with a constant velocity $\underset{\sim}{V}$, the time rate of the plastic distortion is given by [5]

$$\dot{\beta}^*_{ji} = -\varepsilon_{jnh}V_n\alpha_{hi}. \tag{9}$$

The displacement field in an infinite medium is also expressed by (2). If it is expressed in terms of α_{hi} instead of ε^*_{nm}, by using (12) and (13) we have

$$u_m(\underset{\sim}{\bar{x}}) = -(2\pi)^{-3}\int\int_{-\infty}^{\infty} C_{k\ell ij}\varepsilon_{jnh}\alpha_{hi}(\underset{\sim}{y})N_{mk}(\underset{\sim}{\xi},-\underset{\sim}{\xi}\cdot\underset{\sim}{V})D^{-1}(\underset{\sim}{\xi},-\underset{\sim}{\xi}\cdot\underset{\sim}{V})$$
$$\xi_\ell V_n(\underset{\sim}{\xi}\cdot\underset{\sim}{V})^{-1}\exp\{i\underset{\sim}{\xi}\cdot(\underset{\sim}{\bar{x}} - \underset{\sim}{y})\}d\underset{\sim}{\xi}d\underset{\sim}{y}. \tag{10}$$

The plastic distortion is obtained as

$$\beta^*_{ji}(\underset{\sim}{\bar{x}}) = (2\pi)^{-3}\int\int_{-\infty}^{\infty}\varepsilon_{jnh}\alpha_{hi}(\underset{\sim}{y})V_n(i\underset{\sim}{\xi}\cdot\underset{\sim}{V})^{-1}\exp\{i\underset{\sim}{\xi}\cdot(\underset{\sim}{\bar{x}} - \underset{\sim}{y})\}d\underset{\sim}{\xi}d\underset{\sim}{y} \tag{11}$$

and the stress field becomes

$$\sigma_{pq}(\underset{\sim}{\bar{x}}) = i(2\pi)^{-3}C_{pqmn}\int\int_{-\infty}^{\infty}[\xi_\ell C_{k\ell ij}\varepsilon_{njh}\alpha_{ni}(\underset{\sim}{y})N_{km}(\underset{\sim}{\xi},-\underset{\sim}{\xi}\cdot\underset{\sim}{V})$$
$$- \rho(\underset{\sim}{\xi}\cdot\underset{\sim}{V})\varepsilon_{stn}V_s\alpha_{ti}(\underset{\sim}{y})N_{im}(\underset{\sim}{\xi},-\underset{\sim}{\xi}\cdot\underset{\sim}{V})]D^{-1}(\underset{\sim}{\xi},-\underset{\sim}{\xi}\cdot\underset{\sim}{V})$$
$$\exp\{i\underset{\sim}{\xi}\cdot(\underset{\sim}{\bar{x}} - \underset{\sim}{y})\}d\underset{\sim}{\xi}d\underset{\sim}{y}. \tag{12}$$

All the above results can be directly applied to a dislocation loop when we write

$$\int_{-\infty}^{\infty} [\quad] \alpha_{hi}(\underset{\sim}{y}) dy = \oint_{L} [\quad] \nu_h b_i d\ell \tag{13}$$

where $\underset{\sim}{\nu}$, $\underset{\sim}{b}$ are the tangential unit vector along the dislocation loop L and the Burgers vector, respectively, and $d\ell$ is the line element of the dislocation. More explicit form was reported in [2] for a circular dislocation loop. The result will be applied to the high speed punching problems in plastic fubrication. The static solution can be obtained by taking $\underset{\sim}{V} \to 0$ in (10), (11), and (12).

Dislocations and Plasticity

Since Mura's work [6] on the relation between the continuum plasticity and dislocation theory, several papers [7-11] on the related subjects have been published. However, no major breakthrough seems to be made for its applications. One of the difficulties is that equation (7) is not expressed in terms of ε^*_{mn}. As the present author pointed out earlier [12], the anti-symmetric plastic distortion ($\beta^*_{mn} = -\beta^*_{nm}$) provides the impotent distribution of dislocations which has no displacement and no stress fields. This fact can be easily seen from (2) and (3) since $\varepsilon^*_{nm} = 0$. Recently we have developed further classification of dislocation distributions. We write

$$u_{i,j} = \beta^*_{ji} + \beta_{ji} \tag{14}$$

where

$$e_{ij} = (1/2)(\beta_{ij} + \beta_{ji}) \tag{15}$$

is the elastic strain. When (7) is substituted from (14), we have

$$\alpha_{hi} = \varepsilon_{h\ell k} \beta_{ki,\ell} \tag{16}$$

or

$$\alpha_{hi} = \varepsilon_{h\ell k} e_{ki,\ell} + \varepsilon_{h\ell k} \omega_{ki,\ell} \tag{17}$$

where

$$\omega_{ki} = (1/2)(\beta_{ki} - \beta_{ik}). \tag{18}$$

The second term in (17) may be called Nye's dislocation density tensor [4] since it does not produce any stress field but displacement field by rotation. It is easily proved for the static case by using the property of Green's function: $C_{k\ell ij}\xi_\ell \xi_j N_{km} D^{-1} = \delta_{im}$. Namely, when $\alpha_{hi} = \varepsilon_{h\ell k}\omega_{ki,\ell}$ is substituted into (12) for $\dot{V} = 0$, becomes zero whenever $\omega_{ki} = -\omega_{ik}$. A new proposal here is to write

$$\alpha_{hi} = \varepsilon_{h\ell k} e_{ki,\ell} \tag{19}$$

since Nye's dislocations do not contribute to any stress field. Let us call the dislocations defined by (19) the essential distribution of dislocations. Since the elastic strain is related to the stress components by

$$e_{ki} = C^{-1}_{kipq}\sigma_{pq} \tag{20}$$

where C^{-1}_{kipq} are the elastic compliances, (19) states that the essential distribution of dislocations is uniquely determined when the stress field is given. An example is shown in Fig. 1 for the tip of a crack in the plane strain state. Since the slip line theory provides the

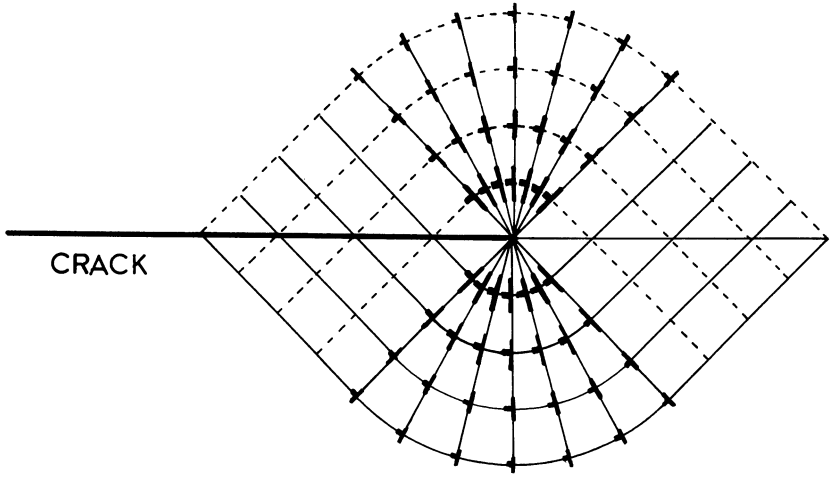

Fig. 1

stress state in the neighborhood of the crack tip for the perfectly elasto-plastic solid, (19) and (20) give the distribution of essential dislocations in the fan-shaped plastic domains as shown in Fig. 1. No dislocation distribution is found in the triangle plastic domains. The strength of the dislocations is obtained as $2(1-\nu)k/\mu r$, where ν is Poisson's ratio, k the yield shear stress, μ the shear modulus and r is the distance from the tip of the crack. The importance of the example is that a statically determined stress field provides information about the plastic deformation through distributions of dislocations. The plastic strain is not uniquely determined but it is reasonably constructed from a dislocation distribution. For an instance, we have

$$\varepsilon^{*}_{ji}(\underset{\sim}{x}) = (2\pi)^{-3}\int\int_{-\infty}^{\infty}(1/2)\{\varepsilon_{jnh}\alpha_{hi}(\underset{\sim}{y}) + \varepsilon_{inh}\alpha_{hj}(\underset{\sim}{y})\}$$

$$v_n(i\underset{\sim}{\xi}\cdot\underset{\sim}{v})^{-1}\exp\{i\underset{\sim}{\xi}\cdot(\underset{\sim}{x}-\underset{\sim}{y})\}d\underset{\sim}{\xi}d\underset{\sim}{y} \qquad (21)$$

which has been obtained from (11) by taking $\underset{\sim}{V} \to 0$ and $V_n/\underset{\sim}{V} \to v_n/\underset{\sim}{v}$. The unit vector $\underset{\sim}{v}$ is arbitrarily given. The physical meaning of $\underset{\sim}{v}$ is the direction of motion by which the dislocation has been brought to the present state from the infinite points in the space. It should be emphasized that the dislocation density is a state quantity while the plastic strain is not.

J Integrals

Equation (9) has an interesting application to fracture mechanics. Let us consider a system where A is a crack, S the boundary of material, and F is the applied force. The displacement, stress, plastic strain at an instant are denoted by u_i, σ_{ij}, and ε^{*}_{ij}.

When the crack A grows by δA these field quantities are changed by δu_i, $\delta\sigma_{ij}$, and $\delta\varepsilon^{*}_{ij}$. The Gauss theorem of integration leads to

$$\int_S F_i\delta u_i dS = \int_V \sigma_{ij}\delta u_{i,j}dV - \int_{\delta A}\sigma_{ij}n_j\delta u_i dS \qquad (22)$$

where the following conditions have been used:

$$\sigma_{ij}n_j = F_i \quad \text{on S}$$
$$\sigma_{ij}n_j = 0 \quad \text{on A}$$
$$\sigma_{ij,j} = 0 \quad \text{in V} \tag{23}$$

where $\underset{\sim}{n}$ is the normal vector on the surfaces and V is the domain of the material. There are relations:

$$\varepsilon_{ij} = (1/2)(u_{i,j} + u_{j,i}) = e_{ij} + \varepsilon^*_{ij}$$
$$\delta\varepsilon_{ij} = (1/2)(\delta u_{i,j} + \delta u_{j,i}) = \delta e_{ij} + \delta\varepsilon^*_{ij}. \tag{24}$$

Equations (22) and (24) give

$$\int_S F_i\delta u_i dS - \int_V \sigma_{ij}\delta e_{ij}dV = \int_V \sigma_{ij}\delta\varepsilon^*_{ij}dV - \int_{\delta A} \sigma_{ij}n_j\delta u_i dS. \tag{25}$$

It has been shown by Eshelby [13] and Rice [14] that

$$-\int_{\delta A} \sigma_{ij}n_j\delta u_i dS = J_\ell\delta\xi_\ell \tag{26}$$

where $\delta\underset{\sim}{\xi}$ is the displacement of the crack tip during the crack increase δA, that is, $\delta\xi = \delta A$. J_ℓ is so called J integral defined by

$$J_\ell = -\int_S \sigma_{ij}u_{i,\ell}n_j dS + \int_S Wn_\ell dS \tag{27}$$

where

$$W = \int_0^{\varepsilon_{ij}} \sigma_{ij}d\varepsilon_{ij}. \tag{28}$$

If dislocations in the neighborhood of the crack tip are displaced with the same amount as the displacement of the crack tip (assumption), (9) can be written as

$$\delta\beta^*_{ji} = -\varepsilon_{j\ell h}\delta\xi_\ell\alpha_{hi}. \tag{29}$$

Then (25) can be written as

$$\partial G/\partial\xi_\ell = -\int_V \sigma_{ij}\varepsilon_{j\ell h}\alpha_{hi}dV + J_\ell \tag{30}$$

where

$$G = \int_S F_i u_i dS - \frac{1}{2} \int_V \sigma_{ij} e_{ij} dV. \tag{31}$$

Equation (30) means that the energy release rate is equal to the sum of the total Peach-Koehler force acting on the dislocations and the J integral. G is the minus of mechanical potential energy. δG is equal to the energy dissipated or the energy released.

Literature

1 Eshelby, J. D.: The determination of the elastic field of an ellipsoidal inclusion. Proc. Roy Soc. A 241 (1957) 376-396.

2 Mura, T.: Method of continuously distributed dislocations. Mathematical Theory of Dislocations, ed. by T. Mura, ASME 1969.

3 Mura, T.; Cheng, P. C.: Elastic fields of uniformly moving inclusions. Unpublished paper. See also P. C. Cheng's Ph.D. Thesis, Northwestern University, 1977.

4 Kröner, E.: Kontinuumstheorie der Versetzungen und Eigenspannungen. Springer 1958.

5 Mura, T.: Continuous distribution of moving dislocations. Phil. Mag. 8 (1963) 843-857.

6 Mura, T.: Continuum theory of plasticity and dislocations. Int. J. Engng. Sci. 5 (1967) 341-351.

7 Eisenberg, M. A.: On the relation between continuum plasticity and dislocation theory. Int. J. Engng. Sci. 8 (1970) 261-271.

8 Owen, D. R. J.: The application of dislocation theory to the determination of stress-strain relationships of composite materials. Int. J. Non-linear Mechanics 6 (1971) 167-175.

9 Shioya, T.; Shioiri, J.: Elastic-plastic analysis of the yield process in mild steel. J. Mech. Phys. Solids 24 (1976) 187-204.

10 Jimma, T.: private communication. Progress of micro-consideration on plasticity. Seimitsu Kikai 42 (1976) 73-80.

11 Weng, G. J.; Philips, A.: On the kinematics of continuous distribution of dislocations in plasticity. Int. J. Engng. Sci. 14 (1976) 65-73.

12 Mura, T.: Continuum theory of dislocations and plasticity. Mechanics of Generalized Continua, ed. by E. Kröner. Springer 1968.

13 Eshelby, J. D.: The force on an elastic singularity. Phil. Trans. Roy. Soc. A 244 (1951) 87-112.

14 Rice, J. R.: A path independent integral and the approximate analysis of strain concentration by notches and cracks. J. Appl. Mech. 35 (1968) 379-386.

On Supersonic and Transonic Impact of Solids*

T. C. T. TING

Department of Materials Engineering
University of Illinois at Chicago Circle
Chicago, Illinois 60680, U. S. A.

Introduction

Consider a one-dimensional wave such as longitudinal wave in a semi-infinite rod or plane strain wave in a half-space which occupies $x \geq 0$. Let the longitudinal stress σ be a given function of the longitudinal strain ε. Moreover, let the $\sigma \sim \varepsilon$ curve be concave downward to the ε-axis. Figure 1 shows an example of the $\sigma \sim \varepsilon$ curve for a commercially pure aluminum. If the wave is generated by a compressive load which is a step function in time t applied at $x = 0$, it is well-known that the solution to the problem is a simple wave solution in which σ, ε and the particle velocity v are constants along the straight lines:

$$x = ct\,, \tag{1}$$

where c is the characteristic wave speed given by

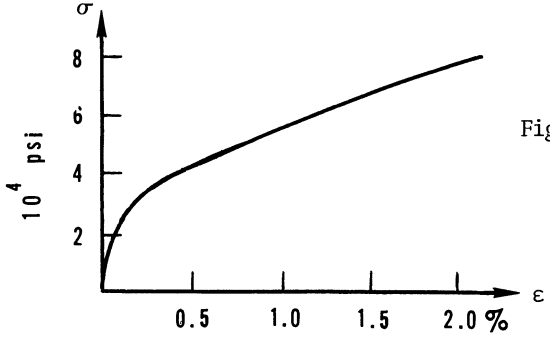

Fig. 1 Stress-strain curve for commercially pure aluminum

*This work is supported by the U.S.Army Research Office-Durham under Grant DAAG 29-G-0121 to the University of Illinois at Chicago Circle.

$$c = \sqrt{d\sigma/\rho d\varepsilon} \ , \tag{2}$$

in which ρ is the mass density. Moreover,

$$v = -\int_0^{\sigma} \frac{d\sigma}{\rho c} = -\int_0^{\varepsilon} c \, d\varepsilon \tag{3}$$

and the particle velocity along any characteristic $x = ct$ can be determined once σ or ε along that characteristic is obtained from (1) and (2). In particular, the impact velocity at $x = 0$ can be obtained in terms of the applied stress at $x = 0$ by using (3).

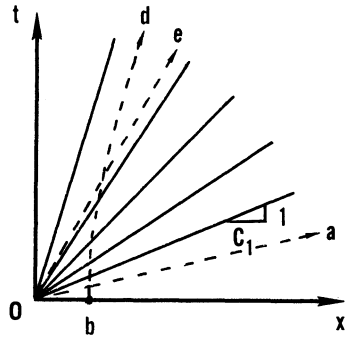

Fig. 2

Let c_1 be the wave speed at $\sigma = 0$. The disturbance at $x = 0$ is propagated at the speed c_1. In the $x \sim t$ plane, the region below $x = c_1 t$ is at rest, Fig. 2. This is irrespective of the impact velocity at $x = 0$. However, the impact velocity obtained from (3) for a given impact load may exceed the wave speed c_1. Thus, at a supersonic impact, the particle at $x = 0$ moves faster than the speed of disturbance c_1 as shown by the dotted line oa in Fig. 2. This creates a physically unacceptable phenomenon in which the particle at $x = 0$ moves through other particles at $x \neq 0$ such as the particle at b whose trajectory in the $x \sim t$ plane is bd.

What went wrong? For the $\sigma \sim \varepsilon$ curve shown in Fig. 1, $c_1 = 16{,}500$ ft/sec and an impact velocity of this magnitude may not be easy to produce in experiments. However, the problem starts way before the impact velocity is supersonic. At a transonic impact in which the impact velocity at $x = 0$ is less than c_1 but larger than the smallest wave speed in the simple wave region, the particle at $x = 0$ still moves through other particles at $x \neq 0$ such as the path oe in Fig. 2. For the $\sigma \sim \varepsilon$ curve shown in Fig. 1, the transonic impact starts at the velocity 1850 ft/sec. This magnitude is not difficult to produce in experiments.

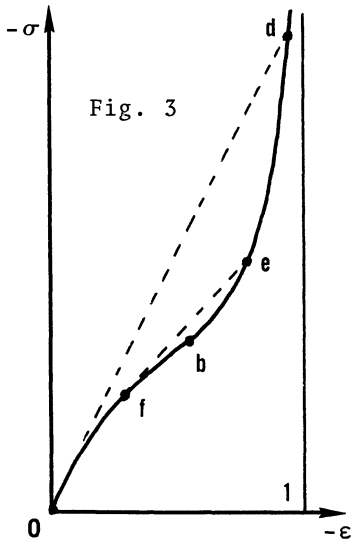

Fig. 3

Again, what went wrong? By considering the rate effect does not explain the problem. By limiting the absolute value of ε to be less than unity does not solve the problem either because in the $\sigma \sim \varepsilon$ curve shown in Fig. 1 the transonic impact starts at $-\varepsilon = 0.675$. By allowing the $\sigma \sim \varepsilon$ curve to consist of one concave downward segment and one concave upward segment as shown in Fig. 3 still cannot explain the problem although it is a more realistic $\sigma \sim \varepsilon$ curve and is a step toward explaining the paradox.

Correct Analysis

Let the particle which is at the position X at time $t = 0$ move to the position x at time t. Hence,

$$x = x(X,t) \ . \tag{4}$$

The strain can be defined in terms of the deformation gradient $\partial x/\partial X$. Of several possible definitions for ε, we will define

$$\varepsilon = \frac{\partial x}{\partial X} - 1. \tag{5}$$

Since any finite length of material cannot be compressed to zero,

$$1 + \varepsilon = \frac{\partial x}{\partial X} > 0. \tag{6}$$

At $\varepsilon = -1$, the material is compressed to zero length. This implies that an infinite stress is required. Hence we assume that the $\sigma \sim \varepsilon$ curve be given by Fig. 3 in which point b is an inflection point.

Let σ, ε and v be functions of x and t. The equation of motion for the finite deformation is

$$\sigma_{,x} = \rho(v_{,t} + vv_{,x}) \ , \tag{7}$$

where ρ is the mass density at any time t and is related to the initial mass density ρ_o by

$$\rho = \rho_o/(1 + \varepsilon) \ . \tag{8}$$

Combining (7) and (8), we obtain

$$\frac{d\sigma}{d\varepsilon}\varepsilon_{,x} = \frac{\rho_o}{1+\varepsilon}(v_{,t} + vv_{,x}) \ . \tag{9}$$

The material continuity is

$$\dot{\varepsilon} = \frac{\partial v}{\partial X} \ , \tag{10}$$

which, in terms of the independent variables x and t, becomes

$$\varepsilon_{,t} + v\varepsilon_{,x} = v_{,x}(1+\varepsilon) \ , \tag{11}$$

Equations (9) and (11) form a system of differential equations for ε and v. The boundary condition for this system is

$$v = \text{constant} = v_o \ , \quad \text{say,} \quad \text{on } x = v_o t \ . \tag{12}$$

It is not difficult to show that the solution of (9), (11) and (12) is a simple wave solution in which v and ε (and hence σ) are constants along the straight lines

$$x = c^* t \ , \tag{13}$$

$$c^* = v + (1+\varepsilon)c \ , \tag{14}$$

where v and c are given by (2) and (3). Notice that c^* is the true wave speed which, in view of (6), is always larger than the particle velocity v. However, the particle velocity v at $X = 0$ can still be larger than c_1. We will explain this by an example later on.

Alternate Analysis

In writing the equations of motion and the continuity, we could have used X and t as the independent variables. We then have

$$\frac{\partial \sigma}{\partial X} = \rho_o \dot{v} \ , \tag{15}$$

$$\frac{d\varepsilon}{d\sigma}\dot{\sigma} = \dot{\varepsilon} = \frac{\partial v}{\partial X} \ . \tag{16}$$

The solution of (15) and (16) subjected to a step load at X = 0 is a simple wave solution in which σ, ε and v are constants along

$$X = ct \ , \tag{17}$$

where c and v are given by (2) and (3). To obtain x(X,t), we integrate the velocity function:

$$x(X,t) - X = \int_0^t v(X/t')\, dt' = X \int_{c_1}^{c} v(c')\, d(1/c') \ . \tag{18}$$

Integrating by parts and using (3), we have

$$x(X,t) = t\{v(X/t) + (1 + \varepsilon(X/t))X/t\} \ . \tag{19}$$

This is identical to (13) and (14). Thus, the characteristics in the X ~ t plane (17) is transformed into the characteristics in the x ~ t plane (13). For a given initial and boundary value problem, it is in general simpler to solve (15) and (16) than (9) and (11). However, the solution in the X ~ t plane has to be transformed to the x ~ t plane for physical interpretations such as the wave speed.

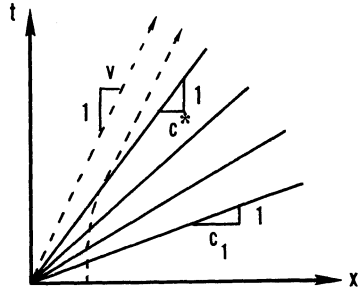

Fig. 4 $\sigma(0,t) = \sigma_f H(t)$

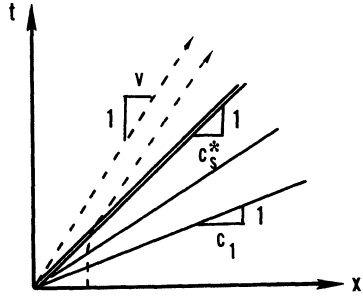

Fig. 5 $\sigma(0,t) = \sigma_e H(t)$

Examples

Figures 4 to 6 show the simple wave solutions in the x ~ t plane when the applied load at X = 0 corresponds to the stress at point f, e and d (Fig. 3), respectively. The particle trajectories at X = 0 and X ≠ 0 obtained from (19) are shown by the dotted lines. For the case shown in Fig. 5, a shock wave speed

$$c_s = \sqrt{\frac{\sigma_e - \sigma_f}{\rho_o(\varepsilon_e - \varepsilon_f)}} \tag{20}$$

is generated. However, this speed is referred to the X ~ t plane. In the x ~ t plane, the true shock wave speed c_s^* is

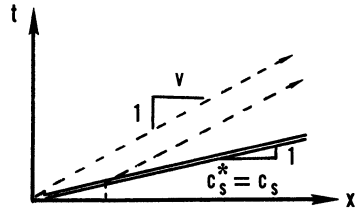

Fig. 6 $\sigma(0,t) = \sigma_d H(t)$

$$c_s^* = v + (1+\varepsilon)c_s \quad . \tag{21}$$

For the case shown in Fig. 6, the shock wave speed

$$c_s = \sqrt{\frac{\sigma_d}{\rho_o \varepsilon_d}} \tag{22}$$

exceeds the speed of disturbance c_1. Again, the true shock wave speed c_s^* should be given by (21). It should be pointed out that although v and ε are discontinuous across a shock wave, $v + \varepsilon c_s$ is continuous. Hence, (21) can be applied to either side of a shock wave. For Fig. 6, v and ε are zero on the lower side of the shock wave and hence $c_s^* = c_s$ for Fig. 6.

Concluding Remarks

The relation between c* and c given by (14) could have been obtained without the presence of a simple wave solution. In fact, (14) is a kinematical relation and is independent of material properties. To see this, we start with (4) and let X be a function of time t such that differentiation of the latter with respect to t yields the wave speed c in the X ~ t plane. With this stipulation, differentiation of (4) with respect to t is

$$c^* = \frac{dx}{dt} = \dot{x} + \frac{\partial x}{\partial X}\dot{X} \tag{23}$$

which is identical to (14).

The three-dimensional counterpart of (14) can be shown to be

$$\underset{\sim}{c}^* = \underset{\sim}{v} + \underset{\sim}{F}\,\underset{\sim}{c}, \qquad \underset{\sim}{F} = \underset{\sim}{x}\nabla \quad . \tag{24}$$

Equation (24) can be applied to the case when $\underset{\sim}{c}$ is the normal wave speed or to the case when $\underset{\sim}{c}$ is the characteristic ray velocity.

Identification of Dynamic Properties and Wave Propagation in Viscoelastic Bars

N. NAKAGAWA, R. KAWAI and T. SASAKI

Department of Mechanical Engineering, Kobe University
Rokko, Nada, Kobe 657, Japan

Summary

The stress distributions in an elastic-viscoelastic bar system subjected to the impact loading are analyzed by the Laplace transform method. Examples are given to the Maxwell, Voigt, and 4-parameter models.
Further the identification of dynamic properties of viscoelastic materials is treated by comparing the analytical results with experimental results. The method of identification is based on the iterative method. Dynamic properties of viscoelastic materials under consideration of the dependence on frequencies are identified.

Introduction

The behavier of material under high rates of deformation is a subject that has recieved considerable attention in recent years. Some methods have been used in order to obtain the dynamic properties of materials. For example Sackman et al.[1] gave the analytical bases for the direct determination of the creep and relaxation functions of linear viscoelastic media for very short times. Authors have analyzed the wave propagation in semi-infinite and finite bars of viscoelastic materials[2)3)].

In this paper the wave propagation in an elastic-viscoelastic bar system subjected to the impact loading is analyzed by the Laplace transform method. Viscoelastic materials are assumed to be represented by the Maxwell, Voigt and 4-parameter models. This system is used to determine the dynamic properties of materials and can be extended to the split-Hopkinson pressure bar. Further the

identification of the dynamic properties of viscoelastic materials is treated. It is generally known that mechanical properties of viscoelastic materials depend on the frequency in testing and the values of these properties used in the past are not unified. However those properties under consideration of the dependence on frequencies can be identified here, because the impact loading obtained by the experiment contains many frequencies and this loading is used directly as the incident wave.

Analysis of Wave Propagation

Thin elastic and viscoelastic bars with the same cross-sectional areas touch at x=1 each other as shown in Fig.1.

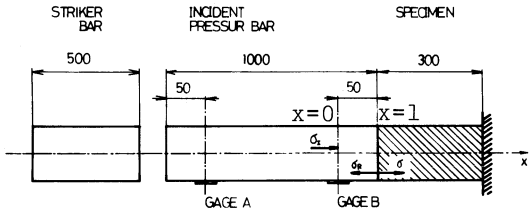

Fig.1. Arrangement of pressure bar experiment

Incident waves in the elastic bar are partly reflected at the interface(x=1) and partly transmitted into the viscoelastic bar. Boundary conditions to the viscoelastic bar depend on the material properties of the both sides of the interface and vary with the time. Hence this problem is complicated. The equation of motion is well known

$$\frac{\partial \sigma}{\partial x}=\rho\frac{\partial^2 u}{\partial t^2} \quad , \quad \frac{\partial^2 \sigma}{\partial x^2}=\rho\frac{\partial^2 \varepsilon}{\partial t^2} \; . \tag{1}$$

The constitutive equation to the viscoelastic material is

$$P\sigma=Q\varepsilon \tag{2}$$

where $P=\sum_{i=0}^{n} a_i\frac{\partial^i}{\partial t^i}$, $Q=\sum_{j=0}^{m} b_j\frac{\partial^j}{\partial t^j}$.

From Eqs.(1) and (2)

$$\frac{\partial^2}{\partial t^2}(P\sigma)=\frac{1}{\rho}\frac{\partial^2}{\partial x^2}(Q\sigma) \; . \tag{3}$$

Boundary conditions are

$$\sigma=\sigma_I+\sigma_R \qquad (x=1) \tag{4}$$

$$v=\frac{c_0}{E_0}(\sigma_I-\sigma_R) \qquad (x=1) \tag{5}$$

$$\sigma=0 \qquad (x=\infty) \tag{6}$$

where subscripts I and R indicate the incident wave and the reflected wave respectively. The incident wave is assumed to be a step wave as follows

$$\sigma_I=\sigma_0 H(t) . \tag{7}$$

The Laplace transform of Eq.(3) gives

$$P(s)\bar{\sigma}=Q(s)\frac{\partial^2\bar{\sigma}}{\partial x^2}\frac{1}{\rho} \tag{8}$$

where

$$P(s)=\sum_{i=0}^{n}a_i s^{i+2}, \qquad Q(s)=\sum_{j=0}^{m}b_j s^j$$

and $\bar{f}$ indicates the Laplace transform of $f(x,t)$.
The general solution of Eq.(8) is given by

$$\bar{\sigma}=C_1\exp[-\sqrt{\frac{P(s)}{Q(s)}}x]+C_2\exp[\sqrt{\frac{P(s)}{Q(s)}}x] . \tag{9}$$

Using the boundary conditions(4)-(6), we obtain

$$\bar{\sigma}=\frac{2\bar{\sigma}_I}{1+\frac{E_0}{c_0}\frac{1}{\rho s}\sqrt{\frac{P(s)}{Q(s)}}}\exp[-\sqrt{\frac{P(s)}{Q(s)}}x] . \tag{10}$$

Inversion of Laplace Transform

When the viscoelastic solids are represented by simpler model (composed of spring and dashpot in series or parallel), the inversion of Eq.(10) is easily obtained. In the case of multi-parameter models, the analytical inversion becomes complicated, so that the numerical inversion of the Laplace transform is used as follows.
The Fourier expansion of the function f(t) by the first N terms leads

$$f_N(t)=e^{ct}\sum_{n=0}^{N}a_n\Phi_n(\frac{t}{T}) \tag{11}$$

where

$$\Phi_n(t)=e^{-t/2}L_n(t) \qquad (n=0,1,2,\cdots) \tag{12}$$

and $L_n(t)$ is the Laguerre function. If $g_N(s)$ is the Laplace transform of $f_N(t)$,

$$g_N(s)=\int_0^\infty f_N(t)e^{-st}dt. \tag{13}$$

Using both the nature that the Laplace transform of Laguerre function is possible and Perseval theory, we obtain

$$a_0=\frac{1}{N+1}\sum_{j=0}^{N} h(\theta_j) \tag{14}$$

$$a_n=\frac{2}{N+1}\sum_{j=0}^{N} h(\theta_j)\cos n\theta_j \tag{15}$$

where

$$h(\theta)=(\frac{1}{2T}+\frac{i}{2T}\cot\frac{\theta}{2})g(c+\frac{i}{2T}\cot\frac{\theta}{2}) \qquad (i^2=-1)$$

$$\theta_j=(\frac{2j+1}{N+1})\frac{\pi}{2}$$

From Eqs.(11),(14) and (15) we can obtain the numerical inversion of $f_N(t)$.

Stress Distribution in the Viscoelastic Bar

The stress distributions in the viscoelastic bar are indicated in Fig.2 to the Maxwell model. The stress distributions by the finite difference method are consistent with those by the Laplace transform. Broken lines indicate the approximate solution by the wave-front expansion. Results to the Voigt model are shown in Fig.3. These results are compared with the results obtained by Lee et al.[4] under the conditions of constant stress and velocity.

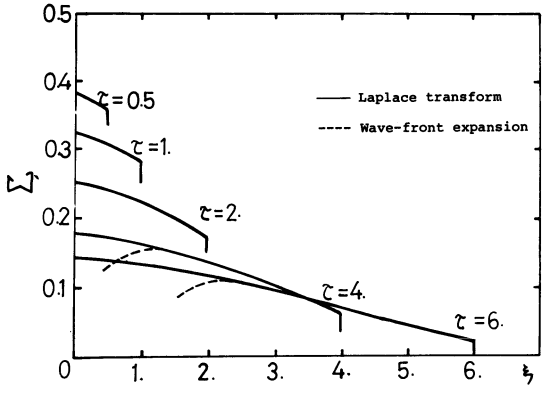

Fig.2. Stress distribution in the viscoelastic bar (Maxwell model)

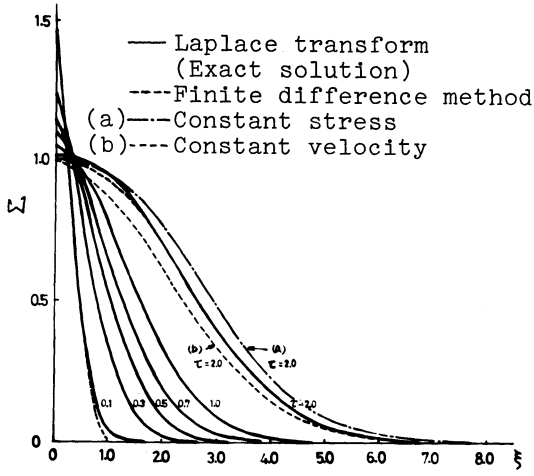

Fig.3. Stress distribution in the viscoelastic bar (Voigt model)

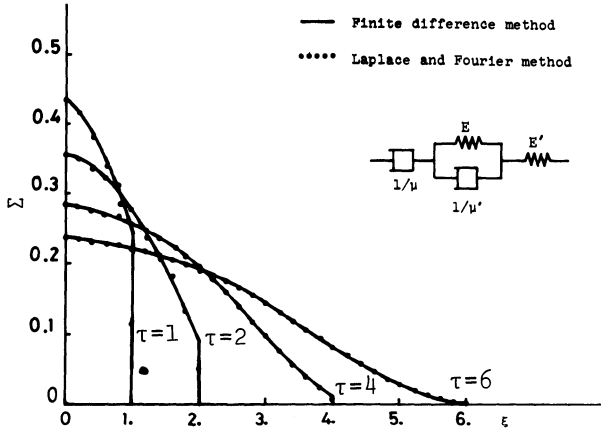

Fig.4. Stress distribution in the viscoelastic bar (4-parameter model)

The stress distributions in the case of 4-parameter model are indicated in Fig.4.

Identification of Dynamic Properties of Viscoelastic Bars

The wave measured by strain gage B at x=0 is (Fig.1)

$$\sigma_B(0,t)=\sigma_I(0,t)=\sigma_{I0}(t) \qquad (0\leqq t\leqq 2l/c_0) \qquad (16)$$

$$\sigma_B(0,t)=\sigma_{I0}(t)-\sigma_{I0}(t-2l/c_0)+2\,L^{-1}\left[\frac{e^{-2sl/c_0}\,\bar{\sigma}_{I0}(s)}{1+\frac{E_0}{c_0}\frac{1}{\rho s}\sqrt{\frac{P(s)}{Q(s)}}}\right]$$

and then

$$L^{-1}\left[\frac{e^{-2sl/c_0}\bar{\sigma}_{I0}(s)}{1+\frac{E_0}{c_0}\frac{1}{\rho s}\sqrt{\frac{P(s)}{Q(s)}}}\right]=\frac{1}{2}\left(\sigma_B(0,t)-\sigma_{I0}(t)-\sigma_{II0}(t-2l/c_0)\right). \quad (2l/c_0 \leq t) \qquad (17)$$

If $P(s)$ and $Q(s)$ are the same values as those of real material, Eq.(17) is valid. In order to get better $P(s)$ and $Q(s)$ we use the optimization technique by the Davies-Swann-Campey method. The objective function is

$$F=\left[\frac{1}{2}\{\sigma_B(0,t)-\sigma_{I0}(t)-\sigma_{II0}(t-2l/c_0)\}-L^{-1}\left[\frac{e^{-2ls/c_0}\bar{\sigma}_{I0}(s)}{1+\frac{E_0}{c_0}\frac{1}{\rho s}\sqrt{\frac{P(s)}{Q(s)}}}\right]\right]^2. \qquad (18)$$

Hence parameters a_i and b_i which minimize the value of F are searched. Parameter identification was done to Acryl resin. Results of parameter identification are shown in Table 1 to the typical data obtained by the experiments.

Table 1. Resulte of parameter identification

	a_0 x10^4 s^{-1}	a_1	a_2 x10^{-11}	b_0 x10^8 Kg/mm^2	b_1 x10^4 Kg/mm^2	b_2 x10^{-8} Kg/mms
Maxwell	0.02	1.00	0.	0.	2.00	0.
Voigt	1.20	0.	0.	1.44	1.20	0.
4-parameter	411.	197.	2.32	0.	0.21	4.88

The authors acknowledge the grant from the Japanese Ministry of Education for their support of this study.

Literature

1 Sackman, J.L.,Kaya, I.: On the determination of very early-time viscoelastic properties. J.Mech.Phy.Solids 16 (1968) 121-132.

2 Nakagawa, N.,Kawai, R. and Akao, M.: Impact waves at the interface of an elastic-viscoelastic bar. Joint JSME-ASME Appl.Mech. Western Conference (1975) 81-88.

3 Nakagawa, N.,Kawai, R. and Akao, M.: An analysis of wave motion in a viscoelstic specimen of the split-Hopkinson pressure bar. Theoretical and Appl.Mech.25 (1977) 175-186.

4 Lee,E.H. and Morrison, J.A.: A comparison of the propagation of longitudinal waves in rods of viscoelastic materials. J.Polymer Science 19 (1956) 93-110.

Results for the Single Ricochet of Spherical-Ended Projectiles off Sand and Clay at up to 400 M/SEC

W. JOHNSON

Engineering Department
University of Cambridge
Cambridge, England

G.H. DANESHI

Department of Metallurgical Engineering
Arya-Mehr University of Technology
Tehran, Iran

Summary

Relevant literature concerning the ricochet of projectiles off water, sand and clay is first reviewed. Experimental findings for the single ricochet of solid spheres, dumb-bell shaped and hemi-spherical ended cylinders, from fine sand and clay when fired at up to 400 m/sec are reported and summarised. Results are presented for small angles of impact of, (i) plough development with time, (ii) the variation of exit speed and angle with entry speed and angle, (iii) rates and directions of spin after impact for the elongated projectiles, when the impact and attitude angle are equal, (iv) crater volume and dimensions as a function of impact speed and (v) the variation of the critical angle of ricochet with speed.

Notation

A	cross-sectional area of projectile
d	diameter of projectile
k, k', c	constants
L	trajectory length
ℓ	inter-sphere distance of a dumb-bell shaped projectile
ℓ'	length of an hemi-spherical end projectile
m	projectile mass

n	velocity exponent
t	time
v_o, v, v_1	entry, instantaneous and exit speed
v_x	longitudinal position of projectile in a Cartesian system of coordinates established at the point of impact
$\bar{v}$	mean speed during impact
ρ, ρ'	density of projectile and impacted medium respectively
θ_o,θ_1	impact and exit angle respectively
θ_c,θ_g	critical angle of ricochet, velocity independent and velocity dependent, respectively
V	volume
f_x	horizontal component of retardation

Introduction

The oblique impact of a projectile against a massive solid or liquid target with the possibility of subsequent ricochet is of especial interest to engineers and ballisticans. Early methodical testing in the subject of ricochet dates back to the late 18th and early 19th century when Douglas[1] and de Jonquières[2] studied the ricochet of cannon balls off sea water and observed the existence of critical angles; multiple ricochet and the number of grazes made for various shapes and angle were also reported. In the early part of the 20th century, the subject received renewed attention in connection with the forces associated with the landing of sea-planes and the launching of air-to-water torpedoes and missiles. Detailed experimental work on the subject was carried out by Birkhoff et al[3] and by Richardson[4] during the Second World War. In the Birkhoff et al[3] studies, full size bombs were dropped from an airplane into a lake to impinge at different angles and speeds and the critical angle of ricochet, exit velocity and shape and dimension effects were measured. Richardson[4] determined the impact forces on a sphere during vertical

and oblique impact into water and discussed the mechanism and forces involved. An extensive literature review and study of the ricochet of spheres off water has recently been given by Johnson and Reid[5]. A simple empirical formula for critical angle of ricochet, θ_c, originally due to Birkhoff et al gives $\theta_c = 18/\sqrt{\sigma}$ degrees where σ is the ratio of the specific gravity of the solid ricocheting sphere to that of the liquid.

Theoretical work on impact between a solid and a liquid is much concerned with the forces developed at the early stages of entry. These forces are due both to compressibility effects and the motion of the solid through the liquid[12]; the compressibility forces arise at high velocities and are of short duration. They are of great importance for engineering design, but are beyond the scope of the present survey. Hydrodynamic forces are generated in any fluid flow situation, but even for the simplest shapes, a mathematical analysis to determine the magnitude of these forces is very difficult. Continuous changes in the flow pattern, disturbances to the shape of the free surface, splash formation and the effects of viscosity and a trailing cavity constitute great obstacles. Almost all the analyses proposed so far have either assumed a two-dimensional fluid flow or a steady flow pattern. Viscosity and cavity formation particularly are neglected in most of these works.

The following feature generally applies to any unsteady fluid motion problem; it is frequently adopted for the particular case of solid-liquid impact and demonstrates one of the difficulties very clearly.

The equation of the free motion of a solid in an ideal fluid may be written as $(M + m)v = Mv_o$ where M and v_o are the mass and the initial velocity of the projectile and v and m are the instantaneous velocity and the virtual mass. Virtual mass is related to the flow pattern of the

fluid and for the (unsteady) entry of a solid into a liquid is a variable; for a well-immersed sphere it is equal to one half of the mass of an equal volume of water.

In 1929 von Karman[6] in his fundamental paper on the landing of sea-planes drew attention to the importance of virtual mass and the use of the momentum conservation principle. In considering landing, the floats were treated as a two dimensional case of a growing flat plate. Shiffman and Spencer[7] analysed the vertical entry of a sphere into water and calculated the pressure and decelerations. The monograph by M. Kornhauser[23] should also be referred to. The oblique entry into water of a sphere was analysed by Trilling[8], but the effects of splash and cavity were not included. Trilling's analysis was extended by Dergarabedian[9] to include compressibility effects. Refs. (10) to (17) give a list of some of the other relevant theoretical work on the subject. A survey of hydrodynamic impact up to 1959 has been given by Szebehly[18].

The effects of the cavity, growing impact area, and non-uniform pressure distribution over the leading surface of the projectile were dealt with by Birkhoff et al[3] in a simple analysis; the contact area and the pressure distribution over it are somewhat arbitrary. They assumed the wetted surface to lie in front of the projectile and below the water surface and assumed the local pressure $p = \rho(v \cos\beta)^2/2$, where v denotes the current velocity of the projectile and β the angle between the normal to the surface element and the instantaneous velocity. Most of the salient features of the ricochet phenomenon are predicted by this simple analysis. In a similar approach, Hutchings[19] applied Rayleigh's pressure formula, originally obtained for the oblique steady motion of a long plate in an infinite liquid, to the ricochet situation and, among other things, obtained a relationship which included the effect of projectile spin on critical ricochet angle.

Most of the experimental work on water entry by projectiles has so far been confined to acquiring test information about actual or model bombs of complicated shape and uneven mass distribution. Tests have often been conducted in open lakes with observation posts stationed nearby. Whip, deceleration rates and forces and coefficients of drag and lift have been calculated for deriving empirical formulae. A number of relevant publications on the planing of non-spherical shapes is listed in Refs. (21) to (23).

The splash profiles from the vertical and oblique impact of a sphere against water have been photographed by White[24]; stainless steel balls 2 in. in diameter were used, fired at 20 ft/sec. His photographs clearly demonstrate changes in the shape of the free surface in front of and behind the sphere.

Critical angles of ricochet for steel and aluminium spheres off water and sand have been reported by Soliman, Reid and Johnson[25] for speeds of up to 250 ft/sec at entry; exit velocities and angles were also measured, an emphasis in that work being on the velocity dependance of critical angle.

The ricochet of spherical and dumb-bell shaped* projectiles off sand has been studied by Daneshi and Johnson[26,27]. Plough development, retardation and rotation were measured by photographing the target area at a number of pre-set time intervals of about 10^{-5} sec, especially during the penetration phase of ricochet.

The work described below is a summary of some recent experimental results obtained by the authors.

---

* Two equal spheres separated by a light rigid rod between their centres.

Equipment

Spherical, d.s.* and o.s.** projectiles were fired into a fine grain sand (150-300 μ or 50-100 Tyler mesh) and into a modelling clay at between 19° and 21°C, (Plasticine), from a specially adapted gun and caused to ricochet. Tests were carried out in a dark room and the projectile's passage through the target area was photographed at pre-determined moments. Details of the equipment and the experimental procedure are given in Refs. (26) and (27). The design and the dimensions of the projectiles are given in Fig. 1 and in Table 1 respectively.

Results

Plough development and retardation

The interaction forces between a projectile and the impact medium were studied through observations of the plough development with time. A high speed rotating camera in conjunction with a spark-flash unit was used to photograph the passage of a projectile at six pre-determined intervals. A typical photograph for the ricochet of a 1/2 in. diameter sphere from clay is given in Fig. 2. The spacings between the images represents the time interval between successive flashes, each mm corresponding to 20 micro-seconds.

Curves of plough progress with time for five d.s. projectiles (d.s. 1 to 5) in sand and five d.s. projectiles (d.s. 6 to 10) in clay are shown in Fig. 3. Curves of velocity and retardation variation with time have been determined by differentiating the x(t) and v(t) curves, see Ref. (28).

---

*d.s.: dumb-bell shaped
**o.s.: hemispherical-end projectile

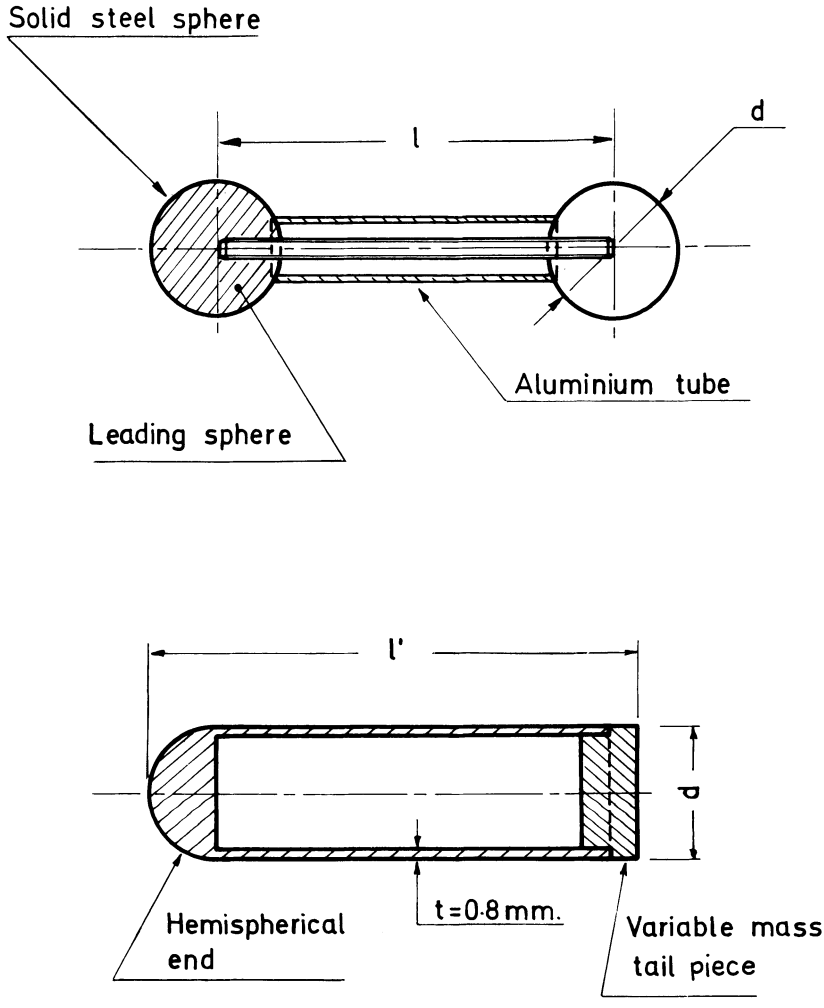

Fig. 1 Arrangement for a dumb-bell shaped and a hemispherical-end cylindrical projectile.

Table 1

Projectile Dimensions mm	sphere d=12.7	sphere d=25.4	d.s.1 d=25.4 ℓ=25.4	d.s.2 d=25.4 ℓ=50.8	d.s.3 d=25.4 ℓ=76.2	d.s.4 d=25.4 ℓ=101.6	d.s.5 d=25.4 ℓ=12.7	d.s.6 d=12.7 ℓ=12.7
mass x 10^3 kg	8.33	66.5	131	135	139	143	147	16.36
Velocity range m/sec	60-400	60-160	50-107	50-107	30-105	50-105	50-105	50-250

Projectile Dimensions mm	d.s.7 d=12.7 ℓ=25.4	d.s.8 d=12.7 ℓ=38.1	d.s.9 d=12.7 ℓ=50.8	d.s.10 d=12.7 ℓ=63.5	o.s.1 d=12.7 ℓ⌙=38.1	o.s.2 d=12.7 ℓ⌙=63.5	o.s.3 d=12.7 ℓ⌙=88.9
mass x 10^3 kg	18.92	21.3	23.8	26.25	23.6	23.71	23.73
Velocity range m/sec	40-240	40-230	40-220	40-210	50-220	50-220	50-220

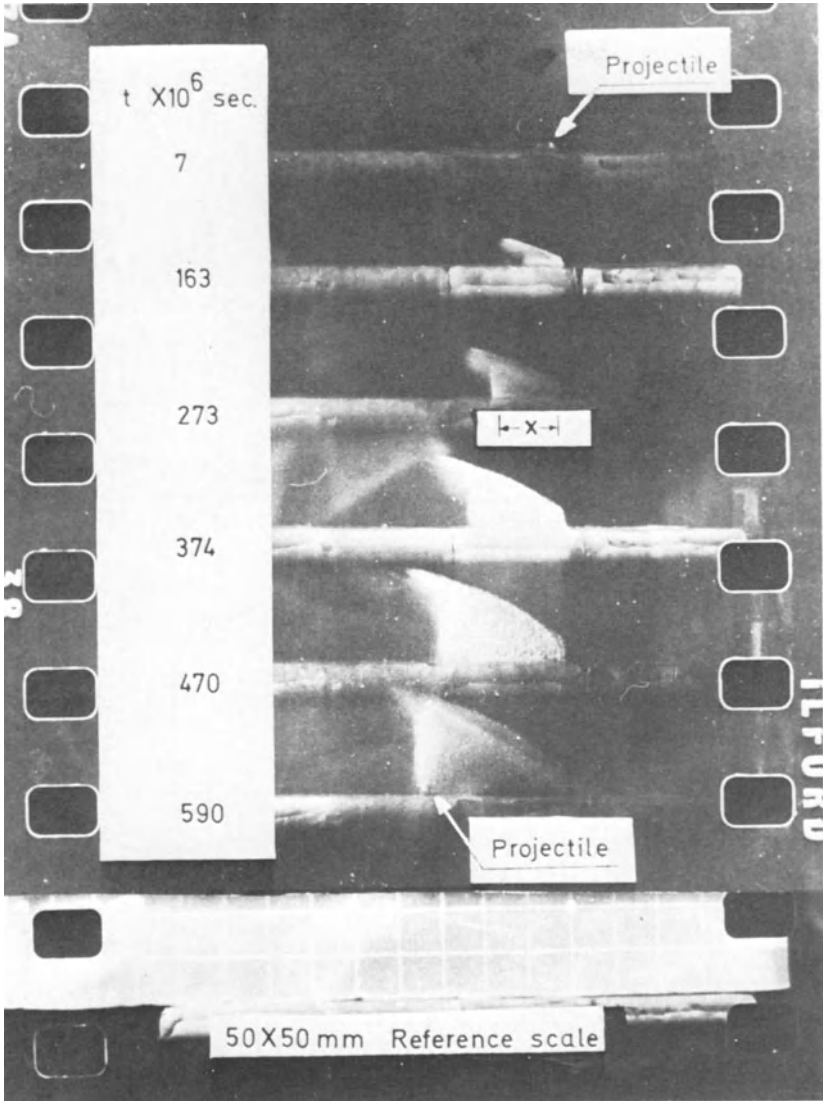

Fig. 2 Plough development after specific intervals of time for a 12.7 mm dia. sphere in Plasticine at θ_o = 5° and v_o = 144 m/sec.

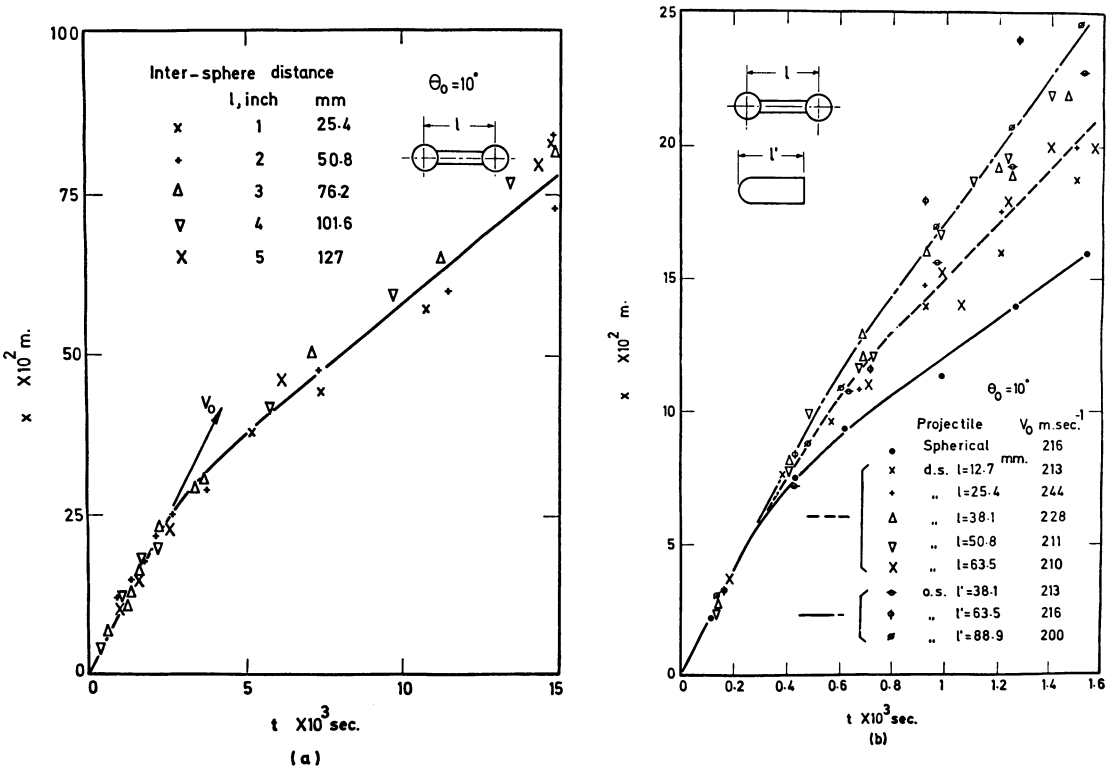

Fig. 3

Longitudinal position (x) versus time (t) for
(a) five d.s. projectiles at $v_o = 100 \pm 5$ m/sec and $\theta_o = 10°$ in sand.
(b) One spherical, five d.s. and three o.s. projectiles at between $v_o = 200$ and 244m/sec with $\theta_o = 10°$ in Plasticine.

Three distinct phases can be distinguished in each ploughing operation:

I: The Entry Phase in which the material piles-up in front of the projectile: retardation rates are comparatively small and velocity changes negligible.

II: The Plough Phase in which material pile-up is complete: retardation rates are at their greatest, as are the rates of velocity decrease.

III: The Exit Phase in which the projectile is ascending: retardation rates have reduced considerably and the speed is almost constant and equal to the exit speed.

For d.s. projectiles ricocheting off sand or off clay, the entry phase occupies approximately one quarter of the plough length. The plough phase, which occurs in the neighbourhood of the point of maximum depth, occupies approximately 1/3 to 1/2 of the total crater length.

In general, the Forces of Ricochet are dependent on the impact speed and the shape and the geometry of the projectile. Tests using a Plasticine target have shown that when everything else is constant, the maximum drag force on our o.s. projectiles is not significantly different from that on a d.s. projectile and both of them are almost twice that of a single sphere whose diameter is equal to the maximum cross-section presented. Aside from the shape of the impact face, the geometry of the remainder of the d.s. or the o.s. projectile and the position of the centre of gravity appear to have little role, in determining the ricochet behavior; tests on five d.s. and three o.s. projectiles sustain this observation. For all the projectiles tested, the maximum drag force in terms of the impact speed seems to fit an equation $F_{x(max)} = kv_o^2$. At $\theta_o = 10°$ for a 12.7 mm sphere, $k = 0.1$ N.sec^2/m^2 and for the d.s. and o.s. projectiles tested, (see Table 1), $k = 0.2$ N.sec^2/m^2. Details of these tests and the

experimental results concerning forces of ricochet are given in Ref. (28).

Exit speed*

A search of the available literature shows that no systematic work on the velocity loss of a ricocheting projectile has yet been carried out and published. A scatter of tests by Birkhoff et al[3] and others[4,25] was not carried out on the same projectiles or at the same entry angle. These tests, however, showed that the velocity loss in water is a function of projectile geometry, density and impact angle.

Experiments were carried out by us on five d.s. projectiles, two spheres and three o.s. projectiles ricocheting off clay. The spherical projectiles were 12.7 mm and 25.4 mm in diameter and weighed 8 and 64 grams respectively. The d.s. projectiles were made up of two 12.7 mm spheres separated by a light weight rod of length ℓ, $12.7 < \ell < 63.5$ mm and weighing between 16.36 and 21.90 grams. The o.s. projectiles were composed of a 12.7 mm hemispherical head and a hollow cylindrical tail and weighed between 23.6 and 23.73 grams**. Details of all the projectiles are given in Fig. 1. Curves of velocity loss for these projectiles are shown in Fig. 4 and indicate that,

(i) At $\theta_o = 5°$, the ratio of the exit to the entry speed, v_1/v_o, is approximately the same for all the spherical, d.s. and o.s. projectiles tested.

(ii) At $\theta_o = 10°$ and at less than approximately 130 m/sec, the v_1/v_o ratio is the same for all these projectiles

* All angles and speeds quoted for d.s. and o.s. projectiles are specified with respect to the centre of mass and axis of symmetry.

** Obtained by changing the mass of the tailpiece, see Fig. 1.

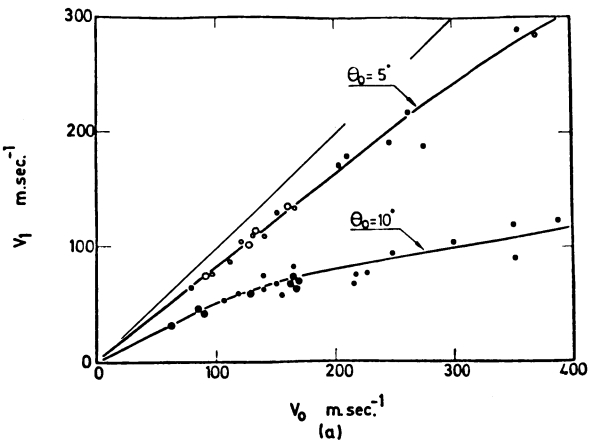

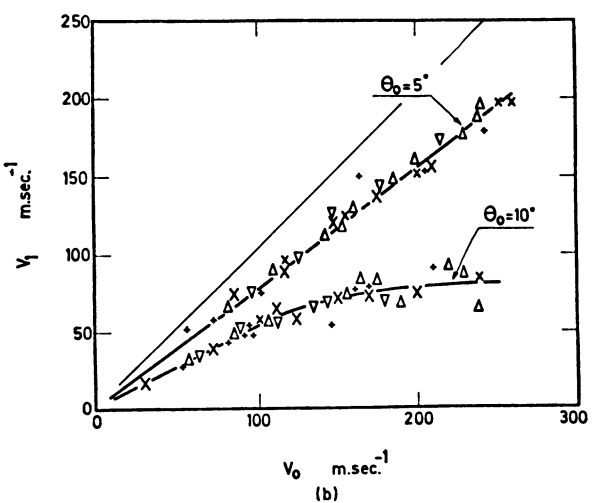

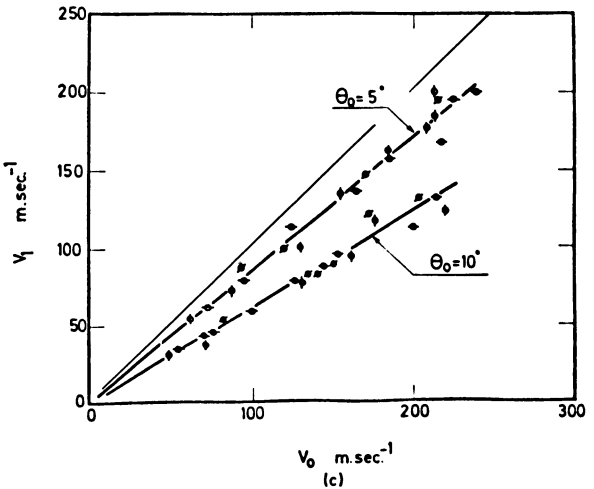

Fig. 4

Showing variations of exit speed with impact speed for spherical, d.s. and o.s. projectiles in Plasticine; °:12.7 mm dia. sphere, 0:25.4 mm dia. sphere, x,+,Δ,∇,X: d.s. 6 to d.s. 10 and ⊖,ϕ,⌀: o.s. 1 to o.s. 3 projectiles at θ_0=5°; •: 12.7 mm dia. sphere, ●: 25.4 mm dia. sphere, x,+,Δ,∇,X: d.s. 6 to d.s. 10 and ⊖,ϕ,⌀: o.s. 1 to o.s. 3 projectiles at θ_0=10°.

and above 130 m/sec it is the same for spherical and d.s. projectiles only.

(iii) At $\theta_o = 10°$ and in excess of 130 m/sec the v_1/v_o ratio for spherical and d.s. projectiles decreases quickly and the exit speed becomes insensitive to the impact speed.

The insensitivity of the v_1/v_o ratio to the projectile shape and its mass suggests that the trajectory length should be proportional to F_x (where F_x is the resistance and m the projectile mass). It is shown, in Ref. (28), that the maximum resistance to the d.s. and o.s. projectiles tested was approximately equal to each other and almost twice that for a 12.7 mm spherical projectile. Measurements of the crater length L against m/A (where A is the maximum cross-sectional area of the specimen normal to the direction of motion) for two spherical, five d.s. and three o.s. projectiles give,

$$(L_s)_{2d} = 2(L_s)_d \qquad \text{for spherical projectiles,}$$

and

$$L_{d.s.\text{ or }o.s.} = 1.4\, L_s \quad \text{for the d.s., o.s. and spherical projectiles tested.}$$

The calculated maximum drag forces, $F_{d.s.\text{ or }o.s.} = 2\, F_s$, and the measured projectile masses, as shown in Table 1, substantiate these results satisfactorily.

The variation of v_1 with v_o for spherical and d.s. projectiles ricocheting off clay are of special interest. At less than approximately 130 m/sec, $v_1 = kv_o$ and above it, v_1 is rather insensitive to large changes in v_o. Measurements of the crater dimensions for $40 < v_o < 260$ m/sec show that the crater length is almost proportional to the impact speed. Crater width and depth do not show similar trends, see the Section on crater volume. The insensitivity of v_1 to changes in v_o may, therefore, be due to the

existence of high impact forces in the early stages of entry or to changes in the physical properties of clay. Photographic data on the early stages of the vertical entry of the d.s. and o.s. projectiles into clay did not reveal excessive retardations.

Exit angle

Experimental results concerning the relationship between the exit and the impact angles of projectiles ricocheting off Plasticine or clay are shown in Fig. 5. For the spherical projectiles the exit angle is always larger than the entry angle; the θ_1/θ_o ratio decreases with increasing impact speeds and at each speed the θ_1/θ_o ratio is larger at $\theta_o = 10°$ than at $\theta_o = 5°$. Richardson[4], Birkhoff et al[3] and Soliman, Reid and Johnson[25] reported that in the ricochet of spherical projectiles off water $\theta_1 < \theta_o$. It is also important to note that in clay and near to the critical angle of ricochet, $\theta_1 >> \theta_o$. This phenomenon will be referred to again later.

d.s. and o.s. projectiles behave differently. At 5° and at high speeds, θ_1/θ_o is greater than unity. As speed reduces, θ_1/θ_o reduces and in some cases becomes less than unity. At $\theta_o = 10°$ and at high speeds, θ_1/θ_o is greater than unity, reducing continuously until the impact velocity is approximately 100 m/sec; in some cases θ_1/θ_o becomes less than unity. Below 100 m/sec, θ_1/θ_o increases again and in a few cases becomes greater than unity again. Unlike the case of spheres, θ_1/θ_o for d.s. and o.s. projectiles at each impact speed at $\theta_o = 5°$ is higher than at $\theta_o = 10°$.

Experimental results on d.s. projectiles ricocheting off sand have shown both $\theta_1 > \theta_o$ and $\theta_1 < \theta_o$; in most of our tests the measurements provide $0.9 < \theta_1/\theta_o < 1.5$.

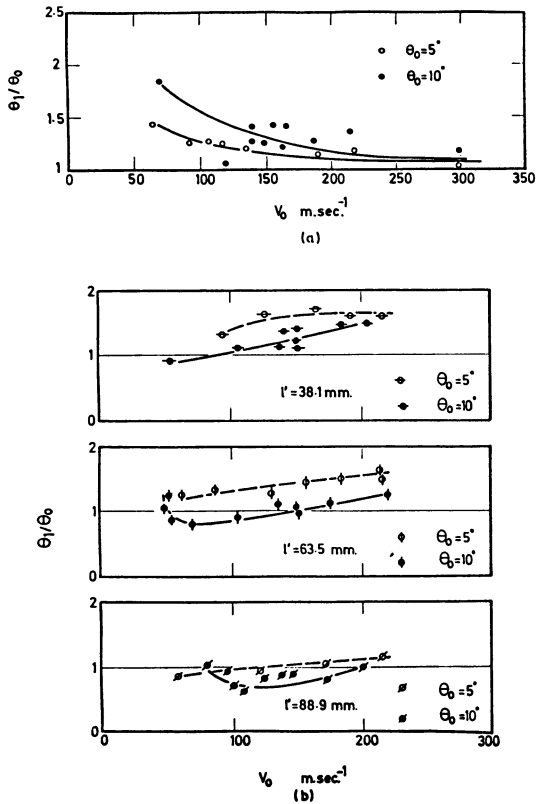

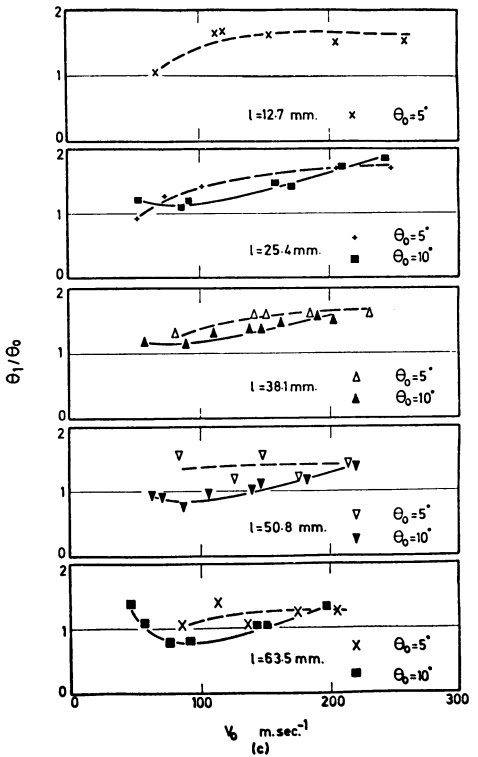

Fig. 5

Showing variations of the ratio of the exit to impact angle with initial speed in Plasticine; ∘: 12.7 mm dia. sphere, x,+,Δ, ∇,X: d.s. 6 to d.s. 10 and ⊖,ϕ,⌀, o.s. 1 to o.s. 3 projectiles at θ_o=5°; •: 12.7mm dia. sphere, ■,▲,▼,■: d.s. 7 to d.s. 10 and ●,◆,⌀, o.s. 1 to o.s. 3 projectiles at θ_o= 10°.

Exit spin

Tests on the three types of projectiles employed showed that during the plough these projectiles acquire rotation and leave the target spinning in the vertical plane. Spherical projectiles show occasional spin about both their lateral and longitudinal axes; d.s. and o.s. projectiles spin about their lateral axis only.

Fig. 6 shows the spinning of a 2.5 in. long d.s. projectile at various entry speeds. At low entry speeds the projectile spins backwards and between 110 and 210 m/sec it spins forwards whilst above 210 m/sec it again spins backwards. Tests on other d.s. and o.s. projectiles show the same type of trend, though backward rotations are not observed in every case.

Variation of the angular velocity of five d.s. projectiles at between 40 and 240 m/sec are shown in Fig. 7. The Birkhoff et al[3] results on model bombs ricocheting from water and the results of the authors'[26,27] tests on d.s. projectiles ricocheting off sand are similar to those presented here.

The direction of the rotation of a projectile may not remain the same during a ploughing operation. Qualitative, photographic tests for the entry phase, in clay and sand, showed that in the beginning all d.s. and o.s. projectiles rotate backwards. In some cases the backward rotations are followed by the impact of the rear end of the projectile into the ricocheting medium and the formation of a second crater inside the main crater. Second craters may be formed whether the exit spin is forwards or backwards, see Ref. (28).

Tests on d.s. and o.s. projectiles ricocheting off clay show that the ratio of the exit to the impact angle, θ_1/θ_o, is related to the projectile spin. When the projectile is spinning forwards*, θ_1/θ_o is generally larger

* anti-clockwise for motion to the left.

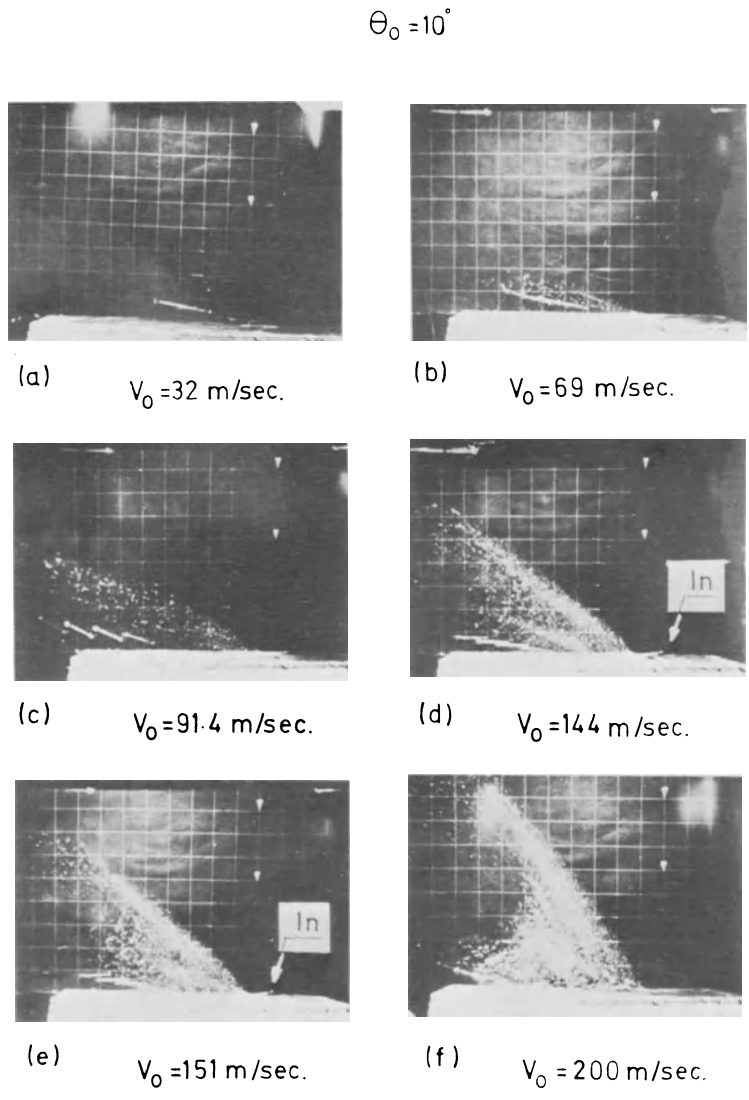

Fig. 6 Photograph of the impact and subsequent rotation of the d.s. 10 projectile in Plasticine: (a) reflection: no plume, clockwise rotation (-ve), (b), (c) clockwise rotation (-ve), (d), (e) anticlockwise rotation (+ve), (f) clockwise rotation (-ve).

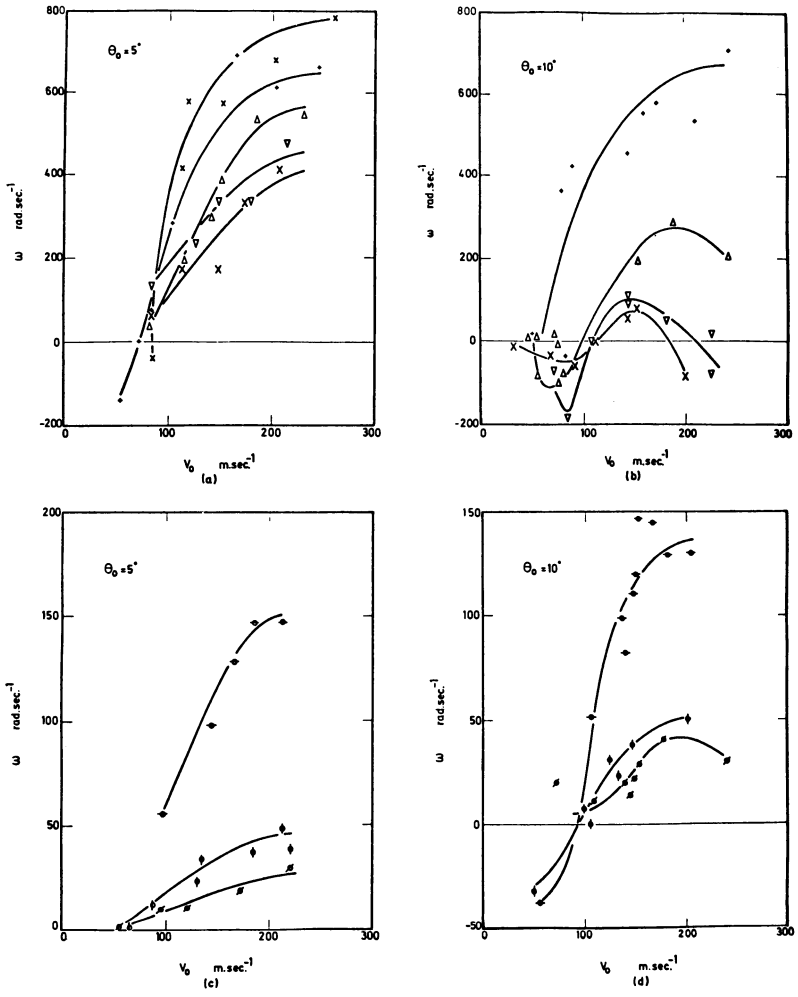

Fig. 7 Showing variation of the angular velocity at exit with impact speed in Plasticine; x,+,Δ,∇,X: d.s. 6 to d.s. 10 and ⊖,ϕ,ø: o.s. 1 to o.s. 3 projectiles at θ_o=5°: +,Δ,∇,X: d.s. 7 to d.s. 10 and ●,◆,ø: o.s. 1 to o.s. 3 projectiles at θ_o=10°. (For the motion from right to left clockwise rotations are considered negative.)

than unity, whilst when the projectile is spinning backwards, it is generally less than unity. Results in Ref.(3) for model bombs show similar trends also, though in these the backward rotation was followed by a sinking of the projectile.

Crater dimensions and volume

A study of the craters produced by projectiles ricocheting off sand and clay reveals that the dimensions of the crater produced by a 1 in. spherical projectile are almost twice those produced by a 1/2 in. projectile. In general, the shape, mass and initial velocity of the projectile and the density of the impacted medium determine the length of a crater, L. We can write

$$L = m \int \frac{v dv}{F}$$

where $F = k' \cdot \rho \cdot v^2 f(\theta)$ is the instantaneous force of the fluid resistance and m and v are the mass and the instantaneous velocity of the projectile.

The dependence of the crater dimensions on the value of the impact speed is not easily understood. All its dimensions depend on the speed but the proportionality factors for length, width and depth, for small changes in speed, are not the same. The width and the depth of a crater increase with speed and approach a critical value asymptotically. The critical depth for ricochet for spherical projectiles is generally agreed to be about 2d.

The volume of a crater, defined as the volume of the material removed from beneath the original surface of the impacted medium, is found experimentally to be represented by a relation of the form $V = c \cdot m \cdot v_o^n f(\theta_o)$, where V is the volume of the crater and v_o and θ_o are the initial speed and the impact angle of the projectile. Tests using two spherical and five d.s. projectiles in sand and two

spherical, five d.s. and three o.s. projectiles in clay have shown that the proportionality coefficient C, the impact angle function $f(\theta_o)$ and the impact velocity exponent n are almost the same for all projectiles which have the same basic shape and dimensions. The value of the velocity exponent, n, depends on the physical properties of the impacted medium. Tests in sand, as shown in Fig. 8, give $n \simeq 1$, i.e. the crater volume is almost directly proportional to the initial momentum of the projectile; in clay and below approximately 200 m/sec, $n \simeq 2$, i.e. the crater volume is proportional to the initial kinetic energy of the projectile and at $v_o > 200$ m/sec, $n \simeq 4$, see Fig. 8(c). At $\theta_o = 5°$ for all the projectiles, and at $\theta_o = 10°$ for the spherical projectiles, $n \simeq 2$, see Figs. 8(b) and 8(d). Experimental results from Finnie[29] and Hutchings, Winter and Field[30-32] using ductile metals struck by quartz projectiles give $2 < n < 2.4$.

Critical angle of ricochet

The critical angle of ricochet, θ_c, is an angle above which ricochet does not occur. The well-known empirical relationship for the value of θ_c for spherical projectiles, is $\theta_c = 18/\sqrt{\rho/\rho'}$ where ρ and ρ' are the densities of the projectile and the impacted medium respectively. According to this relationship the critical angle of ricochet is independent of the entry speed. This is not always true. Tests using clay and sand, as shown in Fig. 9 clearly demonstrate that the critical angle depends not only on the impact speed but also on the projectile size. Both in sand and in clay and at each impact speed, the critical angle for a 1 in. sphere seems to be smaller than that of a 1/2 in. sphere.

In clay the critical angle increases from $\theta_c = 10°$ at 400 m/sec to $\theta_c = 23°$ at 60 m/sec, see Fig. 9(b); the tendency of projectiles to reflect* off clay at low speeds

* ricochet without causing "fracture" - i.e. plastic deformation only; note Fig. 6(a).

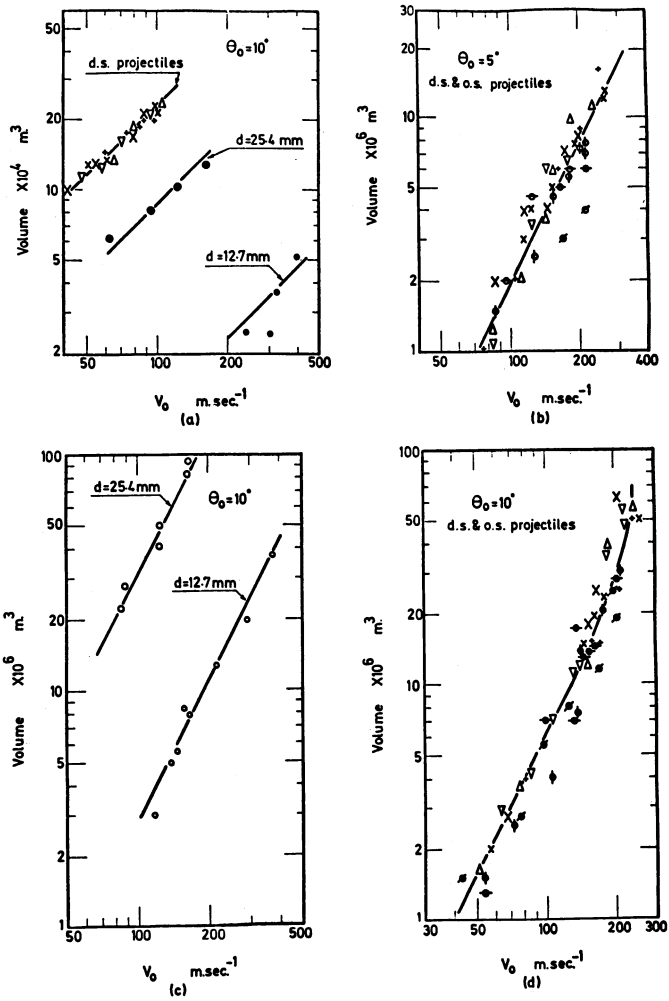

Fig. 8 Showing variation of crater volume with initial speed:
(a) •: 12.7mm dia. sphere, ●: 25.4mm dia. sphere, x,+,Δ,∇,X: d.s. 1 to d.s. 5 projectiles in sand at θ_o=10°.
(b) x,+,Δ,∇,X: d.s. 6 to d.s. 10 and ⊖,ϕ,⌀: o.s. 1 to o.s. 3 projectiles in Plasticine at θ_o=5°.
(c) and (d) ○: 12.7mm dia. sphere, ○:25.4mm dia. sphere, x,+,Δ,∇,X: d.s. 6 to d.s. 10 and ⊖,ϕ,⌀: o.s. 1 to o.s. 3 projectiles in Plasticine at θ_o=10°.

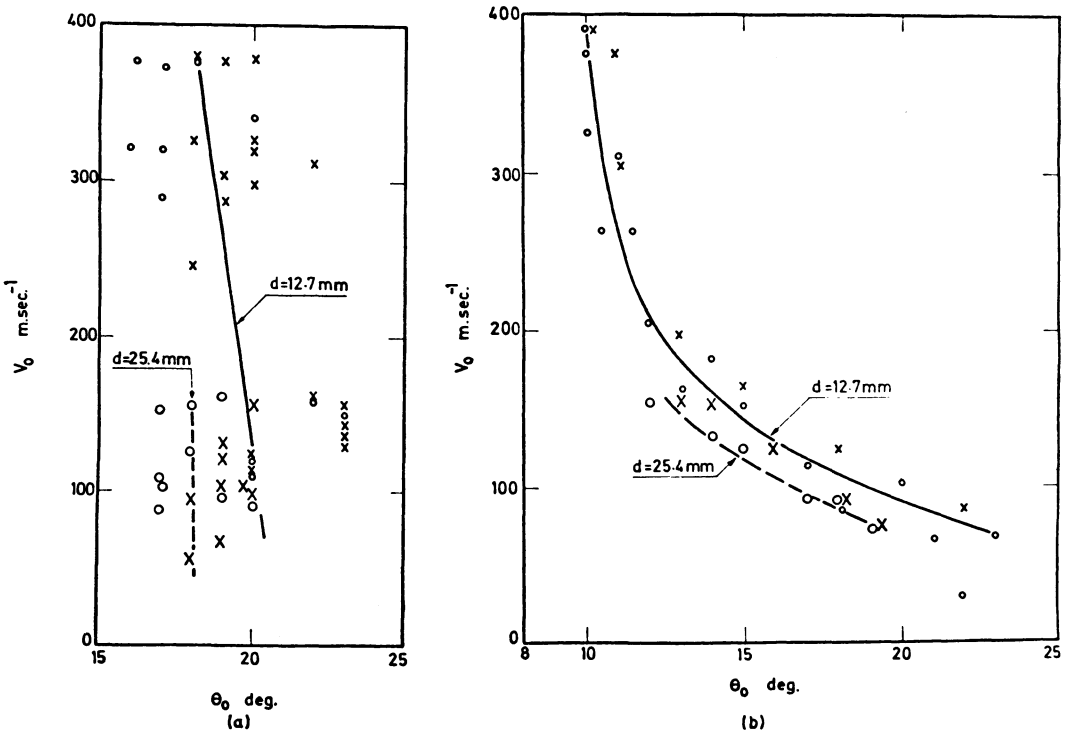

Fig. 9

Showing variations of the critical angle of ricochet of spherical projectiles with entry speed into sand (a) and into Plasticine (b): ∘: 12.7mm dia. ricochet; x:12.7 mm dia. no ricochet; 0:25.4mm dia. ricochet and X:25mm dia. no ricochet.

makes these results the more plausible. In sand, the critical angle of ricochet changes from 20° at 100 m/sec to 18° at 375 m/sec.

Effects of speed have been included in a simple analysis by Soliman, Reid and Johnson[25], according to whom the critical angle is given by $\theta_g = \theta_c - (2dg/\bar{v}^2)$, where θ_g is the critical angle at a given speed and (in radians) $\theta_c = 0.318\sqrt{\rho/\rho'}$. The experimental results in sand and in clay reported above support this analysis qualitatively.

A special phenomenon associated with the critical angle of ricochet

Tests in clay have shown that in the neighbourhood of the critical angle of ricochet the exit angle of the projectile increases suddenly and becomes very large, the exit speed reducing sharply and becoming very small. Data for a typical test, as shown in Fig. 10, are: v_o = 162 m/sec, θ_o = 13 1/2°, v_1 = 6.8 m/sec and θ_1 = 68.5°

Conclusions

Through this and other papers there has now been presented a large amount of experimental information about the single ricochet of projectiles having a spherical leading surface. Thus the validity of the theories of Birkhoff et al, Finnie, Hutchings and others should be better capable of being tested and compared; this should be able to be done in the near future. There is now, in our opinion, a need for, and the possibility of a reliable and general theory of the ricochet of curved rigid bodies from fluid, powder-like and plastically deformable media.

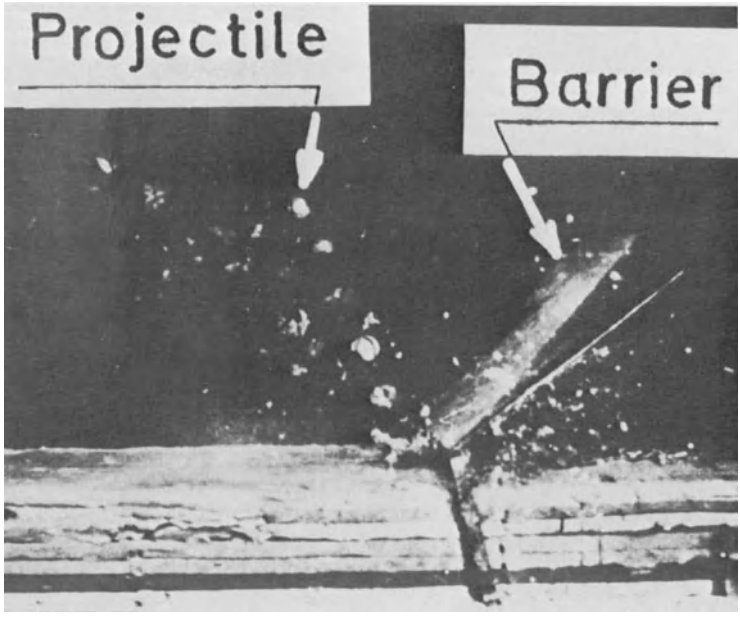

Fig. 10 Demonstrating the large angle of exit near the critical angle exit at 6.8 m/sec and about 68.5° after impact at 162 m/sec and 13.5°. (Barrier inserted to prevent ejected material from obscuring flight of projectile at exit.)

Acknowledgements

The authors are grateful to the Ministry of Defence, U.K., for supporting this work and wish to thank Mr. H.J. James for his interest in it. They also wish to thank Mr. C. Hooper for his help in the design of the photographic equipment. We are grateful to Mr. A. Taylor for his help with the experimental work and to Mrs. S. Venn for the typing of the paper. We also wish to thank Dr. S.R. Reid for reading and commenting on this manuscript.

References

1. Douglas, H., "Naval Gunnery", 1855 (fourth edition).

2. De Jonquières, E., "Comptes Rendus", 1883, 97, 1278.

3. Birkhoff, G., Birkhoff, G.D., Bleick, W.E., Handler, E.H., Murnaghan, F.D. and Smith, T.L., "Ricochet off Water" A.M.P. Memo. 42.4M, 1944.

4. Richardson, E.G., "The Impact of a Solid on a Liquid Surface" Proc. Phys. Soc. 61, 4, 1948, 352-367.

5. Johnson, W. and Reid, S.R., "Ricochet of Spheres off Water", J. Mech. Eng. Sci., 17, 2, 1975, 71-81.

6. Von Karman, T.H., "The Impact on Seaplane Floats during Landing", NACA TM 321, 1929.

7. Shiffman, N. and Spencer, D.C., "The Force of Impact on a Sphere Striking a Water Surface", A.M.P. Report 42.2R, 1943.

8. Trilling, L., "The Impact of a Body on a Surface at an Arbitrary Angle", J. Appl. Phys. 21, 1950, 161-170.

9. Dergarabedian, P., "Compressibility Effects during Water Entry", NAVORD Report 3523, 1955.

10. Pierson, J.D., "The Penetration of a Fluid Surface by a Wedge", Report No. 381, Experimental Towing Tank, Stevens Inst. of Tech., 1950.

11. Tate, M.B., Editor, "Proceedings of the NOL Water Entry Symposium", NAVORD Report 4180, 1955.

12. Johnson, W., Impact Strength of Materials, Arnold, London, 1972.

13. Sivarkrishna Prasad, P. and Subramanian, N.R., "In Compressible Potential Flow Past No-So-Slender Bodies of Revolution at an Angle of Attack", J. Fluid Mech. 70, 4, 1975, 651-661.

14. Hsu-Chieh Yeh, "Method of Solving Potential Field Problems with Complicated Geometries", J. Appl. Phys., 46, 10, 1975, 4431-4440.

15. Ting, L. and Keller, J.B., "Planing of a Flat Plate at High Fronde Number", J. of Fluids, 17, 6, 1974, 1080-1086.

16. Fuchs, O.P., "Impact Phenomenon", AIAA Journal, 1, 9, 1963, 2124-2126.

17. Hatch, Jr. H.G., "Effects of Water-Landing Impact on an Orbital Capsule from the Standpoint of Occupant Protection", NASA TN D-39, 1959.

18. Szebehly, V.G., "Hydrodynamic Impact", Appl. Mech. Review, 12, 5, 1959, 297-300.

19. Hutchings, I.M., "The Ricochet of Spheres and Cylinders from the Surface of Water", I.J.M.S., 18, 1976, 243-247.

20. Rayleigh, Lord, 1876, Phil. Mag. 2, 430-441.

21. Waugh, J.G. and Ager, R.W., "Water Entry Whip and Deceleration of Six Full-scale Torpedo Models with Ogive and Plate-ogive Heads", NAVORD Report 1308, 1951.

22. Waugh, J.G., "Water-entry Whip and Deceleration of Eight Full-scale Torpedo Models with Ogive and Spherogive Heads", NAVORD Report 1223, 1950.

23. Kornhauser, M., "Structural Effects of Impact", 1964, Cleaver-Hume Press, London.

24. White, F.G., "Photographic Studies of Splash in Vertical and Oblique Water Entry of Spheres", NAVORD Report 1228, 1950.

25. Soliman, S.F., Reid, S.R. and Johnson, W., "Ricochet of Spheres off Water and Sand", I.J.M.S., 18, 1976, 279-284.

26. Daneshi, G.H. and Johnson, W., "The Ricochet of Spherical Projectiles off Sand", I.J.M.S., in Press.

27. Daneshi, G.H. and Johnson, W., "The Ricochet of Dumb-bell Shaped Projectiles", I.J.M.S., in Press.

28. Daneshi, G.H. and Johnson, W., "Forces Developed in the Ricochet of Spherical, Ogival and Projectiles of Other Shapes" (to be published).

29. Finnie, I., "Erosion of Surfaces by Solid Particles", Wear, 3, 1960, 87-103.

30. Hutchings, I.M. and Winter, R.E., "The Erosion of Ductile Metals by Spherical Particles", J. Phys. D. Appl. Phys. 8, 1975, 8-14.

31. Winter, R.E. and Hutchings, I.M., "Solid Particle Erosion Studies Using Single Angular Particles", Wear, 29, 1974, 181-194.

32. Hutchings, I.M., Winter, R.E. and Field, J.E., "Solid Particle Erosion of Metals: The Removal of Surface Material by Spherical Projectiles", Proc. Roy. Soc. London, A 348, 1976, 379-392.

An Experimental Study on the Penetration of Rigid Projectiles into Epoxy Resin Targets

T. SHIOYA

Department of Aeronautics, Faculty of Engineering,
University of Tokyo

and

K. KAWATA

Institute of Space and Aeronautical Science,
University of Tokyo

Summary

Problems on the penetration of rigid projectiles into epoxy resin targets are studied experimentally. A light gas gun, a drop weight apparatus and an Instron type loading machine are used as the high speed, middle speed and low speed penetration devices, respectively. The test results are discussed in terms of the resistance force to the projectile in the target material relating to the velocity and the temperature. In the high speed region, the proportional relation between the force and the velocity is deduced, while in the middle and low speed tests, the force becomes proportional to the logarithm of the velocity, which is explained as the activation process in the target material.

1 Introduction

The problems on the penetration of solids has been one of the important theses in the engineering fields. Experiments under various conditions of the projectile

and target have been reported [1-5].
In this paper, the experiments on the penetration of steel balls into epoxy resins varying the penetration velocity widely using three kinds of devices are reported.

2 Experimental Procedure

2.1 Specimens The target materials used in the experiments are epoxy resins the composition and the curing condition of which are shown in Ref.6. The mechanical properties of the resins are largely dependent on the temperature which is exhibited by the creep modulus (30 sec) against temperature curve in Fig.1. The projectiles are sphere balls of steel with the diameter of 3 mm, 5 mm and 7 mm.

2.2 High Speed Impact Tests The high speed penetration tests were performed by the use of a two-stage light gas (Helium) gun with the caliber of 7.6 mm. The tests were carried out at the room temperature up to 2,440 m/s impact velocity. Figure 2 shows the relation between the impact velocity and the penetration depth obtained

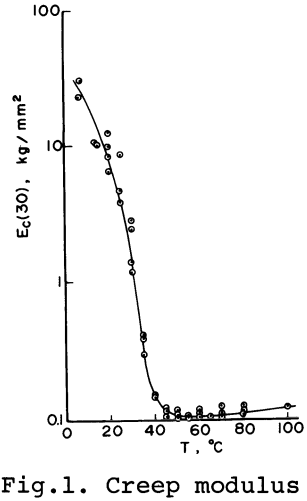

Fig.1. Creep modulus versus temperature

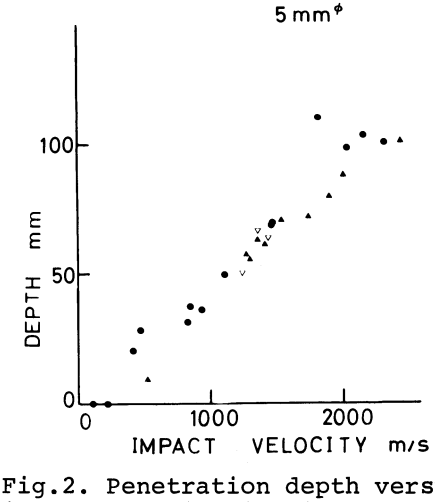

Fig.2. Penetration depth versus impact velocity in high speed tests.

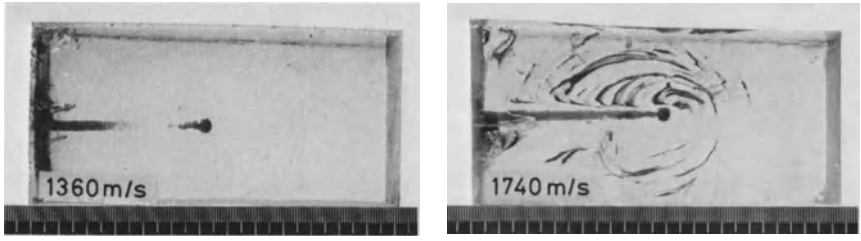

Fig.3. Target specimens after impact tests

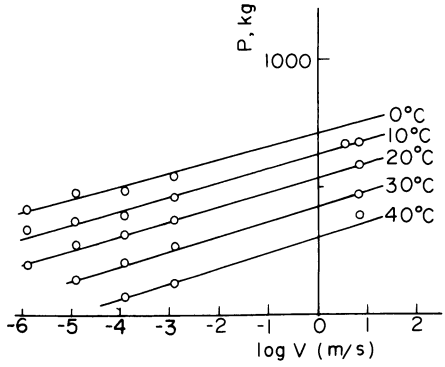

Fig.4. Penetration resistance force versus penetration velocity in middle and low speed tests.

in the tests. The target specimens after the tests are shown in Fig.3.

2.3 Middle and Low Speed Tests A drop weight apparatus (3.5 m height) was used for the middle speed penetration tests (several meters per second). The projectile is pushed into the target block by a thin supporting rod fixed to the drop weight which is taken sufficiently large compared with the presumed penetration load in order to ensure a constant speed penetration. The low speed penetration test (0.1 mm/min-100 mm/min), which is also a constant speed test, was conducted by the use of an Instron type loading machine. In these tests, the temperature was controlled. Figure 4 shows the obtained penetration resistance force versus the penetration velocity

in the logarithmic scale.

3 Discussions

In the case of the high speed impact of hard solids such as metal targets, it is known that in most cases, both the projectile and the target suffer the deformation or sometimes melting, and a large semi-sphere crator is produced on the target surface. There have been reports on the relation between the radius of the crator and the impact velocity or the kinetic energy of the projectile [1]. However, in the present experiments on the epoxy targets, in stead of a large crator, a slender opaque trace or occasionally no trace is formed behind the projectile and cracks spread in the target specimen are often observed in the high speed tests (more than about 1,300 m/s impact velocity) (Fig.3). Further, considering the similarity of the photoelastic fringe patterns of the target after the tests among the different impact velocity tests, it may seem better that the problem of the penetration into the epoxy resins is treated in the aspect of the relation between the resistance force to the projectile motion and the projectile penetration velocity in the target. The proportional relation between the impact velocity and the penetration depth for the same diameter projectiles seen in Fig.2 can be deduced by assuming the proportional relation between the penetration velocity and the resistance force. The results of other experiments in which the velocities in the targets were measured directly from the cut time intervals of the electric wires cast in the target specimens have reinforced this relation between the force and the velocity. The fact that the relation is not distorted remarkably at the tangential sound velocity in the target (875 m/s) may be interpreted that the shear resistance of the tar-

get material is negligible at the high speed penetration process.

The resistance force measured in the middle and low speed tests is not consistent with the extrapolation of the high speed tests, but, the proportional relation between the resistance force and the logarithm of the velocity is seen in Fig.4. This relation suggests that the penetration mechanism in the middle and low speed region is controlled by the activation process, such as,

$$v = A\exp\{ - (U - \lambda P)/RT \} \quad (1)$$

where v, P, R, T, U are the penetration velocity, the penetration resistance force, the gas constant, the temperature and the activation energy, respectively and A and λ are constants.

Determining the constants in Eq.(1) (exhibited as the straight lines in Fig.4) so as to fit the experimental data, 77 Cal/mol is obtained as the value of the activation energy, U. This value seems to be nearer to the energy value of the bond breaking process than to that of the chain slips in the polymers. If the bond breaking process is considered to control the penetration resistance in the epoxy resins, the opaque traces behind the projectile which are composed of small fragments of the target materials may be playing an important role in the penetration process.

The transition from the logarithmic to the proportional in the resistance force versus velocity relation has not been cleared in the present experiments, however, it would seem natural that as the penetration velocity increases, the dynamic pressure in front of the projectile becomes larger, and the problem can be regarded as the fluid impact penetration.

The effect of the projectile size in the experiments appears such that the resistance force is proportional to the square of the projectile length throughout all the

three type tests.
The penetration mode at the temperature higher than 50°C (the target material is in the rubber state) in the low speed tests seems rather elastic and brittle in the sense that a large elastic distortion on the target surface occurs followed by a sudden penetration accompanying a sharp conical crack with the vertical angle of 40-50°.

The authors wish to thank Mr. S. Hashimoto for his co-operation in the experimental works.

References

1 Summers, J.L.: Investigation of high-speed impact: Regions of impact and impact at oblique angles. NASA TN D-94, October 1959.

2 Denardo, B.P.: Penetration of polyethylene into semi-infinite 2024-T351 aluminum up to velocities of 37,000 feet per second. NASA TN D-3369, March 1966.

3 Fish, R.H.: The penetration of porous projectiles in aluminum and plastic targets. NASA TN D-4505, April 1968.

4 Kinard, W.H.; Collins, R.D.,Jr.: An investigation of high-velocity impact cratering into nonmetallic targets and correlation of penetration data for metallic and nonmetallic targets. NASA TN D-726, February 1961.

5 Huth, J.H.; Thompson, J.S.; Van Valkenburg, M.E.: Some new data on high-speed impact phenomena. J.Appl.Mech. Vol.24, March 1957, 65-68.

6 Shioya, T.; Kawata, K.: A preliminary investigation on the penetration of high-speed rigid projectiles into epoxy resins. Trans. Japan Soc. Aeronaut. Space Sci. Vol.19, No.43, March 1976, 15-22.

On the Transient Response of Long Beams Subjected to High Velocity Transverse Impact

S. KAWASHIMA

Department of Aeronautical Engineering,
Kyushu University, Fukuoka, Japan

Summary

This paper deals with the plastic deformation of long beams subjected to high velocity transverse impact. The effects of rotary inertia, shear force and strain-rate on the transient response are discussed from the theoretical and experimental results for pure aluminum.
It is shown that the deflection curves calculated by the strain-rate dependent traveling-wave theory are in much better agreement with the experimental results than those obtained by the elementary theory. In this computation, the linearized constitutive equations by Malvern are used. The values of the strain-rate constants used in the computation were obtained from the high velocity compression and high angular velocity torsional tests on the same material.

1. Introduction

The behavior of beams under transverse impact in plastic range has been studied by many investigators, since the problem was reported in 1950 by Duwez, Clark and Bohnenblust [1]. Their approach is constructed by modifying Boussinesq 's solution for elastic beams so that a plastic material can be handled. The experimental results in their paper are compared with the calculated deflection curves, but the numerical agreement is not good in the case of the copper beam. Other attempts using the rigid-plastic analysis are given by Conroy[2], Lee and Symonds[3], and Parks[4], employing the concept of idealized plastic hinge formation. These efforts in the problem have been directed towards the analyses based on the elementary beam theory with the static relation between bending moment and curvature, that is, elastic-plastic or rigid-plastic.

For high velocity transverse impact loading, it is

required that the traveling-wave theory is applied to predict seriously the transient behavior of beams. As pointed out by Flügge[5], the effects of rotary inertia and transverse shear deformation must be taken into account in application of traveling-wave theory because waves propagate with infinite velocity. In addition, the strain-rate effects become increasingly important. The numerical traveling-wave solution of this type of problem considering the effects of strain-rate has previously been presented in reference[6], in which the strain-rate law of Malvern type[7,8] was used and the flow constants of strain-rate law for both bending stress and shear stress were assumed to be equal. The strain-rate effects as well as the effects of rotary inertia and transverse shear deformation, however, have not as yet been clearly evaluated for an actual transverse impact problem.

In this paper, the author describes the results of the experimental and theoretical investigation for the transient deformation of an annealed pure aluminum beam under high velocity impact loading. In order to study the effects of rotary inertia, transverse shear deformation and strain-rate, experimental results are compared with the theoretical results. The theoretical analysis is made by means of the traveling-wave theory and the strain-rate law of Malvern type is assumed for both bending stress and shear stress. In the numerical calculation, the values of flow constant[9,10] are used, which have been obtained from the experiments of the annealed pure aluminum bars subjected to longitudinal and torsional impact loading.

In the experiment, a long beam of pure aluminum (purity; 99.73%) with square cross section is fixed at one end and is suddenly set into constant velocity motion transversely at the free end by the firing of a steel piston from a compressed air gun. The beam motion is photographed with a high speed camera.

2. Experiment

(1) Specimens

The specimens used in the experiment were pure aluminum (purity; 99.73%) extruded beam, which had a square cross section and the dimensions of the specimens were; length, 1,250 mm; width, 10 mm; depth, 10 mm. The length of the specimens was so chosen that no reflected waves returned to the measuring stations during the time of interest. So, it was possible to compare the experimental results with the theoretical ones for the infinite beam. All specimens were annealed for 1 hr. at 350°C. The composition and static tensile properties of the specimens are given in Table 1.

Material	Composition (%)			Tensile test		
	Cu	Si	Fe	Proof stress (kg/mm^2)	Ultimate strength (kg/mm^2)	Elongation (%)
99.73% Al.	0.01	0.06	0.20	3.1	7.3	52.5

Table 1. Composition and tensile properties for specimens

The static bending moment-curvature curve is shown in Fig. 1. The stress-strain curve was obtained experimentally for the specimens. The bending moment-curvature curve was computed for a beam 10 mm wide and 10 mm deep.

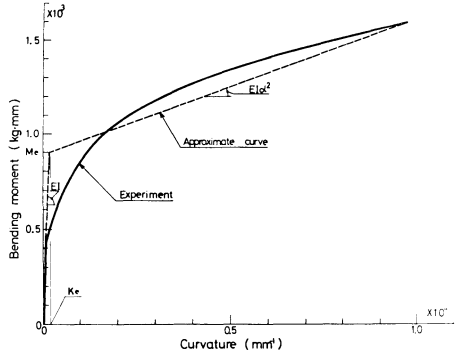

Fig. 1. Static bending moment-curvature curve for annealed aluminum beam

The approximate static bending moment-curvature curve taken for the numerical computation consists of two straight lines as shown in Fig. 1, where Me and Ke are the bending moment and the curvature at the elastic limit, respectively. In the plastic range, the curve makes an angle: $EI\alpha^2$ with the horizontal axis, where α is a constant which indicates the degree of strain-hardening, and its value α is equal to 0.11 for the specimens.

(2) Equipment

The experiments were carried out by the impact air gun. Experimental arrangement and instrumentation are shown in Fig. 2. This equipment consists of : (1) high compressed air source (150 Kg/cm^2), (2) reservoir tank, (3) firing device, (4) acceleration barrel, (5) stopping anvil and (6) measuring instrument and specimen.

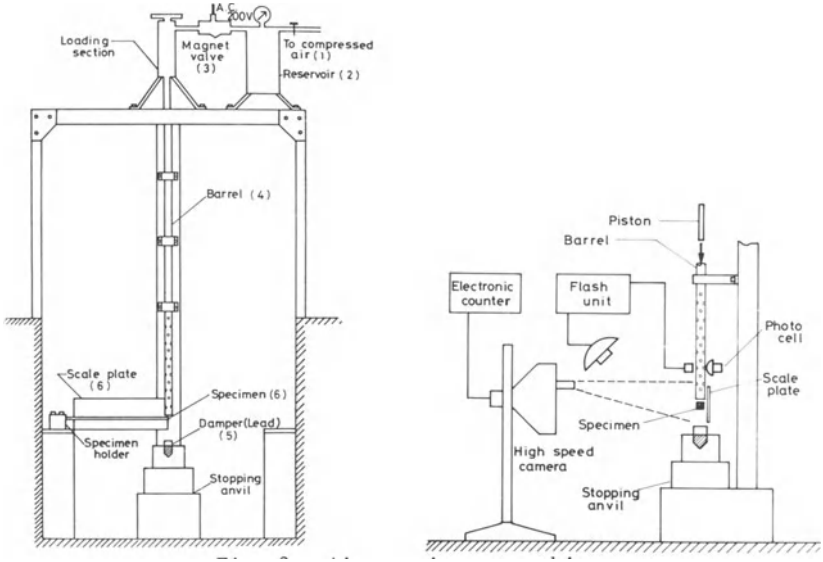

Fig. 2. Air gun impact machine

Tests were carried out on the cantilever beams. A striker piston is 27 mm in diameter, 250 mm in length and made of the quenched Ni.-Cr. steel. The steel piston was fired by the compressed air gun and the beam was struck

camera. These pictures are replotted as deflection curves at any time.

4 Discussion

(1) Impact velcity

As an example, the transverse displacement-time diagram is shown in Fig. 3. The slope of the curve gives the deflection velocity of the impact end of specimens. It may be seen that the transverse velocity at the free end remains approximately constant within 1.0 millisecond. In present experiments, the impact velocity was varied from 30 to 100 m/sec and the beams must be deformed plastically.

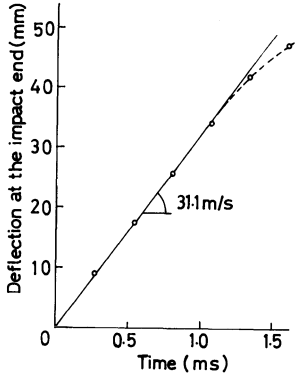

Fig. 3. Transverse displacement-time diagram at the impact end

(2) Transient deflection curves

The theoretical deflection curves are plotted, together with one experimental curve in Fig. 4. It can be seen that there is a considerable discrepancy quantitatively between the experimental curve and the calculated one by the theory [1], in which the approximate bending moment-curvature curve for aluminum beam (given in Fig. 1) is used. Then, in order to study the dependency of deflection on the strain-rate, two cases were calculated with the traveling-wave theory. These results are also shown in Fig. 4. The one is the deflection curve computed by taking account of the strain-rate effects (———). The

transversely at the point, 5 mm from the tip.
The transient motion of the beam and the reference scale were photographed with a high speed camera, Dynafax model 350 (Maximum framing rate; 35,000 pictures per sec.) at the any framing rate. The framing rate was measured with an electronic counter and the rate was used as the scale of time axis for deformation. The framing rate 35,000 pictures per sec. was corresponded to the time interval of each picture being about 30 microsecond.
Upper limit of impact velocity was about 100 m/sec. with this equipment and the 250 mm length steel piston. For the specimens above mentioned, the experiments were performed with the impact velocities, 31.1, 52.6 and 90.5 m/sec.

3. Experimental Results

The typical record with the high speed camera is shown in Photo. 1. The steel piston moved downward with the beam after impact. Photo. 1 shows the motion of the beam of which the portion is 25 cm in length from the tip. As mentioned before, the time interval of each picture can be found from measuring the framing rate of the high speed

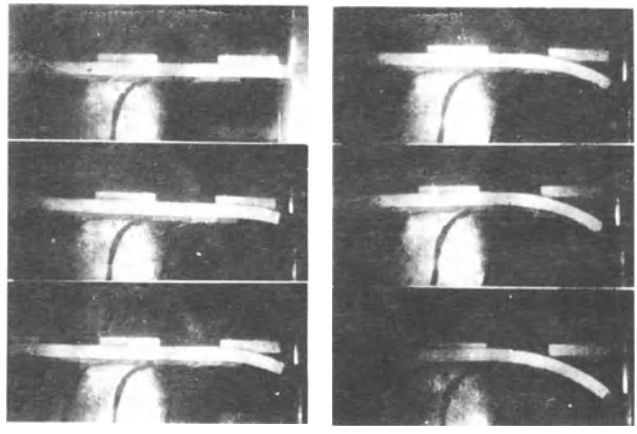

Photo. 1. Typical photographical record of beam deformation (impact velocity: 31.1m/s, framing rate: 62.5μsec. per picture)

strain-rate law of Malvern type is used for both the bending stress and the shear stress. In the numerical calculation, $K_C=5.0 \times 10^6$ and $K_S=5.5 \times 10^6$ 1/sec were used as the values of flow constant. These values were obtained from the longitudinal and the torsional tests, respectively. The other is the curve computed by the use of strain-rate independent theory ($K_C=K_S=0$, —·—·—). It is evident that the result by traveling-wave theory considering the strain-rate effects is in much better agreement with the experiment than those by the elementary theory and the traveling wave theory neglecting the strain-rate effects.

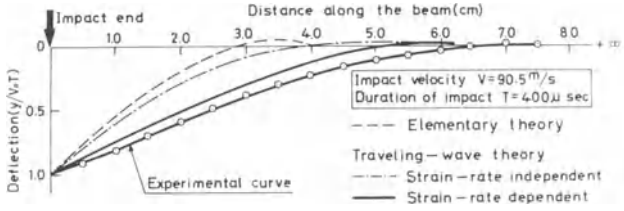

Fig. 4. Deflection curves for annealed-aluminum beam

5 Conclusions

An experimental study has been made in which the deflection curves of long cantilever beams have been obtained during impact. The transient deflection of the pure aluminum beams under high constant velocity transverse impact was compared with three theoretical results. The first theoretical computation was performed by use of the elementary theory. The last ones were made by the strain-rate dependent and independent traveling-wave theories, respectively.

(1) The constants (K_C,K_S) which determine the strain-rate dependency in bending and shear are available from the experimental data which were obtained from the compression and the torsional tests.

(2) The deflection curves obtained by the strain-rate

dependent theory are in much better agreement with the experimental ones than the curves obtained by the strain-rate independent theory.

(3) The effect of shear force on the transverse displacement cannot be neglected, but the effect is smaller than the strain-rate effect.

6 References

1) P.E.Duwez, D.S.Clark and H.F.Bohnenblust, "The Behavior of Long Beams under Impact Loading, J.Appl.Mech., Vol. 17, p.27 (1950)

2) M.F.Conroy,"Plastic-Rigid Analysis of Long Beams under Transverse Impact Loading," J.Appl.Mech., Vol.74, p.465 (1952)

3) E.H.Lee and P.S.Symonds, "Large Plastic Deformations of Beams under Transverse Impact," J.Appl.Mech., Vol.74, p.308 (1952)

4) E.W.Parks, "The Permanent Deformation of a Cantilever struck Transversely at its Tip," Proc.Roy.Soc.London, A228, p.462 (1955)

5) W.Flügge, Die Ausbreitung von Biegungswellen in Staben; Z.A.M.M., Bd.22, Nr.6, Dec. p.312 (1942)

6) H.J.Plass, Jr., "Theory of Plastic Bending Waves in a Bar of Strain Rate Material," Proc. 2nd Midwestern conf. on Solid Mech., p.109 (1955)

7) L.E.Malvern, "Plastic Wave Propagation in a Bar of Material exhibiting a Strain-rate Effect," Q.Appl. Mech., Vol.8, No.4, p.405 (1951)

8) L.E.Malvern, "The Propagation of Longitudinal Waves of Plastic Deformation in a Bar of Material exhibiting a Strain-rate Effect," J.Appl.Mech., Vol.73, p.203(1951)

9) S.Kawashima and R.Kawamura, "An Investigation of the Mechanical Properties of Aluminum Bars at High Rates of Loading," Trans.Japan Soc. Aero. Space. Sci., Vol. 13, No.22, p.27 (1970)

10) S.Kawashima, et. al., "On the Effect of Strain-rate

for shear Deformation," Preprint. Presented at the 18th Conference on Structure and Strength (1976), (Japan soc. Aero. Space Sci. and Japan Soc. Mech. Eng.), to be published in the Transaction of the Japan Soc. Aero. Space Sci.

11) S.Kawashima and H.Okubo, "On the Plastic Deformation of the Aluminum Beams under High Velocity Transverse Impact," Technology Rep. Kyushu Univ., Vol.42, No.3 (1961)

12) S.Kawashima and H.Okubo, "On the Effects of Strain-rate for the Transient Response of Beams under High Velocity Transverse Impact." Preprint, Presented at the Symposium of Western branch of Japan Soc. Aero. Space Sci. (1974)

13) S.Kawashima and H.Okubo, "On the Transient Response of the Aluminum Beams under High Velocity Transverse Impact." Preprint. Presented at the 17th Conference on Structure and Strength (1975), (Japan Soc. Aero.Space Sci. and Japan Soc. Mech. Eng.)

7 Appendix

(1) Strain-rate dependent traveling-wave theory [6,12,13]

The propagation of plastic wave is governed by the following partial differential equations:

$$\left.\begin{aligned} EI\frac{\partial k}{\partial t} &= \frac{\partial M}{\partial t} + K_c(M - \bar{M}) \\ GA_s\frac{\partial \gamma}{\partial t} &= \frac{\partial Q}{\partial t} + K_s(Q - \bar{Q}) \end{aligned}\right\} \text{(material behavior)} \qquad \text{(A-1)}$$

$$\left.\begin{aligned} \frac{\partial M}{\partial x} - Q &= \rho I\frac{\partial \omega}{\partial t} \\ \frac{\partial Q}{\partial x} &= \rho A\frac{\partial v}{\partial t} \end{aligned}\right\} \text{(equation of motion of the element as shown Fig. A-1)} \qquad \text{(A-2)}$$

$$\left.\begin{aligned} \frac{\partial k}{\partial t} &= \frac{\partial \omega}{\partial x} \\ \frac{\partial \gamma}{\partial t} &= \frac{\partial v}{\partial x} + \omega \end{aligned}\right\} \text{(equation of continuity)} \qquad \text{(A-3)}$$

where

M and $\bar{M}$: dynamic and static bending moment
Q and $\bar{Q}$: dynamic and static shear force
Kc and Ks: flow constants for bending stress and shear stress
A and As: area and effective area
I: cross-sectional moment of inertia
ω: angular velocity of the cross section
v: transverse velocity, k: curvature
γ: shear strain, ρ: density
E: Young's modulus, G: shear modulus

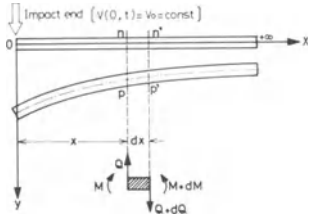

Fig. A-1, Deflection of a beam due to transverse impact

The above equations can be integrated numerically by means of the method of characteristics under appropriate boundary conditions. The characteristics are integrals of the following differential equations:

$$dx = 0 \quad \text{(twice)}$$
$$dx \mp C_M dt = 0 \qquad \text{(A-4)}$$
$$dx \mp C_Q dt = 0$$

where

$$C_M = \sqrt{E/\rho}\ , \qquad C_Q = \sqrt{\frac{GA_s}{\rho A}} \qquad \text{(A-5)}$$

The families of characteristics in the x-t plane are shown in Fig.A-2 (a). The following equations hold respectively along these characteristics;

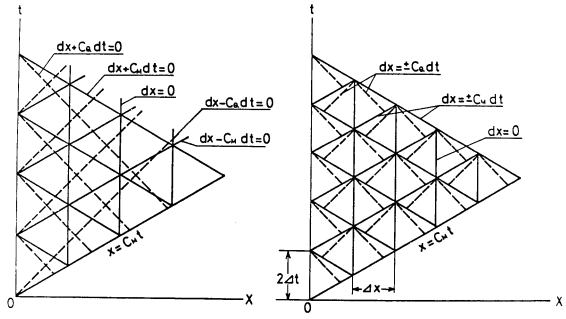

(a) (b)

Fig. A-2. Characteristics in x-t plane

$$
\begin{aligned}
&dM - EIdk = -K_c(M - \bar{M})dt && \text{along } dx = 0\\
&dQ - GA_s d\gamma = -K_s(Q - \bar{Q})dt && \text{along } dx = 0\\
&dM \mp \rho IC_M d\omega = \pm C_M Q - K_c(M-\bar{M})dt && \text{along } dx \mp C_M dt = 0\\
&dQ \mp \rho AC_Q dv = \rho AC_Q\omega - K_s(Q-\bar{Q})dt && \text{along } dx \mp C_Q dt = 0
\end{aligned}
\qquad \text{(A-6)}
$$

Among these six variables, there exists the following relations:

$$
\begin{aligned}
\Delta M &= -\rho IC_M \Delta\omega = EI\Delta k\\
\Delta Q &= -\rho AC_Q \Delta V = GA_s \Delta\gamma
\end{aligned}
\qquad \text{(A-7)}
$$

just behind the leading wave fronts $x=C_M t$ and $x=C_Q t$ respectively.

From the Eqs.(A-6) and (A-7), the following relations are obtained:

$$
\int_{M_o}^{M} \frac{dM}{K_c(M-\bar{M})} = -\frac{1}{2}t \qquad \int_{Q_o}^{Q} \frac{dQ}{K_s(Q-\bar{Q})} = -\frac{1}{2}t \qquad \text{(A-8)}
$$

where $M_o=-\rho IC_M\omega_o$ and $Q_o=-\rho AC_Q v_o$ are the bending moment and the shear force at x=0 and t=0, respectively.

(2) The numerical integration for the constant-velocity impact

Eq.(A-6) can be integrated approximately by replacing the finite difference equations. The numerical computation may be performed to determine the six variables in the x-t plane as shown in Fig.A-2. (b). The computation can

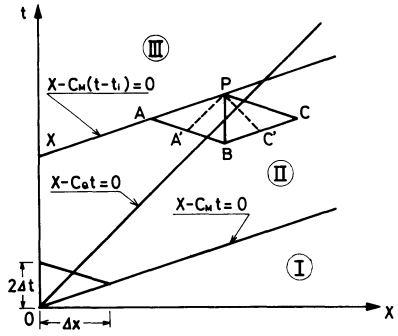

Fig. A-3, Element (P,A,B,C) containing shear discontinuity

be carried out successively for an element in the x-t plane bounded by the characteristics, $dx \mp C_M dt=0$ (solid lines).

The boundary conditions are $M(0,t)=0$ and $v(0,t)=v_o$ for the constant velocity impact. From the Eq.(A-8), the values of M and Q are obtained by the numerical integration along the $x-C_Mt=0$ and $x-C_Qt=0$, respectively. For the constant velocity impact, a shear discontinuity is present, which propagates along the characteristics $x-C_Qt=0$. In our computation, it is assumed that, for the case as shown in Fig.A-3, the values of Q, v and γ at the P point are obtained by superposing their values given by the second equations of Eq.A-7 and Eq.A-8. And also, the following assumptions are used in our computation:

(1) The static values of $\bar{M}$ and $\bar{Q}$ depend only upon k and γ respectively.

(2) The loading conditions are $\Delta k/\Delta t > 0$ or $\Delta\gamma/\Delta t > 0$, independently each other.

The constants used in the computation for the pure aluminum specimens are as follows;

h = depth of section = 10 mm

w = width of section = 10 mm

$A = 100\ mm^2$ $\quad A_s = (2/3)A = 66.67\ mm^2$

$I = 833.3\ mm^4$ $\quad E = 7200\ Kg/mm^2$

$G = 2700\ Kg/mm^2$ $\quad \rho = 2.754 \times 10^{-10}\ Kg\ sec^2/mm^4$

$M_e = 900\ Kg\ mm$ $\quad Q_e = 207\ Kg$

$k_c = 5.0 \times 10^6\ 1/sec$ $\quad k_s = 5.5 \times 10^6\ 1/sec$

$\alpha = 0.11$

High Speed Deformation of Shells

M. S. EL NASCHIE
University of Riyadh, Saudi Arabia

Introduction

In general thin elastic shells subject to a dominantly compressive membrane stress state show a tendency to buckle explosively. The shell will then deform with considerable speed so that it can only be observed using a high speed camera. Furthermore, the loss of stability occurs at loads far below the exact branching loads predicted theoretically.[1] It was not until the pioneering work of von Karman and Koiter that this problem became reasonably understood.[1-12] This was achieved by considering the nonlinear problem of the shell post buckling behaviour. The complimentary character of von Karman's large deflection approach and Koiter's initial post buckling theory was realised in recent years. A short account and criticism of both approaches can be found in Refs. 2,9. Thus, in the last two decades or so, the overwhelming research activity was drawn in the direction of the classical idea of calculating the post buckling path derivatives as accurately as possible and determining the imperfection sensitivity. On the other hand, new interest recently arose in another radically different and very simple approach which treats shell buckling from the stand point of the isometric bending theory.[13-31] The various reasons for initiating this geometrical approach were discussed in Refs. 11, 22, 23. However, the main motive was, in fact, a general feeling that stability analysis of shell structures was becoming incredibly complicated. At the crutial preliminary

design stage, it is more important for the engineer to be able to estimate the critical loads rather than to make an exact calculation of the stability limit of a new shell structure and, consequently, be able to keep his head clear for conceptional thinking.[33] In the following, a few applications of the isometric theory to statical and dynamical buckling of shells will be considered. A general treatment for doubly curved shells under external pressure will also be discussed.

The axially compressed plate

As a first example we will consider the case of coincidental isometric bifurcation, that is to say the upper and lower point of stability coinciding. Consider a rectangular plate with the wall thickness t and the dimension ℓ and b in the x and y directions respectively. The plate is supposed to be simply supported and compressed along b by a uniform axial pressure p. It is helpful to imagine the plate to be composed of longitudinal (y) and transversal (x) elements. The bending and torsion rigidity of the longitudinal elements thus provides an elastic support for the transversal elements. The larger the buckling wave length in y direction, the smaller the elastic support will be. Thus, a buckling configuration with a one half sinuous wave will be considered which corresponds to the case where ℓ is small compared with b. We now imagine a part of the middle of the plate as isolated which has the breadth unity, the length ℓ and the moment of inertia $t^3/12$ and rests on an elastic medium formed by beams of the length b and moment of inertia $t^3/12$. From the geometry of a flat plate with these boundary conditions, we see that there exists no developable surface except the undeflected shape. Therefore, only very small bending deformation can be tolerated without stretching the middle surface of the plate. Consequently, the lower

stability limit is identical to the upper or branching limit. When buckling starts in the direction of compression, the longitudinal elements will not only bend but will aslo twist and thus activated stabilizing lateral forces which act as a stabilizing elastic medium. The problem now is to determine the two constants of this elastic support due to bending and torsional rigidity of the longitudinal elements. Considering the half sin wave deflection form

$$W(x;y) = w(x) \sin \frac{\pi}{b} y \tag{1}$$

these proportionality constants are easily found to be

$$C_{\ell} = \frac{Et^3}{12(1-\nu^2)} (\pi/b)^4 \tag{2}$$

for bending and

$$G_{\ell} = \frac{Et^3}{6(1-\nu^2)} (\pi/b)^2 \tag{3}$$

for torsion. The total potential energy functional is, therefore,

$$V = \int_0^{\ell} \left(\frac{Et^3}{24(1-\nu^2)} w''^2 + \frac{1}{2} G_{\ell} w'^2 + \frac{1}{2} C_{\ell} w^2 - \frac{1}{2} P w'^2 \right) dx \tag{4}$$

The first two terms in this very simple functional represent the total energy functional of a simple Euler strut while the third and fourth terms resemble the energy due to a fictitious supporting elastic medium. Expanding the deflection in the following Fourier series

$$w = \sum_i a_i \sin \frac{i\pi}{\ell} x \tag{5}$$

and inserting this in the quadratic form, minimising with respect to a_i the generalized co-ordinates and then with respect to i, the smallest critical pressure is immediately found to be

$$p^c_{min} = \frac{Et^3}{3(1-\nu^2)} \left(\frac{\pi}{b}\right)^2 \tag{6}$$

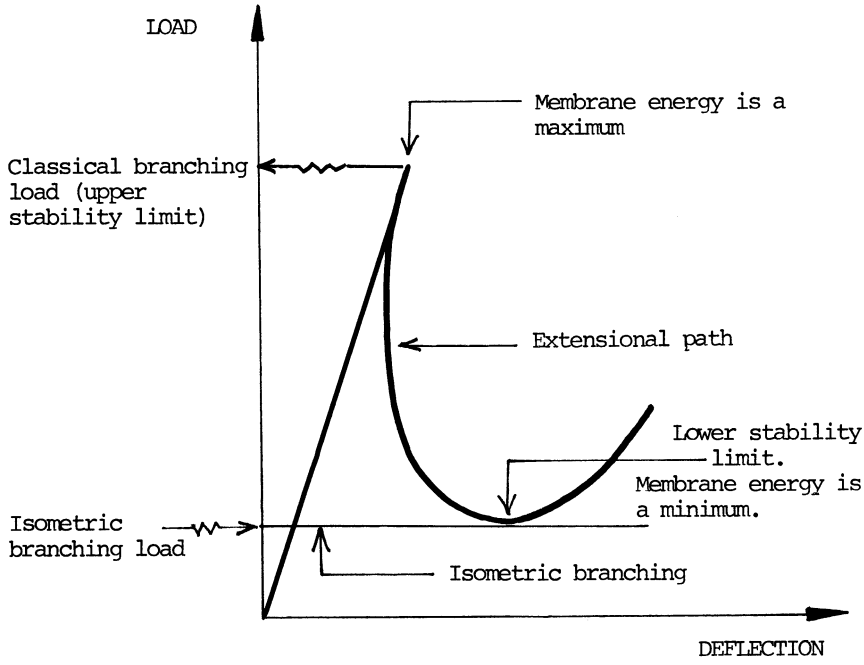

FIG. 1 - Isometric approximation of the lower stability limit.

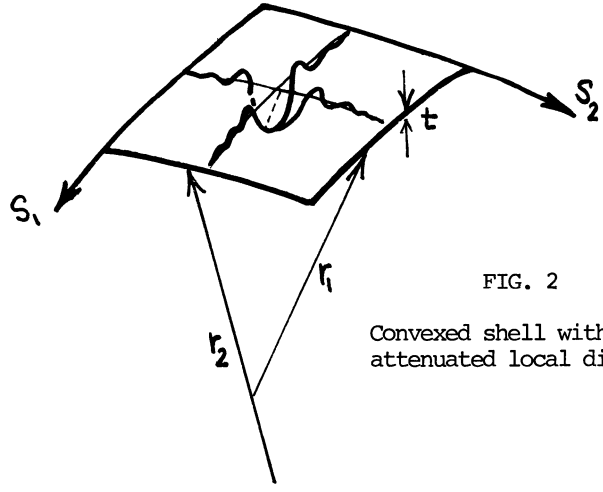

FIG. 2

Convexed shell with attenuated local dimple,

This is identical to the well known exact critical value. Once more, it is important to emphasize that the plate exhibits a symmetric stable type of branching point, as a rigorous nonlinear analysis would reveal. That is the reason why the minimum of the post buckling curve is identical to the branching load itself.

Statical buckling of an axially compressed cylinder

As an example of the general case where the branching point does not coincide with the lower stability limit, a cylindrical shell will be considered. The cylinder is supposed to be of the length ℓ, the radius r and the wall thickness t and subject to axial dead load P. Pogorelov considered this problem from the stand point of geometrical bending and proved the existence of a buckled configuration isometric to the original unbuckled cylinder.[15-17] The remaining main problem is to write down, for the isometric deformed surface, an expression for the corresponding energy density. A linear eigenvalue analysis based upon this energy expression will thus yield a pseudo branching load which is almost equal to the minimum of the post buckling curve of the shell.[18-23] In other words, the lower stability limit which can be used as a reasonable estimate for the actual buckling load of a shell can be obtained using linear analysis and without calculating the whole post buckling path (see Fig. 1). The reason for this is that the isometric surface is, in fact, the ultimate ideal shape of the post buckling configuration of a shell. This fact can be argued in different ways on the basis of the Gauss principle[24] or the principle of minimum potential energy.[18-25] Excluding any extensional deformation of the shell, it is easy to show that the differential equation corresponding to the isometric energy functional is[19-21]

$$W'''' + (\sigma/E)\, K_1\, W'' + K_2\, W = 0 \qquad (7)$$

where

$$K_1 = \frac{1-\nu^2}{b^4} 720r^2 \quad , \quad K_2 = \pi^3 t^2 \frac{120r^2}{b^8}$$

W is the radial deflection and b is the isometric half waves length in the circumference. For an overall transformation of the shell surface, the isometric branching load is easily found to be

$$\sigma^c_{min} = 0.187\ Et/r$$

which is remarkably close to the result obtained from a full nonlinear analysis. For a local transformation, the buckling load is even considerably lower.

General theory of doubly curved shells in the post critical range

In the following we investigate a post critical isometric bending of general nature. We will consider a doubly curved thin elastic shell of arbitrary shape assuming, however, that the Gaussian curvature is positive. As the shell surface is a two dimensional Riemann space, the integrability conditions are given by Peterson-Mainardi-Godazzi and Gauss equations

$$L_{\alpha\beta}|_\gamma = L_{\alpha\gamma}|_\beta \tag{8}$$

$$R_{\varepsilon\alpha\beta\gamma} = L_{\alpha\beta}L_{\gamma\varepsilon} - L_{\alpha\gamma}L_{\beta\varepsilon} \tag{9}$$

where $L_{\alpha\beta}$ and $R_{\varepsilon\alpha\beta\gamma}$ are the second fundamental tensor and the Riemann curvature tensor respectively. In the immediate vicinity of any point it can be shown that these equations are approximately satisfied. Consequently, a small part of a materialized surface can be regarded as quasi-developable. Thus, there exists a one-to-one mapping of the original convex surface on to the concave buckled surface, under which the metric of corresponding curves is preserved. The local deformation

will, therefore, be quasi-geometric bending. Thus, in accordance with the Hamiltonian principle, the deformation will be dominated by isometric energy at least in the advanced post buckling range. N. Kilchevesky[24] et al recently gave an analytical proof of this on the basis of the Gauss principle. In this connection it might be mentioned that H. Weyl was the first to prove the existence of a convexed polyder with fixed matrix in the case of positive Gaussian curvature. Under the same assumption, E. Levi was able to prove that in a sufficient vicinity of any point on an analytical convexed surface, continuous pure bending is geometrically admissable. It should be noted, however, that the condition of positive Gaussian curvature is vital here since W. Efimov proved (for the general case) the existence of certain points where such bending is not permissable. We now consider a shallow region of the shell with the principal radii r_1 and r_2. Again it is helpful to imagine the shell region to be composed of several strips in one of the principle directions S_1, elastically supported by imaginary strips in the perpendicular direction S_2. However, in the present case the strips in both directions are weakly curved beams. This suggests an analysis along very similar lines to that used in the preceding sections. Following Ref. 21, equation No. 10 of that work as well as equation No. 7 of the present work can be generalised to

$$\overset{\cdots\cdot}{W} + (\sigma_1^c/E)\,\underline{K}_1\,\ddot{W} + \underline{K}_2\,W = 0 \qquad (10)$$

where $(\dot{}) = \frac{d(\ )}{d\phi_1}$, ϕ_1 is the angular co-ordinate in S_1 direction, W is the radial displacement, $\sigma_1^c = p^c r_1/2t$ is the membrane stress in S_1 direction, $\underline{K}_1 = 720 r_2^2(1-\nu^2)/b^4$ and $\underline{K}_2 = \pi^3 t^2 120 r_1^2/b^8$. A Galerkin solution associated with $W = \sum_1 a_i \sin i\phi_1$ yields, in this case, the critical pressure

$$p^{c}_{min} \cong 0.37 \sqrt{EE_t} /(r_1 r_2) \qquad (11)$$

where E has been changed to $\sqrt{EE_t}$ in order to account for plasticity effects. For $r_1=r_2=r$ and perfect elastic behaviour, the above formula gives an excellently close result to that obtained by von Karman. Following Ref. 21, the same differential equation can be used for the case of an attenuated local dimple (see Fig. 2) if $\underline{K}_1$ and $\underline{K}_2$ are replaced by the modified Pogorelov-Kirste coefficients for which

$$\overline{K}_1 = \frac{720 r_1^2 (1-\nu^2)}{(b/2)^4} \quad , \quad \overline{K}_2 = \frac{120\pi^3 (t r_2)^2}{(b/2)^8} \qquad (12)$$

The critical value associated with the attenuated local buckling mode

$$W = a e^{-ks_1} (\cos ks_1 + \sin ks_1) \; ; \; S_1 = \phi_1 r_1 \qquad (13)$$

as a Galerkin function is $p^{c}_{min} = \sqrt{0.325\, EE_t t^4}/(r_1 r_2)$. In the case of a spherical shell, this formula yields a lower stability limit which is in fairly good agreement with the experimental results.

Dynamical buckling of an axially compressed cylindrical shell

In all the preceding analysis the inextensional deformation was a special feature of the post buckling range. In the following, however, we will consider an interesting, completely inextensional buckling mode of a shell which is a characteristic of the initial buckling behaviour. This rather surprising phenomena arises in the dynamical buckling of a cylindrical shell under non-conservative tangential axial pressure. To show this we start from the differential equation

$$W'''' + (Et/2r^2)\frac{24(1-\nu^2)}{Et^3} W + \frac{p12(1-\nu^2)}{Et^3} W'' + (\frac{\mu}{2})\frac{24(1-\nu^2)}{Et^3} \overset{**}{W} = 0 \qquad (14)$$

where $(') = \frac{d()}{dx}$, $(^{*}) = \frac{d()}{dT}$, T is the time and μ is the mass density of the cylinder. Assuming

$$W(x;T)=\tilde{W}(x)\ e^{i\lambda T} \tag{15}$$

where λ is the frequency and $i = \sqrt{-1}$, we find that

$$\tilde{W}''''+\frac{12p(1-\nu^2)}{Et^3}\tilde{W}'' + \tilde{W}\left(\frac{Et}{2r^2}\ \frac{24(1-\nu^2)}{Et^3} - \frac{12\lambda\mu(1-\nu^2)}{Et^3}\right)=0 \tag{16}$$

The boundary conditions are

$$\tilde{W} = \tilde{W}' = 0 \qquad x = 0 \qquad (a)$$

and (17)

$$\tilde{W}'' = \tilde{W}''' = 0 \qquad x = \ell \qquad (b)$$

Writing down the general solution of this differential equation and substituting it into the boundary conditions leads to a system of four linear homogeneous algebraic equations for the unknown constants of integration. A nontrivial solution of this system is only possible if the determinant of the coefficients vanish. Expanding this determinant, the frequency equation is obtained. Now for buckling to be triggered, the real part of the frequency equation must vanish. This is analytically equivalent to the vanishing of the discriminant of the frequency equation. Omitting the details of the lengthy standard procedure, the critical pressure is found to be

$$p^c = (1.67)\ \frac{E}{(1-\nu^2)}(t/\ell)^2 \tag{18}$$

The critical value of the rotating nonconservative axial pressure is, therefore, independent of the radius of the shell and considerably smaller than the well known classical critical pressure $P^c = 0.6Et^2/r$. This rather surprising result is due to the fact that this particular dynamical buckling mode is fully isometric. As far as the author is aware, the fact that the buckling load of a cylindrical shell under certain types of external

pressure approach zero as the length tends towards infinity was never pointed out in the literature before and seems to deserve some careful consideration.

Conclusion

Unstable post buckling of a shell structure is marked by the existence of a surface which is noncongruent and isometric to the undeflected shell. This surface is the ultimate post buckling shape of the shell. Based on this idea, a geometrical buckling theory is developed which is sufficiently simple and intuitive to open, for the designer, the path to developing his intuition towards shell buckling. The work, as viewed by the author, is by no means an alternative theory to that of Koiter or von Karman. It is only meant to be complimentary to them. It is thought that the three theories together present a reasonably complete tool for dealing with shell instabilities. The present method is thought to be especially valuable in obtaining fairly accurate estimations for the buckling loads of complicated structures where other methods might fail. It is seen here that having solved the membrane stress state problem of a convexed doubly curved shell with a positive Gaussian curvature under external pressure, the problem of estimating the lower stability limit is rendered more or less trivial. There are many indications for the correctness of the postulates of the isometric buckling theory. These are based on several experiments filmed by high speed camera and the numerical results reported here which are in reasonable agreement with those obtained from a nonlinear post buckling analysis. There is also the paradoxical behaviour of oval cylindrical shells under axial pressure[12] which can be quite well explained by the isometric theory. Using a simple model[31], the complimentary character of Koiter's initial post buckling theory and von Karman's large deflection approach is confirmed for the oval cylindrical

shell. In conclusion, the profound role of isometric deformation in shell buckling is illustrated by a simple but rather surprising dynamical problem. It is found that a fully isometric mode exists for which the buckling load of a cylindrical shell approaches zero as the shell length approaches infinity. Finally, we might note that for reasons which are not explained here, the isometric transformation is most pronounced when the shell is subject to impact loading.[26] Curiously enough, this complicated problem is described by this simple theory much better than in the simple statical loading case.

References

1. Hoff, N.J. Some recent studies of the buckling of thin shells. The Aeronautical Journal of the Royal Aeronautical Society, vol. 3, December (1969), 1057.

2. El Naschie, M.S. A branching solution for the local buckling of a circumferentially cracked cylindrical shell. Int. J. Mech. Sci., vol. 16 (1974), 689-697 and Applied Mechanics Review, Nr. 7900, September (1976).

3. Koiter, W.T. Over de stabiliteit van het elastisch Evenwicht. Dr. Thesis Delft Technical University, H.J. Paris, Amsterdam, Holland (1945).

4. Thompson, J.M.T. and Hunt, G.W. A general theory of elastic stability, John Wiley, London (1973).

5. El Naschie, M.S. Thermal initial post buckling of the extensional elastica. Int. J. Mech. Sci., vol. 18 (1976), p. 321-324.

6. El Naschie, M.S. Der Einfluss von Schubverformung auf die Stabilitat von axial gedruckten Staben im uberkritischen Bereich, Der Stahlbau, 2, (1977), p. 52-54.

7. Esslinger, M. and Geier, B. Gerechnete Nachbeullasten als untere Grenze der experimentellen axialen Beullasten von Kreiszylindern. Der Stahlbau, 41, H12 (1972), p. 353.

8. Hoff, N.H., Madson, W.R. and Mayers, J. Post buckling equilibrium of axially compressed circular cylindrical shells. AIAA Journal, 4 (1966), p. 126.

9. El Naschie, M.S. Durchschlagähnliches Stabilitätsverhalten von Rahmentragwerken. To appear in Der Stahlbau.

10. Thom, R. Structural stability and morphogensis. Translated from French edition by D.H. Fowler, (Addison-Wesley) (1974).

11. El Naschie, M.S. Edlund, B., Wood, J.G.M. and Kaoulla, P. Local post buckling of compressed cylindrical shells (discussion). Proc. Instn. Civil Engs., Part 2, 61, June (1976), p. 483-488.

12. Hutchinson, J.W. Buckling and initial post buckling behaviour of oval cylindrical shells under axial compression. J. Appl. Mech., 35, (1968), p. 66.

13. Yoshimura, Y. On the mechanism of buckling of circular cylindrical shells under end compression. NACA TM, 1390 (1974), p. 1-46.

14. Kirste, L. Abwickelbare Verformung dünnwandiger Kreiszylinder. Österr. Ingenieur-Archiv, 8 (1954), p. 149.

15. Pogorelov, A.V. Topics in the theory of surfaces in elliptic space. Gordon and Breach, New York (1961).

16. Pogorelov, A.V. Die Eindeutige Bestimmung Allgemeiner Konvexer Flächen, Akademie-Verlag-Berlin (1956).

17. Pogorelov, A.V. Geometrical methods in the nonlinear theory of elastic shells (in Russian), Moscow (1967).

18. El Naschie, M.S. Localised diamond shaped buckling patterns of axially compressed cylindrical shells. AIAA Journal, vol. 13, June (1975), p. 837-838. Also in Applied Mechanics Review No. 2073, March (1977). See also reply to P. Kaoulla, AIAA Journal, March (1977), p. 757-759.

19. El Naschie, M.S. An estimation of the lower stability limit of the free edge orthotropic cylindrical shell in axial compression. J. of Appl. Math. and Mech. (ZAMM), vol. 55 (1975), p. 694.

20. El Naschie, M.S. Abschätzung der untere Stabilitätsgrenze einer örtlich ausgebeulten Zylinderschen Schale unter axial druck. Die Bautechnik, No. 5, (1976), p. 163.

21. El Naschie, M.S. Estimation of the lower stability limit of locally buckled spherical shells. J. of Spacecraft and Rockets, vol. 14, No. 3, March (1977), p. 189-191.

22. El Naschie, M.S. Imperfection sensitivity and isoperimetric variational problems in stability theory. J. of Spacecraft and Rockets, vol. 13, No. 12, (1976), p. 761-763.

23. El Naschie, M.S. Nonlinear isometric bifurcation and shell buckling. J. of Appl. Math. and Mech. (ZAMM), 57, 46, p. 293-296 (1977).

24. Kilchevsky, N.A. and Nikulinskaya, S.N. Substantiation of the theory of stability of cylindrical shells on the basis of the Gauss principle. Proc. IUTAM Symp. Instability of Continuous Systems. Herrenalb, Springer-Verlag, Editor H. Leipholz (1969).

25. Fung, Y.C. and Wittrick, W.H. A boundary layer phenomenon in the large deflection of thin plates. Quart. J. Mech. and Appl. Math., vol. VIII, Part 2, (1955), p. 191-210.

26. Coppa, A.P. Inextensional buckling configuration of conical shells. AIAA Journal, April (1967), p. 750-754.

27. Wolmir, A.S. Flexible shells and plates. Berlin BEB Verlag fur Bauwesen. (German title 'Biegsame platten und schalen', translated to German from Russian), (1962).

28. Edlund, B.L.O. Thin-walled cylindrical shells under axial compression, prebuckling, buckling and post buckling behaviour. Monte Carlo Simulation of the scatter in load carrying capacity. DSC Thesis, Chalmers Tekniska Hogskola, Gotenborg, Sweden, (1974).

29. Soden, P.D., Al-Hassani, S.T.S. and Johnson, W. The crumpling of polyvinylchloride tubes under static and dynamic axial loads. Institute of Physics Conf. Ser. No. 21.

30. Miura, K. Inextensional buckling deformations of general cylindrical shells. AIAA Journal, vol. 6, No. 5, May (1968), p. 966-968.

31. Miura, K. Proposition of pseudo-cylindrical concave polyhedral shells. A.I.S.S. Symposium on folded plates and prismatic structures. Vienna, (1970).

32. Basar, Y. and Krätzing, W. Structure konsistenten Grundgleichungen für Beul-und Nachbeulverhalten allgemeiner Flächentragwerke. Der Stahlbau, 5, (1977), p. 138.

33. Croll, J.G.A. Towards simple estimates of shell buckling loads. Der Stahlbau, vol. 44, No. 8 (1975), p. 243.

Acknowledgement:
The author is deeply indebted to Prof. S. Athel for his continuous encouragement as well as to the University of Riyadh for the generous financial help which made this work possible.

Shock and Vibration Characteristic of Solid Rocket Vehicles

D. MORI AND J. ONODA

Institude of Space and Aeronautical
Science, University of Tokyo
Komaba, Meguro-ku, Tokyo 153, JAPAN

Summary

In order to acquire the knowledge on the dynamic characteristics of the solid propellant launch vehicle and to assess the dynamic environment of the satellite or installed electronics, two kinds of study have been carried out. The one is measurement of the response of the actual vehicle in flight and the other is an analytical and experimental approach to the shock and vibration characteristics of small test rocket segments containing solid propellant.

1. Introduction

In order to prevent the aeroelastic instability or the structural failure of the launch vehicle with solid propellant motors and also to assess the flight environment of the installed electronics or satellite, the knowledges on the dynamic characteristics of the vehicle in flight are fundamental one.

The authors have been engaged in the development of the solid propellant launch vehicles for scientific satellite, and here, the results of two research works on the dynamic characteristics of the vehicle body are presented.

2. An Example of Dynamic Environment of a Solid Propellant Vehicle

Shock and vibration environment of a three stage solid propellant vehicle Mu-3H-1 has been measured.
Mu-3H-1, and newly designed vehicle, was launched in February 1977 and put in orbit the test satellite "Tansei 3" in the medium earth orbit. Figure 1 shows the vehicle just before launch, and Figure 2 shows the location of sensors for dynamic measurement of the upper stages.
Five accelerometers, five vibration meters and one sound level gage were installed.
Figure 3 shows the acceleration response at launch. Bending vibrations of the body (5 Hz, 13 Hz, and 22 Hz) were excited, and lateral vibration of 3.1 G and base of the spacecraft is the biggest one thoughout its lifetime. Separation of sub-boosters excited vibration of 1 G.
The acceleration caused by the shock and vibration during the second and third stages are not so significant as in the first stage.
Vibration records were obtained by the peizo type vibration meters, whose overall response being flat up to 2 kHz.
Figure 4 is an overall vibration recorded by pen-oscillograph in the first stage powered flight. At ignition, the effect of the exhausted gas reflecting at the base ground is significant. The vibration amplitude in the following phase is roughly proportional to the dynamic

pressure of the vehicle, and so, these vibration seem to be generated by the acoustic excitation induced by the turbulent airsteam. The response at the base of the spacecraft is moderate.
Figure 5 is an acceleration and acoustic noise sensed at the wall of the nose fairing. It can be seen that the levels at ignition are quite large.

3. Longitudinal Dynamic Characteristics of the Solid Rocket Models

To understand the effect of the solid propellant on the vehicle, the longitudinal response displacements and accelerations developed within the propellant and motor cases under impulsive or vibrational axial loads have been investigated employing small test models.
Figure 6 shows the test models. Polybutadien and ammonium perchrolate are the main components of the propellant and the motor case is a steel cylinder with end plates. Two models having the length of 1000 mm and 300 mm have been used.

In this analysis, the axial displacement is assumed to be presented by

$$u_r(r,x,t) = U_o(x,t) + \sum_{i=1}^{Nr} \phi_i(r)\, U_i(x,t) \qquad (1)$$

where

u: axial displacement at r, x point, t: time
r: radial axis, x: longitudinal axis
U_o: axial displacement of the case
U_i: generalized coordinate of the ith mode
ϕ_i: ith natural mode of the propellant, moving axisymmetrically clamped at the motor case.

The stress-strain relationships are

$$\sigma_c = E_c \frac{\partial U_o}{\partial x} \quad , \quad \sigma_x = E_p \frac{\partial u_x}{\partial x} \quad , \quad \tau = G_p \frac{\partial u_x}{\partial r} \qquad (2)$$

$$E_p = 2(1+\nu_p)G_p \Big/ \left(1 - \frac{2\nu_p}{1+\left(\frac{a_1}{a}\right)^2 + \left(\frac{E_{pr}a}{E_c h_c} - \nu_p\right)\left\{1-\left(\frac{a_1}{a}\right)^2\right\}}\right) \qquad (3)$$

where

c: motor case, p: propellant, 2a: diameter of the cylinder.

The complex moduli of the propellant were obtained by exciting a rectangular column under the boundary conditions of clamp-free ends.

Figure 7 and 8 show the frequency response of the two test models comparing with the analytical values. It can be seen that the motor have several resonant peak and notches, and the experimental results seem to coincide with the analytical value up to the second resonance mode.

Figure 9 shows the similar results for another test model treated two years ago. It can be seen that the present analysis is also valid in describing the test, but the old FEM analysis could not follow the second resonance mode in which the shear motion of the propellant plays a dominant role.

In addition, the longitudinal impact test has been carried out (Figure 10). A small steel ball hunged by a string strikes against one end plate of the test motor and acceleration response of the case was measured at ten points.

Figure 11 shows the typical response of the motor case under a half sinusoidal impulsive force. Decrease of acceleration amplitude along with the propagation of the impulsive wave is significant.

Figure 12 shows an example of comparison between the test and analysis on the propagation of shock along the test motor.

These results show the adequacy of the employed analytical method, and this method can be applied to estimate the overall longitudinal dynamic response of the total Vehicle under dynamic loads such as ignition and burning of the motor, or separation of stages.

Fig.1 Mu-3H-1 on Launcher

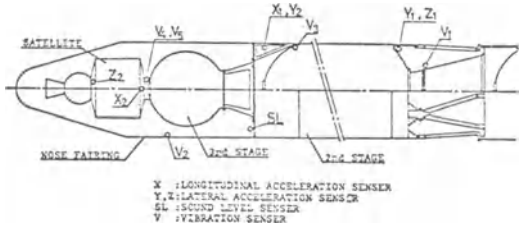

Fig.2 Location of Sensors for Dynamic Measurement

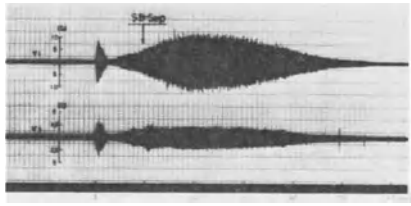

Fig.4 Vibration in the First Stage Powered Flight

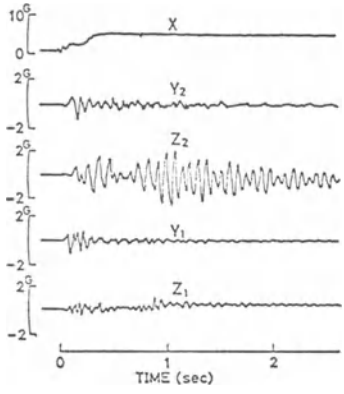

Fig.3 Acceleration Response at Launch

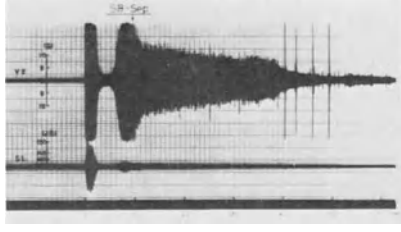

Fig.5 Vibration and Acoustic Noise at the Nose Fairing

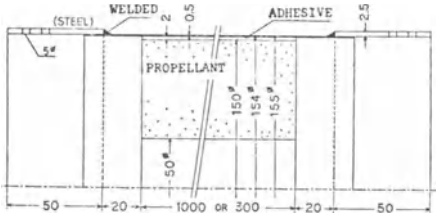

Fig.6 The Model of Solid Rocket

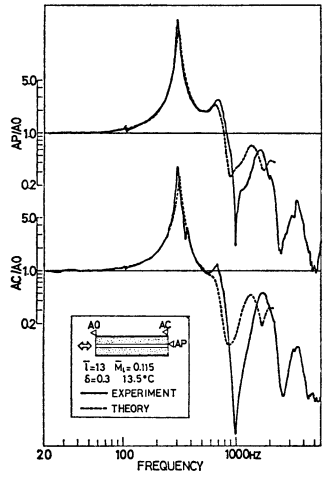

Fig.7 Frequency Response of the Long Model

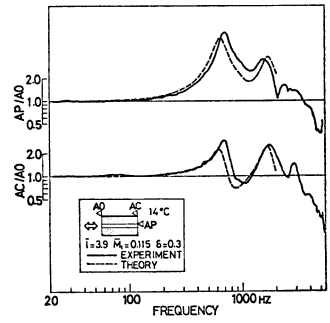

Fig.8 Frequency Response of the Short Model

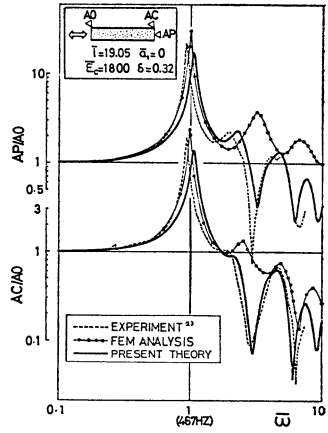

Fig.9 Frequency Response of the Another Model

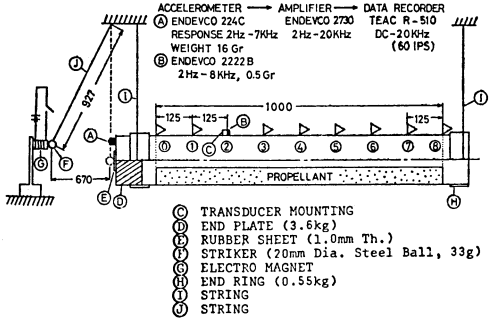

Fig.10 Longitudinal Impact Test Setup

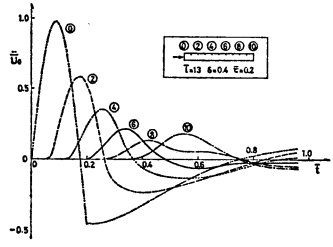

Fig.11 Response to Half Sinusoidal Impulsive Force

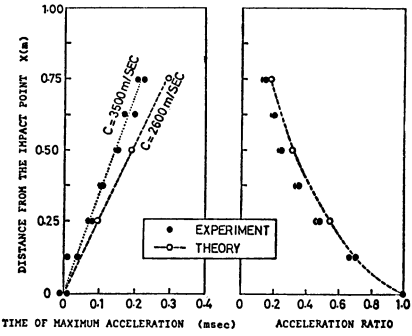

Fig.12 Propagation Characteristics

Some Phenomena at the Interface in Hypervelocity Impact of Metals and Its Application to Lamination of Metal Plates

K. KIYOTA Yatsushiro College of Technology and
M. FUJITA Faculty of Engineering, Kumamoto University

Summary

When two metal plates collide obliquely with a high velocity, the contact surfaces are cleaned by jet formation and they are bonded by a high pressure owing to a high velocity collision. The authors are successfully investigating a weld forming process by shock wave in water using this effect.

Introduction

When two metal plates collide obliquely with a high velocity, metal jet is formed by Munroe Effect at the collision point, because thin layers of contact surfaces of both plates behave as fluid under extremely high pressure caused by a high velocity collision.[1] Fig.1 is a

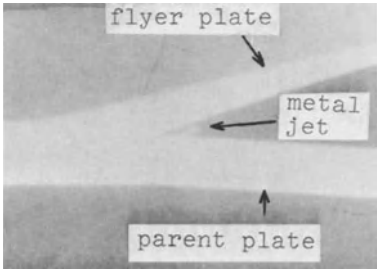

Fig.1. Generation of metal jet between two metal plates by oblique collision with high velocity

photograph of the jet formation taken by a pulse X-ray radiation. When the jet is formed, the contact surfaces of both plates are scarfed or cleaned near the collision point. Succeedingly the two metal plates are forced to bond metallurgically by the extremely high pressure. Since a proper quantity of jet is necessary for good bonding, it is necessary for values of the collision

angle and velocity to be held within required ranges throughout all bonded area. Colliding under the required condition produces the wave-like bonded interface which is the typical phenomenon of the explosive welding, and the wave formation depends on the collision condition.[2] The authors recently have been investigating an explosive weld-forming process by shock wave in water. The differences of this process from the conventional explosive clad method are the followings: A flyer plate is accelerated by shock wave pressure in water caused by an underwater explosion of explosive, but not by the direct explosion pressure; and also the forming process of the composite plate, succeeded in the welding process, into the required shape is achieved by the rest of the kinetic energy of the flyer plate and the pressure energy in water during a shot of the underwater explosion. By means of this process, end plates of small scale have been made of mild steel plates, whose inner face is lined by a copper plate during the same shot.

Method of experiment

An equipment for explosive weld-forming process by shock wave in water is shown in Fig.2. This process has been designed as an improvement of an explosive forming technique using an auxiliary plate[3]; the auxiliary plate plays

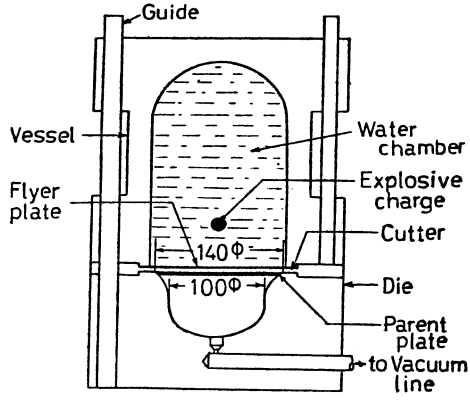

Fig . 2. Equipment of explosive weld-forming process by shock wave in water

the role as a flyer plate of the clad plate in this process.

A circular steel parent plate, 6 mm in thickness and 140 mm in diameter, is placed on the top of a die on which the plate is pressed by gather forming technique. A copper flyer plate, 0.5 mm in thickness, is placed on a cutter put on a circular die. An explosive is set in water a little apart from the flyer plate. The explosive used in this investigation was sheet explosive (SEP),whose detonation velocity is about 6,500 m/s, and the charge weight was constantly 30 gramms in every experiment. In the experiments, a shock wave in water and a deforming process of a flyer plate were photographed by a high speed camera and a bonded interface of a product was observed by a microscope.

Elementary experiments

Photographs of the deforming in three case are shown in Fig.3, each of which is a frame of successive high speed photographs: A spherical explosive has been used in (A), a circular flat explosive in (B) and a conical shock wave generator in (C).

(A) In case of using a spherical explosive

(B) In case of using a circular flat explosive

(C) In case of using a conical shock wave generator

Fig. 3. Deformed shapes of flyer plate

And in Fig.4, wave amplitudes and wave lengths of bonded interfaces are plotted in radial position. ① is the result in the case of using a spherical explosive (the diameter Of the explosive is 35 mm and the stand-off of explosion

position is 30 mm from the surface of the flyer plate), ② is the result in the case of using a circular flat explosive (the diameter of the explosive is 90 mm and the thickness is 5 mm and the explosion position is 20 mm from the surface of the flyer plate) and ③ is the result in the case of using a conical shock wave generator (the top of the explosive is 5 mm apart from the flyer plate).

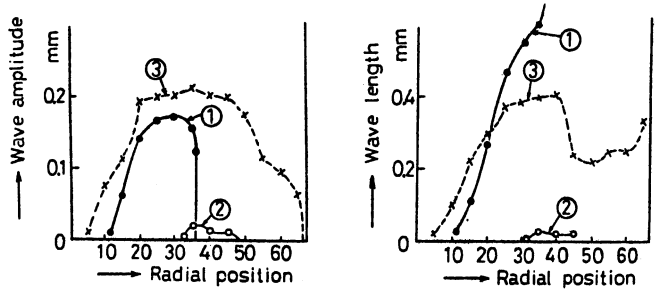

① In case of using a spherical explosive ② In case of using a circular flat explosive ③ In case of using a conical shock wave generator

Fig. 4. Wave amplitudes and wave lengths of bonded interface

The following phenomena are found from the results of (A) and (B) in Fig.3 and ① and ② in Fig.4 (the results of (C) in Fig.3 and ③ in Fig.4 will be discussed in the following chapter): Since a shock wave starting from a spherical explosive propagates as a spherically diverging wave, a flyer plate becomes roundish by its action. Therefore, the collision angle between the flyer plate and the parent plate increase as the collision point progresses outward. As the result the wave of the bonded interface changes remarkably with the radial position; In the case of a circular flat explosive since the flyer plate is flat at the central part, the bonding cannot be achieved. The appearance of the wavy interface is therefore limited within a small area responding to the periphery of the explosive and the outer part except the area is not well bonded, because the collision velocity is too low.

Experiment using a conical shock wave generator

To get good bonding over whole area, a conical shock wave generator has been designed, which is shown in Fig.5. At the central part, an explosive is formed into a conical shell shape, and is pasted on a reflector made of mild steel block. And at the outer part except the projection area of the explosive, an outside reflecting wall inclining forward is added to the reflector in order to increase the shock wave energy there. The deformed shape of the

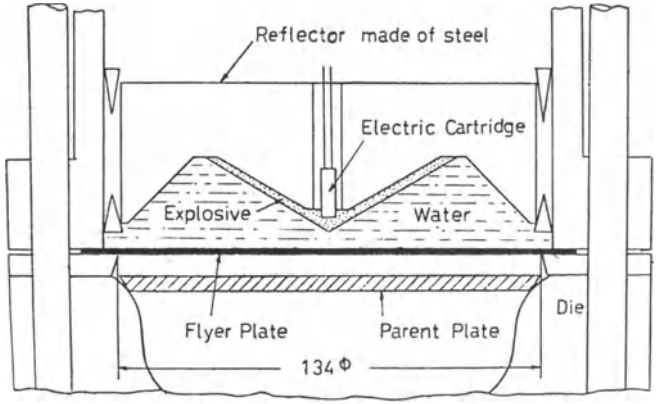

Fig.5. A conical shock wave generator

flyer plate in process of the forming is shown in Fig.3 (C). The flyer plate becomes gradually a conical shell shape, as the shock wave starting from the generator moves outward on the surface of the flyer plate with a

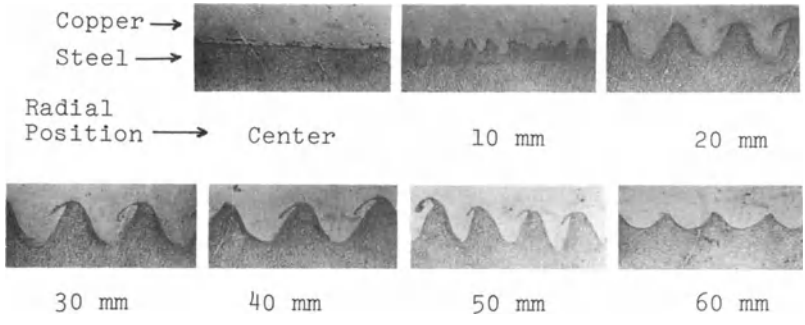

Fig. 6. Microscopic photographs of bonded interface

nearly constant velocity. And microscopic photographs of the bonded interface are shown in Fig.6. The curve ③ in Fig.4 shows the changes of wave amplitude and wave length of the bonded interface in radial positions on the flyer plate. Waves continue at almost all area, though the interface is nearly flat at the small areas of the center and the periphery.

Discussions and conclusions

In order to obtain good bonding, the collision between two metal plates should be done under the required conditions. Such colliding conditions can be produced also by an action of shock pressure in water. In this investigation, the good bonding over almost all area has been obtained by the use of a conical shock wave generator newly designed; especially at the outer part except the projection area of an explosive, the shock wave energy has been increase by adding the reflected shock from the outside wall of the reflector. Lastly, we wish to emphasize also the following merits on our process: The surface of the flyer plate is not damaged by the heat of explosion at all; both explosion noise and several damages caused by flying substance such as fragments are extremely reduced in comparison with the conventional method in which the explosions is done in air.

Literature

(1) Holtzman, A.H. and Cowan, G.R. : Bonding of Metals with Explosives, Welding Research Council Bulletin, 1965.

(2) Crossland, B. and Bahrani, A.S. : A Review of Explosive Welding Research Carried Out in the Queen's University of Belfast, Proc. of 1st Int. Conf. of the Center for High Energy Forming, 1976.

(3) Kiyota, K. Fujita, M. Izuma, T. and Hamasaki, M. : A New Method in High Energy Rate Forming, Proc. of 2nd Int. Conf. of the Center for High Energy Rate Forming, 1969.

A Fundamental Study on Head Impact Problem by Finite Element Method

Shigeo KOBAYASHI
Department of Aeronautics, University of Tokyo

Takashi KOBAYASHI
Nagoya Aircraft Works, Mitsubishi Heavy Industries, LTD

Hiroaki TOMITA
Graduate Student, Department of Aeronautics, University of Tokyo

Introduction

Hayashi[1] analytically clarified the property of pressure response in brain to head impact by using one dimensional model on the assumption of a rigid skull. However, neurosurgeons require mechanical analysis on a model more close to human head itself in order to study and protect the head injury. The finite element method will be only one technique to find a solution for this problem. In the present paper an axi-symmetric impact of an axi-symmetric elastic shell model filled with a soft elastic continuum is treated in order to overcome a difficulty in application of the finite element method to this problem and to disclose the essential property of the impact response of the skull and brain combined system. Recently two papers[2),3)] have been presented for the head impact analysis by the finite element method in the United States. These papers have employed the reduced integration technique in evaluating the element stiffness matrix for nearly incompressible materials. Now in the present paper a different treatment is employed. The present paper is only a part of our study.

Formulation by Finite Element Method

The shear modulus G of the brain is extremely smaller than its bulk modulus K as shown in Table 1. Then Poisson's ratio ν calculated from G and K using the formula

$$K = 2G (1 + \nu) / [3 (1 - 2\nu)] \qquad (1)$$

is very close to 0.5. Namely the brain is a neary incompressible material. In this case the standard displacement method in the

finite element method yields erroneous results as shown in Table 2. The equation of equilibrium for displacement u_i in three dimension is

$$G\Delta u_i + \frac{G}{1 - 2\nu} \frac{\partial e}{\partial x_i} + F_i = 0 \quad (i = 1 \sim 3) \tag{2}$$

Where e is a dilatation. In the case of $\nu = 0.5$ the second term becomes an indeterminate form of 0/0, because $e \fallingdotseq 0$ and $(1 - 2\nu) \fallingdotseq 0$. This is the reason why the displacement method yields erroneous results. In order to overcome this difficulty a stress parameter H defined by[4]

$$H = \frac{3\sigma}{2G (1 + \nu)} \qquad \left(\longrightarrow H = \frac{e}{1 - 2\nu} \right) \tag{3}$$

where σ is the mean stress at a point, is introduced as an independent function and Herrmann's variational principle[5] is used in the finite element formulation in the present paper.

An axi-symmetric triangular element as shown in Fig.1, is used for brain. A displacement $\mathbf{f} = [u, w]^T$ in the element is expressed by the nodal displacement $\mathbf{u}^e = [u_i, w_i, u_j, w_j, u_k, w_k]^T$ as

$$\mathbf{f} = [N] \mathbf{u}^e \tag{4}, \qquad N = \begin{bmatrix} N_i & 0 & N_j & 0 & N_k & 0 \\ 0 & N_i & 0 & N_j & 0 & N_k \end{bmatrix} \tag{5}$$

$$N_i = (a_i + b_i r + c_i z)/2\Delta \tag{6}$$

where Δ is the area of a triangle i j k and

$$a_i = r_j z_k - r_k z_j, \quad b_i = z_j - z_k, \quad c_i = r_k - r_j \tag{7}$$

in cyclic for i, j and k. Substituting $\mathbf{f}$ into the formula of strain in cylindrical coordinates, we get the expression

$$\boldsymbol{\varepsilon} = [\varepsilon_r, \varepsilon_\theta, \varepsilon_z, \gamma_{zr}]^T = [B_i, B_j, B_k] \mathbf{u}^e \tag{8}$$

where

$$[B_i]^T = \begin{bmatrix} 0 & b_i & a_i/r + b_i + c_i z/r & c_i \\ c_i & 0 & 0 & b_i \end{bmatrix} \tag{9}$$

The expression of strain energy in Herrmann's variational principle is

$$A_H(\varepsilon, H) = \frac{1}{2}\varepsilon^T[C_{11}]\varepsilon + H[C_{12}]\varepsilon + \frac{1}{2}H^2[C_{22}] \quad (10)$$

$$[C_{11}] = 2G\begin{bmatrix} 1 & 0 & 0 & 0 \\ & 1 & 0 & 0 \\ & & 1 & 0 \\ \text{sym} & & & 1/2 \end{bmatrix}, \quad [C_{12}]^T = [\nu \ \nu \ \nu \ 0] \quad (11)$$

$$[C_{22}] = -\nu(1 - 2\nu)$$

The stress parameter H is expressed as

$$H = [N_H]\{h^e\} \qquad [N_H] = [N_i, N_j, N_k] \quad (12)$$

where $\{h^e\} = [H_i \ H_j \ H_k]^T$ is the values at the three nodes. Using Herrmann's variational principle, we get the equation of equilibrium for an element :

$$\begin{bmatrix} k_{UU} & k_{UH} \\ k_{UH}^T & k_{HH} \end{bmatrix}\begin{Bmatrix} u^e \\ h^e \end{Bmatrix} + \begin{bmatrix} m_U & 0 \\ 0 & 0 \end{bmatrix}\begin{Bmatrix} \partial^2 u^e/\partial t^2 \\ \partial^2 h^e/\partial t^2 \end{Bmatrix} = \begin{Bmatrix} F^e \\ 0 \end{Bmatrix} \quad (13)$$

where

$$\begin{aligned} [k_{UU}] &= \iiint_{V^e}[B]^T[C_{11}][B]\,r\,dr\,d\theta\,dz \\ [k_{UH}] &= \iiint_{V^e}[B]^T[C_{12}][N_H]\,r\,dr\,d\theta\,dz \\ [k_{HH}] &= \iiint_{V^e}[N_H]^T[C_{22}][N_H]\,r\,dr\,d\theta\,dz \\ [m_U] &= \iiint_{V^e}[N]^T\rho[N]\,r\,dr\,d\theta\,dz \end{aligned} \quad (14)$$

For the skull an axi-symmetric truncated conical shell element is used. The formulation is shown in the text book of Zienckiewicz.[6)]

In the present paper we use the condition of perfect connection between the skull and the brain without a slip and a gap. Then their displacements are connected at the nodes in the finite element method. Superposing the element stiffness and mass matrices, we get the equation of motion of the system in the following form :

$$\begin{bmatrix} K_{UU} & K_{UH} \\ K_{UH}^T & K_{HH} \end{bmatrix}\begin{Bmatrix} u \\ h \end{Bmatrix} + \begin{bmatrix} M & 0 \\ 0 & 0 \end{bmatrix}\begin{Bmatrix} \partial^2 u/\partial t^2 \\ \partial^2 h/\partial t^2 \end{Bmatrix} = \begin{Bmatrix} R(t) \\ 0 \end{Bmatrix} \quad (15)$$

Impact Problem and Method of Calculation

An example problem is that a ball having a velocity V =30 m/sec strikes a head. The model of skull is a spherical shell. The material constants of the skull and brain are shown in Table 1. The ball is analytically modeled as a mass-spring system of which weight m x g is 140^{gr} and spring constant k is 30 kg/mm as shown in Fig.2. Fig.2 shows element divisions.

If the head is rigid, the impact load is a half sine calculated by the following formula :

$$F(t) = F_{max}\sin\omega t, \quad 0 \leq t \leq \pi/\omega$$
$$F_{max} = kV/\omega, \quad \omega = \sqrt{(k/m)[1 + (m/m_h)]} \tag{16}$$

where m_h is the mass of head. However, in the present calculation we treated the ball as a node during the contact between the ball and the head. The impact load is calculated by

$$F = k(U_b - U_{c_1}) \tag{17}$$

where U_{c_1} is the axial displacement of the impact point on the shell.

The numerical integration by time was carried out by Wilson's θ-method[7] with $\theta = 1.4$. In the calculation we took a time interval $\Delta t = 1 \times 10^{-5}$sec and displayed the output in each 20 x Δt sec.

Results and Discussion

The figure 3 shows the impact load and the axial displacements U of the impact point, i.e. node 1, and the counter pole, i.e. node 17. The response of an empty skull is also shown for comparison. There is not much difference between the load of the elestic, elastic-empty and rigid models. The difference in the velocity of displacement is explained as the effect of the brain mass. A time lag is observed for the displacement of the counter pole.

The figure 4 shows membrane and bending stresses in the meridional direction of the closest shell element to the impact point, i.e. element 1. The stresses of the empty skull, which are also shown for comparison, are lower than those of the skull-brain system, because the response velocity of the empty skull is higher. The magnitude of the stresses in the shell element not close to the

impact point is very small. Namely high stresses in the skull are localized in the vicinity of the impact point.

The solid lines in Fig.5 show the pressure response of the representative three elements in the brain. The figure 6 shows equi-pressure contours at 0.8 m sec. For comparison the pressure response in a rigid spherical skull is also calculated and is shown by dashed lines in Fig.5. The figure 7 shows the pressure distribution along symmetric axis in the case of the rigid skull at 0.2 m sec and 1.0 m sec. In the rigid spherical model of skull the pressure response property is very simple and is similar to Hayashi's result. At the element 29 a negative pressure appears immediately after the impact. On the other hand the response property of the elastic model is very complicated depending on the elastic deformation of the skull.

For comparison the figure 8 shows the pressure response of the brain in an elastic cylindrical skull model of which length and diameter are 150 mm and thickness is 5 mm. At the element 91 a negative pressure does not appear during the time when the impact load is being applied. It is considered that this property is due to the flexibility of the end circular plates.

In the case where the spring constant of the ball is one hundred times as hard as the original one and velocity is one-tenth times as high as the original one, we get the impact load and pressure response shown in Fig.9. The maximum load is about one-thirds and the impact duration is about three times of the values calculated from Eq.(16). This property is due to the fact that the elastic skull is more flexible than the hardened spring. Very high pressure is observed at the element 1 immediately after the impact. The pressure response is very complicated. On the other hand, in the case where the spring constant of the ball is one-hundredth times as hard as the origin and the velocity is ten times as high as the origin, we get a very simple pressure response as shown in Fig. 10.

The shear strain was also calculated, but not displayed, because it was so small as about 3×10^{-2}. In the real head the shape of skull and the load are not axi-symmetric and the brain is not homogeneous. Therefore the shear strain may be an important item for the head injury. Clarifying this property is a future problem.

Conclusion

The followings will be concluded by the present study.

1) If Herrmann's variational principle is used, the finite element method yields a powerful technique to analyse the impact response of the head.

2) The coupling response property of the skull and brain combined system is disclosed.

Table 1. Material constants of skull and brain

	skull	brain
K kg/mm^2	———	250
G kg/mm^2	———	7.50×10^{-4}
E kg/mm^2	570	2.25×10^{-3}
ν	0.22	0.4999985
ρ kg sec^2/mm^4	1.44×10^{-10}	1.02×10^{-10}

Table 2. Fundamental natural frequency of axi-symmetric vibration of elastic continuum in rigid cylindrical container

ν	displacement method	Herrmann's method	K kg/mm^2
0.3	3.781 Hz	3.775 Hz	8.02×10^{-5}
0.49	6.256	6.083	1.84×10^{-3}
0.499	8.192	6.746	1.85×10^{-2}
0.49999	43.75	6.854	1.85
0.4999999	431.5	6.858	185
0.5	———	6.875	∞

* diameter 155 mm, length 281 mm, shear modulus G = 3.70×10^{-5} kg/mm^2

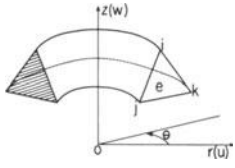

Fig. 1

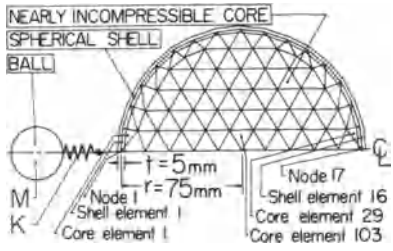

Fig. 2

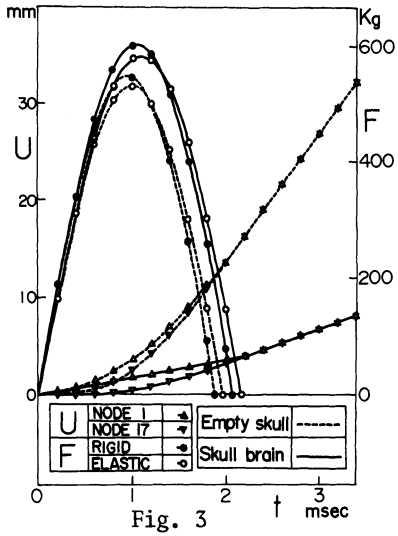

Fig. 3

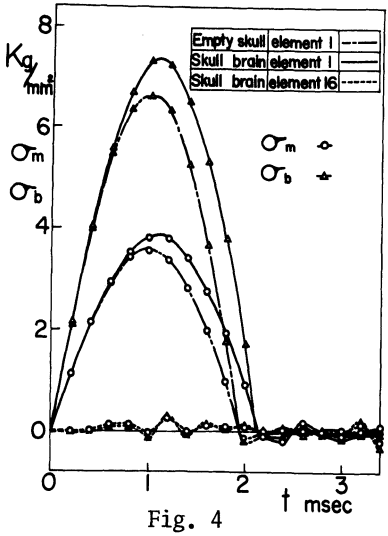

Fig. 4

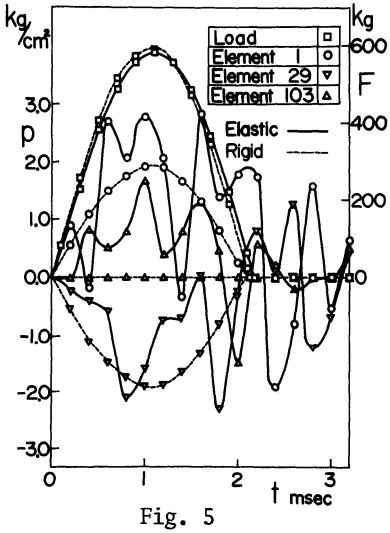

Fig. 5

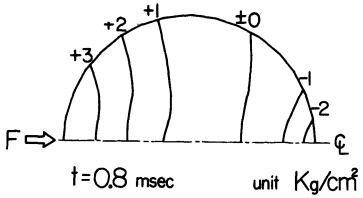

Fig. 6

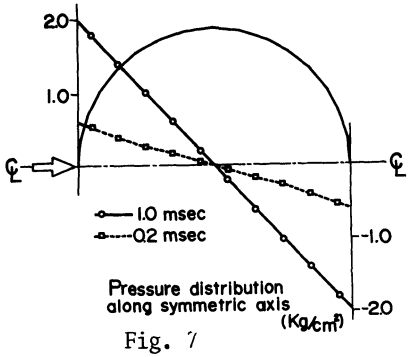

Fig. 7

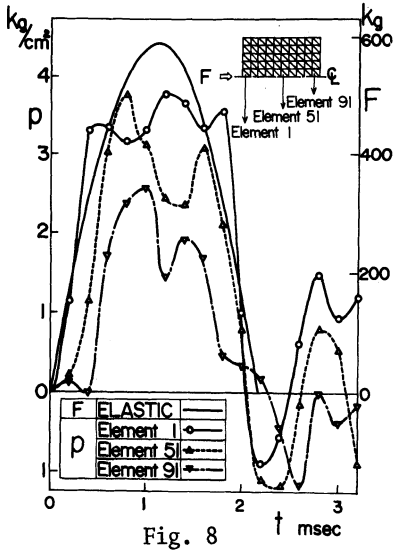

Fig. 8

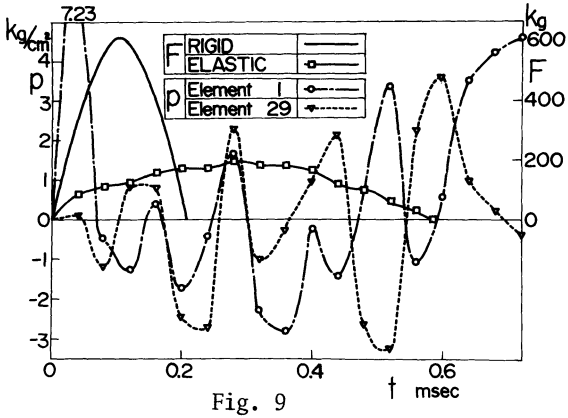

Fig. 9

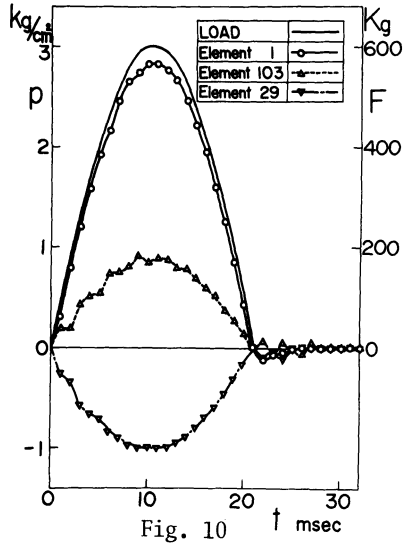

Fig. 10

References

1 Hayashi,T.: Study of intracranical pressure caused by head impact. J.Faculty of Engineering. University of Tokyo, Vol.XXX, No.1(1969)
2 Chan,H.S.: Mathematical model for closed head impact. Proc.18th Stapp Car Crash Conference (1974) p.557.
3 Shugar, T.A.: Transient structural response of the linear skull-brain system. Proc. 19th Stapp Car Crash Conference (1975) p.581.
4 Herrmann, L.R. and Toms, R.M.: A reformulation of the elastic field equation in terms of displacements,valid for all admissible values of Poisson's ratio. J.Appl.Mech., Vol.31,March(1964)p.140.
5 Herrmann, L.R.: Elastic equations for incompressible and nearly incompressible materials by a variational theorem. AIAA Journal, Vol.3, No.10 (1965) p.1896.
6 Zienkiewicz, O.C.: The finite element method in engineering science. McGraw-Hill 1971.
7 Clough, R.W. and Wilson, E.L.: Dynamic finite element analysis of arbitrary thin shells. Computer and Structures, Vol.1(1971) p.33.

High Velocity Impact of Mild Steel Cylinder

H.Fukuoka and H.Toda

Faculty of Engineering Science,
Osaka University, Toyonaka, Japan

Summary

Behavior of elastic/viscoplastic cylindrical specimen with strain hardening under axial impact is considered. As governing equation of the axisymmetric problem is of nonlinear type, difference method by means of bicharacteristics is employed. Numerical results for distribution of strain are compared with experiment carried out for mild steel and observed by high speed camera.

Introduction

Previously, we had carried out axial impact test of mild steel cylindrical specimen and observed the process of deformation by high speed camera having the capacity of 200,000 frames per second and compared the result with one dimensional analysis for rigid-viscoplastic model [1]. This time, we assume elastic/viscoplastic constitutive relation with strain hardening and solved the impact of the cylinder as two dimensional axisymmetric problem by means of the integration method developed by Clifton [2].

Theory

The problem is a normal impact of a finite rod on a rigid wall as is shown in Fig.1.

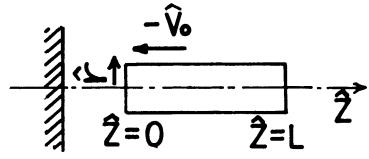

Fig.1

Constitutive equation of Perzyna type are used:

$$\dot{e}_{ij} = \frac{s_{ij}}{2\mu} + \Gamma\,\Phi(F)\frac{s_{ij}}{\sqrt{J_2}} \qquad \text{for } F \geq 0$$
$$\dot{e}_{ij} = \frac{\dot{s}_{ij}}{2\mu} \qquad \text{for } F < 0 \tag{1}$$

$$\dot{\varepsilon}_{kk} = \frac{\dot{\sigma}_{kk}}{3K} \tag{2}$$

where $\mu, K, \Gamma, \sigma_{ij}, s_{ij}, \dot{\varepsilon}_{ij}, \dot{e}_{ij}, J_2$ and F are rigidity, bulk modulus, viscous coefficient, stress tensor, stress deviator tensor, strain rate tensor, strain rate deviator tensor, the second invariant of stress deviator and the yield function, respectively. To take account of strain hardening effect as well as strain rate sensitivity, we employ three kinds of function $\Phi(F)$ as follows:

$$\text{C-1:}\quad \Phi(F)=\left(\frac{\sqrt{J_2}}{k}-1\right)^P, \quad k=\sqrt{\{(\sigma_0^2+2HW_p)/3\}}$$

$$\text{C-2:}\quad \Phi(F)=\left(\frac{\sqrt{J_2}}{k}-1\right)^P, \quad k=(\sigma_0+H\varepsilon_{eq}^p)/\sqrt{3} \tag{3}$$

$$\text{C-3:}\quad \Phi(F)=\left(\frac{\sqrt{J_2}-k}{\sigma_0/\sqrt{3}}\right)^P, \quad k=(\sigma_0+H\varepsilon_{eq}^p)/\sqrt{3}$$

where σ_0, k, W_p, H, P and ε_{eq}^p are initial yield stress in tension, yield stress in shear, plastic work, hardening coefficient, material constant and equivalent plastic strain, respectively. With (r,θ,z) cylindrical coordinate and using Clifton's notation in which demensionless independent variables are defined by means of their dimensional counterparts denoted with hat symbol and the radius of the cylinder R by

$$t=(c_1/R)\hat{t},\quad r=\hat{r}/R,\quad z=\hat{z}/R$$

and dimensionless velocities and stresses are defined by

$$u=v_r/c_1,\quad v=v_z/c_1,\quad p=(\sigma_r+\sigma_\theta)/2\rho c_1^2,$$
$$q=(\sigma_r-\sigma_\theta)/2\rho c_1^2,\quad s=\sigma_z/\rho c_1^2,\quad \tau=\tau_{rz}/\rho c_1^2$$
$$J_2=\{(p-q)^2+3(q^2+\tau^2)\}/3$$

and

$\gamma=(R/c_1)\Gamma$, $a=c_1/c_2$, $c_1=\sqrt{\{4\mu+3K)/3\rho\}}$, $c_2=\sqrt{(\mu/\rho)}$,

then, the governing equation for the problems considered can be written in the following form.

$$\underset{\sim}{L}(\underset{\sim}{w})\equiv\underset{\approx}{A}^t\underset{\sim}{w}_t+\underset{\approx}{A}^r\underset{\sim}{w}_r+\underset{\approx}{A}^z\underset{\sim}{w}_z-\underset{\sim}{B}=\underset{\sim}{0} \qquad (4)$$

where subscript notation for independent variable denotes partial differentiation and in which $\underset{\sim}{w}$ and $\underset{\sim}{B}$ denote vectors and $\underset{\approx}{A}^t$, $\underset{\approx}{A}^r$ and $\underset{\approx}{A}^z$ denote symmetric matrices:

$$\underset{\sim}{w}=\begin{bmatrix} u \\ v \\ p \\ q \\ s \\ \tau \end{bmatrix},\quad \underset{\sim}{B}=\begin{bmatrix} 2q/r \\ \tau/r \\ (u/r)-(2/3)\langle D\rangle(p-s) \\ -(u/r)-2\langle D\rangle q \\ (2/3)\langle D\rangle(p-s) \\ -2\langle D\rangle\tau \end{bmatrix},$$

$$\underset{\approx}{A}^t=\begin{bmatrix} 1 & 0 & 0 & 0 & 0 & 0 \\ 0 & 1 & 0 & 0 & 0 & 0 \\ 0 & 0 & M & 0 & Q & 0 \\ 0 & 0 & 0 & 1 & 0 & 0 \\ 0 & 0 & Q & 0 & N & 0 \\ 0 & 0 & 0 & 0 & 0 & a^2 \end{bmatrix},\quad \underset{\approx}{A}^r=\begin{bmatrix} 0 & 0 & -1 & -1 & 0 & 0 \\ 0 & 0 & 0 & 0 & 0 & -1 \\ -1 & 0 & 0 & 0 & 0 & 0 \\ -1 & 0 & 0 & 0 & 0 & 0 \\ 0 & 0 & 0 & 0 & 0 & 0 \\ 0 & -1 & 0 & 0 & 0 & 0 \end{bmatrix},$$

$$\underset{\approx}{A}^z=\begin{bmatrix} 0 & 0 & 0 & 0 & 0 & -1 \\ 0 & 0 & 0 & 0 & -1 & 0 \\ 0 & 0 & 0 & 0 & 0 & 0 \\ 0 & 0 & 0 & 0 & 0 & 0 \\ 0 & -1 & 0 & 0 & 0 & 0 \\ -1 & 0 & 0 & 0 & 0 & 0 \end{bmatrix},$$

where $M=a^4/(3a^2-4)$, $N=a^2(a^2-1)/(3a^2-4)$,

$Q=a^2(2-a^2)/(3a^2-4)$, and $\langle D\rangle=\begin{cases}\gamma\Phi(F)/\sqrt{J_2} & \text{for } F\geq 0\\ 0 & \text{for } F<0.\end{cases}$

Numerical computation

Integration of the system of partial differential equation (4) is carried out by integrating difference equation along bicharacteristics which was developed by Clifton for plane elastodynamic problem. This method was applied to plane elastic/viscoplastic problem by Bejda [3]. The differnce equations are derived for computing the solution at a mesh point (t_o,r_o,z_o) from known data at neighboring mesh points on the plane

$t=t_o-k$. If we write the increment of variable as

$$\delta\underline{w}=\underline{w}(t_o,r_o,z_o)-\underline{w}(t_o-k,r_o,z_o)$$

then, finally we obtain six equations for six unknown increments within the order of k^3 as follows.

$$\delta u-\frac{k}{r_o}\delta q = \frac{k^2}{2}\{\frac{a^2-2}{a^2}(\frac{u_{r_o}}{r_o}-\frac{u_o}{r_o^2})+u_{rr_o}+\frac{u_{zz_o}}{a^2}+\frac{a^2-1}{a^2}v_{rz_o}$$
$$-\frac{2}{3a^2}(D_{r_o}p_o+D_op_{r_o}-D_{r_o}s_o-D_os_{r_o}+3D_{r_o}q_o+3D_oq_{r_o}+3D_{z_o}\tau_o$$
$$+3D_o\tau_{z_o})\}+k(p_{r_o}+q_{r_o}+\frac{2}{r_o}q_o+\tau_{z_o})$$

$$\delta v-\frac{k}{2r_o}\delta\tau = \frac{k^2}{2a^2}\{(a^2-2)\frac{u_{z_o}}{r_o}+(a^2-1)u_{rz_o}+v_{rr_o}+a^2v_{zz_o}$$
$$+\frac{4}{3}(D_{z_o}p_o+D_op_{z_o})-\frac{4}{3}(D_{z_o}s_o+D_os_{z_o})-2(D_{r_o}\tau_o+D_o\tau_{r_o})\}$$
$$+k(s_{z_o}+\frac{\tau_o}{r_o}+\tau_{r_o})$$

$$-\frac{k(a^2-2)}{2a^2r_o}\delta u+(1+\frac{kD^o}{3a^2})\delta p+(1+\frac{kD^o}{a^2})\delta q-\frac{kD^o}{3a^2}\delta s = \frac{k^2}{2}\{p_{rr_o}$$
$$+q_{rr_o}+\frac{2q_{r_o}}{r_o}-\frac{2q_o}{r_o^2}+\frac{2(a^2-1)}{a^2}\tau_{rz_o}+\frac{a^2-2}{a^2}(s_{zz_o}+\frac{\tau_{z_o}}{r_o})\}$$
$$+k\{u_{r_o}+\frac{a^2-2}{a^2}(\frac{u_o}{r_o}+v_{z_o})-\frac{D^o+D_o}{3a^2}(p_o+3q_o-s_o)\} \qquad (5)$$

$$\frac{\kappa}{2r_o}\delta u+(a^2+kD^o)\delta q = \frac{k^2}{2}(p_{rr_o}+q_{rr_o}+\frac{2q_{r_o}}{r_o}-\frac{2q_o}{r_o^2}+\tau_{rz_o})$$
$$+k\{u_{r_o}-\frac{u_o}{r_o}-(D^o+D_o)q_o\}$$

$$(N+\frac{kD^o}{3})\delta s-(\frac{a^2-2}{a^2-1}N+\frac{kD^o}{3})\delta p = \frac{k^2}{2}(\tau_{rz_o}+\frac{\tau_{z_o}}{r_o}+s_{zz_o})$$
$$+k\{v_{z_o}+\frac{D^o+D_o}{3}(p_o-s_o)\}$$

$$(a^2+kD^o)\delta\tau = \frac{k^2}{2}(p_{rz_o}+q_{rz_o}+\frac{2q_{z_o}}{r_o}+s_{rz_o}+\tau_{rr_o}+\tau_{zz_o}$$
$$+\frac{\tau_{r_o}}{r_o}-\frac{\tau_o}{r_o^2})+k\{u_{z_o}+v_{r_o}-(D^o+D_o)\tau_o\}$$

in which subscript $_o$ denotes the value evaluated at the point (t_o-k,r_o,z_o) and superscripted quantity D^o denotes the value of D at the point (t_o,r_o,z_o) and symbol <> for D is omitted for economy of space. As (5) includes unknown quantity D^o, the system is solved by successive

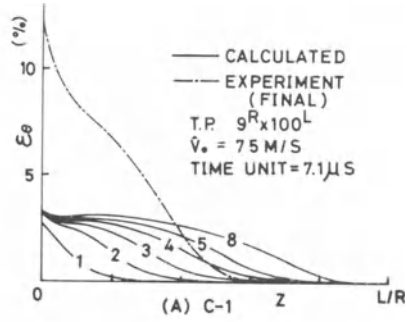

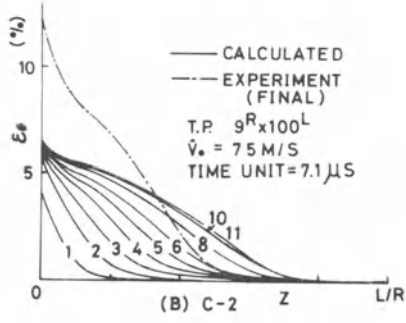

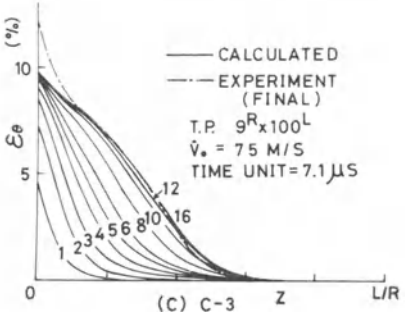

Fig.2 Distribution of circumferential strain at boundary surface. Abscissa is Lagrangian coordinate. Nimerical results shown in these figures should compared with experimental results shown in Fig.3.

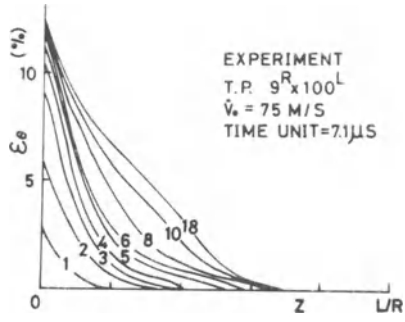

Fig.3 Distribution of circumferential strain. Experiment.

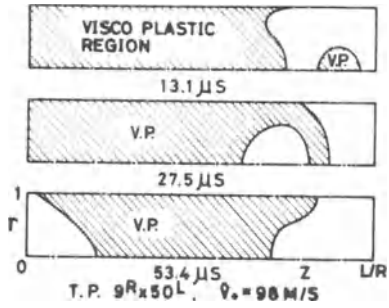

Fig.4 Elastic and visco-plastic boundary in axial plane.

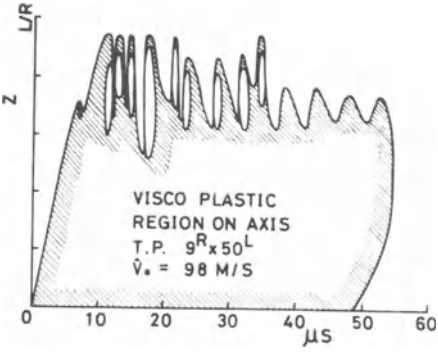

Fig.5 Elastic and visco-plastic boundary on axis.

approximation. For point on cylinder axis, computation is carried out same as for inner point if we notice that $\delta u=\delta q=\delta\tau=0$ on the axis because of symmetry. For point on the boundary or at the corner we can make use of boundary conditions instead of lost relations along bicharacteristics which are out of region. Data used for computation are: Young's modulus=2.1×10^{6}kg/cm^2, Poisson's ratio=0.29, $\rho=0.80\times10^{-5}$kg$\cdot$s^2/cm^4, σ_o=1560 kg/cm^2, H=1.9×10^{4}kg/cm^2, Γ=35 1/s and P=5 [4]. Ratio of dimensionless time interval k to dimensionless spatial interval is 0.25. Accuracy of computation is evaluated by comparing energy imparted to the specimen $E_o=2\pi\int\int(sv+\tau u)rdtdr$ with total energy of specimen at any instant $E=2\pi\int\int\frac{1}{2}(u^2+v^2)rdrdz+2\pi\int\int\frac{1}{2}(Mp^2+Ns^2+2Qps+a^2q^2+a^2\tau^2)rdrdz+2\pi\int\int\int\{\frac{2}{3}(p-s)^2+2(q^2+\tau^2)\}<D>rdtdrdz$. Relative errors $(E-E_o)/E_o$ are within 0.8 % for this case.

Results and conclusion

Results are shown in Figs.2 to 5. The constitutive relation which employs the type C-3 of (3) agrees best with experiment. Although elastic and viscoplastic boundary varies in complicated way, it is found that one dimensional rigid-viscoplastic analysis [1] gave fairly well feature.

References

1. Hayashi, T.; Fukuoka, H.; Toda, H.: Axial impact of low carbon mild steel rod. Bulletin of Japan Soc. Mech. Eng. 14 (1971) 901-908.

2. Clifton, R.J.: A difference method for plane problems in dynamic elasticity. Q. Appl. Math. 25 (1967) 97-116.

3. Bejda, J.: Propagation of two-dimensional stress waves in an elastic/viscoplastic material. Proc. 12th Int. Congr. Appl. Mech. (1969) 121-134.

4. Manjoine, M.J.: Influence of rate of strain and temperature on yield stresses of mild steel. J. Appl. Mech. 11 (1944) 211-218.

Dynamic Frictional Effects as Measured from the Split Hopkinson Pressure Bar

J. KLEPACZKO and Z. MALINOWSKI

Institute of Fundamental Technological Research,
Warsaw, Poland

Summary

This paper presents the results of a simplified theoretical analysis to estimate both the effects of friction and inertia durting fast compression of a cylinder. The solution enables to eliminate stress errors developed in experiment due to presence of friction and inertia. Using this analysis it was attempted to estimate the static and dynamic coefficient of friction by compression of aluminum specimens of ten height-to-diameter ratios in the range from 0.1 to 1.0. It is concluded that the dynamic coefficient of friction, as estimated from experiments with the split Hopkinson bar /lubrication by the MoS_2 powder/, is a bit larger than that estimated from the quasi-static experiments.

Introduction

The split Hopkinson pressure bar technique is presently a very useful and popular tool to obtain stress-strain properties of metals within the high strain rate region. However, during data reduction there is a problem how to deal with both friction and lateral or axial inertia. In spite of some previous analyses by different authors there is no simple relation which takes into consideration these effects. Such an estimation is needed to evaluate frictional and inertial errors in the measured stress during dynamic compression of the wafer specimen.

The main topic of this paper is to derive such relation-ship and to estimate on this basis the dynamic coefficient of friction as measured from the fast compression performed with the aid of the split Hopkinson pressure bar.

The early papers, in which only the interface friction during plastic compression of a cylindrical specimen was taken into consideration are those by Sibel [1], Cook and Larke [2], Schroeder and Webster [3], also by Van Rooyen and Backofen [4]. Recently, many additional papers have been published on this subject, especially with the aid of the finite elements technique.

On the other side, some papers have been published in which only inertial effects at the fast upsetting are taken into consideration, for example, Kolsky [5], Haddow [6], Davies and Hunter [7], Klepaczko [8], Samanta [9], and others.

Recently, Bertholf and Karnes [10] performed the comprehensive two-dimensional numerical analysis of the split Hopkinson bar technique, and they were able to describe quantitatively both the effects of realistic friction and inertia. However, their analysis is not very useful in the laboratory practice since computation of each case for assumed specimen geometry and interface friction needs relatively long time for the CDC 7000 series computer.

In description of the frictional effects in the classical manner, as it was done in paper [1], the equation of equilibrium is integrated together with Tresca yield condition, taking into account in addition a proper boundary condition. The solution for the mean axial true stress σ_z takes the form

$$\sigma_z = \sigma_o \frac{2}{\alpha^2} \left(e^{\alpha} - \alpha - 1 \right) \; ; \quad \alpha = \frac{\mu d}{h} \; , \qquad /1/$$

where σ_o is the true one-dimensional flow stress, μ denotes the coefficent of Coulomb friction, d and h denote respectively the current diameter and height of a compressed disc.

This paper represents the energy approach which enables to consider both friction and inertia.

The energy approach

The shadowed area in Fig. 1 demonstrates the additional work for the unit of specimen volume, which is lost for friction and inertia during a small increment of strain $\Delta\varepsilon$. Curve a of Fig. 1 is the

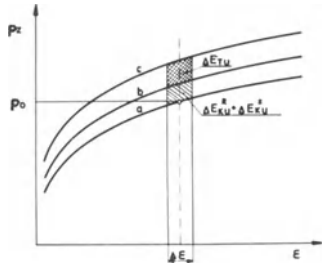

Fig. 1. Stress-strain diagram, a-one dimensional stress $p_o(\varepsilon)$; b-inertial effects added; c - both friction and inertia effects - the curve $p_z(\varepsilon)$, this curve is measured experimentally.

one-dimensional strain hardening curve $p_o(\varepsilon)$. Curve b in the same Fig. 1 is adequate to an apparent one when longitudinal and radial inertia effects are taken into consideration. Curve c represents the measured response when both effects are present. The energy increments ΔE_K^r and ΔE_K^z may be positive or negative within some strain regions mainly due to changes in the axial strain rate $\dot{\varepsilon}(t)$ and in the axial acceleration $\ddot{\varepsilon}(t)$. The total increment of energy which is lost for a small increment of strain $\Delta\varepsilon$ is equal

$$\Delta E = \Delta E_T + \Delta E_K^r + \Delta E_K^z \qquad /2/$$

where ΔE_T is the energy increment due to frictional effects which are present between specimen interfaces and plattens, ΔE_K^r and ΔE_K^r denotes respectively radical and axial increment of the kinetic

energy. Assuming, as it is shown in Fig. 2, that the distributions of axial and radial velocities are linear, i.e.

$$v_z = -\frac{zV}{h} \quad ; \qquad v_r = \frac{r\,V}{2h} \quad , \qquad /3/$$

The following expressions can be derived to obtain components of the kinetic energy E_K^r and E_K^z

$$\Delta E_K^r = \frac{\pi h^2 a^4}{16}\,\varrho\,V^2\left[\frac{1}{(h-\Delta h)^3} - \frac{1}{h^3}\right] + \frac{\pi h^2 a^4 \Delta h}{8(h-\Delta h)^3}\,\varrho\,\frac{\Delta V}{\Delta t} \quad , \qquad /4/$$

$$\Delta E_K^z = \frac{\pi h a^2 \Delta h}{3}\,\varrho\,\frac{\Delta V}{\Delta t} \quad , \qquad /5/$$

Δh is the increment of height, ϱ is the mass density of a specimen and V denotes the velocity of upsetting for $z = h$. Expression for the frictional energy ΔE_T which is dissipated at two interfaces of a specimen has been derived earlier [11]. This expression was derived under assumption that the deformation of the disc is uniform and the distribution of shear stress τ at the interfaces is constant, $\tau(r) = \text{const.}$, then

$$\Delta E_T = \frac{2}{3}\pi a^3 \mu\left[\left(\frac{h}{h-\Delta h}\right)^{\frac{1}{2}} - 1\right]\left(p_{zL} + p_{zR}\right) \quad , \qquad /6/$$

where p_{zL} and p_{zR} denotes respectively the average pressures at the interfaces for $z = h$ and $z = 0$, see Fig. 2.

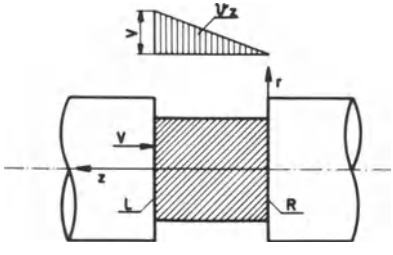

Fig. 2. Specimen configuration between Hopkinson bars together with velocity field

The total increment of energy ΔE is simply the increment of the height Δh times the increment of the force ΔP caused by friction and inertia,

$$\Delta E = \pi a^2 \Delta h \left(p_{zL} - p_o \right) \qquad /7/$$

After introduction /4/, /5/, /6/, and /7/ into eq. /2/ one yields the balance of energy relationship for the unit volume

$$\left(p_{zL} - p_o \right) \frac{\Delta h}{h} = \frac{2}{3} \mu \frac{a}{h} \left[\left(\frac{h}{h-\Delta h} \right)^{\frac{1}{2}} - 1 \right] \left(p_{zL} + p_{zR} \right) + \frac{\varrho \Delta h}{3} \frac{\Delta V}{\Delta t}$$

$$+ \frac{\varrho h a^2 V^2}{16} \left[\frac{1}{(h - \Delta h)^3} - \frac{1}{h^3} \right] + \frac{\varrho h a^2 \Delta h}{8(h - \Delta h)^3} \frac{\Delta V}{\Delta t} \qquad /8/$$

Multiplying eq. /8/ by $h/\Delta h$ and for $\Delta \varepsilon \to 0$ or $\Delta h \to 0$ one yields finally the limiting case

$$p_{zL} = p_o + \frac{\mu a}{3h} \left(p_{zL} + p_{zR} \right) + \frac{\varrho}{h} \left(\frac{a^2}{8} + \frac{h^2}{3} \right) \frac{dV}{dt} +$$

$$+ \frac{3 \varrho a^2}{16} \frac{V^2}{h^2} \qquad /9/$$

From the equation of equilibrium and for the linear velocity field, which is shown in Fig. 2, the relationship between the averaged pressures at the contact surfaces left and right, i.e. for $z = h$ and $z = 0$, is as follows

$$p_{zL} = p_{zR} + \frac{\varrho h}{2} \frac{dV}{dt} \qquad /10/$$

Taking into account eq. /10/, and having in mind that the one-dimensional flow stress $\sigma_o = - p_o$, eq. /8/ can be rewritten in the form

$$\sigma_o = - \frac{1}{2} \left(p_{zL} + p_{zR} \right) \left(1 - \frac{2 \mu a}{3h} \right) + \frac{\varrho}{h} \left(\frac{a^2}{8} + \frac{h^2}{12} \right) \frac{dV}{dt} + \frac{3 \varrho a^2}{16} \frac{V^2}{h^2} \qquad /11/$$

When one introduces strain rate and strain acceleration terms

$$\dot{\varepsilon} = - \frac{V}{h}, \qquad \ddot{\varepsilon} = - \left(\frac{1}{h} \frac{dV}{dt} + \frac{V^2}{h^2} \right)$$

Eq. /11/ can be rewritten once again as follows

$$\sigma_o = -\frac{1}{2}\left(p_{zL} + p_{zR}\right)\left(1 - \frac{2\mu a}{3h}\right) - \left(\frac{a^2}{8} + \frac{h^2}{12}\right)\ddot{\varepsilon} + \left(\frac{a^2}{16} - \frac{h^2}{12}\right)\dot{\varepsilon}^2 \qquad /12/$$

Relationship /12/ is also correct for the case when the convective term is taken into consideration assuming the axial velocity field ϑ_z in the form $\vartheta_z = -\left(U + \frac{zV}{h}\right)$. However, when eq. /10/ is used and σ_o depends exclusively upon p_{zR}, i.e. p_{zL} is eliminated, in relationship /12/ the convective part will be present, and U also $\dot{U}$ will enter the equation.

For non-frictional case, i.e. $\mu = 0$ and when the term at $\dot{\varepsilon}^2$ is small i.e. $\dot{\varepsilon}^2 \approx 0$, the eq. /12/ reduces to the relationship derived by Davies and Hunter [7]. On the other hand, where intertial effects are small and can be neglected, eq. /12/ reduces to the following form

$$\sigma_o = -p_z\left(1 - \frac{2\mu a}{3h}\right) \qquad /13/$$

where $p_z = p_{zL} = p_{zL}$ is the average pressure at the interfaces.

The above analysis was done by the energy balance approach. The estimation of frictional effects can also be performed via analysis by the power balance, as it has been dealt with inertial effects by Davies and Hunter [7], and also Samanta [9]. For the power balance approach the time derivative of the frictional energy E_T must be introduced as follows

$$\dot{E}_T = \int_o^a 2\pi r\left(\tau_L + \tau_R\right) V_r dr \; ; \quad \dot{E}_T = \frac{\pi a^3 V}{3h}\mu\left(p_{zL} + p_{zR}\right) \qquad /14/$$

where τ_L and τ_R are the shear stresses at the interfaces.

Experimental investigation of the quasi-static co-efficent of friction

Assuming the definition of engineering strain $\varepsilon = (h_o - h)/h_o$ from eq. /13/, the coefficent of friction can be obtained as follows

$$\mu = 3\, s_o \left(1 - \varepsilon \right)^{\frac{3}{2}} \frac{p_z - p_o}{p_z} \qquad /15/$$

where s_o is the initial height -to-diameter ratio, $s_o = h_o / d_o$. Pressures p_z and p_o, which enter into eq. /15/, must be obtained experimentally for the current value of strain. Relationship $p_o(\varepsilon)$ is adequate for the axial one-dimensional true stress σ_o as a function of strain, and can be obtained for example by the Cooke and Larke method. This method is based on the plot extrapolation

$p_o(\varepsilon) = \lim_{s_o \to \infty} p_z(\varepsilon)$ at particular values of ε for the family of experimental curves $p_z(\varepsilon)$ obtained at several values of s_o. Analysis provided in the paper [11] makes possible to calculate p_o for a particular strain ε from the formula

$$p_o = \frac{\sum_{i=1}^{n-1} s_{oi} - (n-1)\, s_{on}}{\sum_{i=1}^{n-1} \frac{s_{oi}}{p_{zi}} - (n-1)\, \frac{s_{on}}{p_{zn}}}, \qquad \varepsilon = \text{const.} \qquad /16/$$

where the average pressures $p_{zi} \ldots p_{zn}$ must be obtained experimentally by compression tests performed for n different values of height-to-diameter ratios from s_{o1} to s_{on}. Relationship /16/ may be derived by solving according to p_o the following set of equations

$$p_{zi} = p_o + \frac{\Delta E_{Ti}}{u_i \Delta \varepsilon} \qquad /17/$$

where u_i is the specimen volume. Set of equations like /17/ denotes n ponts on the experimental curve $p_z(s_o)$, $\varepsilon = \text{const.}$ In order to solve set /17/ in respect to p_o, the relationship for ΔE_T has been used, assuming that value of μ does not depend upon s_o. As it has been shown in the paper [11], for the experimental data which show a low scatter, values of p_o obtained from the Cook and Larke method and those obtained from eq. /16/ are very close.

In order to estimate the coefficent of friction for the quasi-static case, function p_z (ε , s_o) was obtained from the series of compression tests. Specimens of different height -to-diameter ratio, i.e. ten different s_o , 0.1; 0.125; 0.162; 0.2; 0.25; 0.33; 0.4; 0.5; 0.667; 1.0, prepared carefully from polycrystalline aluminum and annealed, were compressed in the special device [12]. The initial diameter of all specimens was 14 mm . Specimen faces before each test were lubricated by the molybdmun disulphide powder. Strain rate in all tests, independently on the specimen height, was kept constant $\sim 8 \times 10^{-4} s^{-1}$.

The obtained experimental results are shown in Fig. 3

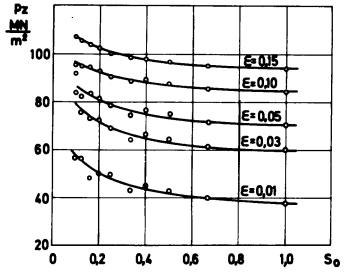

Fig. 3 Axial stress p_z as measured in quasi-static tests for different height-to-diameter ratio s_o, and for particular strain levels, $p_z(s_o)_\varepsilon$.

These results are the cross-sections $p_z(s_o)_\varepsilon$; ε = const, of the surface p_z (ε , s_o) for constant strains: 0.03; 0.05; 0.10; 0.15. Values of the coefficent of friction μ , obtained numerically from eq. /15/ for slow loading conditions, are shown as a function of strain ε in Fig. 4.

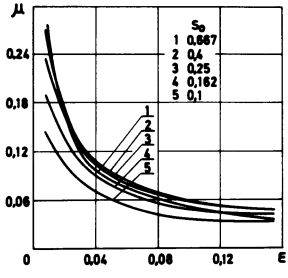

Fig. 4 . Coefficient of friction μ calculated from eq. /15/ on the basis of experimental data for quasi-static tests.

These values were calculated independently for five specimen geometries and do show similar trends, i.e. μ diminishes as strain increases. However, as it was demonstrated by Van Rooyen and Backofen [4] , changes of μ may strongly depend on a specimen material, its quality of surfaces, preparation of plattens and used lubricant A similar result for $\mu(\varepsilon)$ was obrained for aluminum with molybdemun disulphate lubricant by Van Rooyen and Backofen [4].

Dynamic coefficent of friction

The fundamental question arises as to whether in equation /12/ , in the estimation of the error devolped by the inerial effects an friction, the same values of the friction coefficent μ may be used as for the quasi-static situations. To clarify this point a series of experiments were performed with the modified split Hopkinson pressure bar. Similarly, as in the quasi-static tests, dynamic compression test was performed for ten height -to-diameter ratios, i.e. $0.1 \leqslant s_o \leqslant 1$. Specimen material was the same as for the quasi-static tests polycrystalline annealed aluminum as well as the same initied diameter of specimen do = 14 mm. To compensate the length influence of individual specimen geometry, in keeping the strain rate constant, a different velocities of the striker bar was applied. For all tests performed the strain rate values were within the range $5 \times 10^2\ s^{-1} \leqslant \leqslant \dot{\varepsilon} \leqslant 1.5 \times 10^3 s^{-1}$. For each specimen geometry three good tests were performed and next, after data reduction /oscillograms/, a set of p_z (s_o) curves were obtained.

In Fig. 5a, b, and c three oscillograms are shown for three

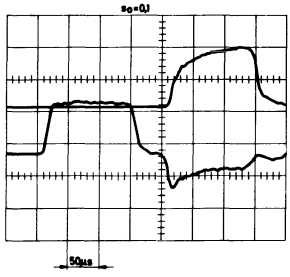

Fig. 5 a. Transmitted /upper trace/, incident and reflected /lower trace/ pulses recorded for aluminum specimen from the modified Hopkinson apparatus for s_o = 0.1.

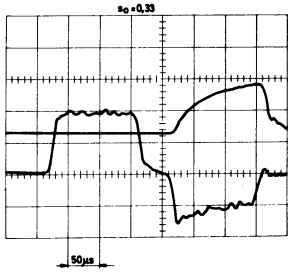

Fig. 5b. Transmitted /upper trace/, incident and reflected /lower trace/ pulses recorded for aluminum specimens from the modified Hopkinson apparatus for $s_o = 0.33$.

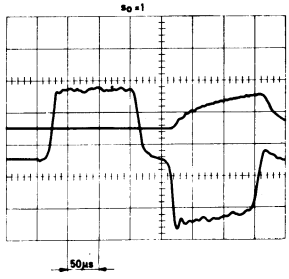

Fig. 5c. Transmitted /upper trace/, incident and reflected /lower trace/ pulses recorded for aluminum specimens from the modified Hopkinson apparatus for $s_o = 1.0$

different values of s_o, minimal $s_o = 0.1$, medium $s_o = 0.33$, and maximal $s_o = 1.0$. On each of them three pulses are visible, incident $\varepsilon_I(t)$, reflected $\varepsilon_R(t)$, /lower channel/, and transmitted $\varepsilon_T(t)$ /upper channel/. It is clearly visible that the transmitted pulse, which is basically proportional to the average pressure in a specimen $p_z(t)$, is larger, as expected, for shorter specimens. A more detailed description of the split Hopkinson bar technique can be found, for example, in [13].

In the data reduction, to obtain a pressure-strain curve $p_z(\varepsilon)$, the computer program was employed and $p_z(t)$, $\varepsilon(t)$, $p_z(\varepsilon)$, and $\dot{\varepsilon}(\varepsilon)$ data were calculated and plotted. The simplified expressions for $\varepsilon(t)$ and $p_z(t)$ were used

$$\varepsilon(t) = \frac{2C_{oE}}{h_o} \int_o^t \varepsilon_R \quad (t) \qquad dt,$$

$$p_z\ (t) \quad = \quad E \quad \frac{D^2}{d_o^2} \left[1 - \varepsilon(t)\right]\left[- \quad \varepsilon_T \quad (t)\right] \quad ,$$

when C_{oE} and E are respecively the longitudinal ware speed and Young modulus of the Hopkinson bars, D is the bar diameter, h_o and d_o are the initial specimen height and specimen diameter respectively.

Fig. 6 is the final result, where by the solid lines $p_z(s_o)_\varepsilon$, ε = const curves for the high strain rat deformation are shown

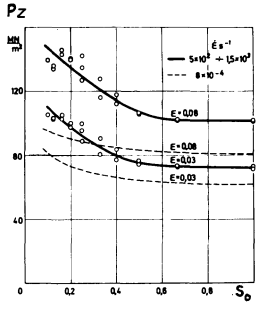

Fig. 6 . Dynamic axial stress /solid lines/ and quasi-static /dashed lines/ as measured respectively from the split Hopkinson bar and at a slow loading.

at two strain levels, ε = 0.03 and 0.08. in order to compare these results with the quasi-staic data, $p_z(s_o)_\varepsilon$, ε = const. curves for the same two strain levels were also shown in Fig. 6 by the dashed lines. Besides the influence of the lengh -to-diameter ratio, the strain rate effect is also visible. It may be first concluded that the strain rate sensitivity can be measured with a high reliability for s_o larger than 0.5.

It has been concluded on the basis of eq. /12/ that for the measured changes in strain rate $\dot{\varepsilon}(t)$, met in those experiments, for strain levels 0.03 and 0.08 the inertial effects are less than 1 % of the flow

stress, and they can be neglected. Thus, the dynamic coefficent of friction was calculated from eq. /15/ making use of Fig. 6 data, and results are shown in Fig. 7. The results are presented in the

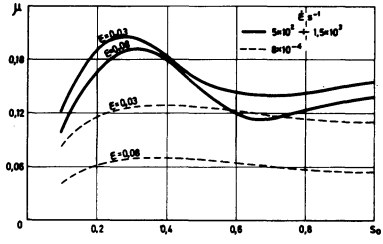

Fig. 7. Dynamic and static coefficients of Coulomb friction estimated for the M_oS_2 powdered lubricant; the polycrystalline annealed aluminum specimen and the silicon steel bar.

form of plots $\mu(s_o)$ for both quasi-static and dynamic conditions of deformation. The comparison shows that, for the applied lubrication- powdered M_oS_2, and for applied aluminum, the dynamic coefficent of Coulomb friction at (at $\dot{\varepsilon} \approx 10^3\ s^{-1}$) shows larger values than that measured by the Cook and Larke method at quasi-static tests ($\dot{\varepsilon} \approx 8x10^{-4}\ s^{-1}$) . But the differences in μ are not so large. The largest differences in static and dynamic values of μ are observed for $s_o \approx 0.3$, but the order of μ , can be fairly said, is the same.

Discussion and conclusions

Derived in the present paper relation /12/ makes possible to take into account both ineartia and friction influences in the dynamic compression test. Equation /8/, which was the basic one for eq./12/, is the conservation of energy principle for a finite increment of strain $\Delta\varepsilon$.

Relationship /16/, derived from the set of equations /17/, and from the frictional energy relation /6/, makes possible to estimate, for a particular strain ε , value of one dimensional stress σ_o . Experimental in put to the eq. /16/ is $p_z\ (s_o)_\varepsilon$. One dimen-

sional stress σ_o estimated from eq. /16/ for slow loading tests are in agreement with values of σ_o obtained from the Cook and Larke method. However, even for the last method there are some inaccuracies because in reality some quantites change along radius of the interfaces, i.e. $\mu(r)$, $p_z(r)$ and $\tau(r)$. Usually coefficent of friction is assumed constant. In this paper τ is assumed to be independent of the interface radius. It has been observed experimentally [4], that and μ and τ diminish in the direction of the specimen axis.

As it was mentioned above, calculations of the dynamic coefficent of friction resulted in the variation of μ as a function of height -to-diameter ratio s_o, Fig. 7. In the range $0.10 \leqslant s_o \leqslant 0.25$ the dynamic coefficient of friction for two considered strain levels shows diminishing tendency as the length-to-diameter ratio is lowered, which may be well developed by increasing unit pressures $p_z(s_o)_\varepsilon$ for shorter specimens, see Fig. 6. Whereas in the range of larger values of height -to-diameter ratio $0.25 \leqslant s_o \leqslant 1.0$, variation in the coefficient of friction is less pronounced and may be developed by inherent features of the split Hopkinson bar technique, e.g. wave processes in specimen and bars.

Generally, the results of this simplified analysis are in qualitative agreement with two dimensional more exact numerical analysis of the split Hopkinson pressure bar system 10. In view of that the derived here formulas can find a practical application in designing and stress error estimation in dynamic compression tests. However, much experimental work is needed toward measurements of the dynamic coefficient of friction for different situations, especially when there is a contact between elastic and plastically deforming material at the interface.

References

1 Siebel, E.; Grundlagen zur Berechnung des Kraft und Arbeitdorf vei Schmieden und Walzen, Stahl u. Eisen. Düsseldorf, 43 /1923/ 1295.

2 Cook, M., Larke, E. C.; Resistance of copper and copper alloys to homogeneous deformation in compression, I. Inst. Metals, 71/1945/371.

3 Schroeder, W., Webster, D. A.; Press-forging thin sections: effect of friction, area, and thickness on pressures required, J. Appl. Mech., 16/1949 289.

4 Van Rooyen, G. T., Backofen, W. A.; A study of interface friction in plastic compression, Int. J. Mech. Sciences 1, /1960/ 1.

5. Kolsky , M.; An investigation of the mechanical properties of materials of very high rates of loading, Proc. . Phys. Soc., B62 /1949/ 676.

6. Haddow, J. B.; On the compression of a thin disk, Int. J. Mech. Sciences., 7/1965 / 657.

7. Davies, E. D. and Hunter, S. C.; The dynamic compression testing of solids by the method of the Split-Hopkinson pressure bar, J. Mech. Phys. Solids, 11/1963/ 155

8. Klepaczko, J.; Lateral inertia effects in the compression impact experiments, Inst. Fund. Tech. Res. Report 17 /1969/.

9 Samanta, S. K.; Dynamic deformation of aluminum and copper at elevated temperatures, J. Mech. Phys. Solids 19 /1971/117

10 Bertholf, L. D. and Karnes, C. H.; Two-dimensional analysis of the split Hopkinson pressure bar, J. Mech. Phys. Solids 23 /1975/, 1.

11 Malinowski, Z.; On a method of friction analysis in plastically compressed cylindrical specimens, Theoretical and Applied Mechanics, 14/1976/347, /in Polish/.

12 Malinowski, Z., Klepaczko, J.; Estimation of the coefficient of friction on the interfaces of the plastically deformed cylindrical specimen, Theorectical and Applied Mechanics, 10/1972/ 561 /in Polish/.

13 Lindholm, U. S.; High strain rate tests, in Measurement of Mechanical Properties, Part 1, ed. R. F. Bunshah, Interscience Publ. /1971/.

Activities of the Research Committee of Shock-Resistant Structures for Automobile

TSUYOSHI HAYASHI

Department of Mathematics, Faculty of Science and Engineering, Chuo University, 1-13-27 Kasuga, Bunkyo-ku, Tokyo 112, Japan

Summary

The Research Committee of Shock-Resistant Structures for Automobile, consisting of twelve members* from Universities and Institutes, has been organized in 1976 under the sponsorship of the Japan Automobile Research Institute (JARI).

The scope of the Committee is to study the impact properties of the main structural components of car and the structural characteristics as a system of car and then to find the feasible shock-resistant configurations.

In 1976, all of members have cooperated in the survey and review of the published literatures concerned and every member has promoted the study for the prearranged projects.

As to the individual study, Prof. K. Kawata presented an impact analysis of an elasto-plastic one-dimensional structure, taking into consideration of the effect of decreasing mass. Prof. T. Sato analyzed the load-contraction behaviors of a rectangular tubler steel plate structure with the assumption of plastic hinge and carried out the impact tests and obtained a good agreement between theory and experiments. Prof. K. Takehi carried out the compression tests on steel conical shells and studied their compressive strength and load-deformation properties.

Prof. T. Hayashi derived a correlation law between structural weight and gross weight for similar car structures, and analyzed quantitatively the effectiveness of weight reduction of a structure for impact. He has also discussed a structure having a shock absorbing element with rigid-plastic type compressive behavior, taking into account the Human Tolerance Limit for impact.

Prof. M. Uemura has been studying the impact behavior of structural components by using a falling weight tower.

Dr. S. Shimamura has been conducting the collision tests of full scale cars with Glass Reinforced Plastics body.

The other members are also extending their contributions.

*Committee Members:

T. Hayashi (Prof., Chuo Univ.; Chairman)
T. Sato (Prof., Dept. of Mech. Engng., Keio Univ.)
M. Uemura (Prof., ISAS, Univ. of Tokyo)
K. Kawata (Prof., ISAS, Univ. of Tokyo)
S. Shimamura (Dr., Div. Chief, Mech. Engng. Labo., MITI)
T. Hirata (Prof., Agricultural Engng. Univ.)
K. Takehi (Prof., Dept. of Mech. Engng., Tamagawa Univ.)
Y. Takeishi (Prof., Chiba Industrial Univ.)
H. Kobayashi (Prof., Dept. of Mech. Engng., Univ. of Tokyo)
Y. Okami (Director, JARI)
H. Ishikawa (Research Engnr., JARI)
F. Matsukawa (Research Engnr., JARI)

Discussion

1-1

W. Goldsmith: If this model is to be compared to experiment to check its validity, impact and wave processes must be used to attain a strain rate of $\dot{\varepsilon}$ = 100/s or greater. Now there is a drastic variations of stress, strain and strain rate at each section of the bar that rapidly change with time. How does one measure this, and what value of $\dot{\varepsilon}$ would be used to compare model and test data? If the final strain distribution is used, it may not be unique. If the split Hopkinson is used, this problem does not arise.

K. Kawata: The problem of high velocity tension of bars of finite length arises very frequently in the practical problems of structures under high velocity loading. The high velocity tension of bars of finite length is the most fundamental and also the simplest at first sight, but intrinsic nature is rather complicated. We think the behaviours of bars of finite length under high velocity tension should be clarified using the constitutive equations based upon microscopic standpoint, for this reason. The first object of our study is to know the difference of the behaviours of BCC materials from of FCC materials in high velocity tension of bar of finite length.

In the present paper, the stress-strain relations at various constant strain rates are also calculated basing upon the constitutive equations deduced, and these would be convenient to compare directly with the split Hopkinson bar data.

1-2

E. H. Lee: You emphasized the advantage of using computational methods which eliminate the generation of discontinuities in solutions in order to obtain ease of computation and accuracy. What about problems in which discontinuities do arise in the physical problem, such as shock waves? Surely an accurate analysis must then incorporate these phenomena in the computational approach utilized.

J. P. Wright: By authors Wright and Baron (also I. Sandler, of the same office). The types of discontinuities which should be eliminated are those which correspond to major changes in the solution when minor changes are made in the problem definition. In the solution to a given problem, temporal and spatial discontinuities in stress and velocity (i.e., shocks) may arise, but these should be of a stable kind and should not be drastically altered if the problem specification is only slightly changed. If we symbolically denote the solution as S (x, t; P) where S is the solution (stresses or velocities), x denotes position, t is time and P represents the set of parameters that defines the problem (loading and support conditions, material properties, geometric configuration, etc.) then S may be discontinuous in x and t (so long as it satisfies the appropriate jump conditions), but it should depend continuously on P.

D. C. Drucker: Would you comment on the likely differences to be found in the solutions that would be obtained with other less realistic cap shapes as, for example, the spherical cap that Gibson, Henkel, and I proposed originally as a crude approximation to reality, or the planar cap proposed by Shield as a great mathematical simplification?

J. P. Wright: By authors Wright and Baron (also I. Sandler, of the same office). The differences in behavior which arise between models using elliptical caps and spherical or planar caps occur most significantly in the stress paths associated with given strain histories; the modeling of the cap shape is consequently most important for problems in which residual stresses are to be determined. In general, the importance of this particular aspect of the cap model depends strongly on the problems at hand. It should be noted that for problems solved by numerical methods on the computer, the use of a planar or spherical cap does not result in any significant simplification, as might be the case when analytic methods are employed.

W. Goldsmith: How do the predictions of the cap model compare with those of a two-phase system (voids and core, with the possibility of no voids), particularly under dynamic conditions (wave propagation)?

J. P. Wright: By authors Wright and Baron (also I. Sandler, of the same office). The cap model is not intended to represent true two-phase phenomena such as void or pore water migration, but is instead intended to describe the behavior of materials in situations where time scales are so short that such effects are unimportant. The nonmigratory effects of pore fluid pressure can easily be incorporated in the cap model by an effective stress approach.

2-1

R. J. Clifton: Do you have a mechanism in mind to which you would ascribe the reported thermally activated deformation at low temperatures? In particular, is it possible that the apparent change in mechanism at high stresses and low temperatures is related to a change in the kinetics of dislocation generation instead of in the mechanism governing the mobility of dislocations?

U. S. Lindholm: In the paper it is suggested that thermally activated cross slip may become controlling as the stress is increased, either by reducing the temperature or increasing the strain rate. Your suggestion that nucleation kinetics may be involved is also a possibility. However, the mobile dislocation density is included in the preexponential term, $\dot{\gamma}_0$. It is generally found that this value is relatively constant, with inference, thereby, that mobile density is also constant.

T. Mura: This is a complementary comment to the question of Dr. H. Suzuki addressed to Dr. U. S. Lindholm, asking the effect of inclusions to the macroscopic mechanical properties of material. The inclusions usually give a back stress to the matrix of material. If the matrix, for instance, is perfectly plastic, the hard inclusions provides macroscopically a work-hardening behavior of the composite. If the matrix is a Newtonian flow, the hard particles give Kelvin's solid as a whole.

U. S. Lindholm: Strengthening by hard precipitate inclusions is common in alloys since these inclusions form strong barriers to dislocation mobility. The Newtonian linear viscous behavior of dislocations relates only to their motion through the uniform lattice. The combination of viscous drag and interaction with local barriers occurring simultaneously is discussed in Reference 2 of this paper.

2-2

J. R. Klepaczko: How would you describe the plastic strain-rate in terms of the Orowan equation, i.e.,

$$\dot{\gamma} = \chi N b v \qquad (*)$$

where χ is an orientation factor, N is the mobile dislocation density, b is the Burgers' vector and v is the average velocity of dislocations.

R. J. Clifton: This equation applies directly for slip on a single family of slip planes in a single slip direction, provided that the deformation is sufficiently uniform for the macroscopic plastic strain-rate to be described adequately by parameters characterizing the average motion of dislocations. In the plate impact experiments, under ideal conditions, the rate of shearing is the same on the four active slip systems. Then, the plastic shear strain-rate associated with each of the slip systems is given by (*) with $\chi = 1$ and the plastic strain-rate $\dot{\varepsilon}_{11}^{P}$ in the direction of wave propagation is

$$\dot{\varepsilon}_{11}^{P} = \frac{-b}{2} (4N) v$$

where N is the line length, per unit volume, of mobile dislocations on each of the four active slip systems and v is the average velocity of these dislocations. From the equivoluminal character of plastic deformation, the plastic strain rates in the other two principal directions are $\dot{\varepsilon}_{22}^{P} = \dot{\varepsilon}_{33}^{P} = -\dot{\varepsilon}_{11}^{P}/2$.

2-3

U. S. Lindholm: In your experiments the transition from thermally activated to a viscous drag mechanism appears to occur at nearly constant strain rate. In the absence of a coupled analytical model, I would expect the transition to occur more nearly at a constant stress level.

Do you think there are any significant effects of the large area miss-match between specimen and pressure bar in your experiments?

J. Shioiri:

(1) Theoretical estimation of the strain rate or the stress at which the transition in the rate controlling mechanism will occur seems to require such an analysis as equation (16) of the text, because the transition should appear in the region where two mechanisms are simultaneously operative. Results obtained from equation (16) indicate that the transition will appear rather at a nearly constant strain rate when the temperature is changed [figure 8 of the text].

(2) I think, in our experiment, the effect of the area mismatch upon the output of the transmitter bar gauge will be not so significant. This is due to the following reasons:

(i) Since the dispersion effect in the incident bar makes the front shape of the incident pulse gentle, the higher order oscillations caused in the transmitter bar by a large area mismatch will be not so strong; mathematically this implies that the high frequency components in the response function to a step load concentrated near the center are averaged in the process of the Duhamel integral [equation (13) of the text];

(ii) the dynamic Saint Venant's effect [reference [11] of the text] seems to weaken the effect of the area mismatch, since in our experiment the ratio z_0/a (distance from the specimen to the gauge/radius of the pressure bar) is as high as 60.

3-1

S. Tanimura: Is there any relation between that one cannot observe any stress peak during compression tests for single crystals and that a large error is usually accompanied to observe stress-strain relation at the beginning of deformation by the split Hopkinson bar method?

M. Stelly: In the compressive experiments performed with the split Hopkinson pressure bar, there exists non uniformities in the spatial stress and strain distribution in the specimen at the beginning of the test. Thus it would be erroneous to determine stress-strain curves during the first microseconds of the test. Nevertheless, it is possible to know the stresses behavior versus time at each specimen's end, although the stress levels are not always the same. So, if a peak existed, we would be able to observe it on the recordings.

In the case of dynamic tensile tests, many anterior experiments have shown that copper specimens take a long time to reach an homogeneous state of deformation. Despite this fact, a very pronounced peak is observed at the beginning of the deformation of copper single crystals, deformed at a loading rate similar to compressive tests.

J. Klepaczko: It is good that the incremental experiments have been performed on monocrystals. They do clarify some doubts on the role of grain boundary relaxation in the strain rate history effects observed previously on polycrystalline copper* and other metals. It would be also interesting to compare your results with those obtained for polycrystalline copper at Brown University with the aid of split Hopkinson torsional bar.

* J. KLEPACZKO - Strain Rate Incremental Tests on Copper, Brown University Report, NSF - GK - 40213/6 (1974).

M. Stelly: Results obtained during incremental strain rate experiments are recent and supplementary tests would be useful for a good understanding of the phenomenon. Especially, it would be necessary to determine the upper bound of the domain where thermal activation is prevalent.

However, we have compared some of our results on copper single crystals with those obtained on polycrystals and we discuss about it in the written text. In summary, the following points may be noted:

In the strain rate range between $10^{-4}s^{-1}$ to $2 \cdot 10^{3}s^{-1}$, where the deformation mechanism still seems to be thermal activation, the activation volume and its variations with strain are not very different from those found in Klepaczko's works.

But a difference appears in the mechanical behavior of single crystals for which there is no fading memory effect as observed on polycrystals. This difference can be due to experimental procedure and studies are now in progress to perform incremental dynamic compressive tests with rapid change of strain rate and no unloading.

3-2

J. Klepaczko: Would you like to comment why in the case of incremental experiments some alloys you tested show the maxima of rate sensitivity at higher temperatures?

K. Tanaka: When a deformation is controlled by a thermally activated process, the relation between the stress and the temperature is illustrated schematically in the following figure. The difference of the thermal components of stress, $\sigma_2^*-\sigma_1^*$, is zero at 0°K and increases with the increase of the temperature. It has a maximum value at or around $(T_c)_1$. Therefore, it is reasonable to show the maxima of strain rate sensitivity. The temperature T_c increases with the increase of the strain rate.

In Al alloys, the maxima appear at rather low temperatures. The maxima observed at high temperatures are caused by the interactions between mobile dislocations and solute elements such as Mg and Cu.

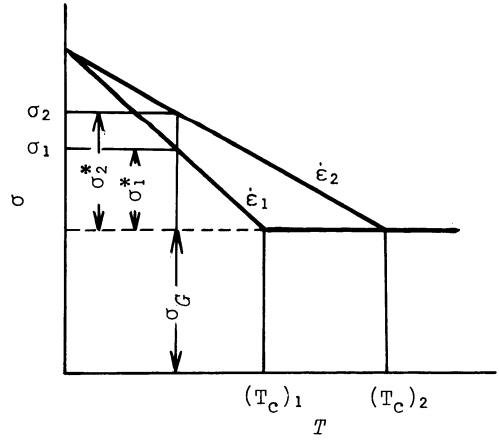

3-3

T. Mura: This is not a question but a comment. As you will see in my talk in the latter session, there are two types of dislocations namely Nye's dislocations and the essential dislocations. Nye's dislocations are related to recrystallization and polygonization, on the other hand, the essential dislocations play an important role for work-hardening. The competition between the recrystallization and work-hardening as Prof. T. Nakamura mentioned may be interpreted by the competition between the two types of dislocations above mentioned.

T. Nakamura: I appreciate Professor Mura's comment. Certainly, the two competing phenomena occur during high temperatures. For example, in such a material as aluminum, the rearrangement of dislocations to form Nye's type configuration is predominant, thus, resulting in dynamic recovery in ordinary cases. The opposite case is for the low stacking fault energy materials, making Nye's rearrangement difficult. In other words, the two competing dislocation rearrangements can be discussed in terms of dislocation core structures.

4-1

R. J. Clifton: If the surface energy required for fracture is believed to be dependent on crack velocity, would you still expect a linear relationship between kinetic energy absorbed and fracture surface area?

L. E. Malvern: It could be that the major part of the dynamic delamination takes place at approximately constant crack propagation speed, high compared to the speeds in static loading tests, although this has not been demonstrated experimentally.

D. C. Drucker: Have you had the time yet to examine the effect of the shape of the impactor? What would happen with a conical point, a chisel point, or a spherical shape?

L. E. Malvern: Up to now we have used only blunt-ended impactors. I would expect a rounded end to produce a less sharply defined generator strip, but would still expect to see sequential delamination in the multilayer lamina 0-90° layup plates. We expect to explore this question in future experiments.

4-2

D. C. Drucker: You have shown excellent agreement between theory and experiment at lower temperatures. The agreement at the higher temperatures of test was not as good. What additional features are needed in the theory for those higher temperatures?

A. T. Yokobori, Jr.: It is very nice question. The trend is similar in the case of applying[1)2)] Cottrell-Bilby dislocation locking mechanism. Concerning this point, one of the author (T. Yokobori) made a modification by taking into account of frictional stress τ_i and using effective stress $\tau-\tau_i$ instead of τ, applied stress for the case of dislocation locking mechanism, and the theory is in better agreement with the experimental data.[1)2)] We believe similar modification by taking into account of frictional stress will improve the agreement.

1) Yokobori, T., J. Appl. Phys., Vol. 25 (1954), 593.
2) Yokobori, T., Kolloid - Z., Band 166, (1959), 20.

R. J. Clifton: I have both a comment and a question. The comment is that I am pleased to see the attention you are giving to dislocation group dynamics with emission of dislocations as opposed to the motion of isolated dislocations. The question is "What is the criterion used for emission of a dislocation?"

A. T. Yokobori, Jr: We have analysed the problem of the instability of dislocation emission from the crack tip, from the force and the energy balance requisites, respectively.[3)4)] As a result it is concluded that a dislocation will spontaneously be emitted if stress intensity factor is larger than a specific or critical value, which is very small.[3)4)] In such case as the present paper, dislocation will probably be emitted from within the specimen, and applied stress may be used instead of stress intensity factor. However, in this case also a dislocation will be spontaneously emitted if applied stress is larger than a specific or critical value, which is very small.

3) Yokobori, T., Yokobori, A.T., Jr. and Kamei, A., Int. J. Fracture, Vol. 11 (1975) 781; Vol. 12 (1976) 519.
4) Yokobori, T., Konosu, S. and Yokobori, A.T., Jr., Fracture, Vol. 1 (1977) 665, Univ. of Waterloo, Proc. 4th Int. Conf. Fracture.

4-3

U. S. Lindholm: In your modeling of adiabatic shear band formation, what is your criteria for nucleation?

D. A. Shockey: In the present model, the shear bands are nucleated when both an empirically-determined critical strain and a critical strain rate are exceeded. Typical values used for steels are a critical strain of 0.15 to 0.3 and a critical strain rate of $10^3 s^{-1}$. However, we are

currently developing a different nucleation criterion based on localization of plastic strain resulting when the local plastic wave velocity is too small to allow local perturbations in strain to propagate away. This criterion is similar to that developed by von Karman, G.I. Taylor, and others to explain localization of plastic strain in wires subjected to tensile impact. For quasi static loads, the criterion reduces to the usual one for plastic instability, namely that the work hardening modulus be zero or negative.

M. Stelly: You have developed a general model to describe fracture. Have you been interested by the initiation of cracks and especially by its relation with metal microstructures.

D. A. Shockey: We have been very interested in identifying the microstructural features responsible for microfailure initiation,[16] and in relating the size distributions of these features to crack and void size distributions. We found that different microstructural features served as the dominant nucleating defect in different materials. Manganese sulfide inclusions are the main nucleation defects in many steels,[18] grain boundary triple points in α-titanium,[12] trapped spherical bubbles in polycarbonate,[3] and intergranular flaws in a fine-grained quartzite rock.[7,8] In the latter case, we measured the inherent flaw size distribution and made use of it in the fracture model to calculate the number of activated cracks. We are currently using the inclusion size distribution we measured in A533B steel to calculate the failure behavior of a tensile bar.

18) D. A. Shockey, L. Seaman, K. C. Dao, and D. R. Curran, "A Computational Model for Fracture of Pressure Vessel Steel Derived from Experimental Data," Paper No. 78-PVP-92, The Amer. Soc. of Mech. Engrs., New York 1978.

4-4

D. A. Shockey: You mentioned that you computed temperature increases of about 20°C in the midplane zone of impacted aluminum plates. This implies very high local temperatures near expanding voids. Do you account for the effects of the high temperatures on the constitutive equations? Do the void surfaces melt?

Lee Davison: The average temperature in the damaged region of a spalling body is greater than it would be if damage were suppressed. In the specific example mentioned (see Fig. 6 of Ref. 1) the temperature increased from 300 K to almost 320 K during the formation of voids eventually comprising 6 1/2% of the volume of the central region of the sample. If we were to suppose that the internal energy associated with a 20 K increase in average temperature were actually stored in a volume of material comparable to that of the voids, then the average temperature increase of this small volume of material would be about 300 K -- enough to alter the mechanical properties markedly but not quite sufficient to cause melting. In cases where larger amounts of damage are produced more rapidly we have calculated overall increases in temperature of almost 100 K. A calculation similar to that suggested above results in temperatures very close to the melting point and we belive that melting could occur. The crudeness of the local temperature estimate, neglect of melting kinetics, etc. leave the situation so uncertain that the question remains open.

None of the effects of localized heating are incorporated into the present theory, although some shortcomings could be removed on an ad hoc basis. A more careful treatment of the problem would necessitate taking account of localized inertia and other microstructural effects as well as the heating, and seriously complicate the theory.

5-1

A. Kobayashi: Do you think that the crack velocity is predominantly affected by the plastic region ahead of a running crack?

K. B. Broberg: At small scale yielding the crack tip velocity is governed by a balance condition: The energy flow to the dissipative region (the process region and the plastic region) equals the energy "demanded", i.e. the energy irrecoverably trapped near the crack tip. The energy flow can be calculated very accurately at small scale yieldning from a purely elasto-dynamic model, since the dissipative region is very small. The energy irrecoverably trapped near the tip (material deterioration in the process region, plastic flow, and to some very small extent residual elastic strain energy) depends on the material and on the tip velocity, as explained in the paper. Thus the crack tip velocity depends on the amount of plastic flow, but since the energy flow depends strongly on the crack length it would perhaps be misleading to say that the crack tip velocity is predominantly affected by the plastic region.

At large scale yielding the balance condition should regard the energy flow to the process region, only, and the energy consumption of the process region, because the process region can almost always be assumed to be very small.

H. G. Suzuki: Can we extend your argument to the crack tip configuration of brittle fracture? When the area of the region where plastic deformation occurs at the crack tip is narrow, usually brittle fracture does occur. If it is broad, then ductile fracture yields. If so, how can we adjust between ductile and brittle fracture?

K. B. Broberg: I avoid nowadays the term "brittle fracture", because it seems to mean so many different things. For the theoretical case of perfect cleavage without plastic deformation, especially in the weak direction at the strong anisotropy, one could perhaps assume that the minimum energy argument holds up to the Rayleigh wave velocity. However, real materials, glass, PMMA, etc. certainly exhibit plastic flow type energy dissipation and isolated micro-separations. Thus, I think, the ideas expressed in the paper are pertiment to practically seen all materials, except very ductile ones, where small scale yielding does not occur on normal laboratory or structural scales.

M. Stelly:

(1) In your model you have supposed that, for fast moving crack tip, many micro-separations are created ahead of the crack tip and out of its plane. Have you experimental evidence to support this model?

(2) You explain existence and influence of the micro-separations by the fact that interactions between them are impeded by the short times involved. I ask if, due to the high sound speed and little distance between microseparations, there are not rather many interactions creating a complex stress state ahead of the crack tip?

(3) Crack tip velocity may attain sound speed but it is known that plastic deformation deplacement velocities are about on order smaller than sound speed. How do you correlate these two facts?

K. B. Broberg:

(1) There exists a lot of evidence that the fracture surfaces become more and more rough as the crack tip velocity increases. Also so called parabolic marks (in, for instance, PMMA) increase in number when the tip velocity increases. See, for instance, Carlsson, J., Dahlberg, L., and Nilsson, F.: "Experimental studies of the unstable phase of crack propagation in metals and polymers", (Proceedings of an international conference on) Dynamic Crack Propagation, edited by George C. Sih, Noordhoff International Publ., 1973.

(2) In the plastic region the sound velocities may be even lower than the velocity of a very fast running crack tip. This means that the interaction between microseparations becomes impeded. It is certainly correct that the stress state between the microseparations becomes highly complex.

(3) The Rayleigh wave velocity is the theoretical limiting speed for mode I cracks. In practice about 70 per cent of this velocity is frequently obtained. This is, certainly, higher than the sound velocities in the plastic region. The implications of this fact was studied in refs. 8 and 9.

5-2

A. Kobayashi:

(1) Did you observe preceding strain disturbances ahead of the running crack?

(2) Was your experiment done at room temperature?

W. Goldsmith:

(1) It is assumed that the question refers to waves released at the crack tip as the result of energy conversion at that point. Although it is well-known that such waves are generated there (cf. the work by J. Miklowitz, JAM, 20, 122 (1952); J. W. Phillips, Int. J. Sol. Struc., 6, 1403 (1971); References 3-7 of the paper; various photoelastic studies by A. S. Kobayashi and associates (1970-1976), etc.) and such waves were undoubtedly present in the current experiments, it had not been intended to examine this particular aspect of the phenomenon. In consequence, the optical and strain gage equipment employed was not appropriately arranged and, further, its sensitivity may not have been sufficient to permit detection of these transients.

(2) Yes.

D. A. Shockey:

(1) Theoreticians have analyzed the situation of a high rate load striking a stationary crack and find that, at early times, the crack tip intensity rises parabolically with time, overshoots the equilibrium static stress intensity, and attains the static value after a few damped oscillations. Were you able to observe in your experiments corresponding behavior of the caustic?

(2) You report a single value for the dynamic crack tip stress intensity, implying crack speed independence. Other workers report a pronounced increase in crack tip stress intensity with crack speed in polymers. Could you comment on this apparent discrepancy?

W. Goldsmith:

(1) The variations in the crack intensity factor upon initiation of crack propagation as well as those recently found to occur upon crack arrest (Ref. 13 of the paper) involved loading conditions substantially different from those of the present investigation. In the case of crack initiation, loading consisted of an idealized ramp or step function, whereas the study involving crack arrest utilized the force produced by driving a wedge into the preexisting crack of a double cantilever beam specimen. In the present tests, the loading produced by the longitudinally striking sphere could be approximated by a sine-squared function, traversing the length of the specimen alternatingly as a compression and tension wave. Thus, no quasi-dynamic equilibrium state was ever attained during the process, particularly not during crack propagation. In consequence, the results of the present tests can not be compared with those cited, particularly with respect to the behavior of the dynamic stress intensity factor relative to the static value. In any event, no oscillations in the size of the caustic were observed when identical or nearly identical strain levels existed at the crack cross section; in view of the timing of the film exposures, such a situation would occur only by accident.

(2) There is no discrepancy, apparent or otherwise, in the values reported for the stress intensity factor. It should be borne in mind that all the data were obtained under conditions of unstable (or catastrophic) crack propagation. For PMMA, the crack speeds were found to differ by a factor of approximately 2 depending upon whether or not complete failure of the specimen occurred in a single tensile wave passage or as the result of two or three such

passages. Slight differences were found in the values of the critical stress intensity factor for these two cases, although well within experimental error. In fact, for all runs involving both PMMA and Lexan, variations in both the intensity factor and the critical stress resulting in fracture initiation were considered to be within the measurement limitations of the experiment. This result is due to the fact that all data were obtained for initial strain rates varying by less than one decade, a small band compared to the rates ranging from 10^{-6} to more than 10^{3} utilized by other investigators. Thus, the rates employed in these other tests encompass the domains from extremely slow, stable propagation to catastrophic failure, where surely some rate dependence can be expected; in the present investigation, only unstable crack propagation was examined.

5-3

U. S. Lindholm: How did you determine the strain rate you employed?

A. Kobayashi: The strain rate I employed is based on the crosshead speed divided by the specimen gage length, V/L. Especially for higher strain rate of 48/sec, a strain gage was placed and the strain rate was also measured, obtaining almost the same strain rate value as obtained from V/L.

6-1

W. Goldsmith: Would you expect your estimate of crater volume to apply also to a rock target or other granular material where the substance would fracture, pulverize, comminute and/or produce grain fracture or fracturing of intergranular bonds?

D. C. Drucker: The cratering of a brittle or granular target was, in fact, the original impetus for the study reported here. A few truncated computer solutions and a few experimental results had just become available for small particles impacting a graphite composite target. As a first step toward answering some of the questions raised, the approximate response of a ductile target was found. The statement was made in the unpublished report from which this paper is abstracted that the zone of high plastic strain extending out from the crater in a ductile target would be a shattered or powdered zone in a friable material. The very crude estimate was that the crater radius therefore would be about twice the radius for a ductile target when the shear strength of the friable material and the flow strength of the ductile material are equal under the extremely high hydrostatic pressures and strain rates of the problem. Consequently the crater volume would be 8 times larger for a friable target material with the same σ_t as a ductile target.

6-2

T. C. T. Ting: The three fractures in the sphere which you called F1, F2, and F3 occurred at the location of the caustics. Theoretically, after the occurrence of the first fracture at the caustic F1, the subsequent wave motion is altered because of the presence of the fracture at F1. In particular, the location and the shape of the caustic at F2 will be affected. In your analysis, you

seem to ignore this effect; and yet you obtain a very good agreement with the experimental observation. Do you have any physical explanations for the good agreement?

W. Johnson: We agree Prof. Ting's comments and observations. We believe that the effect on F2 (or F3) of fracture at F1 is too small to significantly affect its position. There are many assumptions in our explanations and only further investigations by us and other will reveal the degree to which they are acceptable.

S. Tanimura: It is very interesting that some patterns of fracture and void development in hemi-spherical ended bodies are shown. Isn't it better to explain the patterns to take account of all the dilatational and the distortional waves reflected at free surface by the each wave?

W. Johnson: We considered the patterns made by both the P and S-waves but on this occasions could find no void to correlate with the focus to the P-wave. In previous work (on spheres, see the references) we have noted 3 independent void zones.

6-4

K. Asada: Perforated plates (porous metals) is used at heat exchangers and steam generaters. So static macro equivalent σ-ε relations was made for design of perforated plates. But there was no dynamic macro equivalent σ-ε relations. (These relations are important for explosive loadings) Are you planning to make the dynamic equivalent σ-ε relations by changing the ligament efficiency?

E. H. Lee: The application you suggest to perforated plates of heat exchangers is an interesting one. The problem would presumably be modeled as plane stress, or perhaps some average between plane stress and plane strain depending on the thickness of the plate relative to the tubes size. The problem you suggested could certainly be carried out, but we have not attempted it.

R. J. Clifton: Since finite element techniques are used in the computations you can presumably obtain corresponding results for holes with initially elliptical shape. Have you examined such cases to determine the effect of the aspect ratio of the holes on the macroscopic strain rate effect that would be observed?

E. H. Lee: It would be feasible to consider initially elliptical pores, but we have not carried out such calculations. We have not pursued the matter in greater detail since for most cases the calculation cannot be more than qualitative since pores would probably be much closer to spheres than cylinders, and the problem of treating spherical holes on a cubical network poses a much more difficult finite-element problem.

6-5

E. H. Lee: You mention the use of several stress measures in analysing elastic plastic problems and the selection of a particular stress measure, such as the Euler stress, for particular types of problems. On what basis do you selection a particular stress measure for a particular type of problem?

Y. Yamada: The choice of stress measure is closely related to the use of stress rate in the constitutive equations in the updated formulation adopted here. The author bases his choice on the rotation of the principal stress axes

direction rather than that of the material element. There are a number of problems, e.g. steady flow of metals in material processing and diffuse neck in stability in tensile specimen, which validate the use of the Jaumann rate of Kirchhoff or Euler stress associated with the spin of material element. However, for the problem where the spin of the element does not necessarily accompany the rotation of the principal stress axes, it is considered the intrinsic rate of Kirchhoff or Euler stress would be more appropriate. The torsion of thin walled tube is such an example and more details on this problem are discussed in the following paper:

Y. Yamada, T. Hirakawa, and A. S. Wifi, Analysis of Large Deformation and Bifurcation in Plasticity Problems by the Finite Element Method, A paper to appear in Finite Elements in Nonlinear Solid and Structural Mechanics, Tapir Publishers, Trondheim, Norway, 1978.

7-2

U. S. Lindholm: Subsequent to the work you referenced, we have performed high strain rate ($<10s^{-1}$) biaxial tests on Al, Ti, Be and steel. The results of these tests also confirm that the expansion of the yield surface is isotropic with increasing strain rate under proportional stress loading, and that the yield criteria is of the Mises type.

T. Hayashi: The authors are interested in two problems. One is the yield surface under dynamic combined stresses to which we had the same results as you had shown in your papers. The other is the flow rule, namely the relations between the increments of each strain components and stress state in the plastic region under dynamic forces. Our experiments showed that Prandtl-Reuss flow rule holds even in the dynamic loading.

R. J. Clifton: I would like to join Drs. Malvern and Lindholm in complimenting you on this significant extension of dynamic testing methods to cases of combined tension and torsion. As a comment I would like to underscore the importance of investigating cases of non-proportional loading in order to interpret experimental results for combined longitudinal and torsional plastic waves. Our experimental results for longitudinal impact of pre-torqued tubes indicate that the slow plastic wave arrives much earlier than predicted by an isotropic hardening model of the type you are inferring from proportional loading experiments. Better agreement in the arrival time of the slow plastic wave is obtained with a theory based on a self-consistent slip model of the plastic deformation. The important new feature of the latter model is the relatively smaller change in stiffness that occurs when the loading path is changed from a direction essentially tangent to an isotropic yield surface to a direction perpendicular to such a yield surface. This smaller change in stiffness corresponds to a smaller change in wave speed with the result that the slow plastic wave follows immediately behind the fast plastic wave, in better agreement with experiments.

T. Hayashi: We would like to perform the experiments on the flow rule under non-proportional loading. But in order to observe the difference clearly between the behavior under proportional loading and non-proportional loading, it is desirable that the change of the loading path is as clear and sharp as possible. It is very difficult technically and we have not succeeded yet to make such a suitable device for our use.

7-3

R. J. Clifton: Why are you modelling the plastic wave as a discontinuous wave when experiments indicate that plastic waves are generally continuous?

T. Jimma: Because, the analysis of a discontinuous plastic wave is a good example of dislocation theory. In our paper, the material is assumed to be a linearly work-hardening solid so that the plastic wave becomes the discontinuous wave. We can analyze a continuous plastic wave in a similar way by assuming that the moving dislocations are distributed continuously behind the plastic wave front.

7-6

W. Goldsmith: The experimental set-up shown in the slide indicates the impact of a flat-ended striker on a flat-ended bar. This is impossible to achieve; there is an angular impact with contact indentation that strongly influence the wave parameters, and hence the parameters to be identified experimentally. How is this problem resolved?

N. Nakagawa: In the experimental set-up, the incident pressure bar contacts initially with the specimen at x=1. On the other hand, the end of the striker is rounded with a radius of about 100 mm, because of the difficulty to achieve the impact of a flat-ended striker on a flat-ended bar. We consider that the incident waves propagate in one dimension, through the incident bar, since the length of the incident pressure bar is sufficiently long in comparison with its diameter. Hence, it would be possible to use the results of our analysis in order to identify the dynamic properties of viscoelastic bars.

7-7

K. Asada: You arranged your experimental results of the crater depth by the velocity of the projectiles. But if the weights of the projectiles change, then we must arrange it by the energy of the projectiles. Though I have never found such energy arranged experimental results, have you ever arranged it by the energy?

W. Johnson: All tests were conducted by impacting against semi-infinite targets. However the plot of crater volume is against the logarithm of the velocity; the volume then turns out to be proportional to the square of the velocity in most cases so that with a constant mass projectile, volume is proportional to energy. (Workers have frequently found volume to correlate better with momentum than energy in high speed impact work, so that the choice of a linear abscissae is understandable.)

8-1

W. Goldsmith: If the solution was to demonstrate the effect of strain-rate sensitivity, why was aluminum used for the specimen which has one of the lowest rate-sensi tivities known, rather than steel, which has much higher sensitivity?

S. Kawashima: The agreement between the experimental result and the calculated one presented in a paper by Duwez, Clark, and Bohnenblust is not good in the case of the copper beam. This paper deals with the same problem and the effects of rotary inertia, shear force and strain-rate on the transient response are discussed from the theoretical and experimental results for pure aluminum.

8-2

K. Miura: In case of the circular cylindrical shell, the experimentally observed post-buckling deformation can be certainly approximated by the isometric transferred surface. It seems that the author's approach depends on this fact.

This is not necessarily the case, however, with the oval cylindrical shell. That is, the observed deformation can not be approximated by a complete surface built up with the tessellation of diamond patterns. Instead, it is the complex surface composed of diamond patterns of different sizes and irregularly deformed zones, which necessarily accompany the considerable amount of extensional deformation.

I would like to ask the author about the matter.

M. S. El Naschie: I do agree completely with Prof. Miura that it is not possible to construct an overall isometric surface to that of an oval cylindrical shell. Incidentally, this does not violate the theory of isometric buckling. On the contrary, it confirms it. As I mentioned previously in my talk, the non-existence of an overall isometric surface is an indication of a stable post buckling path. On the other hand, Kempner showed some time ago that on the whole, the oval cylindrical shell possesses a stable post buckling path for an assumed overall buckling form. However, it should be remembered that my paper mainly deals with a special form of isometric transformation, namely a localised one. This is based on the assumption that buckling is first triggered locally in a very small shallow region and then spreads dynamically, with high speed, over a large portion of the shell surface. The corresponding buckling formula is considered to be an absolute lower stability limit estimation. In the

absence of measurements for an oval cylindrical shell, the usefulness of this formula could not be directly verified.

8-3

D. A. Shockey: Are the amplitudes of the vibrations caused by the burning propellant sufficient to cause fracture of the propellant or debonding of the propellant from the motor casing? What is the propellant composition?

D. Mori: In the case of small soudnig rockets, we have experienced some relatively great amplitudes of vibration of solid propellant motor which caused some problems with installed equipment or fracture of structural elements, however, we think we have never experienced a fracture of the solid propellant or debonding.

Our study is not concerned with the investigation of the fracture of the propellant but aimed to understand the effect of solid propellant on the overall dynamic characteristics of rockets.

The composition of the solid propellant we used in the experiment is CTPB (binder), NH_4ClO_4 and Aluminum powder.

9-1

W. Johnson:

(1) Can you say what is the standoff distance and how is the best distance decided upon.

(2) What is the pressure developed against the flyer plate?

K. Kiyota:

(1) The best stand-off distance, which is the distance between the top of the conical explosive and the flyer plate, was 5 millimeters for 0.5 millimeter thickness of the flyer copper plate in this experiment. As the distance becomes large, the unwelded area spreads at the central part, because the shock front becomes roundish. When it is too small, the central part of the flyer plate is torn by partially too high pressure.

(2) The pressure developed against the flyer plate was not measured directly. Usually the shock pressure propagating in fluid can be obtained from the velocity of shock front. It was about 5 kilobars, obtained from the high speed photographs of the shock front, though its accuracy was not good on account of small pictures on the film. However it is not the pressure developed against the flyer plate. In order to obtain the pressure, the structure of flow in the shock wave and its relative motion to the flyer plate should be observed. The accurate observations of them are difficult in this case.

9-2

W. Goldsmith:

(1) Experiment, closed form solution and finite element analysis for axisymmetric head impact problem correlated well and was not disturbed by the incompressibility of the fluid, for radial impact on a uniform elastic shell.

(2) Loading approximation on shell is much better-given by a sine-squared load function $F = F_0 \sin^2 \frac{\pi t}{\tau}$ than by a sinusoidal loading.

(3) Head injury model only good for 2-3 passages of the wave ($\sim$400μs) because flow the constraining effects of the neck must be considered.

(4) There is a tremendous difference on the stress distribution in certain critical regions when a point load as opposed to an areal load is used. The latter must be used here.

S. Kobayashi:

(1) As far as the intracranial pressure response caused by axisymmetric impact is concerned, we know the results stated in your comment. However, we have an opinion that in the case where a shear strain is predominant in causing brain injury the brain should be treated as a nearly imcompressible material and the usual displacement method in the finite element method yields erroneous results.

(2) We know that a real loading pattern is rather a sine-squared function because the load-displacement relation of the ball is nonlinear. However, in the present numerical example we have not focused our attention on the effect of the loading pattern. We have considered that we should treat the ball as an element without giving a loading function, and as the first and simplest example we have used a linear spring, although the calculation can be easily carried out in the case of a nonlinear spring.

(3) As the head model and load are axisymmetric in the present framework of the computer program of the finite element method, we cannot treat the effect of neck. The final purpose of our study is to treat the real head including neck subjected to arbitrary impact load by using a generalized three dimensional finite element. The present paper is only a fundamental study.

(4) The comment is a matter of course. The main purpose of the present study is to clarify the response property of the intracranial pressure and shear strains in the brain. Although the stresses in the skull have also been calculated and displayed in our paper, they are nothing but the representation for your information. If we focus our calculation on the skull stresses, we have to divide it into more fine elements in the critical region and employ an areal load as your comment.

W. Johnson:

(1) I would like to support Prof. Goldsmith in saying that for a real head impact problem, the effect of tensing the neck muscles soon becomes important.

(2) Have you tried to correlate your results with the notion of the GADD seventy index as used to assess liability to serious head injury in motor car accidents?

(3) A very important loading system is that of tangential loading ; this is similar is the "hook" in boxing and is the cause of death in this sport. (see UNTERSCHARNSCHEIDT's papers). Can the model be usefully used to deal with this real head impact problem? (The skull would rotate and "leave behind" the brain - due to inertia - so that bridging veins are stretched and ruptured.)

S. Kobayashi:

(1) The answer has been dealt with in the reply to Dr. Goldsmith's third comment.

(2) We are sorry we have not tried so, because unfortunately we have no information of such a literature.

(3) The present computer program cannot deal with the tangential loading as it is suitable only for axisymmetric load. We know that the tangential load is a very important factor in head injury problem. This mechanism was first suggested by Holbourn, and analytical model was proposed by, e.g., Hayashi*. However, it is a future problem for us as stated in the reply to Dr. Goldsmith's third comment.

* T. Hayashi: Brain Shear Theory of Head Injury due to Rotational Impact. Jour. Fac. Engng., Univ. of Tokyo, Vol. 30, No. 4 (1970), p. 307.

9-3

S. Tanimura: Is it not necessary for a comparison between the high velocity impact test results and the theoretical results to deal with the boundary of impact face as the impact of a deformable elastic body and an elastic-visco-plastic body?

H. Fukuoka: In case the specimen and the target have same diameters and same elastic properties, the particle velocity of the impact face of the specimen after impact is half of the impact velocity. But if the target material has much higher yield stress than the specimen, we can model this case as an impact of elastic-viscoplastic specimen on the elastic target. Then, a typical numerical example shows that the particle velocity of the impact face of the specimen after impact is less than the impact velocity by only a few percent. Therefore, if we take the consideration that the target wall has much larger area than that of the specimen into account, we can equate the particle velocity of the impact face of the spcimen to the impact velocity and thus the assumption of the rigid target wall is justified.

9-4

U. S. Lindholm: Have you investigated other types of lubricants than MoS_2 or non-lubricated surfaces?

J. Klepaczko: Yes, we performed experiments on lead specimens lubricated with a silicon oil; see results on the attached figure. Besides, we used other limited data by some authors /i.e. p_Z/S_C/plots/ to calculate dynamic coefficient of friction with our computer program. Generally, obtained from dynamic compression tests shows the same order as from quasi-static tests.

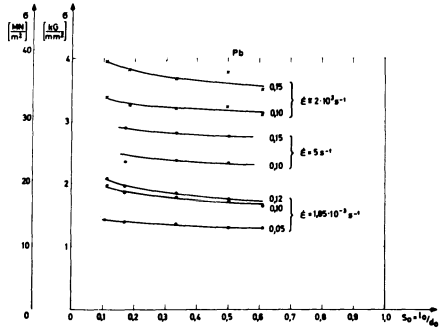

IUTAM Symposia

International Union of Theoretical and Applied Mechanics

Applied Mechanics
Proceedings of the Eleventh International Congress of Applied Mechanics, Munich (Germany) 1964. Editor: H. Görtler. In cooperation with P. Sorger.
1966. 740 figures. XXVIII, 1189 pages (161 pages in French, 132 pages in German, 8 pages in Italian)
ISBN 3-540-03462-5

Applied Mechanics
Proceedings of the Twelfth International Congress of Applied Mechanics. Stanford University, August 26-31, 1968. Editors: M. Hetényi, W.G. Vincenti
1969. 318 figures. XXIV, 420 pages
ISBN 3-540-04420-5

Creep in Structures
Colloquium held at Standford University, Calif. July 11-15, 1960. Editor: N.J. Hoff
1962. 156 figures. VIII, 375 pages
ISBN 3-540-02796-3

Creep in Structures, 1970
Symposium Gothenburg (Sweden), August 17-21, 1970. Editor: J. Hult
1972. 171 figures. XI, 429 pages
ISBN 3-540-05601-7

Dynamics of Satellites / Dynamique des Satellites
Symposium Paris, Mai 28-30, 1962. Editor: M. Roy
1963. 94 figures. XII, 335 pages (41 pages in French)
ISBN 3-540-02958-3

Dynamics of Satellites (1969)
Proceedings of a Symposium held in Prague. May 20-24, 1969 (COSPAR-IAU-IAG/IUGG-IUTAM) Editor: B. Morando
1970. 89 figures. VII, 312 pages (27 pages in French)
ISBN 3-540-04792-1

Flow-Induced Structural Vibrations
IUTAM / IAHR Symposium Karlsruhe, Germany, August 14-16, 1972. Editor: E. Naudascher
1974. 360 figures. XX, 774 pages
ISBN 3-540-06317-X

Grenzschichtforschung. Boundary Layer Research
Symposium Freiburg/Br. 26.-29. August 1957. Editor: H. Görtle
1958. 206 figures. XII, 411 pages (175 pages in German, 8 pages in French)
ISBN 3-540-02273-2

Instability of Continuous Systems
Symposium Herrenalb (Germany) September 8-12, 1969. Editor: H. Leipholz
1971. 147 figures. XII, 422 pages (23 pages in German, 7 pages in French)
ISBN 3-540-05163-5

Irreversible Aspects of Continuum Mechanics. – Transfer of Physical Characteristics in Moving Fluids
Symposia, Vienna, June 22-28, 1966. Editors: H. Parkus, L. I. Sedov
1968. 87 figures. XII, 424 pages (16 pages in German)
ISBN 3-211-80869-8

Mechanics of Generalized Continua
Symposium on The Generalized Cosserat Continuum and the Continuum Theory of Dislocations with Applications. Freudenstadt and Stuttgart (Germany) 1967. Editor: E. Kröner
1968. 64 figures. XII, 358 pages
ISBN 3-540-04264-4

Mechanics of Visco-Elastic Media and Bodies
Symposium Gothenburg/Sweden, September 2–6, 1974. Editor: J. Hult
1975. 60 figures. XII, 391 pages (28 pages in French)
ISBN 3-540-07228-4

Optimization in Structural Design
Symposium Warsaw, Poland, August 21-24, 1973. Editors: A. Sawczuk, Z. Mróz
1975. 216 figures, 27 tables.
XV, 585 pages
ISBN 3-540-07044-3

Rheology and Soil Mechanics. Rhéologie et Mécanique des sols.
Symposium Grenoble, April 1–8, 1964. Editors: J. Kravtchenko, P.M. Sirieys
1966. 325 figures. XVI, 502 pages (with contributions in English and French)
ISBN 3-540-03652-0

Satellite Dynamics
COSPAR - IAU - IUTAM, Symposium Sao Paulo, June 19-21, 1974. Editor: G.E.O. Giacaglia. Executive Editor: A.C. Stickland
1975. 86 figures. VIII, 376 pages
ISBN 3-540-07087-7

Stress Waves in Anelastic Solids
Symposium held at Brown University, Providence, R.I., April 3–5, 1963. Editors: H. Kolsky, W. Prager
1964. 145 figures. XII, 342 pages (29 pages in French)
ISBN 3-540-03221-5

Symposium Transsonicum
Aachen, September 3-7, 1962. Editor: K. Oswatitsch
1964. 238 figures. XX, 490 pages (85 pages in German and 29 pages in French)
ISBN 3-540-03223-1

Symposium Transsonicum II
Göttingen/Germany, September 8-13, 1975. Editors: K. Oswatitsch, D. Rues
1976. 324 figures. XVI, 574 pages
ISBN 3-540-07526-7

Theory of Thin Shells
2nd Symposium Copenhagen, September 5-9, 1967. Editor: F. I. Niordson
1969. 86 figures. VIII, 388 pages
ISBN 3-540-04735-2

Thermoinelasticity
Symposium East Kilbride, June 25-28, 1968. Editor: B.A. Boley
1970. 133 figures. XII, 344 pages (36 pages in French)
ISBN 3-211-80961-9

Trajectories of Artificial Celestial Bodies as Determined from Observations. Trajectoires des corps célestes artificiels déterminées d'après les observations
(COSPAR - IAU - IUTAM). Proceedings of a Symposium held in Paris, April 20-23, 1965. Editor: J. Kovalevsky
1966. 55 figures. XVI, 265 pages (15 pages in French)
ISBN 3-540-03681-4

Verformung und Fließen des Festkörers. Deformation and Flow of Solids
Kolloquium Madrid 26. - 30. September 1955. Herausgeber: R. Grammel
1956. 188 Abbildungen.
XII, 324 Seiten (19 Beiträge in Englisch, 8 in Deutsch, 4 in Französisch und 2 in Spanisch)
ISBN 3-540-02095-0

Springer-Verlag
Berlin
Heidelberg
New York